THE EVOLUTION OF THE MAGMATIC PLUMBING SYSTEM ASSOCIATED WITH THE FRANKLIN LARGE IGNEOUS PROVINCE (VICTORIA ISLAND, ARCTIC CANADA)

Ben Hayes

Submitted in partial fulfilment of the requirements for the degree of PhD.

September 2014

Declaration

This work has not previously been accepted in substance for any degree and is not concurrently submitted in candidature for any degree

Signed …… (candidate)

Date ……

Statement 1

This thesis is being submitted in partial fulfilment of the requirements for the degree of PhD.

Signed …… (candidate)

Date ……

Statement 2

This thesis is the result of my own independent work/investigation, except where otherwise stated.

Other sources are acknowledged by explicit references

Signed …… (candidate)

Date ……

Statement 3

I hereby give consent for my thesis, if accepted, to be available for photocopying and for inter-library loan, and for the title and summary to be made available to outside organisations.

Signed …… (candidate)

Date ……

Statement 4

I hereby give consent of my thesis, if accepted, to be available for photocopying and for inter-library loans after expiry of a bar on access previously approved by the Graduate Development Committee.

Signed …… (candidate)

Date ……

Abstract

This thesis is an investigation of the magmatic processes that operated in the plumbing system of the Franklin Large Igneous Province (LIP). The Franklin LIP (~723-716 Ma) extends >2500 km across northern Canada and is superbly exposed in the Minto Inlier of Victoria Island. The exposed plumbing system is dominated by sills, with subordinate fault-guided feeder dykes. Locally, sills are characterised by olivine-enriched bases, with overlying doleritic gabbros. One example is the Lower Pyramid Sill. This sill was investigated in detail using petrography, whole-rock chemistry and *in-situ* mineral chemistry. Petrological and geochemical observations, combined with inverse melt modelling show that the olivine-enriched layer formed by olivine slurry replenishment into a resident gabbroic mush. In contrast, the overlying gabbros formed by *in-situ* differentiation. Intervening clinopyroxene-rich cumulates formed by a metasomatic reaction between different pore melts. The study emphasises that both slurry emplacement and *in-situ* differentiation played a role in the formation of cumulate layering in this sill.

Sections examined through the same sill along strike, collectively termed the Fort Collinson Sill Complex, reveal that the olivine slurry propagated >50 km downstream. Radiogenic and stable isotope data support this interpretation. The geochemical consequences of cumulate remobilisation and mixing in the sill complex are demonstrated, as well as quantified, using Fe=Mg modelling. Additionally, the effects of dolostone assimilation are considered, which can potentially affect phase equilibria.

This thesis also investigates the Ni-Cu-PGE potential of the Franklin LIP by studying the Southern Feeder Dyke Complex. This dyke complex was fault-guided and brecciated dykes contain microdoleritic microxenoliths that are impregnated by sulphides. Immiscible sulphide liquids formed when the magma became sulphur saturated due to the ingestion of local sulphur-rich wallrock. This study demonstrates the importance of external sulphur addition to magma in triggering sulphide mineralisation and highlights the economic potential of the Franklin LIP.

Acknowledgements

Firstly, I'd like to thank my supervisors, Jean Bédard and Johan Lissenberg. They've both pushed me hard all the way through. Jean has been an inspiration throughout and his knowledge of igneous petrology is terrifying. There are no 'silly questions' with Jean. He's really been awesome all the way through. Johan was there for discussions, hours on end. They were really enjoyable and without his commitment to the project, things would have been much more difficult.

I shared two summers in the land of the midnight sun with a wonderful group of people. We were all lucky to be apart of such a fantastic project, and we made the most of it. I'll remember those nights in the 'lounge'. Cheers to Durbano and Chuck – we had a good laugh.

There are plenty of people in Cardiff I could name who have shared in some good times. In particular, I'd like to say 'cheers lads' to Rob and Sam, also Scott. It was a brilliant three years or so building the best 'Tuesday 5-a-side team in Cardiff'. To Ella, without your help and support over the last four years, I would never have finished.

Finally, I wouldn't be here without the unconditional love and support of my family. Mum (Jacqueline), Dad (John) and big brothers, Richard and Adam. The five of us have always stuck together and have helped pull each other through. They've taught me that hard work and commitment is rewarded, eventually. Looking up to Adam and seeing him work hard and achieve so much has been my inspiration throughout.

Contents

1. Introduction

1.1 Project rationale & aims

The principal subject of this thesis is an investigation of the magmatic processes that operated in the magma plumbing system of the Franklin Large Igneous Province (LIP). The study has three aims. The first is to understand the broader scale processes of how LIPs differentiate. The Franklin LIP as exposed on Victoria Island (Arctic Canada), comprises a sill-dominated magmatic plumbing system overlain by flood basalts. Sills act as an intermediary stage for magma traversing the crust, from mantle source to the Earth's surface, and are the location of igneous differentiation. Hence, by studying the Franklin sills, I aim to understand the processes of emplacement, melt transport and crystallisation during the evolution of a LIP plumbing system.

The second aim is to investigate smaller scale differentiation mechanisms that operate in sills. The importance of sills is emphasised by their presence in many igneous terranes; they are common in Proterozoic and Phanerozoic continental flood basalt provinces (Baragar, 1976, Francis & Walker, 1986, Hawkesworth *et al.*, 1995, Chevallier & Woodford, 1999, Bédard *et al.*, 2007); ophiolites and oceanic crust (Bédard, 1991a, Lissenberg *et al.*, 2004, Canales *et al.*, 2009); oceanic plateau complexes (Kerr *et al.*, 1998); and Archean tholeiitic lava plains (Bédard *et al.*, 2009). Therefore, the importance of studying sills cannot be understated, and the Franklin sills on Victoria Island represent an excellent target to study magmatic processes operating in sills. Extensive work has been undertaken and our understanding of magmatic processes has advanced considerably over the past ~80 years, however, many unresolved issues remain, particularly with regard to how cumulate layering forms. The Franklin sills offer the opportunity to investigate the differentiation mechanisms that operated in a basaltic magma chamber. Such investigations have typically focused on large layered intrusions such as the Skaergaard Intrusion and Bushveld Complex. However, the slow cooling times of large layered intrusions allows extensive post-cumulus diffusive exchange, which overprints the primary magmatic signature. The Franklin sills are thin and cooled relatively rapidly in comparison to large layered intrusions. Faster cooling rates of magma allows the preservation of the primary magmatic signature, which provides insights into the differentiation mechanisms that

operated in the sills. Additionally, some of the Franklin sills are characterised by well developed cumulate layering, similar to that observed in large layered intrusions.

The final aim relates to the economic geology of the Franklin LIP. The Franklin LIP is considered to be prospective for Ni, Cu and PGE mineralisation (Jefferson *et al.*, 1985, Jefferson *et al.*, 1994, Jowitt & Ernst, 2013). The Franklin sills have been compared to the Noril'sk-Talnakh intrusions in Siberia (Jefferson *et al.*, 1994). There are known native copper occurrences in the Natkusiak flood basalts, the extrusive part of the Franklin LIP (Jefferson *et al.*, 1985). This thesis aims to constrain and further understand the Ni-Cu-PGE economic potential of the Franklin LIP on Victoria Island.

1.2 Fieldwork

Fieldwork for this project took place during the summer months of 2010 and 2011 on Victoria Island. The summer months and short lengths (~7 weeks each) of the field season were necessary because of the high latitude (~72°N). The Geological Survey of Canada organised and sponsored the project fieldwork, which was one component of a mapping initiative called GEM (Geomapping for Energy & Minerals Project). The principal aim of GEM is to open the Canadian Arctic to geological mapping and research in order to improve understanding of its economic potential. The field base camp was located in different locations for each field season. In 2010, the field base camp was located ~15 km NE of the easternmost end of Minto Inlet, and the 2011 base camp was located ~10 km NW of Ulukhaktok (both are labelled on Fig. 2.2). Helicopter support provided transport throughout both field seasons.

Dr Robert Rainbird and Dr Jean Bédard, both of the Geological Survey of Canada, were co-leaders of the mapping expedition to Victoria Island. The expedition consisted of ~15 students, all of whom were undertaking either an undergraduate, masters or Ph.D. project on the rocks. Other senior researchers also contributed during fieldwork. I was involved in both field seasons, as both a mapping geologist and a researcher for this thesis. The majority of the 2010 field season involved mapping in order to understand the geology, particularly the architecture and composition of the Franklin igneous rocks. The Lower Pyramid Sill (chapter 4) was sampled during the 2010 field season, as were the majority of

the rocks comprising the Fort Collinson Sill Complex (chapter 5). The Uhuk Massif was identified during the 2010 field season and I was involved in the detailed mapping of this important locality. The field relationships of the Uhuk Massif were the focus of an article published in Geological Society of America Bulletin in May 2012, which I co-authored (appendix A). More specific mapping and sampling was targeted during the 2011 field season, following mapping in 2010. I mapped and sampled the Southern Feeder Dyke Complex (chapter 6) during the 2011 field season. Both the Uhuk Massif and Southern Feeder Dyke Complex localities were included in a contact metamorphism article published in Journal of Metamorphic Geology in November 2012, on which I am a co-author (appendix B).

1.3 Thesis outline

Chapter 2 provides a summary of the geological setting of the Franklin LIP, specifically its manifestation in the Minto Inlier of Victoria Island. Chapter 3 provides a summary of the methods used by the author and co-authors. The aim of chapter 4 was to investigate the differentiation of a layered mafic sill called the 'Lower Pyramid Sill'. I carried out a detailed petrological, textural and *in-situ* mineral chemical investigation of the Lower Pyramid Sill. This study has important implications for how igneous layering forms. Chapter 5 expands on the Lower Pyramid Sill by examining sections through the same sill at other localities > 50 km along strike. Collectively this sill is called the 'Fort Collinson Sill Complex', because of its occurrence just above the prominent Fort Collinson Formation. Chapter 5 provides insights into how the magmatic plumbing system of the Franklin LIP differentiated. Chapter 5 also has implications for how other LIPs differentiate on a regional scale, as well as having implications for the origin of lateral compositional variability that is observed in igneous intrusions. Chapter 6 is an investigation of a fault-guided feeder dyke system known as the 'Southern Feeder Dyke Complex'. Chapter 6 is a field-based study, which includes small-scale geological maps that are central to the chapter. Chapter 6 has important implications for how Ni-Cu-PGE sulphide deposits form, specifically the role crustal sulphur assimilation in the generation of immiscible sulphide liquids. Chapter 6 also considers the regional economic potential of the Franklin LIP. Chapter 7 provides a short conclusion of the overall study.

1.4 Author contributions

1.4.1 Chapter 4

Chapter 4 has been accepted for publication in *Journal of Petrology*.

Ben Hayes: I sampled the Lower Pyramid Sill during the 2010 field season. I carried out all of the rock preparation (for whole-rock chemistry and thin sectioning), analytical and data collection work on the Lower Pyramid Sill samples. I conducted all of the geochemical modelling within the chapter. I wrote the chapter with guidance from both supervisors, which helped improve the flow, organisation and scientific impact of the study presented. All interpretations are my own and have not changed during editing from my supervisors.

Jean Bédard: Jean provided guidance during the 2010 field season and through many discussions, provided direction in terms of the modelling carried out in chapter 4. He edited earlier versions of the manuscript to help clarify the arguments that are presented.

Johan Lissenberg: Johan, as my supervisor based at Cardiff University, was available for discussions throughout the course of analytical work, data interpretation and modelling. Johan edited earlier versions of the manuscript and helped clarify data presentation and the scientific impact of the interpretations.

1.4.2 Chapter 5

Chapter 5 is currently under review for publication in *Contributions to Mineralogy & Petrology*.

Ben Hayes: Chapter 5 builds on chapter 4, and therefore includes a large part of the data and interpretations presented in chapter 4, which are all my own work. Jean Bédard and myself, as well as Dick Naslund and Kathryn Steigerwaldt of Binghamton University sampled the sills of the Fort Collinson Sill Complex, during the 2010 field season. I carried

out all of the modelling and interpretations (except the radiogenic and stable isotopes) that are presented in chapter 5. I wrote the chapter with guidance from the co-authors.

Johan Lissenberg: Johan provided guidance during the geochemical modelling that is included in the chapter. Johan edited earlier versions of the chapter that helped improve the clarity of the study.

Jean Bédard: Jean helped sample the sills of the Fort Collinson Sill Complex studied in chapter 5. Jean provided direction and guidance during the Fe=Mg and trace element inversion modelling. Jean edited earlier versions of the chapter, which improved the flow and organisation of the chapter.

Charlie Beard: Charlie was part of the Victoria Island mapping team in 2011, specifically to carry out a radiogenic isotope investigation of the Franklin sills and Natkusiak flood basalts, principally to understand melt source evolution in the Franklin LIP. Charlie worked on samples from the Fort Collinson Sill Complex, and provided radiogenic isotope methods (chapter 3; section 3.4.1), data and modelling to the chapter. Charlie edited earlier versions of the chapter, helping to improve the clarity of the study.

1.4.3 Chapter 6

Chapter 6 has been submitted to *Economic Geology* for publication.

Ben Hayes: I spent a week mapping and sampling the Southern Feeder Dyke Complex in detail during the 2011 field season. I prepared the samples for whole-rock (including PGE) chemistry and thin sectioning. I undertook all of the petrographic work, data collection and the interpretations of the data. I wrote the chapter, with guidance from the co-authors.

Jean Bédard: Jean assisted in the field in 2011 by helping to plan the strategy for mapping and sampling the Southern Feeder Dyke Complex. Jean provided guidance during the writing of the chapter, which helped improve the flow and organisation of the study.

Matt Hryciuk: Matt assisted me with sampling during fieldwork on the Southern Feeder Dyke Complex. Matt undertook a sulphur isotope based thesis on rocks from the Minto Inlier at McGill University in Montréal. Matt provided details of the sulphur isotope methods (chapter 3; section 3.4.2). Matt provided sulphur isotope interpretations and he edited earlier versions of the chapter, which helped improve the clarity of the material presented, particularly the economic implications of the study.

William MacDonald: Bill spent 3 days sampling at the Southern Feeder Dyke Complex in 2011. Bill processed the samples for magnetic fabrics in his laboratory at Binghamton University, New York state. Bill provided details of the method he used (chapter 3; section 3.4.3) and interpreted the magnetic fabric data that is included in the chapter.

Johan Lissenberg: Johan edited earlier versions of the chapter, which greatly improved the flow, organisation and scientific impact of the study.

2. Franklin Large Igneous Province

2.1 Extent and age

The Franklin Large Igneous Province (LIP) extends for > 2500 km from the west coast of Greenland as far as the Great Bear Lake and Victoria Island in northern Canada (Fig. 2.1). The Franklin LIP is thought to have formed during Neoproterozoic break-up of Rodinia as Siberia separated from northern Laurentia (Heaman *et al.*, 1992, Rainbird, 1993, Pehrsson & Buchan, 1999, Ernst *et al.*, 2008, Denyszyn *et al.*, 2009). Geochemically correlative intrusions are thought to be present in Siberia (Ariskin *et al.*, 2009). The emplacement of the Franklin LIP has been dated at between ~723-716 Ma, using concordant U/Pb ages on baddeleyite/zircon from the Coronation sills and Franklin sills (Heaman *et al.*, 1992, Macdonald *et al.*, 2010). The emplacement of the Franklin LIP has been correlated with the early stages of the Neoproterozoic Sturtian glaciation (Macdonald *et al.*, 2010).

Fig. 2.1: The extent of the Franklin LIP across northern Canada. The Franklin LIP has a radiating dyke swarm, which has been used to infer the location of the melt source (red start located NW of Victoria Island: see Ernst *et al.* (2008) for details). Franklin sills, dykes and volcanics (Natkusiak) outcrop in the NW region of Victoria Island (western Canadian Arctic). The Coronation sills, on mainland Canada, are also thought to be related to the Franklin LIP (Shellnutt *et al.*, 2004).

2.2 Minto Inlier

The Minto Inlier is located on Victoria Island (Fig. 2.2). The Minto Inlier is a NE-SW trending syncline of Neoproterozoic Shaler Supergroup sedimentary rocks (Rainbird, 1993). The Shaler Supergroup comprise intra-cratonic clastic and carbonate sediments that were deposited in the Amundsen Basin (Rainbird *et al.*, 1996). The basin formed during break-up of Rodinia (Young, 1981). The Amundsen Basin is thought to represent an embayment along a larger epeiric basin within the Rodinia supercontinent (Young, 1981, Rainbird *et al.*, 1996). This epeiric sea was episodically connected to open ocean via seaways (Williams & Stelck, 1975).

The Shaler Supergroup was first defined by Thorsteinsson and Tozer (1962), after their investigations of the Minto Inlier. The Neoproterozoic Shaler Supergroup unconformably overlies Paleoproterozoic (~1.9 Ga) sedimentary rocks of the Goulburn Supergroup, which themselves overlie granite of suspected late Archean age, on the northeast side of Minto Inlier (*cf.* Rainbird et al. 1996). The Shaler Supergroup is up to ~5 km thick. It includes, in ascending stratigraphic order, the Rae Group, Reynolds Point Group, Minto Inlet Formation, Wynniatt Formation, Kilian Formation, and Kuujjua Formation (Thorsteinsson & Tozer, 1962, Jefferson, 1985, Rainbird *et al.*, 1996, Jones *et al.*, 2010, van Acken *et al.*, 2013, Thomson *et al.*, 2014). These Formations generally consist of carbonate rocks with subordinate clastics and sulphate evaporites.

At the top of the Shaler Supergroup are the Natkusiak flood basalts, a sequence of ~1 km thick lavas that are coeval to the Franklin LIP. These rocks were gently folded about ENE-trending axes, eroded, and then unconformably overlain by a Palaeozoic clastic and carbonate sequence (Thorsteinsson & Tozer, 1962, Mathieu *et al.*, 2013), itself dissected by a prominent ENE-trending normal fault system (Bédard *et al.*, 2012, Dewing *et al.*, 2013).

Franklin sills and feeder dykes intrude the Shaler Supergroup within the Minto Inlier. There are ~20 Franklin sills, which range in thickness from a few meters to ~150 m. The Franklin sills are mostly conformable to bedding (Fig. 2.3) and, where exposures permit, are seen to be laterally continuous for tens of kilometres along strike with little change in

thickness (Bédard *et al.*, 2012). There are narrow (~2-10 m) contact metamorphic haloes around Franklin sills (Nabelek *et al.*, 2013) with wider haloes enveloping some dykes (Hryciuk et al. Submitted).

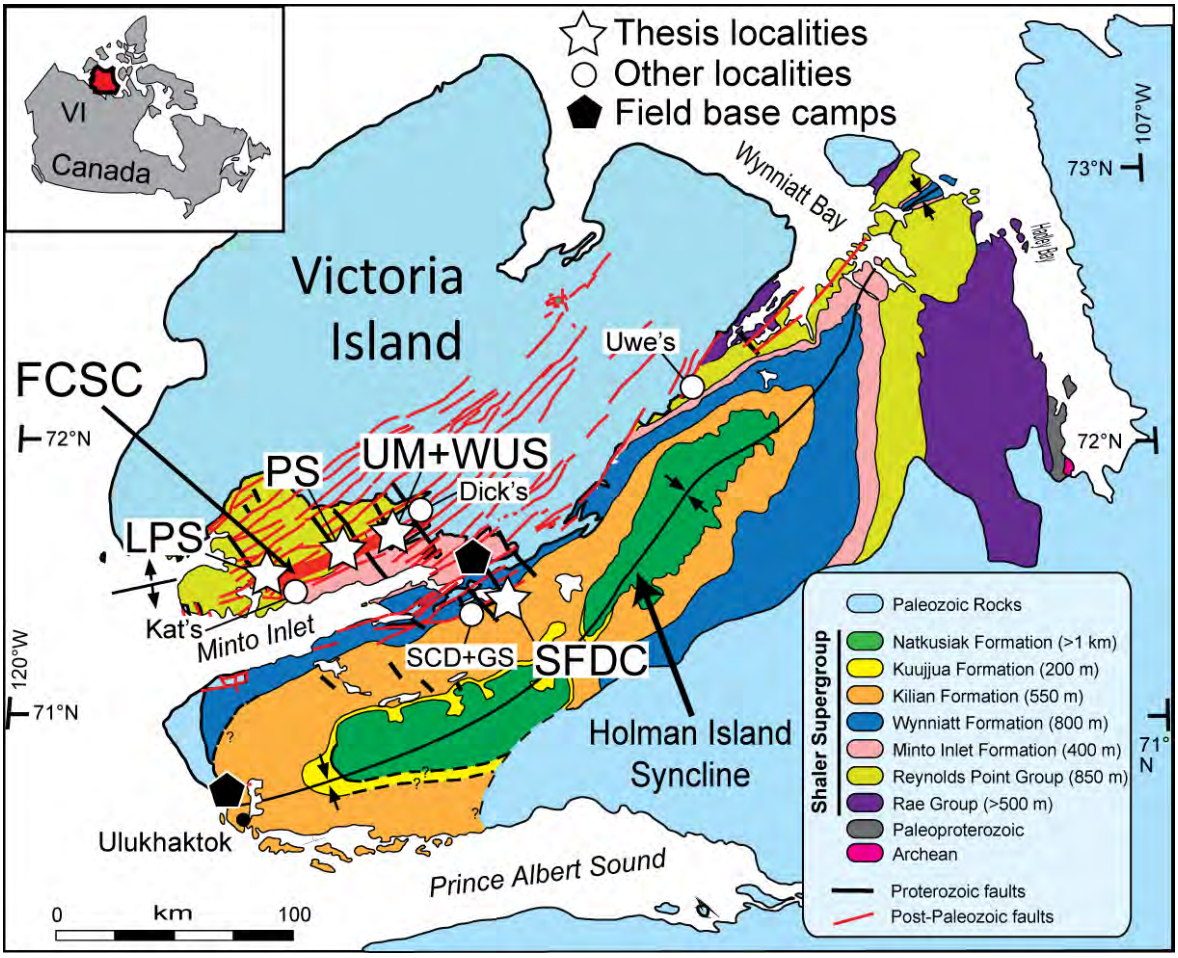

Fig. 2.2: A simplified geological map of the Minto Inlier on Victoria Island, modified after Thorsteinsson and Tozer (1962), following fieldwork in 2010 and 2011. The localities of the rocks studied in this thesis are labelled. The Lower Pyramid Sill (LPS) is situated near the western end of Minto Inlet and is studied in detail in chapter 4. The LPS is part of the Fort Collinson Sill Complex (FCSC), which is a series of olivine-rich sills that are emplaced just above the Fort Collinson Formation marker unit (within the Reynolds Point Group). The FCSC includes the West Uhuk Sill (WUS) and P-sill (PS). The Uhuk Massif (UM) is a major fault-guided dyke feeder system (appendix A) that is thought to have fed the FCSC. The FCSC magmatic plumbing system is discussed in chapter 5. The Southern Feeder Dyke Complex (SFDC), studied in chapter 6, is situated at the Wynniatt/Kilian Formation boundary, south of the Minto Inlet and ~1 km stratigraphically beneath the Natkusiak Formation flood basalts. Other locations mentioned in this thesis are also labelled (SCD = Sulphide City Dyke & GS = Gossan Sill).

A new aeromagnetic map reveals prominent NW-trending magnetic lineaments (Kiss & Oneschuk, 2010) that correspond to major topographic lows. These topographic lows locally contain breccias and cataclasites and have been interpreted to be faults (Bédard *et al.*, 2012). Some of these magnetic lineaments correspond to sharp breaks in stratigraphy indicating east-side-down throws and exhibit associated structures indicating normal

motion synchronous with emplacement of magmas with Franklin affinities, and are therefore interpreted to be Neoproterozoic syn-magmatic normal faults. These field relationships are described in detail in Bédard *et al.* (2012) for the Uhuk Massif (appendix A). The Southern Feeder Dyke Complex (SFDC: Fig 2.2) exhibits very similar field relationships (described in chapter 6), with brecciated country rocks that are intruded by basaltic Franklin dykes, themselves brecciated due to Neoproterozoic syn-magmatic faulting.

Fig. 2.3: Field photo looking towards the SE showing a typical section view within the Minto Inlier of Victoria Island. Sills are brown/black in colour with orange lichen staining at their bases and mostly show poorly developed columnar jointing. Photo by Charlie Beard.

2.3 Natkusiak Flood Basalts

The Natkusiak flood basalts (Fig. 2.2), at the top of the Shaler Supergroup, are a ~1 km thick sequence of basaltic volcanics that are coeval to Franklin sills (Baragar, 1976, Jefferson *et al.*, 1985, Williamson *et al.*, 2013). The Natkusiak flood basalts are preserved as two erosional remnants in the Holman Island syncline (Fig. 2.2). The Shaler Supergroup sedimentary rocks beneath the Natkusiak flood basalts were subjected to pre-magmatic uplift just prior to eruption, thought to be due to thermal doming above a mantle plume (Rainbird, 1993). The lowermost extrusive unit (~50-100 m thick) is a primitive basalt (~7-

11 wt% MgO) characterised by LREE (light-rare earth element)-LILE (large ion lithophile element)-enrichment, also referred to as Type-1 magmas (Bédard *et al.*, 2013). Overlying this thin unit are laterally extensive basaltic (~6-10 wt% MgO) sheet flows with less strongly enriched L/HREE signatures, also referred to as Type-2 magmas (Bédard *et al.*, 2013).

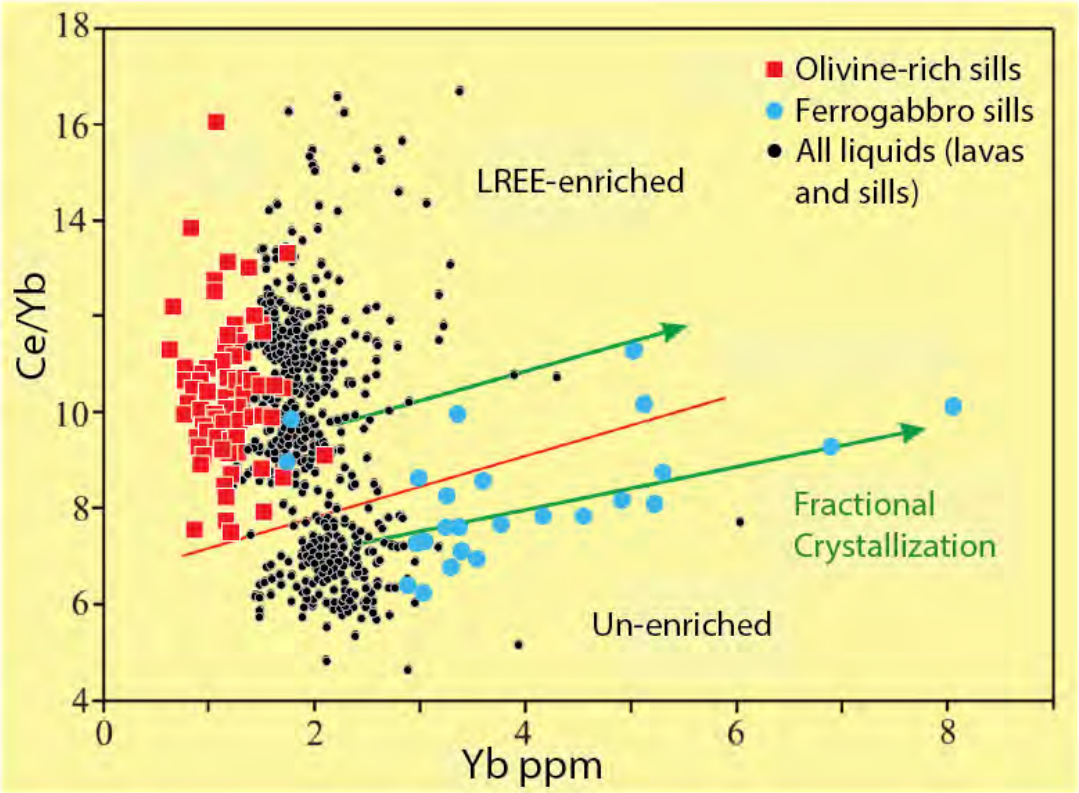

Fig. 2.4: A trace element discrimination plot showing Ce/Yb versus Yb (in ppm). The plot includes all liquid (i.e. sill and dyke chills and Natkusiak lavas) and quasi-liquid (i.e. dolerite and ferrogabbro) compositions that were sampled across the Minto Inlier during fieldwork in 2010 and 2011. These data reveal two populations of magma fed the Franklin LIP. Type-1 magmas are LREE-enriched (high Ce/Yb) while Type-2 magmas have low L/HREE ratios. Based on crosscutting relationships preserved in drill core (sampled by GNME in 2008), Type-1 magmas are older than Type-2 magmas.

The two populations (Type-1 and Type-2) of magma recognised in the Natkusiak volcanics can be correlated with those in the underlying sills. Both magma types form gabbroic/doleritic sills that exhibit systematic inward enrichment of FeO, TiO_2 and incompatible elements as a result of *in-situ* fractional crystallisation (Naslund *et al.*, 2013). Type-1 sills (including the Lower Pyramid Sill and other sills of the Fort Collinson Sill Complex: chapter 4 & 5) mostly occur in the lower part of the Shaler Supergroup and are commonly characterised by olivine-rich bases and gabbroic upper parts. They correspond

geochemically to the lower primitive Natkusiak lavas. Intrusions formed from the younger, Type-2 magma population lack olivine-rich layers, but may be prominently plagioclase-clinopyroxene phyric or sub-ophitic in texture (including the majority of the Southern Feeder Dyke Complex: chapter 6).

3. Methods

3.1 Introduction

This chapter aims to give an overview of the methods used for the data that are presented in this thesis. Section 3.2 will explain the whole-rock chemistry methods utilised at Cardiff University, specifically for major, trace and platinum group elements (PGEs). A selection of samples that are presented in chapter 5 were analysed for whole-rock chemistry in laboratories in Canada, and a brief summary is provided. Section 3.3 will summarise the *in-situ* mineral chemistry methods used at Laval University in Québec City. Section 3.4 will summarise the methods used by co-authors for other data that form part of this thesis.

3.2 Whole-rock chemistry

Rock samples (N = 81) were prepared for whole-rock analyses using the rock preparation facilities at Cardiff University. Initially, samples were trimmed using a diamond bladed mechanical rock saw in order to remove weathered edges. The rock samples were then dried before the next stage of the process. Chunks of each sample were crushed to coarse grit with a steel jaw crusher. Each sample was then reduced to a fine powder in a agate planetary ball mill. Approximately 2 g of each sample was ignited for two hours in a furnace at ~900° in order to drive off volatiles. This allowed the loss on ignition (LOI) values to be calculated.

Samples were then prepared as solutions for inductively coupled plasma-atomic emission spectrometry or ICP-OES (Jobin Yvon Horiba Ultima 2) and inductively coupled plasma-mass spectrometry or ICP-MS (Thermo Elemental) analysis, following the lithium metaborate fusion method described in McDonald and Viljoen (2006). Approximately 0.1 +/- 0.001 g of each sample was mixed with 0.6 g +/- 0.004 g of lithium metaborate flux in a platinum crucible. Lithium iodide wetting agent was added to each mixture, which was then fused with a Claisse Fluxy automated fusion system. Each mixture was then dissolved in a 50 ml solution of 20 ml of 10% HNO_3 and 30 ml of 18.2 deionised water obtained

from a Milli-Q purification system. Once the mixture had fully dissolved, 1 ml of 100 ppm Rh spike was added to the solution, which was then filled with 100 ml of 18.2 deionised water. The samples (~20 ml of each) were then run on the ICP-OES in order to obtain major element and some trace element (Sc, V, Cr, Co, Ni, Cu, Zn, Sr, Y, Zr, Ba) abundances. An aliquot of 1 ml of each solution was added to 1 ml of In and Tl and 8 ml of 2% HNO_3 and run on the ICP-MS to obtain trace element abundances (V, Cr, Co, Ni, Cu, Zn. Ga, Rb, Sr, Y, Zr, Nb, Sn, Ce, Pr, Nd, Sm, Eu, Gd, Tb, Dy, Ho, Er, Tm, Yb, Lu, Hf, Ta, Pb, Th, U). Dr. Iain McDonald and Dr. Ley Wooley operated the ICP-OES and ICP-MS. In order to assess the accuracy and precision of the whole-rock data, external and internal standards were analysed. The external standards were JB-1a and NIM-G (included in appendix E1). The percentage errors of the measured values compared with the certified values are included in appendix E1.

A suite of samples (N = 51) presented in chapter 5 were analysed in IRNS-ETE laboratories in Québec City, Canada. Rock samples were initially trimmed and then reduced to a coarse grit with a steel jaw crusher before being powdered with a planetary agate mortar. Sample fusion was operated on a Claisse fluxer using $LiBO_2$ and LiBr. The HNO_3-HCl sinter technique was employed to circumvent potential problems associated with high field-strength elements (HFSE) and rare-earth elements (REE) in refractory minerals. The major elements and Ba, Sr, Sc, V, Co, Cr, Cu, Ni and Zn compositions were determined by ICP-OES. Trace elements were determined by ICP-MS using a similar method to that described by Varfalvy *et al.* (1997). Full details of the detection limits, and the accuracy and precision of the data are summarised in Leclerc *et al.* (2011).

A suite of samples (N = 16) that are presented in chapter 6, were analysed for platinum group elements (PGE) at Cardiff University. PGE concentrations for each sample were obtained by Ni sulphide fire assay, followed by ICP-MS following the method of Huber *et al.* (2001) and McDonald and Viljoen (2006).

3.3 Mineral chemistry

In-situ mineral chemical analyses were carried out using a Cameca SX-100 Electron Microprobe at Laval University in Québec City, Canada. The probe was fitted with 5 wavelength-dispersive spectrometers. All phases were analysed on polished thin sections using a focused beam (1 µm diameter), 20 nA current and a 15.0 kV accelerating potential. Counting times were typically 30 seconds on peak and background levels. Core to rim profiles were measured on the major silicate phases. Where grain size was very fine or only a representative core composition was required, single spot analyses were obtained. The dataset for each phase analysed and the analytical conditions for each mineral species are supplied in appendix C. Preparation before undertaking the data collection using the Electron Microprobe was carried out using the Scanning Electron Microscope (Cambridge 360 instrument) at Cardiff University.

3.4 Other methods used by co-authors

3.4.1 Radiogenic lead isotopes

A suite of samples (N = 6) that are presented in chapter 5 were analysed for radiogenic Pb-isotopes at the Pacific Centre for Isotopic and Geochemical Research (PCIGR), University of British Columbia, Vancouver, by chapter 5 co-author, Charlie Beard. Rock samples were carefully prepared before being crushed to gravel and then milled to a fine powder. 100 g of gravel for each sample was milled in agate jars containing agate marbles. Doleritic samples were dissolved using the hot plate method as described in Weis *et al.* (2006), whilst olivine-rich rocks were digested in high-pressure bombs to produce dissolution of resistant accessory phases such as Zircon (Pretorius *et al.*, 2006, Weis *et al.*, 2006). Elements were separated and purified before isotopic analyses using ion exchange chromatography. Pb was isolated by a two-pass ion exchange chromatography separation method, described by Nobre Silva *et al.* (2009). Pb-isotopic ratios were corrected for instrumental drift using a Ln-Ln trend function, determined by bracketed analyses of NBS981 Pb standard solution. External reproducibility was ensured by measurement of USGS reference materials BCR-2 Columbia River Basalt and G-2 Granite, normalised

values for which were within the 2σ range of historical values within PCIGR. Internal reproducibility was tested by multiple replicate and complete procedural duplicate analyses. Pb-isotopic compositions were age-corrected to initial ratios at 723 Ma. Full details of the method used are available in Beard (2012) and a more comprehensive description of laboratory methods can be found in Dell'Oro *et al.* (2012).

3.4.2 Sulphur isotopes

A suite of samples (N = 15) presented in chapter 5 and a suite of samples (N = 32) presented in chapter 6 were analysed for sulphur isotopes in the laboratories at McGill University, Montréal. Sulphur isotope powders were ground using case hardened steel and tungsten carbide mills. Sulphate evaporites were extracted using a boiling Thode reduction solution (Forrest & Newman, 1977). All other samples were extracted using a Cr-reducible solution (Canfield *et al.*, 1986). H_2S was reacted with zinc acetate and $AgNO_3$ to produce an Ag_2S precipitate. This precipitate was weighed into packets, which were fluorinated overnight in nickel bombs to produce SF_6. Analysis was completed with a Thermo Finnigan MAT 253 mass spectrometer using a dual inlet method monitoring ion beams at a mass/charge ratio of 127-131. Analytical reproducibility (2σ) for the full measurement procedure from rock powders to the final mass spectrometer data for $\delta^{34}S$ is estimated to be better than 0.2‰. All data is reported relative to the Vienna Canyon Diablo Troilite standard (VCDT). Full details of the method used are available in Hryciuk et al. (Submitted).

3.4.3 Anisotropy of magnetic susceptibility fabrics

Oriented blocks were taken at 17 sites along the Southern Feeder Dyke Complex (chapter 6) using magnetic and solar compasses. Eleven sites were in dykes, and 6 were in adjacent sills. Typically 5 cores were drilled from each block, producing 85 oriented cores. The anisotropy of magnetic susceptibility (AMS) of each core was measured using the AGICO KLY-3 Kappabridge susceptibility metre. Prof William MacDonald (co-author on chapter 6) carried out this work in his laboratory at Binghamton University, New York state.

4. Olivine slurry replenishment and the development of igneous layering in a Franklin sill

4.1 Abstract

The Franklin sills and dykes on Victoria Island in the Canadian Arctic represent the sub-volcanic plumbing system to the Natkusiak flood basalts, which are associated with late Neoproterozoic (*ca.* 723-716 Ma) break-up of Rodinia. The Lower Pyramid Sill (LPS) is the distal end of a sill complex that may be rooted in the Uhuk Massif, a major fault-guided feeder system. The LPS is unusual for a thin (*ca.* 21 m), shallow, tholeiitic intrusion because it displays well-developed cumulate layering similar to that seen in large layered intrusions. The LPS has an aphanitic, olivine-phyric (*ca.* 5%) Lower Chilled Margin (LCM); a (<1 m thick) dendritic, olivine-phyric Lower Border Zone (LBZ); an (*ca.* 7 m thick) olivine-dominated (up to *ca.* 55%) melagabbro/feldspathic-peridotite zone (OZ); a thin (*ca.* 1 m) clinopyroxene-rich cumulate gabbro (CPZ) containing sector-zoned euhedral clinopyroxene; a (*ca.* 10 m thick) doleritic gabbro zone (DZ); an (<1 m thick) aphyric, dendritic Upper Border Zone (UBZ); and an aphanitic, olivine-phyric (*ca.* 5%) Upper Chilled Margin (UCM). Distinct compositional groups recognized in olivines from the OZ can be associated with specific crystal morphologies, some showing significant reverse zoning. Melt compositions were calculated through application of the olivine-melt Fe=Mg exchange coefficient. The calculations suggest that phenocrystic and primocrystic olivine (Fo_{88-82}) in the LCM/LBZ and lower OZ formed from melts with *ca*. 13-10 wt% MgO. Modeling implies that reversely zoned olivine primocrysts and chadacrysts have rims in equilibrium with melts of *ca*. 10-8 wt% MgO that were saturated only in olivine (+ minor chromite), whereas some olivine cores formed from melts as evolved as *ca*. 6-5 wt% MgO that would have coexisted with a gabbroic assemblage. The presence of multiple olivine populations in the OZ (some reverse zoned) indicates that the LPS did not crystallize from a single pulse of melt that evolved by closed-system fractional crystallization. We propose that the reverse zoning pattern records incorporation of evolved crystals, most derived from the mushy gabbroic host, when an olivine-charged replenishment under/intraplated

the partly crystallized basaltic magma, now preserved as the DZ. The intervening CPZ may also owe its origin to the emplacement of the olivine slurry; possibly as a result of pore-scale melt mixing at this interface. The DZ shows inward differentiation trends that can be explained by *in-situ* differentiation. The data implies that late emplacement of olivine-rich crystal-slurries and *in-situ* differentiation both played a role in the development of the layered LPS.

4.2 Introduction

There is considerable petrological and geochemical evidence from active volcanoes for periodic replenishment of high-level magma chambers by the influx of new magma from depth (Murphy *et al.*, 2000, Tepley *et al.*, 2000, Garcia *et al.*, 2003, Humphreys *et al.*, 2006, Morgan *et al.*, 2006, Ginibre & Wörner, 2007). Replenishment is also well documented in layered intrusions (Wager & Brown, 1968, Huppert & Sparks, 1980, Ballhaus & Glikson, 1989, Cawthorn, 1996, Wallace & Bergantz, 2002, Namur *et al.*, 2010). Influxes of replenishing primitive magma can: (1) prolong the life of a magma chamber (Usselman & Hodge, 1978, Annen *et al.*, 2014); (2) modify chemical fractionation trends (O'Hara, 1977, Dungan & Davidson, 2004, Reubi & Blundy, 2008); (3) affect the cumulate stratigraphy in layered intrusions (Wager & Brown, 1968, Cawthorn, 1996, Gibb & Henderson, 2006); and (4) trigger eruption (Brown, 1956, Sparks *et al.*, 1977, Field *et al.*, 2013). It is widely believed that primitive replenishments play a role in the formation of cyclic/macrorhythmic layering in mafic-ultramafic intrusions (Brown, 1956, Irvine & Smith, 1967, Wager & Brown, 1968, Irvine, 1977, Huppert & Sparks, 1980, Smewing, 1981).

Huppert and Sparks (1980) developed a model to explain cyclic olivine-rich/plagioclase-rich macrorhythmic layers by ponding of dense, hot, primitive magma recharges beneath a resident, more evolved basaltic magma. In their model (as applied to the Rum intrusion), the contrast in composition and temperature between the two liquid layers drove vigorous convection, holding olivine in suspension in the lower layer until its eventual *en masse* deposition formed an olivine-rich macro layer. Continuous re-equilibration with the convecting melt prior to deposition would cause olivine compositional variations to approach end-member equilibrium crystallisation paths (Tait, 1985), and explain a lack of

cryptic olivine compositional variation in the Rum olivine-rich macro layers. More recent reviews on the mechanisms of magma influx during replenishment, and the development of igneous layering, can be found in Gorring and Naslund (1995), Cawthorn (1996), Puffer *et al.* (2009) and Zieg and Marsh (2012).

Recent discussion about how large-scale cyclic/macrorhythmic olivine-rich/plagioclase-rich layers form has been strongly polarised. One school of thought advocates the late emplacement of crystal-laden slurries into pre-existing, partly crystallised intrusions (Marsh, 2004, Marsh, 2013). Another favours the emplacement of largely aphyric magmas that evolve by fractional crystallisation to produce *in-situ* differentiation trends (Latypov, 2009). In this chapter, we present data that bear on this debate, showing that olivine-enriched basal layers in the Franklin sills of Victoria Island formed as a result of slurry injection, much as proposed by Marsh (2004, 2013), but that the overlying gabbroic rocks are internally differentiated, as advocated by Latypov (2009) and others (Shirley, 1985, Parsons, 1986, Naslund, 1989).

Slow cooling of large intrusions allows significant post-cumulus textural (Hunter, 1996, Holness *et al.*, 2007) and compositional re-equilibration (Barnes, 1986) that may obscure primary magmatic signatures. This is especially true for olivine due to the rapid exchange of Fe and Mg between crystal and melt at magmatic temperatures (Chakraborty, 1997), whereas 'primary magmatic' zoning patterns of clinopyroxene (Müller *et al.*, 2013) and especially plagioclase (Grove *et al.*, 1984, Morse, 1984) seem to better survive the post-cumulus stage. In contrast, thin (< 100 m) intrusions would cool quickly (Carslaw & Jaeger, 1959) and might better preserve the textural and mineral-chemical evidence of the magmatic processes by which they formed.

The sills constituting the Neoproterozoic Franklin sub-volcanic plumbing system on Victoria Island are examples of such thin, quickly cooled systems. These sills are well exposed, unmetamorphosed and the suite has a capping, cogenetic flood basalt sequence (Natkusiak flood basalts). The excellent preservation and availability of liquid compositions allow the physical and chemical linkages between sills, feeder/transfer dykes and the capping Natkusiak flood basalts to be established. In this chapter, we reconstruct the differentiation history of the Lower Pyramid Sill (LPS), a thin (~21 m) sill that is prominently layered, with an olivine-enriched lower layer and an olivine-poor gabbroic

upper layer. Our textural and mineral-chemical observations from the LPS are best explained by mixing between a resident gabbroic mush with a late invading olivine slurry, and we propose that this is how the first-order olivine-rich/plagioclase-rich macro layering formed.

4.3 Lower Pyramid Sill

The LPS (Fig. 4.1a) is located near Boot Inlet at the western end of the Minto Inlier (Fig. 2.2). It formed from the LREE-LILE-enriched magma population (Type-1 magma). The LPS was emplaced at a depth of ~3 km based on its stratigraphic position. It is one of many olivine-rich sills that were emplaced just above the Fort Collinson Formation quartz-arenites within a broad corridor along the Collingwood hills. Collectively these olivine-enriched sills are known as the Fort Collinson Sill Complex (discussed in chapter 5). The thin (~50-100 m) Fort Collinson marker unit is embedded in much thicker sequences of dolostone and limestone, and this mechanical discontinuity appears to have greatly facilitated intrusion of the early Type-1 magma pulse in the Franklin province. The western, sill-like part (~40 m thick) of the Uhuk Massif (UM), located ~50 km to the east (Fig. 2.2: *cf* Bédard *et al*., 2012), is another example of an olivine-enriched sill emplaced at this stratigraphic position. The LPS has a thin (*ca.* 5-6 m) metamorphic halo surrounding it, similar to other Franklin sills (Nabelek *et al.*, 2013).

The LPS is unusual for such a thin hypabyssal intrusion in having a well-defined basal olivine-rich cumulate layer, which is overlain by a sub-ophitic doleritic gabbro (Fig. 4.1b). The LPS has chilled contacts against a thin septum of fissile Jago Bay Formation carbonates, only a few meters above the top of the Fort Collinson quartz-arenites (Fig. 4.1a). The LPS (Fig. 4.1b) has an aphanitic Lower Chilled Margin (LCM); a thin (< 1 m) dendrite-textured Lower Border Zone (LBZ); a ~7 m thick sequence of olivine cumulate melagabbro to feldspathic-peridotite with ~40-55% modal olivine (OZ); a ~1 m thick layer of clinopyroxene-rich gabbro (CPZ); a ~10 m thick layer of sub-ophitic doleritic gabbro (DZ); a thin (< 1 m), dendrite-textured Upper Border Zone (UBZ); and a thin (< 1 m) aphanitic Upper Chilled Margin (UCM). We have taken 26 samples from a single LPS profile with sample locations constrained by a global positioning system, and height above the lower contact measured in the field (data in appendix E1). We analysed all samples for

their whole-rock major element concentrations (Fig. 4.1b) and 22 for mineral compositions.

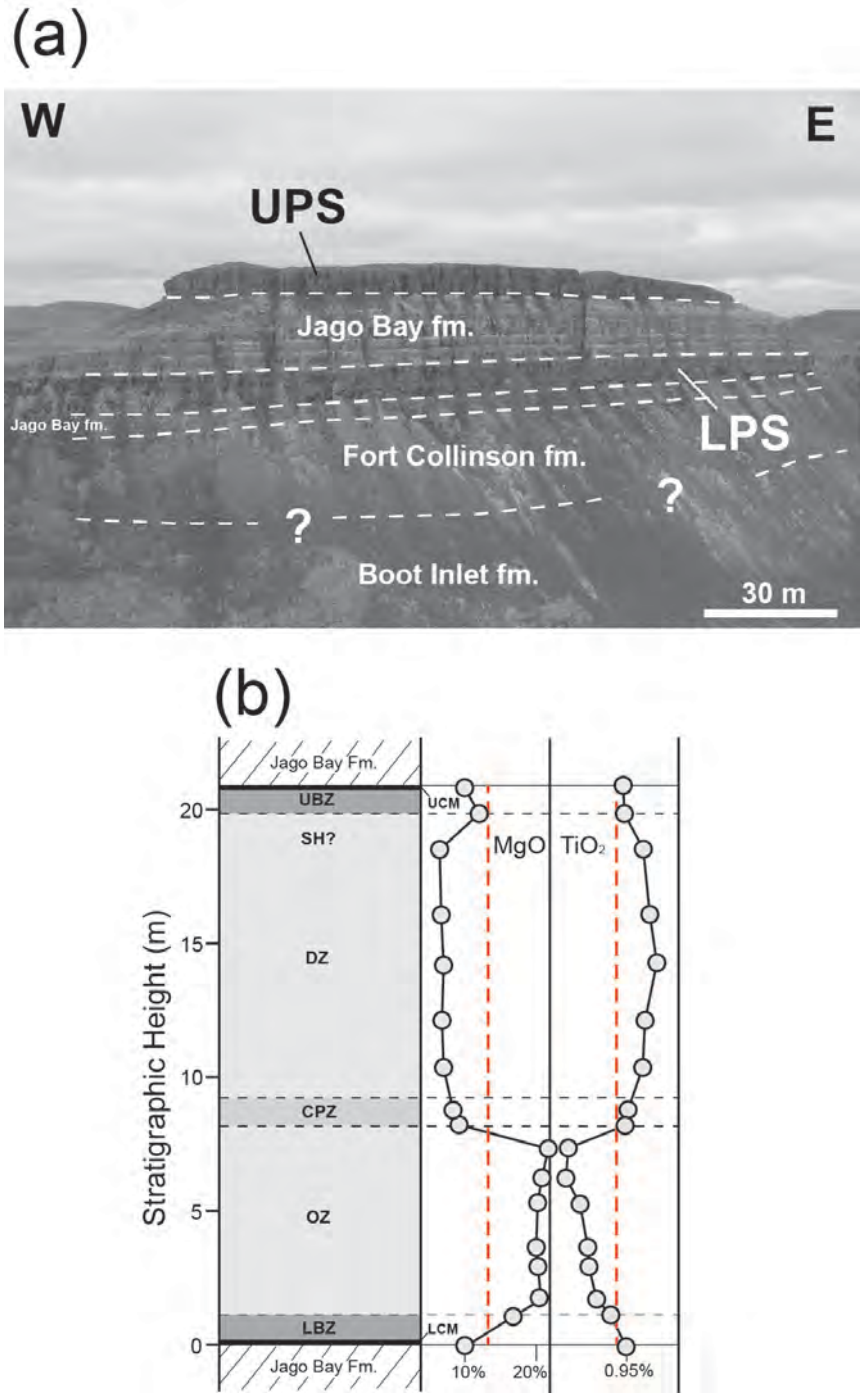

Fig. 4.1: (a) Field photo of the LPS, with a lower contact just above the Fort Collinson Formation, which is a prominent marker unit. The upper contact is abutted against the Jago Bay Formation. The Upper Pyramid Sill (UPS) is a younger, porphyritic Type-2 sill (unenriched L/HREE magma). In (b), the stratigraphy of the LPS is shown, along with MgO and TiO_2 whole-rock compositions (in wt%). MgO is highest (up to ~25 wt%) in the OZ, which is dominated by olivine. The DZ has lower MgO contents, similar to the chill (~10 wt% MgO) and higher TiO_2 contents in comparison to the LCM/OZ. The red dashed lines show the mean sill composition. All whole-rock data is provided in appendix E1.

4.4 Results

4.4.1 Petrography

4.4.1.1 Lower Chilled Margin (LCM)

The LCM (sampled at ~5 cm above the contact) has ≤ 5% euhedral olivine phenocrysts (~0.5-2 mm), which may contain tiny chromite microphenocrysts as inclusions. The olivine phenocrysts are surrounded by a very-fine grained (~0.1 mm) groundmass (Fig. 4.2a) that grades from massive aphanitic material to a felted mass of dendritic plagioclase and clinopyroxene.

4.4.1.2 Lower Border Zone (LBZ)

In the LBZ, the proportion of olivine phenocrysts (~1-2 mm, also with minor Cr-spinel inclusions) increases to ~10-15% (at ~20 cm above the lower contact). The dendritic intergrowths of plagioclase and clinopyroxene reach ~1-2 mm grain sizes with dendrites commonly nucleating on the surface of olivine phenocrysts (Fig. 4.2b). The rims of some olivine crystals are intergrown with the plagioclase-clinopyroxene dendrites suggesting that the 3-phases cosaturated during crystallisation of the LBZ (Fig. 4.2b). The textures, with the presence of cumulus olivine, are consistent with a weakly olivine-cumulative composition for the LBZ.

4.4.1.3 Olivine Zone (OZ)

There is a noticeable textural change ~1 m above the lower contact of the LPS. At this height, modal olivine increases over a few cm to ~40% and the groundmass texture changes from dendritic to medium-grained poikilitic. We define this modal and textural transition as the boundary between the LBZ and the OZ. The OZ is ~7 m thick and is composed of cumulate olivine melagabbro to feldspathic-peridotite. Cr-spinel microphenocrysts are present throughout the OZ, typically as inclusions in olivine primocrysts and as grains embedded in interstitial clinopyroxene and plagioclase.

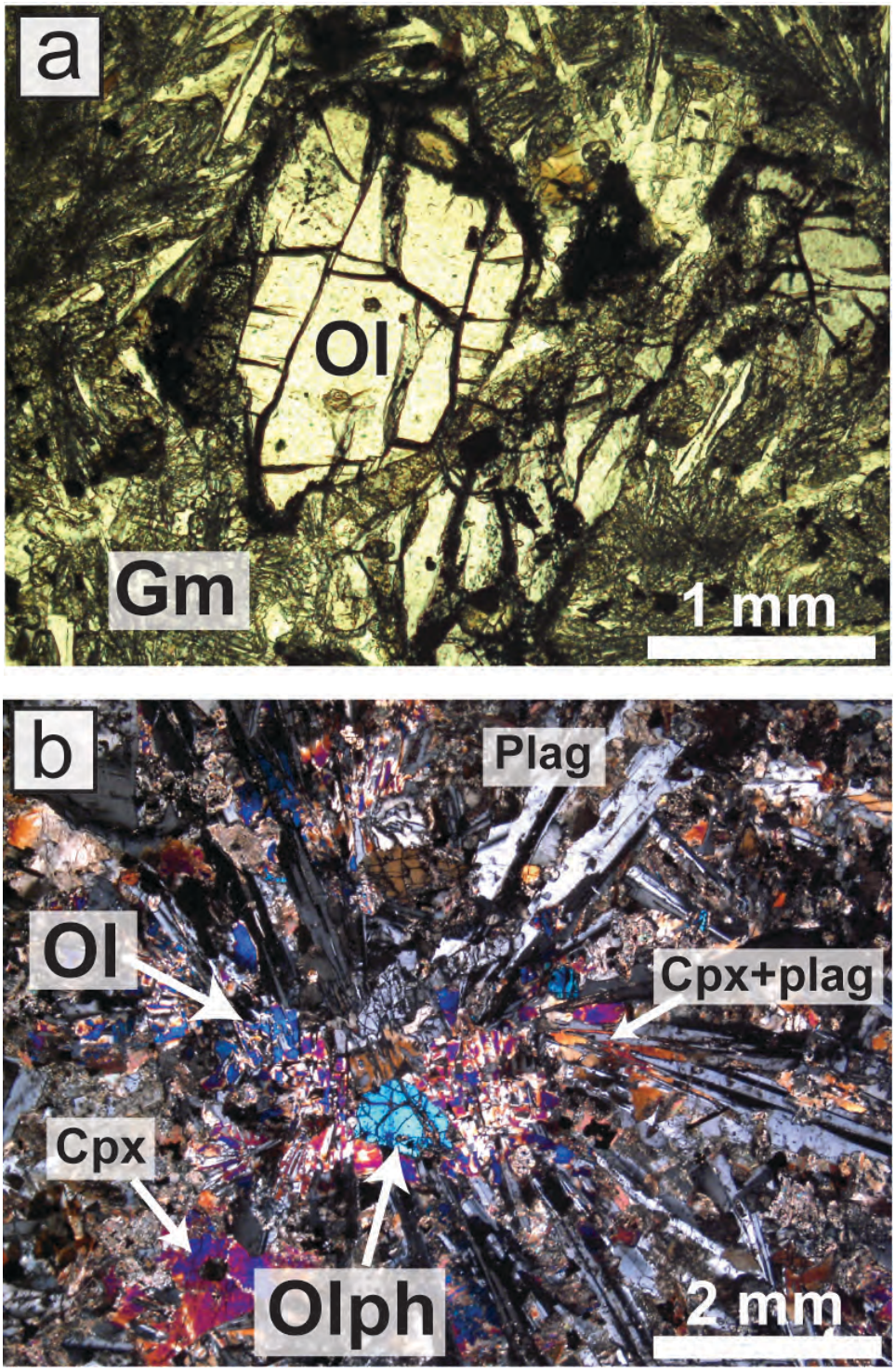

Fig. 4.2: Photomicrographs of the textures observed in the LCM and LBZ. (a) At the lower contact, euhedral olivine (Ol) phenocrysts reside in a fine-grained quenched groundmass (Gm) (image in plane-light). (b) ~20 cm above the lower contact within the LBZ, the textures grade into coarser dendrites of plagioclase (Plag) and clinopyroxene (Cpx) that cement olivine phenocrysts (Olph). Olivine (Ol) is also intergrown with the dendrites suggesting the melt may have reached the 3-phase cotectic early in its crystallisation history (image in crossed-nicols).

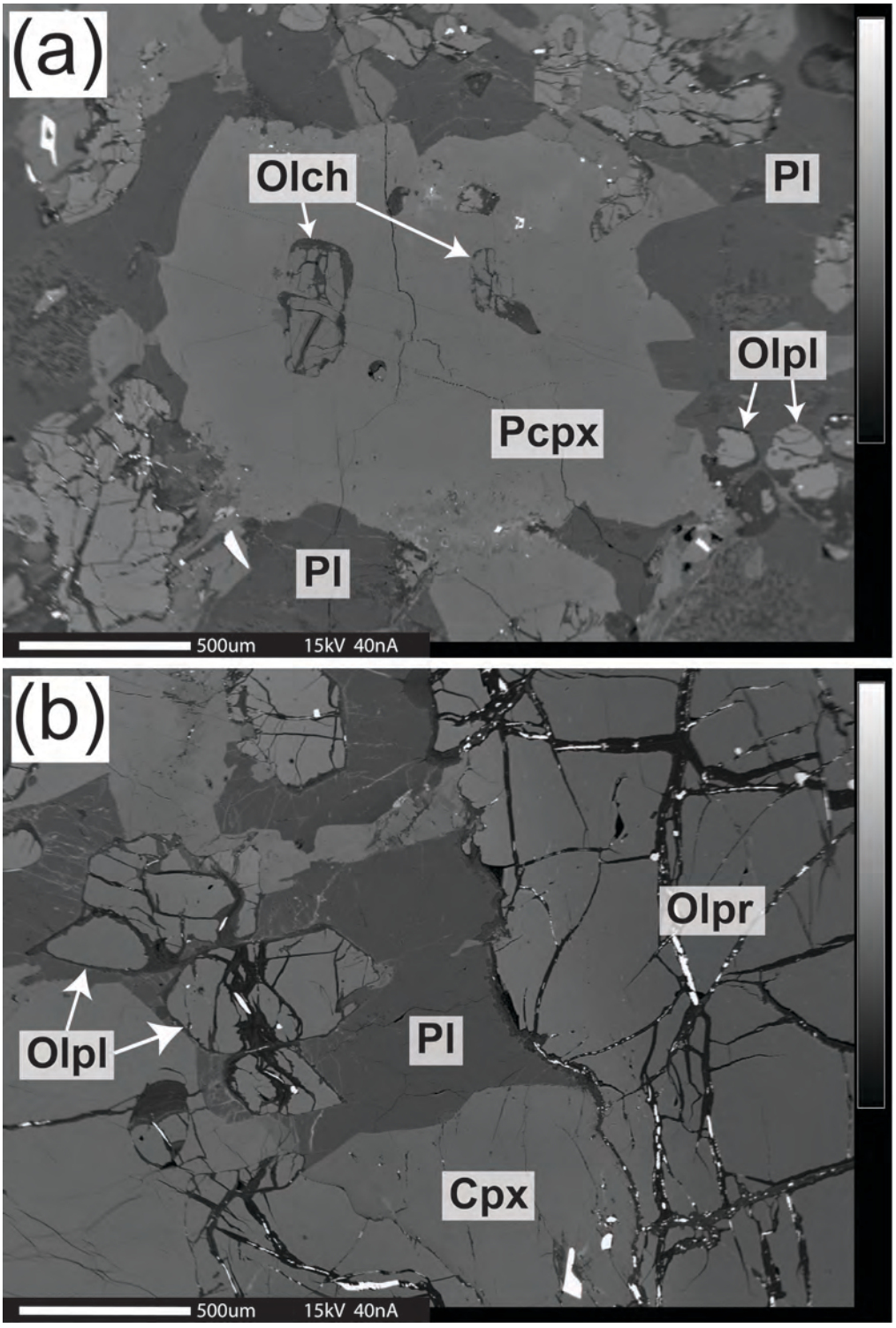

Fig. 4.3: Backscattered electron (BSE) images showing LOZ olivine morphologies. (a) A clinopyroxene oikocryst (Pcpx) encloses olivine chadacrysts (Olch), and is surrounded by anhedral, interstitial plagioclase (Pl), which encloses groundmass olivines (Olpl). (b) Euhedral and clustered groundmass olivines (Olpl) enclosed by anhedral, interstitial plagioclase (Pl). The edge of a large, normally zoned olivine primocryst (Olpr) is also visible.

Olivine within the OZ can be broadly assigned to four different textural groups: (1) euhedral olivine primocrysts (*ca.* 0.5-2 mm), which commonly contain euhedral Cr-spinel microphenocrysts (Fig. 4.3b & 4.4a); (2) chadacrystic fine-grained (*ca.* 0.2-0.5 mm) euhedral-subhedral olivine crystals (some bearing Cr-spinel inclusions), which are enclosed by clinopyroxene oikocrysts (Fig. 4.3a, 4.4a & 4.5f); (3) fine-grained (*ca.* 0.2-0.5 mm) groundmass olivine crystals (some bearing Cr-spinel inclusions) surrounded by interstitial plagioclase (Fig. 4.3b, 4.4a & 4.5f); (4) hopper olivines (*ca.* 0.2-2 mm), which are hopper in habit in cross-section and orthorhombic in basal sections where it appears to enclose clinopyroxene and plagioclase (Fig. 4.4d, e & f). Hopper olivines also have anhedral margins indicating co-crystallization with plagioclase (Fig. 4.4d & e). We sub-divide the OZ based on the spatial distribution of these olivine textures into: a basal pyroxene-poikilitic olivine-melagabbro, which mainly consists of euhedral olivine primocrysts, olivine chadacrysts and groundmass olivines (LOZ; Fig. 4.3a, 4.4a & 6), with only minor (*ca.* 5%) proportions of fine-grained (<0.5 mm) hopper olivine; a middle subzone dominated by hopper olivine crystals that are typically intergrown with clinopyroxene, with subordinate primocrystic, chadacrystic, groundmass and hopper olivine (MOZ; Fig. 4.4b & c); and an upper subzone (UOZ) dominated by hopper olivine morphologies with subordinate euhedral primocrystic and groundmass olivines that lacks olivine chadacrysts in poikilitic clinopyroxene (Fig. 4.4d, e & f).

Clinopyroxene (~1-2 mm) habits range from euhedral to subhedral in the LOZ and it commonly encloses olivine chadacrysts (Fig. 4.3a). Clinopyroxene becomes more subhedral to anhedral in the MOZ, where intergrowths with olivine are common (Fig. 4.4b). In the UOZ, euhedral cumulus clinopyroxene crystals appear (~1-2 mm; Fig. 4.4d, f), substituting for now rare clinopyroxene oikocrysts that typify the LOZ/MOZ. Subordinate inter-granular, interstitial clinopyroxene occurs throughout the OZ.

Plagioclase is anhedral throughout the OZ and is interstitial to cumulus olivine and mostly interstitial to clinopyroxene, except for local co-crystallisation textures (Fig. 4.4a, c, d). There are minor accessory amphibole and biotite, and there are traces of groundmass Fe-Ti oxides and Fe-Ni-Cu sulphides.

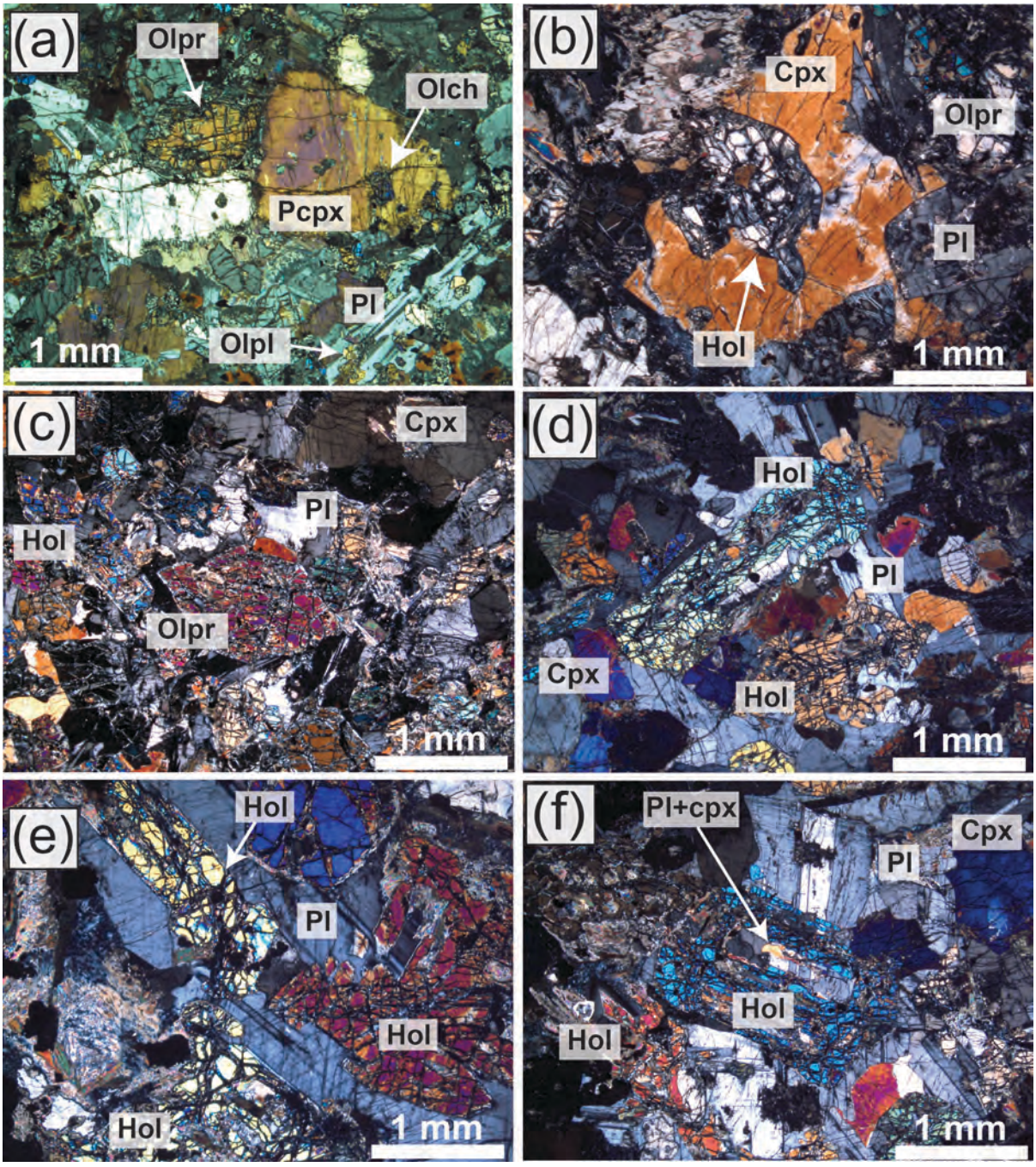

Fig. 4.4: Photomicrographs of OZ textures (all in crossed-nicols). (a) An image from the LOZ showing an olivine primocryst (Olpr) and poikilitic clinopyroxene (Pcpx), which encloses smaller olivine chadacrysts (Olch). Finer-grained olivine crystals (Olpl) can also be seen, surrounded by interstitial plagioclase (Pl). (b) An image from the MOZ showing a hopper olivine (Hol), which is overgrown by clinopyroxene (Cpx). (c) Image showing the abundant olivine of the MOZ, with olivine primocrysts (Olpr) and hopper olivines (Hol). (d) Hopper olivines (Hol) in the UOZ. (e) UOZ hopper olivines (Hol) that are intergrown with interstitial plagioclase (Pl). (f) UOZ hopper olivine (Hol) that appears to enclose plagioclase and clinopyroxene (Pl+cpx). Euhedral clinopyroxene crystals (Cpx) are also present as well as interstitial plagioclase (Pl).

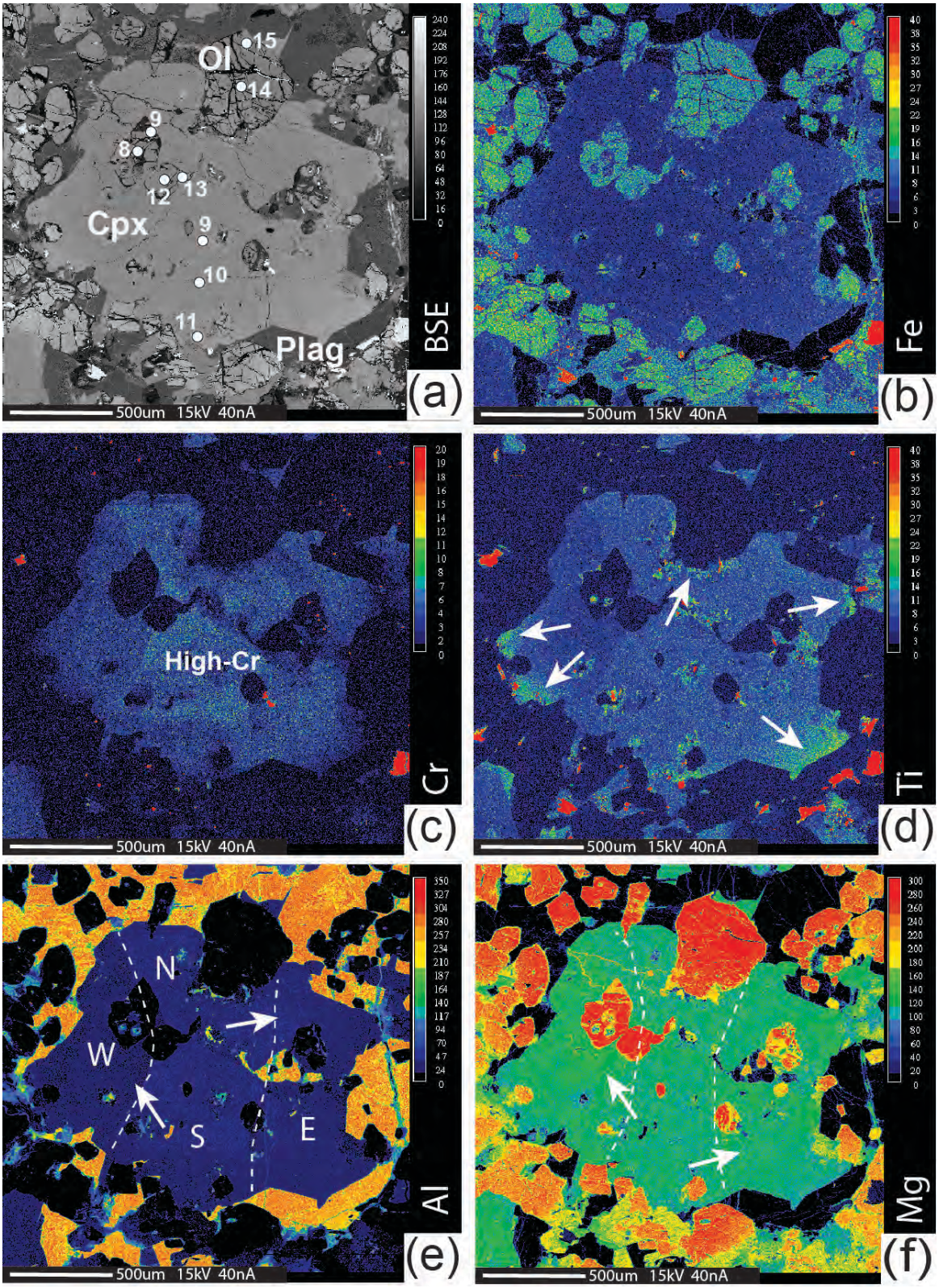

Fig. 4.5: Back scattered electron (BSE) image and element maps of a clinopyroxene oikocryst from the LOZ with olivine chadacrysts (Fo_{83-81}): (a) BSE image showing analysis spot numbers (core composition is Mg#85), (b) Fe, (c) Cr, (d) Ti, (e) Al, (f) Mg. The clinopyroxene oikocryst appears to display sector-zoning, visible in the Mg and Al element maps. The clinopyroxene oikocryst also has a narrow Fe-Ti enriched rim (white arrows in d). Interstitial plagioclase is visible in (e). The Fe-rich groundmass olivines are hosted by interstitial plagioclase. N = north; S = south = E = east. W = west. Additional element maps are included in appendix E7-1.

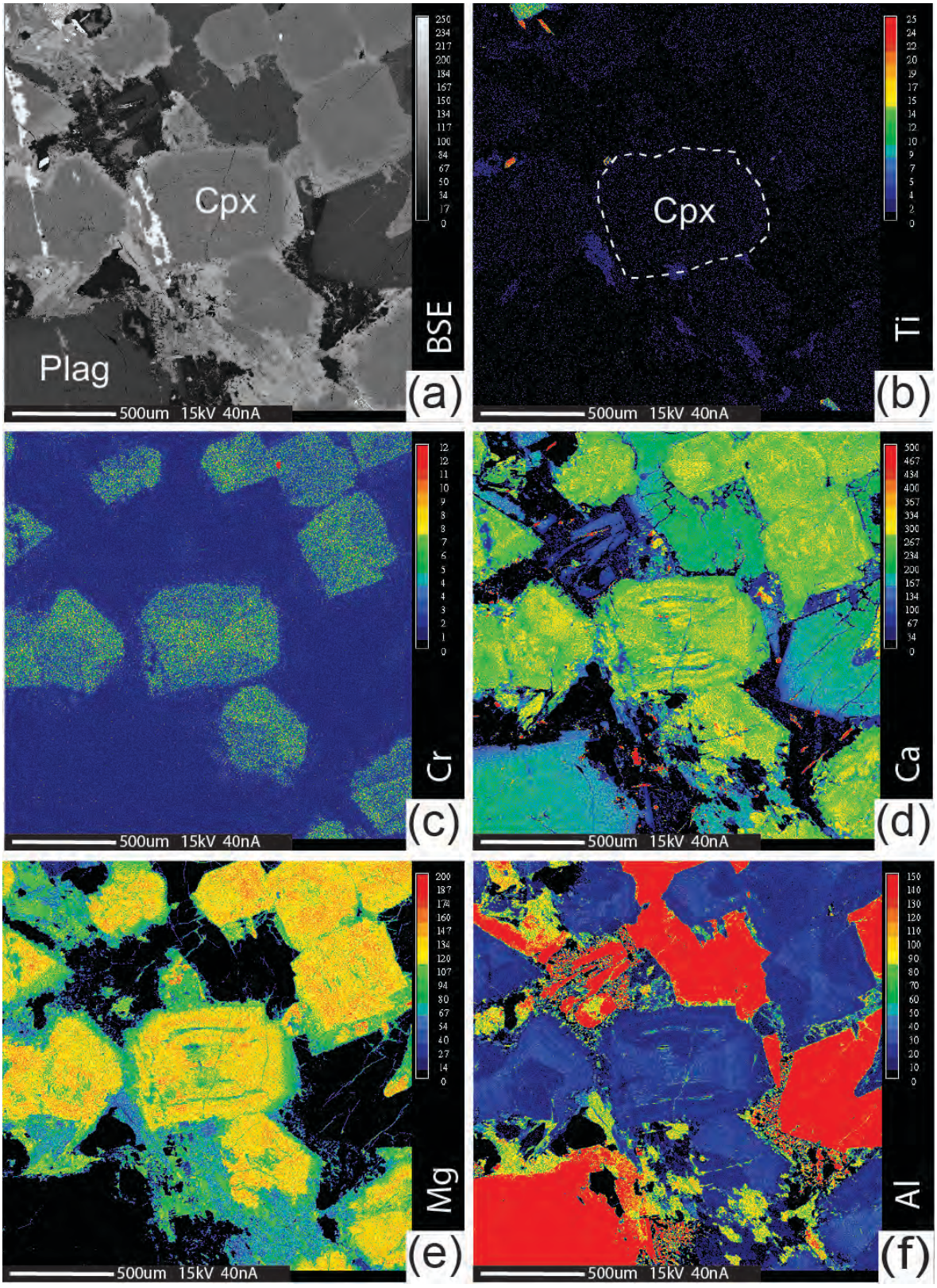

Fig. 4.6: BSE and element maps of sector-zoned clinopyroxenes from the CPZ: (a) BSE, (b) Ti, (c) Cr, (d) Ca, (e) Mg, (f) Al. Zones characterise the hourglass style sector-zoning with 2-3 times more enrichment in both Cr and Al. Additional element maps are included in appendix E7-1.

4.4.1.4 Clinopyroxene Zone (CPZ)

The CPZ is ~1 m thick. The diffuse base of the CPZ is characterised by a drop in the mode of olivine (to ~5%), and a corresponding increase in the proportion of euhedral cumulus clinopyroxene (~0.5-1 mm) to ~30-40%. The euhedral clinopyroxene crystals are often sector-zoned (Fig. 4.6) and are distributed as trains of grains that may record its formation in some type of channel (Fig. 4.7). Between these trains of sector-zoned clinopyroxene is a gabbroic matrix consisting of serpentinised olivine (~5%), euhedral-subhedral clinopyroxene and interstitial plagioclase with subordinate interstitial clinopyroxene. There is minor (< 5%) magnetite and ilmenite, as well as accessory amphibole and biotite.

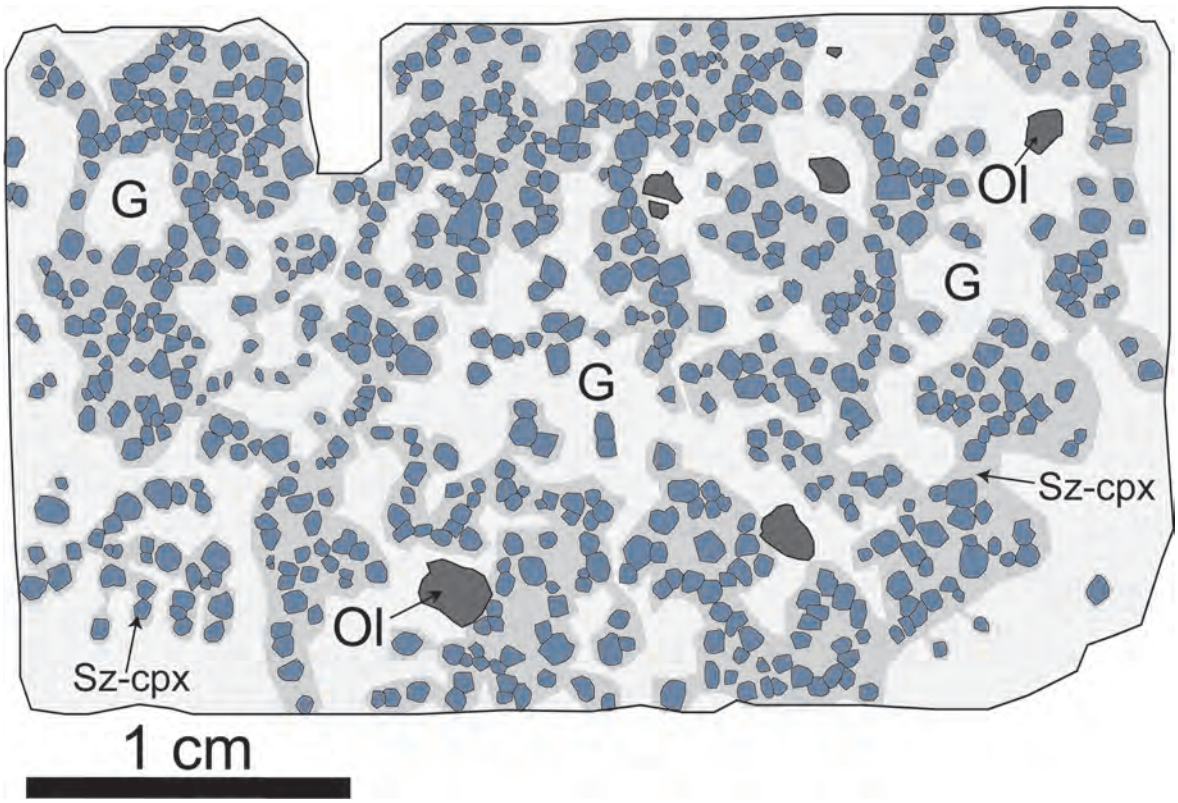

Fig. 4.7: A digitised version of a thin section from the CPZ (~8 m), which shows how the sector-zoned clinopyroxene (Sz-cpx) may form an interconnected network. The lighter grey is the gabbroic matrix (G) consisting of cumulus clinopyroxene (+ low-Ca pigeonite) and interstitial plagioclase, and minor (< 5%) Fe-Ti oxides. The gabbroic matrix also includes minor (~5%) olivine (Ol), which has been completely serpentinised. The darker grey surrounding the sector-zoned clinopyroxene outlines the morphology of these 'trains'.

4.4.1.5 Dolerite Zone (DZ)

The DZ is characterised by the absence of olivine and modal increases in plagioclase (from ~25% in the OZ to ~40% in the DZ) and clinopyroxene (from ~30% in the OZ to ~40% in the DZ). The DZ is also marked by a change in the morphology of plagioclase, from subhedral-anhedral interstitial textures to coarser (~2-3 mm) lath-shaped crystals that mostly form doleritic intergrowths with clinopyroxene. Around 5-10% of the plagioclase/clinopyroxene mode is comprised of cumulus crystals that do not display intergrowth textures. Full thin section scans show domains of sub-ophitic dolerite with varying grain sizes (varitextured), with coarser pegmatitic patches (~5 mm plagioclase & ~3-4 mm clinopyroxene) and finer-grained domains (~2-3 mm plagioclase & ~1-2 mm clinopyroxene) present in the DZ.

Clinopyroxene is typically euhedral-subhedral and intergrown with plagioclase, but both augite and low-Ca pigeonite also occur as separate cumulus crystals. Low-temperature alteration is more common in the DZ compared with other zones of the LPS, with plagioclase and clinopyroxene being partly altered to fine-grained albite and saussurite, or chlorite and actinolite (respectively). This is interpreted to represent deuteric alteration caused by volatile exsolution during the final stages of LPS crystallisation. Olivine was not observed in the DZ, but sparse orthopyroxene grains (~5-10%) in the lower DZ may be pseudomorphous after olivine. Interstitial ilmenite and magnetite is present (~5-10%) as are interstitial sulphides (~5%), with associations of pyrrhotite-pyrite in the lower DZ grading into associations of pyrite-chalcopyrite in the upper DZ. Minor accessory amphibole and biotite occur throughout the DZ, and may be associated with interstitial granophyre in the uppermost DZ (~19-20 m height). Also, in the uppermost DZ, long (~5-10 mm), blade-like clinopyroxene crystals are present with preferred growth directions roughly perpendicular to the upper contact of the LPS (element maps are included in the appendix E7-1).

4.4.1.6 Upper Border Zone (UBZ)

The UBZ (from ~20 m to ~21 m height) consists largely of fine-grained (< 1 mm) plagioclase and clinopyroxene dendrites. There are also coarser subhedral-anhedral

clinopyroxene grains (~1-2 mm), which shows both sector-zoning and complex concentric zoning, locally with sieve-textures (element maps included in appendix E7-1). No olivine phenocrysts (nor its pseudomorphs) were observed in the UBZ.

4.4.1.7 Upper Chilled Margin (UCM)

The LPS at its upper contact with the Jago Bay Formation carbonate is similar to the LCM in that it is a very fine grained, almost glassy, chilled contact. It contains ~5% olivine phenocrysts (~1-2 mm) that have been completely pseudomorphed by secondary serpentine. The groundmass appears to consist of very fine-grained dendrites, but it is more altered in comparison to the LCM. A few amygdules (< 5%; ~2 mm) are filled with biotite and chlorite.

4.4.2 Mineral chemistry

The main silicate phases present in each layer in the LPS were analysed using the electron microprobe. Chemical zonations were mapped to constrain the crystallisation history of the LPS. We use ‘core’ when referring to the central region of a crystal; ‘mantle’, for the intermediate part between the core and rim (often with weak compositional gradients); and ‘rim’ for the strongly zoned edges of a crystal. We use ‘primocryst’ when we refer to euhedral cumulus crystals, which are typically ≥ 1 mm in size, and ‘phenocryst’ for euhedral crystals in the chills and border zones.

4.4.2.1 Olivine

Compositional variations of olivine in the LCM, LBZ and OZ are summarised in Fig. 4.8. Variations in Fo (molar Fo = 100 x Mg/[Mg+Fe^{2+}]) are typically correlated with olivine NiO (wt%) contents.

Olivine phenocrysts in the LCM are normally zoned with near-constant core and mantle compositions and narrow, evolved rims. The average core and rim compositions are Fo_{87} and Fo_{82}, respectively. The cores and mantles of olivine phenocrysts in the LCM have an average NiO content of 0.32 wt%, whilst the rims have a lower NiO content of 0.28 wt%.

Some euhedral olivine phenocrysts show subtle core to mantle increases in Fo-content (~0.3 & 0.4 mol% increases) followed by decreasing Fo at the rim. A small olivine phenocryst in the LCM displays unusually strong zoning from Fo_{86} (0.28 wt % NiO) in the core to Fo_{75} (0.24 wt% NiO) at its rim.

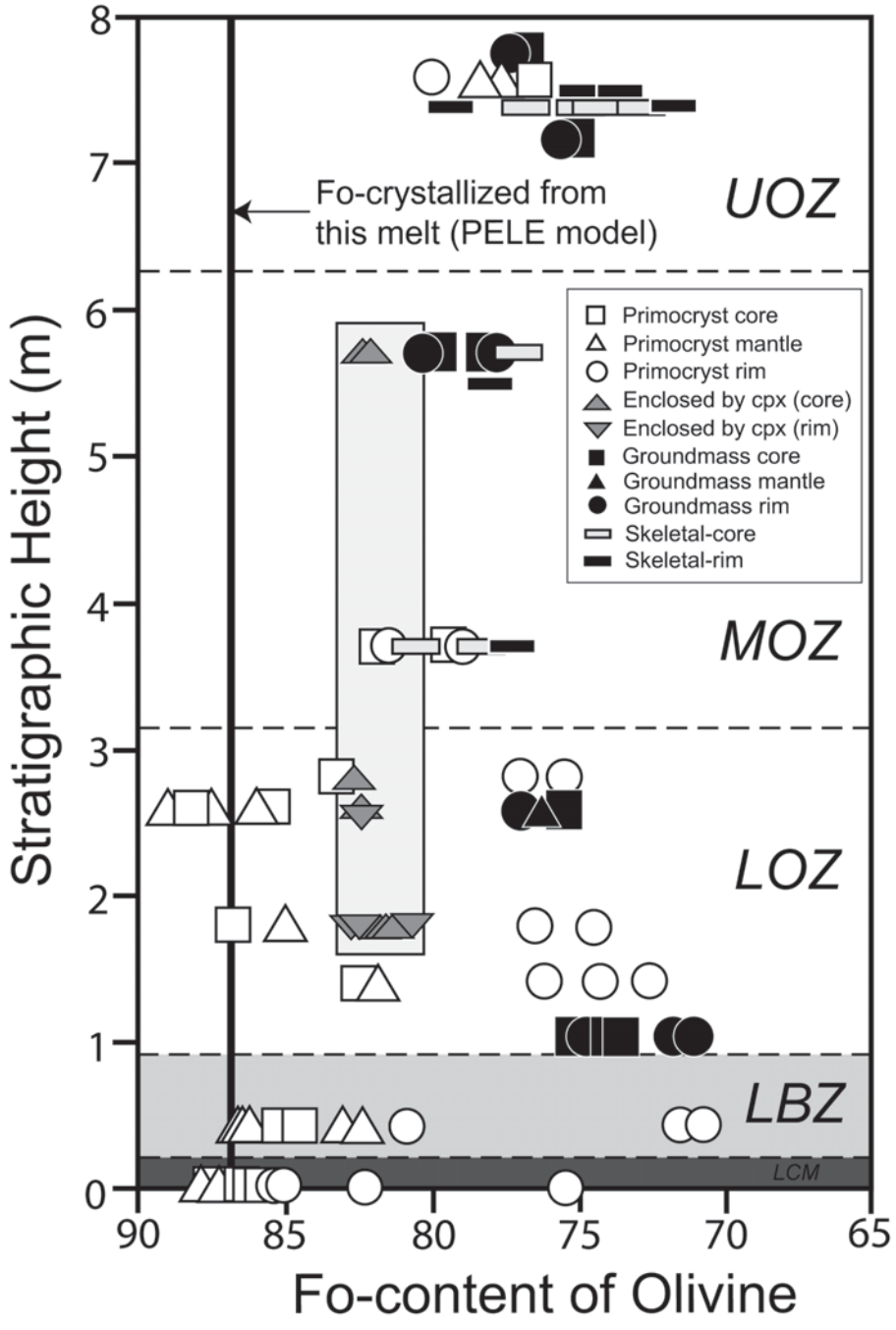

Fig. 4.8: Stratigraphic column showing olivine compositional variations of molar forsterite (Fo) content, through the LCM, LBZ and OZ, which is further subdivided into the lower OZ (LOZ); middle OZ (MOZ); and upper OZ (UOZ). The grey box covers the compositional range of olivines that are enclosed by clinopyroxene, which is tightly clustered around $Fo_{83\text{-}81}$. 'This melt' refers to the lower chill composition. NiO (wt%) olivine compositions are closely coupled with olivine Fo-compositions. NiO (wt%) contents are coupled with Fo, in that they show the same zoning patterns. NiO data is provided in appendix xx.

In the LBZ, the average core composition of olivine phenocrysts is Fo_{85} (0.29 wt% NiO). Many olivine phenocrysts in the LBZ show weak reverse zoning from core to mantle (~1 mol%), but with little corresponding change in the NiO content (average ~0.32 wt%). Olivine commonly shows strong normal zoning with an average rim composition of Fo_{75} (0.2 wt% NiO).

In the LOZ, olivine primocrysts have core compositions ranging between Fo_{88} and Fo_{82} (0.4-0.25 wt% NiO). Smaller olivine chadacrysts (enclosed by clinopyroxene oikocrysts) have systematically lower Fo-contents and a restricted range of compositions with an average core composition of Fo_{83} (0.25 wt% NiO) and an average rim composition of Fo_{81} (0.2 wt% NiO). Groundmass olivine surrounded by plagioclase has still more evolved compositions with average core and rim compositions of Fo_{81} (0.21 wt% NiO) and Fo_{70} (0.1 wt% NiO), respectively. Most olivines in the LOZ are zoned. The larger olivine primocrysts commonly exhibit normal zoning with near-constant core and mantle compositions (Fig. 4.8), and narrow Fe-rich rims as evolved as Fo_{77-75}. Chadacrystic olivines enclosed by clinopyroxene oikocrysts are mostly normally zoned (typically a ~1-2-mol% change from core to rim) except for a weakly reverse-zoned olivine grain, which has a core composition of Fo_{82} (0.2 wt% NiO) that increases to Fo_{83} (0.24 wt% NiO) at its rim. Groundmass olivines that are surrounded by plagioclase are generally normally zoned and reach very low Fo compositions at the rims (~Fo_{77-70}), but may also show weak reverse zoning with core to rim increases of ~0.5 mol% (with NiO contents < 0.2 wt% for both core and rim).

In the MOZ and UOZ, the relative proportion of olivine primocrysts decreases, whereas the total olivine mode increases (up to ~55%). Olivines enclosed by clinopyroxene oikocrysts become less common, but where present they have a restricted compositional range (Fo_{83-81}). In the MOZ, the average Fo composition of groundmass olivines is generally more primitive (~Fo_{80}) than the average groundmass olivines from the LOZ (~Fo_{75}). Subtle (~1 mol%) reverse zoning is observed in both groundmass and hopper olivines in the MOZ.

In the UOZ, common hopper olivines have core compositions as low as Fo_{73} and commonly display reverse zoning with rims between Fo_{80-77} (Fig. 4.8). An olivine primocryst in the UOZ displays reverse zoning (Fig. 4.9) with a core to rim increase from

Fo_{77} (0.16 wt% NiO) to Fo_{80} (0.23 wt% NiO). Groundmass olivine in the UOZ shows reverse zoning for Fo, with cores of ~Fo_{77} and rim compositions ranging between $Fo_{80\text{-}78}$ (with NiO content for core and rim typically < 0.22 wt%).

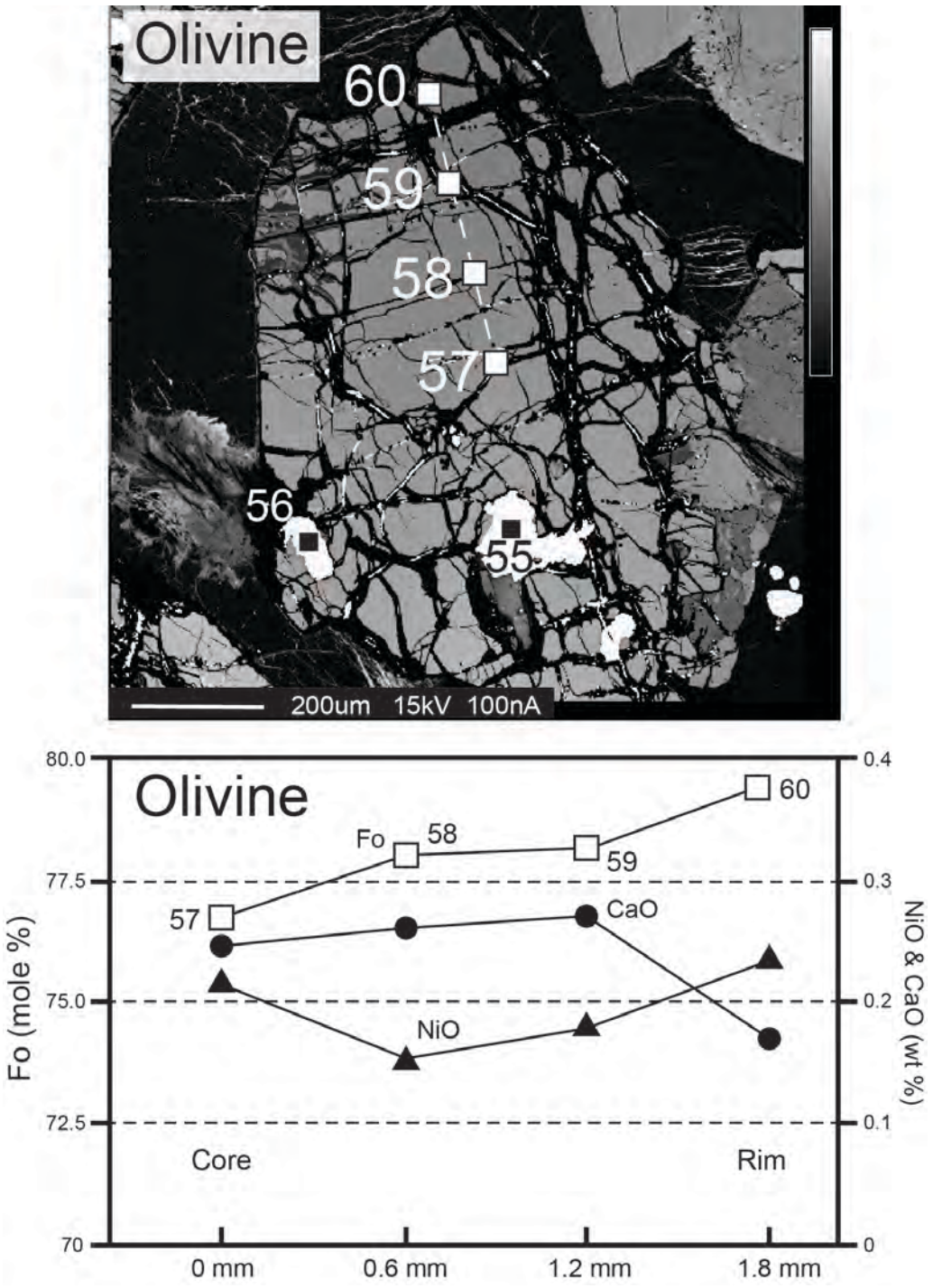

Fig. 4.9: A BSE image and corresponding microprobe traverse of an olivine primocryst from the UOZ. Spot analysis numbers are plotted on the image and correspond to the microprobe traverse. The spot analysis numbers for the Cr-spinel inclusions are also plotted (data in appendix E5). The olivine is reversely zoned, with increasing Fo towards the rim (increasing from Fo_{77} to Fo_{80}), as well as increasing NiO (wt%) and decreasing CaO (wt%) at the rim.

4.4.2.2 Cr-spinel

Cr-spinel microphenocrysts enclosed by phenocrystic olivine in the LCM have compositions that depend on their location in the host olivine phenocryst. For example, a Cr-spinel in the core of an olivine phenocryst has a Cr# (=100 x Cr/[Cr+Al]) of 50, while a Cr-spinel included in the rim of the same olivine has a higher Cr# of 58. Neither Fe3# (=100 x Fe^{3+}/[Fe^{3+}+Cr+Al]) nor Fe2# (=100 x Fe^{2+}/[Mg+Fe^{2+}]) for these LCM Cr-spinel microphenocrysts show any variation, however.

In the LOZ, Cr-spinels inclusions have very similar compositions (Cr# 73-46; Fe3# 18-10; Fe2# 84-41) to those of the LCM/LBZ, whereas they show more significant compositional variations in the UOZ. For example, a Cr-spinel in the core of a reversely zoned UOZ olivine primocryst (Fo_{77}; Fig. 4.9) has a Cr# of 67, Fe3# of 67 and Fe2# of 84, whereas the Cr-spinel located in the olivine rim (Fo_{80}; Fig. 4.9) has a higher Cr# of 71, and markedly lower Fe3# of 59 and a lower Fe2# of 80.

4.4.2.3 Clinopyroxene

The Mg# (molar Mg# = 100 x Mg/[Mg+Fe^{2+}+Mn]) of clinopyroxene versus stratigraphic height is summarised in Fig. 4.10. The Mg# of groundmass clinopyroxene in the LBZ is relatively low ($Mg\#_{77-70}$) compared with clinopyroxenes of the overlying OZ. Most LBZ clinopyroxene crystals are normally zoned (decreasing Mg# towards the rims), but some are reversely zoned, with Mg# increasing by up to ~3 mol% towards the rim (Fig. 4.11b).

In the OZ, clinopyroxene core compositions show little variation with stratigraphic position (Figs 4.10, 4.11a & Fig. 4.12) with $Mg\#_{86-83}$ (average Cr_2O_3 ~0.8 wt% and TiO_2 ~0.4 wt%). Clinopyroxene oikocrysts have near-constant core-mantle compositions, but may have narrow Fe-Ti-rich rims (~$Mg\#_{75}$; Fig. 4.11a; also see Fig. 4.5b, d). The evolved rim compositions of oikocrystic and cumulus clinopyroxene in the OZ overlap with the compositions of interstitial OZ clinopyroxene, and with those of LBZ groundmass clinopyroxene (Fig. 4.10). Some LOZ clinopyroxene oikocrysts show subtle sector-zoning, visible on element maps of Cr, Al and Mg (Fig. 4.5c, e, f). Cr and Al (Fig. 4.5c, e) appear

to show similar behaviour and are slightly enriched in a N-S sector, whilst Mg (Fig. 4.5f) is more enriched in the E-W sector of the clinopyroxene.

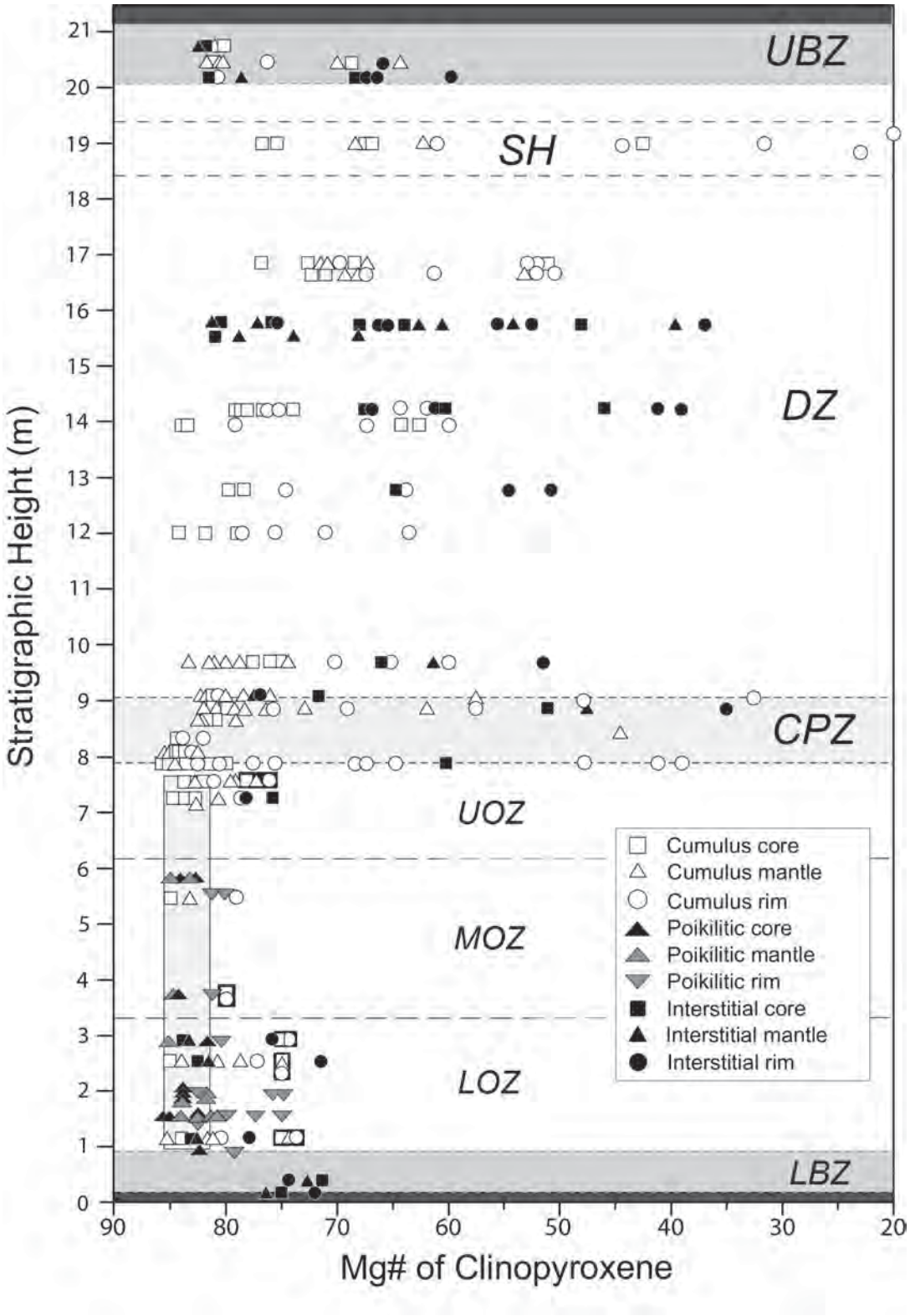

Fig. 4.10: Stratigraphic column showing clinopyroxene compositional variations in molar magnesium content (Mg# = 100 x Mg/[Mg+Fe^{2+}+Mn]) through the entire LPS. The grey box in the OZ covers the range of poikilitic and cumulus clinopyroxene core compositions in the OZ (between Mg#85-82), illustrating their restricted range in composition.

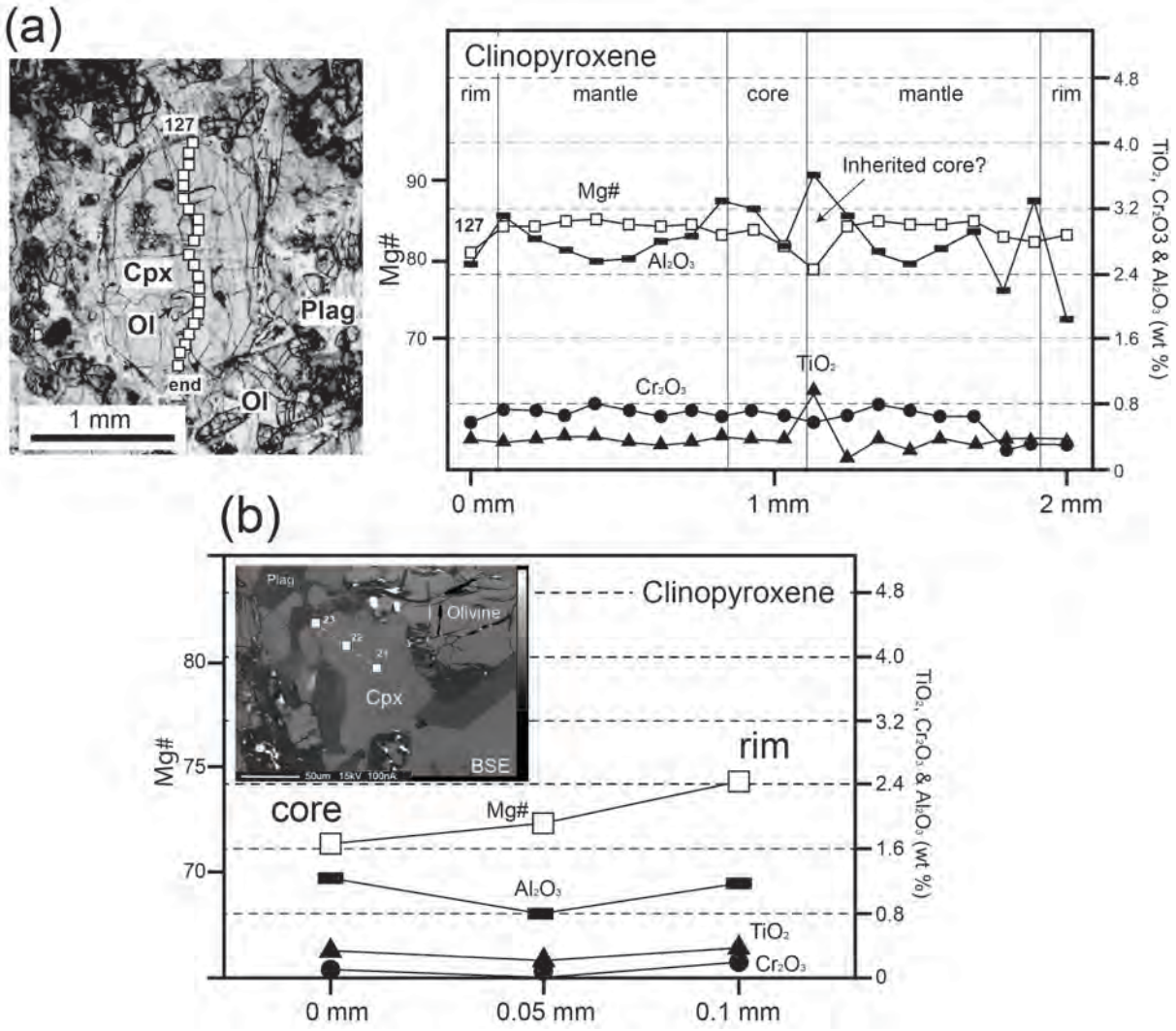

Fig. 4.11: (a) Poikilitic clinopyroxene crystal (~1.5 mm) from the LOZ (plane-light photomicrograph), with the corresponding microprobe traverse. The profile starting at 127 traverses the crystal in a N-S direction and avoids the olivine chadacrysts. The clinopyroxene is normally zoned with narrows rims. (b) A subhedral (interstitial?) clinopyroxene from the LBZ, which is adjacent to an olivine phenocryst (BSE image). The corresponding microprobe traverse exhibits increasing Mg# towards its rim (i.e. reverse zoning).

In the CPZ, euhedral cumulus clinopyroxenes, which are often sector-zoned, have core compositions similar to those of OZ clinopyroxene (Mg#83: Fig. 4.10), whilst rims extend to compositions that are more Fe-rich (Mg#70-30) than clinopyroxene rims in the underlying OZ. The sector-zoning of clinopyroxene is apparent on element maps (Fig. 4.6), with different zones showing weak contrasts in Cr and Al abundance (Fig. 4.6c, f), whereas Ca and Mg show no clear inter-zone differences (Fig. 4.6d, e). Cr_2O_3 typically decreases from ~0.6 wt% in the cores to ~0.2 wt% in the rims, whilst Al_2O_3 increases from ~1.8 wt% in the cores to ~2 wt% at the rims. TiO_2 contents also increase slightly from the cores (~0.4 wt%) to the rims (~0.5 wt%); which contrasts with the much greater increase in

TiO_2 (to ~1 wt%) seen in OZ clinopyroxene rims. We suspect the deficit in TiO_2 of CPZ clinopyroxene rims may be due to sequestration of TiO_2 into interstitial ilmenite in the case of the CPZ. The CPZ grades upward over ~0.8 m into slightly more evolved clinopyroxene core compositions (Mg#80), which have reversely zoned mantles (up to Mg#83), suggesting interaction with a more MgO-rich melt. The presence of wide, strongly evolved rims on all forms of clinopyroxene in the CPZ suggests that all have interacted with abundant, late, evolved pore melts during the final stages of crystallisation, possibly suggesting higher trapped melt fractions in these rocks.

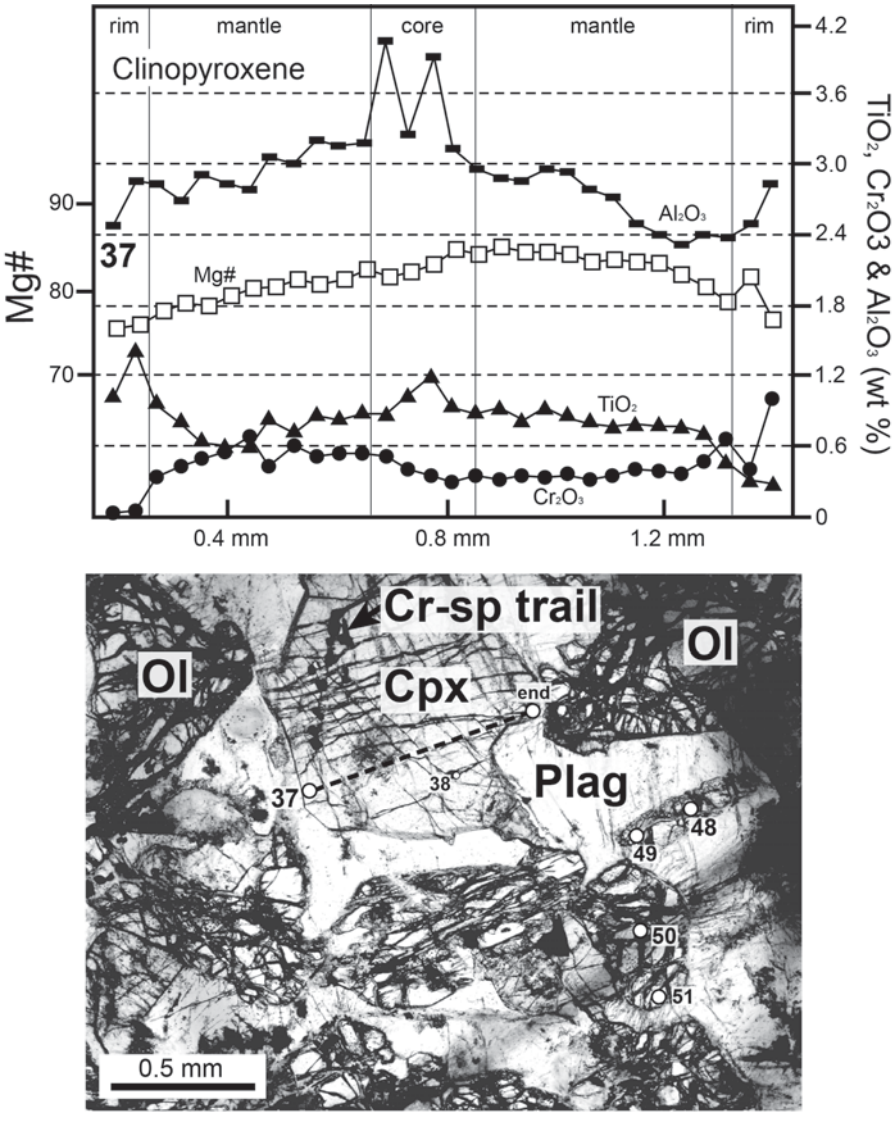

Fig. 4.12: A microprobe traverse across a subhedral clinopyroxene crystal (37), which is surrounded by interstitial plagioclase (the corresponding photomicrograph is in plane-light). The clinopyroxene is normally zoned with narrow Fe-enriched rims. Cr_2O_3 (wt %) shows increases towards one rim, but decreases towards the other. A hopper olivine (48 to 49) surrounded by plagioclase shows reverse zoning (core $Fo_{77.6}$ to rim $Fo_{79.5}$: data in appendix E2).

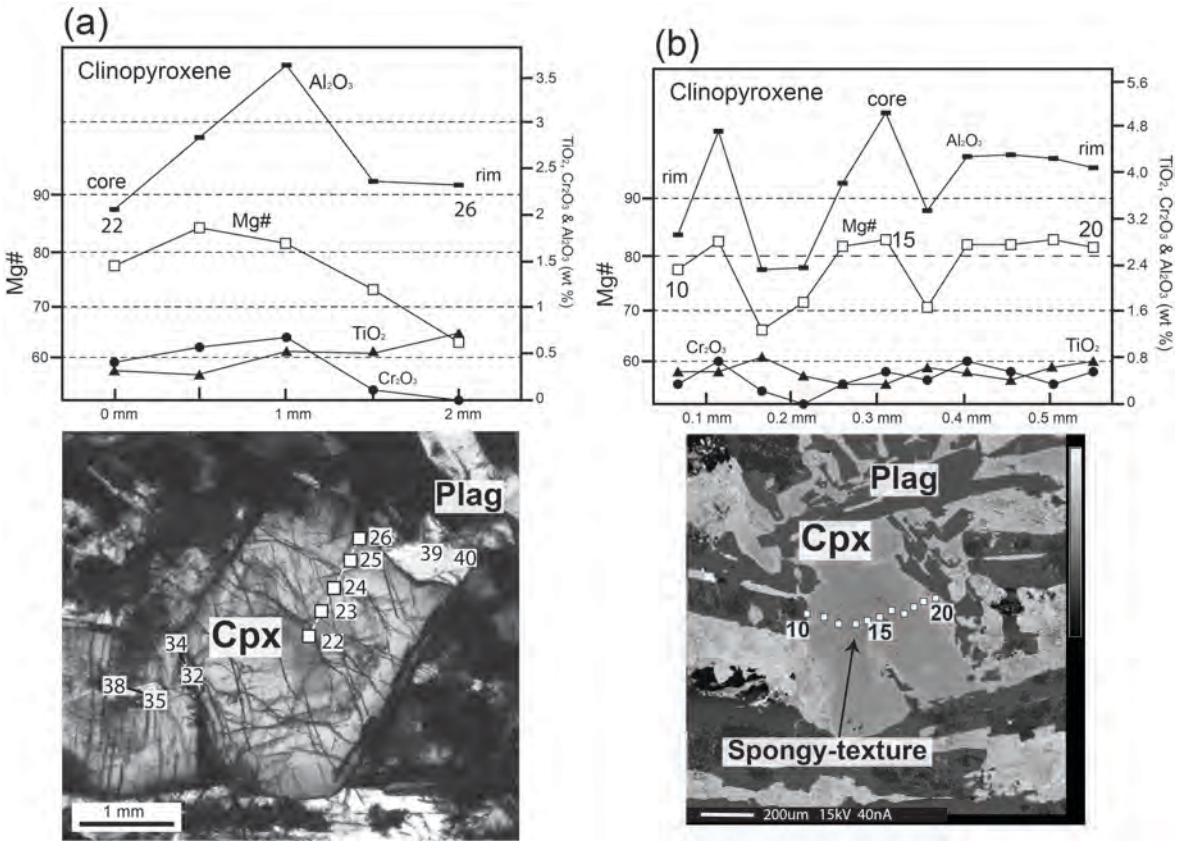

Fig. 4.13: (a) Plane-light photomicrograph of a euhedral clinopyroxene crystal from the DZ, with the corresponding microprobe traverse (23 to 26). The clinopyroxene has increasing Mg# and Cr_2O_3, within its mantle before developing normal zoning at its rim, suggesting it may have mixed with more primitive melt during crystallisation. (b) A BSE image of a clinopyroxene crystal from the UBZ that has a sieve-textured core/mantle. The microprobe traverse (10 to 20) shows complex zoning with a high-Mg# core, followed by low-Mg# mantles and outwardly decreasing Mg# at the rims, a pattern that is resembled by Al_2O_3.

In contrast to the muted variations of clinopyroxene compositions in the OZ, clinopyroxene in the DZ shows systematic up-section cryptic variations (Fig. 4.10). At the base of the DZ, clinopyroxene compositions overlap with those of clinopyroxene from the OZ and CPZ (~Mg#84). A cumulus-textured clinopyroxene at the base of the DZ (Fig. 4.13a) shows complex zoning, with a core composition of Mg#84 that increases outward gradually to Mg#85 and then shows a sudden decrease out to Mg#63 in the rim. This pattern of Mg-enrichment in the mantle of cumulus clinopyroxene occurs sporadically in the DZ (Fig. 4.10). More generally, clinopyroxene displays strong normal core to rim zoning throughout the DZ with changes in Mg# ranging between ~10-20 mol%. Rims of euhedral clinopyroxene overlap with the compositions of evolved interstitial clinopyroxene in the DZ. Interstitial clinopyroxene from the DZ is more evolved than interstitial clinopyroxene from the OZ. In the upper DZ, clinopyroxene (including bladed clinopyroxene crystals) have core compositions of Mg#75 and strong normal zoning at the

rims (to Mg#30-20). The peak in clinopyroxene Fe-enrichment, just below the UBZ, may represent a type of ‘sandwich’ horizon.

The UBZ contains rare, euhedral (~1 mm), sector-zoned clinopyroxene with compositions of Mg#81 in the crystal core (Fig. 4.13b), with a narrow Fe-Ti-enriched rim (element maps of this crystal are included in appendix E7-1). This specific crystal is sieve-textured with mantle depletions in Mg# (Mg#70-67; Fig. 4.13b) relative to the rims, that may indicate a thermal spike, or a reaction with more primitive melt. Interstitial clinopyroxene is intergrown with plagioclase and has evolved compositions (~Mg#67).

4.4.2.4 Plagioclase

Plagioclase anorthite (An; molar An =100 x Ca/[Ca+Na+K]) content versus stratigraphic height is shown in Fig. 4.14. Plagioclase dendrites within the LCM groundmass have relatively low An values, averaging An_{64}. In the LBZ, the coarser plagioclase dendrites become slightly more primitive with compositions of ~An_{71}.

Plagioclase has core compositions of An_{73-68} throughout the OZ. Most grains show normal zoning with sporadic occurrences of reverse zoning. Plagioclase rim compositions extend to An contents as low as An_{58}, with the lowest An values adjacent to olivine crystals. Core compositions of interstitial plagioclase in the CPZ (Fig. 4.15a) are between An_{72-70}, whereas rims are strongly evolved (~An_{40}). CPZ plagioclase core compositions overlap the composition of OZ plagioclase. In the CPZ, minor euhedral cumulus plagioclase is more primitive with core and mantle compositions up to An_{76}.

Plagioclase core and mantles are typically ~An_{70-60} in the DZ, with strongly evolved rims as low as An_{45}. Rare, cumulus-textured plagioclase in the lower DZ has some of the most primitive An compositions (An_{77-76}; Fig. 4.15b) in the LPS. In some plagioclase crystals in the middle DZ, the cores are mantled by higher An plagioclase suggesting interaction with a more primitive melt prior to the initiation of *in-situ* fractional crystallisation. The core and rim compositions with the lowest An values occur in the upper DZ (Fig. 4.14) where clinopyroxene has the lowest Mg# (Fig. 4.10), corresponding to the inferred position of the sandwich horizon.

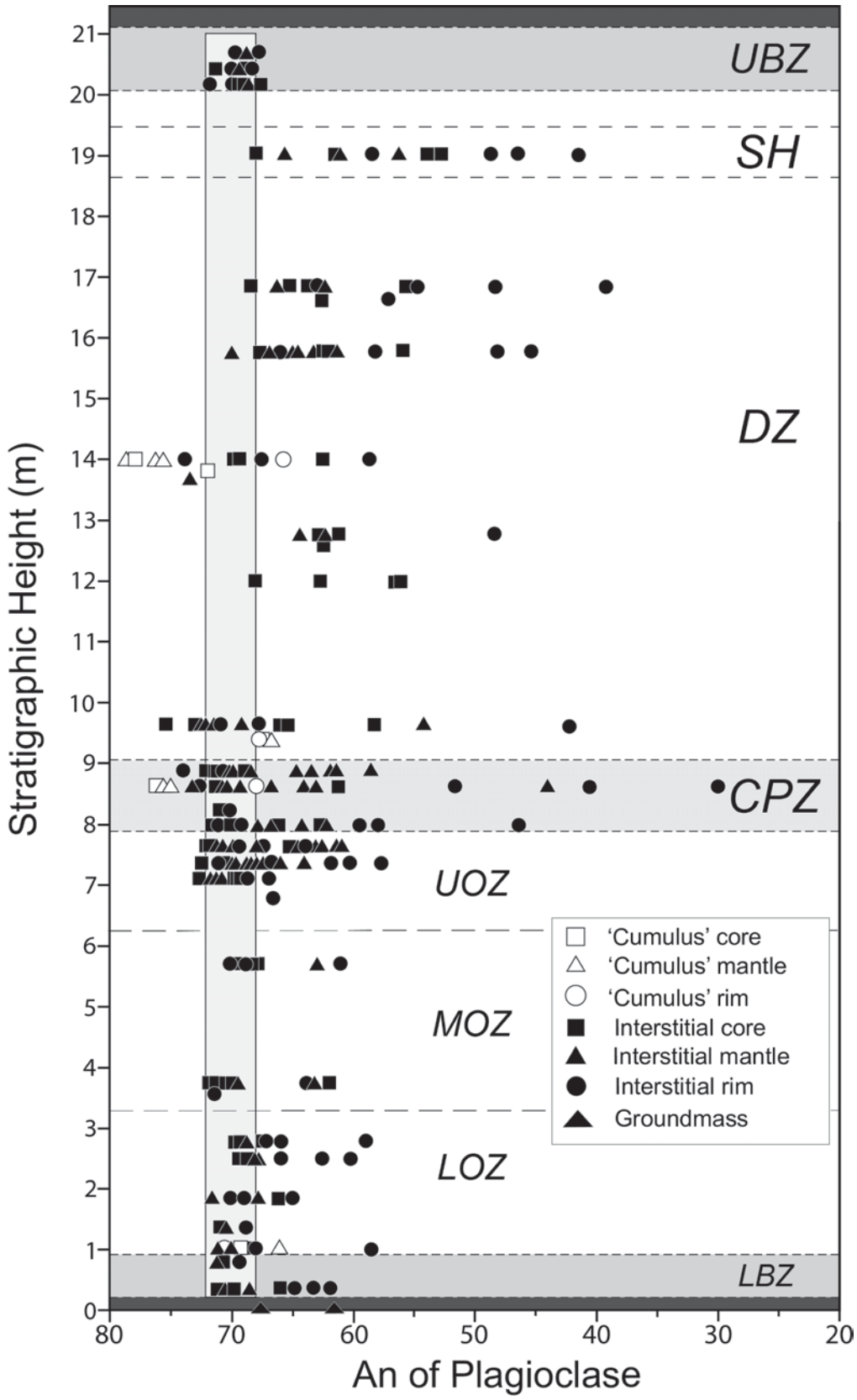

Fig. 4.14: Stratigraphic column showing plagioclase compositional variations in molar anorthite (An = 100 x Ca/[Ca+Na+K]) content through the entire LPS. The vertical grey box covers the typical range of core compositions throughout the LPS (An_{72-68}).

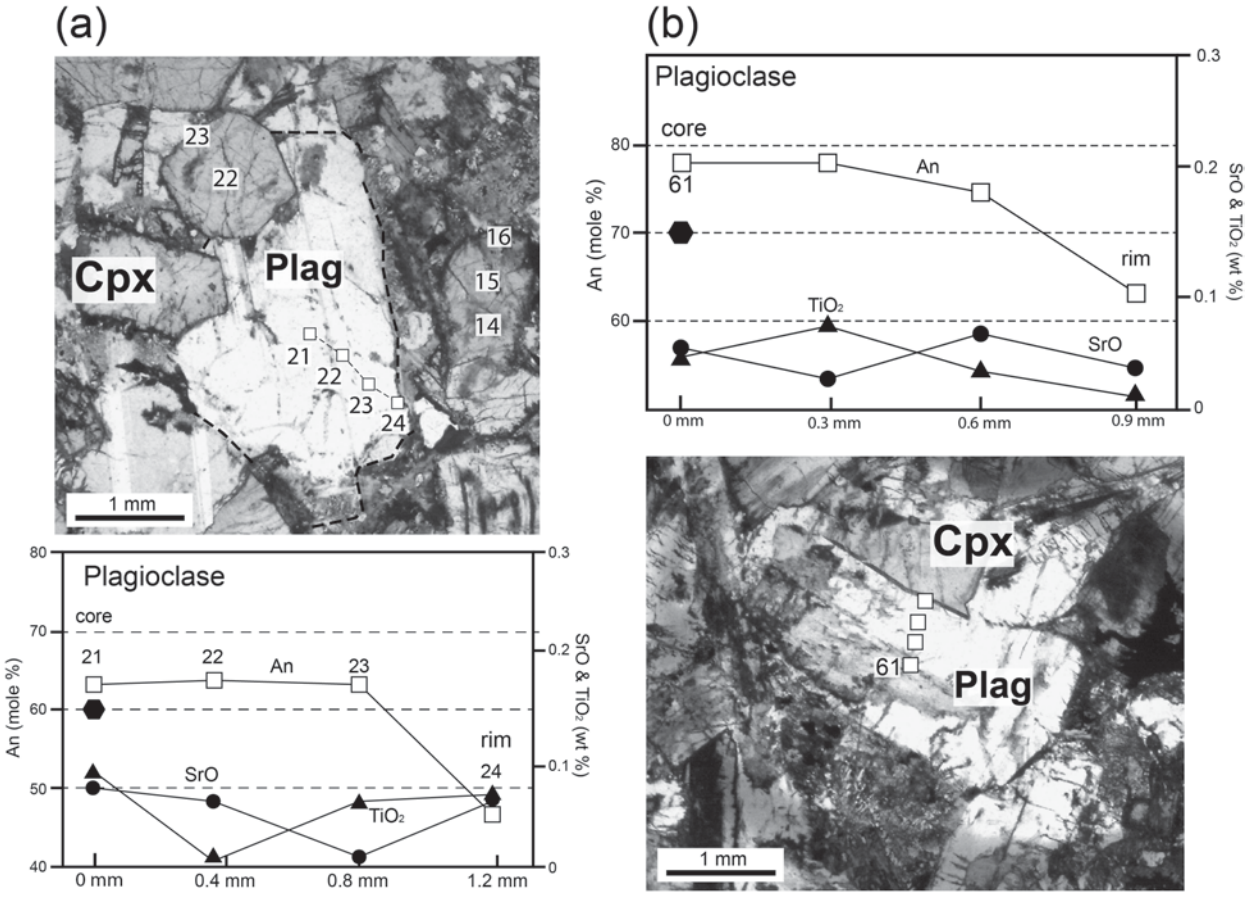

Fig. 4.15: (a) Plane-light photomicrograph of an interstitial plagioclase crystal from the CPZ with the corresponding microprobe traverse. A ~1 mm sized euhedral sector-zoned clinopyroxene can also be seen (22 to 23). The plagioclase is strongly normally zoned with An values of < 50 mol% at the rims. (b) A plane-light photomicrograph of a euhedral plagioclase lath (possibly cumulus?) in the DZ, with the corresponding microprobe traverse (61). This plagioclase has the highest core An (An_{77}) content recorded in the LPS and is normally zoned towards its rim.

A fine-grained (~0.2 mm) plagioclase dendrite in the UBZ is reversely zoned at its rim (Fig. 4.16) and, as for clinopyroxene (Fig. 4.13b), may record a temperature increase and/or a primitive replenishment event in the UBZ.

4.4.3 Calculated melt chemistry

The Fe/Mg ratio of a crystal can be used to calculate the Fe/Mg of its equilibrium melt if the Fe=Mg exchange coefficient is known (Roeder & Emslie, 1970). Data from Franklin sill chilled margins and the coeval Natkusiak flood basalts were used to parameterise covariations of melt Fe/Mg ratio with melt MgO, allowing melt MgO in equilibrium with both olivine and clinopyroxene to be calculated (model anchors are included in appendix D).

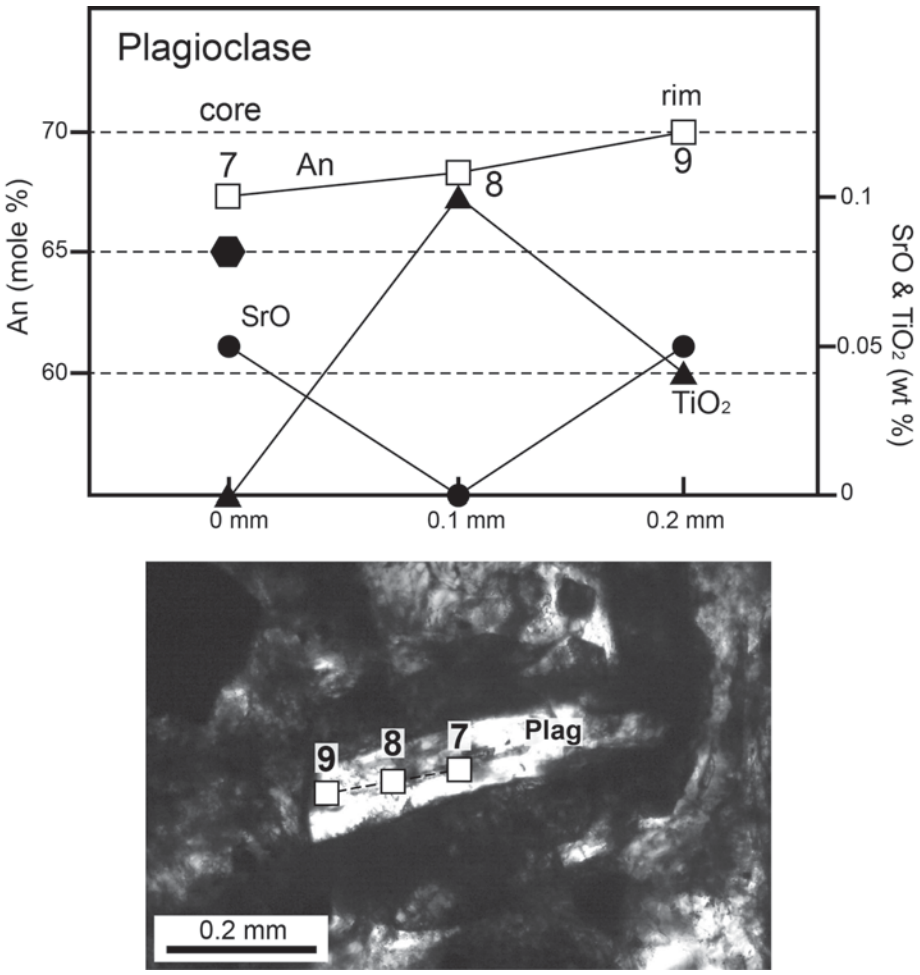

Fig. 4.16: A plane-light photomicrograph and microprobe traverse (7 to 9) of a plagioclase crystal in the UBZ. This plagioclase is reversely zoned with increasing An towards its rim.

4.4.3.1 Olivine

An exchange coefficient (Kd) of 0.34 as experimentally determined by Matzen *et al.* (2011) was used to calculate the exchange of molar FeO and molar MgO between olivine and melt. The cores and mantles of euhedral olivine phenocrysts in the LCM yield model melts with up to ~13 wt% MgO. The narrow evolved rims on these grains yield model melts of ~11-10 wt% MgO, closer to the LPS chill composition. The most evolved olivine phenocryst rims yield model melts of ~6.5 wt% MgO. In the LBZ, phenocrystic olivines have cores equivalent to model melts of ~11 wt% MgO, and have narrow, Fe-rich rims equivalent to model melts of ~5 wt% MgO.

Olivine primocryst cores from the LOZ yield model melts between ~13.5-10 wt% MgO, while their rims yield a melt range of ~8-6 wt% MgO. Olivine chadacrysts enclosed by clinopyroxene oikocrysts yield magnesian model melts between ~10-8.5 wt% MgO. A reversely zoned olivine chadacryst has a core in equilibrium with a model melt of 9.8 wt% and a rim in equilibrium with a model melt of 10.2 wt% MgO. Groundmass olivines in the LOZ are in equilibrium with model melts ranging between ~7-5 wt% MgO. In the UOZ, primocrystic olivine and hopper olivine cores yield evolved model melts ranging between ~8-5 wt% MgO. A reversely zoned olivine primocryst (Fig. 4.9) in the UOZ has a core in equilibrium with a model melt of ~6.3 wt% MgO, whereas its rim yields a model melt of ~8.5 wt% MgO. Groundmass olivines in the MOZ and UOZ yield model melts of ~8 wt% MgO.

4.4.3.2 Clinopyroxene

To calculate the MgO and FeO of the melt in equilibrium with clinopyroxene we used the clinopyroxene Fe/Mg ratio and a clinopyroxene-melt Kd calculated using equation 14 from Bédard (2010). Interstitial LBZ clinopyroxene yields evolved model melts of ~5-3.5 wt% MgO. In the LOZ and MOZ, clinopyroxene oikocryst cores yield primitive model melts between ~9-7 wt% MgO, as do euhedral cumulus clinopyroxene cores in the UOZ. All clinopyroxene rims in the OZ yield Fe-rich compositions with model melts < 7 wt% MgO. The cores of cumulus clinopyroxenes from the CPZ yield compositions (~9-6 wt% MgO), similar to the range of model melts recorded in OZ clinopyroxene, whereas their evolved rims and interstitial clinopyroxene in the CPZ yield very evolved model melts with < 5 wt% MgO. Model melts calculated from the DZ clinopyroxene cores show cryptic up-section variation with melt MgO broadly ranging between ~8-1 wt%. In the UBZ, dendritic clinopyroxenes correspond to model melts ranging between ~7-1 wt% MgO. A coarser, sector-zoned clinopyroxene in the UBZ yields model melts of ~6.5 wt% MgO, with values of ~2 wt% MgO in the sieve-textured mantle and more primitive melts of ~5 wt% at its rims.

4.5 Discussion

4.5.1 Constraints provided by the mineral-chemical data and inverse melt compositions

Olivine and clinopyroxene in the LPS yield a broad range of model melt MgO compositions. When coupled with the textural observations, these allow us to track the chemical evolution of melts within the LPS. The cores of euhedral olivine phenocrysts and primocrysts within the LCM, LBZ and LOZ yield the most primitive model melt MgO compositions (~13.5-10 wt% MgO), equal or higher than the MgO content of their host chills (10.3 wt%), but similar to the most primitive chilled margins from other Type-1 Franklin sills (Bédard *et al.*, 2013). The majority of olivine phenocryst rims from the LCM as well as olivine phenocryst cores from the LBZ are, however, in approximate equilibrium with the LCM composition. The model melt compositions in equilibrium with olivine chadacrysts included in clinopyroxene oikocrysts have MgO values between ~10-8 wt%. The melt values calculated to be in equilibrium with the most primitive poikilitic clinopyroxene (~9-8 wt% MgO) fall within this range of melt compositions. Since these clinopyroxene oikocrysts contain both normally and reversely zoned olivines, the clinopyroxene oikocrysts in the OZ must have formed after some of their enclosed olivines were exposed to a higher-MgO melt.

The primitive melt values calculated from the cores of olivine and clinopyroxene are in stark contrast to the melts calculated from olivine cores in the UOZ. Melt values in equilibrium with UOZ olivine cores are as low as ~5 wt% MgO, whilst the rims extend to melt values of ~8 wt% MgO. These reversely zoned trends are seen in hopper olivines, groundmass olivines and rare primocrystic olivines in the UOZ. Reversely zoned primocrystic olivines contain Cr-spinels that mirror the Fo trend (Fig. 4.9). Cr-spinel hosted within the low-Fo olivine core has lower Cr# and higher Fe2# and Fe3# than the Cr-spinel hosted by the more primitive olivine rim. This pattern suggests that the Cr-spinel in the primocryst rim formed from a less evolved melt than the one in the core, similar to the host olivine primocryst zoning.

In addition to the common occurrence of reversely zoned olivines in the UOZ, groundmass olivines become more primitive upward in the OZ. In the LOZ, groundmass olivines typically have compositions of Fo_{75} (~5 wt% MgO model melt). This increases to Fo_{80} (~8 wt% MgO model melt) in the MOZ. MOZ and UOZ groundmass olivines are therefore in equilibrium with the rims of reversely zoned UOZ olivines, suggesting they may have crystallised from the same melt. The shift to more primitive groundmass olivine compositions upward through the OZ may indicate a change in the crystallisation conditions or differing proportions of trapped melt in this region of the OZ.

Recorded clinopyroxene model melt variations at the base of the DZ are in equilibrium with OZ clinopyroxenes (~9-7 wt% MgO), before becoming more evolved up-section to reach minimum MgO contents (< 4 wt% MgO) in the upper DZ (sandwich horizon). Rims to euhedral clinopyroxenes in the DZ are in equilibrium with DZ interstitial clinopyroxenes (~4-1 wt %). Throughout the LPS, clinopyroxene rims locally record extreme Fe-Ti-enrichment, presumably as pore melts evolved extensively through *in-situ* differentiation (*cf*. Humphreys (2009)). If the interstitial clinopyroxenes crystallised from late, evolved pore melt then this implies that the larger clinopyroxenes may also have crystallised or equilibrated with this melt. The upward evolution in clinopyroxene rim compositions (eventually to values of ~Mg#20) is matched by the plagioclase rim/interstitial plagioclase compositions (~An_{40}) suggesting the presence of a sandwich horizon, possibly as a result of the migration of evolved pore melt (Boudreau & Philpotts, 2002) towards the last part of the sill to solidify, i.e. the upper DZ. A coarse UBZ clinopyroxene crystal has a broader range of model melts (~7-4 wt% MgO) compared to dendrites in the LBZ (~4-3 wt% MgO) and may therefore be a ‘xenocrystic’ crystal that was carried in with the first pulse of LPS magma.

4.5.2 PELE modelling

To help constrain the crystallisation history of the sill, we ran the PELE program (Boudreau, 1999) using a chill with 10.3 wt% MgO (defined as the average chill composition of the LPS and related intrusions; clarified in chapter 5) as a starting composition. A fractional crystallisation model was run at a pressure of ~0.8 kbar, corresponding to the estimated height of the overlying stratigraphic column. Melt CO_2 was

set at 0.2 wt%, S at 0.12 wt% and H_2O at 0.2 wt%, and chromite was excluded from the assemblage (justifications are provided in the appendix E6-2). PELE predicts a liquidus at 1245°C where Fo_{88} olivine crystallises, values similar to compositions of olivine phenocrysts in the LCM. After ~8% olivine was extracted, PELE predicts that the melt cosaturates in clinopyroxene (Mg#87) and plagioclase (An_{80}) at ~7.5 wt% MgO (1175°C), at which juncture the composition of olivine is Fo_{84}. PELE predicts that olivine reaches compositions of Fo_{75} (similar to primocryst rims in the LOZ and the most evolved primocryst cores from the UOZ) at ~1115°C, at which point the sill would be 40% solidified, comprising 11% olivine + 16% plagioclase + 13% clinopyroxene + 60% pore melt with an MgO of 6 wt%. In conclusion, the crystallisation pathway predicted by PELE is broadly compatible with the observed compositions and textures of olivine in the LPS OZ. However, the most primitive model melts calculated to be in equilibrium with clinopyroxene (~9 wt%) exceed the melt MgO composition at which clinopyroxene becomes cosaturated according to the PELE model (~7.5 wt%). Conversely, the model melts calculated to be in equilibrium with most DZ clinopyroxene are in accord with the PELE results. We now discuss the role that fractional crystallisation may have played in the differentiation of the LPS.

4.5.3 The role of closed-system fractional crystallisation in the LPS

Mineral compositional trends in a related suite of igneous rocks are commonly explained by fractional or equilibrium crystallisation (Bowen, 1928). The classic example is the Skaergaard intrusion, which exhibits unambiguous mineralogical and cryptic mineral-chemical trends, interpreted to reflect closed-system fractional crystallisation of a single pulse of magma (Wager & Deer, 1939, McBirney, 1996, Tegner, 1997). In the LPS we see similar signs of compositional evolution that could be interpreted as being due to *in-situ* fractional crystallisation. Such an interpretation would imply that the sill was initially filled with an olivine + chromite phyric magma; that all of the olivine settled out to yield the OZ; that after the olivine settled out, cosaturation of clinopyroxene yielded the CPZ, followed almost immediately by plagioclase cosaturation and reaction of olivine to low-Ca pyroxene to produce the basal DZ. The diffuse inward trends seen in the DZ mineral chemistry of both clinopyroxene (Fig. 4.10) and plagioclase (Fig. 4.14) suggest that the DZ solidified mainly at the floor and reached its furthest chemical evolution in a sandwich horizon just

below the UBZ. In such a model, the systematic decrease in Fo from olivine primocrysts, to chadacrysts, to groundmass in a single thin section would record *in-situ* evolution of trapped pore melt that partly reacted with its cumulate matrix. While many aspects of such a scenario are plausible, the petrology of the LPS suggests a more complex differentiation history.

None of the main mineral species within the OZ exhibits trends suggesting systematic up-section fractional crystallisation by sequential crystallisation against the floor (Fig. 4.8, 4.10 & 4.14). Given the extreme compatibility of nickel in olivine (Arndt, 1977, Hart & Davis, 1978), nickel in accumulated olivine should show a marked and rapid up-section decrease, a pattern that is not observed in the LPS OZ. Alternatively, the uniform compositions of the various olivine morphologies in the LPZ OZ could be explained if these olivines remained in suspension and re-equilibrated with melt (equilibrium crystallisation path) prior to deposition, as in the model proposed by Huppert and Sparks (1980) and Tait (1985). This scenario also fails to explain the observations, because in such a model the deposited olivines should be essentially unzoned, or at least show a consistent zoning pattern, whereas olivines in the LPS OZ show marked and diverse zoning patterns. The common preservation of hopper olivine habits in the LPS OZ also seems inconsistent with this scenario, because hopper olivines would have recrystallized during settling to become more euhedral (Welsch *et al.*, 2012).

Nor are the modal abundances of olivine in the LPS compatible with the amounts of olivine predicted to crystallize from the magma using the PELE modeling. The olivine present in the OZ (when redistributed throughout the LPS) represents *ca.* 15-20% of the volume of the LPS (assuming constant thickness). This is far in excess of the *ca.* 8% olivine-only crystallization predicted by PELE. This suggests that the amount of olivine in the LPS OZ was not extracted by *in-situ* crystallization of a magma similar to the LPS chill. PELE models with a starting composition corresponding to some of the most primitive Franklin chills (*ca.* 13.5 wt% MgO) crystallize slightly more olivine (*ca.* 10-15%) prior to cosaturation in plagioclase and clinopyroxene and are better fits to the observed modal abundances of olivine in the LPS OZ. It might be possible to explain the observed olivine modal abundances if the LPS sill was filled with a more primitive magma (in comparison with the observed chilled margin composition), or if the initial melt pulse carried a significant cargo of olivine crystals (*ca.* 20%). However, neither of these

alternative models is compatible with the variety of olivine zoning patterns and their organized distribution within the OZ.

In conclusion, we contend that the common occurrence of reversely zoned olivines in the UOZ and the occasional presence of evolved Cr-spinel inclusions in the low-Fo olivine cores of such grains (Fig. 4.9) cannot be explained by *in-situ* fractional crystallisation of a single melt pulse and require the operation of an additional mechanism during sill formation and differentiation.

4.5.4 The significance of reversely zoned olivine

The survival of strongly zoned olivine in the LPS, particularly the reversely zoned olivines, and the heterogeneous olivine compositions from single thin sections, imply preservation as a result of rapid cooling. The presence of heterogeneous olivine compositions within single thin sections is reminiscent of the diversity of olivine Fo compositions observed in Hawaiian picrites (Garcia *et al.*, 2003). Preliminary olivine Fe=Mg diffusion calculations following the method of Costa and Dungan (2005) suggest that the residence times of olivine at magmatic temperatures (with a closure temperature of ~1150°C), were between *ca.* 2-5 years. Following the method of Carslaw and Jaeger (1959) for 'simple' conductive heat loss of a sill to wallrock at 75°C, between 3-6 years are needed to cool magma to its solidus, similar to that calculated above. Using a method similar to that described by Cawthorn and Walraven (1998) yields a very similar cooling rate. These calculations indicate that the LPS cooled rapidly and imply that opportunities for re-equilibration were limited. Consequently, we conclude that the mineral-chemical signatures recorded in the LPS are primary igneous features.

Reversely zoned olivines are present throughout the OZ but they are particularly common in the UOZ. In the LOZ, olivine chadacrysts enclosed by clinopyroxene preserve subtle reverse zoning, indicating reaction with primitive melts containing *ca.* 10 wt% MgO. According to the PELE modeling, such melts would only be saturated in olivine + chromite. One of the most extreme examples of a reversely zoned olivine in the UOZ has an evolved core (Fo_{77}) that formed from a low-MgO (*ca.* 6 wt%) melt that would have been in equilibrium with an olivine + clinopyroxene + plagioclase assemblage. The core of

this olivine also contains an evolved (low-Cr#, high-Fe3#, high Fe2#) Cr-spinel that must have formed from a melt that had a low Mg# and high concentrations of ferric iron. In contrast, the Fo_{80} rim of this reversely zoned olivine indicates formation from a more primitive melt with *ca.* 8 wt% MgO, and it contains Cr-spinel inclusions with compositions (high Cr#, low Fe3#, low Fe2#) that also imply an outward shift to more primitive melt compositions. Reverse zoning (rimward Mg# and An increases) are also seen in both clinopyroxene and plagioclase (Fig. 4.12 & 4.16) throughout the LPS. We hypothesize that these reverse mineral-chemical zoning trends in clinopyroxene and plagioclase may possibly be related to the same mechanism that produced the reversely zoned olivines in the OZ.

The different textural types of olivine, and their distinct compositions, when considered together with the presence of reverse zoning (in both olivine + Cr-spinel inclusions) in the OZ strongly suggest that the OZ rocks are hybrids, representing a mixture of multiple generations of crystallisation products and liquids. Similar textural and phase relationships have been observed in the Lower, Critical and Main Zones of the Bushveld Complex, which have been linked to replenishment (Eales *et al.*, 1991, Mitchell *et al.*, 1998). Other intrusions and volcanic products also bear imprints of variable crystal cargoes, as shown by *in-situ* isotopic modelling (Davidson *et al.*, 2007, Font *et al.*, 2008, Martin *et al.*, 2010). We will now attempt to constrain the different components involved the differentiation of the LPS using the mineral and melt chemistry in combination with the PELE modelling results.

4.5.5 The origin of the OZ/DZ duality

4.5.5.1 The source of the high-MgO melts – an olivine slurry?

The presence of reversely zoned olivines in the OZ excludes an origin by simple fractional or equilibrium crystallisation of a single pulse of melt. We propose that this reverse zonation is the result of an intra-sill melt replenishment event, and that the primitive rims record the arrival of a replenishing magma. The range of primitive melt compositions calculated from the reversely zoned rims of olivine in the OZ is between ~10-8 wt% MgO. These melts resemble the chilled margin composition and would have had about the same

composition as the melts from which most of the primitive olivine primocrysts in the LOZ formed. Some of the olivine primocrysts are too primitive to have crystallised from a LPS melt similar to the chilled margin, and may be exotic to the LPS. The highest model melt MgO contents (up to ~13.5 wt%) recorded in the OZ may represent the replenishing melt, but it is also possible that the high-Fo primocrysts that yielded these high melt MgO contents are un-re-equilibrated antecrysts derived from a less-evolved magma that was actively fractionating olivine somewhere upstream as it flowed towards the LPS.

The melt-crystal systematics lead us to infer that that a magma containing olivine primocrysts was emplaced into the LPS as a replenishing olivine slurry. In this scenario, the primitive carrier melt is responsible for the reverse zoning of OZ olivines, with the low-Fo cores of these grains being relicts of the crystal mush that was present in the sill before the slurry arrived. The late arrival of a crystal-liquid slurry carrying a cargo of primitive olivine primocrysts would account for the excess modal olivine in the LPS as a whole compared to the PELE fractional crystallization model. On the other hand, the diverse zoning patterns observed in the OZ, particularly the reverse zoning, appears inconsistent with models invoking simple redistribution of entrained olivine carried in by an initial magma. In this context, the low-Fo hopper olivines in the MOZ and UOZ might also reflect contamination of the primitive slurry by host DZ rocks. Radiogenic and $\delta^{34}S$ isotope data (chapter 5) show that the OZ and DZ are not in isotopic equilibrium and represent separate intrusive events, strongly supporting a multiple intrusion model.

We propose that a slurry of olivine primocrysts was emplaced immediately above the dendritic LBZ (at *ca*. 1 m above the lower contact) and beneath the DZ, to form the LPS OZ. We speculate that the boundary between the (solidified) dendritic LBZ and the relatively buoyant feldspar-rich resident mush above was an important mechanical discontinuity, facilitating emplacement of a slightly denser olivine slurry. The primitive melts in the replenishing magma would have partly mixed with the resident, evolved, gabbroic mush. Some of the evolved olivines in the OZ may be true relicts, whilst others may record more extensive, earlier hybridization steps. Since the primitive olivine primocrysts with normal zoning patterns typify the LOZ, we suggest that this sub-zone is the least-hybridized facies of the OZ and mostly contains olivines carried in by the replenishing slurry. Reversely zoned mantles to some olivine phenocrysts from the LBZ (Fig. 4.10) that we infer are derived from the first magma pulse emplaced into the LPS,

may also have developed as a result of olivine slurry emplacement, through heating and impregnation of a porous floor. However, reversely zoned mantles are also observed in LCM olivine phenocrysts, so we cannot rule out the possibility that the reversed zoning signatures were created further upstream in the plumbing system prior to emplacement in the LPS. It is also possible that the melt directly in contact with host dolostone may have increased its Mg/Fe by assimilating some of the wallrock dolostone (*cf.* Gaeta *et al.* (2009), Di Rocco *et al.* (2012)).

Other examples of reversely zoned olivines and chromite microphenocrysts have been observed in many of the olivine-cumulate sills in the Fort Collinson Sill Complex, suggesting that late olivine slurry emplacement may be ubiquitous in these older Franklin sills (see chapter 5).

4.5.5.2 The DZ – a relict of the resident mush?

Thin hypabyssal sills and dikes (like the LPS) are typically considered to have been emplaced near instantaneously and to have cooled rapidly. As a result, they should show limited internal differentiation. They commonly have doleritic textures, which would have hindered crystal-liquid separation, so giving them only a weak cumulate component (Gunn, 1966, Philpotts *et al.*, 1998). The compositions of model melts in equilibrium with DZ clinopyroxene cores are typical of cotectic melt compositions (*ca.* 7.5 wt% MgO). The compositions, textures, scarcity of cumulus minerals (<10%) and abundance of Fe-Ti oxides of the LPS DZ are therefore typical of relatively quickly-crystallized hypabyssal sills.

If the evolved cores of reversely zoned olivines in the UOZ are relicts of the earlier material filling the LPS, as argued above, then we can use their composition to constrain the DZ composition prior to the replenishment. The most evolved olivine core (~Fo_{75}) in the UOZ that has a reversely zoned rim that is in equilibrium with a model melt composition of ~6 wt% MgO. The PELE and Fe=Mg modelling indicate that plagioclase and clinopyroxene joined olivine on the DZ liquidus at ~7.5 wt% MgO. This implies that the low-Fo (Fo_{75}) cores in the OZ should have been part of a 3-phase cotectic gabbroic assemblage. If the DZ crystallised from a melt similar to the LPS LCM, then the PELE modelling suggests that at the moment when the replenishing event occurred, the DZ

would have comprised 60% pore melt with about 11% olivine, 16% plagioclase, and 13% clinopyroxene. We will refer to this assemblage as the resident mush. The hopper olivines of the UOZ that enclose clinopyroxene and plagioclase (Fig. 4.4b, c, f) are also inferred to record ingestion of the DZ mush by the olivine slurry.

One disparity between this model and the observations is that no olivine has been observed in the DZ, whereas PELE predicts ~10% to have been present in the LPS. However, there is commonly a thin olivine-gabbro subzone at the base of the DZ in other Franklin sills of this type (e.g. Bédard *et al*. 2012). On this basis we infer that the sparse (~5-10%) orthopyroxene from the basal LPS DZ is pseudomorphous after olivine. This implies that the interstitial melt in the LPS DZ became sufficiently evolved to have reached the olivine-orthopyroxene peritectic, which is consistent with the highly evolved compositions of crystal rims in the DZ (e.g. clinopyroxene Mg#20).

The primitive plagioclase (An_{77}) and clinopyroxene (Mg#85) crystals in the DZ may be relicts of early DZ crystallisation or possibly antecrystic phases carried in the first pulse of LPS magma that are embedded in a mass of later crystallisation products. It is possible that localised reverse zoning in cumulus plagioclase in the DZ may record the arrival of the OZ replenishing magma, but this remains conjectural since plagioclase An-content is sensitive to many other potential effects (e.g. build-up of water content). Reversely zoned mantles in cumulus-textured clinopyroxene in the CPZ and DZ may also be a record of olivine slurry emplacement. The cumulus crystals bearing this signal may have then been entrained and emplaced into the DZ followed mixing with the olivine slurry.

Following olivine slurry emplacement, we suggest that the DZ continued to evolve, reaching its most extreme mineral compositions (Fig. 4.12 & 4.16) and highest proportions of accessory phases (Fe-Ti oxides, amphibole, biotite) at a high-level sandwich horizon, a pattern suggestive of progressive *'in-situ'* fractional crystallization (*cf.* Boudreau & Philpotts, 2002). Although we cannot unequivocally determine whether the DZ sandwich horizon developed prior to, or after olivine slurry emplacement, we will argue below that it post-dates it.

4.5.5.3 Mixing and hybridisation between the resident DZ and replenishing slurry

As argued above, we propose that a partly crystalline DZ characterised by a high melt proportion (~60%) was resident in the LPS when a replenishing olivine-charged magma was emplaced. The replenishing magma must have contained a high melt proportion (~50%), since otherwise flow would have been impeded (Paterson, 2009). Mixing between the slurry and resident magma led to the formation of a hybrid melt with an composition of ~10-8 wt% MgO, from which the most primitive reversely zoned olivine rims and overgrowing clinopyroxene oikocrysts crystallised.

Clinopyroxene oikocryst cores have similar Mg# throughout the entire OZ, indicating that they all formed from pore melts with ~9-8 wt% MgO. Conversely, the rims of reversely zoned olivines become less forsteritic up-section, from Fo_{83} in the LOZ to Fo_{80} in the UOZ, where olivine rims are calculated to have been in equilibrium with ~8 wt% MgO melts. The lack of differentiation in OZ clinopyroxene compositions suggests they cosaturated when local pore melt reached the same point in its compositional evolution. The model melts calculated to be in equilibrium with OZ clinopyroxene exceed their cotectic melt MgO content (according to PELE), suggesting that these clinopyroxenes did not form through fractional crystallisation from a LCM melt composition. Instead, OZ clinopyroxene saturation appears to have been triggered at the point of magma hybridisation when initial hybrid magmas were primitive (~9 wt% MgO).

The compositions of groundmass olivines in the MOZ are more primitive than LOZ groundmass olivines and are in equilibrium with reversely zoned rims in the UOZ. The transition to more primitive groundmass olivine in the MOZ/UOZ suggests these groundmass olivines crystallized from hybrid magma percolating up through this mass as the OZ cumulates compacted. As such, the UOZ rim compositions were buffered by throughflow from hybrid pore melt expelled from below. However, compaction of the OZ may have been limited by the relatively rapid cooling rate of the LPS (<6 years). We suggest that the UOZ is a strongly hybridized facies of the OZ that retains undissolved traces of the resident mush, now represented by plagioclase and clinopyroxene inclusions in hopper olivines (Fig. 4.5d & f), evolved olivine cores and evolved Cr-spinel inclusions (Fig. 4.9). The less common MOZ hopper olivines (Fig. 4.5b) may also have crystallised from hybrid magma, possibly suggesting a weaker contamination signature in the MOZ.

4.5.6 Evidence for rapid crystallisation in the centre of the LPS

4.5.6.1 Hopper olivine morphologies in the UOZ

The UOZ is characterized by abundant hopper olivine morphologies (Fig. 4.4d, e & f), some of which are reversely zoned. The hopper olivines of the UOZ that enclose clinopyroxene and plagioclase (Fig. 4.4d & f) are also inferred to record ingestion of the DZ mush by the olivine slurry. Experiments carried out by Donaldson (1976) show that olivine crystal morphology is related to the cooling rate and melt MgO composition, and that hopper olivine morphologies form at high growth rates. Huppert and Sparks (1980) suggested that hopper and elongate olivines could be produced by rapid cooling when a hot, primitive basaltic magma quenches beneath a cooler basaltic melt. A very similar mechanism was proposed more recently for the origin of cyclic harristic layering in the Rum intrusion (O'Driscoll *et al.*, 2007). The hopper olivines in the UOZ of the LPS seem to indicate rapid cooling, even though the UOZ is near the middle of the LPS (at *ca.* 8 m height) where cooling rates should be the slowest. We suggest that the hopper olivine in the LPS OZ formed when the hotter, primitive olivine slurry intruded a cooler resident gabbroic mush. In this scenario, the 'supercooled' hybrid melt crystallized olivine (hopper-type) around the xenocrystic cores sourced from the resident gabbroic mush.

4.5.6.2 Sector-zoned clinopyroxene in the CPZ

Above the OZ there is a striking modal and textural change, as olivine cumulates grade rapidly into a thin layer dominated by euhedral, sector-zoned clinopyroxene (Fig. 4.6). The passage from olivine-dominated cumulates to a clinopyroxene-rich cumulate assemblage (CPZ) could be interpreted as being due to fractional crystallization with cosaturation in clinopyroxene briefly preceding cosaturation with plagioclase. However, as discussed previously, our preferred interpretation is that the OZ formed as a replenishment into a resident gabbroic mush (DZ). This suggests that the CPZ may be related to this event, rather than representing an intermediate fractional crystallization step.

The development of sector-zoning in clinopyroxene has been attributed to rapid growth brought about by rapid cooling, or quenching by magma decompression and volatile exsolution (Nakamura, 1973, Brophy *et al.*, 1999). However, as emphasized in the

discussion about the origin of hopper olivines, the CPZ is roughly in the middle of the sill (at *ca.* 8-9 m height), where cooling rates should be slowest. Also, clinopyroxene was not a liquidus phase upon emplacement of the initial LPS melt (assumed to have had a composition corresponding to the LCM), so decompression and volatile exsolution are not plausible causes. In the context of the OZ emplacement model, we suggest that the rapid growth textures and abundant clinopyroxene modes of the CPZ record compositional super-saturation induced by pore scale melt mixing. If the DZ was underplated by an olivine slurry, then the OZ/DZ interface may have been overprinted by the migration of pore melts from one system into the other. We speculate that the buoyant, hybrid melts from the OZ percolated upwards, possibly driven by compaction of the OZ below, and infiltrated the base of the DZ, where pore melts would have had cotectic compositions. The phase topology (Fig. 4.17) suggests that mixtures of two such melts could result in a clinopyroxene-only saturated melt (Onuma & Tohara, 1983, Bédard, 1993). Clinopyroxenes that form from such compositionally super-saturated melts may have crystallized rapidly, much as we suggested for the hopper olivine of the UOZ. This interpretation for the origin of the CPZ is consistent with the distribution of sector-zoned clinopyroxene into ‘channel-like’ trains (Fig. 4.7). It is also supported by the compositions of the sector-zoned clinopyroxene, which have cores compositions ($Mg\#_{85\text{-}83}$) that overlap with core compositions of clinopyroxene oikocrysts in the OZ below (Fig. 4.10). Since the latter are interpreted to have crystallised from the hybrid melt of the OZ, this compositional similarity is consistent with derivation of the sector-zoned clinopyroxene from pore melt expelled from the OZ.

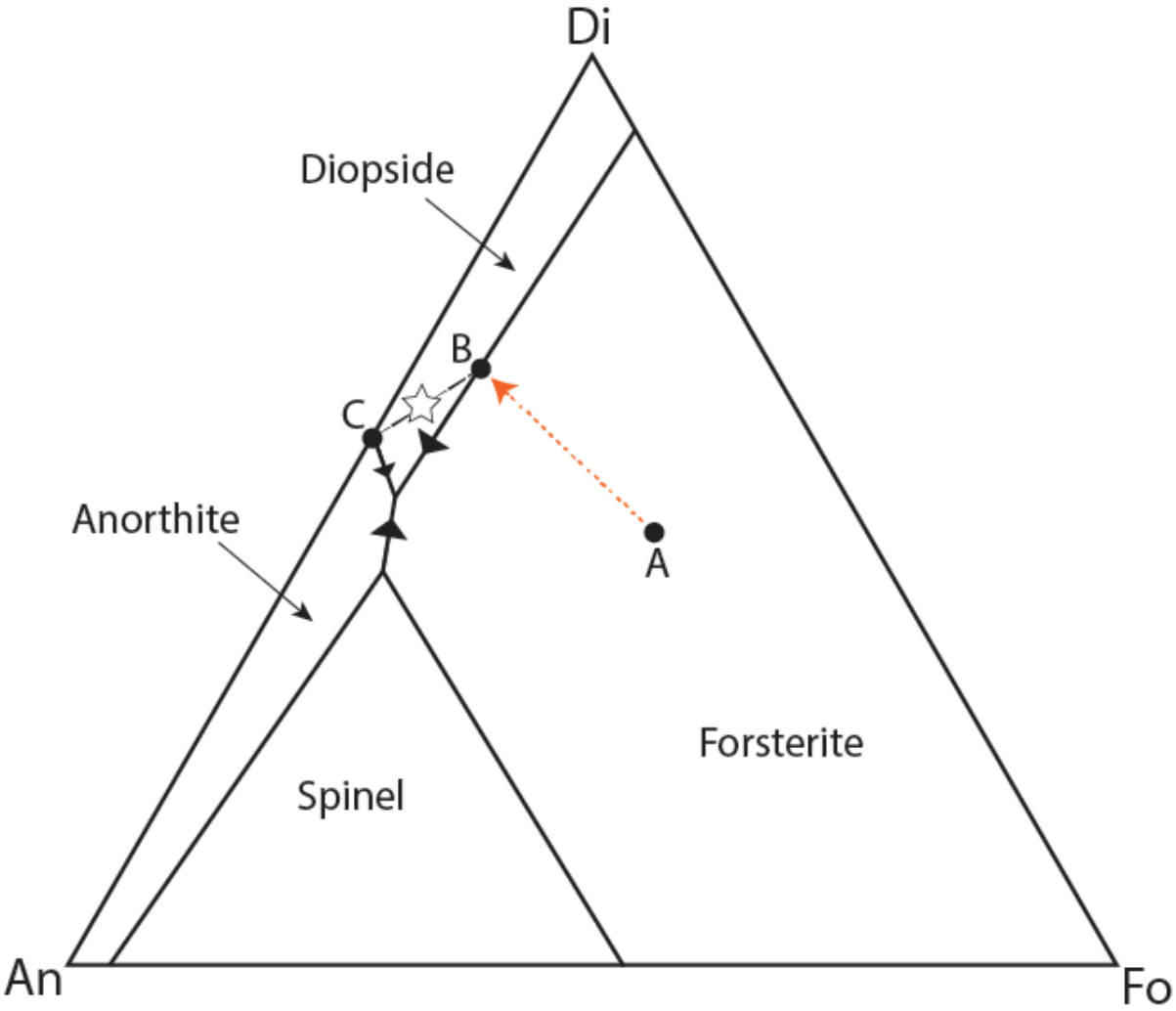

Fig. 4.17: A Di-An-Fo phase diagram modified after Onuma and Tohara (1983) and Bedard (1993), indicating how mixtures of melt that has crystallised on a pathway between olivine (Fo) and clinopyroxene (Di), with melt that has crystallised plagioclase (An), fall in the clinopyroxene-only field (labelled with a star). Melt A would originally be olivine slurry derived carrier melt that became hybridised and crystallised olivine and clinopyroxene (Melt B). Melt C would be derived from the DZ, which had crystallised plagioclase. Melt C was most likely Fe-enriched pore melt that percolated down through the DZ mush.

4.5.7 Model – the development of igneous layering in the LPS

Based on the textural and mineral-chemical evidence presented above, we propose that the LPS records three main magmatic stages (Fig. 4.18): (1) initial magma (a dilute crystal slurry) emplacement followed by fractional crystallization; (2) replenishment and partial hybridization with an olivine slurry; (3) late-stage pore melt migration, and limited re-equilibration with cooling, trapped pore melt.

4.5.7.1 Stage 1 – initial magma emplacement and fractional crystallisation

The presence of *ca.* 5% modal olivine phenocrysts (*ca.* 1-2 mm) in the LPS chills suggests that the initial magma pulse probably carried small amounts of olivine, though we cannot exclude the possibility that higher proportions of olivine were concentrated in the centre of the flow (Bhattacharji, 1967, Simkin, 1967). It is also possible that the initial magma carried a cargo of clinopyroxene and plagioclase, as evidenced by the presence of rare cumulus crystals in the DZ. Model melts in equilibrium with the most primitive olivine phenocryst in the LCM are higher (at *ca.* 13 wt%) than the LPS chill (10.3 wt% MgO). As such, some of the olivine carried in with the first pulse may be antecrystic relicts (or products of an earlier crystallization step) carried downstream as the magma fractionated. After emplacement, this basaltic magma crystallized from both margins, producing the LBZ and UBZ, where high cooling rates formed plagioclase and clinopyroxene with dendritic habits that overgrew and cemented olivine phenocrysts. The olivine phenocrysts of the LBZ have core compositions that are in equilibrium with the LCM melt composition suggesting they are derived from this magma. The lack of any olivine crystals in the UBZ suggests that any phenocrysts that were present settled fast enough to evade entrapment by the downward solidification front.

The intergrowth of olivine with clinopyroxene and plagioclase dendrites in the LBZ suggests that the initial magma rapidly reached the 3-phase cotectic after emplacement. If the LCM accurately reflects the melt composition, then only *ca.* 8% olivine extraction is needed to reach 3-phase saturation according to the PELE model. However, if the olivine phenocrysts in the chill are ‘cumulate’ phases, then the LCM composition is slightly biased towards higher MgO contents and <8% crystallization may be needed to reach 3-phase saturation. If we deduct the average olivine core composition of LBZ olivines from the LCM (considering a 10% olivine mode for the LBZ), then the residual melt would contain *ca.* 6 wt% MgO, similar to our estimate of the resident mush composition using the Fe=Mg modeling. The olivine that crystallized from this initial magma pulse into the LPS may have settled to form a first-stage olivine cumulate, but this cannot be determined with certainty. If such a basal olivine-rich layer developed at this stage, then there may have been a weak S-shaped profile with the most evolved material concentrated in the upper third of the sill, as seen in other intrusions (Shirley, 1985, Meurer & Boudreau, 1998) and in thick lava flows (Bédard, 1987, Boudreau & Philpotts, 2002). The sandwich horizon

defined by the clinopyroxene and plagioclase data from the LPS (Fig. 4.10 & 4.14) may have developed early, or might have developed after emplacement of the olivine slurry (see below).

4.5.7.2 Stage 2 – the emplacement of an olivine slurry and hybridisation with the basal DZ

The mineral zonation patterns and compositions from the LPS OZ suggest that a crystal-charged olivine slurry was injected near the base of the LPS, beneath most of the buoyant DZ and above the more consolidated, dendritic-textured LBZ. This olivine slurry could have scoured out and mixed with weakly consolidated (olivine-enriched?) host material resting on the sill floor, with only the better-consolidated, largely solidified LBZ adjacent to the cooling surface surviving. The relative coarseness of the LBZ dendrites (Fig. 4.2b) suggests relatively slow cooling rates, possibly due to the emplacement of the hot olivine slurry above. If this is correct, it would imply that the olivine slurry arrived not long after the initial magma was emplaced into the LPS.

Fig. 4.18 (page 58): Cartoons that illustrate the differentiation and subsequent formation of the OZ/DZ duality within the LPS. Stage 1 depicts the emplacement of the first magma in the sill. The initial magma was olivine + chromite phyric (Ol 1). Evidence of this early cargo of normally zoned olivine phenocrysts was quenched in, in both lower (A) and upper (A') chilled margins. As the melt began to crystallise inwardly from its lower and upper margins, it crystallised plagioclase and clinopyroxene dendrites that cemented LBZ olivine phenocrysts (B). No olivine phenocrysts were preserved in the dendritic UBZ due to rapid olivine settling. As the melt crystallised, the sill inflated, crystallising olivine (Fo_{75}) + clinopyroxene (Cpx 1) + plagioclase (Plag) mush with ~60% pore melt (with 6 wt% MgO: Melt 1) (C). In stage 2, the olivine slurry is emplaced from the east (D), carrying a suspended cargo of primitive olivine primocrysts (Fo_{88-82}: Ol 2) and its equilibrium carrier melt (13-10 wt% MgO: Melt 2). As the olivine slurry was emplaced, it partly mixed with and ingested the resident gabbroic mush in the sill (E). The main bulk of the buoyant resident gabbroic mush would have been underplated by the denser olivine slurry (F). As the olivine slurry under/intraplates the resident mush, the DZ, as we see it was emplaced and continued to crystallise (G). In stage 3, the layering becomes enhanced. The majority of the primitive olivine primocrysts delivered into the sill settle in the LOZ (H) whilst the two melts (Melt 1+2) hybridise (Melt 3). This hybridised melt percolates through the OZ, crystallising olivine and poikilitic clinopyroxene (Cpx 2) in the MOZ, as well as the reversely zoned rims of olivine in the UOZ (I). The hybridised melt eventually encounters DZ derived Fe-rich residual liquids, saturating the melt in sector-zoned clinopyroxene (J). The DZ continued to crystallise, with evolved clinopyroxene and plagioclase rims in the upper DZ representing a sandwich horizon where late-stage, evolved pore melt may have pooled (K).

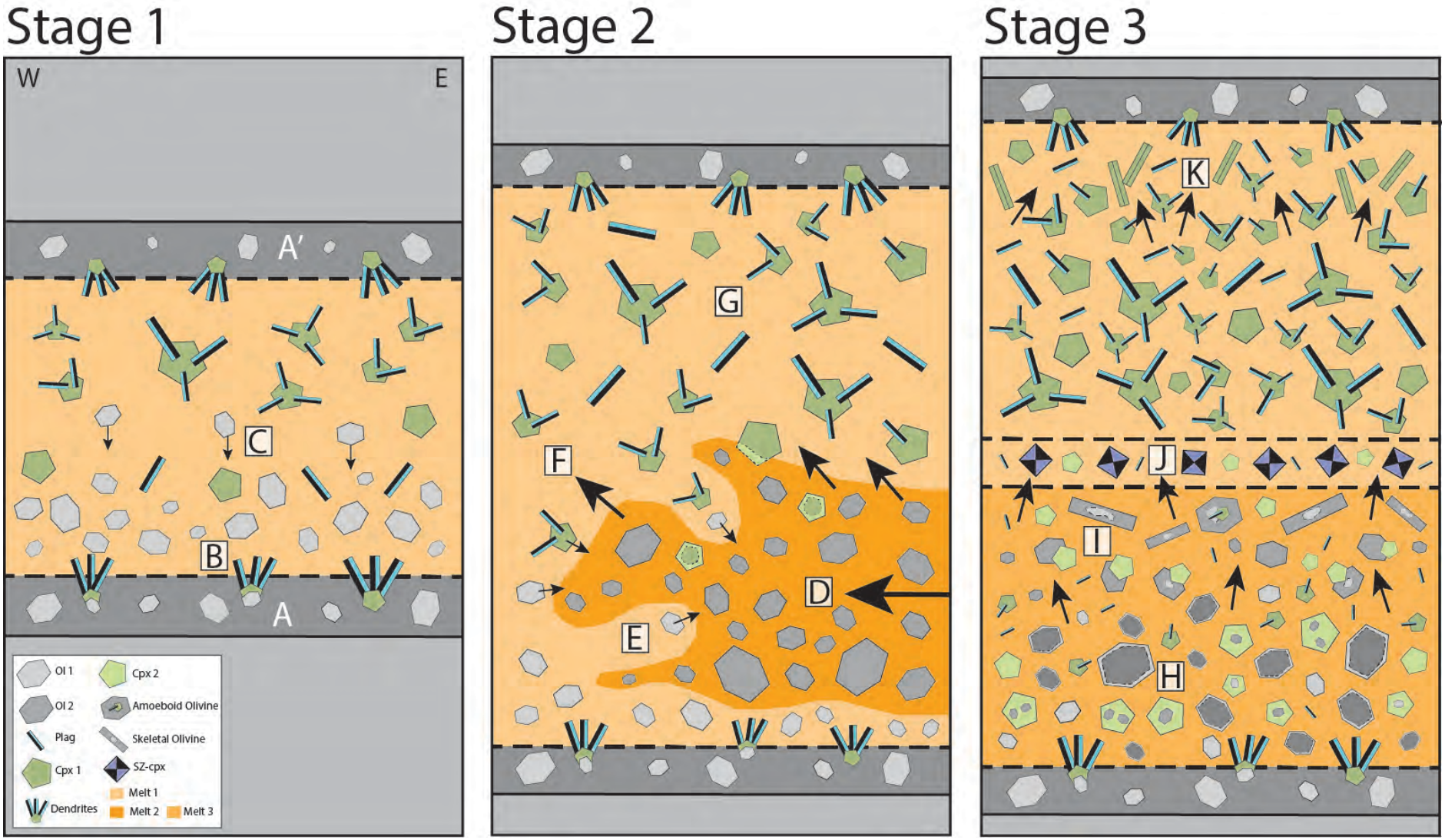
Stage 1
W
E
A'
A
B
C
Ol 1
Ol 2
Plag
Cpx 1
Cpx 2
Amoeboid Olivine
Skeletal Olivine
SZ-cpx
Melt 1
Melt 2
Melt 3
Dendrites
Stage 2
G
F
D
E
Stage 3
K
J
I
H

The olivine slurry would have been denser than a partly-solidified, feldspar-rich dolerite and so it would probably have underplated the host DZ, much as was proposed previously for the replenishment of magma chambers (Huppert & Sparks, 1980, Tegner *et al.*, 1993). On the basis of major element geochemical systematics, Hayes et al. (Submitted) calculated that the olivine slurry contained *ca.* 20-25% olivine, making it slightly denser than a resident mush that was *ca.* 40% solidified. Also, the 40% solidified resident mush may have been mechanically strong due to formation of feldspar chains (Philpotts *et al.*, 1998), and so the weakest part of the LPS may have been the interface between the dendritic LBZ and the overlying partly-crystalline resident mush. We infer that the emplacement of the olivine slurry at the base of the LPS created the S-type basal MgO bulge (Fig. 4.1b). During emplacement, we suggest that the incoming olivine slurry mixed to some extent with the resident mush (corresponding to the missing basal DZ) and created a hybrid melt with *ca.* 10-8 wt% MgO. The evolved olivine cores (and evolved Cr-spinel inclusions) and possibly the gabbroic inclusions in hopper olivines are interpreted to be partially digested relicts of this basal DZ. The high-An cumulus plagioclase and high-Mg# cumulus clinopyroxene in the DZ may be remnants of the primitive base of the DZ, much of which may have mixed with and dissolved into the feldspar- and pyroxene-undersaturated olivine slurry. However, the DZ may have had a complex history prior to OZ emplacement, so we cannot exclude the possibility that the uncommon primitive plagioclase and clinopyroxene from the DZ are unrelated to OZ formation. Olivines in the MOZ and especially the UOZ commonly have hopper-type morphologies (Fig. 4.4b-f). These may record the chilling effect of extensive hybridization, coupled with heat loss to the cooler DZ host, similar to models for the harristic layering of the Rum intrusion (Huppert & Sparks, 1980, O'Driscoll *et al.*, 2007).

4.5.7.3 Stage 3 – late-stage processes

After emplacement of the olivine slurry and hybridization with the basal DZ host, the hybrid melt in the resulting OZ had a composition of *ca.* 10-8 wt% MgO. This range may represent heterogeneities in the amount of admixed DZ material. Alternatively, the variability of the MgO content may reflect post-hybridization fractional crystallization of the hybrid melt as the OZ solidified. During this consolidation and cooling phase, interstitial and poikilitic clinopyroxene and then plagioclase began to form. The cores of the most primitive clinopyroxenes that envelop the reverse zoned olivines are in

equilibrium with a maximum melt MgO content of *ca*. 9 wt%, recording clinopyroxene cosaturation from the hybrid melt. We do not yet have a clear explanation for why clinopyroxene appears earlier on the OZ crystallization path in comparison with the PELE model results.

It is plausible to infer that pore melt from the OZ was expelled by compaction to mix with the overlying DZ, and we suggest that this is the origin of the sector-zoned clinopyroxene in the CPZ. At this juncture, the melt being expelled from the OZ would have had compositions roughly corresponding to the compositions of the reversely zoned olivine rims and clinopyroxene in the UOZ (*ca.* 8 wt% MgO). When it penetrated the overlying DZ, this OZ-derived pore melt would have mixed with more evolved pore melts, possibly triggering rapid growth of sector-zoned clinopyroxene (Fig. 4.6). We suspect that mixing occurred in dissolution channels in what is now the CPZ and that clinopyroxene formed by this reaction overgrew and replaced the olivine-bearing gabbroic matrix of the CPZ (Fig. 4.7).

When permeability dropped to the point where interstitial melts could no longer move, the trapped pore melts began to evolve via *in-situ* fractional crystallization (Humphreys, 2009, Holness *et al.*, 2011). Permeability drops may be linked with inwardly migrating solidification fronts (Marsh, 1996). In OZ rocks this generated narrow Fe-rich rims on olivine primocrysts, evolved groundmass olivines, Fe-Ti enriched rims on clinopyroxene, sodic rims on plagioclase, and a cortège of minor phases (Fe-Ti oxides, mica, amphibole, and sulphides). The effects of *in-situ* differentiation are most prominent just beneath the UBZ in the DZ, where clinopyroxene (Fig. 4.10) and plagioclase (Fig. 4.14) cores reach their most evolved compositions at a sandwich horizon. We tentatively suggest that this sandwich horizon developed late in the crystallization history of the LPS and post-dates the emplacement of the olivine slurry. This is based on the constraints provided from our data, which suggests that the LPS was only *ca.* 40% solidified at the time of olivine slurry emplacement, rather than >70% solidification required to produce the strongly evolved/fractionated mineral compositions seen in the sandwich horizon.

4.5.8 Implications for the differentiation and formation of cyclic/macrorhythmic layering in large layered intrusions

The LPS preserves first order igneous layering that is similar to cyclic/macrorhythmic cumulate layering observed in large layered intrusions (Eales & Cawthorn, 1996, Wilson, 2012). The rapid cooling rate of the thin LPS preserves fine details of mineral textures and zoning that provide insights into the differentiation and layer-forming mechanisms. Similar mechanisms may also have operated in larger, more slowly cooled, magma chambers. We have presented evidence that suggests that the LPS OZ was emplaced as an olivine slurry near the base of a pre-existing gabbroic mush. The prominent layering seen in the LPS is in marked contrast with most dolerite-textured gabbroic sills. For example, the 150 m thick Beacon sill of the Ferrar suite in Antarctica (Zieg & Marsh, 2012) shows only limited internal differentiation, and does not develop significant modal layering, even though it is seven times thicker than the *ca.* 21 m LPS. Our data imply that the first order cumulate layering structure (OZ/DZ duality) of the LPS was not formed by *in-situ* closed system differentiation of a single magma pulse, and that the LPS is a composite intrusion that records multiple intrusive pulses, a conclusion that is supported by our unpublished isotopic data (chapter 5: Beard et al. In Preparation). Similar textural and phase relationships have been observed in the Lower, Critical and Main Zones of the Bushveld Complex, which have been linked to replenishment (Eales *et al.*, 1991, Mitchell *et al.*, 1998). Other intrusions and volcanic products also bear imprints of variable crystal cargoes, as shown by *in-situ* isotopic modeling (Davidson *et al.*, 2007, Font *et al.*, 2008, Martin *et al.*, 2010).

Our results bear on a debate that has created very polarised views in the literature about how magma chambers form and differentiate. The DZ of the LPS (and most other sills of the Franklin suite) shows a D-shaped profile, with the development of an Fe-Ti enriched zone (sandwich horizon) as a result of inward crystallisation, much as argued by Shirley (1985), and others (Latypov, 2009). However, the OZ/DZ duality and S-shaped profile of the LPS as a whole appears to have formed through multiple injections, as advocated by Marsh (2004, 2013). We emphasise that the demonstration that some types of layering (in this instance, a basal olivine-rich layer) formed from a replenishing crystal-charged slurry does not imply that magma cannot differentiate by *in-situ* fractional crystallisation.

The late emplacement of an olivine slurry in the LPS has other implications for magma chamber evolution. It seems axiomatic that such an event could only occur if the incoming slurry was driven by some type of magmatic overpressure. As the olivine-charged slurry is injected into a previously existing sill, space needs to be created to accommodate it. Either the sill inflates by floor subsidence and/or roof uplift, or an equivalent volume of pre-existing resident mush needs to be expelled. This remobilised gabbroic mush could be forced onwards to more distal zones as the overpressure allows the sill to expand laterally, or it could be expelled into parasitic dykes, or could be injected up-section to erupt at the surface if favourable structures are present to facilitate this. A multiple emplacement process similar to what we have documented in the LPS could also have operated in other basaltic provinces and possibly other settings, explaining common glomerocrystic and disequilibrium crystal-melt assemblages (Larrea *et al.*, 2012, Passmore *et al.*, 2012, Leuthold *et al.*, 2014).

We also suggest the formation of a clinopyroxene-enriched layer at the interface between the two systems as a result of post-emplacement migration of interstitial melt. The possible development of the CPZ by mixing between OZ and DZ pore melts is similar to the mechanism of formation proposed for gabbros in the Rum intrusion (Bédard *et al.*, 1988), pyroxenites in the Bay of Islands complex (Bédard, 1991a) and is similar to that proposed for the formation of high-Mg# clinopyroxene in actively spreading mid-ocean crust (Lissenberg & Dick, 2008); emphasising the need to better understand the effects of igneous metasomatic processes during the solidification of igneous bodies.

4.6 Conclusions

The Lower Pyramid Sill (LPS) forms part of the sill-dominated Franklin magmatic plumbing system that is well exposed in the Minto Inlier of Victoria Island, Arctic Canada. For a thin sill (~21 m), the LPS is remarkably well layered, characterised by a ~7 m thick layer of olivine-cumulate melagabbro/feldspathic peridotite (OZ) that is capped by a thin (~1 m) layer of sector-zoned clinopyroxene-rich cumulate gabbro (CPZ) and a ~10 m thick layer of sub-ophitic doleritic gabbro (DZ). The OZ is sub-divided based on textures into a basal pyroxene-poikilitic OZ (LOZ); a middle OZ (MOZ); and an upper OZ (UOZ). The

absence of systematic cryptic mineral compositional variations in the LPS OZ; the high proportions of modal olivine; the presence of reversely zoned olivines; and the variety of olivine morphologies within the OZ, when considered together, appear to preclude formation by *in-situ* fractional crystallisation of a single pulse of magma. Data from the LPS OZ are best explained by an intra-sill mixing event between an invading olivine slurry and a resident gabbroic mush that was ~40% solidified. The olivine slurry was emplaced just above the LBZ. During its emplacement, the primitive, MgO-rich melts (~13-10 wt%) mixed with the more evolved resident mush (with ~6 wt% MgO pore melt) that was already present in the LPS. Mixing between these two magmas produced a hybrid magma, with higher proportions of DZ contaminant in the UOZ. As the OZ solidified, interstitial melt percolated up through the compacting olivine cumulate, forming reversed rims on olivine, as well as clinopyroxene oikocrysts. The intervening CPZ is dominated by enigmatic sector-zoned clinopyroxene that may have formed when this hybrid melt expelled from the OZ reacted with more Fe-rich residual melts in the DZ. The DZ shows inward fractional crystallisation trends culminating in a sandwich horizon just beneath the UBZ. Our differentiation model for the LPS illustrates that both crystal-slurries and *in-situ* differentiation were crucial to the development of the OZ/DZ duality seen in the LPS. Such a style of magma emplacement and differentiation may also be prominent in the construction of cyclic/macrorhythmic layering of larger layered intrusions.

5. The Geochemical Effects of Olivine Slurry Replenishment and Dolostone Assimilation in the Plumbing System of the Franklin Large Igneous Province

5.1 Abstract

The Neoproterozoic (~723-716 Ma) Franklin Large Igneous Province exposed on Victoria Island (Arctic Canada) is comprised of a sill-dominated magma plumbing system overlain by coeval lavas. We have investigated three sections, separated by a total of > 50 km of distance, of a sill emplaced just above a prominent sedimentary marker unit. The sill is characterised by a basal olivine-enriched layer (OZ: up to 55% olivine) overlain by gabbroic rocks. Olivine compositional variations in the OZ can be linked to crystal habit and paragenesis. The diversity of olivine compositions observed in the OZ implies that bulk-rock arrays on an MgO *vs* FeO diagram reflect accumulation of a heterogeneous olivine crystal cargo. We suggest that the OZ represents a late olivine slurry replenishment in a gabbroic sill. This is consistent with radiogenic isotope data, which show that at least three geochemically distinct magmas were emplaced into the sill. The OZ MgO *vs* FeO arrays exhibit a gradual lateral westward shift towards more Fe-rich bulk compositions. We rule out progressive fractionation or varying amounts of compaction as a cause of this shift. Instead, downstream mixing between the replenishing olivine slurry and a resident gabbroic mush can best explain the westward shift towards more Fe-rich bulk compositions in the OZ. Pb isotopic signatures suggest that magmas near the inferred conduit feeder assimilated small amounts (< 10%) of dolostone (possibly local host rock), which may have locally buffered olivine compositions to high-Fo contents by increasing initial melt MgO contents.

5.2 Introduction

To understand the geochemical evolution of basalts we need to constrain the processes active in the associated magmatic plumbing system. Sill-dominated plumbing systems are prominent in Proterozoic and Phanerozoic continental flood basalt provinces (Baragar, 1976, Francis & Walker, 1986, Hawkesworth *et al.*, 1995, Chevallier & Woodford, 1999, Bédard *et al.*, 2007), oceanic crust formed by seafloor-spreading (Bédard, 1991b, Lissenberg *et al.*, 2004), oceanic plateau crust (Kerr *et al.*, 1998) and Archaean greenstones (Bédard *et al.*, 2009). Documenting lateral changes in bulk-rock and mineral chemistry in the constituent sills of such basaltic plumbing systems would shed light on mechanisms of magma emplacement in the crust, of magma interaction with host rocks, on igneous differentiation processes, and may enable reconstruction of magma flow directions (Marsh, 2004). In addition to constraining fundamental properties of magmatic systems, this type of information is an important element in the search for Noril'sk type Ni-Cu-PGE sulphide deposits (Naldrett, 1992).

Separation of crystals from melt in magma chambers is frequently assumed to be responsible for the observed geochemical diversity of lavas (Bowen, 1928) and also plays a role in the development of layering in fossil magma chambers (Wager & Deer, 1939, Irvine, 1980, Irvine, 1987, Naslund & McBirney, 1996). Recent discussions have emphasised the importance of remobilisation of previously deposited crystal cumulates or crystal slurries, and associated consequences for the magmatic evolution of plutonic systems (Marsh, 2013, Neave *et al.*, 2013, Leuthold *et al.*, 2014). It has also been proposed that the abundant phenocrysts seen in some basalts are remobilised cumulates that were flushed out of underlying feeder systems (Larrea *et al.*, 2012, Passmore *et al.*, 2012). Examples of crystal slurry emplacement have been documented in the Ferrar sills of Antarctica (Bédard *et al.*, 2007); the Shiant Isles sills in NW Scotland (Gibb & Henderson, 2006); and the Franklin sills on Victoria Island (chapter 4). The emplacement of crystal slurries is also pertinent for the construction of large layered intrusions such as the Bushveld Complex (Mondal & Mathez, 2007, Roelofse & Ashwal, 2012, Wilson, 2012). Slurry remobilisation is also implicated in the genesis of the anomalous concentrations of immiscible sulphide liquid observed in some Ni-Cu-PGE deposits (Naldrett, 1992).

An additional factor that can affect melt and crystal evolution is the assimilation of (and/or reaction with) country rocks. It is widely accepted that mantle-derived melts may undergo modification of their isotopic signatures as a result of crustal assimilation e.g. Hildreth and Moorbath (1988). Assimilation of carbonate rocks in particular may impact on the liquid line of descent (LLD) of magma by buffering melt Mg/Fe ratios and preferentially stabilising clinopyroxene on the liquidus (Di Rocco *et al.*, 2012, Mollo & Vona, 2014). The impacts of carbonate assimilation have been demonstrated for Merapi Volcano (Chadwick *et al.*, 2007, Troll *et al.*, 2013) and the Colli Albani volcanic district (Gaeta *et al.*, 2009, Di Rocco *et al.*, 2012), but are not commonly described in tholeiitic systems. Assimilation of carbonate rocks by magma can potentially release significant volumes of CO_2 (Iacono Marziano *et al.*, 2007), which may perturb global climate. CO_2 excursions in the geological record have been correlated with the formation of Large Igneous Provinces (Wignall, 2001).

The well-preserved and exposed Neoproterozoic Franklin Large Igneous Province (LIP) on Victoria Island provides a unique natural laboratory to address many of these issues. The Franklin LIP has a sill-dominated magmatic plumbing system with local fault-mediated shifts in emplacement level that facilitated magma transgression (Bédard *et al.*, 2012). Franklin sills were emplaced primarily into limestones and dolostones, and calc-silicate skarns that formed by magma-carbonate interaction are locally prominent (Nabelek *et al.*, 2013). Chapter 4 documented the development of first-order modal layering in a composite Franklin sill as a result of two intrusive pulses. In chapter 4, we proposed that the basal olivine-enriched layer of the ~21 m thick Lower Pyramid Sill (LPS) represents a late olivine slurry replenishment into a resident gabbroic mush. Here we present data from two other localities situated north of the Minto Inlet on Victoria Island (Fig. 2.2), that we believe represent sections through coeval and possibly correlative sills. The P-sill (PS) is located ~20 km to the ENE of the LPS, whilst the West Uhuk sill (WUS) is another ~30 km to the ENE (Fig. 2.2). Both have olivine-enriched bases and were emplaced at the same stratigraphic level. The WUS is adjacent to a prominent fault-guided magma upflow zone known as the Uhuk Massif (UM: described in Bédard *et al.* (2012)), which preserves calc-silicate facies at some intrusive contacts (Nabelek *et al.*, 2013). These three olivine-enriched sills (WUS, PS and LPS) are collectively termed the Fort Collinson Sill Complex (FCSC). We will compare sections through them and document how bulk-rock compositions, mineral chemistry and isotopic compositions vary along strike. We will

suggest that the FCSC records a regional scale (> 50 km) olivine slurry replenishment event in a previously emplaced sill. The along-strike changes in composition recorded in the FCSC provide constraints on the geochemical and textural impacts of cumulate remobilisation and slurry emplacement. We also discuss how small amounts of dolostone assimilation could have increased the Mg/Fe ratio of the magma and buffered the Fo-content of equilibrium olivine in some parts of the FCSC.

5.3 Fort Collinson Sill Complex

The Fort Collinson Sill Complex (FCSC), comprising the West Uhuk Sill (WUS), the P-sill (PS) and the Lower Pyramid Sill (LPS), outcrops in the Collingwood Hills region of the Minto Inlier, just north of the Minto Inlet (Fig. 2.2). The FCSC was emplaced ~3 km stratigraphically beneath the coeval Natkusiak flood basalts. Previous work has documented the field relationships at the Uhuk Massif (Bédard *et al.*, 2012), showing that the Uhuk Massif (UM) is a magma upflow zone that extends towards the west as a conformable sill-like body, the WUS (Fig. 5.1). The WUS was emplaced into the dolostone-dominated Jago Bay Formation, only ~10 m above the contact with the underlying Fort Collinson Formation, which is dominated by quartz-arenites. The WUS is ~40 m thick, has sharp chilled upper and lower contacts, and contains a ~12 m thick olivine-enriched layer in its lower section that we refer to as the Olivine Zone (OZ). About 30 km to the WSW, we sampled a section through another olivine-rich sill (PS) that is located at exactly the same stratigraphic level as the WUS. No chilled margins are exposed at the PS, which has a slightly thinner OZ (~10 m thick) in comparison to the WUS. About 20 km to the WSW of the PS is the ~21 m thick LPS (chapter 4), which, again, is at the same stratigraphic position as the WUS and PS. Both chilled margins are exposed at the LPS, which has an OZ that is only ~7 m thick. The petrology and mineral chemistry of the LPS was described in detail by in chapter 4, where we argued on the basis of textural and mineral-chemical data that the LPS OZ is a hybrid rock that formed by mixing between a late olivine slurry and a resident gabbroic mush.

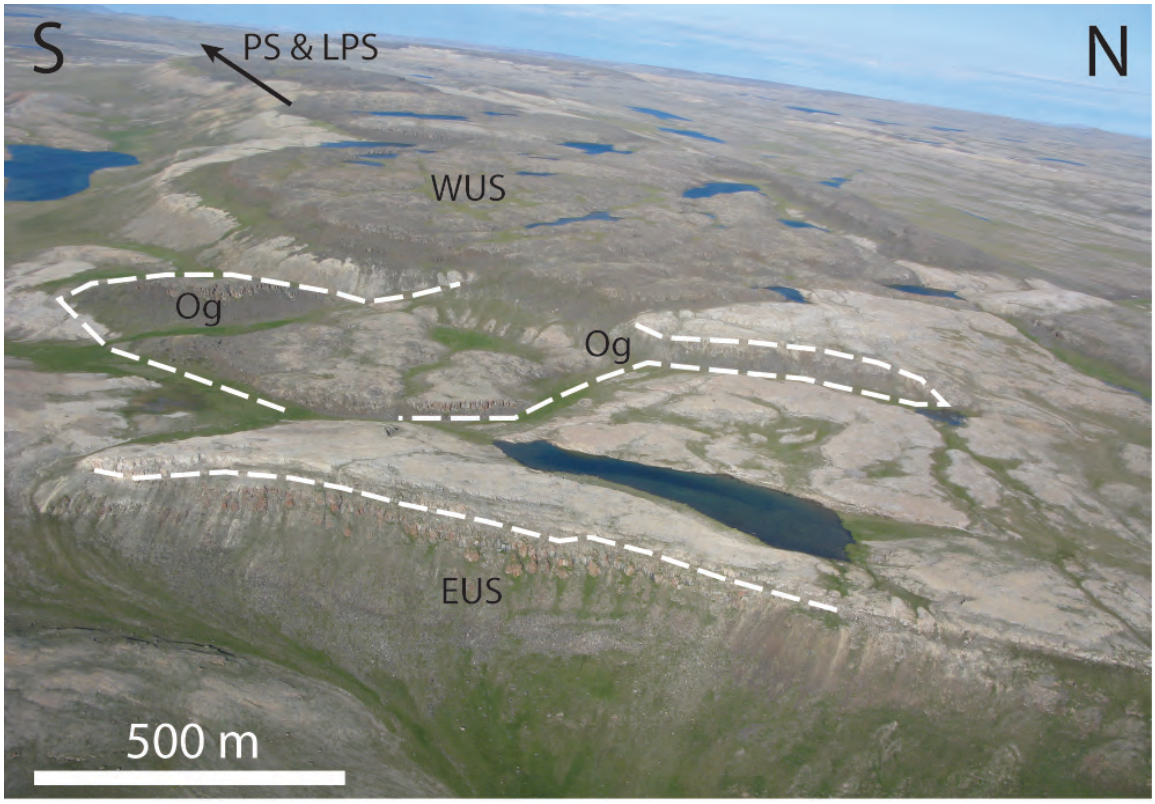

Fig 5.1: Field photo of the UM feeder system (looking west). The olivine-enriched East Uhuk Sill (EUS) jogs up-section into the WUS, with minor olivine-enriched (Og) sills between the two main sills. The WUS extends towards the west, towards to the PS and LPS.

5.4 Results

5.4.1 Petrography

The sills constituting the FCSC exhibit near-identical internal stratigraphies, albeit with differences in layer thicknesses. From bottom to top they have: an olivine-phyric (~5%) Lower Chilled Margin (LCM); an olivine-phyric (~10%) Lower Border Zone (LBZ); an Olivine Zone (OZ) composed of olivine-melagabbro to feldspathic-peridotite with olivine modes up to ~55%; a clinopyroxene-rich cumulate gabbro zone (CPZ), which is most prominent at the LPS; a doleritic gabbro zone (DZ) comprised of sub-ophitic clinopyroxene and plagioclase with a minor (< 10%) cumulate component; an aphyric Upper Border Zone (UBZ); an olivine-phyric (~5%) Upper Chilled Margin (UCM). The key features of each layer are summarised in an idealised FCSC stratigraphic log (Fig. 5.2). We will now describe the key features of each layer of the FCSC following the nomenclature of Irvine (1982), and then discuss along-strike sill-to-sill variations.

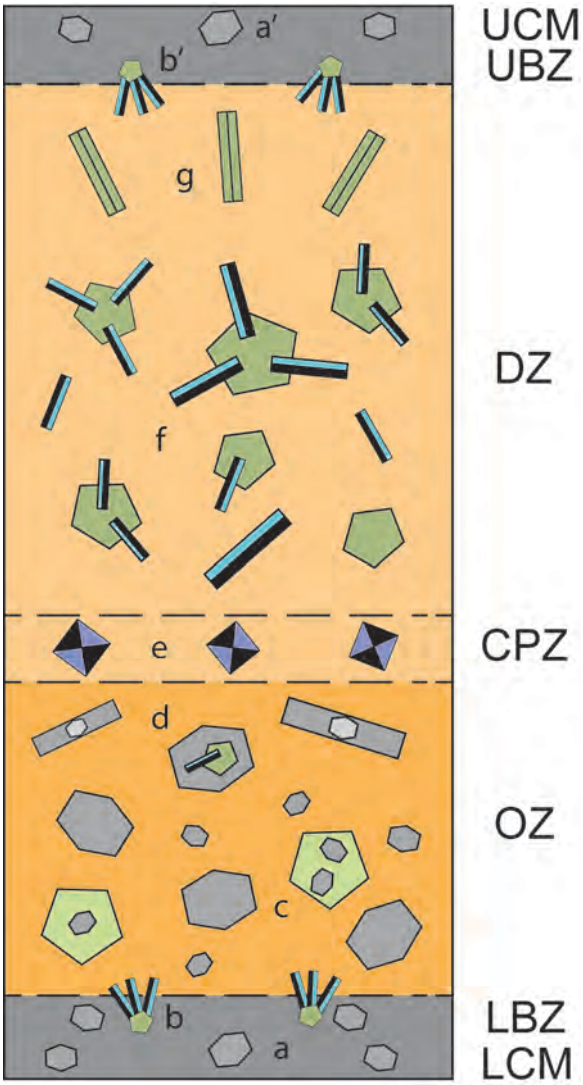

Fig. 5.2: A schematic log through the FCSC, showing key features of each layer. Both Lower and Upper Chilled Margins (LCM and UCM respectively) contain olivine phenocrysts (a; ~5%). The chilled margins grade into Lower and Upper Border Zones (LBZ and UBZ respectively) characterised by plagioclase and clinopyroxene dendrites (b; with local nucleation on the surfaces of olivine phenocrysts). The Olivine Zone (OZ) is characterised by high olivine modes (up to 55%) with primitive olivine primocrysts, pyroxene-poikilitic textures (c) and hopper olivine-clinopyroxene textures. The OZ also contains hopper olivines (d). The Clinopyroxene Zone (CPZ) is characterised by abundant (40-50%) sector-zoned clinopyroxene in an olivine-poor (5-10%) gabbroic matrix (e). The Doleritic Zone (DZ) consists of sub-ophitic plagioclase and clinopyroxene (f) with minor olivine, sometimes pseudomorphed by orthopyroxene. The top part of the DZ is characterised by acicular pyroxenes (g) and an increase in late-stage accessory phases (quartz, alkali-feldspar, hornblende and biotite).

Where it is visible, the thin (~5 cm) LCM contains 5% euhedral (0.5-2 mm) olivine phenocrysts in a very fine-grained groundmass (0.1 mm) of plagioclase and clinopyroxene dendrites. Small chromite microphenocrysts occur as inclusions in olivine and in the groundmass. In the WUS LCM, hopper olivine is also present (Fig. 5.3a). The UCM is exposed at both the LPS and WUS and also contains 5% olivine phenocrysts (or its

pseudomorphs) in a very-fine grained groundmass (0.1 mm). Amygdules (1-2 mm) filled with secondary chlorite, biotite and quartz, are present in the UCM.

The LPS LCM grades up into a ~1 m-thick LBZ, where euhedral (1-2 mm) olivine phenocrysts are embedded in a matrix composed of plagioclase and clinopyroxene dendrites (1-2 mm). The LBZ at the WUS and PS is generally similar, although the slightly thicker (~5 m) WUS LBZ also contains olivine with hopper morphologies (Fig. 5.3b). At the PS and WUS, the dendrite-textured basal LBZ grades up into an upper LBZ facies with a gabbroic-textured groundmass (Fig. 5.3c). Some olivine primocrysts appear to have been fractured and veined by groundmass plagioclase. Clinopyroxene oikocrysts contain inclusions of olivine, chromite and euhedral plagioclase laths. Minor groundmass orthopyroxene is also observed.

The LPS UCM grades down to an UBZ that is free of olivine phenocrysts, and which is composed of plagioclase and clinopyroxene dendrites. In chapter 4, we suggested that the absence of phenocrysts was due to crystal settling of olivine, such that the upper crystallisation front was no longer able to capture fast-settling phenocrysts. The WUS has a very thin UBZ, whereas the uppermost facies are missing from the PS as a result of erosion. The UBZ at the WUS grades down rapidly into varitextured DZ gabbros, some markedly pegmatitic with acicular pyroxene morphologies.

The LPS LBZ grades up into a ~7 m thick OZ composed of olivine orthocumulate melagabbro to feldspathic peridotite with 40-55% modal olivine. The OZ is slightly thicker (~9-10 m) at the PS, and thicker again (~12 m) at the WUS. In chapter 4, we subdivided the LPS OZ based on olivine morphologies. The LPS Lower OZ (LOZ) contains euhedral (1-2 mm) olivine primocrysts and finer-grained (0.5-1 mm) olivine that are enveloped by clinopyroxene oikocrysts and interstitial plagioclase. The LPS Middle OZ (MOZ) has fewer olivine primocrysts, and is dominated by hopper olivine that is intergrown with clinopyroxene (Fig. 5.3d). The LPS Upper OZ (UOZ) mostly contains hopper olivine (Fig. 5.3e), with subordinate primocrystic and groundmass olivine. The UOZ clinopyroxene is commonly euhedral and does not contain chadacrystic olivine inclusions.

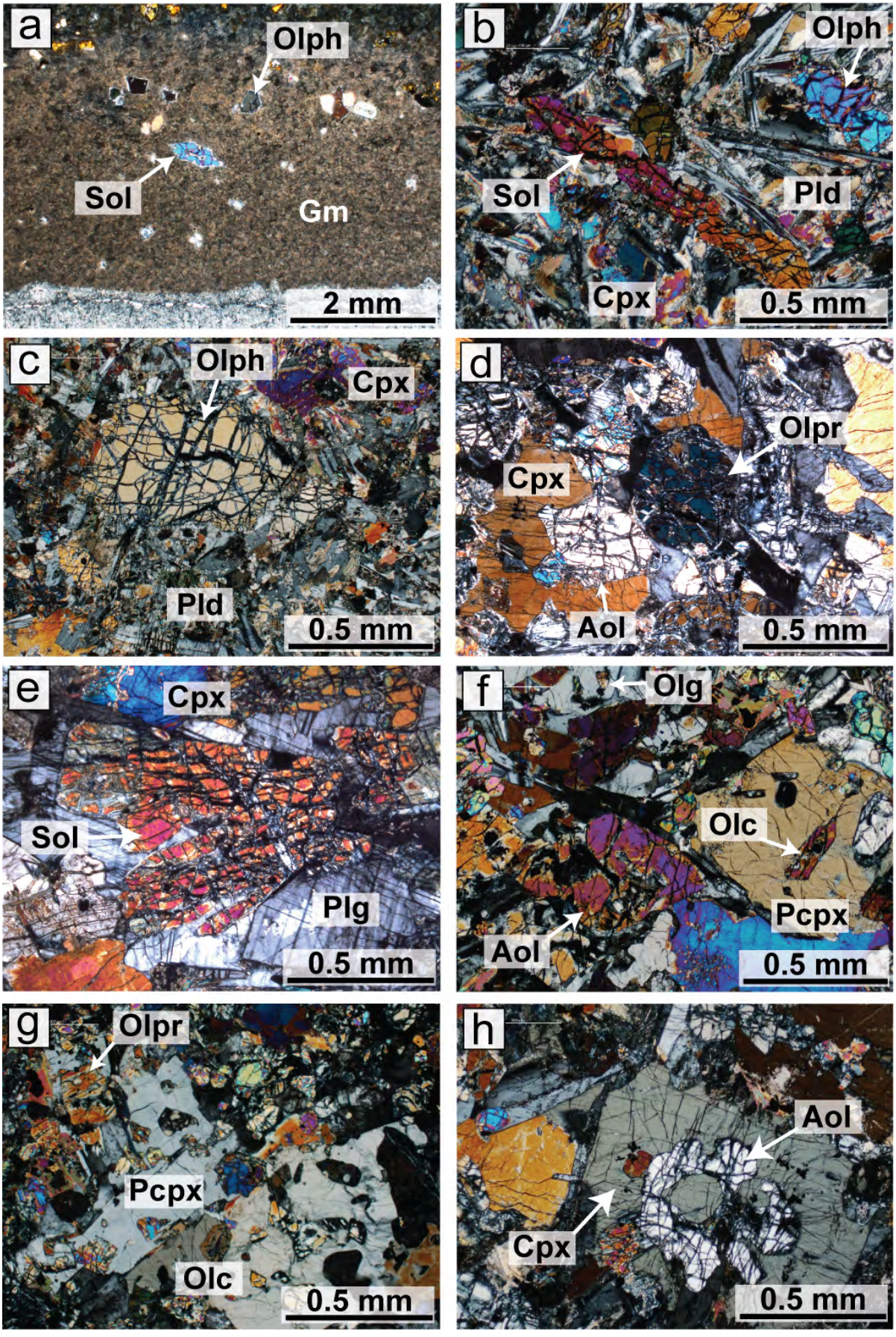
a
Olph
Sol
Gm
2 mm
b
Olph
Sol
Pld
Cpx
0.5 mm
c
Olph
Cpx
Pld
0.5 mm
d
Olpr
Cpx
Aol
0.5 mm
e
Cpx
Sol
Plg
0.5 mm
f
Olg
Olc
Pcpx
Aol
0.5 mm
g
Olpr
Pcpx
Olc
0.5 mm
h
Aol
Cpx
0.5 mm

Fig. 5.3 (page 71): Photomicrographs (all in crossed-nicols) of olivine morphologies and textural relationships in the FCSC. (a) The olivine-phyric WUS LCM with the lower contact with the Jago Bay formation visible. Olivine phenocrysts (Olph) and hopper olivines (Sol) are shown, residing in a very-fine grained groundmass (Gm). (b) The WUS LBZ contains both phenocrystic and hopper olivine can be seen residing in a fine-grained matrix of clinopyroxene (Cpx) and plagioclase dendrites (Pld). (c) The PS LBZ showing a euhedral olivine phenocryst residing in a dendritic matrix. (d) The LPS OZ (specifically the MOZ) showing both olivine primocrysts and hopper olivines that are overgrown by clinopyroxene. (e) The LPS OZ (specifically the UOZ) showing hopper olivines that are intergrown with interstitial plagioclase (Plg). (f) The WUS OZ showing hopper (resorbed?) olivine (Aol), olivine chadacrysts (Olc) enclosed in poikilitic clinopyroxene (Pcpx) and groundmass olivines (Olg) residing in interstitial plagioclase. (g) The WUS OZ showing euhedral olivine primocrysts (Olpr) and a coarse poikilitic clinopyroxene enclosing abundant olivine chadacrysts. (h) The PS OZ showing a hopper olivine that is overgrown by clinopyroxene.

In the PS and WUS, the divisions into LOZ, MOZ and UOZ are less clear than at the LPS. In the WUS OZ, hopper olivine can be seen at various levels rather than being restricted to the UOZ (Fig. 5.3f). Near the base of the PS and WUS OZ, clinopyroxene occurs both as oikocrysts (Fig. 5.3g) and as euhedral ’cumulus’ grains, some with internal ’fairy-rings’ of chromite microphenocrysts. Higher in the PS and WUS OZ, subordinate orthopyroxene occurs as oikocrysts, as euhedral prisms or is intergrown with clinopyroxene. Some olivine inclusions in clinopyroxene oikocrysts have hopper shapes and contain clinopyroxene inclusions (Fig. 5.3h). Plagioclase occurs as subhedral inclusions in clinopyroxene oikocrysts, as interstitial grains and as fine groundmass laths.

Overlying the LPS OZ is a thin (~1 m) CPZ, which is dominated by euhedral sector-zoned clinopyroxene (40-50%). Equivalents of the CPZ were observed at the PS interlayered with olivine-rich cumulates. CPZ-type rocks were not identified in our section through the WUS. In the PS, the euhedral sector-zoned clinopyroxene commonly has sieved internal zones, and may have alternating normal and reversed zones (in terms of Mg#). The matrix of the PS CPZ preserves hopper olivine that is cemented by plagioclase.

Above the LPS CPZ is a ~9-10 m thick DZ, which mostly consists of sub-ophitic clinopyroxene and plagioclase. Orthopyroxene (~10%) in the LPS DZ may be pseudomorphous after olivine. The habit of clinopyroxene changes gradually from more blocky prismatic crystals at the base of the LPS DZ to more acicular elongated prisms in the upper LPS DZ. The PS DZ and WUS DZ show a general similarity to the LPS DZ, but with some differences. At the WUS, the DZ is markedly thicker (~27 m) than at the LPS. The basal DZ at the WUS and PS contains 10% euhedral olivine (1-3 mm) in a gabbroic matrix (1-2 mm) with only minor Fe-Ti oxides (1-2%) and granophyric patches. Some

clinopyroxene grains are equant to euhedral, with optically distinct cores reminiscent of CPZ clinopyroxene. Plagioclase is generally anhedral, with a few coarser (1-2 mm) euhedral (cumulus?) laths that may have spongy internal zones. In the PS, this basal olivine-bearing DZ facies is thin and grades up rapidly into a varitextured doleritic gabbro that contains abundant Fe-Ti oxides and shows marked variations of grain size through the development of pegmatoidal patches. The basal WUS DZ described above is succeeded by a thick, doleritic-textured gabbro with acicular clinopyroxene habits. Approximately 12 m below the upper contact, the proportion of Fe-Ti-oxides and sulphides in this gabbro increases markedly (to ~10%), as does the amount of granophyre (to ~10%) and hornblende (~5%). The uppermost portions of the WUS DZ resemble the upper varitextured gabbroic facies seen at the PS, with abundant pegmatoidal patches and acicular pyroxene habits. We interpreted the increase in these accessory phases in the upper DZ at the LPS to represent an evolved residue (sandwich horizon) that formed by *in-situ* fractional crystallisation (as described for the LPS chapter 4).

5.4.2 Bulk-rock chemistry

The chilled margin compositions of the WUS and LPS are very similar (10.6 *vs* 10.5 wt% MgO, respectively: appendix F1). Metre-scale dykes emplaced near the contacts of the UM also have similar compositions (appendix F1). We calculated an average FCSC chill composition of 10.3 wt% MgO (appendix F1) from 10 samples (chills, thin sills and dykes). This chill composition was used in chapter 4 as a starting composition for PELE (Boudreau 1999) fractional crystallisation modelling, which will be used to anchor some of the models in the chapter 5 discussion section below.

Many of the OZ rocks from the FCSC show MgO-enrichment and Al_2O_3-depletion trends indicating that they contain cumulus olivine (appendix F1). The OZ rocks have MgO contents between 18 and 27 wt%, Al_2O_3 between 6 and 10 wt%, and Ni contents up to 720 ppm (appendix F1). The CPZ rocks have high CaO contents, with values between 12 and 14 wt%, and high Cr and Sc (1500 and 52 ppm, respectively), indicating a cumulate clinopyroxene component. The major element chemistry of DZ rocks is very similar in all three sections of the FCSC, with MgO contents ranging between 6 and 10 wt%. FCSC DZ rocks show clear trends of increasing FeO and TiO_2 and decreasing Al_2O_3 as MgO

decreases that imply fractionation along a multiphase cotectic (Fig. 5.4). Many DZ rocks have high Al_2O_3 contents (11 to 15 wt%) and Sr contents (250 ppm), and some show positive Eu anomalies on MORB-normalised spidergrams (not shown), implying a plagioclase cumulate component, consistent with plagioclase crystal habits.

The similarity of igneous stratigraphy, petrography and major element compositions at the WUS, PS and LPS, indicates very similar differentiation paths of a common (or at least very similar) magma. The most notable difference between the three sills is that the OZ rocks show a systematic trend towards more Fe-rich bulk compositions towards the west (Fig. 5.4 and appendix F1), which will be discussed below.

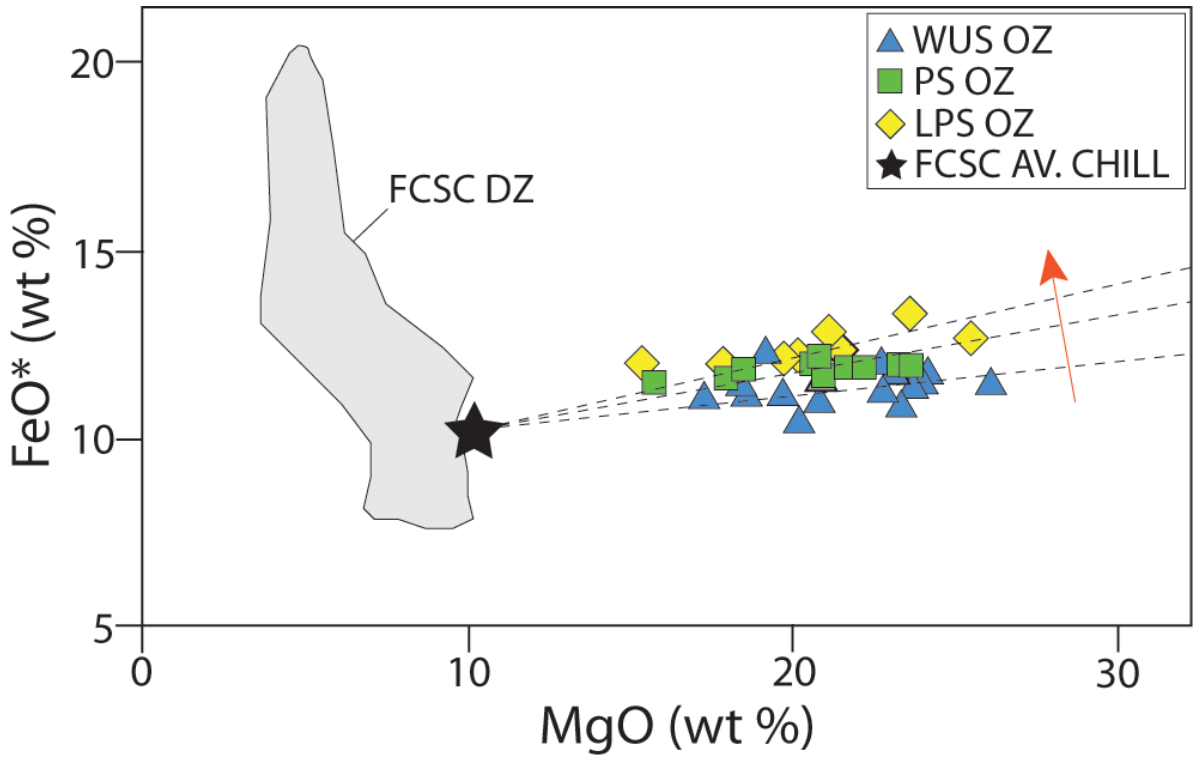

Fig. 5.4: A bulk-rock FeO* versus MgO diagram. The FCSC OZ arrays extend towards MgO-enrichment as well as rotating towards more FeO* compositions (shown by the arrow). The FCSC DZs extend towards FeO* enrichment, with decreasing MgO. The dashed lines are least square regression fits to the WUS, PS and LPS OZ arrays that are forced through the average FCSC chill (appendix F1). FeO* has been recalculated from total Fe, with the proportion of Fe^{2+} to Fe^{3+} set at 0.9.

5.4.3 Olivine chemistry

Olivine chemical data (appendix F2) provides *in-situ* compositional constraints on the crystals and melts involved in the formation of OZ rocks in the FCSC. An array of different olivines can be recognised in the FCSC OZ and we will show that there is a linkage between the morphology, composition and style of zonation. The chemistry and zonation of olivine within the LPS OZ was described in detail in chapter 4 and we will summarise those findings here before comparing them to the PS and WUS. NiO (wt%) compositions of olivine range between 0.4-0.1 wt% and are coupled with Fo behaviour.

Five different types of olivine morphologies were observed within the LPS OZ, each with a particular range of forsterite (molar Fo = 100 x Mg/[Mg+Fe^{2+}]) content and distinctive core-to-rim zoning styles. Euhedral olivine primocrysts in the LPS Lower OZ (LOZ) are the most primitive, with core compositions ranging between Fo_{88-82}. These olivine primocrysts have narrow Fe-rich rims (Fo_{75}). This group of primitive olivine primocrysts was interpreted to have been carried as suspended 'phenocrysts' in a late olivine slurry replenishment (e.g. Fig. 4.17), with the Fe-rich rims recording *in-situ* differentiation of the melt after emplacement. Euhedral-subhedral chadacrystic olivines that are enclosed by clinopyroxene oikocrysts are more evolved than the primocrysts and have a restricted range of composition, between Fo_{83-81}. Although many are normally zoned, some olivine chadacrysts show reverse zoning. The crystallisation of clinopyroxene oikocrysts must therefore post-date the origin of this reverse or normal olivine zoning. Groundmass olivines are similar in size and shape to chadacrysts enclosed by clinopyroxene oikocrysts but are more evolved (Fo_{81-72}). Groundmass olivines are typically normally zoned, but some also show reverse zoning. The hopper olivines of the LPS Upper OZ (UOZ) have similar compositional ranges (Fo_{80-73}) to groundmass olivines. The hopper olivines commonly exhibit reverse zoning with the most primitive rim compositions reaching Fo_{80} in the LPS UOZ.

Olivine primocrysts are also common in the WUS OZ and PS OZ, with core compositions up to Fo_{90} being observed at the PS. Olivine chadacrysts enclosed by clinopyroxene oikocrysts have Fo_{83-78} compositions, similar to the LPS range. Groundmass olivines at the WUS and PS range to lower Fo contents (Fo_{80-77} and Fo_{83-68} respectively), as for the LPS.

The Fo-contents of hopper olivines at the WUS and PS sites are very similar to those of the LPS OZ, but at the WUS and PS, they are mostly normally zoned.

5.4.4 Lead and sulphur isotopes

Discrimination plots of $^{208}Pb/^{204}Pb$ *vs* $^{206}Pb/^{204}Pb$ and $^{207}Pb/^{204}Pb$ *vs* $^{206}Pb/^{204}Pb$ are presented in Fig. 5.5. The WUS and LPS of the FCSC are plotted (we did not analyse PS samples for Pb-isotopes), along with other olivine-enriched sills (Kat's, Dick's and Uwe's) from the Minto Inlier, some of which may be correlative with the FCSC. The WUS OZ and DZ are in approximate isotopic equilibrium in both Pb-isotope plots, consistent with derivation from the same magma. In contrast, the LPS OZ and DZ are isotopically distinct in both Pb-isotope plots, indicating that these layers were derived from discrete magmas. This observation supports the replenishment model developed in chapter 4.

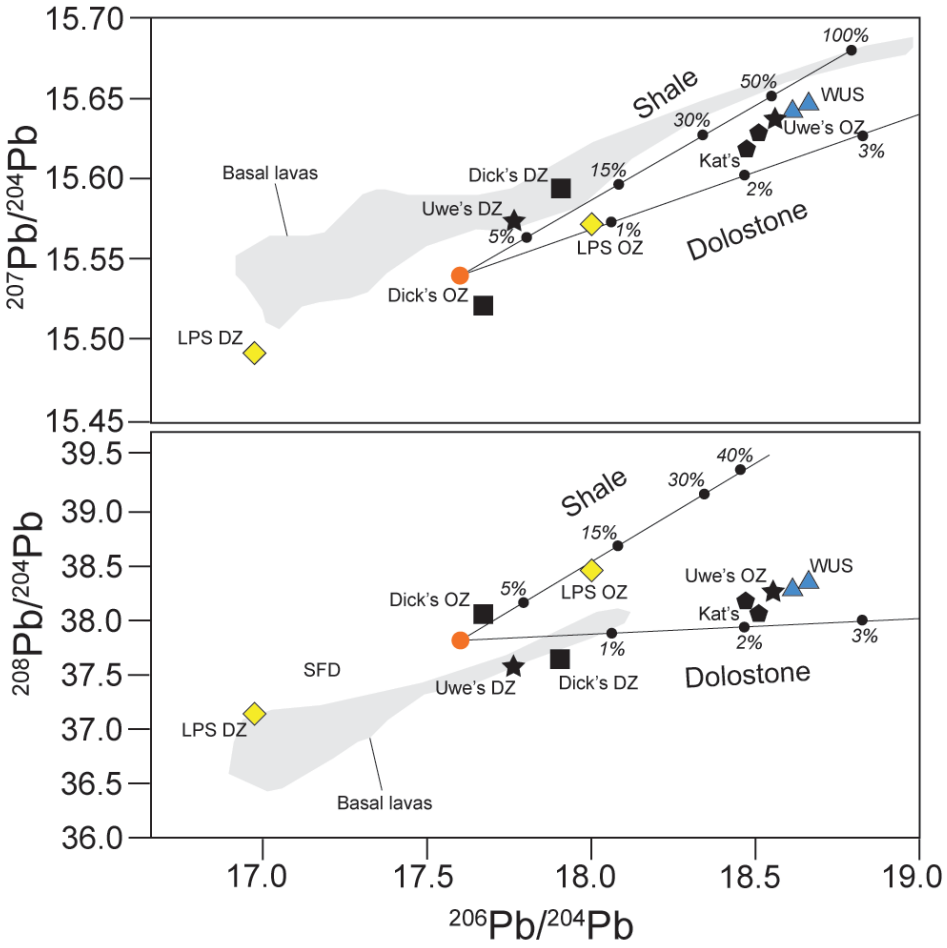

Fig. 5.5: Pb-isotope discrimination plots with OZ and DZ rocks of the FCSC shown, along with other possibly correlative sills (Dick's, Kat's and Uwe's). (a) $^{207}Pb/^{204}Pb$ *vs* $^{206}Pb/^{204}Pb$ and (b) $^{208}Pb/^{204}Pb$ *vs* $^{206}Pb/^{204}Pb$. The compositional field of the basal lava unit of the Natkusiak Flood Basalts are plotted (grey field) showing Pb-isotope compositions that overlap with those of the Type-1 olivine-enriched Franklin sills.

Assimilation trajectories for dolostone and shale are shown with the starting composition set as the average Type-1 Franklin magma composition.

Dick's and Uwe's OZ and DZ are also in Pb-isotope disequilibrium, indicating these are also composite sills. Kat's sill (a few kilometres SE of the LPS: Fig. 2.2) is also located along the top of the Fort Collinson Formation contact, which based on field relationships is thought to be an offshoot of the FCSC. Isotopically, Kat's sill is similar to the WUS, with an OZ and DZ that are in approximate isotopic equilibrium.

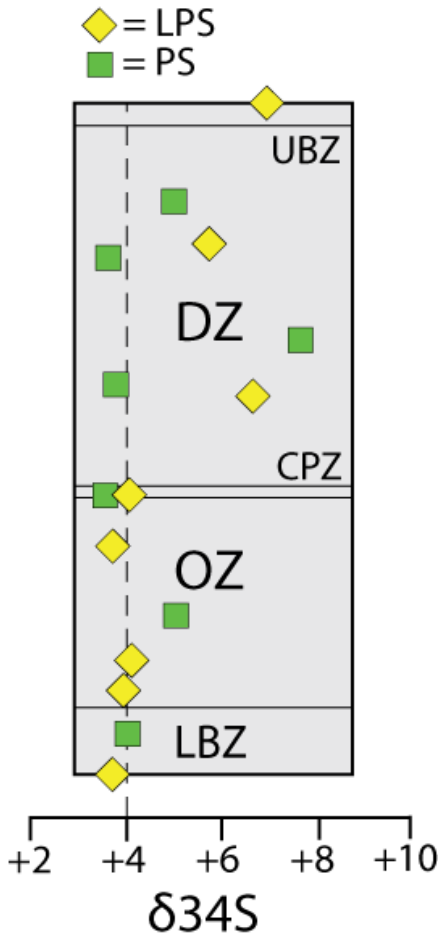

Fig. 5.6: S-isotope values for the PS and LPS. The stratigraphic log thickness has been normalised in order to compare the data from the two sills.

S-isotopes for the PS and LPS are presented in Fig. 5.6. The PS and LPS exhibit similar $\delta^{34}S$ profiles, with contrasting ranges for their OZ and DZ rocks. The LPS exhibits more of a 'step-change' between OZ and DZ. In general OZ rocks have $\delta^{34}S$ values ranging between +3‰ and +5‰, whilst the DZ rocks have a greater range in $\delta^{34}S$ values between +3‰ and +8‰. The apparent decoupling between the OZ and DZ shown by the S-isotopes

is consistent with the Pb-isotope disequilibrium observed in the LPS. Values of +3 to +4‰ are common for the Franklin magmas and are suggestive of a slightly anomalous melt source composition (Hryciuk et al. Submitted); whereas the range to higher $\delta^{34}S$ seen in the DZ rocks suggests these facies include a sedimentary crustal component.

5.5 Discussion

5.5.1 Are the three FCSC sills a single sill?

The WUS, PS and LPS are all exposed at the same stratigraphic horizon, immediately above the upper contact of the Fort Collinson Formation marker unit. They share a similar internal stratigraphy with similar first-order bimodal layering (OZ/DZ), and have similar petrographic features (Fig. 5.3), chilled margin compositions (appendix F1) and olivine compositions (appendix F2). Additionally, the LPS and PS show a roughly similar split between the S-isotope signatures of the OZ versus the DZ (Fig. 5.6). Dykes at the UM branch towards the west (see Fig. 6 in Bédard et al., (2012) – appendix A) suggesting westward sill propagation. The thickness of the OZ decreases systematically from 12 m at the WUS to 7 m at the LPS, as does the total sill thickness (from 40 m at the WUS to 20 m at the LPS). These relationships suggest that the WUS, PS and LPS may be a single, laterally extensive sill (> 50 km), that propagated westward from a feeder dyke at the UM. We cannot completely exclude the null hypothesis, however, that these three sills are separate injections of a similar magma that was emplaced at the same stratigraphic level, and that all three evolved by similar differentiation paths to generate similar igneous layering, bulk-rock chemistry, OZ/DZ S-isotope dichotomy (LPS and PS), petrographic features and mineral compositions. Indeed, many olivine-enriched Type-1 sills from the Minto Inlier that were emplaced at other stratigraphic levels develop very similar facies sequences. However, it would be extremely fortuitous for three separate intrusions to not only share so many characteristics, but also show a systematic westward thinning of the OZ, as well as total sill thickness. We will argue that the systematic westward Fe-enrichment trend in the FCSC OZ (Fig. 5.4) is consistent with a westward magma propagation hybridisation model, a scenario that is difficult to explain if the WUS, PS and LPS were three completely separate intrusions.

5.5.2 Are the sills of the FCSC composite intrusions?

In chapter 4, we presented mineral-chemical and textural data indicating that the LPS OZ is a hybrid rock that was produced when a primitive olivine slurry was emplaced into a resident gabbroic mush. The OZ from the PS and WUS show similar features and we infer from this that they formed in a similar manner. S-isotope data (Fig. 5.6) support the distinct origin of the OZ and DZ and seem to preclude a simple fractional crystallisation relationship between the two layers at the PS and LPS. Our limited database of bulk rock radiogenic isotope compositions (Fig. 5.5) provides additional constraints and suggests an even more convoluted intra-sill differentiation story for the FCSC. 1) It reinforces the S-isotope conclusion that LPS OZ is distinct from its DZ (Fig. 5.6). 2) It suggests that the WUS DZ and OZ are in approximate Pb-isotopic equilibrium. This could suggest that the WUS DZ developed by internal differentiation of the same magma from which the WUS OZ accumulated; yet the two are very different in terms of S-isotopes (unpublished data). 3) It suggests that magmas either experienced open-system processes with an extremely heterogeneous host stratigraphy as they migrated through the crust, or that magmas originated in an extremely heterogeneous source mantle and were not homogenised *en-route*, or both. Thus, the LPS OZ acquired radiogenic isotope signatures that are distinct from those in the LPS DZ, and which also differ from those in the WUS. We will now examine the Fe=Mg systematics of the FCSC, so as to determine the compositions of crystals and melts involved in intra-sill differentiation. We will reconsider the isotopic constraints afterwards.

5.5.3 FCSC OZ Fe=Mg systematics

5.5.3.1 Crystal-melt constraints - a westward shift towards more evolved magmas?

The Fe=Mg relationships help us to constrain the composition of magmas and crystals involved in the formation and differentiation of the sills constituting the FCSC. Fig. 5.7 shows the average FCSC chill composition, together with analyses of DZ and OZ rocks from the FCSC sills we have sampled. We have also plotted the LLD pathway predicted from PELE (Boudreau 1999) for the average FCSC chill composition, and labelled the point where plagioclase and clinopyroxene join Fo_{84} olivine on the liquidus. This model LLD pathway overlaps the compositions of DZ rocks from the FCSC, supporting the

notion that these are cotectic precipitates derived from fractional crystallisation of a tholeiitic melt similar to the average FCSC chill composition.

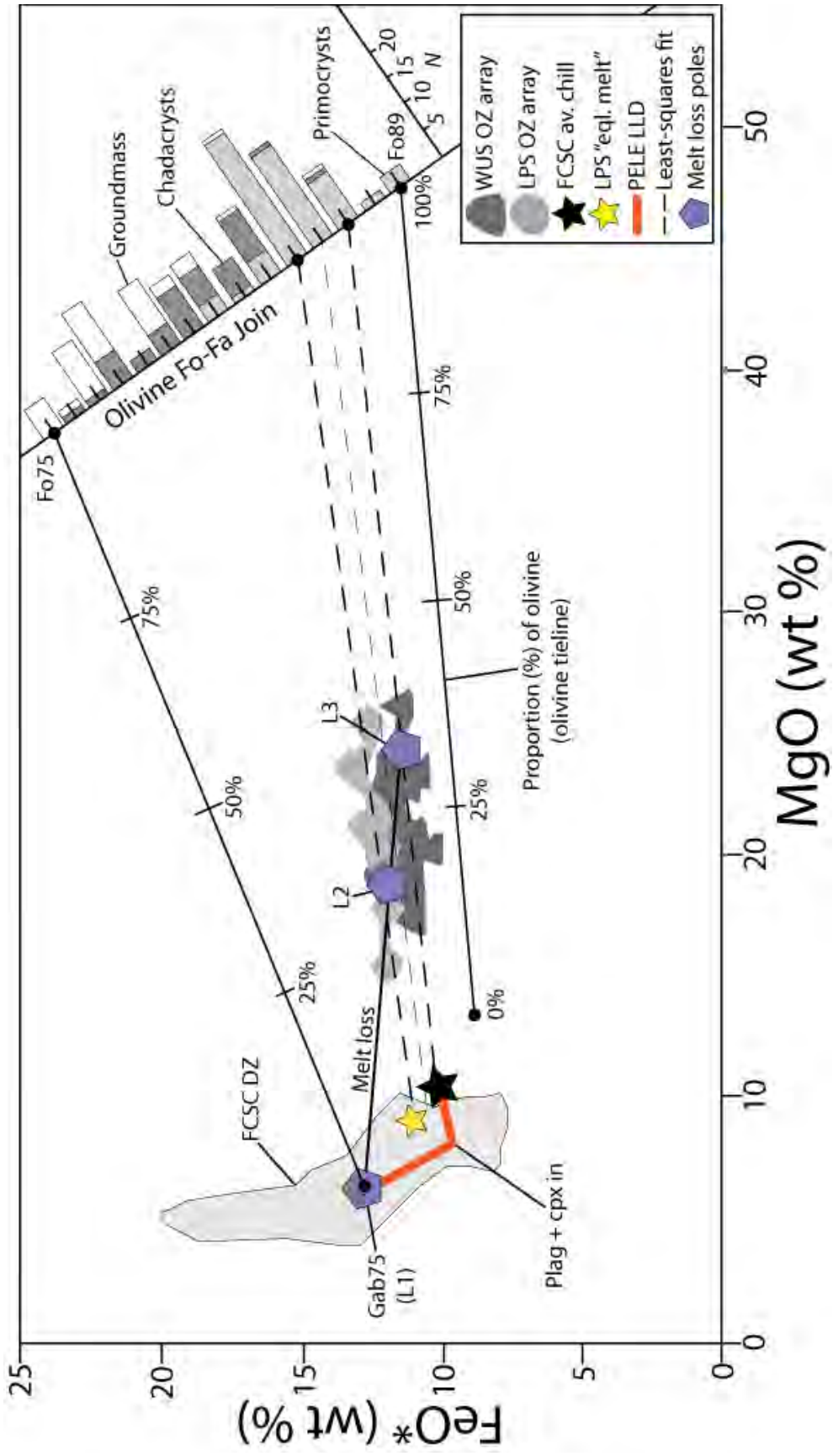

Fig. 5.7 (page 82): The Fe=Mg systematics of the FCSC with bulk-rock compositional fields as well as the constraints provided by the olivine compositional data and their inverse melt compositions. The histogram attached to the olivine Fo-Fa join shows the distribution of primocrystic, chadacrystic and groundmass olivine compositions observed in the FCSC OZ from all three sills belonging to the FCSC. Also shown on the diagram is a melt loss trajectory with collinear L1, L2 and L3 poles (see text for details).

Although the petrography (Fig. 5.3) and MgO-enrichment trends of the FCSC OZ rocks (Fig. 5.4) imply olivine accumulation, the OZ arrays in the FCSC sills (WUS, PS and LPS) show distinct trends (Fig. 5.4). In principle, each individual OZ bulk rock composition represents a two-component mixture of cumulus olivine and trapped melt, now mostly represented by clinopyroxene and plagioclase. The modal proportion of olivine in these rocks ranges between 20-55% (Fig. 5.7), of which most is 'cumulus' textured. A least squares regression trend was fitted to each OZ array, defining both the composition of (bulk) olivine that accumulated from the melt (Cawthorn *et al.*, 1992, Wilson, 2012) and the composition of the dominant entrapped basaltic melt (Fig. 5.7). The WUS OZ array intersects the average FCSC chill composition (10.3 wt% MgO) and projects towards an olivine composition of $Fo_{87,}$ which we will later show is not in equilibrium with this melt composition. The PS OZ array projects towards a more evolved basaltic melt composition (9 wt% MgO) and a more evolved olivine composition of Fo_{86}. The LPS OZ array projects toward a still more evolved basaltic melt composition (8 wt% MgO) and a still more evolved olivine composition of Fo_{85}. If we force the regression of the LPS OZ through the average FCSC chill composition (shown in Fig. 5.4), then the bulk-extract olivine compositions that are required to satisfy the bulk-rock mass balance for the PS and LPS OZ rocks are even more Fe-rich (~Fo_{83}) than the dominant primocrystic olivines (~Fo_{86}) that these rocks contain. Although the bulk-rock Fe=Mg systematics imply that the olivine cumulates in the FCSC were derived from increasingly more Fe-rich melts towards the west, the observed compositions of olivine in these rocks only approximately matches the required crystal 'cumulates', and do not show systematic Fe-enrichment towards the west (Fig. 5.7 and appendix F2). The diversity of olivine compositions (histograms on the Fo-Fa join: Fig. 5.7) observed within each OZ does not fit an idealised equilibrium crystal-extract model (Cawthorn *et al.*, 1992), and implies that the OZ cumulate arrays reflect an average cumulate formed from a heterogeneous olivine crystal cargo.

5.5.3.2 Determining OZ porosities using inverse melt modelling

The fossil porosity of each OZ sample from the FCSC is defined from its position on the Fe=Mg diagram (Fig. 5.7), with the proportion of olivine in each rock ranging between 20-55%. We tested these porosities using the equilibrium distribution method of Bédard (1994). The equilibrium distribution method uses the bulk-rock trace element contents of plutonic rocks to evaluate the relationships between the compositions of cumulate crystals and the amount and composition of its trapped melt fraction (TMF). It can be used to constrain the TMF if the melt composition is known. To begin, we assumed that all WUS OZ cumulates formed from a melt similar to the average FCSC chill composition (supported by the position of the WUS OZ array least squares regression: Fig. 5.7). The model melts calculated from the WUS OZ rocks resemble the average FCSC chill composition for TMFs ranging between 50-70%, for complementary olivine modes of 30-50% (results included in appendix F1). The WUS OZ model melt solutions are almost identical to the olivine modes defined on the Fe=Mg diagram (Fig. 5.7). We fitted the LPS OZ model melts to typical 8 wt% MgO Franklin suite melt (average of Type-1 chills between 7.5 and 8.5 wt% MgO) because the LPS OZ array least squares regression intersects a melt with this more evolved composition (Fig. 5.7). The model melts calculated from the LPS OZ rocks yield close matches to this 8 wt% MgO melt with TMFs that are very similar to those defined on the Fe=Mg diagram (Fig. 5.7). The LPS OZ rocks range to slightly lower modal TMF (higher olivine modes), in comparison to those calculated for the WUS OZ.

In summary, the porosities calculated using the equilibrium distribution method closely resemble the porosities defined on the Fe=Mg diagram, supporting the inference that OZ rocks are principally composed of olivine and trapped melt with compositions that match those defined by regression of OZ rocks on the Fe=Mg diagram (Fig. 5.7). Only 2-3% fractional crystallisation is needed to explain the incompatible trace element variation between melts calculated to be in equilibrium with the WUS OZ and the LPS OZ (Fig. 5.7). PELE fractional crystallisation modelling implies that ~5% olivine-only fractionation is required to shift melt MgO from 10 to 8 wt%, consistent with what was calculated from the trace elements.

5.5.4 Can progressive magma fractionation explain the westward FCSC OZ differentiation trend?

The westward Fe-enrichment trend in the FCSC OZ (Fig. 5.4) could perhaps be interpreted as a result of olivine fractionation during flow. However, the absence of a systematic trend towards more evolved olivine compositions towards the western end of the FCSC OZ is inconsistent with this hypothesis. Instead, the data show that the compositions of olivine primocrysts and chadacrysts are almost identical in the three OZ sections (appendix F2). The Fe=Mg systematics imply that the WUS OZ formed from an accumulation of primitive olivine crystals originating from a melt almost identical in composition to the average FCSC chill composition (Fig. 5.7). Such a melt (10.3 wt% MgO) would be saturated only in olivine (+ minor chromite). Therefore, the WUS OZ could plausibly be interpreted to have formed by partial separation of olivine from a melt similar in composition to the average FCSC chill (Cawthorn *et al.,* 1992). In contrast, the LPS OZ array implies extraction of less forsteritic olivines from an evolved melt composition (8 wt% MgO), which would have been very close to cosaturation in pyroxene and plagioclase (Fig. 5.7). Consequently, this melt should not have been able to create a 7 m thick sequence of olivine cumulates in the LPS, suggesting that the LPS OZ contains 'excess' olivine. One might have inferred that the LCM of the LPS (being only ~1 m below the LPS OZ) should have been the melt from which the LPS OZ crystallised. However, the misfit between the entrapped melt composition predicted from the LPS OZ array (Fig. 5.7) and the LPS LCM (appendix F1) implies that the melts in equilibrium with the LPS OZ had a different and more complex origin. We contend that the westward Fe-enrichment trend in the OZ cannot be explained solely by fractional crystallisation during magma flow in the FCSC.

5.5.5 Can variable degrees of compaction explain the lateral Fe-enrichment trend in the FCSC OZ?

Compaction of cumulates is one mechanism by which pore melt can be expelled from a crystal mush (Sparks *et al.*, 1985, Mathez *et al.*, 1997, Meurer & Boudreau, 1998). The FCSC thins from 40 to 20 m towards the west. One would predict faster cooling and consequently less efficient compaction at the thinner LPS, in comparison to the thicker

WUS. Preferential retention of an Fe-enriched trapped melt fraction (TMF) might explain why LPS OZ bulk-rock Fe-contents are higher than in the WUS OZ. A similar mechanism was proposed to explain the along-strike increase in TMF within gabbronorites below the pyroxenite marker in the eastern Bushveld Complex (Lundgaard *et al.*, 2006).

We can graphically determine the amount of pore melt loss required to shift the LPS OZ array to the lower Fe-contents that are typical of the WUS OZ array (Fig. 5.7). The composition of this hypothetical extracted pore melt can be determined by drawing a line that passes through two OZ rocks, one from the WUS array and one from the LPS array (Fig. 5.7). The composition of this hypothetical extracted pore melt (Gab75 or L1 on Fig. 5.7) corresponds to a melt in equilibrium with Fo_{75} olivine and is similar to what was calculated to be in equilibrium with groundmass olivine from the LPS OZ in chapter 4. The amount of pore melt loss required to shift the LPS OZ (L2 pole on Fig. 5.7) array to the WUS OZ (L3 pole on Fig. 5.7) array is ~30% (Fig. 5.7). We tested this hypothesis by subtracting Gab75 pore melt (corresponding to the trace element composition of a DZ rock matching this Fe/Mg bulk-rock composition from the Victoria Island database) from the LPS OZ rock, to see if the result matched the target WUS OZ rock (e.g. L2 – L1 = L3: Fig. 5.7). The best-fit trace element profile requires the loss of ~15% Gab75 from LPS OZ to reproduce WUS OZ (Fig. 5.8). This is substantially less than the ~30% melt loss calculated graphically from the Fe=Mg diagram (Fig. 5.7), indicating that the systematic westward Fe-enrichment trend in the FCSC is not a function of variable pore melt loss during compaction.

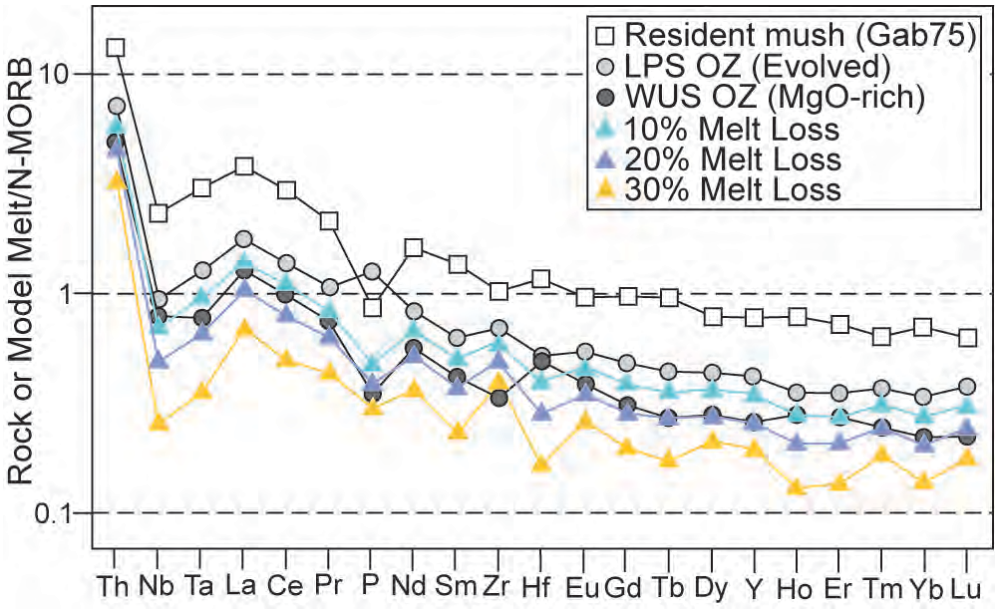

Fig. 5.8 (page 86): Spidergram showing the trace-element composition of the inferred resident mush pore melt (Gab75; with 6 wt% MgO and 13 wt% FeO*) taken from the database of FCSC DZ compositions (appendix F1). Also plotted are the LPS OZ and WUS OZ rocks that fall on a collinear array with Gab 75 on Fig. 5.7 (L2 – L1 = L3). The calculated trace-element signatures of the LPS OZ with Gab75 removed from this (in proportions of 10, 20 and 30%) are also shown. This melt loss trace-element signature best fits the WUS OZ with ~15% Gab75 removed from the LPS OZ (see text for details). N-MORB normalizing values are from McDonough and Sun (1995).

5.5.6 Mixing between an olivine slurry and a resident gabbroic mush?

In chapter 4, we argued that the LPS OZ is a hybrid rock that formed from a mixture of an evolved component similar in composition to the DZ and an injected magma charged with olivine. This inference is supported by the isotopic data (Fig. 5.5 and 5.6) that demonstrate that the LPS OZ and DZ are not strictly consanguineous. We first constrain the compositions of the components involved, and then quantify the proportions of each component in the mixture using the Fe=Mg diagram (Fig. 5.9), in order to evaluate whether variable degrees of mixing can explain the lateral differentiation trend in the FCSC OZ.

5.5.6.1 Component 1 - resident gabbroic mush

In chapter 4, we argued that the LPS contained a partly crystallised gabbroic mush at the time of olivine slurry replenishment. The composition of the gabbroic mush at this juncture was constrained by comparing the PELE LLD of the average FCSC chill with the melt composition calculated to be in equilibrium with evolved olivine cores located in the LPS OZ. These cores were interpreted to be xenocrystic, being derived from the host gabbro mush. In fact, the composition of evolved xenocrystic olivine cores is very similar across the FCSC, ranging between $Fo_{77\text{-}75}$. In chapter 4, we calculated from Fe=Mg olivine-melt equilibria that these olivine xenocrysts were in equilibrium with melts of ~6 wt% MgO. The LLD for fractional crystallisation of the average FCSC chill is plotted on Fig. 5.7. At 6% MgO, the PELE model predicts that 40% of the melt has solidified, containing 11% olivine, 16% plagioclase and 13% clinopyroxene. The location of this resident mush-mixing pole is labelled as Gab75, and it lies approximately in the middle of the FCSC DZ compositional field (Fig. 5.9a & b). Olivine cores as evolved as Fo_{73} are present in the LPS UOZ. We label this more evolved resident mush as Gab73 (Fig. 5.9c). We also define a third possible resident mush mixing pole (Sandwich Horizon: SdH: Fig. 5.9c) that would correspond to the most evolved possible FCSC DZ compositions.

5.5.6.2 Component 2 - olivine slurry

The olivine primocrysts (Fo_{88-82}) in the LPS OZ were interpreted to have been derived from an olivine slurry that was injected into the evolved resident gabbroic mush (e.g. Fig. 4.17). The most primitive olivine primocrysts observed in the FCSC OZ have core compositions up to Fo_{90}, but the median Fo-content of olivine primocrysts/phenocrysts is Fo_{86} (see histograms on Fig. 5.7). The WUS OZ array links the average FCSC chill composition to olivine compositions (Fo_{87}) that are similar to the olivine primocrysts found within these rocks. Therefore, the WUS OZ appears to represent a mixture of a melt similar to the average FCSC chill and forsteritic olivine. In order to be mobile, such an olivine slurry must have contained > 50% melt (Paterson, 2009); so it seems plausible to suggest that the lower-MgO, melt-rich part of the WUS OZ may approximate the olivine slurry mixing component. We use the average WUS OZ composition (OS87a: Fig. 5.9a) as one potential olivine slurry-mixing pole. This composition (OS87a) corresponds to 20% olivine (Fo_{87}) in a primitive carrier melt (13 wt% MgO). The composition of this primitive carrier melt was determined by calculating the melt in equilibrium with Fo_{87} olivine using the Fe=Mg olivine-melt exchange coefficient (Kd = 0.34) of Matzen *et al.* (2011) with all Fe as FeO. This calculated carrier melt is more primitive than the FCSC chill, indicating that the melts in equilibrium with this olivine were unfractionated and that the WUS OZ array defined in Fig. 5.7 is not in equilibrium with the projected olivine composition. However, given the large spread of olivine primocryst compositions in the FCSC OZ (Fig. 5.7) it is likely that the olivine slurry was compositionally heterogeneous. The median of olivine primocryst core compositions from the FCSC OZ is Fo_{86} (see histograms on Fig. 5.7). This second potential olivine slurry-mixing pole (OS86a: Fig. 5.9b & c) would contain 30% olivine (Fo_{86}) and a carrier melt with 12 wt% MgO, also calculated using the olivine-melt Fe=Mg exchange coefficient of Matzen *et al.* (2011). More olivine-rich slurry poles can also be defined. One, which contains 45% olivine, is on the WUS array (OS87b) and another with 55% olivine is on the Fo_{86} tieline (OS86b: Fig. 5.9c).

5.5.6.3 Mixing calculations

Mixing the Gab75 and OS87a components in a proportion of 70:30 creates a hybrid, olivine charged magma that falls on the LPS OZ array (Fig. 5.9a). Mass balance implies

that this hybrid magma would contain ~15% olivine primocrysts, primarily inherited from the OS87a component, and would have bulk MgO values between ~15-17 wt%. These hybrid magmas could then unmix to generate the LPS OZ array. Such unmixing was argued to play an important role in the development of the LPS OZ, with upward melt expulsion leading to the formation of the clinopyroxene that dominates the CPZ that overlies the OZ (section *4.5.6.2* & Fig. 4.16). The mixing lines (Fig. 5.9a) also passes through the PS OZ array, indicating that the PS OZ would contain a slightly (~5%) higher proportion of olivine slurry. This pattern is consistent for the PS OZ in all the mixing calculations presented below. It is possible to produce a more MgO-rich 1-stage hybrid that could match the more olivine-rich facies of the OZ (19-21 wt% MgO or LOZ). To do so, the olivine slurry would need to contain a higher proportion of olivine (e.g. OS87b). Mixing OS87b (containing 45-50% olivine), with Gab75 can produce these more MgO-rich compositions as one event, without the need for post-hybridisation unmixing (Fig. 5.9a).

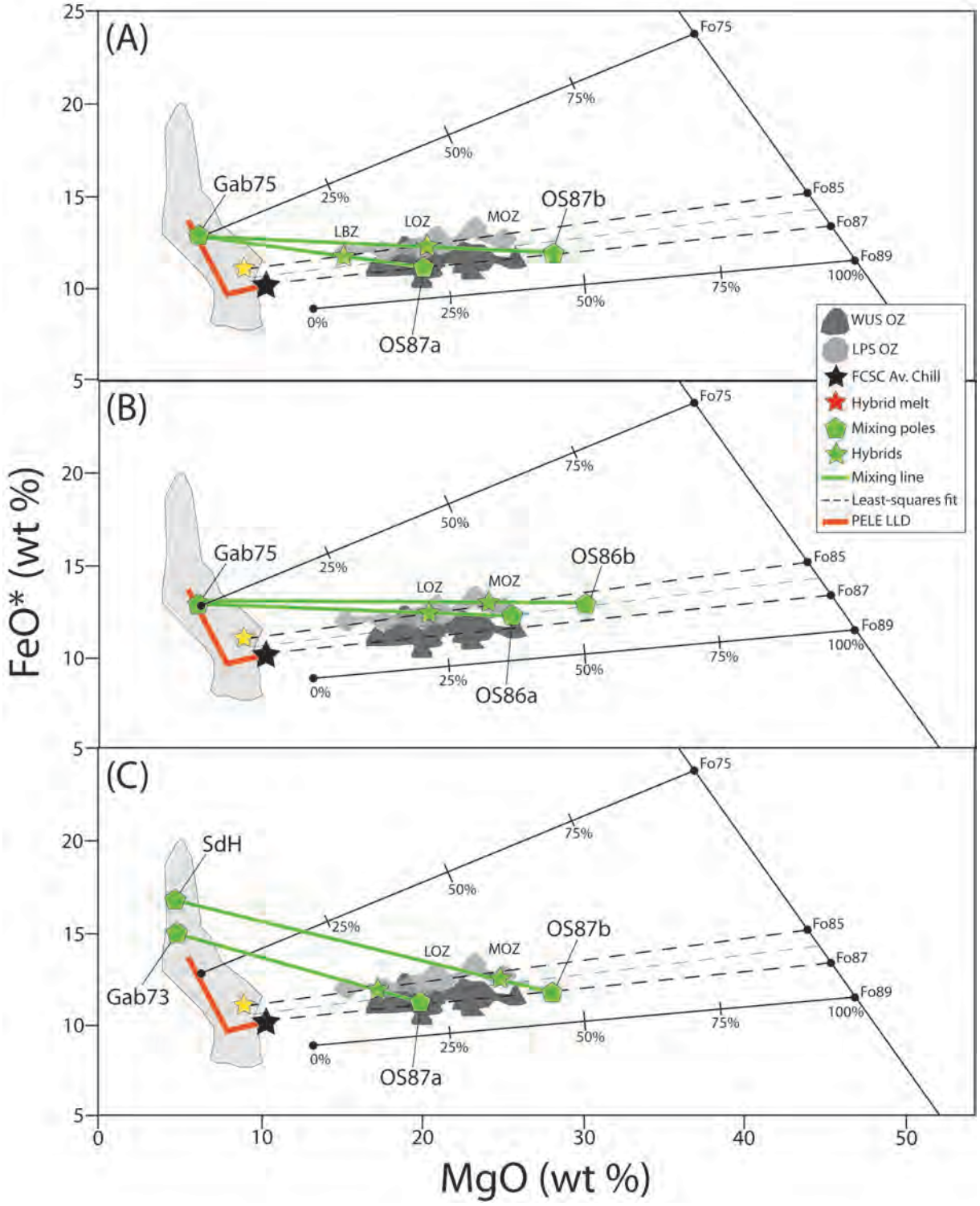

Fig. 5.9: Various Fe=Mg mixing models using different mixing poles. (a) OS87a containing ~20% olivine (Fo_{87}) mixed with Gab75 (with ~6 wt% MgO), and OS87b containing ~45% olivine (Fo_{87}) mixed with Gab75. (b) OS86a containing ~40% olivine (Fo_{86}) mixed with Gab75, and OS87b with >50% olivine (Fo_{86}) mixed with Gab75. (c) OS87a mixed with Gab73 (with ~5 wt% MgO) and OS87b mixed with SdH (with ~4 wt% MgO).

Mixing Gab75 with the OS86a mixing pole in a proportion of 75:25 also generates a more MgO-rich hybrid (Fig. 5.9b). Mass balance implies that this hybrid magma would contain 20-25% olivine primocrysts, primarily inherited from the OS86a component, and would have bulk MgO values between ~19-21 wt%. The most bulk-MgO-rich OZ compositions along the LPS array contain up to 25 wt% MgO. The more MgO-rich hybrid magmas defined above could have unmixed to produce these higher-MgO bulk-rock compositions. On the other hand, if the high-MgO compositions formed in one event then a more olivine-rich slurry would be needed. An 80:20 mix of Gab75 and OS86b (which contains > 50% olivine) can produce such hybrid magmas. However, this last model is probably unrealistic because the high proportion of olivine in the slurry would probably inhibit flow and mixing (Paterson, 2009). Alternatively, instead of high olivine modes in the slurry, the resident gabbroic mush may have been more evolved than Gab75. Mixing Gab73 with OS87a in a proportion of 80:20 can produce hybrid magmas with ~19-21 wt% MgO (Fig. 5.9c). This is a 5% reduction in the proportion of olivine slurry required, compared to models that use the Gab75 mixing pole.

What these mixing models show, is that it is easy to reproduce the more evolved (low-MgO) part of the LPS OZ array by some variant of this mixing process, but that it is difficult to generate the more primitive parts of the LPS OZ array (e.g. LPS MOZ with ~25 wt% MgO) by a 1-stage mixing process unless a very high proportion (> 50%) of olivine is present in the recharging olivine slurry (e.g. OS86b). If we only consider 'reasonable' olivine modes in the olivine slurry (e.g. OS87b) then the more primitive part of the LPS OZ array can only be attained in a single stage if the resident gabbroic mush had a SdH composition, with mixtures of 80:20 (SdH:OS87b). However, it seems implausible that the invading olivine slurry could have ingested large volumes solely of late-stage evolved magmas that only constitute a small (~5%) proportion of Type-1 sills. We therefore favour a scenario whereby the MgO-rich part of the OZ array is formed by unmixing of the hybrid magma.

5.5.7 Post-hybridisation unmixing and the formation of high-MgO olivine cumulates

The propagation of a primitive olivine slurry and its hybridisation with a resident gabbroic mush can produce hybrid magmas that account for the formation of the FCSC OZ. The

apparent westward decrease in the proportion of the olivine-rich component in the mixture from which the different OZs accumulated, suggests that the olivine slurry progressively hybridised with an evolved resident gabbroic mush as it migrated through the sill. This progressive hybridisation scenario accounts for the downstream bulk Fe-enrichment trend seen in the FCSC OZ. Following mixing, the resultant hybrid magmas would have unmixed to produce the high-MgO cumulate arrays displayed in Fig. 5.9. These are recorded as the primocrystic olivine in the LPS LOZ. In addition, there are texturally different olivines within OZ rocks containing the highest olivine modes (Fig. 5.7). These rocks, preserved in the LPS MOZ, are predominantly composed of hopper olivine that is intergrown with clinopyroxene (Fig. 5.3d, f, h), with few (~5%) euhedral olivine primocrysts, and have high-MgO contents (~25 wt% MgO). Also, the LPS MOZ olivine compositions (Fo_{83-81}) are more evolved than the euhedral olivine primocrysts that characterise the olivine slurry. Based on these textural and compositional constraints we interpret the LPS MOZ to have crystallised directly from the hybrid melt that was produced from the mixing process explained above. To test this scenario we ran an assimilation-fractional-crystallisation (AFC) model in PELE, to see whether the mixing process described above can produce 'excess' olivine crystallisation and so account for the higher olivine modes (~55%) and by extension, the higher MgO (~25 wt% MgO) contents observed in the LPS MOZ. We simulated in PELE an olivine slurry (containing 30% olivine and 70% melt) that assimilates a gabbroic mush (corresponding to an average FCSC DZ composition). The output from this model shows that ~5% more olivine crystallisation is produced prior to the cotectic. Olivine Fo-contents are also buffered at Fo_{82}, compared to closed-system models where Fo decreases rapidly with crystallisation. These olivine compositions are similar to the composition of olivines observed in the LPS MOZ. The AFC model results (appendix F4) support the hypothesis that the LPS MOZ rocks crystallised from the hybrid melt, consistent with the bulk-mixing model presented above (Fig. 5.9).

5.5.8 Lead and sulphur isotopic constraints on the petrogenesis of the FCSC

The spread of Pb-isotope compositions (Fig. 5.5) indicates that several different magmas were involved in the generation of the olivine-enriched Franklin sills. The distribution of compositions in $^{208}Pb/^{204}Pb$ *vs* $^{206}Pb/^{204}Pb$ and $^{207}Pb/^{204}Pb$ *vs* $^{206}Pb/^{204}Pb$ plots could in part

be explained by the assimilation of Shaler Supergroup crustal rocks. The problem is that it is unclear which isotopic composition represents the 'uncontaminated' component. Some of the spread towards the WUS OZ/DZ isotopic compositions could be explained by small (< 10%) amounts of dolostone assimilation, since the composition of Shaler dolostone falls along a suitable mixing trajectory (Beard, 2012). Because the WUS OZ/DZ have similar trace element compositions with enriched Pb concentrations and distinctive radiogenic $^{206}Pb/^{204}Pb$ and $^{207}Pb/^{204}Pb$ isotope compositions, we suggest they shared a similar melt source composition and contamination history. Conversely, the unradiogenic Pb isotopic composition seen in the LPS DZ might reflect assimilation of Archaean Basement (Beard, 2012). Whether the range of isotopic compositions in the Franklin magmas is best explained by a heterogeneous mantle source, or a common source magma that was variably contaminated by different crustal components will be discussed in Beard et al. (In Prep).

What is pertinent here is that the LPS OZ and LPS DZ have different Pb- and S-isotope signatures (Fig. 5.5 & 5.6), consistent with the composite intrusion model presented in chapter 4. In Pb-isotope plots, mixing lines between two geochemical reservoirs are straight lines. As the LPS OZ plots above a tie line between the WUS OZ/DZ and the LPS DZ, a simple mixture of these two magmas cannot explain its isotopic signature (Fig. 5.5b), in apparent contradiction with the hybridisation model we favour (Fig. 5.9). If the FCSC does indeed represent a single sill system, then the olivine slurry replenishment event may have been internally heterogeneous or there were two isotopically distinct olivine slurry replenishment events in the FCSC. This is discussed further below.

We suggest that the igneous rocks preserved at the WUS represent a vigorous replenishment event, which may have pushed previously emplaced magmas downstream towards the LPS. Pb-isotope compositions suggest that this final pulse of magma assimilated small amounts of dolostone (< 10%) relative to the average Type-1 magma (Fig. 5.5). We speculate that early injections of magma, which created the WUS, are preserved only at the hybrid LPS OZ. These assimilated a smaller fraction of dolostone than the final pulse of magma, now preserved as the WUS. The original, pre-hybridisation olivine-rich LPS OZ component would have been isotopically distinct from the WUS. In this context, the gradual shifts in OZ Fe/Mg in the FCSC that we attribute to downstream hybridisation (Fig. 5.9) are superimposed on a secular variation in the

geochemical/isotopic signatures of the incoming primitive magmas. Fe/Mg ratios are buffered by fractional crystallisation, however, radiogenic isotope compositions are unaffected by crystallisation. Therefore, the FCSC records the injection of isotopically distinct magmas.

5.5.9 The potential effects of dolostone assimilation on the FCSC magma(s)

The Franklin intrusions of the Minto Inlier are hosted by a predominantly carbonate/dolostone sedimentary sequence (Thomson *et al.*, 2014), and calc-silicate reaction products are locally prominent (Nabelek *et al.*, 2013). We also see field and thin section evidence of dolostone assimilation in the UM (Bédard et al., 2012). If we are correct in our inference that the FCSC magmas are rooted in the UM upflow zone, then fault-related brecciation of host dolostones at the UM (Bédard *et al.*, 2012) may have allowed more extensive assimilation as magma migrated up the fault before propagating laterally along the mechanical discontinuity represented by the contact between the Fort Collinson and Jago Bay Formations.

We investigated the potential impacts of dolostone assimilation on melt and mineral chemistry using PELE. We used the average FCSC chill as our starting composition (10.3 wt% MgO) and added a dolostone contaminant to the magma (0.2g, 0.4g, 0.5g and 1g of contaminant added per fractionation step). The composition of the contaminant was taken as the average of 26 dolostone bulk-rock analyses from sedimentary rocks of the Minto Inlier (appendix F5). The addition of this high-MgO (~20 wt%) and low-FeO (< 1 wt%) dolostone contaminant to the magma has major impacts on the LLD, when compared to regular fractional crystallisation. Prior to olivine saturation, the AFC models with the most dolostone contaminant predict an increase in melt MgO content up to 11.7 wt% and decrease the melt FeO/MgO ratio. In this early stage, abundant CO_2 gas is released. Primitive olivine (up to Fo_{89}) crystallises at temperatures of ~1260°C, earlier than in closed-system models for this melt composition (Fig. 5.10). Between 1260°C and 1200°C, ~7% olivine crystallises, ~16% dolostone is assimilated, and 7% CO_2-rich gas is released. In contrast to fractionation models without dolostone assimilation where olivine Fo-contents decrease rapidly (Fig. 5.10), assimilation of MgO-rich dolostone buffers olivine Fo-contents at values of ~Fo_{88-87} in the 1260-1200°C interval (Fig. 5.10). Clinopyroxene

begins to crystallise earlier in the dolostone-AFC models compared to the closed-system model due to the high CaO-contents (24-47 wt%) of the dolostone contaminant, with up to ~20% clinopyroxene being extracted before the arrival of plagioclase. In contrast, both clinopyroxene and plagioclase join olivine on the liquidus simultaneously in closed-system models.

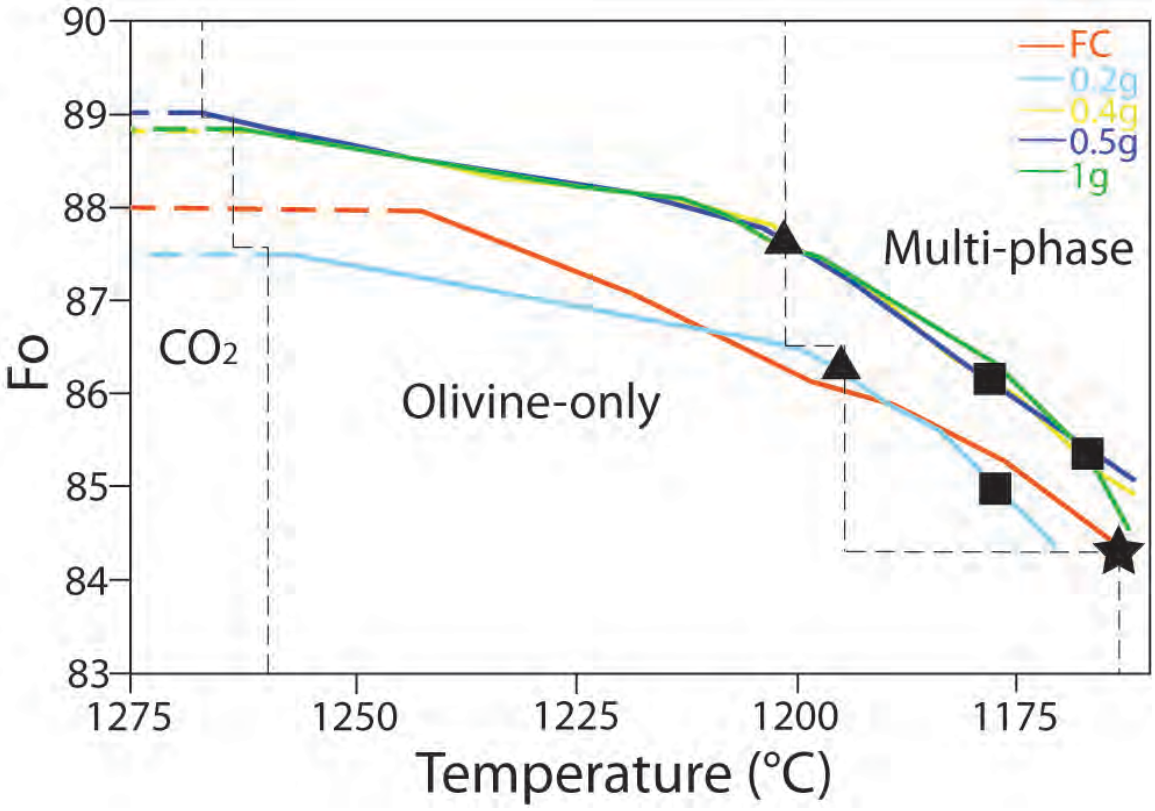

Fig. 5.10: Forsterite (Fo) versus temperature diagram showing the LLD of the average FCSC magma during fractional crystallisation (FC) and AFC. Dolostone is the contaminant, which has been added to the magma in varying proportions per fractionation step. Symbols indicate the arrival of a phase on the liquidus (triangles = clinopyroxene; squares = plagioclase; star = both clinopyroxene and plagioclase). Models are included in appendix F6.

The modelled effects of dolostone assimilation on the FCSC magma are very similar to those observed experimentally (Iacono Marziano *et al.*, 2008, Mollo & Vona, 2014) and resemble products of volcanic and plutonic systems where assimilation of host carbonates occurred (Wenzel *et al.*, 2002, Chadwick *et al.*, 2007, Di Rocco *et al.*, 2012, Troll *et al.*, 2013). Dolostone assimilation in the FCSC magma could help explain the high-Fo compositions of olivine cores in the WUS OZ. Additionally, the effects of volatile and gas budgets within crystal-mushes have been shown to affect their viscosity. Therefore the

production of CO_2 caused by dolostone assimilation may have reduced the viscosity of the crystal-rich FCSC olivine slurry during downstream propagation (Pistone *et al.*, 2013) and facilitated hybridisation.

5.5.10 Differentiation model for the FCSC plumbing system

The evidence presented is consistent with a model where the FCSC OZ formed from a late injection of olivine-enriched magma that mixed with a resident, partly consolidated gabbroic mush. This olivine slurry was sourced from upstream in the FCSC, possibly from the UM feeder system.

The isotopic data indicate that there are multiple isotopic signatures within the FCSC. One potential explanation for this is that the olivine slurry replenishment was internally isotopic heterogeneous upon emplacement. The olivine slurry may have acquired varying isotopic signatures deeper in the plumbing system when fresh batches of magma were injected into the plumbing system, possibly during remobilisation of the olivine cargo. However, in this scenario it would be highly fortuitous for the WUS OZ and DZ to be in isotopic equilibrium. We therefore favour a model in which the replenishing olivine-rich magma was injected as two pulses, showing secular shifts in radiogenic isotope composition. Magmas may have been variably contaminated with a diverse range of crustal facies, including dolostone. Even though the olivine slurry was isotopically heterogeneous, the FCSC solidified to form similar textural and petrological facies at the WUS, PS and LPS. In this model, the LPS DZ isotopic signature (Fig. 5.5) represents the earliest pulse of magma into the FCSC. This component could record minor amounts of Archaean basement or sedimentary rock contamination (Beard et al. In Prep). Whether isotopically distinct magma pulses represent a diversity of contamination paths imposed on a common magma stem, or whether these are discrete samples of an isotopically heterogeneous mantle, is beyond the scope of this chapter. An olivine-enriched replenishment seems to have propagated westward through the FCSC, mixing *en route* with a resident gabbroic mush to create the LPS OZ. A second olivine slurry pulse seems to have experienced more extensive dolostone contamination, as recorded by the Pb isotopes (Fig. 5.5). The olivine slurry replenishment events appear to have been widespread, since Type-1 olivine-enriched sills (Kat's, Dick's and Uwe's sills) are common at the stratigraphic level where the FCSC

was emplaced. Kat's sill is similar to the WUS in that it shows isotopic equilibrium between OZ and DZ, and has isotopic signatures that are very similar to those of the WUS. Kat's sill is located just to the south of the FCSC (Fig. 2.2) and may represent another branch of the WUS-forming pulse. In contrast, Dick's and Uwe's sills are isotopically distinct and would record different, non-unique sources/differentiation paths. As the OZ of Uwe's sill has similar radiogenic isotope and trace element ratios to rocks from the WUS and Kat's sill, olivine with the dolostone assimilation signature probably crystallised prior to emplacement of this pulse of magma.

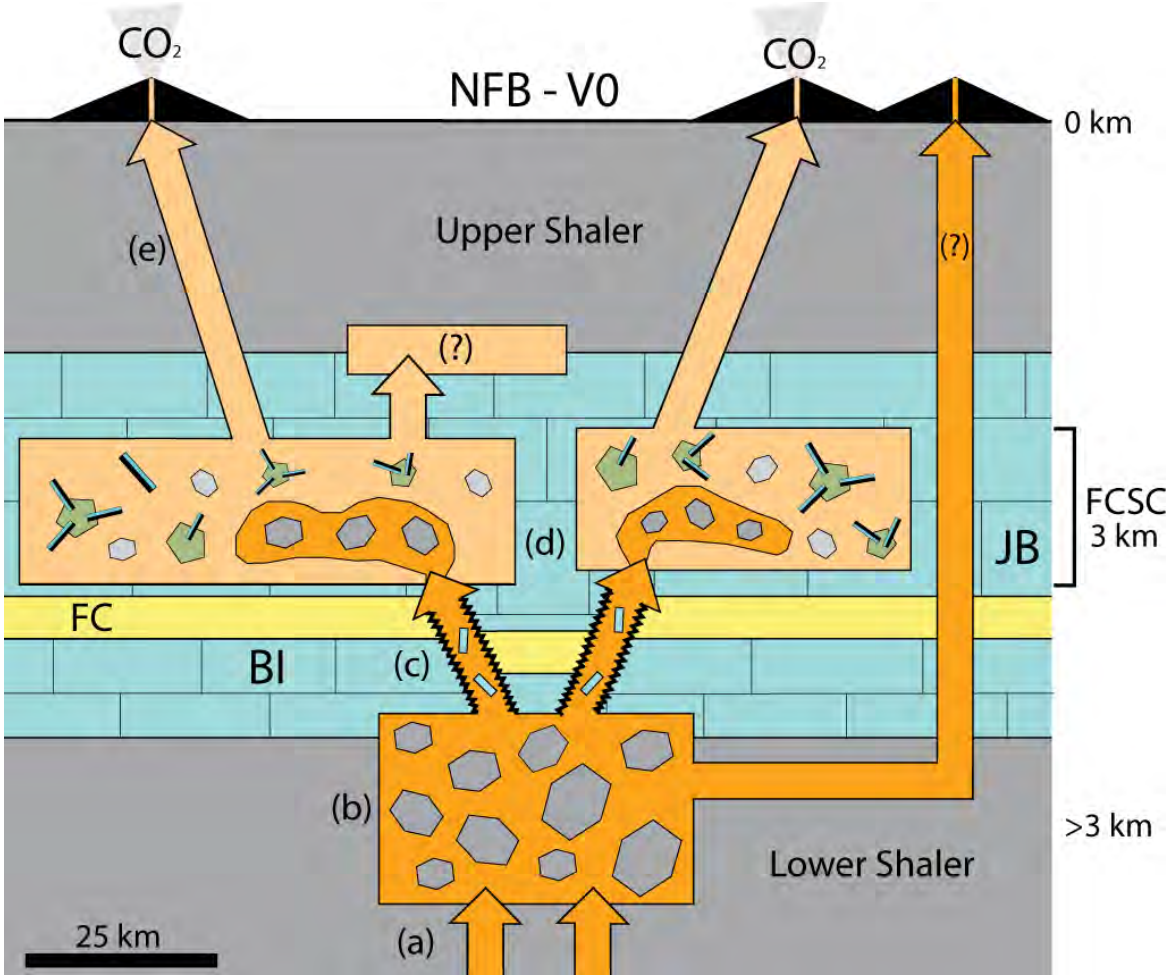

Fig. 5.11: Schematic diagram illustrating the formation of the FCSC and the basal lava sequence of the Natkusiak flood basalts (NFB). (a) Deep (> 3 km) holding sills or feeder conduits are fed by fresh batches of primitive melt from isotopically distinct mantle sources; (b) After initial residual magmas escape from the holding system, primitive olivine cumulates with equilibrium melts are left behind before being remobilised (by overpressure from fresh melt deliveries?); (c) The remobilised olivine slurry ascends up syn-magmatic Neoproterozoic faults (arrows with squiggly contacts), where they assimilate dolostone country rock; (d) Olivine slurry is emplaced into the FCSC, which already hosts a partly-crystallised gabbroic mush derived from an earlier magma; (e) Residual melts to the sills may be erupted at the surface, if structures facilitate melt escape. The erupted melt forms the basal NFB lava sequence, and if melts affected by dolostone assimilation were erupted, then significant quantities of CO_2 may have been released. BI = Boot Inlet Formation; FC = Fort Collinson Formation; JB = Jago Bay Formation.

We present a possible model for the development of the olivine-enriched rocks of the FCSC in Fig. 5.11. The emplacement dynamics of these heterogeneous olivine slurry replenishment events are similar to the 'braided sills' differentiation model of the Torres Del Paine Mafic Complex in Patagonia (Leuthold *et al.*, 2014). Also, our assimilation-replenishment scenario is analogous to the Roelofse and Ashwal (2012) model proposed for the formation of the Main Zone in the Bushveld Complex. In their model, crustal contamination of crystal-mushes occurred in sub-compartments of an underlying feeder system. A similar scenario may have operated beneath the FCSC at > 3 km depth in the Franklin plumbing system. It is also possible that extensive contamination occurred during transport of magma up fault-guided conduits populated by cataclastic breccias (Bédard *et al.*, 2012). Ultimately, our database of lateral variations in the compositions of the olivine-enriched sills of the Minto Inlier provides insight into magma/crystal-slurry flow directions. These have important implications for the evolution of magma plumbing systems, intra-sill mixing and in the search of economic deposits.

5.6 Conclusion

The Fort Collinson Sill Complex (FCSC) of the Franklin Large Igneous Province, extends for > 50 km along strike, and its constituent sills are characterised by basal olivine-enriched layers (OZ) and capping gabbros (DZ). We investigated three sections through the FCSC. At its eastern end is the West Uhuk Sill (WUS), in the centre is the P-sill (PS) and at its western end is the Lower Pyramid Sill (LPS). The FCSC OZ rocks exhibit a gradual shift towards more Fe-rich bulk compositions towards the west. Olivine cumulate arrays on Fe=Mg plots were used to define bulk crystal-extracts and equilibrium melts, which shift to more evolved compositions towards the west. However, the predicted PS and LPS olivine compositions only approximately match the olivine cargo they contain suggesting excess olivine was added, perhaps by injection of a crystal slurry. The primitive olivine primocrysts within the FCSC OZ were derived from a replenishing olivine slurry, which was emplaced into and mixed with a partly crystalline gabbroic mush. Downstream propagation and hybridisation between these two components can explain the westward Fe-enrichment trend in the FCSC OZ. Radiogenic isotope data suggest that there were at least three geochemically distinct pulses of magma in the FCSC. Isotopic signatures in the WUS in particular can be explained by small amounts of dolostone assimilation, which

buffers the melt Mg/Fe ratio enabling crystallisation of the higher-Fo olivine that characterises the WUS. In addition, clinopyroxene is preferentially stabilised on the liquidus ahead of plagioclase and significant quantities of CO_2 are released, during dolostone assimilation. The similarities between the FCSC and other olivine-enriched Franklin sills suggest that olivine slurry replenishment events are common, and that the olivine-rich slurries were able to propagate > 50 km along strike.

6. Sulphide immiscibility induced by wallrock assimilation in a fault-guided Franklin magmatic feeder system

6.1 Abstract

The Southern Feeder Dyke Complex (SFDC) is part of the Franklin Large Igneous Province (LIP), which is well exposed in the Minto Inlier of Victoria Island (Arctic Canada). Previous work on the Franklin LIP considers its igneous rocks to be prospective for Ni-Cu-PGE sulphide mineralisation. We investigated the SFDC, which comprises a series of NW-SE trending gabbroic outcrops and sedimentary panels with contact zones that correspond to 1st derivative magnetic anomalies. Field and textural relationships show that the SFDC was emplaced contemporaneously with regional Neoproterozoic faulting. Gabbroic dykes intruded brecciated country rock, and microdoleritic microxenoliths in basaltic matrices indicate multiple intrusive/brecciation events. Host rocks are commonly overprinted by greenschist facies assemblages, with calcite + pyrite veins filling open spaces between breccia fragments. Dykes emplaced into these breccias show globular and net-textured sulphides within microdoleritic microxenoliths that appear to impregnate a porous crystal mush suggesting that immiscibility was triggered on a local scale, presumably by assimilation of local wallrock. Heavy $\delta^{34}S$ isotopic signatures in these dykes also indicate assimilation of sulphur-bearing country rocks. Wallrock assimilation would have been facilitated by fault-related brecciated of the country rocks, which would expose extensive xenolith surface areas to fresh magma. Significant gossan showings associated with a sill up-section from the SFDC suggests that immiscible sulphide liquids may have been flushed downstream by composite dyke systems that experienced magma replenishment. Fault-mediated melt ascent along NW-SE faults has been documented elsewhere in the Minto Inlier, providing opportunities for similar wallrock assimilation and sulphide redistribution events. The evidence preserved in the SFDC confirms the Ni-Cu-PGE potential of the Franklin LIP.

6.2 Introduction

Magma conduits such as dikes are dynamic systems that provide a setting for magma-crust interaction (Naldrett, 1992, Li *et al.*, 2000, Maier *et al.*, 2001, Ding *et al.*, 2010, Lightfoot & Evans-Lamswood, 2015), and are important sites of Ni-Cu-PGE sulfide mineralization (Ripley & Li, 2011). Economic conduit-type Ni-Cu-PGE sulfide deposits are typically associated with olivine-rich magmas (Li & Naldrett, 1999); are commonly situated close to major crustal faults (Naldrett, 1992, Begg *et al.*, 2010, Song *et al.*, 2012, Lightfoot & Evans-Lamswood, 2015); are generally hosted by (or related to) intrusive or extrusive facies that show a depletion in chalcophile elements (Naldrett, 1992); are commonly emplaced into (or traverse) sulfur-bearing country rocks (Naldrett, 1992, Li *et al.*, 2009); and may show field and/or geochemical evidence of interaction between magma and country rock (Ripley *et al.*, 2003, Li *et al.*, 2009, Keays & Lightfoot, 2010, Ganino *et al.*, 2014). Most economic Ni-Cu-PGE sulfide deposits of this type are thought to have involved addition of external sulfur to a sulfur-undersaturated magma. Other possible mechanisms to induce sulfide immiscibility include changes of melt composition (Irvine, 1975, Czamanske & Moore, 1977, Wendlandt, 1982), temperature (Haughton *et al.*, 1974) or fO_2 (Buchanan & Nolan, 1979, Liu *et al.*, 2007). Additionally, a hydraulic trap is commonly invoked to concentrate sufficient volumes of immiscible sulfide liquids (Naldrett, 1992); with an appropriate R-factor, a measure of the ratio of silicate magma to the sulfide liquid, being needed to upgrade the metal tenor of immiscible sulfide liquids (Campbell & Naldrett, 1979). In conduit-type deposits, upgrading would most likely occur in the context of an open magmatic system, where a previously concentrated sulfide melt would see its PGE tenor upgraded by magma throughflow (Naldrett, 1992).

Examples of conduit-type Ni-Cu-PGE sulfide deposits include the Noril'sk-Talnakh intrusions in Siberia (Naldrett, 1992, Arndt, 2011), Voisey's Bay in Labrador (Naldrett *et al.*, 2000, Ripley & Li, 2011) and the Eagle deposit in northern Michigan (Ding *et al.*, 2010). Each of these magma conduits is associated with craton margins, regional fault-systems and are comprised of differentiated (mafic-ultramafic intrusions). Additionally, there is petrological and geochemical evidence that magma-crust interaction triggered the formation of immiscible sulfide liquids in each of these magma conduits. Data on $\delta^{34}S$ isotopes is especially informative about incorporation of crustal sulfur, because crustal

sulfur is typically enriched in comparison to mantle sulfur (Fiorentini *et al.*, 2012, Ripley & Li, 2013, Black *et al.*, 2014). The heavy $\delta^{34}S$ isotopic values (6 to 14‰) of mafic rocks at Noril'sk have been explained by the ingestion of crustal sulfur into the magma (Grinenko, 1985, Li *et al.*, 2009). However, other Ni-Cu-PGE sulfide deposits such as Jinchuan in China (Ripley *et al.*, 2005, Lehmann *et al.*, 2007) and Nebo-Babel in Australia (Seat *et al.*, 2009) do not show isotopic evidence for the involvement of external sulfur. For deposits where external sulfur is considered an important factor, a key issue is how and where in the magma plumbing system the sulfur was incorporated into the magma (Ripley *et al.*, 2003, Ripley & Li, 2013).

The metallogenetic setting of the Franklin Large Igneous Province (LIP) in northern Canada (Fig. 1) shares many similarities with those of other economic conduit-type Ni-Cu-PGE sulfide deposits (Jefferson *et al.*, 1994). The Franklin LIP is situated at the margin of the Slave craton, a typical feature of Ni-Cu-PGE sulfide deposits (Begg *et al.*, 2010). A Geological Survey of Canada mapping project (2010 and 2011) aimed to constrain the Ni-Cu-PGE potential of the Franklin LIP, considered prospective by Jowitt and Ernst (2013). The associated Natkusiak flood basalts have a known native copper potential (Jefferson *et al.*, 1985), not unlike the Keewenawan Basalts, which are associated with sulfide mineralization in the Duluth Complex (Miller *et al.*, 2002). In the Minto Inlier (Fig. 1), the Franklin igneous suite is dominated by mafic and ultramafic-mafic sills with subordinate NNW/NW-trending feeder dikes (Bédard *et al.*, 2012). There are small (~ mm disseminated sulfides) sulfide showings in the Franklin sills and dikes, as well as larger (~1 km diameter) surface gossans of uncertain origin (Peterson *et al.*, 2014). The Southern Feeder Dike Complex (SFDC) within the Minto Inlier is a NNW/NW-trending dike system with associated sulfide showings. The SFDC preserves evidence of magma emplacement that was contemporaneous with regional-scale Neoproterozoic normal faulting. We carried out a field, geochemical (bulk-rock and *in-situ*), $\delta^{34}S$-isotope and anisotropy of magnetic susceptibility study of the SFDC in order to constrain how magmas were emplaced, how magmas interacted with host rocks, how the associated sulfides formed, and to better understand the impact of the syn-magmatic faulting on the overall system. Field evidence (Bédard *et al.*, 2012) and results of a companion $\delta^{34}S$-isotope study (Hryciuk et al. submitted), suggest that fault-related brecciation commonly facilitated the ingestion of crustal sulfur into Franklin magmas. In the SFDC, some of the small- and medium-scale processes by which this occurred are preserved. Our results bear on the Ni-Cu-PGE sulfide

potential of the Franklin LIP, and provide insights into the processes involved in the generation of magmatic Ni-Cu-PGE sulfides elsewhere, particularly those that operated in conduit-type magmatic plumbing systems.

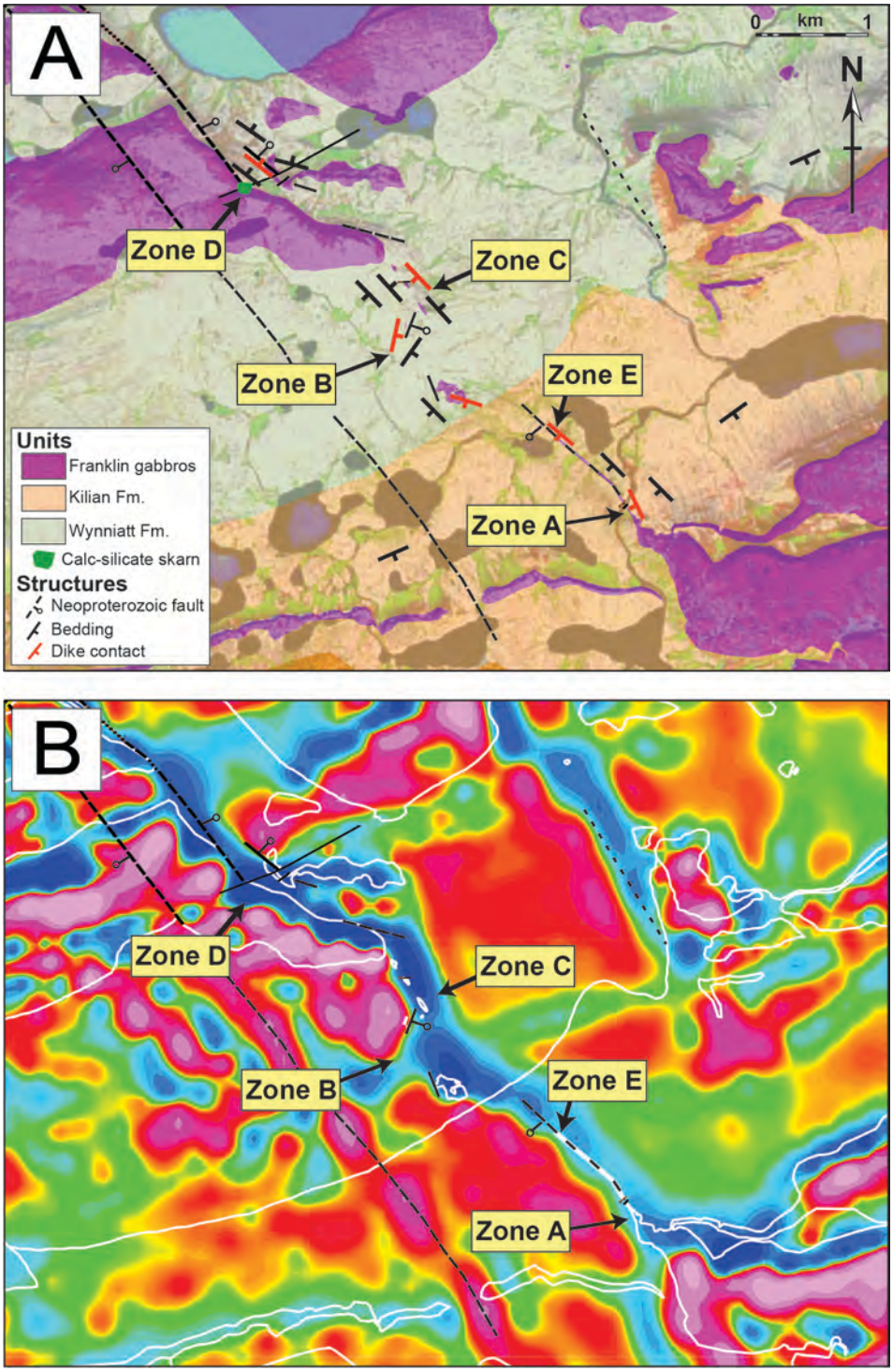

Fig. 6.1: (A) Geological map of the SFDC with each zone labelled. Regional bedding typically dips a few degrees towards the SE, except for perturbations near to the SFDC. (B) The SFDC coincides with a 1st derivation NNW/NW-trending magnetic anomaly (Kiss & Oneschuk, 2010). The locations of the mapped Zones are labelled. Circles with labels correspond to outcrop localities or 'stations' that were used to sync the SFDC with the Geological Survey of Canada mapping system. The 'climbing sill' is a separate locality that will not be discussed here.

6.3 Southern Feeder Dyke Complex

The SFDC (Fig. 6.1) was briefly discussed in Bédard *et al.* (2012) as an example of a syn-faulting dyke system. The SFDC is situated ~10 km south of the Minto Inlet (Fig. 2.2), and is located along a NNW/NW-trending magnetic lineament (Fig. 6.2). On the kilometer scale, the area is characterised by a series of NW- or SE-trending gabbroic and sedimentary panels that are separated by prominent linear valleys or scarps, and which are interpreted to be faults and/or intrusive contacts (Fig. 6.1). The gabbroic outcrops comprise sills that form capping mesas, and dyke-like bodies that are locally exposed in valleys that commonly have a thick Quaternary cover. The intrusive rocks were emplaced into southeasterly younging and shallowly SE-dipping bedded carbonates and evaporites of the Wynniatt and Kilian Formations of the Shaler Supergroup at ~1 km paleodepth. We examined the SFDC in five, well-exposed areas along a ~6 km transect. We will describe the field relationships of each from NW to SE (i.e., moving up-section). Also labeled on Fig. 2.2 are the locations of the Gossan Sill (GS) and the Sulphide City Dyke (SCD), which both represent gabbroic bodies emplaced at a similar stratigraphic level. These will be discussed in future studies.

6.3.1 Zone D

Zone D is at the northwestern end of the SFDC (Fig. 6.1). In this area, a large gabbroic body (SW end of Fig. 6.3) at the ridge top forms a capping mesa (Figs. 6.3 and 6.4A). Preserved contact relationships imply that this body is a sill that extends for tens of kilometers towards the SW. Contacts with the host Wynniatt Formation are poorly exposed as the SFDC is approached, however, probably due to renewed post-intrusive motion on faults. The contact region of this capping sill with the SFDC (labeled ‘b’ on Fig. 6.3) shows a bench of strongly recrystallised bedded marble (labeled ‘m’ on Fig. 6.3) and a disrupted outcrop of interlayered calc-silicate and Fe-oxide skarn rock. These facies closely resemble contact metamorphic rocks seen at the Uhuk Massif where there are fault-guided up-section magmatic transgressions (Bédard *et al.*, 2012, Nabelek *et al.*, 2013). About 50 meters NE of this hidden fault contact is an irregular body of gabbro, ~20 m thick (labeled ‘a’ on Fig. 6.3) that is embedded in contact-metamorphosed limestone. The

gabbro has chilled margins at both contacts, as well as internal chills. Bedding in the host Wynniatt Formation increases markedly in dip towards the margins of the dyke (from 5° to >70°), with drag fold polarity indicating NE-side-down motion on a NNW/NW-trending fault (Fig. 6.3). The host Wynniatt Formation adjacent to the dyke is recrystallised as well as heavily fractured and brecciated. We interpret this part of Zone D to be a downdropped hanging wall limestone panel. Magma was injected into parasitic faults within this downdropped panel to form a gabbroic roof apophysis, similar to what was seen at the Uhuk Massif (Bédard *et al.* (2012).

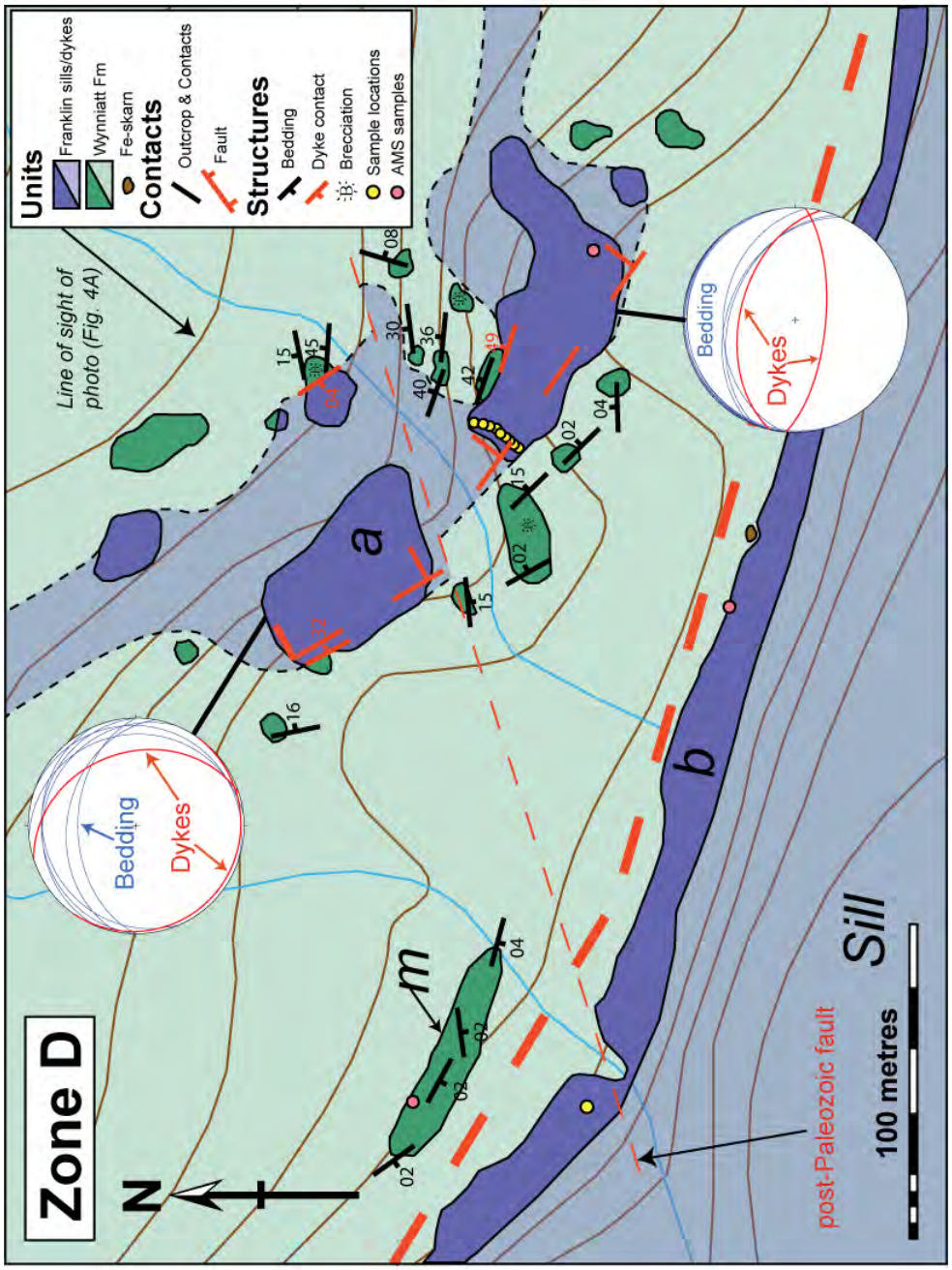

Fig. 6.3: A detailed geological map of Zone D, showing the moderately dipping NNW/NW-trending dyke-like roof apophysis emplaced into moderately dipping Wynniatt Formation country rock. The line of sight for the field photo in Fig. 6.4A is shown.

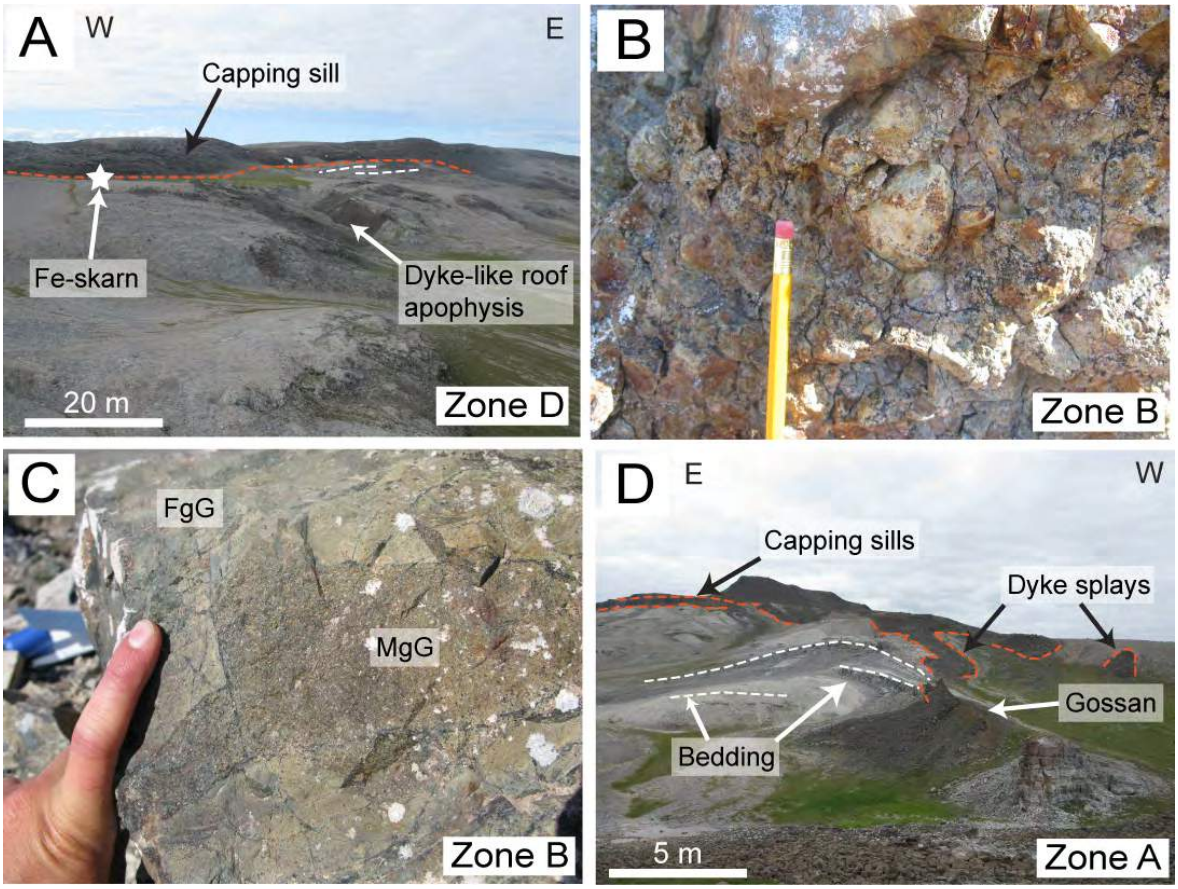

Fig. 6.4: (A) Field photo of Zone D, showing the dyke-like roof apophysis feeding towards the capping sill (dashed red line shows inferred contact region and dashed white lines show gently dipping Wynniatt Formation rocks adjacent to the sill). (B) Brecciated and Fe-stained Wynniatt Formation country rocks at Zone B (pencil is 5 cm). (C) Igneous breccia with the dyke propagator tips at Zone B. Microphyric basalt (FgG) hosts xenoliths of microdoleritic sulphide-bearing gabbro (MgG). The dyke propagator tips have a green colouration, possibly because of greenschist grade alteration. (D) Field photo of Zone A showing the steeply dipping dyke feeding and splaying towards the capping sills (dashed red lines are igneous contacts). The Kilian Formation bedding dips steeply towards the dyke (dashed white lines). The dyke is gossan stained (labelled) and dips towards the SW, with the dark material extending towards the viewer being talus of basalt deposited on limestone. It is unclear from the outcrop, which sill the dyke feeds into.

6.3.2 Zone C

Zone C (Fig. 6.5) is situated ~2 km to the SE of Zone D (Fig. 6.1). Limited exposures reveal a ~20 m thick NNW-trending gabbroic dyke that has steeply dipping margins (~75° to the SW), and preserves a chilled margin on the western side (Fig. 6.5). The Wynniatt Formation in contact with this chilled margin is heavily fractured and bedding increases in dip towards the dyke (Fig. 6.5: up to ~27° to the NE). The dip directions on either side of

the gabbroic dyke indicate NE-side-down motion on a fault, as for Zone D. There is a thinner parallel (~1 m) near-vertically dipping (~85°) dyke that appears to merge into the thicker dyke over a distance of ~15 m (Fig. 6.5). The gabbroic body at Zone C is interpreted to be an extension of the main gabbroic intrusion (labeled 'b' on Fig. 6.3) of Zone D.

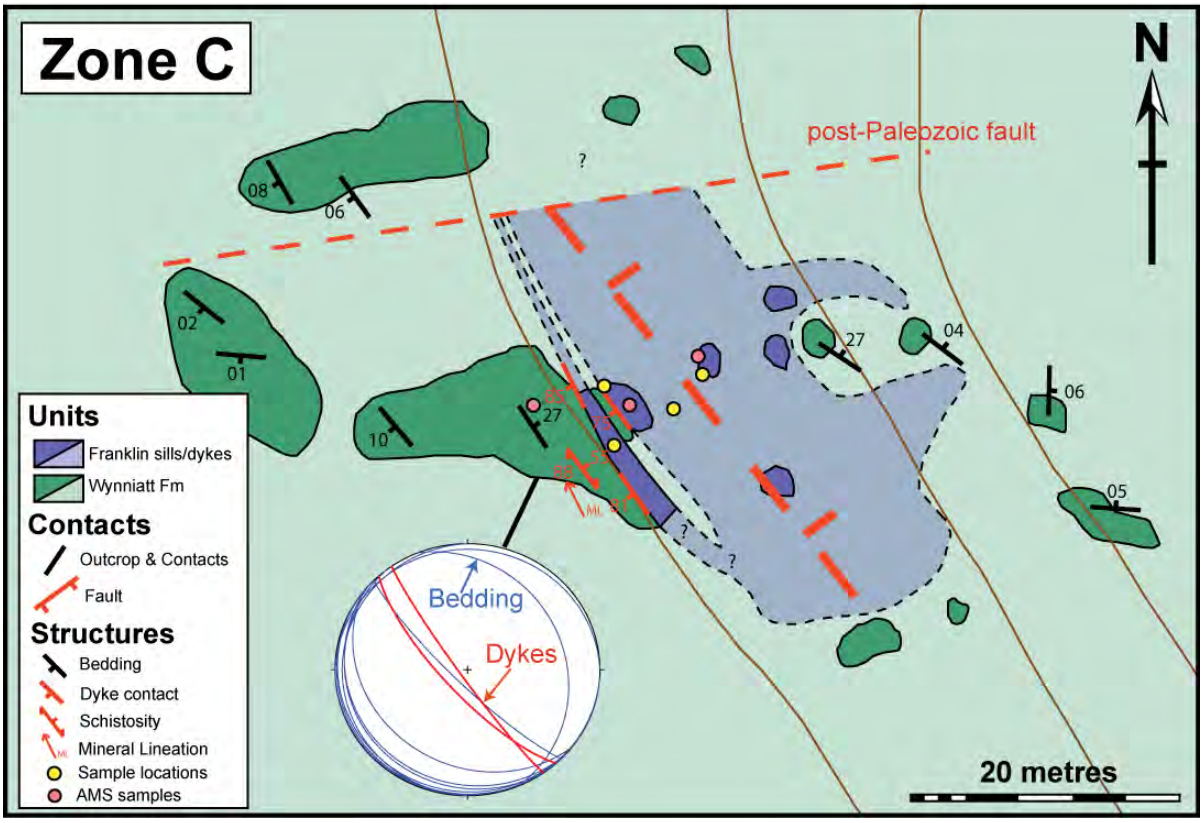

Fig. 6.5: A detailed geological map of Zone C showing the dyke and local Wynniatt Formation bedding perturbations.

6.3.3 Zone B

Zone B (Fig. 6.6) is located ~0.5 km to the SE of Zone C (Fig. 6.1). A rubbly mound (~20 m thick) of dark, NNW/NW-trending gabbroic rock can be seen at the poorly exposed northeastern end of Zone B. No contacts are preserved, but the thickness and orientation of the gabbro mound, as well as its proximity to Zone C, suggests it may be a continuation of the Zone C dyke. At the SW end of Zone B (Fig. 6.6) there are several, thinner (~0.5-2 m thick) N/NNE-trending dykes, which are oblique to the larger NNW/NW-trending dyke. Some of these thinner dykes can be traced for hundreds of meters through the host

Wynniatt Formation and may connect to the larger NNW/NW-trending dyke (Fig. 6.6). The bedding in the Wynniatt Formation limestone hosting the thinner dykes dips (up to ~45°) towards the SE, and is commonly brecciated, with veins being filled by calcite, prehnite, quartz, pyrite and sparse chalcopyrite (Fig. 6.4B). The thin N/NNE-trending dykes intrude the brecciated country rocks, and we infer them to be dyke propagator tips that were emplaced into an active fault. In places, the breccias are igneous, with microdoleritic microxenoliths cemented by microphyric basalt (Fig. 6.4C). Many of these breccias have a distinctly green colouration, indicating a strong greenschist-grade hydrothermal overprint (Fig. 6.4C) that may have been driven by heat derived from repeated emplacement of dykes into the active fault. These greenschist facies breccias are cut by brown weathered, weakly altered, and locally brecciated dykes, which appear to represent the last igneous event. These late dykes and breccias commonly contain disseminated sulphides, typically pyrite, pyrrhotite and minor chalcopyrite.

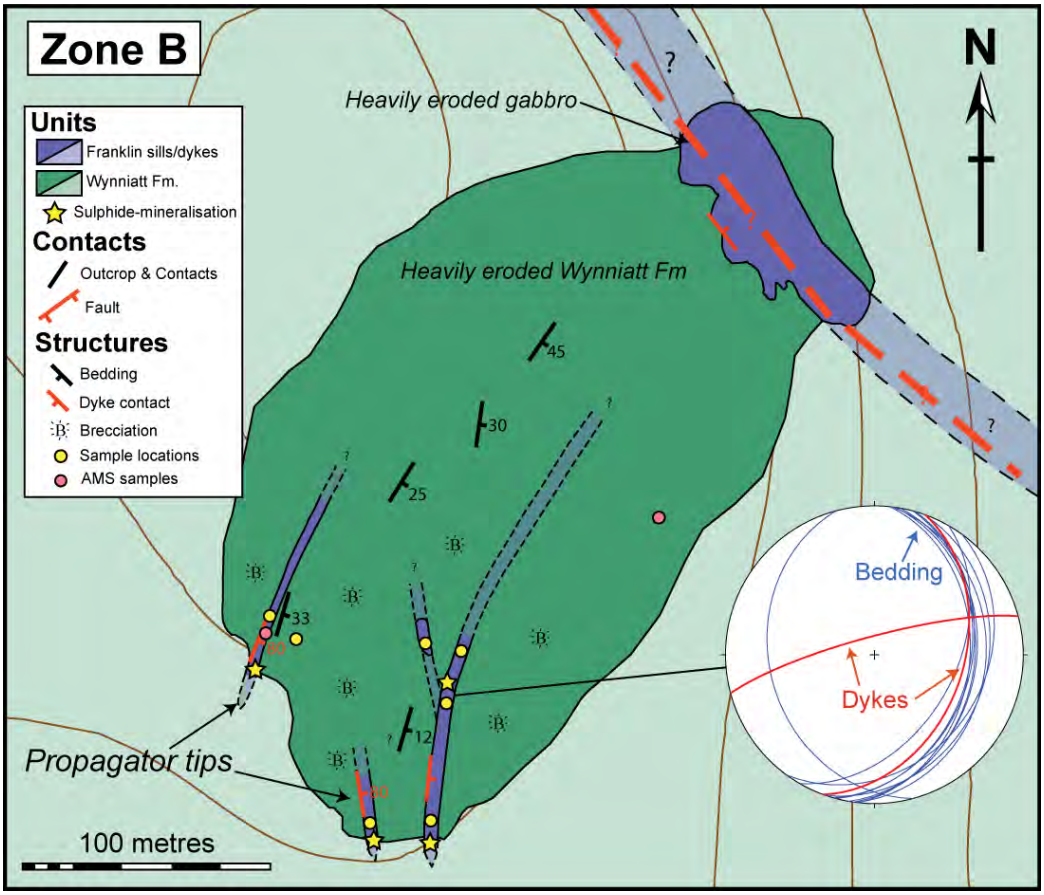

Fig. 6.6: A detailed geological map of Zone B showing the inferred location of the main NNW/NW-trending dyke as well as the N/NNE-trending dyke propagator tips that extend towards the south into brecciated Wynniatt Formation country rock.

6.3.4 Zone E

Zone E (Fig. 6.7) is located midway between Zones B and A (Fig. 6.1). We did not create a detailed map of Zone E because of the limited size of the outcrop (Fig. 6.7A). Zone E consists of a ~20 m thick NNW-trending gabbroic body emplaced into the Kilian Formation. Both margins of the gabbroic body are preserved, dipping very steeply towards the SW (~80°), and both are chilled contacts. This gabbroic body is interpreted to be a dyke, which is parallel to the NNW-trending dykes of Zone D-C-B. The host Kilian Formation, near to the dyke margins, is strongly discoloured (Fig. 6.7B), has steeper dips (~40° to the SW), and is heavily brecciated, with the fractures containing coarse (1 cm sized) pyrite and calcite. Parasitic folds with NW-trending hinge lines are observed up to ~10 m away from the dyke contact (Fig. 6.7B). The deflection of the Kilian Formation bedding indicates SW-side-down motion on a NNW-trending fault, the opposite sense to Zone D-C.

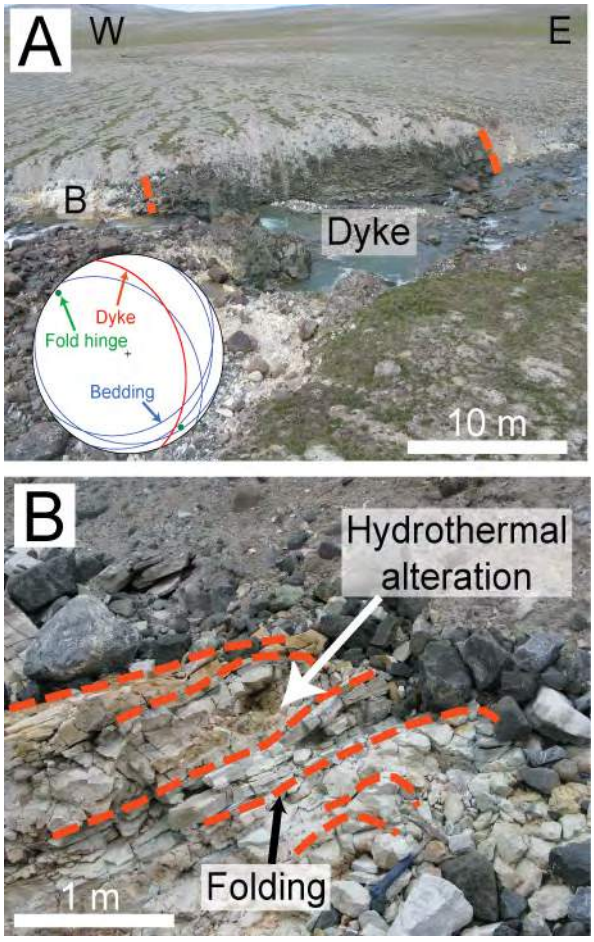

Fig. 6.7: (A) Field photo of Zone E showing the dyke outcrop (dashed red lines show igneous contacts). The location of photo B is shown at the western margin of the dyke. (B) Folded and discoloured Kilian Formation bedding at the western margin of the dyke. Hinge lines trend NW, parallel to the dyke.

6.3.5 Zone A

Zone A (Fig. 6.8) is at the southeastern end of the SFDC, and represents the highest stratigraphic level of the SFDC we have examined. A ~20 m thick gabbroic dyke that trends NNW/NW has chilled margins against Kilian Formation sulphate evaporates that dip ~80° to the SW (Fig. 6.4D). The dyke is slightly offset (< 10 m) by ENE-trending post-Palaeozoic faults (Fig. 6.8). The dips of the bedding in host rocks increases (up to ~32° to the SW) at dyke margins, indicating SW-side-down motion on a NNW/NW-trending fault, as for Zone E. We interpret this dyke to be a direct continuation of the Zone E dyke (Fig. 6.1). The dyke at Zone A contains disseminated sulphides at its margin, as well as sulphide staining in its core (Fig. 6.4D). The dyke appears to terminate where it joins a set of conformable gabbroic sills (Figs. 6.1 and 6.4D). Two sills are well developed towards the NE, but only one, poorly exposed sill can be traced towards the SW. The junction of these two sets of sills with the Zone A dyke is rubbly and poorly exposed (Fig. 6.4D), such that we cannot ascertain from field relationships if the dyke fed the sills.

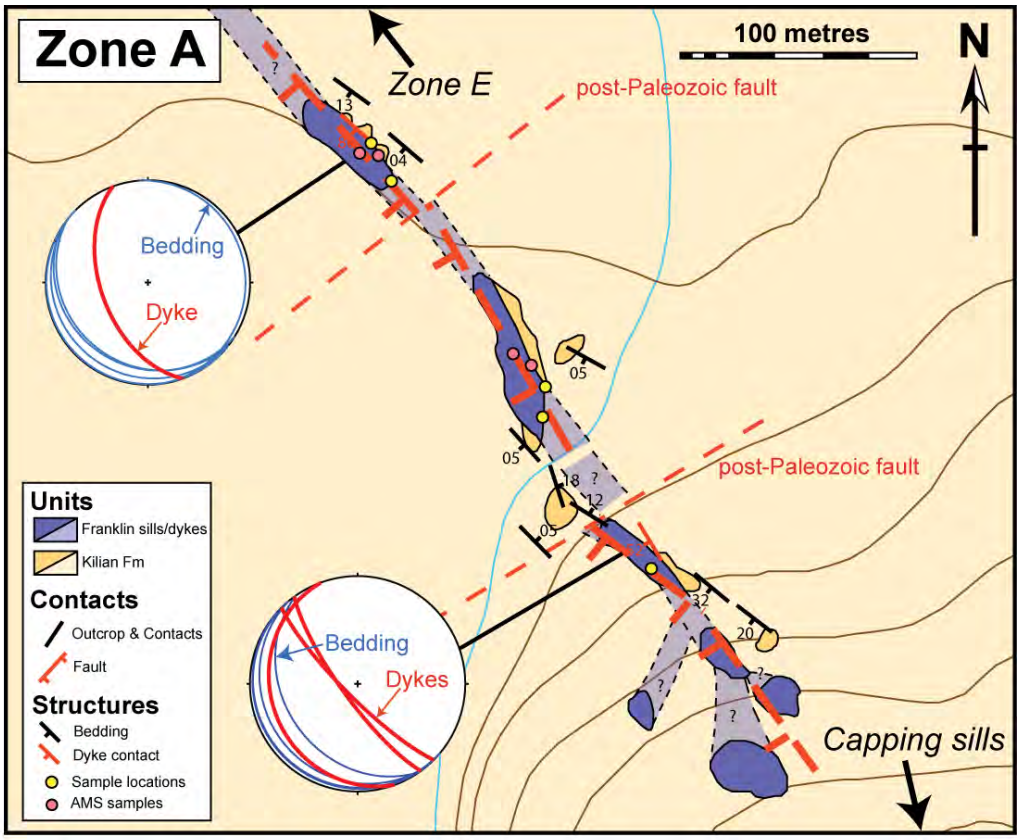

Fig. 6.8: A detailed geological map of Zone A, showing an inferred continuous dyke that splays towards two capping sills. The local Kilian Formation (sulphate-bearing) bedding is significantly perturbed near to where the dyke splays.

6.4 Results

6.4.1 Petrography and mineral chemistry

There are a variety of igneous and country rock facies preserved in the SFDC, including chilled intrusive contacts, medium-grained doleritic to gabbroic rocks, brecciated host rocks, all of which may show hydrothermal overprints. Chilled contacts typically grade inwards over a few cm to medium-grained doleritic facies. *In-situ* mineral compositions for olivine (Fo = 100 x Mg/(Mg+Fe2+)), clinopyroxene (Mg# = 100 x Mg/(Mg+Fe^{2+}+Mn)) and plagioclase (An = 100 x Ca/(Ca+Na+K)) are provided where analysed. 'Core' corresponds to the centre of the crystal, 'mantle' corresponds to the intermediate region and 'rim' corresponds to the edge of the crystal.

At Zone D, the capping sill is composed of sub-ophitic gabbro with euhedral, normally zoned (core An_{70}; rim An_{50}) plagioclase chadacrysts hosted by anhedral, normally zoned (core Mg#80; rim Mg#45) clinopyroxene oikocrysts (Fig. 6.9A). Minor (< 15%) olivine and interstitial ilmenite-magnetite are also present. The gabbroic body/roof apophysis (labeled 'a' on Fig. 6.3) has a chilled margin that is microphyric with phenocrysts of olivine (core Fo_{80} and NiO 0.25wt%) and clinopyroxene (core Mg#83; rim Mg#80) residing in a very fine-grained groundmass. This chilled margin grades into medium-grained gabbro that is texturally identical to the capping sill gabbro, with intergrown plagioclase (core An_{60}; rim An_{50-45}) and clinopyroxene (core Mg#75; rim Mg#40) and isolated olivine crystals (core Fo_{75} and NiO 0.15wt%). The internal chill in the gabbroic roof apophysis is very similar to the outer chilled margin with sparse clinopyroxene (core Mg#79; rim Mg#76) and plagioclase (core An_{70}; rim An_{68}) phenocrysts (no olivine was observed in the internal chill).

The Zone C dyke is very similar to the gabbroic roof apophysis at Zone D. A chilled margin grades into a medium-grained gabbro. However, at Zone C the dyke contains interstitial-textured olivine (Fig. 6.9B) with compositions that are more evolved (~Fo_{50} and NiO < 0.1wt%) in comparison to Zone D olivine. Both clinopyroxene (core Mg#80; rim Mg#63) and plagioclase (core An_{70}; rim An_{55}) core compositions at Zone C are very similar to those of Zone D, but crystal rims are more evolved at Zone C.

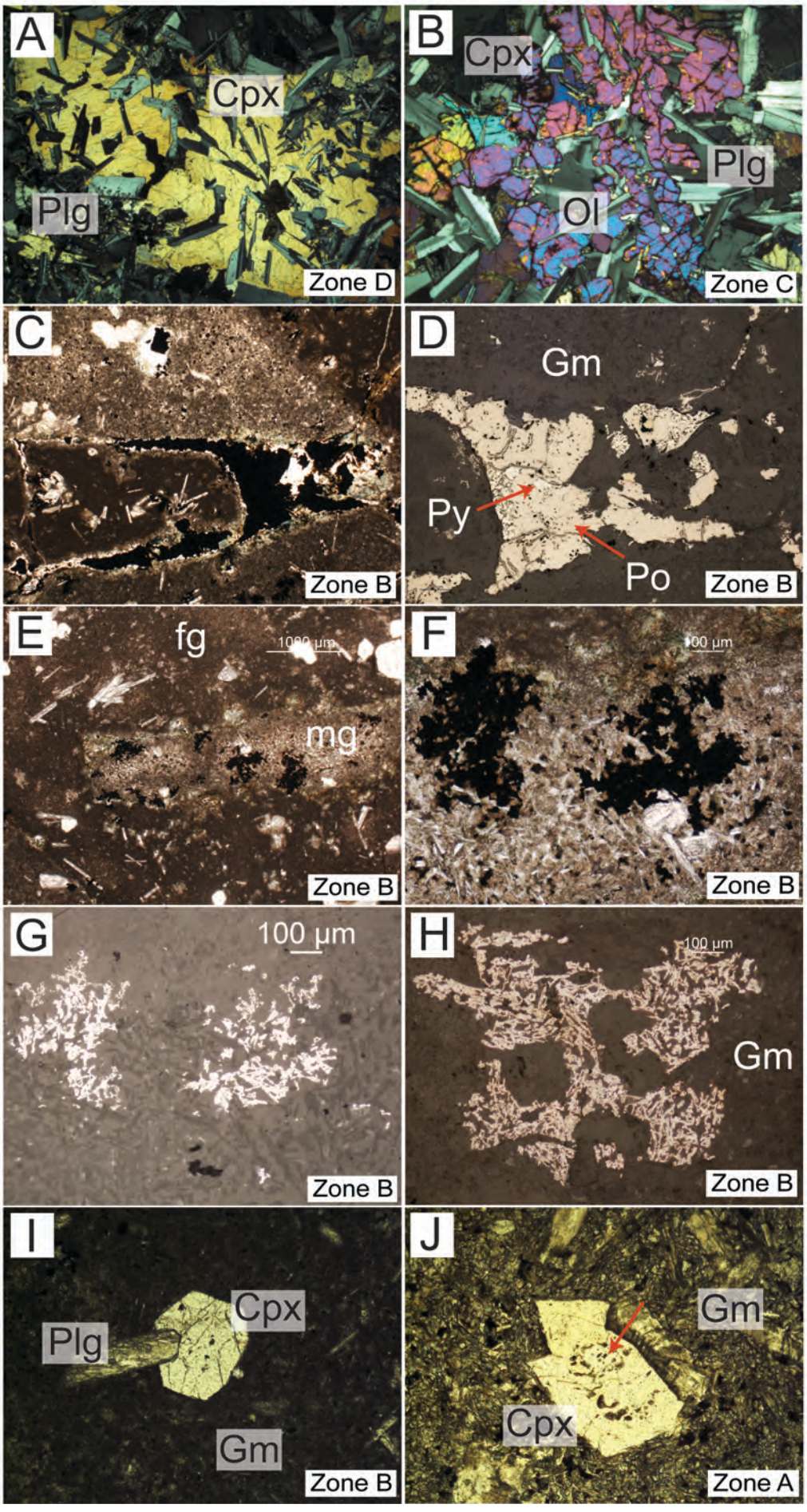
A
Cpx
Plg
Zone D
B
Cpx
Plg
Ol
Zone C
C
Zone B
D
Gm
Py
Po
Zone B
E
fg
mg
Zone B
F
Zone B
G
100 µm
Zone B
H
100 µm
Gm
Zone B
I
Cpx
Plg
Gm
Zone B
J
Gm
Cpx
Zone A

Fig. 6.9 (page 109): Photomicrographs of minerals and textures from the SFDC (FOV = field of view): (A) Clinopyroxene (Cpx) oikocryst enclosing plagioclase (Plg) chadacrysts (image in crossed-polars and FOV = 4 mm) at Zone D. (B) Interstitial olivine (Ol) intergrown with plagioclase and clinopyroxene in the Zone C dyke (image in crossed-polars and FOV = 4 mm). (C) Plane-light image (FOV = 2 mm) of igneous sulphide trapped in a wedge-shaped pore in Zone B dyke-propagator tip igneous breccia. (D) Reflected light image (FOV = 1 mm) of sulphide from image (C), which consists of pyrite (Py) and pyrrhotite (Po). (E) Plane-light image (FOV = 1 mm) of microdoleritic microxenolith in the Zone B dyke propagator tip igneous breccia. Note that the microdoleritic microxenolith is coarser than the quenched microphyric basalt in which it is embedded, suggesting it represents a wallrock fragment, and that it hosts several globular concentrations of sulphide. (F) Plane-light image (FOV = 1 mm) and (G) reflected light image (FOV = 1 mm) close-ups of the two patches in lower centre of the microdoleritic microxenolith shown in (E). Note that sulphide impregnates the doleritic textured silicates. (H) Another example of sulphide melt impregnation of microphyric dolerite (reflected light with FOV = 1 mm). (I) Clinopyroxene phenocryst intergrown with plagioclase in the microphyric basalt of the Zone B dyke propagator tips (plane-light and FOV = 1 mm). (J) Clinopyroxene phenocryst with spongy core (red arrows) hosted within groundmass at Zone A (plane-light and FOV = 1 mm).

At Zone B, the Wynniatt Formation limestones surrounding the narrow dykes we interpret to be propagator tips are heavily brecciated (Fig. 6.4B) with fractures/veins containing abundant calcite and hydrothermal pyrite crystals up to 1 cm in size. Veins also contain prehnite, quartz and sparse chalcopyrite. The brecciated limestone is crosscut by the dyke propagator tips, which themselves are brecciated by younger basaltic dykes. These brecciated propagator tips are composed of microdoleritic microxenoliths, cemented by microphyric basalt (Fig. 6.9I), which has reversely zoned clinopyroxene (core Mg#81; rim Mg#83) and normally zoned plagioclase (core An_{60}; rim An_{50}) microphenocrysts. The microdoleritic microxenoliths have granular clinopyroxene (core Mg#80; rim Mg#55) and fine, randomly oriented plagioclase laths (core An_{68}; rim An_{48}). Small (~2-3 μm) euhedral grains of pentlandite, pyrrhotite and pyrite were observed within plagioclase crystals in some of these microdoleritic microxenoliths. Large (~200 μm) grains of pyrite and pyrrhotite were observed infilling voids between microxenoliths in these dykes (Fig. 6.9 C-D), suggesting that the sulphide melt was mobile during brecciation. The microdoleritic microxenoliths also contain globular masses of net-textured sulphide (Fig. 6.9 E-H) that appear to have impregnated the porous dolerite.

The Zone E dyke displays very similar patterns to the dyke at Zone D-C, with a chilled margin that grades into medium-grained gabbro. Olivine in the chill is present as isolated, normally zoned phenocrysts (core Fo_{80}; rim Fo_{65}) and as more evolved crystals in olivine glomerocrysts (core Fo_{72}; rim Fo_{70}). Microphenocrysts of clinopyroxene in the chill are normally zoned (core Mg#80; rim Mg#55), with more evolved variants in the dyke core (core Mg#75; rim Mg#35). The Kilian Formation directly at the dyke margins at Zone E is

brecciated with fractures being infilled with euhedral pyrite and calcite crystals (up to 1 cm in size), similar to those observed in the brecciated Wynniatt Formation limestones at Zone B. Pyrite in these fractures appears to have been deposited in the permeable host rock breccia by hydrothermal fluids.

The Zone A dyke contains very similar textures and compositions to those observed in the Zone E dyke. However, there is an occurrence of a microporphyritic texture in a dolerite from the gossan-stained dyke core (Fig. 6.4D) at Zone A. Here, microphenocrysts of clinopyroxene are normally zoned (core Mg#83; rim Mg#80) with sieve-textured cores (Fig. 6.9J) suggesting resorption. Plagioclase phenocrysts are typically normally zoned with primitive cores (core An_{85}; rim An_{75}). However, reversely zoned plagioclase phenocrysts are also observed with rims in equilibrium with the cores of normally zoned plagioclase phenocrysts (core An_{72}; rim An_{85}). Sparse pyrite and chalcopyrite grains (< 1 mm in size) are present in the gossan stained core region of the Zone A dyke (Fig. 6.4D).

6.4.2 Bulk rock geochemistry

The majority of gabbroic samples from the SFDC have MgO contents < 10 wt%. Most gabbros show an FeOt-enrichment trend (Fig. 6.10B), suggesting melt evolution was controlled by the olivine + clinopyroxene + plagioclase cotectic. Most show L/HREE-ratios typical of Type-2 Franklin magmas (Fig. 6.10A). However, there are isolated occurrences of slightly more primitive (~10-12 wt% MgO) Type-1 Franklin magma in the SFDC (Fig. 6.10B). These occur in the dyke propagator tips at Zone B and in the Zone D dyke core.

Primitive mantle normalised multi-element spidergrams show a general similarity of magmas emplaced in the SFDC (Fig. 6.11). The large-ion-lithophile-elements (LILEs), including Pb, show erratic behaviour, however, suggesting hydrothermal alteration of the rocks and remobilisation of these elements (Fig. 6.11). There may be subtle differences between dyke core and chilled margin compositions. For example, at Zone D, the dyke core is more enriched in incompatible trace elements than the dyke chill (Fig. 6.11A). A sample from within the Zone D gabbroic roof apophysis shows higher L/HREE-ratios similar to the Type-1 Franklin magma (Fig. 6.11A). The gabbro from the sill-like body in

the SW region of Zone D is the most depleted in incompatible trace elements (Fig. 6.11A). The Zone C dyke has a trace element pattern identical to the Zone D gabbros, while the dyke chill at Zone C is most enriched (Fig. 6.11B). Zone B dyke propagator tip trace element patterns are very similar to Zone D-C gabbros, indicating they are Type-2 Franklin magmas (Fig. 6.11C). LILEs and high-field-strength-elements (HFSEs) are notably more enriched in the Zone B propagator tips compared to Zones D-C (Fig. 6.11C). Dyke rocks from Zone A-E are very similar to one another, indicating they formed from the same, or a very similar magma (Fig. 6.11 D-E).

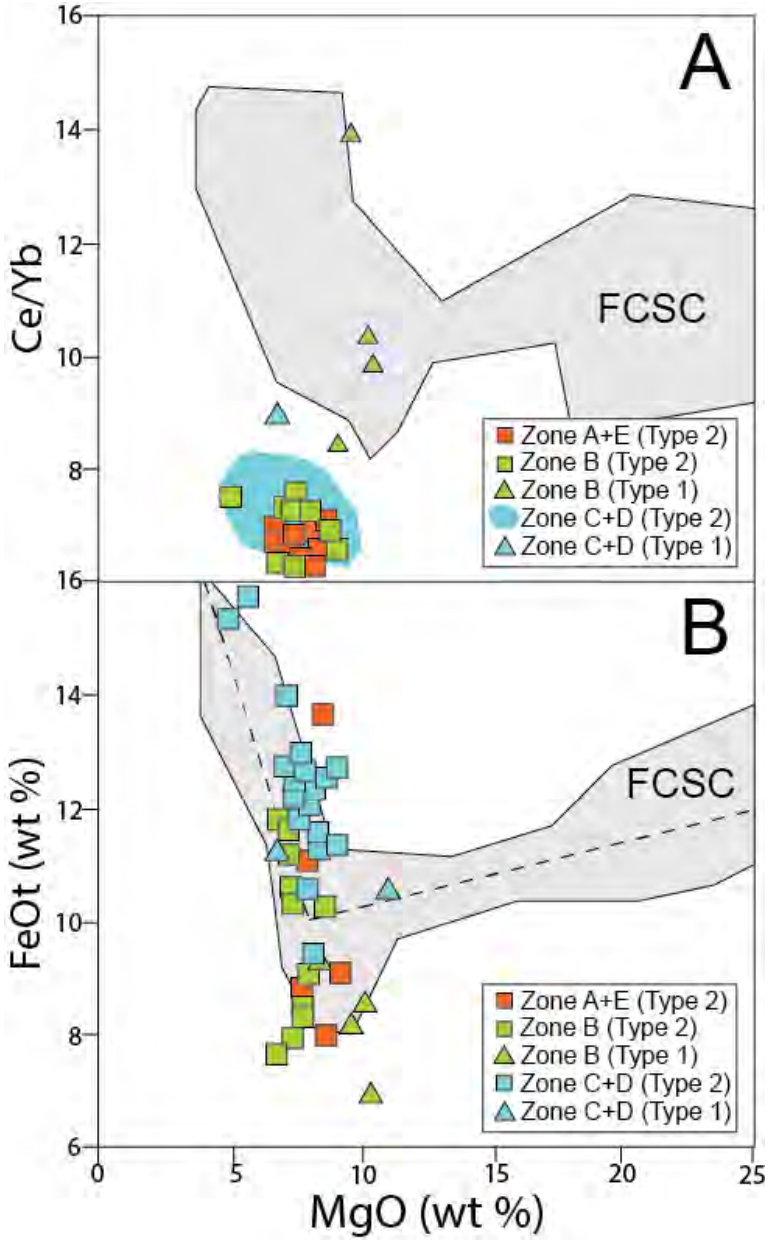

Fig. 6.10: (A) Ce/Yb versus MgO showing SFDC data. (B) FeOt versus MgO showing the SFDC data. The FCSC field, which is composed of Type-1 Franklin magma, is shown for reference on both plots.

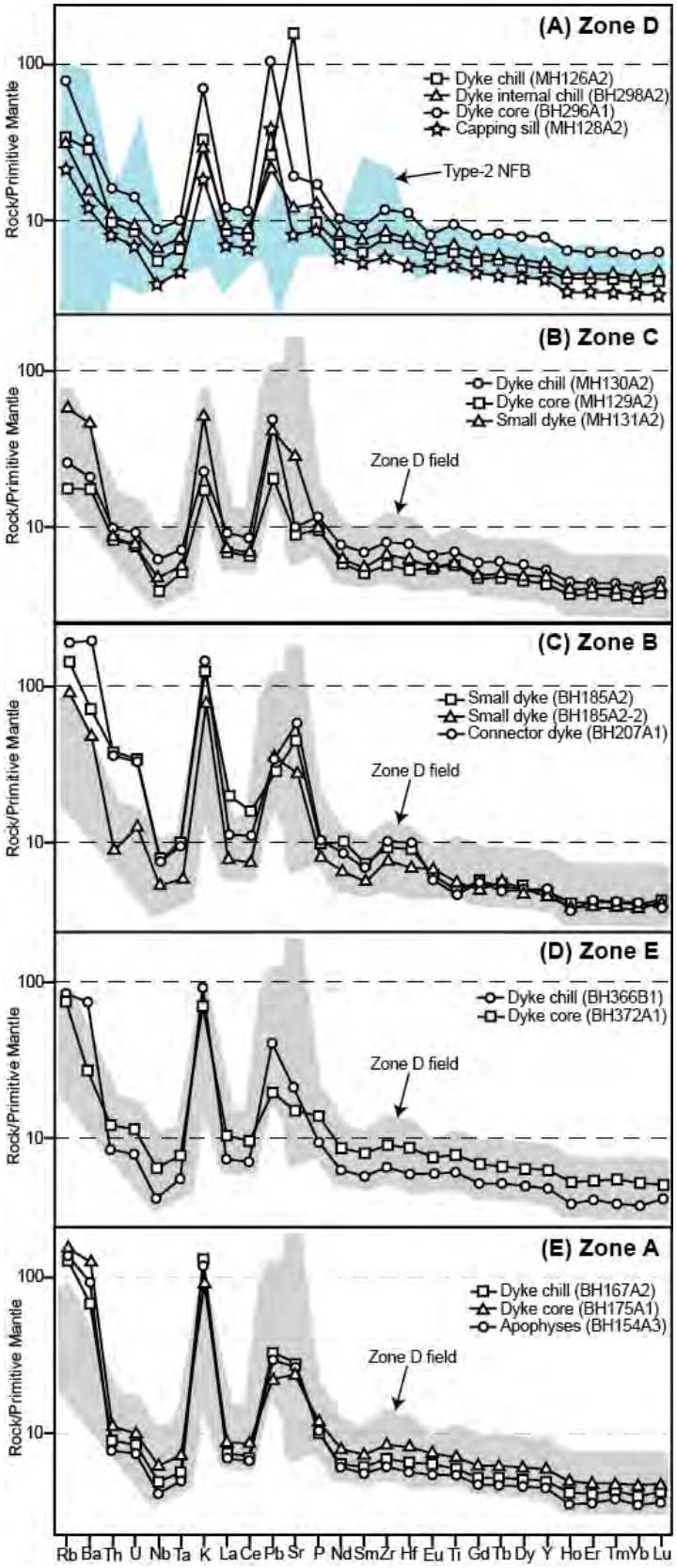

Fig. 6.11: Primitive mantle normalised spidergrams showing gabbroic samples from the SFDC: (A) Zone D; including in blue the Type-2 Natkusiak Flood Basalts, which are very similar to Zone D gabbros. (B) Zone C. (C) Zone B. (D) Zone E. (E) Zone A. Normalizing values are from Sun and McDonough (1989).

Chondrite normalised PGE profiles from the SFDC show that the gabbroic samples contain relatively low amounts of PGE, compared to chondrite abundances (Fig. 6.12). The IPGEs are strongly depleted, suggesting either retention of Os-Ir alloys in the source or fractionation of minor chromite/alloys or olivine (Capobianco & Drake, 1990, Tredoux *et al.*, 1995, Brenan *et al.*, 2003) or in local reduction fronts at chromite grain boundaries (Finnigan *et al.*, 2008). SFDC gabbros show a minor enrichment in Pt and Pd, relative to other PGEs. Pt is particularly enriched in the dykes at Zone E-A (Fig. 6.12A).

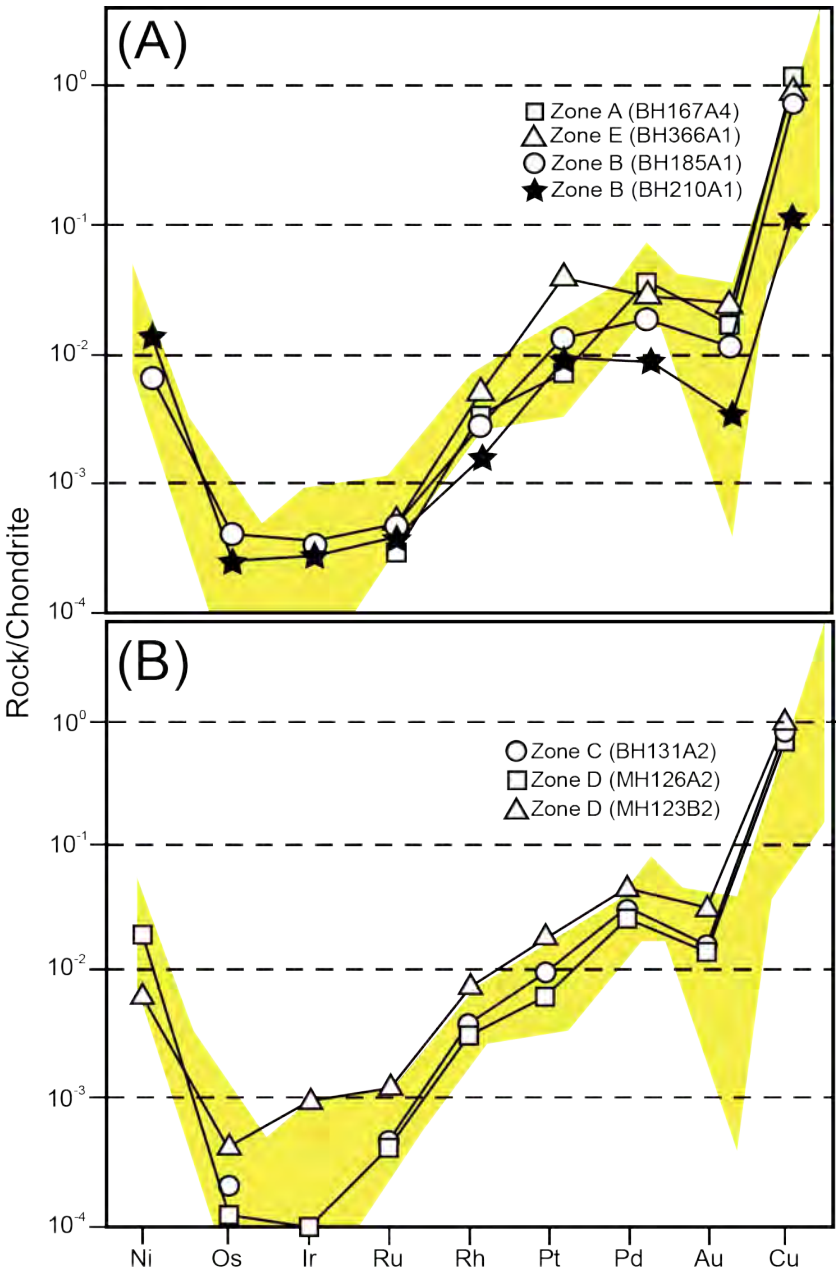

Fig. 6.12: Chondrite mantle normalised PGE spidergrams showing data from gabbroic samples from the SFDC: (A) Zones A, E and B. (B) Zones C and D. Normalizing values are from McDonough and Sun (1995). The yellow field is Type-2 Natkusiak Flood Basalts (N = 45). PGE data can be found in appendix G1.

6.4.3 Sulphur isotopes

The sulphur isotope data ($\delta^{34}S$) for the SFDC is presented in Fig. 6.13 and appendix G5. Samples are plotted from bottom (NW) to top (SE) in stratigraphic order. Gabbroic samples at Zone D have $\delta^{34}S$ values between +2.7 and +4.5‰. This is consistent with many Minto Inlier Franklin magmas, which commonly have $\delta^{34}S$ values between +2 and +4 possibly reflecting a slightly anomalous mantle source (Beard, 2012, Hryciuk *et al.*, 2014). The Wynniatt Formation limestone at Zone D has $\delta^{34}S$ values between +7.4 and +11.5‰, suggesting that only limited (if any) host-rock contamination is recorded in the gabbros of Zone D. In contrast, Zone C gabbroic samples have heavier $\delta^{34}S$ values between +9.0 and +11.0‰, suggesting more extensive contamination of the magma. At Zone B, Wynniatt Formation limestone has $\delta^{34}S$ values between +12.7 and +19.6‰. The thin N/NNE-trending dyke propagator tips at Zone B have $\delta^{34}S$ values between +4.8 and +12.7‰, and have higher sulphur contents (0.24 to 0.58 wt%) than most igneous rocks in the SFDC, implying significant wallrock contamination at Zone B. The Zone E dyke has $\delta^{34}S$ values of +9.7 to 10.4‰, suggesting contamination by Kilian Formation sulphates, which generally have $\delta^{34}S$ values between +17.0 to +24.0‰. A sample traverse from the Kilian Formation to the west of the Zone E dyke shows a pattern of bulk sulphur-depletion towards the dyke contact, with values decreasing from 0.43 to 0.13 wt% (appendix G5). Kilian Formation carbonates at Zone A have $\delta^{34}S$ values between +19.1‰ and +21.5‰, whereas the sulphates have $\delta^{34}S$ values between +31.8‰ and +32.6‰. The Zone A dyke has $\delta^{34}S$ values between +5.0‰ and +8.9‰, also consistent with wallrock contamination.

In summary, the SFDC shows an unambiguous up-section $\delta^{34}S$ enrichment trend between Zone D and B, with elevated $\delta^{34}S$ at Zone E, that suggests incorporation of heavy sedimentary sulphur by the magma. The most enriched $\delta^{34}S$ values occur in the dykes that are hosted by brecciated sulphur-bearing country rocks in Zone B (Fig. 6.13).

Fig. 6.13: $\delta^{34}S$ (relative to VCDT = Vienna Canyon Diablo Troilite) plot showing dyke, sill and local country rock $\delta^{34}S$ compositions across the SFDC, in stratigraphic order. Sulp = Sulphate evaporites.

6.4.4 Anisotropy of magnetic susceptibility fabrics

AMS was performed on 17 samples from the SFDC to constrain magma flow directions (appendix G6). Variation of susceptibility in cores of igneous rocks can be represented by a susceptibility ellipsoid, with maximum, intermediate and minimum axes K1, K2 and K3, respectively (Tarling & Hrouda, 1993). The plane of 'flattening' of the ellipsoid is the K1-K2 plane, and the axis of elongation is the K1 axis. Studies of AMS in magnetite-bearing rocks show that the magnetofoliation, for convenience represented by the K3 axis normal to the K1-K2 plane, and the magnetolineation, represented by the K1 axis, correspond to the preferred shape orientation of multi-domain magnetite (Borradaile & Henry, 1997).

Thus the principal AMS axes, K3 and K1, in unstrained pristine igneous rocks, are used as proxies for planes and lines of magmatic flow, respectively.

For the SFDC, the mean magnetic susceptibility (Km) is generally slightly higher and more variable for the sills (5.25 +/- 2.6 x 10^{-2} SI: Fig. 6.14 B-D) than for the dykes (3.38 +/- 1.4 x 10^{-2} SI: Fig. 6.14 A-C). This is probably due to more abundant and larger grain size of magnetite in the sills. The parameter P, for the degree of anisotropy, is low, < 1.066 for both sills and dykes, and is typical for fabrics of intrusive igneous rocks (Hrouda, 1982). The range of P is about the same for the sills as for the dykes (Fig. 6.14). For both sills and dykes, the shape factor U suggests that prolate magnetofabrics (U < 0) are more common than oblate magnetofabrics (U > 0), the ratio being about 1.4:1, respectively (Fig. 6.14 C-D).

In Fig. 6.14 E-F, poles for the AMS axes are shown for dykes and sills, respectively. Squares represent poles of K1 axes and circles represent poles of K3 axes. The AMS axial distributions for the dykes are somewhat scattered, consistent with both variable dyke orientation and variable flow patterns within dykes (Fig. 6.14E). In general, the K1 axes are better grouped than the K3 axes. The mean K3 of combined dyke sites corresponds to a magnetofoliation striking N33°W and dipping 73°SW. The dyke mean magnetolineation K1 in the plane of the magnetofoliation is steeply inclined to the SW at 72° towards azimuth 237°. However, these are *'in-situ'* orientations in the northern flank of a regional syncline (Fig. 2.2). Nearby to the west, the host Wynniatt Formation bedding strikes N67°E and dips 12°SE. If dyke emplacement preceded tilting of the bedding, as seems likely, then the present attitudes can be corrected for structural tilt, to estimate the original attitudes at the time of dyke emplacement. Using the above estimate for tilt correction, the 'tilt-corrected' orientation of the mean K1 axis for the dykes becomes approximately 65° inclined towards azimuth 205°. This supports the interpretation that steep upward flow of magma during dyke emplacement was from a southern source.

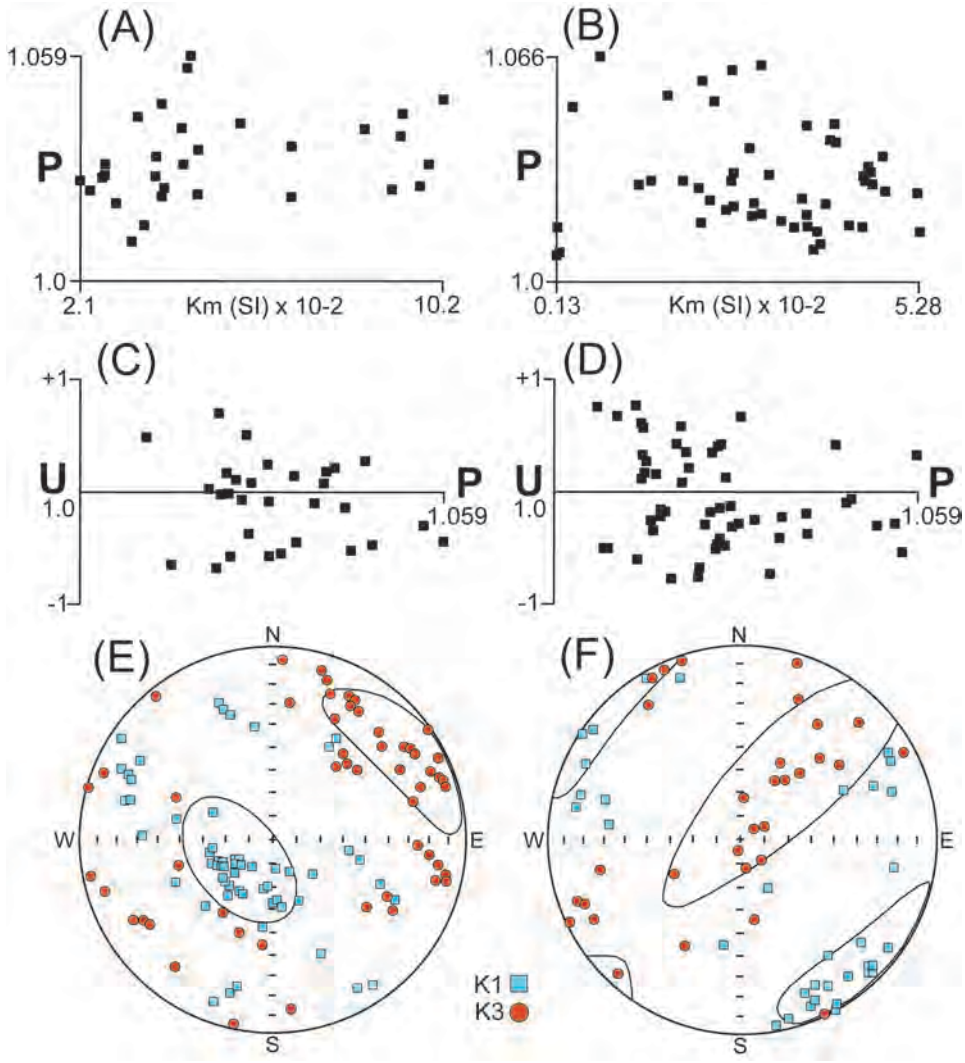

Fig. 6.14: Summary plots of magnetic susceptibility parameters for sills (A, C) and dykes (B, D) along the SFDC. P is degree of anisotropy, U is shape parameter, and Km is mean sample susceptibility in S.I. units. Stereoprojection of AMS K1 axes (blue squares, maximum susceptibility) and of K3 axes (red circles, minimum susceptibility) for dykes (E) and sills (F) of the SFDC; equal area, lower hemisphere projection. The contours are clustered around the majority of data points for each population shown (K1 and K3).

The AMS axial distributions for the sills (Fig. 6.14F) tend to be more streaked along great-circle trends and less irregularly scattered than for the dykes. The mean magnetofoliation of combined sill sites, interpreted from the mean K3 axis, strikes N55°W and dips 31°SW, significantly steeper than typical sill-margin contacts. The sills sampled along the SFDC exhibit mainly gently plunging K1 axes of NW/SE trend. This could be consistent with near-horizontal flow, but tectonic influences may also be involved. K1 axes are mainly well clustered at individual sill sites with larger scatter between sites. In deformed rocks, finite strain may affect AMS axial orientations (Borradaile & Henry, 1997). Combined magmatic-tectonic influences may produce streaked AMS axial patterns of primary and

secondary (i.e. of magmatic and tectonic), origins. Such transitional magnetofabrics (Borradaile & Henry, 1997) could occur especially in the sill samples of the SFDC.

6.5 Discussion

6.5.1 The structure and emplacement of the Southern Feeder Dyke Complex

The SFDC is located along a set of prominent regional NNW-trending 1st-derivative magnetic lineaments (Fig. 6.2), interpreted to represent syn-magmatic normal faults by Bédard *et al.* (2012). The SFDC consists of NNW/NW-trending dykes and NE-SW striking, SE-dipping sills (Fig. 6.1). In many cases, host rocks show evidence of brecciation (Fig. 6.4B) and at Zone B, previously brecciated and hydrothermally altered dyke material was reinjected by fresh dykes, indicating syn-magmatic faulting. The rheologically weak country rock carbonates soften markedly during magma emplacement and thus preserve shear sense directions on the faults (Žák *et al.*, 2012). At Zone D-C (Fig. 6.3 & 6.5), metre-scale drag folds indicate east-side-down motion on a NE-dipping normal fault. The softening of the country rock implies significant heat loss from the dykes, which could have driven hydrothermal cells around the SFDC.

Zone D is the stratigraphically deepest part of the SFDC. It preserves a ~20 m thick gabbroic roof apophysis (labeled ‘a’ on Fig. 6.3) that injected a parasitic fault in the downdropped limestone roof panel. The edge of the main gabbroic mass may also be a dyke (labeled ‘b’ on Fig. 6.3), the contact subsequently being sharpened by faulting. These syn-faulting dykes probably fed the capping sill, which extends for tens of kilometers towards the SW, but no direct linkage between the sill and the dyke-like facies is observed. However, interlayered calc-silicate and Fe-oxide skarn rocks occur in the inferred contact region. The calc-silicates in the skarn suggest intense contact metamorphism during sill emplacement (Nabelek *et al.*, 2013). The Fe-oxide facies of the skarn was inferred to represent the expulsion of late-Fe-rich magmatic fluids from the sills into the roof panel limestones at the Uhuk Massif (Bédard *et al.*, 2012, Nabelek *et al.*, 2013). If the analogy with the field relationships at the Uhuk Massif holds, then the skarn facies at Zone D would be remnants of a metamorphic aureole that sheathed the conduit-system that fed the

Zone D sill. This is consistent with the idea that the carbonate and discrete dyke ('a' on Fig. 6.3) that composes most of Zone D is a downdropped roof panel, and that the dyke-like feeder of the sill located near the gabbro/limestone contact ('b' on Fig. 6.3) was partly faulted out. The proximity of the Zone C dyke to Zone D, together with its similar size and orientation, suggest it is an extension to a higher stratigraphic level of the Zone D feeder dyke. The Zone C dyke contains more evolved mineral compositions in comparison to the Zone D gabbros, suggesting the magma fractionated as it traversed the crust. This is consistent with the AMS data that indicate dominant up-flow in the dykes (Fig. 6.14). At the present erosional level, the SFDC is segmented, but the dykes constituting this system may be connected at depth, as is typical of many dyke systems (Delaney & Pollard, 1981).

We infer that the NNW/NW-trending rubbly gabbro at the NE-end of Zone B is also an up-section continuation of the Zone D-C feeder dyke. However, Zone B also has numerous thinner (~0.5-2 m) N/NNE-trending dykes that splayed off from the main fault-guided dyke (Fig. 6.6). The orientation of the thinner N/NNE-trending dykes suggests injection of magma into a conjugate fracture system. The sulphide-bearing igneous breccias in the thin dykes are cemented by microphyric basalt, confirming the syn-faulting nature of magmatism. The overprinting hydrothermal system generated by dyke intrusion appears to have remobilised country rock sulphides, and deposited them in the surrounding, permeable limestone breccia. We interpret the thinner dykes at Zone B to be propagator tips emplaced into an active fault.

Zone E-A consist of a single NNW/NW-trending dyke emplaced into sulphates and carbonates of the Kilian Formation. This is the stratigraphically highest region of the SFDC. No dykes are present above this level (at this location), suggesting that the dykes may have fed the overlying sills (Figs. 6.4D & 6.8). At Zone E-A (Fig. 6.7 & 6.8), SW-side-down motion on a normal fault is preserved, the opposite of that seen at Zone D-C. This suggests that the SFDC fault system has a horst-and-graben geometry, and is composed of numerous, synchronously active fault strands, many of which were exploited by the Franklin magma.

6.5.2 Evidence for a composite magmatic system

The presence of internal chills within the dyke-like roof apophysis at Zone D, and the presence of igneous breccias (Figs. 6.4C and 6.9 E-F) at Zone B, implies that the SFDC was a composite magmatic system. Sieve-textured clinopyroxene phenocrysts indicate resorption caused by magmatic replenishment in the plumbing system. Geochemically, the SFDC is mostly composed of relatively fractionated Type-2 Franklin magma (Fig. 6.10A). However, there are occurrences of more primitive Type-1 magma (Fig. 6.10A) at Zone D-B. The presence of both populations of Franklin magma suggests that the SFDC acted as a conduit system for the 1st (Type-1 magma) stage of Franklin LIP magmatic activity, and that this older conduit system was then reactivated and flooded by Type-2 magma during the main basaltic effusion stage. AMS fabrics in the dykes show steep upflow fabrics indicating that magma ascended from depth along fault-guided dykes (Fig. 6.14). The apparent northerly magma flow direction measured in the SFDC is probably a local effect caused by the channelling of Franklin magmas through a complex underlying plumbing system.

6.5.3 Downstream/up-section $\delta^{34}S$ increase in the SFDC caused by crustal assimilation

Various mechanisms that trigger sulphur-saturation in magma have been suggested, such as: 1) fractional crystallisation (Czamanske & Moore, 1977, Wendlandt, 1982): 2) changing fO_2 conditions (Haughton *et al.*, 1974): 3) magma mixing (Irvine, 1975): and 4) addition of external crustal sulphur (Ripley *et al.*, 2003, Keays & Lightfoot, 2010). The assimilation of crustal sulphur into magma is considered a particularly potent way to trigger formation of an immiscible sulphide liquid. The $\delta^{34}S$ data imply that magmas in the SFDC interacted with and commonly assimilated their host rocks (Fig. 6.13).

Heavy $\delta^{34}S$ values imply ingestion of crustal sulphur (Li *et al.*, 2009), because mantle-like $\delta^{34}S$ values are typically ~0‰ (Labidi *et al.*, 2014). Franklin magmas have $\delta^{34}S$ values typically between +2 and +4‰, however, which we believe reflects derivation from a slightly anomalous source mantle (Beard, 2012, Hryciuk *et al.*, 2014). $\delta^{34}S$ values in the

gabbros at Zone D are similar to typical Franklin magmatic values and therefore preserve minimal evidence of host rock contamination. Slightly up-section at Zone C, the $\delta^{34}S$ values increase to ~10‰, indicating host rock assimilation. The dyke propagator tips at Zone B also have enriched $\delta^{34}S$ values between +4.8 and +12.7‰, trending towards the composition of their host country rocks (Fig. 6.13). The Wynniatt and Kilian Formation sedimentary rocks hosting the SFDC have elevated $\delta^{34}S$ values typical of sedimentary rocks deposited in a restricted basin (Prince, 2014). This may account for the elevated $\delta^{34}S$ values (up to +32.6‰) of Kilian Formation sulphate evaporites compared to the lighter values (+15 to +17‰) of the Minto Inlet Formation evaporites. The Zone E dyke has $\delta^{34}S$ values of +9.7 to 10.4‰, indicating significant contamination by host rocks. The hydrothermally altered and sulphur-depleted country rock that occurs in proximity to the Zone E dyke suggests that sulphur was liberated by metamorphic devolatilization reactions, as suggested for the Northern Feeder Dyke Complex (Hryciuk et al. In Prep). The $\delta^{34}S$ values (+5.0‰ and +8.9‰) of the Zone A dyke also indicate minor evaporite or carbonate assimilation (Fig. 6.13). The most elevated Zone B $\delta^{34}S$ values and sulphur contents can be explained by a simple mixing model (Ripley & Li, 2003). Assuming an uncontaminated magma with 620 ppm sulphur and $\delta^{34}S$ of +3.6‰, then 0.05 to 0.06wt% anhydrite assimilation (with $\delta^{34}S$ of +32‰) is required to generate $\delta^{34}S$ values greater than +8‰.

In summary, the $\delta^{34}S$ data indicate that most gabbroic rocks of the SFDC have been contaminated by local country rocks, which may have induced sulphide immiscibility in the magma. We will now discuss in more detail the evidence preserved at Zone B, where sulphide immiscibility caused by wallrock assimilation appears to have been 'caught in the act'.

6.5.4 Sulphide immiscibility induced by wallrock assimilation

There is an ongoing debate about how and where magma becomes sulphur-saturated within the magmatic plumbing systems of Ni-Cu-PGE sulphide deposits (Naldrett, 1992, Ripley *et al.*, 2003, Ripley & Li, 2013). The dyke-fault relationships of the SFDC share many similarities to conduit-style ore deposits such as Noril'sk (Naldrett, 1992, Li *et al.*, 2009), Jinchuan (Lehmann *et al.*, 2007) and the Eagle deposit (Ding *et al.*, 2012), where it has been inferred that faulting associated with rifting facilitated ore genesis. At Noril'sk it

is thought that the ingestion of sulphate-bearing country rocks into a PGE-enriched magma generated the orebodies (Li *et al.*, 2009). The latter is supported by the heavy $\delta^{34}S$ composition of the magma, which is higher than mantle-like values and trends towards the $\delta^{34}S$ composition of the surrounding sulphate-bearing country rocks (Grinenko, 1985). However, the actual mechanism for ingestion of sulphur-rich country rock into the Noril'sk magma is unclear (Ripley *et al.*, 2003). Naldrett (1999) proposed that thermal erosion of the magma chamber walls during multiple magmatic pulses led to the ingestion of Devonian evaporites and carbon-bearing country rocks. In the SFDC, the country rock is heavily brecciated as a result of Neoproterozoic faulting. Emplacement of magma into fault zones could allow more extensive interaction because of the increased surface area provided by the brecciated country rock. At Zone B in particular, the dyke propagator tips intrude sulphur-bearing brecciated carbonates and older brecciated dyke material (Fig. 6.4C). The $\delta^{34}S$ values of the Zone B propagator tips are especially high (up to +12.7‰), and trend towards $\delta^{34}S$ values of the surrounding country rock (Fig. 6.13).

Sulphur contents of ~1400 ppm are typically required to trigger sulphur saturation in a basaltic magma (Jugo *et al.*, 2005) similar to the Type-2 magmas (Fig. 6.10A), which constitute most of the SFDC. However, this value is dependent upon various factors such as temperature, pressure, magma composition and oxygen fugacity. The sulphur contents of the Zone B dyke propagator tips (up to 0.58 wt% ppm: appendix G5) are typically greater than the value required to trigger sulphur saturation. The sulphur-bearing local country rocks represent plausible sulphur-sources. The abundance of sulphur-minerals in the hydrothermal breccia-fills suggest that hydrothermal cells generated by magmatism stripped sulphides from host country rocks (and possibly earlier dyke pulses) and reconcentrated them within the breccia zone (Fig. 6.4B), where they would have the greatest likelihood of being assimilated by the next pulse of magma. In turn, such hydrothermal cells would have been made more efficient by local country rock brecciation, which would have greatly enhanced the permeability of the country rocks.

The microdoleritic microxenoliths within the syn-faulting dyke propagator tips at Zone B host globular impregnations of sulphides that provide direct evidence of syn-faulting magmatic sulphide immiscibility (Fig. 6.9 E-H). The textures show that immiscible globules of magmatic sulphide impregnated a porous microdoleritic matrix (Fig. 6.9 C-H). These sulphide-impregnated microdoleritic rocks were then reworked (brecciated) by the

next magma pulse. It is possible that the injecting basaltic melt that now cements the microdoleritic microxenoliths could have scavenged and ingested sulphide hosted within microdoleritic microxenoliths, in addition to incorporating external crustal-derived sulphur directly.

The Zone B dyke propagator tips appear to represent magmatic dead ends where rapid cooling limited the upgrading process. Conversely, this is why textural evidence for immiscible sulphide generation has been preserved there. The processes involved in the early stages of ore-genesis that are preserved in Zone B may be applicable to the entire SFDC, given the elevated $\delta^{34}S$ values recorded in other parts of the system (Fig. 6.13). However, in larger, more robust parts of the system (e.g. Zone D: Fig. 6.3), where large amounts of magma flowed through the conduits to inflate a major sill, the contaminated signatures and any immiscible sulphides formed this way may have been flushed downstream (*cf* Hryciuk et al. Submitted). Given the availability of structural or hydraulic traps in these sills, it is possible that immiscible sulphides may have been trapped there.

In summary, the SFDC on Victoria Island represents a fossilised magmatic feeder system that was emplaced into an active normal fault system. Our data imply that external sulphur was ingested by the magma, triggering local sulphide saturation and the formation of immiscible sulphide liquids. Brecciation associated with this faulting may have facilitated the assimilation of host sulphur, both by increasing available reactant surface area, and more speculatively, by pre-concentrating sulphur and Cu through forced hydrothermal circulation in high-permeability fault breccias. Similar mechanisms may have been involved in forming Ni-Cu-PGE ore-bodies in other conduit-style magmatic systems; the evidence having been obliterated by repeated magma throughflow.

6.5.5 Economic Ni-Cu-PGE potential of the Franklin LIP

The evidence that sulphide immiscibility occurred in Zone B of the SFDC raises the question of where any possible immiscible sulphide liquids were deposited. A hydraulic trap is required in order to produce economically viable quantities of immiscible sulphide liquids (Naldrett, 1992). The most probable targets would be the downstream extensions of sills that were fed by SFDC dykes. Approximately 10 km SW of the capping sill at Zone A

there are sulphide-rich (~5%) dykes (e.g. Sulphide City Dyke: Fig. 2.2) with small semi-massive sulphide concentrations at its contacts, and there are large calcite-pyrite-rich gossans (GS: Fig. 6.15 and Peterson *et al.* (2014)). Although the sulphide at the GS appears to be mainly hydrothermal (Fig. 6.15B), it is possible that some of it was scavenged from immiscible sulphide previously concentrated in one of the adjoining sills.

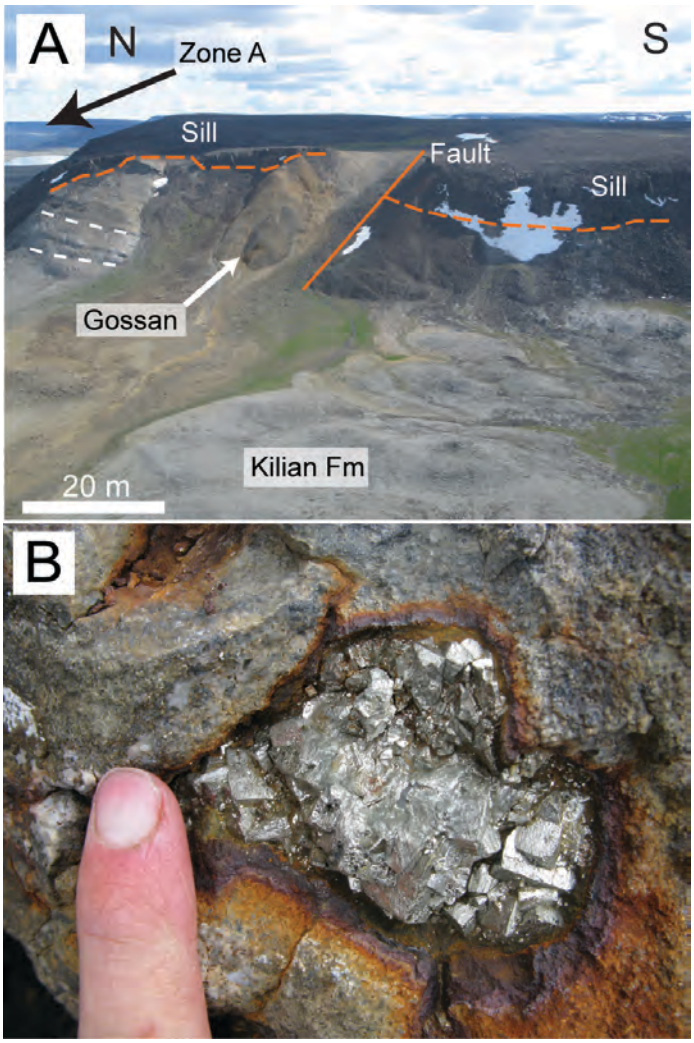

Fig. 6.15: (A) Field photo of the Gossan Sill (GS) situated ~10 km WSW of the SFDC (Fig. 2.2). The dashed red line shows the sill contact with the Kilian Formation country rocks (dashed white lines for bedding). (B) Hydrothermal pyrite globules with oxidised halos in the Kilian Formation just below the contact with the sill.

The syn-faulting scenario for magma emplacement and contamination documented in the SFDC and the Uhuk Massif (Bédard *et al.*, 2012) probably also applies to the entire Franklin event in the Minto Inlier. The NNW/NW-trending magnetic lineaments (Fig. 6.2) are found throughout the Minto Inlier (Kiss & Oneschuk, 2010), and each may represent a syn-faulting dyke that could have transported significant quantities of magma up-section. In these syn-magmatic fault systems, where cataclasis increases reactant surface areas,

flowing magma could have ingested crustal sulphur, triggering the formation of immiscible sulphide liquids. This is the scenario that appears to be preserved at Zone B of the SFDC. The intersections of these syn-magmatic faults with sulphate-rich sediments of the Kilian and Minto Inlet Formations would appear to be particularly promising exploration targets. Such fault systems could also be favourable sites for the emplacement of subsequent magma pulses, generating composite magma systems with the capacity to upgrade the tenor of early sulphides. Where the magma systems are better developed, as at Zone D, prior evidence of contamination (if it indeed occurred) would have been flushed downstream.

In addition to the dyke-fault systems acting as dynamic environments, the occurrence of Type-1 magma in the SFDC is significant (Fig. 6.10A). Type-1 magmas were the first to be emplaced in the Franklin LIP and are commonly found deeper in the Shaler Supergroup. Type-1 rocks are often primitive (up to ~13 wt% MgO) with high Ni-contents up to 250 ppm (appendix E1). Type-1 Franklin magmas were hotter (~1300°C) than Type-2 Franklin magmas, and therefore would have had more potential to reactivate crustal rocks. The Uhuk Massif was inferred to be the major melt and crystal-slurry feeder to the Type-1 olivine-enriched Fort Collinson Sill Complex (chapter 5). Pulses of magma and crystal slurries may have waxed and waned during episodic fault-slip, and upstream sill collapse during melt evacuation at the Uhuk Massif. It has been proposed that melt evacuation triggered by sill collapse played a role in the generation of the Voisey's Bay Ni-Cu-PGE sulphide deposit (Cruden *et al.*, 2008). There is also evidence for magmatic replenishment and magma mixing in sills associated with Type-1 magmas (chapter 5), which can act as mechanism for triggering sulphur-saturation (Irvine, 1975). Later Type-2 magma pulses that utilised the SFDC may have ingested earlier sulphides associated with Type-1 magmas. The association of Type-1 magmas in the SFDC as well as other dyke feeder systems in the Minto Inlier therefore enhances the Ni-Cu-PGE economic potential of the Franklin LIP.

6.6 Conclusion

The Southern Feeder Dyke Complex (SFDC) on Victoria Island in the Canadian Arctic is part of the Franklin Large Igneous Province (LIP). The Franklin LIP on Victoria Island is

primarily composed of gabbroic sills, with sub-ordinate NNW/NW-trending feeder dykes. Igneous breccias cemented by basalt and drag folds within wallrocks indicate that Franklin magmas were emplaced contemporaneously with regional Neoproterozoic normal faulting. The SFDC dykes acted as dynamic magma conduits that facilitated the ingestion of crustal sulphur into the magma, which we believe triggered the formation of immiscible sulphide liquids. This scenario is supported by heavy $\delta^{34}S$ values of the dykes. There are sulphide showings associated with Franklin sills and dykes across the Minto Inlier, including the SFDC area. At the SFDC, globular and locally net-textured sulphides are associated with microdoleritic microxenoliths that were cemented by later basaltic magmas. Evidence that the SFDC was a composite magmatic system suggests that previously formed immiscible sulphides may have been ingested by fresh magma. In the more robust part of the SFDC where dykes and sills are well developed, the evidence for sulphide immiscibility may have been flushed downstream. The SFDC appears to feed laterally extensive sills at different crustal levels. These sills may represent hydraulic traps that could have concentrated immiscible sulphide liquids. There are gossan showings in the sills downstream from the SFDC, which may represent late hydrothermal reworking of such sulphides. Similar processes of wallrock induced sulphide immiscibility may have operated in dyke-feeder systems across the Franklin LIP in the Minto Inlier, suggesting that the Franklin igneous rocks on Victoria Island are indeed prospective for Ni-Cu-PGE. The textures and field relationships documented in the SFDC support models where sulphide immiscibility is triggered by sedimentary wallrock assimilation during fault-guided magmatic activity.

7. Conclusions and future work

7.1 Introduction

This thesis has investigated the magmatic processes that operated in the Neoproterozoic Franklin plumbing system. The excellent exposure and preservation (lack of metamorphism and deformation) of the Franklin sills, dykes and flood basalts within the Minto Inlier of Victoria Island has enabled a detailed petrological and *in-situ* mineral chemical investigation of the igneous rocks.

At the beginning of this project, three aims were set out: 1) Investigate the large-scale processes that operated in the magmatic plumbing systems of LIPs. 2) Investigate the small-scale differentiation mechanisms operating in sills. 3) Provide insights into the economic Ni-Cu-PGE potential of the Franklin LIP.

7.2 Large-scale processes operating in the Franklin magmatic plumbing system

In chapter 5, I studied the larger-scale differentiation mechanisms of the Franklin magmatic plumbing system. This was achieved by examining the Fort Collinson Sill Complex (FCSC) for > 50 km along strike. The FCSC has a continuous olivine zone with an overlying doleritic gabbro zone, with the former exhibiting an along strike bulk-rock Fe-enrichment trend. Fe=Mg systematics and trace element modelling show that this differentiation trend is the result of olivine slurry replenishment into a resident, more evolved gabbroic mush.

The FCSC study provides important insights into the regional differentiation dynamics of the Franklin magmatic plumbing system. Other olivine-enriched sills have been observed at a similar stratigraphic level to the FCSC, and some of them show isotopic disequilibrium between their olivine and dolerite zones. Therefore, a similar olivine slurry replenishment scenario may have operated in these other Franklin sills. If this is the case, then there may

have been a magma chamber system beneath the level of emplacement of the sills, where primitive magmas similar to the parental magmas to the sills, crystallised olivine cumulates. Periodic replenishment into this underlying feeder system could have triggered cumulate remobilisation events with olivine slurries emplaced up-section into sills containing partly crystalline gabbroic mushes. Such an emplacement process may have operated in other LIPs or large layered intrusions elsewhere, and can potentially account for the lateral variability seen in some of these rocks.

7.3 Small-scale differentiation mechanisms operating in sills

In chapter 4, I studied a layered mafic Franklin sill, called the Lower Pyramid Sill (LPS), in detail. The LPS is characterised by a basal olivine-enriched layer (OZ) that is overlain by a sequence of doleritic gabbro (DZ). This study utilised field relationships, whole-rock chemistry, petrography and *in-situ* mineral chemistry, to help understand how its igneous layering formed. The rapid cooling and preservation of the LPS enabled the use of reliable inverse melt modelling, which was used to assess the compositions of crystals and melts involved during differentiation of the sill. I showed that the LPS OZ formed by an olivine slurry replenishment into a resident, more evolved gabbroic mush. The DZ shows upward *in-situ* fractional crystallisation trends in comparison to the underlying OZ. Intervening clinopyroxene-rich cumulates were shown to have formed by a metasomatic reaction between pore melts derived from the OZ and DZ.

The differentiation model developed for the LPS has implications for the development of igneous layering in layered intrusions elsewhere, particularly with regards to the formation olivine-rich layers. Also, the study fits into a current debate about how magma(s) are emplaced and how igneous layering forms. One school of thought advocates the emplacement of aphyric liquids that evolved by *in-situ* fractional crystallisation, while another suggests the emplacement of crystal-charged slurries. The model presented for the LPS shows that its cumulate layering formed from both of these mechanisms. In addition, the LPS model also shows the importance of porous melt flow within crystal mushes, which can potentially overprint primary igneous facies. The differentiation mechanisms that operated in the LPS may have operated in the development of igneous layering large layered intrusions. For example, in the Bushveld Complex, large-scale up-section isotopic

shifts have been observed, as well as crystal-scale isotopic disequilibrium within individual layers. The larger-scale isotopic shifts suggest the periodic emplacement of replenishing magmas, whilst the smaller-scale isotopic disequilibrium between constituent crystals of individual layers suggest that slurry emplacement, as shown for the LPS, may have been an important differentiation mechanism in the Bushveld Complex.

7.4 Economic Ni-Cu-PGE potential of the Franklin LIP

The Franklin LIP is considered to be prospective for Ni-Cu-PGE mineralisation. In chapter 6, I investigated a fault-guided Franklin feeder dyke network, called the Southern Feeder Dyke Complex (SFDC). The SFDC provided an ideal target to investigate the economic potential of the Franklin LIP on Victoria Island. The exceptionally exposed field relationships, sulphide mineralisation and emplacement into sulphate-bearing country rocks of the SFDC allowed the processes involved in the formation of immiscible sulphide liquids to be investigated.

At the SFDC, magmas were fault-guided and they may have fed the adjacent sills. Dykes at the SFDC are brecciated and contain microdoleritic microxenoliths cemented by basalt. The microdoleritic microxenoliths contain globular and locally net-textured sulphides that impregnated a porous doleritic mush. I inferred, based on the field and textural relationships, that sulphide immiscibility in the SFDC magma was triggered by local wallrock assimilation. This would have been facilitated by fault-related brecciation. Our interpretation of external sulphur addition into the magma is supported by elevated $\delta^{34}S$ values of the dykes, which are towards the values of the local sulphur-bearing country rocks.

NW-trending syn-magmatic Neoproterozoic faults are pervasive across the Minto Inlier, and based on the evidence preserved in the dykes at the SFDC, I infer that that similar mechanisms inducing sulphide immiscibility operated throughout the Franklin magmatic plumbing system. However, in composite magmatic systems that experienced renewed magmatism, immiscible sulphide liquids may have been flushed downstream into neighbouring sills. There is evidence in the SFDC for magmatic replenishment and coupled with the slurry replenishment mechanisms preserved in the Franklin sills, indicates

that the Franklin magmatic plumbing system was a dynamic environment. The SFDC ultimately emphasises the importance of external, crustal-derived sulphur in the formation of immiscible sulphide liquids in basaltic magmas. The SFDC allows for a reconstruction of the mechanisms by which this external sulphur is incorporated into the magma, providing insights into Ni-Cu-PGE mineralisation processes.

7.5 Future work

The superbly exposed Neoproterozoic Franklin LIP on Victoria Island provides an excellent opportunity to understand the differentiation of LIPs. Further work on the olivine-enriched sills that may be related to the Fort Collinson Sill Complex (FCSC: chapter 5) could help determine if they formed from a similar emplacement process to that preserved in the Lower Pyramid Sill (LPS: chapter 4) and the other sills constituting the FCSC. If indeed Kat's sill is related to the FCSC (as inferred in chapter 5), then there may have been a regional olivine slurry replenishment event. The exposure of the Franklin sills would enable this olivine slurry replenishment event and its geochemical consequences to be characterised in 3D.

The next phase of the LPS study (chapter 4) would be to characterise in detail the nature of the hybrid melt and its porous flow through the proto-OZ mush. Detailed *in-situ* trace element quantification and inverse melt modelling using partition coefficients parameterised using the Franklin melt database would provide constraints on porous melt flow in the LPS and its role in redistributing incompatible trace elements in the sill. Also, sector-zoned clinopyroxenes that appear to be preserved in a channel-like network in the geometric centre of the LPS can be investigated to understand the impacts of sector-zoned growth on trace element partitioning.

The majority of Franklin sills exposed in the Minto Inlier are geochemically related to the Type-2 magma population. These Type-2 sills are characterised by doleritic and porphyritic textures. The porphyritic sills are comprised of isolated phenocrysts and glomerocrysts that appear to be ripped up gabbroic mushes. The porphyritic sills show S- and D-shaped whole-major element profiles that characterises other layered sills. Considering the 'random' constituents of these sills, it is surprising that they form well-

developed geochemical profiles. One of these porphyritic sills should be examined in detail, much like the LPS in chapter 4, with crystal and melt compositions constrained to see how their geochemical profiles formed and if similar processes operated in these sills to those in the LPS/FCSC. This work would therefore transcend both Franklin magma populations (Type 1 & 2) and reveal any linkages between differentiation mechanisms and specific magma types.

To further improve our understanding of the Franklin magmatic plumbing system and the processes operating during the remobilisation of cumulates, the Natkusiak flood basalts need to be studied. A ~1 km thick sequence of Natkusiak lavas are preserved in the Minto Inlier and they have been geochemically correlated to the underlying Franklin intrusives. Therefore, detailed whole-rock and *in-situ* mineral chemical work on the Natkusiak flood basalts would provide an opportunity to understand the dynamics of the Franklin plumbing system. It would be interesting to see if the processes preserved in the sills (chapter 4 & 5) are preserved in the coeval flood basalts, or if, in addition, the lavas preserve a record of other processes. Additionally, geothermobarometry studies of the phenocrysts preserved in the Natkusiak flood basalts would provide constraints on the depth distribution of magma chambers in the Franklin LIP.

8. References

Annen, C., Paulatto, M., Sparks, R. S. J., Minshull, T. A. & Kiddley, E. J. (2014). Quantification of the intrusive magma fluxes during magma chamber growth at soufrière hills volcano (montserrat, Lesser Antilles). *Journal of Petrology* **55**, 529-548.

Ariskin, A. A., Konnikov, E. G., Danyushevsky, L. V., Kislov, E. V., Nikolaev, G. S., Orsoev, D. A., Barmina, G. S. & Bychkov, K. A. (2009). The Dovyren intrusive complex: Problems of petrology and Ni sulfide mineralization. *Geochemistry International* **47**, 425-453.

Arndt, N. T. (1977). Partitioning of nickel between olivine and ultrabasic and basic komatiite liquids. *Carnegie Institution of Washington Year Book* **76**, 553-557.

Arndt, N. T. (2011). Insights into the geologic setting and origin of Ni-Cu-PGE sulfide deposits of the Noril'sk-Talnakh region, Siberia. *Reviews in Economic Geology* **17**, 199-215.

Ballhaus, C. G. & Glikson, A. Y. (1989). Magma Mixing and Intraplutonic Quenching in the Wingellina Hills Intrusion, Giles Complex, Central Australia. *Journal of Petrology* **30**, 1443-1469.

Baragar, W. R. A. (1976). The Natkusiak basalts, Victoria Island, District of Franklin; in Report of Activities, Part A. *Geological Survey of Canada Paper* **76-1A**, 347-352.

Barnes, S. (1986). The effect of trapped liquid crystallization on cumulus mineral compositions in layered intrusions. *Contributions to Mineralogy and Petrology* **93**, 524-531.

Beard, C. (2012). Magmatic plumbing and melt source characterisation: A Hf-Pb-Sr-Nd isotopic study of the sill-dominated intrusive complex of the Franklin Large Igneous Province, Victoria Island, Arctic Canada. *Unpublished thesis*.

Bedard, J. H. (1993). Oceanic crust as a reactive filter: synkinematic intrusion, hybridization, and assimilation in an ophiolitic magma chamber, western Newfoundland. *Geology* **21**, 77-80.

Bédard, J. H. (1987). The development of compositional and textural layering in Archaean komatiites and in Proterozoic basaltic komatiites from Cape Smith, Quebec, Canada. *In: I. Parsons (Ed) The origin of layering in igneous rocks* **Proceedings of a NATO workshop. D. Reidel Publ. Co. Dordrecht, Holland**, 399-418.

Bédard, J. H. (1991a). Cumulate recycling and crustal evolution in the Bay of Islands ophiolite. *Journal of Geology* **99**, 225-249.

Bédard, J. H. (1991b). Cumulate recycling and crustal evolution in the Bay of Islands ophiolite. *Journal of Geology* **99**, 225-249.

Bédard, J. H. (1993). Oceanic crust as a reactive filter: Synkinematic intrusion, hybridization, and assimilation in an ophiolitic magma chamber, western Newfoundland. *Geology* **21**, 77-80.

Bédard, J. H. (1994). A procedure for calculating the equilibrium distribution of trace elements among the minerals of cumulate rocks, and the concentration of trace elements in the coexisting liquids. *Chemical Geology* **118**, 143-153.

Bédard, J. H. (2010). Parameterization of the Fe=Mg exchange coefficient (Kd) between clinopyroxene and silicate melts. *Chemical Geology* **274**, 169-176.

Bédard, J. H., Hayes, B., Hryciuk, M., Wing, B., Beard, C., Dell'Oro, T. A., Weis, D., Scoates, J. S., Williamson, N., Cousens, B., Naslund, H. R., MacDonald, W. & Nabelek, P. (2013). The Neoproterozoic Franklin Large Igneous Province on Victoria Island. *Geological Asssociation of Canada - Mineralogical Association of Canada annual meeting. Program with Abstracts* **35**, 82.

Bédard, J. H., Leclerc, F., Harris, L. B. & Goulet, N. (2009). Intra-sill magmatic evolution in the Cummings Complex, Abitibi greenstone belt: Tholeiitic to calc-alkaline magmatism recorded in an Archaean subvolcanic conduit system. *Lithos* **111**, 47-71.

Bédard, J. H., Naslund, H. R., Nabelek, P., Winpenny, A., Hryciuk, M., Macdonald, W., Hayes, B., Steigerwaldt, K., Hadlari, T., Rainbird, R., Dewing, K. & Girard, É. (2012). Fault-mediated melt ascent in a Neoproterozoic continental flood basalt province, the Franklin sills, Victoria Island, Canada. *Geological Society of America Bulletin* **124**, 723-736.

Bédard, J. H., Sparks, R. S. J., Renner, R., Cheadle, M. J. & Hallworth, M. A. (1988). Peridotite sills and metasomatic gabbros in the Eastern Layered Series of the Rhum complex. *Journal of the Geological Society* **145**, 207-224.

Bédard, J. H. J., Marsh, B. D., Hersum, T. G., Naslund, H. R. & Mukasa, S. B. (2007). Large-scale mechanical redistribution of orthopyroxene and plagioclase in the basement sill, ferrar dolerites, McMurdo Dry Valleys, Antarctica: Petrological, mineral-chemical and field evidence for channelized movement of crystals and melt. *Journal of Petrology* **48**, 2289-2326.

Begg, G. C., Hronsky, J. A. M., Arndt, N. T., Griffin, W. L., O'Reilly, S. Y. & Hayward, N. (2010). Lithospheric, Cratonic, and Geodynamic Setting of Ni-Cu-PGE Sulfide Deposits. *Economic Geology* **105**, 1057-1070.

Bhattacharji, S. (1967). Mechanics of flow differentiation in ultramafic and mafic sills. *Journal of Geology* **75**, 101-112.

Black, B. A., Hauri, E. H., Elkins-Tanton, L. T. & Brown, S. M. (2014). Sulfur isotopic evidence for sources of volatiles in Siberian Traps magmas. *Earth and Planetary Science Letters* **394**, 58-69.

Borradaile, G. J. & Henry, B. (1997). Tectonic applications of magnetic susceptibility and its anisotropy. *Earth Sciences* **42**, 49-93.

Boudreau, A. E. (1999). PELE—a version of the MELTS software program for the PC platform. *Computers & Geosciences* **25**, 201-203.

Boudreau, A. E. & Philpotts, A. R. (2002). Quantitative modeling of compaction in the Holyoke flood basalt flow Hartford Basin, Connecticut. *Contributions to Mineralogy and Petrology* **144**, 176-184.

Bowen, N. L. (1928). The evolution of igneous rocks. *Princeton University, Princeton*.

Brenan, J. M., McDonough, W. F. & Dalpé, C. (2003). Experimental constraints on the partitioning of rhenium and some platinum-group elements between olivine and silicate melt. *Earth and Planetary Science Letters* **212**, 135-150.

Brophy, J. G., Whittington, C. S. & Young-Rok, P. (1999). Sector-zoned augite megacrysts in Aleutian high alumina basalts: implications for the conditions of basalt crystallization and the generation of calc-alkaline series magmas. *Contributions to Mineralogy and Petrology* **135**, 277-290.

Brown, G. M. (1956). The layered ultrabasic rocks of Rhum Inner Hebrides. *Philosophical Transactions of the Royal Society of London* **B240**, 1-53.

Buchanan, D. L. & Nolan, J. (1979). Solubility of sulfur and sulfide immiscibility in synthetic tholeiitic melts and their relevance to Bushveld-Complex rocks. *The Canadian Mineralogist* **17**, 483-494.

Campbell, I. H. & Naldrett, A. J. (1979). The influence of silicate:sulfide ratios on the geochemistry of magmatic sulfides. *Economic Geology* **74**, 1503-1506.

Canales, J. P., Nedimovi, M. R., Kent, G. M., Carbotte, S. M. & Detrick, R. S. (2009). Seismic reflection images of a near-axis melt sill within the lower crust at the juan de fuca ridge. *Nature* **460**, 89-93.

Canfield, D. E., Raiswell, R., Westrich, J. T., Reaves, C. M. & Berner, R. A. (1986). The use of chromium reduction in the analysis of reduced inorganic sulfur in sediments and shales. *Chemical Geology* **54**, 149-155.

Capobianco, C. J. & Drake, M. J. (1990). Partitioning of ruthenium, rhodium, and palladium between spinel and silicate melt and implications for platinum group element fractionation trends. *Geochimica et Cosmochimica Acta* **54**, 869-874.

Carslaw, H. S. & Jaeger, J. C. (1959). Conduction of heat in solids. *Oxford University Press, Oxford*, 510.

Cawthorn, R. G., Sander, B. K. & Jones, I. M. (1992). Evidence for the trapped liquid shift effect in the Mount Ayliff Intrusion, South Africa. *Contributions to Mineralogy and Petrology* **111**, 194-202.

Cawthorn, R. G. & Walraven, F. (1998). Emplacement and Crystallization Time for the Bushveld Complex. *Journal of Petrology* **39**, 1669-1687.

Cawthorn, R. G. e. (1996). Layered Intrusions. *Elsevier*.

Chadwick, J. P., Troll, V. R., Ginibre, C., Morgan, D., Gertisser, R., Waight, T. E. & Davidson, J. P. (2007). Carbonate assimilation at Merapi Volcano, Java, Indonesia: Insights from crystal isotope stratigraphy. *Journal of Petrology* **48**, 1793-1812.

Chakraborty, S. (1997). Rates and mechanisms of Fe-Mg interdiffusion in olivine at 980°–1300°C. *Journal of Geophysical Research: Solid Earth* **102**, 12317-12331.

Chevallier, L. & Woodford, A. (1999). Morph-tectonics and mechanism of emplacement of the dolerite rings and sills of the western Karoo, South Africa. *South African Journal of Geology* **102**, 43-54.

Costa, F. & Dungan, M. (2005). Short time scales of magmatic assimilation from diffusion modeling of multiple elements in olivine. *Geology* **33**, 837-840.

Cruden, A. R., Burrows, D. R. & Evans-Lamswood, D. (2008). Structure and emplacement of the Voisey's Bay troctolite and associated Ni-Cu-Co mineralisation. *GAC-MAC-SEG-SGA program with abstracts, Quebec City, May 26-28 2008*, 39.

Czamanske, G. K. & Moore, J. G. (1977). Composition and phase chemistry of sulfide globules in basalt from the Mid-Atlantic Ridge rift valley near 37°N lat. *Geological Society of America Bulletin* **88**, 587-599.

Davidson, J. P., Morgan, D. J., Charlier, B. L. A., Harlou, R. & Hora, J. M. (2007). Microsampling and isotopic analysis of igneous rocks: Implications for the study of magmatic systems. 273-311.

Delaney, P. T. & Pollard, D. D. (1981). Deformation of host rocks and flow of magma during growth of minette dikes and breccia-bearing intrusions near Ship Rock, New Mexico. *U.S. Geological Survey Professional Paper* **1202**, 61.

Dell'Oro, T. A., Weis, D., Scoates, J. S. & Bédard, J. H. (2012). Sr-Nd-Hf-Pb Isotope and Trace Element Geochemistry of the Natkusiak Formation Continental Flood Basalts of the Neoproterozoic Franklin Large Igneous Province, Victoria Island, Canada. *Unpublished thesis*.

Denyszyn, S. W., Halls, H. C., Davis, D. W. & Evans, D. A. D. (2009). Paleomagnetism and U–Pb geochronology of Franklin dykes in High Arctic Canada and Greenland: a revised age and paleomagnetic pole constraining block rotations in the Nares Strait region. *Canadian Journal of Earth Sciences* **46**, 689-705.

Dewing, K., Pratt, B. R., Hadlari, T., Brent, T., Bédard, J. & Rainbird, R. H. (2013). Newly identified "Tunnunik" impact structure, Prince Albert Peninsula, northwestern Victoria Island, Arctic Canada. *Meteoritics and Planetary Science* **48**, 211-223.

Di Rocco, T., Freda, C., Gaeta, M., Mollo, S. & Dallai, L. (2012). Magma Chambers Emplaced in Carbonate Substrate: Petrogenesis of Skarn and Cumulate Rocks and Implications for CO2 Degassing in Volcanic Areas. *Journal of Petrology* **53**, 2307-2332.

Ding, X., Li, C., Ripley, E. M., Rossell, D. & Kamo, S. (2010). The Eagle and East Eagle sulfide ore-bearing mafic-ultramafic intrusions in the Midcontinent Rift System, upper Michigan: Geochronology and petrologic evolution. *Geochemistry, Geophysics, Geosystems* **11**, Q03003.

Ding, X., Ripley, E. & Li, C. (2012). PGE geochemistry of the Eagle Ni–Cu–(PGE) deposit, Upper Michigan: constraints on ore genesis in a dynamic magma conduit. *Mineralium Deposita* **47**, 89-104.

Donaldson, C. (1976). An experimental investigation of olivine morphology. *Contributions to Mineralogy and Petrology* **57**, 187-213.

Dungan, M. A. & Davidson, J. (2004). Partial assimilative recycling of the mafic plutonic roots of arc volcanoes: An example from the Chilean Andes. *Geology* **32**, 773-776.

Eales, H. V. & Cawthorn, R. G. (1996). The Bushveld Complex. In: Richard Grant, C. (ed.) *Developments in Petrology*: Elsevier, 181-229.

Eales, H. V., Maier, W. D. & Teigler, B. (1991). Corroded plagioclase feldspar inclusions in orthopyroxene and olivine of the Lower and Critical Zones, Western Bushveld Complex. *Mineralogical Magazine* **55**, 479-486.

Ernst, R. E., Wingate, M. T. D., Buchan, K. L. & Li, Z. X. (2008). Global record of 1600-700 Ma Large Igneous Provinces (LIPs): Implications for the reconstruction of the proposed Nuna (Columbia) and Rodinia supercontinents. *Precambrian Research* **160**, 159-178.

Field, L., Blundy, J., Calvert, A. & Yirgu, G. (2013). Magmatic history of Dabbahu, a composite volcano in the Afar Rift, Ethiopia. *Geological Society of America Bulletin* **125**, 128-147.

Finnigan, C. S., Brenan, J. M., Mungall, J. E. & McDonough, W. F. (2008). Experiments and Models Bearing on the Role of Chromite as a Collector of Platinum Group Minerals by Local Reduction. *Journal of Petrology* **49**, 1647-1665.

Fiorentini, M. L., Bekker, A., Rouxel, O., Wing, B. A., Maier, W. & Rumble, D. (2012). Multiple Sulfur and Iron Isotope Composition of Magmatic Ni-Cu-(PGE) Sulfide Mineralization from Eastern Botswana. *Economic Geology* **107**, 105-116.

Font, L., Davidson, J. P., Pearson, D. G., Nowell, G. M., Jerram, D. A. & Ottley, C. J. (2008). Sr and Pb isotope micro-analysis of plagioclase crystals from skye lavas: An insight into open-system processes in a flood basalt province. *Journal of Petrology* **49**, 1449-1471.

Forrest, J. & Newman, L. (1977). Silver-110 microgram sulfate analysis for the short time resolution of ambient levels of sulfur aerosol. *Analytical Chemistry* **49**, 1579-1584.

Francis, E. H. & Walker, B. H. (1986). Emplacement of alkali-dolerite sills relative to extrusive volcanism and sedimentary basins in the Carboniferous of Fife, Scotland. *Transactions of the Royal Society of Edinburgh* **77**, 309-323.

Gaeta, M., Di Rocco, T. & Freda, C. (2009). Carbonate Assimilation in Open Magmatic Systems: the Role of Melt-bearing Skarns and Cumulate-forming Processes. *Journal of Petrology* **50**, 361-385.

Ganino, C., Arndt, N., Chauvel, C. & Tornos, F. (2014). Metamorphic degassing of carbonates in the contact aureole of the Aguablanca Cu–Ni–PGE deposit, Spain. *Contributions to Mineralogy and Petrology* **168**, 1-21.

Garcia, M. O., Pietruszka, A. J. & Rhodes, J. M. (2003). A Petrologic Perspective of Kīlauea Volcano's Summit Magma Reservoir. *Journal of Petrology* **44**, 2313-2339.

Gibb, F. G. F. & Henderson, C. M. B. (2006). Chemistry of the Shiant Isles Main Sill, NW Scotland, and Wider Implications for the Petrogenesis of Mafic Sills. *Journal of Petrology* **47**, 191-230.

Ginibre, C. & Wörner, G. (2007). Variable parent magmas and recharge regimes of the Parinacota magma system (N. Chile) revealed by Fe, Mg and Sr zoning in plagioclase. *Lithos* **98**, 118-140.

Gorring, M. L. & Naslund, H. R. (1995). Geochemical reversals within the lower 100 m of the Palisades sill, New Jersey. *Contributions to Mineralogy and Petrology* **119**, 263-276.

Grinenko, L. I. (1985). Sources of sulfur of the nickeliferous and barren gabbro-dolerite intrusions of the northwest Siberian platform. *International Geology Review* **27**, 695-708.

Grove, T. L., Baker, M. B. & Kinzler, R. J. (1984). Coupled CaAl-NaSi diffusion in plagioclase feldspar: Experiments and applications to cooling rate speedometry. *Geochimica et Cosmochimica Acta* **48**, 2113-2121.

Gunn, B. M. (1966). Modal and element variation in Antarctic tholeiites. *Geochimica et Cosmochimica Acta* **30**, 881-920.

Hart, S. R. & Davis, K. E. (1978). Nickel partitioning between olivine and silicate melt. *Earth and Planetary Science Letters* **40**, 203-219.

Haughton, D. R., Roeder, P. L. & Skinner, B. J. (1974). Solubility of Sulfur in Mafic Magmas. *Economic Geology* **69**, 451-467.

Hawkesworth, C. J., Lightfoot, P. C., Fedorenko, V. A., Blake, S., Naldrett, A. J., Doherty, W. & Gorbachev, N. S. (1995). Magma differentiation and mineralisation in the Siberian continental flood basalts. *Lithos* **34**.

Heaman, L. M., LeCheminant, A. N. & Rainbird, R. H. (1992). Nature and timing of Franklin igneous events, Canada: Implications for a Late Proterozoic mantle plume and the break-up of Laurentia. *Earth and Planetary Science Letters* **109**, 117-131.

Hildreth, W. & Moorbath, S. (1988). Crustal contributions to arc magmatism in the Andes of Central Chile. *Contributions to Mineralogy and Petrology* **98**, 455-489.

Holness, M. B., Stripp, G., Humphreys, M. C. S., Veksler, I. V., Nielsen, T. F. D. & Tegner, C. (2011). Silicate liquid immiscibility within the crystal mush: late-stage magmatic microstructures in the skaergaard intrusion, east greenland. *Journal of Petrology* **52**, 175-222.

Holness, M. B., Tegner, C., Nielsen, T. F. D., Stripp, G. & Morse, S. A. (2007). A textural record of solidification and cooling in the skaergaard intrusion, East Greenland. *Journal of Petrology* **48**, 2359-2377.

Hrouda, F. (1982). Magnetic anisotropy of rocks and its application in geology and geophysics. *Geophysical surveys* **5**, 37-82.

Hryciuk, M., Bédard, J. H., Nabelek, P. & Wing, B. A. (2014). (Submitted) Dynamic dikes and sterile sills: Contamination in the Neoproterozoic Franklin large igneous province, Victoria Island, Canada. *Geology*.

Huber, H., Koeberl, C., McDonald, I. & Reimold, W. U. (2001). Geochemistry and petrology of Witwatersrand and Dwyka diamictites from South Africa: search for an extraterrestrial component. *Geochimica et Cosmochimica Acta* **65**, 2007-2016.

Humphreys, M. C. S. (2009). Chemical Evolution of Intercumulus Liquid, as Recorded in Plagioclase Overgrowth Rims from the Skaergaard Intrusion. *Journal of Petrology* **50**, 127-145.

Humphreys, M. C. S., Blundy, J. D. & Sparks, R. S. J. (2006). Magma evolution and open-system processes at Shiveluch Volcano: Insights from phenocryst zoning. *Journal of Petrology* **47**, 2303-2334.

Hunter, R. H. (1996). Texture Development in Cumulate Rocks. In: Richard Grant, C. (ed.) *Developments in Petrology*: Elsevier, 77-101.

Huppert, H. E. & Sparks, R. S. J. (1980). The fluid dynamics of a basaltic magma chamber replenished by influx of hot, dense ultrabasic magma. *Contributions to Mineralogy and Petrology* **75**, 279-289.

Iacono Marziano, G., Gaillard, F. & Pichavant, M. (2007). Limestone assimilation and the origin of CO2 emissions at the Alban Hills (Central Italy): Constraints from experimental petrology. *Journal of Volcanology and Geothermal Research* **166**, 91-105.

Iacono Marziano, G., Gaillard, F. & Pichavant, M. (2008). Limestone assimilation by basaltic magmas: an experimental re-assessment and application to Italian volcanoes. *Contributions to Mineralogy and Petrology* **155**, 719-738.

Irvine, T. N. (1975). Crystallization sequences in the Muskox intrusion and other layered intrusions—II. Origin of chromitite layers and similar deposits of other magmatic ores. *Geochimica et Cosmochimica Acta* **39**, 991-1020.

Irvine, T. N. (1977). Origin of chromitite layers in the Muskox intrusion and other stratiform intrusions: A new interpretation. *Geology* **5**, 273-277.

Irvine, T. N. (1980). Magmatic density currents and cumulus processes. *American Journal of Science* **280A**, 1-58.

Irvine, T. N. (1982). Terminology for Layered Intrusions. *Journal of Petrology* **23**, 127-162.

Irvine, T. N. (1987). Layering and related structures in the Duke Island and Skaergaard Intrusions: Similarities, differences, and origins. In. In: Parsons, I. (ed.) Origins of Igneous Layering. NATO ASI Series C. *Mathematical and Physical Sciences* **196**, 185-245.

Irvine, T. N. & Smith, C. H. (1967). The ultramafic rocks of the Muskox intrusion, Northwest Territories, Canada. *In: Wyllie, P.J. (ed.) Ultramafic and Related Rocks. New York: John Wiley & Sons, Inc*, 38-49.

Jefferson, C. W. (1985). Uppermost Shaler Group and its contact with the Natkusiak Basalts, Victoria Island, District of Franklin: in Current Research Part A. *Geological Survey of Canada Paper* **85-1A**, 103.

Jefferson, C. W., Hulbert, L., Rainbird, R., H., Hall, G. E. M., Gregoire, D. C. & Grinenko, L. I. (1994). Mineral resource assessment of the Neoproterozoic Franklin igneous events of Arctic Canada: comparison with the Permo-Triassic Noril'sk-Talnakh Ni-Cu-PGE deposits of Russia. *Geological Survey of Canada Open File Report* **2789**, 48.

Jefferson, C. W., Nelson, W. E., Kirkham, R. V., Reedman, J. H. & Scoates, R. F. J. (1985). Geology and Copper Occurrences of the Natkusiak Basalts, Victoria Island, District of Frankalin. Current Research, Part A. *Geological Survey of Canada Paper* **85-1A**, 203-214.

Jones, D. S., Maloof, A. C., Hurtgen, M. T., Rainbird, R. H. & Schrag, D. P. (2010). Regional and global chemostratigraphic correlation of the early Neoproterozoic Shaler Supergroup, Victoria Island, Northwestern Canada. *Precambrian Research* **181**, 43-63.

Jowitt, S. M. & Ernst, R. E. (2013). Geochemical assessment of the metallogenic potential of Proterozoic LIPs of Canada. *Lithos* **174**, 291-307.

Jugo, P. J., Luth, R. W. & Richards, J. P. (2005). An Experimental Study of the Sulfur Content in Basaltic Melts Saturated with Immiscible Sulfide or Sulfate Liquids at 1300°C and 1·0 GPa. *Journal of Petrology* **46**, 783-798.

Keays, R. & Lightfoot, P. (2010). Crustal sulfur is required to form magmatic Ni–Cu sulfide deposits: evidence from chalcophile element signatures of Siberian and Deccan Trap basalts. *Mineralium Deposita* **45**, 241-257.

Kerr, A. C., Tarney, J., Nivia, A., Marriner, G. F. & Saunders, A. D. (1998). The internal structure of oceanic plateaus: inferences from obducted Cretaceous terranes in western Colombia and the Caribbean. *Tectonophysics* **292**, 173-188.

Kiss, F. & Oneschuk, D. (2010). First vertical derivative of the magnetic field, Minto Inlier aeromagnetic survey, Victoria Island, NTS 87 G/SE and parts of 87 G/NW, 88B/SE and 88 B/SW, Northwest Territories, . *Geological Survey of Canada Open File Map 6705, scale 1:100,000*.

Labidi, J., Cartigny, P., Hamelin, C., Moreira, M. & Dosso, L. (2014). Sulfur isotope budget (32S, 33S, 34S and 36S) in Pacific–Antarctic ridge basalts: A record of mantle source heterogeneity and hydrothermal sulfide assimilation. *Geochimica et Cosmochimica Acta* **133**, 47-67.

Larrea, P., França, Z., Lago, M., Widom, E., Galé, C. & Ubide, T. (2012). Magmatic Processes and the Role of Antecrysts in the Genesis of Corvo Island (Azores Archipelago, Portugal). *Journal of Petrology* **54**, 769-793.

Latypov, R. (2009). Testing the Validity of the Petrological Hypothesis 'No Phenocrysts, No Post-emplacement Differentiation'. *Journal of Petrology*.

Leclerc, F., Bédard, J. H., Harris, L. B., McNicoll, V. J., Goulet, N., Roy, P. & Houle, P. (2011). Tholeiitic to calc-alkaline cyclic volcanism in the Roy Group, Chibougamau area, Abitibi Greenstone Belt — revised stratigraphy and implications for VHMS explorationGeological Survey of Canada Contribution 20100254. Ministère des Ressources naturelles et de la Faune Contribution 8439-2010-2011-17. *Canadian Journal of Earth Sciences* **48**, 661-694.

Lehmann, J., Arndt, N., Windley, B., Zhou, M.-F., Wang, C. Y. & Harris, C. (2007). Field Relationships and Geochemical Constraints on the Emplacement of the Jinchuan Intrusion and its Ni-Cu-PGE Sulfide Deposit, Gansu, China. *Economic Geology* **102**, 75-94.

Leuthold, J., Müntener, O., Baumgartner, L. P. & Putlitz, B. (2014). Petrological Constraints on the Recycling of Mafic Crystal Mushes and Intrusion of Braided Sills in the Torres del Paine Mafic Complex (Patagonia). *Journal of Petrology* **55**, 917-949.

Li, C., Lightfoot, P. C., Amelin, Y. & Naldrett, A. J. (2000). Contrasting Petrological and Geochemical Relationships in the Voisey's Bay and Mushuau Intrusions, Labrador, Canada: Implications for Ore Genesis. *Economic Geology* **95**, 771-799.

Li, C. & Naldrett, A. J. (1999). Geology and petrology of the Voisey's Bay intrusion: reaction of olivine with sulfide and silicate liquids. *Lithos* **47**, 1-31.

Li, C., Ripley, E. M. & Naldrett, A. J. (2009). A new genetic model for the giant Ni-Cu-PGE sulfide deposits associated with the Siberian flood basalts. *Economic Geology* **104**, 291-301.

Lightfoot, P. C. & Evans-Lamswood, D. (2015). Structural controls on the primary distribution of mafic–ultramafic intrusions containing Ni–Cu–Co–(PGE) sulfide mineralization in the roots of large igneous provinces. *Ore Geology Reviews* **64**, 354-386.

Lissenberg, C. J., Bédard, J. H. & van Staal, C. R. (2004). The structure and geochemistry of the gabbro zone of the Annieopsquotch ophiolite, Newfoundland: implications for lower crustal accretion at spreading ridges. *Earth and Planetary Science Letters* **229**, 105-123.

Lissenberg, C. J. & Dick, H. J. B. (2008). Melt–rock reaction in the lower oceanic crust and its implications for the genesis of mid-ocean ridge basalt. *Earth and Planetary Science Letters* **271**, 311-325.

Liu, Y., Samaha, N.-T. & Baker, D. R. (2007). Sulfur concentration at sulfide saturation (SCSS) in magmatic silicate melts. *Geochimica et Cosmochimica Acta* **71**, 1783-1799.

Lundgaard, K. L., Tegner, C., Cawthorn, R. G., Kruger, F. J. & Wilson, J. R. (2006). Trapped intercumulus liquid in the Main Zone of the eastern Bushveld Complex, South Africa. *Contributions to Mineralogy and Petrology* **151**, 352-369.

Macdonald, F. A., Schmitz, M. D., Crowley, J. L., Roots, C. F., Jones, D. S., Maloof, A. C., Strauss, J. V., Cohen, P. A., Johnston, D. T. & Schrag, D. P. (2010). Calibrating the Cryogenian. *Science* **327**, 1241-1243.

Maier, W. D., Li, C. & De Waal, S. A. (2001). WHY ARE THERE NO MAJOR Ni–Cu SULFIDE DEPOSITS IN LARGE LAYERED MAFIC-ULTRAMAFIC INTRUSIONS? *The Canadian Mineralogist* **39**, 547-556.

Marsh, B. D. (1996). Solidification fronts and magmatic evolution. *Mineralogical Magazine* **60**, 5-40.

Marsh, B. D. (2004). A magmatic mush column rosetta stone: the McMurdo Dry Valleys, Antarctica. *EOS Trans Am Geophys Union* **85**.

Marsh, B. D. (2013). On some fundamentals of igneous petrology. *Contributions to Mineralogy and Petrology* **166**, 665-690.

Martin, V. M., Davidson, J., Morgan, D. & Jerram, D. A. (2010). Using the Sr isotope compositions of feldspars and glass to distinguish magma system components and dynamics. *Geology* **38**, 539-542.

Mathez, E. A., Hunter, R. H. & Kinzler, R. (1997). Petrologic evolution of partially molten cumulate: the Atok section of the Bushveld Complex. *Contributions to Mineralogy and Petrology* **129**, 20-34.

Mathieu, J., Kontak, D. J. & Turner, E. C. (2013). A fluid inclusion study of diagenetic fluids in Proterozoic and Paleozoic carbonate rocks, Victoria Island, NWT. *Geofluids* **13**, 559-578.

Matzen, A. K., Baker, M. B., Beckett, J. R. & Stolper, E. M. (2011). Fe–Mg Partitioning between Olivine and High-magnesian Melts and the Nature of Hawaiian Parental Liquids. *Journal of Petrology* **52**, 1243-1263.

McBirney, A. R. (1996). The Skaergaard Intrusion. In: Richard Grant, C. (ed.) *Developments in Petrology*: Elsevier, 147-180.

McDonald, I. & Viljoen, K. S. (2006). Platinum-group element geochemistry of mantle eclogites: a reconnaissance study of xenoliths from the Orapa kimberlite, Botswana. *Applied Earth Science* **115**, 81-93.

McDonough, W. F. & Sun, S. s. (1995). The composition of the Earth. *Chemical Geology* **120**, 223-253.

Meurer, W. P. & Boudreau, A. E. (1998). Compaction of Igneous Cumulates Part I: Geochemical Consequences for Cumulates and Liquid Fractionation Trends. *The Journal of Geology* **106**, 281-292.

Miller, J. D., Green, J. C., Severson, M. J., Chandler, V. W., Hauck, S. A., Peterson, D. M. & Wahl, T. E. (2002). Geology and mineral potential of the Duluth Complex and related rocks of northeastern Minnesota. *Minnesota Geological Survey Report of Investigations* **58**, 207.

Mitchell, A. A., Eales, H. V. & Krueger, F. J. (1998). Magma replenishment, and the significance of poikilitic textures, in the Lower Main Zone of the western Bushveld Complex, South Africa. *Mineralogical Magazine* **62**, 435-450.

Mollo, S. & Vona, A. (2014). The geochemical evolution of clinopyroxene in the Roman Province: A window on decarbonation from wall-rocks to magma. *Lithos* **192–195**, 1-7.

Mondal, S. K. & Mathez, E. A. (2007). Origin of the UG2 chromitite layer, Bushveld Complex. *Journal of Petrology* **48**, 495-510.

Morgan, D. J., Blake, S., Rogers, N. W., De Vivo, B., Rolandi, G. & Davidson, J. P. (2006). Magma chamber recharge at Vesuvius in the century prior to the eruption of A.D. 79. *Geology* **34**, 845-848.

Morse, S. A. (1984). Cation Diffusion in Plagioclase Feldspar. *Science* **225**, 504-505.

Müller, T., Dohmen, R., Becker, H. W., Heege, J. & Chakraborty, S. (2013). Fe–Mg interdiffusion rates in clinopyroxene: experimental data and implications for Fe–Mg exchange geothermometers. *Contributions to Mineralogy and Petrology* **166**, 1563-1576.

Murphy, M. D., Sparks, R. S. J., Barclay, J., Carroll, M. R. & Brewer, T. S. (2000). Remobilization of andesite magma by intrusion of mafic magma at the Soufriere Hills volcano, Montserrat, West Indies. *Journal of Petrology* **41**, 21-42.

Nabelek, P. I., Bédard, J. H., Hryciuk, M. & Hayes, B. (2013). Short-duration contact metamorphism of calcareous sedimentary rocks by Neoproterozoic Franklin gabbro sills and dykes on Victoria Island, Canada. *Journal of Metamorphic Geology* **31**, 205-220.

Nakamura, Y. (1973). Origin of Sector-Zoning of Igneous Clinopyroxenes. *American Mineralogist* **58**, 986-990.

Naldrett, A. J. (1992). A Model for the Ni-Cu-PGE Ores of the Noril'sk Region and Its Application to Other Areas of Flood Basalt. *Economic Geology* **87**, 1945-1962.

Naldrett, A. J. (1999). World-class Ni-Cu-PGE deposits: key factors in their genesis. *Mineralium Deposita* **34**, 227-240.

Naldrett, A. J., Asif, M., Krstic, S. & Li, C. (2000). The Composition of Mineralization at the Voisey's Bay Ni-Cu Sulfide Deposit, with Special Reference to Platinum-Group Elements. *Economic Geology* **95**, 845-865.

Namur, O., Charlier, B., Toplis, M. J., Higgins, M. D., Liégeois, J.-P. & Vander Auwera, J. (2010). Crystallization Sequence and Magma Chamber Processes in the Ferrobasaltic Sept Iles Layered Intrusion, Canada. *Journal of Petrology* **51**, 1203-1236.

Naslund, H. R. (1989). Petrology of the Basistoppen Sill, East Greenland: A Calculated Magma Differentiation Trend. *Journal of Petrology* **30**, 299-319.

Naslund, H. R., Bédard, J. H., Steigerwaldt, K. & Dye, D. (2013). Origin of S and M and reversed S and M shaped profiles in two Proterozoic mafic sills from the Franklin magmatic event, Victoria Island, NWT, Canada. *Geophysical Research Abstracts* **15**.

Naslund, H. R. & McBirney, A. R. (1996). Mechanisms of Formation of Igneous Layering. In: Richard Grant, C. (ed.) *Developments in Petrology*: Elsevier, 1-43.

Neave, D. A., Passmore, E., Maclennan, J., Fitton, G. & Thordarson, T. (2013). Crystal–Melt Relationships and the Record of Deep Mixing and Crystallization in the ad 1783 Laki Eruption, Iceland. *Journal of Petrology* **54**, 1661-1690.

Nobre Silva, I. G., Weis, D., Barling, J. & Scoates, J. S. (2009). Leaching systematics and matrix elimination for the determination of high-precision Pb isotope compositions of ocean island basalts. *Geochemistry, Geophysics, Geosystems* **10**, Q08012.

O'Driscoll, B., Donaldson, C. H., Troll, V. R., Jerram, D. A. & Emeleus, C. H. (2007). An Origin for Harrisitic and Granular Olivine in the Rum Layered Suite, NW Scotland: a Crystal Size Distribution Study. *Journal of Petrology* **48**, 253-270.

O'Hara, M. J. (1977). Geochemical evolution during fractional crystallization of a periodically refilled magma chamber. *Nature* **266**, 503-507.

Onuma, K. & Tohara, T. (1983). Effect of chromium on phase relations in the join forsterite-anorthite-diopside in air at 1 Atm. *Contributions to Mineralogy and Petrology* **84**, 174-181.

Parsons, I. (1986). Origins of Igneous Layering. NATO ASI Series C. *Mathematical and Physical Sciences* **196**, 666.

Passmore, E., Maclennan, J., Fitton, G. & Thordarson, T. (2012). Mush Disaggregation in Basaltic Magma Chambers: Evidence from the ad 1783 Laki Eruption. *Journal of Petrology* **53**, 2593-2623.

Paterson, S. R. (2009). Magmatic tubes, pipes, troughs, diapirs, and plumes: Late-stage convective instabilities resulting in compositional diversity and permeable networks in crystal-rich magmas of the Tuolumne batholith, Sierra Nevada, California. *Geosphere* **5**, 496-527.

Pehrsson, S. J. & Buchan, K. L. (1999). Borden dykes of Baffin Island, Northwest Territories: a Franklin U-Pb baddeleyite age and a paleomagnetic reinterpretation. *Canadian Journal of Earth Sciences* **36**, 65-73.

Peterson, R. C., Williamson, M.-C. & Rainbird, R. H. (2014). Gossan Hill, Victoria Island, Northwest Territories: An analogue for mine waste reactions within permafrost and implication for the subsurface mineralogy of Mars. *Earth and Planetary Science Letters* **400**, 88-93.

Philpotts, A. R., Shi, J. & Brustman, C. (1998). Role of plagioclase crystal chains in the differentiation of partly crystallized basaltic magma. *Nature* **395**, 343-346.

Pistone, M., Caricchi, L., Ulmer, P., Reusser, E. & Ardia, P. (2013). Rheology of volatile-bearing crystal mushes: Mobilization vs. viscous death. *Chemical Geology* **345**, 16-39.

Pretorius, W., Weis, D., Williams, G., Hanano, D., Kieffer, B. & Scoates, J. (2006). Complete Trace Elemental Characterisation of Granitoid (USGS G-2, GSP-2) Reference

Materials by High Resolution Inductively Coupled Plasma-Mass Spectrometry. *Geostandards and Geoanalytical Research* **30**, 39-54.

Prince, J. K. G. (2014). Sequence stratigraphic, lithostratigraphic and stable isotope analysis of the Minto Inlet Formation and Kilian Formation, of the Shaler Supergroup, Northwest Territories. *Thesis. Carleton University, Ottawa*, 127.

Puffer, J. H., Block, K. A. & Steiner, J. C. (2009). *Transmission of Flood Basalts through a Shallow Crustal Sill and the Correlation of Sill Layers with Extrusive Flows : The Palisades Intrusive System and the Basalts of the Newark Basin, New Jersey, U.S.A.* Chicago, Il, ETATS-UNIS: University of Chicago Press.

Rainbird, R. (1993). The Sedimentary Record of Mantle Plume Uplift Preceding Eruption of the Neoproterozoic Natkusiak Flood Basalt. *Journal of Geology* **101**, 305-318.

Rainbird, R. H., Jefferson, C. W. & Young, G. M. (1996). The early Neoproterozoic sedimentary Succession B of northwestern Laurentia: Correlations and paleogeographic significance. *Geological Society of America Bulletin* **108**, 454-470.

Reubi, O. & Blundy, J. (2008). Assimilation of Plutonic Roots, Formation of High-K 'Exotic' Melt Inclusions and Genesis of Andesitic Magmas at Volcán De Colima, Mexico. *Journal of Petrology* **49**, 2221-2243.

Ripley, E. M. & Li, C. (2003). Sulfur isotope exchange and metal enrichment in the formation of magmatic Cu-Ni-(PGE) deposits. *Economic Geology* **98**, 635-641.

Ripley, E. M. & Li, C. (2011). A Review of Conduit-Related Ni-Cu-(PGE) Sulfide Mineralization at the Voiseys Bay Deposit, Labrador, and the Eagle Deposit, Northern Michigan. *Reviews in Economic Geology* **17**.

Ripley, E. M. & Li, C. (2013). Sulfide Saturation in Mafic Magmas: Is External Sulfur Required for Magmatic Ni-Cu-(PGE) Ore Genesis? *Economic Geology* **108**, 45-58.

Ripley, E. M., Lightfoot, P. C., Li, C. & Elswick, E. R. (2003). Sulfur isotopic studies of continental flood basalts in the Noril'sk region: implications for the association between lavas and ore-bearing intrusions. *Geochimica et Cosmochimica Acta* **67**, 2805-2817.

Ripley, E. M., Sarkar, A. & Li, C. (2005). Mineralogic and Stable Isotope Studies of Hydrothermal Alteration at the Jinchuan Ni-Cu Deposit, China. *Economic Geology* **100**, 1349-1361.

Roeder, P. L. & Emslie, R. F. (1970). Olivine-liquid equilibrium. *Contributions to Mineralogy and Petrology* **29**, 275-289.

Roelofse, F. & Ashwal, L. D. (2012). The Lower Main Zone in the Northern Limb of the Bushveld Complex—a >1·3 km Thick Sequence of Intruded and Variably Contaminated Crystal Mushes. *Journal of Petrology* **53**, 1449-1476.

Seat, Z., Beresford, S. W., Grguric, B. A., Gee, M. A. M. & Grassineau, N. V. (2009). Reevaluation of the Role of External Sulfur Addition in the Genesis of Ni-Cu-PGE Deposits: Evidence from the Nebo-Babel Ni-Cu-PGE Deposit, West Musgrave, Western Australia. *Economic Geology* **104**, 521-538.

Shellnutt, J. G., Dostal, J. & Keppie, J. D. (2004). Petrogenesis of the 723 Ma Coronation sills, Amundsen basin, Arctic Canada: implications for the break-up of Rodinia. *Precambrian Research* **129**, 309-324.

Shirley, D. N. (1985). Compaction of igneous cumulates. *Journal of Geology* **94**, 795-809.

Simkin, T. (1967). Flow differentiation in the picritic sills of North Skye. *In Wyllie, P.J., ed, Ultramafic and Related Rocks, John Wiley, Hoboken, N.J.*, 64-69.

Smewing, J. D. (1981). Mixing characteristics and compositional differences in mantle-derived melts beneath spreading axes; evidence from cyclically layered rocks in the ophiolite of North Oman. *Journal of Geophysical Research* **86**, 2645-2659.

Song, X.-Y., Danyushevsky, L., Keays, R., Chen, L.-M., Wang, Y.-S., Tian, Y.-L. & Xiao, J.-F. (2012). Structural, lithological, and geochemical constraints on the dynamic magma plumbing system of the Jinchuan Ni–Cu sulfide deposit, NW China. *Mineralium Deposita* **47**, 277-297.

Sparks, R. S. J., Huppert, H. E., Kerr, R. C., McKenzie, D. P. & Tait, S. R. (1985). Postcumulus processes in layered intrusions. *Geological Magazine* **122**, 555-568.

Sparks, R. S. J., Sigurdsson, H. & Wilson, L. (1977). Magma mixing: a mechanism of triggering acid explosive eruptions. *Nature* **267**, 315-318.

Sun, S. S. & McDonough, W. F. (1989). Chemical and isotopic systematics of oceanic basalts: implications for mantle composition and processes. *Geological Society, London, Special Publications* **42**, 313-345.

Tait, S. R. (1985). Fluid dynamic and geochemical evolution of cyclic unit 10, Rhum, Eastern Layered Series. *Geological Magazine* **122**, 469-484.

Tarling, D. H. & Hrouda, F. (1993). The Magnetic Anisotropy of Rocks. *Chapman and Hall, London*, 217.

Tegner, C. (1997). Iron in plagioclase as a monitor of the differentiation of the Skaergaard intrusion. *Contributions to Mineralogy and Petrology* **128**, 45-51.

Tegner, C., Wilson, J. R. & Brooks, C. K. (1993). Intraplutonic Quench Zones in the Kap Edvard Holm Layered Gabbro Complex, East Greenland. *Journal of Petrology* **34**, 681-710.

Tepley, F. J., Davidson, J. P., Tilling, R. I. & Arth, J. G. (2000). Magma Mixing, Recharge and Eruption Histories Recorded in Plagioclase Phenocrysts from El Chichón Volcano, Mexico. *Journal of Petrology* **41**, 1397-1411.

Thomson, D., Rainbird, R. H. & Dix, G. (2014). Architecture of a Neoproterozoic intracratonic carbonate ramp succession: Wynniatt Formation, Amundsen Basin, Arctic Canada. *Sedimentary Geology* **299**, 119-138.

Thorsteinsson, R. & Tozer, E. T. (1962). Banks, Victoria and Stefansson Islands, Arctic Archipelago. *Geological Survey of Canada Memoir* **330**, 85.

Tredoux, M., Lindsay, N. M., Davies, G. & McDonald, I. (1995). The fractionation of platinum-group elements in magmatic systems, with the suggestion of a novel causal mechanism. *South African Journal of Geology* **98**, 157-167.

Troll, V. R., Deegan, F. M., Jolis, E. M., Harris, C., Chadwick, J. P., Gertisser, R., Schwarzkopf, L. M., Borisova, A. Y., Bindeman, I. N., Sumarti, S. & Preece, K. (2013). Magmatic differentiation processes at Merapi Volcano: inclusion petrology and oxygen isotopes. *Journal of Volcanology and Geothermal Research* **261**, 38-49.

Usselman, T. M. & Hodge, D. S. (1978). Thermal control of low-pressure fractionation processes. *Journal of Volcanology and Geothermal Research* **4**, 265-281.

van Acken, D., Thomson, D., Rainbird, R. H. & Creaser, R. A. (2013). Constraining the depositional history of the Neoproterozoic Shaler Supergroup, Amundsen Basin, NW Canada: Rhenium-osmium dating of black shales from the Wynniatt and Boot Inlet Formations. *Precambrian Research* **236**, 124-131.

Varfalvy, V., Hébert, R., Bedard, J. H. & Laflèche, M. R. (1997). Petrology and geochemistry of pyroxenite dykes in upper mantle peridotites of the North Arm Mountain massif, Bay of Islands Ophiolite, Newfoundland: Implications for the genesis of boninitic and related magmas. *Canadian Mineralogist* **35**, 543-570.

Wager, L. R. & Brown, G. M. (1968). Layered igneous rocks. *Olivier Boyd, Edinburgh*.

Wager, L. R. & Deer, W. A. (1939). Geological investigations in East Greenland Part III. The petrology of the Skaergaard Intrusion, Kangerdlugssuaq, East Greenland. *Meddelelser om Grønland* **105**, 1-352.

Wallace, G. S. & Bergantz, G. W. (2002). Wavelet-based correlation (WBC) of zoned crystal populations and magma mixing. *Earth and Planetary Science Letters* **202**, 133-145.

Weis, D., Kieffer, B., Maerschalk, C., Barling, J., de Jong, J., Williams, G. A., Hanano, D., Pretorius, W., Mattielli, N., Scoates, J. S., Goolaerts, A., Friedman, R. M. & Mahoney, J. B. (2006). High-precision isotopic characterization of USGS reference materials by TIMS and MC-ICP-MS. *Geochemistry, Geophysics, Geosystems* **7**, Q08006.

Welsch, B., Faure, F., Famin, V., Baronnet, A. & Bachèlery, P. (2012). Dendritic Crystallization: A Single Process for all the Textures of Olivine in Basalts? *Journal of Petrology*.

Wendlandt, R. F. (1982). Sulfide saturation of basalt and andesite melts at high pressures and temperatures. *American Mineralogist* **67**, 877-885.

Wenzel, T., Baumgartner, L. P., Brugmann, G. E., Konnikov, E. G. & Kislov, E. V. (2002). Partial Melting and Assimilation of Dolomitic Xenoliths by Mafic Magma: the Ioko-Dovyren Intrusion (North Baikal Region, Russia). *Journal of Petrology* **43**, 2049-2074.

Wignall, P. B. (2001). Large igneous provinces and mass extinctions. *Earth-Science Reviews* **53**, 1-33.

Williams, G. D. & Stelck, C. R. (1975). Speculations on the Cretaceous paleogeography of North America. In: Caldwell, W.G.E. (Ed.), The Cretaceous system in the Western Interior of North America. . *Geological Association of Canada, Special Paper Number* **13**, 1-20.

Williamson, N., Bédard, J. H., Ootes, L., Rainbird, R., Cousens, B. & Zagorevski, A. (2013). Volcanostratigraphy and significance of the southern lobe Natkusiak Formation flood basalts, Victoria Island, Northwest Territories. *Geological Survey of Canada, Current Research* **2013-16**, 13.

Wilson, A. H. (2012). A Chill Sequence to the Bushveld Complex: Insight into the First Stage of Emplacement and Implications for the Parental Magmas. *Journal of Petrology* **53**, 1123-1168.

Young, G. M. (1981). The Amundsen Embayment, Northwest Territories, relevance to the Upper Proterozoic evolution of North America, *in* Campbell, F.H.A., ed., Proterozoic Basins of Canada. *Geological Survey of Canada Paper* **81-10**, 203-211.

Žák, J., Verner, K., Johnson, K. & Schwartz, J. J. (2012). Magma emplacement process zone preserved in the roof of a large Cordilleran batholith, Wallowa Mountains, northeastern Oregon. *Journal of Volcanology and Geothermal Research* **227–228**, 61-75.

Zieg, M. J. & Marsh, B. D. (2012). Multiple Reinjections and Crystal-mush Compaction in the Beacon Sill, McMurdo Dry Valleys, Antarctica. *Journal of Petrology* **53**, 2567-2591.

9. Appendices

A. Copy of “Bédard et al. (2012) Fault-mediated melt ascent in a Neoproterozoic continental flood basalt, the Franklin sills, Victoria Island, Canada” published in Geological Society of America Bulletin in 2012

B. Copy of “Nabelek et al. (2013) Short Duration contact metamorphism of calcareous sedimentary rocks by Neoproterozoic Franklin gabbro sills and dykes on Victoria Island, Canada” published in Journal of Metamorphic Geology in 2013

C. Electron microprobe methods for mineral species analysed

D. Model anchors
    - D1. Franklin liquid line of descent
    - D2. Model melt parameterisations for mineral chemistry

E. Chapter 4 “Olivine slurry replenishment and the development of igneous layering in a Franklin sill” appendix
    - E1. Whole-rock data
    - E1-A. Point counting results and error
    - E1-B. Additional sill whole-rock profiles and descriptions
    - E2. Olivine chemical data and inverse melt compositions
    - E3. Pyroxene chemical data and inverse melt compositions
    - E4. Plagioclase chemical data
    - E5. Spinel chemical data
    - E6-1. PELE modelling
    - E6-2. PELE modelling
    - E7-1. Element maps
    - E7-2. Element map descriptions and interpretations

F. Chapter 5 “The geochemical effects of olivine slurry replenishment and dolostone assimilation in the plumbing system of the Franklin large igneous province” appendix
    - F1. Whole-rock data
    - F2. Olivine chemical data and inverse melt compositions

F3. Sulphur isotope data

F4. PELE assimilation-fractional-crystallisation modelling (olivine slurry)

F5. Dolostone whole-rock data from the Minto Inlier

F6. PELE assimilation-fractional-crystallisation modelling (with dolostone)

G. Chapter 6 “Sulphide immiscibility induced by wallrock assimilation in a fault-guided Franklin magmatic feeder system” appendix

G1. Whole-rock data

G2. Olivine chemical data

G3. Clinopyroxene chemical data

G4. Plagioclase chemical data

G5. Sulphur isotope data

G6. AMS data

G7. Additional plots and descriptions

Geological Society of America Bulletin

Fault-mediated melt ascent in a Neoproterozoic continental flood basalt province, the Franklin sills, Victoria Island, Canada

J.H. Bédard, H.R. Naslund, P. Nabelek, A. Winpenny, M. Hryciuk, W. Macdonald, B. Hayes, K. Steigerwaldt, T. Hadlari, R. Rainbird, K. Dewing and É. Girard

Geological Society of America Bulletin published online 6 February 2012;
doi: 10.1130/B30450.1

Notes

Geological Society of America Bulletin, published online on 6 February 2012 as doi:10.1130/B30450.1

Fault-mediated melt ascent in a Neoproterozoic continental flood basalt province, the Franklin sills, Victoria Island, Canada

J.H. Bédard[1,†], H.R. Naslund[2], P. Nabelek[3], A. Winpenny[4], M. Hryciuk[5], W. Macdonald[2], B. Hayes[6], K. Steigerwaldt[2], T. Hadlari[7], R. Rainbird[8], K. Dewing[7], and É. Girard[9]

[1]*Geological Survey of Canada (GSC-Québec), 490 de la Couronne, Québec, Québec G1K 9A9, Canada*
[2]*Department of Earth Sciences, State University of New York, Binghamton, New York 13902, USA*
[3]*Department of Geological Sciences, University of Missouri, Columbia, Missouri 65211, USA*
[4]*Department of Earth Sciences, University of Bristol, Wills Memorial Building, Bristol BS8 1RJ, UK*
[5]*Department of Earth and Planetary Sciences, McGill University, 3450 University Street, Montréal, Québec H3A 2A7, Canada*
[6]*School of Earth, Ocean and Planetary Sciences, Cardiff University, Cardiff CF10 3YE, Wales, UK*
[7]*Geological Survey of Canada (GSC-Calgary), 3303 33rd Street NW, Calgary, Alberta T2L 2A7, Canada*
[8]*Geological Survey of Canada (GSC-Ottawa), 601 Booth Street, Ottawa, Ontario K1A 0E8, Canada*
[9]*Institut National de la Recherche Scientifique – Eau Terre et Environnement, 490 de la Couronne, Québec, Québec G1K 9A9, Canada*

ABSTRACT

The Neoproterozoic Franklin large igneous province on Victoria Island, Canada, is characterized by continental flood basalts and a sill-dominated feeder system. Field relationships indicate that fault-guided transfer zones allowed magma to jump up-section to form higher-level intrusions. Where sills connect to dikes and magmas moved up-section, roof and wall rocks are characterized by wide and intense contact-metamorphic haloes, consistent with throughflow of magma. The geometric constraints suggest that conduits may have opened episodically and then closed when magma pressure waned. The episodic nature of conduit opening events can explain the pulsed ascent of crystal slurries, and may also play a role in the deposition of Ni-sulfides.

INTRODUCTION

Most flood basalt provinces are dominated by evolved lava compositions, requiring significant intracrustal differentiation (Cox, 1980; Dostal and Dupuy, 1984, Hooper and Hawkesworth, 1993; Hawkesworth et al., 1995; Elliot and Fleming, 2004; Jourdan et al., 2007; Larsen and Pedersen, 2009). Tholeiitic dike swarms riddle shields and pericratonic areas and are thought to be the root zones of flood basalt events, possibly related to mantle plumes (e.g., Fahrig, 1987; Ernst et al., 1995; Bryan and Ernst, 2008). Where dike swarms can be related to well-developed passive-margin sequences with associated volcanic rocks, dike orientations reflect the interplay between preexisting structural anisotropy and the stress field that is developed as continental breakup proceeds (May, 1971; Sykes, 1978; Ernst et al., 1995; Watanabe et al., 1999; McHone et al., 2005). On the other hand, sills dominate many tholeiitic feeder systems beneath Proterozoic and Phanerozoic continental flood basalt provinces (e.g., Baragar, 1976; Francis and Walker, 1986; Hawkesworth et al., 1995; Chevallier and Woodford, 1999; Bédard et al., 2007; Bryan and Ernst, 2008), magmatically active rifted margins (Bédard et al., 1984; Thomson and Hutton, 2004; Rocchi et al., 2007; White et al., 2008), oceanic plateaus (Kerr et al., 1998), ophiolitic and oceanic lower crust (Bédard, 1991; Dick et al., 2000; Lissenberg et al., 2004), and Archean tholeiitic lava plains (Bédard et al., 2009a). In sill-dominated plumbing systems, there is generally a dearth of steeply dipping conduits that could explain ascent of melt to the surface from their mantle sources.

Dikes are thought to change into sills as a consequence of the dike propagator intersecting a discontinuity or stress barrier, such as an anomalously weak or strong unit (e.g., Watanabe et al., 1999; Gudmundsson and Brenner, 2001; Gudmundsson, 2011). In contrast, much less is known about how sills change into dikes. Some basalt provinces are dominated by saucer-shaped sills (Thomson and Hutton, 2004; Hansen and Cartwright, 2006; Galerne et al., 2008; Polteau et al., 2008), where the up-curved edges of a lower sill fed higher-level sills (Thomson and Hutton, 2004), such that "feeder" dikes are steep offshoots from the terminations of underlying sills. In saucer-shaped sills from the Karoo (South Africa) and Rockall Trough (west of Great Britain), the data imply shallow, nearly "subvolcanic" emplacement (Thomson and Hutton, 2004; Hansen and Cartwright, 2006; Galerne et al., 2008), and it has been proposed that their upward transgression is a consequence of lateral expansion and interaction with the free surface (Fialko, 2001; Malthe-Sørenssen et al., 2004; Galland et al., 2009). On the basis of a comparison between observed thicknesses and emplacement depth, Polteau et al. (2008) proposed that sills with diameters less than 10 km would correspond to emplacement depths of less than 2 km. While these transgression mechanisms may characterize subvolcanic sill-dominated feeder systems, they may not apply to more deeply emplaced sills, where interactions with the free surface should not be a factor. There seem to be two end-member possibilities to explain upward transgression of deeply emplaced sills.

(1) The pathway by which a sill migrated up-section did not exist prior to sill emplacement and was generated by an interplay among the stress field, magma flow, magma pressure, and host-rock deformation (Pollard and Segall, 1987; Lister and Kerr, 1991; Rubin, 1995; Gerya and Burg, 2007; Gudmundsson, 2011). Because magmatic intrusion rates are much faster than any possible tectonic accommodation rates (Paterson and Tobisch, 1992; Vigneresse et al., 1999), the local stress field in a rapidly inflating and propagating sill will be dominated by magmatic flow. Menand (2008) suggested that during rapid lateral propagation of magma in a

†E-mail: jbedard@nrcan.gc.ca

 doi: 10.1130/B30450.1; 10 figures.

sill, viscously controlled dynamics may lead to upward transgression of the intrusion along an induced reverse fault where the sill propagator has its maximum curvature.

(2) Magma may jog up-section because of the presence of preexisting steep structures such as faults. This possibility is often suggested but rarely demonstrated (but see Hutton and Ingram, 1992; Thomson, 2007). Structurally mediated melt ascent is intuitively attractive, but unambiguous demonstration of a genetic relationship between guiding structures and magma emplacement from field relationships requires exceptional exposures and preservation of fabrics and contacts. Perversely, robust melt channels tend to consume and recrystallize the wall rocks that contain the evidence (e.g., Huppert and Sparks, 1988; Holness and Humphreys, 2003). In addition, well-exposed crustal sections beneath basaltic lava fields are rare, and in seismic-reflection profiles, steeply dipping up-flow conduits would be difficult to image. Consequently, the poor documentation of structurally controlled magmatic ascent in sill-dominated basaltic feeder systems may partly be an observational problem. In this paper, we present evidence from the superbly exposed and preserved Neoproterozoic Franklin magmatic suite of Victoria Island, Canada, that strongly supports an ephemeral, fault-mediated, magma transfer mechanism to explain up-section sill transgression.

VICTORIA ISLAND GEOLOGY

The Neoproterozoic Shaler Supergroup (Rainbird, 1993) is located in the Minto Inlier, central Victoria Island, Canada (Fig. 1; Thorsteinsson and Tozer, 1962). The Shaler Supergroup is dominated by shallow-water carbonate rocks, with subordinate mud rocks, sandstones, and sulfate evaporites, and it represents a shallow-water Proterozoic intracontinental basin developed within the supercontinent Rodinia (Young, 1981; Rainbird, 1993). Archean granites and Paleoproterozoic sedimentary rocks underlie the Neoproterozoic strata (Rainbird et al., 1994). The Natkusiak flood basalts (Baragar 1976; Jefferson, 1985; Jefferson et al., 1985; Dostal et al., 1986; Dupuy et al., 1995) are the uppermost formation of the Shaler Supergroup. The Natkusiak Formation has a thin, heterogeneous basal unit (flows, volcaniclastics, and lahars), succeeded by sheet flows defining two geochemical volcanic cycles (each ~500 m thick; Dostal et al., 1986). In each cycle, basalts range from high-MgO olivine-phyric basal flows (up to 11 wt% MgO), to evolved plagioclase + clinopyroxene + magnetite-phyric upper flows (~3–4 wt% MgO). The upper contact is a Cambrian erosional unconformity upon which a Paleozoic clastic and carbonate sequence was deposited.

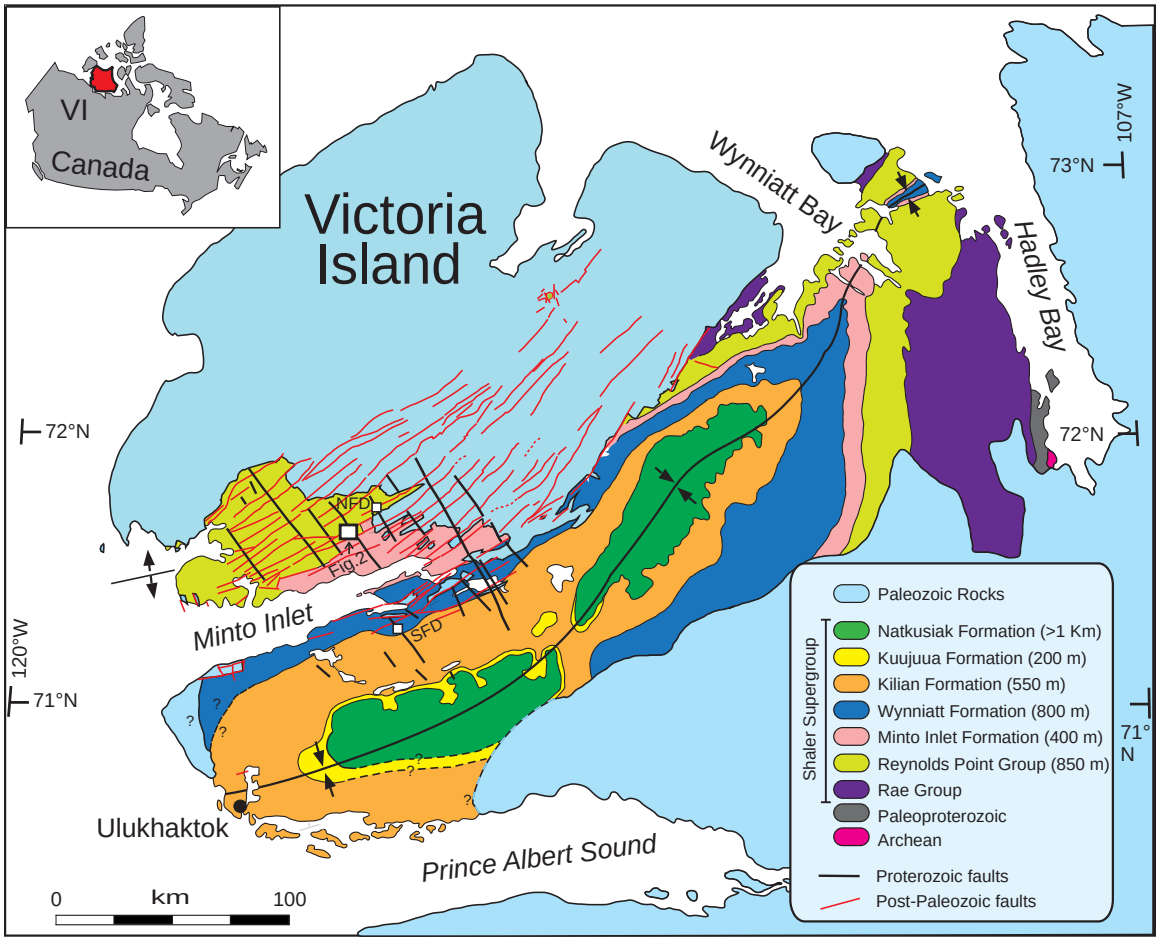

Figure 1. Simplified regional map of Victoria Island (Red polygon on inset labeled VI for Victoria Island, which shows location in Canada), based on the compilation of Hulbert et al. (2005) and our new observations from 2010 and 2011 mapping. The boxes show the locations of the northern and southern feeder dikes (NFD and SFD), and of Figure 2. Individual sills are not represented.

Geological Society of America Bulletin, published online on 6 February 2012 as doi:10.1130/B30450.1

The Franklin sills occur throughout the Shaler Supergroup, and some of them may represent feeders to the lavas (Baragar, 1976; Rainbird et al., 1994; Jefferson et al., 1994; Hulbert, 1998; Hulbert et al., 2005). Franklin sills range in thickness from less than 1 m to over 100 m, but most are 20–60 m thick. Individual sills commonly extend for 20 km or more along-strike with little obvious change in thickness. Depending on the specific location, sills constitute anywhere from 10% to 75% of the section. Sills of similar type and age also occur in the Coronation Gulf to the south (Rainbird et al., 1996; Shellnutt et al., 2004), and coeval, geochemically very similar magmas correlated with the Franklin event extend from Greenland to Siberia (Heaman et al., 1992; Pehrsson and Buchan, 1999; Denyszyn et al., 2009; Richard Ernst, 2011, personal commun.). Two age populations are present in the sills, ca. 723 and 716 Ma (Heaman et al., 1992; Michael Hamilton, 2009, personal commun.).

Shaler Supergroup rocks are gently folded along NE-trending axes into open upright folds with a wavelength of ~200 km (Fig. 1). Beds typically dip no more than 5° or 10°, however, and there is rarely a cleavage or other apparent outcrop-scale fabric related to folding. The total thickness (excluding sills) of the Supergroup is ~4 km, including the ~1.1-km-thick Natkusiak Formation flood basalts that cap the sequence.

A new aeromagnetic map reveals prominent NNW-trending magnetic lineaments (Kiss and Oneschuk, 2010; Fig. 2B) that correspond to prominent linear topographic lows, locally containing cataclasites, which we interpret to represent faults. Some of these lineaments mark sharp breaks in stratigraphy indicating east-side-down throws (maps in preparation) and exhibit associated structures indicating normal motion synchronous with emplacement of magmas with Franklin affinities (this paper)—and so we interpret them to be Neoproterozoic synmagmatic normal faults.

The Neoproterozoic rocks are unconformably overlain (Fig. 1) by a Paleozoic sequence ranging in age from Cambrian to Devonian, composed of clastic sedimentary rocks at the base grading up into dominant carbonate rocks (Thorsteinsson and Tozer, 1962; Durbano et al., 2010). The feather-edge of the unconformity is very irregular in detail, with development of an oxidized regolith and local paleotopographic effects. All rocks are dissected into horst and graben structures by ENE- to E-W–trending block faults of post-Devonian age (Hadlari and Bédard, 2008; this study), which we call post-Paleozoic faults henceforth. The distribution of these faults on Figure 1 represents the limit of the 2010 mapping, and they are more widespread than is shown.

Franklin Sills

Most Franklin sills contain fairly homogeneous, evolved diabasic rocks and show only modest internal differentiation (e.g., Shellnutt et al., 2004), but there are subordinate occurrences of plagioclase + clinopyroxene + olivine-porphyritic sills and of strongly differentiated primitive sills with olivine cumulate bases. Apparent contact-metamorphic haloes are typically less than a few meters wide. Olivine-rich sills have lower chilled margins with up to 12 wt% MgO, and olivine up to Fo_{87} with NiO up to 0.35 wt%. Minor chromite microphenocrysts are also present (Cr/[Cr + Al] between 0.5 and 0.7). Diabasic sills typically contain plagioclase and clinopyroxene (±olivine) microphenocrysts and generally have chilled margins with MgO around 6%–8%. Most sills are concordant with bedding in host sedimentary rocks and, where later block faulting has spared the evidence, extend along-strike for many tens of kilometers with no apparent change in thickness or position in the host stratigraphy. In the course of a regional mapping program (Rainbird et al., 2010), several occurrences and types of sill terminations were observed, the most significant of which are described next. In this paper, we focus

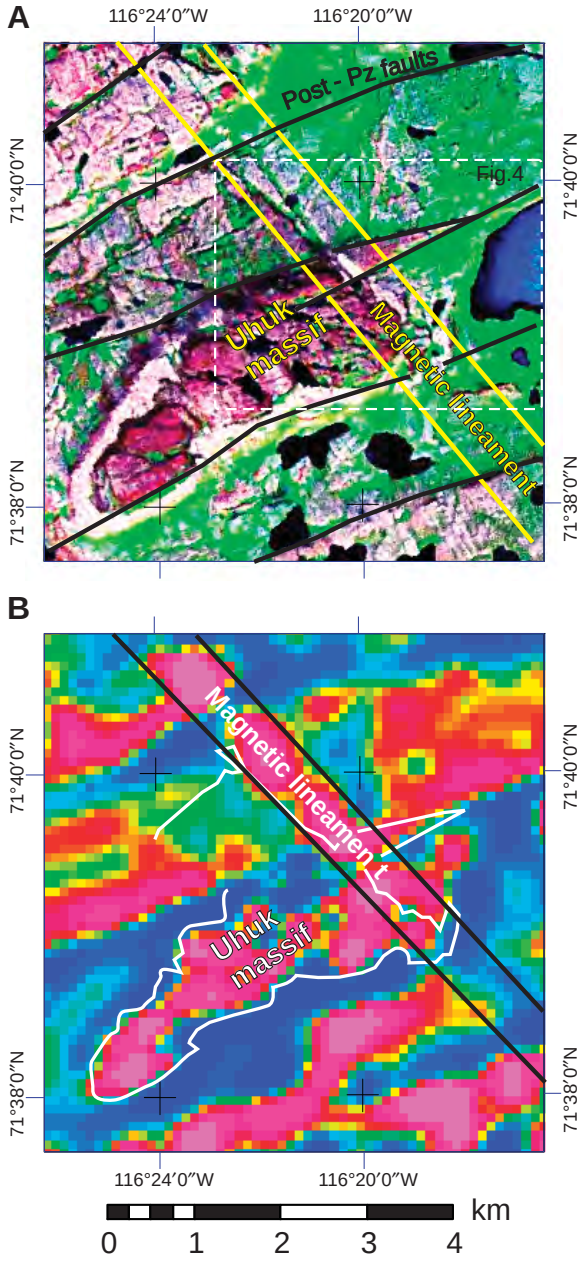

Figure 2. (A) Landsat image showing the Uhuk Massif. The purple colors correspond to mafic igneous rocks. A few of the larger faults and units are also shown, as is the location of Figure 4 (box). (B) The first derivative of the magnetic field (Kiss and Oneschuk, 2010) for the same area. Note the prominent NNW-trending lineament that crosses the eastern end of the Uhuk Massif. The igneous rocks from part A are outlined by a white line. Pz—Paleozoic.

Geological Society of America Bulletin, published online on 6 February 2012 as doi:10.1130/B30450.1

on three areas that show evidence for up-section sill migration.

(1) The northern feeder dike (NFD; Figs. 1, 3A, 3B, and 3C) records injection of magma from a sill into a normal fault, intense thermal metamorphism of capping strata, and possible deflation of the lower sill and partial closure of the feeder channel as the capping strata subsided.

(2) The southern feeder dike (SFD; Figs. 1 and 3D) contains blocks of limestone that are tilted over 60° in a magmatically dominated up-flow zone in a synmagmatic normal fault.

(3) The Uhuk Massif (Figs. 1, 2, and 4–9) exposes a complex up-flow zone, where olivine-rich magma migrated up-section and then extended to the west for tens of kilometers (Figs. 2A and 6A) as a concordant sill. Capping and floor strata are intensely metamorphosed, consistent with the existence of a magmatic throughflow system. The roof zone is characterized by breccias, branching dikes, and partially detached slivers (Figs. 4–7 and 9), implying synkinematic magmatic emplacement along an east-dipping normal fault. The contact-metamorphosed roof zone carbonates were injected by Fe-rich fluids, leading to the development of oxide-sulfide–rich skarns (Fig. 8).

Northern Feeder Dike

The thin-bedded limestones and silty limestones of the Boot Inlet Formation (~3–4 km paleodepth) dip ~5° toward the southeast in this area, and they are intruded by two sills linked by a dike (Fig. 3A). The diabasic upper sill extends at least 2 × 5 km and forms a prominent mesa that terminates abruptly on valley walls. Sill-capped mesas on the other sides of wide valleys to the east and west may be extensions of the same sill. In the area pictured in Figure 3A, the upper sill's roof has been eroded away, but exposed portions are up to 50 m thick. Lower chilled margins are well exposed locally, but talus generally obscures the contact. The lower sill is separated from the upper sill by ~25–30 m (stratigraphic thickness) of thin-bedded limestone, which is exposed on a shallowly south-sloping bench, ~250 m wide (Fig. 3A). The lower sill is also diabasic and is at least 20 m thick. Its floor is buried in turf, but its roof is well exposed along a south-facing cliff (an ENE-trending post-Paleozoic fault scarp), and as two erosional windows in the sloping limestone bench (Fig. 3A). The lower sill's roof zone does not show a well-developed chill, but it has granular textures, is affected by pervasive deuteric hydrothermal alteration, and is enriched in pyrite and minor chalcopyrite. A prominent NNW-trending diabase dike (which we call the northern feeder dike) has well-developed chilled margins on both sides and cuts the limestone bench. The dike is ~3 m wide at the southern end (Fig. 3B) and widens to ~30 m where it approaches the contact with the upper sill. This widening effect is primarily an along-strike change, unlike the dikes documented by Gudmundsson et al. (2008). Where it is widest, the feeder dike is composed of medium-grained diabase at its core. Preliminary magnetic susceptibility data suggest a steep flow fabric. Locally, sulfides are concentrated along the hanging-wall contact. The upper sill does not show any trace of the northern feeder dike within it, and we now believe that the upper sill is a later intrusion. Dikes with similar orientations, spaced 1–2 km apart, many plagioclase + clinopyroxene + olivine-phyric, occur along this same limestone bench to the east, indicating that this dike is not an isolated or unique occurrence. A series of post-Paleozoic ENE-trending faults cuts the limestone bench, generating small offsets in the northern feeder dike and obscuring the contact zone with the upper sill.

Along the southern cliff exposure, the lower sill merges seamlessly with the dike, which dips ~45° toward the east (Fig. 3B). Immediately above the junction with the sill on the southern scarp, the dike is only ~3 m wide and has chilled margins. The limestone above the sill's roof shows textures indicating extensive recrystallization. This probably represents a combination of thermal metamorphism, reaction between invading magma and host carbonates, and fluid-mediated metasomatism. Brittle normal offsets of limestone laminae in the hanging wall indicate extension. The limestone on the footwall side of the dike appears to be less metamorphosed, with a brownish halo that is only ~2 m wide. A few, small, 0.5-m-wide plagioclase + clinopyroxene + olivine-phyric splay dikes penetrate the footwall. Limestone in contact with the dike locally exhibits drag folds on a 1–3 m scale (Fig. 3C), indicating that the eastern (hanging-wall) block moved down, making this a normal fault. Tiny back bends on bent laminae suggest either fluctuations to the overall motion, or compression of hot, ductile limestone related to elevated magmatic pressure.

Southern Feeder Dike Complex

In this area, the bedded limestone of the Upper Wynniatt Formation (~1–2 km paleodepth) and evaporites of the Kilian Formation are intruded by large bodies of diabase and gabbro. On the kilometer scale, the outcrop pattern is characterized by a series of NNW-trending gabbroic and limestone panels, separated by prominent linear valleys or scarps that we interpret as faults and/or intrusive contacts. The area corresponding to the southern feeder dike shows a prominent NNW-trending positive magnetic anomaly similar to the one shown on Figure 2A, suggesting that this may be a magmatic up-flow zone. The action of the faults on the wall rocks and metasedimentary septa is pronounced. A large intrusive apophysis shows a shallowly dipping limestone bench (Fig. 4A) that bends abruptly down into the fault-feeder zone. Limestone of the roof is broken up into large (e.g., 2 m thick × 25 m long) slabs of layered marble that dip 60°–70° to the east (Fig. 4B) near the fault zone. Both the steeply dipping and flat-lying limestones along this structure are intensely recrystallized to white marble over many meters. Pipe-like magmatic structures drill up into thermally softened limestone/marble and are surrounded by prominent calc-silicate coronas. The steeply dipping metasedimentary block is sheathed in diabase, some of which shows chilled margins.

Uhuk Massif

A major feeder system is superbly exposed and preserved on the eastern edge of the Uhuk Massif (Fig. 2). The eastern part of the Uhuk Massif is located above a prominent positive NNW-trending magnetic lineament (Fig. 2B) that also corresponds to a major regional-scale lithostratigraphic break, suggesting that the rocks to the east have dropped along a normal fault. The common occurrence of dikes with this orientation (see previous and following sections), commonly associated with breccias and other evidence for faulting, implies that faults with this orientation are synmagmatic faults of Franklin age. The sill-like western part of the Uhuk Massif has a thick olivine-cumulate base and extends toward the west for ~10 km (Figs. 2A and 6A). We have yet to unambiguously correlate a sill from one fault block to another, and so we cannot be certain how far this sill actually extends. Except for its eastern end (described later herein), the sill appears to have a planar, conformable lower contact against bedded limestones and dolostones of the Jago Bay Formation (~2–3 km paleodepth). Unlike footwall contacts of most diabasic sills, the carbonate rocks that underlie the distal flat-lying parts of the Uhuk sill show a wide contact-metamorphic halo.

Near-vertical, E-W–trending, post-Paleozoic faults break the massif into four main blocks, exposing cross sections, preserving different levels of emplacement, and facilitating interpretation of geological relationships (Figs. 4 and 6A). The post-Paleozoic faults cut and offset N- to NNW-trending faults that are parallel to the prominent magnetic lineament of Figure 2B,

Geological Society of America Bulletin, published online on 6 February 2012 as doi:10.1130/B30450.1

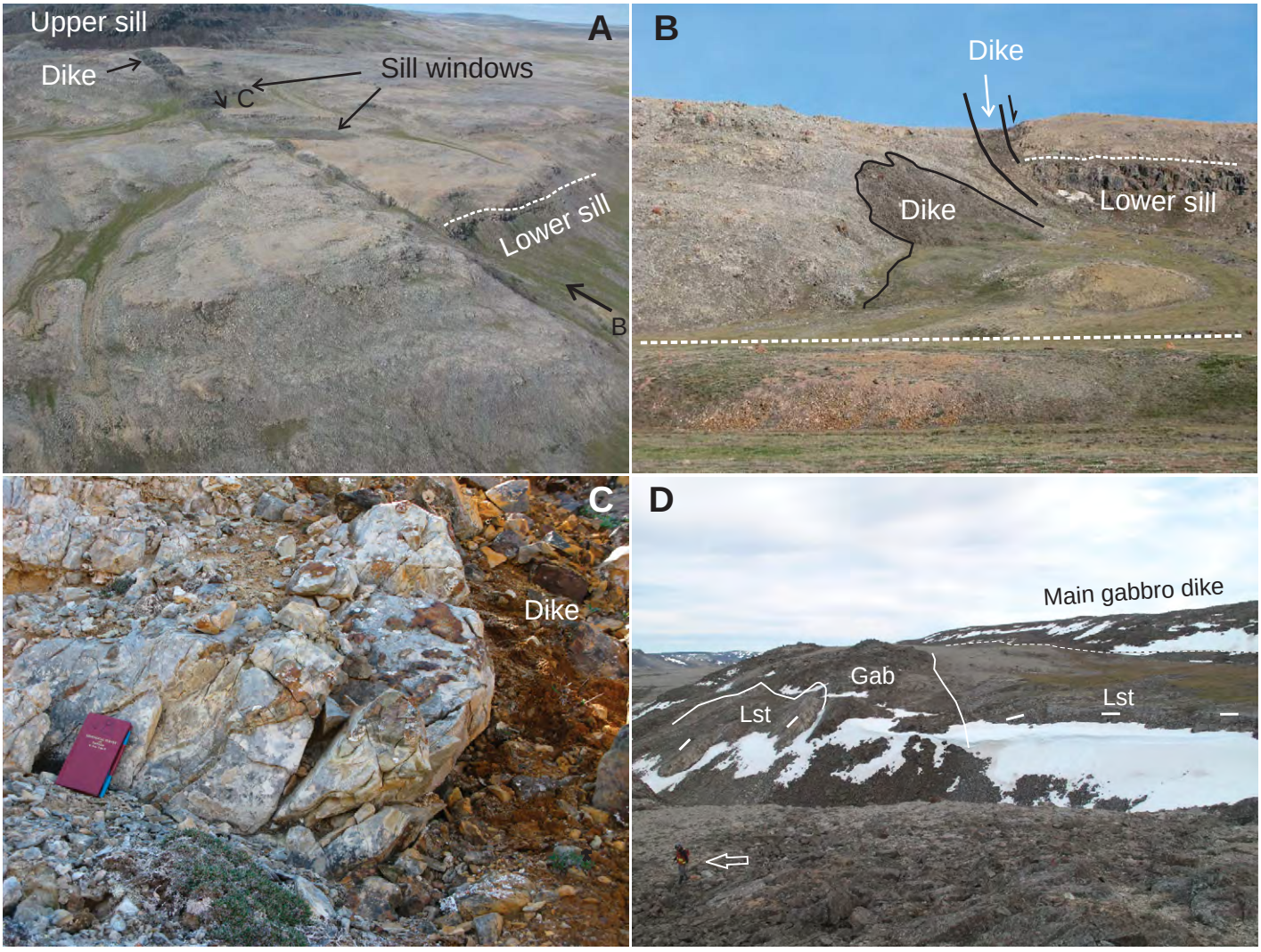

Figure 3. Northern and southern feeder dikes. (A) General view from the air looking northeast of the northern feeder dike (extending from top left to lower right). The dike is over 30 m wide at its northern end, where it nearly joins the upper sill. The dotted white line shows the upper contact of the lower sill. The "B" and "C" arrows show the viewpoints for Figures 4B and 4C. Note the small dark patches labeled "sill windows" where the upper contact of the lower sill peeps through the thin limestone cap. (B) View looking northwest, nearly along the strike of the feeder dike/fault. The irregular surface labeled "dike" on the left is a plating of dike on the cliff surface. The dotted line in the foreground is the trace of a post-Paleozoic normal fault (foreground down). (C) View looking south at the upper contact of the northern feeder dike against intensely deformed and metamorphosed limestone. Note that the disrupted bedding dips steeply to the left (east), suggesting that the hanging wall moved down (normal fault). (D) Southern feeder dike. View looking S-SW. In the background, forming the ridge, there is a large dike of diabase and gabbro (Gab). The dotted line shows the approximate trace of the inferred contact. The white lines next to the limestone (Lst) outcrops show the bedding dip. This varies from nearly flat-lying on the right to steeply dipping to the left. The steeply dipping limestone is bounded by fine-grained diabase at its base and beyond. We interpret the outcrop pattern and change in dip as the result of movement along a Proterozoic synmagmatic fault (down to left). The arrow shows the geologist for scale.

and that are associated with cataclastic breccias into which dikes are emplaced (Fig. 7B). These are unambiguously synmagmatic normal faults (down to the east). A third, less-well-developed fault population trends NNE. The NNE-trending faults appear to cut many of the NNW-trending faults, but not all of them, and so their age remains uncertain. We suspect that they may also be Proterozoic, but we cannot be sure. To facilitate the presentation, major panels separated by intrusive contacts or Neoproterozoic faults are referred to as domains, with igneous rocks having a number code and metasedimentary rocks having a letter code.

The Southern Block (Figs. 4 and 6A) is a deeply foundered graben where the Uhuk Massif (if present) is hidden below Shaler Supergroup rocks and unconformably overlying Cambrian clastic and carbonate rocks. The Uhuk Main Block is ~1.5 km wide (N-S direction). It preserves the main conformable part of the sill to the west and downdropped panels of sill, roof limestone, and contact zone rocks to the east. The next block to the north is the 500-m-wide Horst Block, which exposes the same relationships as the Main Block, but at a different level. The Northern Block is a

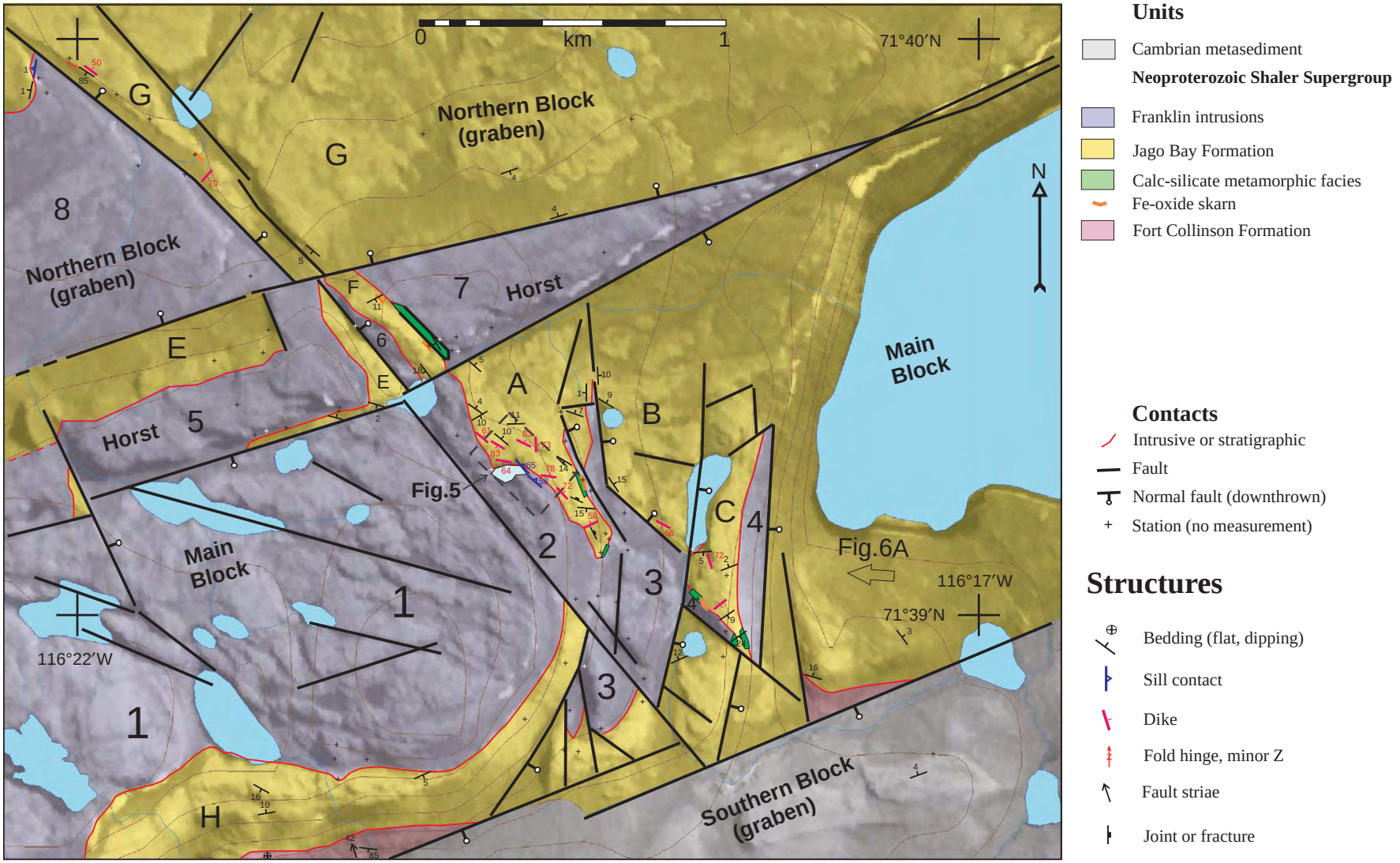

Figure 4. Map of the eastern termination of the Uhuk Massif. The geology is shown as a color wash over a rectified air photo base. Contour lines and lakes are also shown. Letters and numbers are domains referred to in the text. Black lines are faults. Interpreted motion on normal faults is shown by the stick-ball symbol (ball-side down). Skarns are shown as bold orange lines. The location of Figure 5 and viewpoint of Figure 6A are shown.

Geological Society of America Bulletin, published online on 6 February 2012 as doi:10.1130/B30450.1

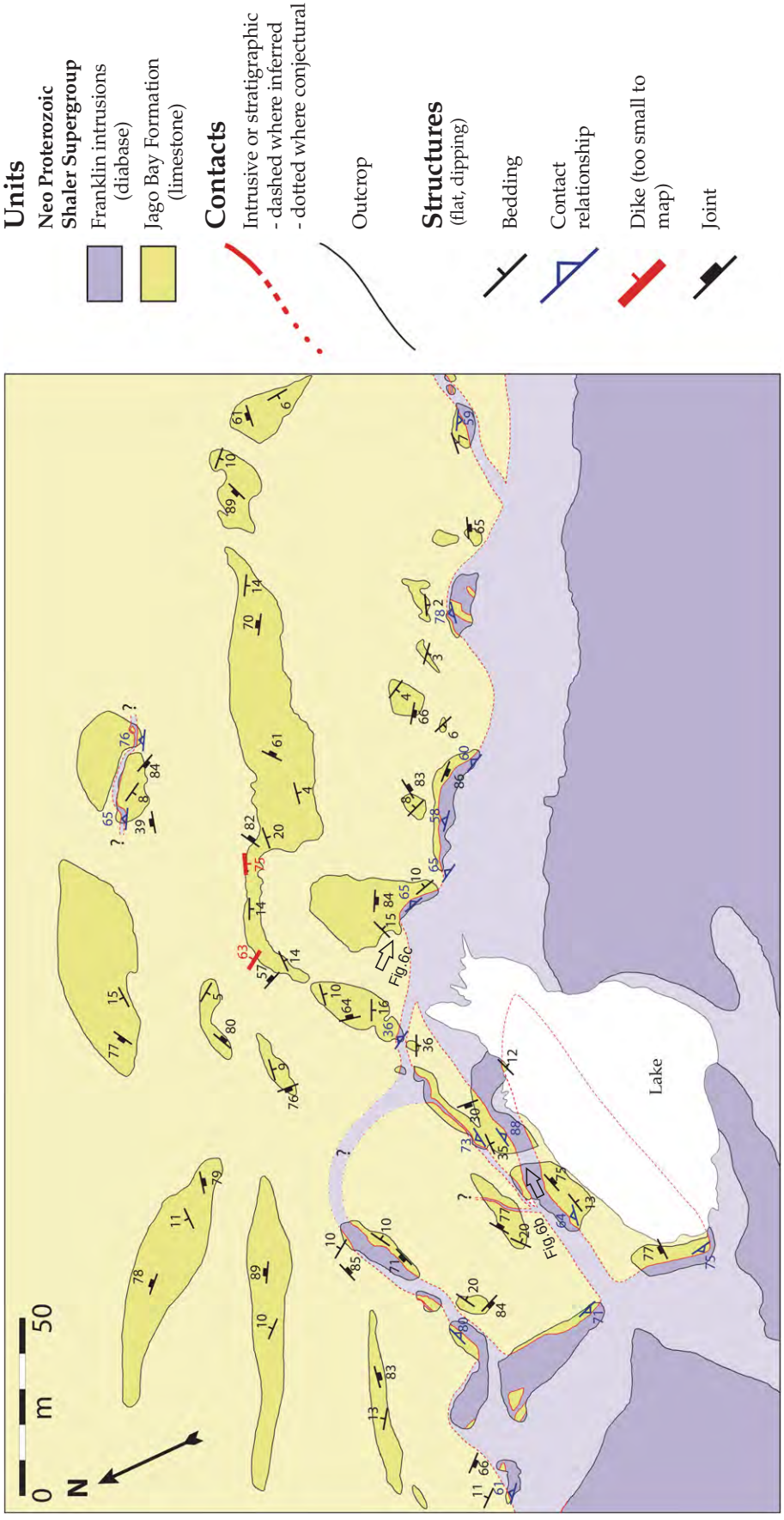

Figure 5. Detail map of the sill/limestone upper contact zone, showing two incipient limestone roof pendants and the scalloped shape of the sill/limestone contact. Viewpoints of Figures 6B and 6C are shown as arrows. Center of map is at ca. 116°19.3′W, 71°39.15′N.

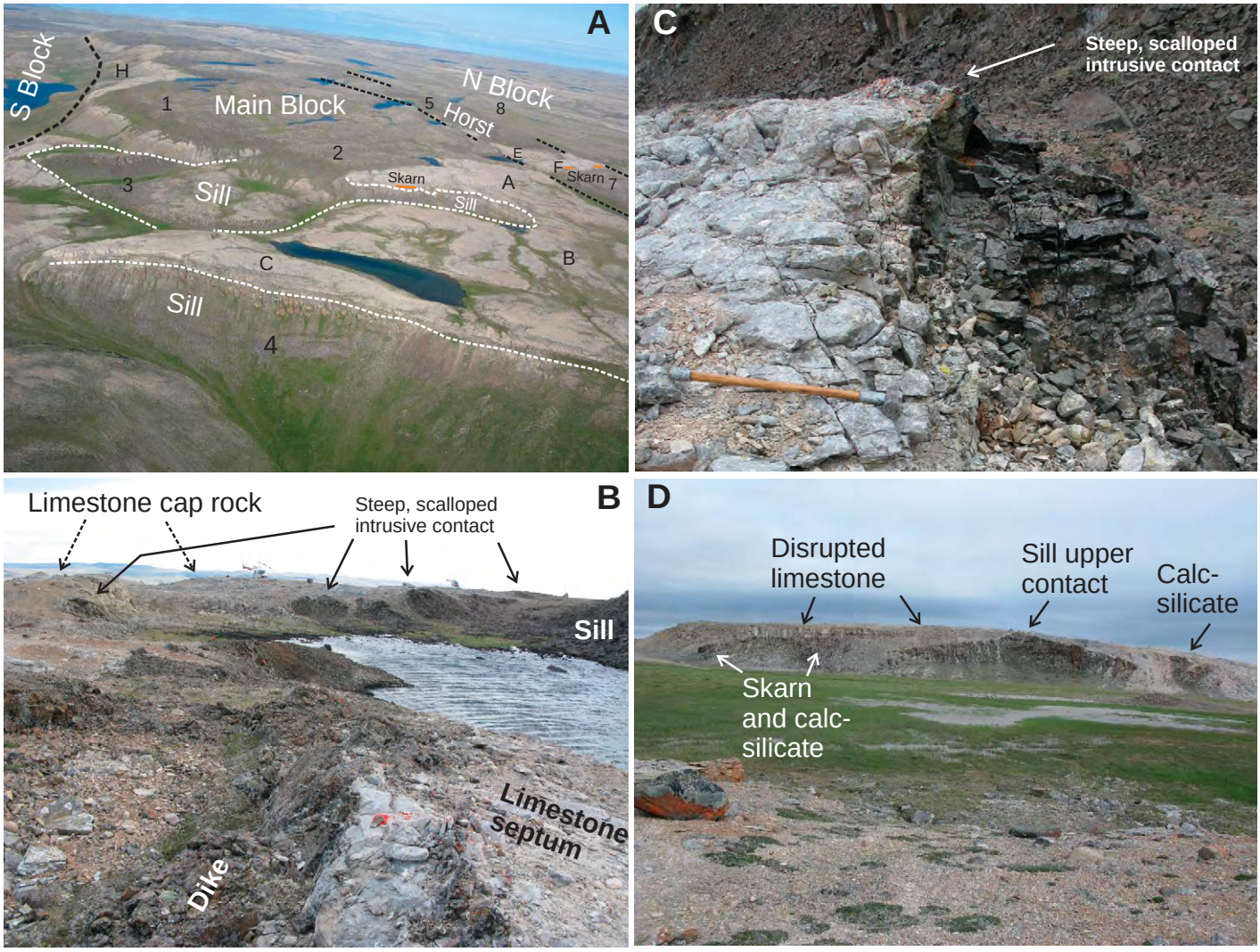

Figure 6. (A) General view from the air of the Uhuk Massif, looking west (see Fig. 4 for viewpoint). Some of the domains are marked. Dashed white lines highlight sill contacts. Black dashed lines highlight post-Paleozoic faults. Thick orange lines show the locations of skarns. (B) View looking southeast. Photo was taken from the small lake between the 2 and the A on Figure 6A; and the viewpoint is marked on Figure 5. The pale gray in the foreground is a partly detached marble roof pendant, dissected by dikes. The black lenses to the left of, and just beyond, the small lake are the intrusive upper contact of the sill (detail in Fig. 6C). The helicopters in the background are on a large limestone roof panel (domain A). (C) Detail of one of the steeply dipping, scalloped upper intrusive contacts from Figure 2B; viewpoint shown on Figure 5. Hammer is 1 m long. (D) View looking ENE at the sill upper contact (ridge in foreground of Figure 6A, domain 4-C contact; photo taken from just below the 3). The cliff face extends ~200 m from left to right (N to S). Note how the irregular contact comes to a point and breaches the limestone surface.

1.5-km-wide graben that preserves the uppermost facies of the sill to the west and a down-dropped panel of roof limestone and contact zone rocks to the east.

Main Block

In the western part of the Uhuk Massif, the sill is conformable (domain 1, Figs. 4 and 5A), and it is divisible into a lower border zone with upwardly increasing proportions of olivine, a peridotite zone dominated by cumulate olivine (commonly with a poikilitic top), a lower, medium-grained gabbroic zone, and an upper gabbroic zone characterized by more acicular pyroxene and coarser patches. The upper chilled margin is not exposed. Metasedimentary rocks beneath (e.g., domain H) show a prominent contact-metamorphic halo.

In the next sill domain (domain 2) to the east, the intrusive upper contact of the sill against roof limestone (domain A) dips steeply toward the east. The contact is irregular, showing a scalloped pattern that may represent "conchoidal" fracture of massive, annealed roof rocks (Figs. 5, 6B, and 6C). This process was fossilized in action as arcuate dikes that partly detach slivers of roof-contact limestone, each ~5–10 m wide (Figs. 5 and 6B). The roof limestone is cut by many thin (1 cm to 3 m), NNW-trending dikes that locally flatten out parallel to bedding and branch toward the west (Fig. 7A), suggesting westward fracture propagation and emplacement. Domain A limestone is most intensely metamorphosed where it abuts sill rocks. The upper sill contact is exposed along the NE-fac-

Geological Society of America Bulletin, published online on 6 February 2012 as doi:10.1130/B30450.1

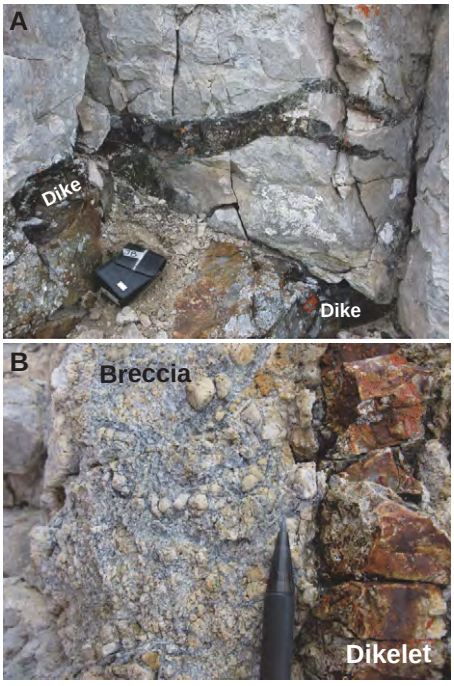

Figure 7. (A) Branching dike emplaced within limestone cap rock of domain A. The branching suggests emplacement toward the northwest. Camera case is ~12 cm long. (B) Close-up of fault breccia injected by microdike, indicating the synkinematic nature of the magmatism. This is from the roof limestone of the ridge shown in Figure 6D (domain C).

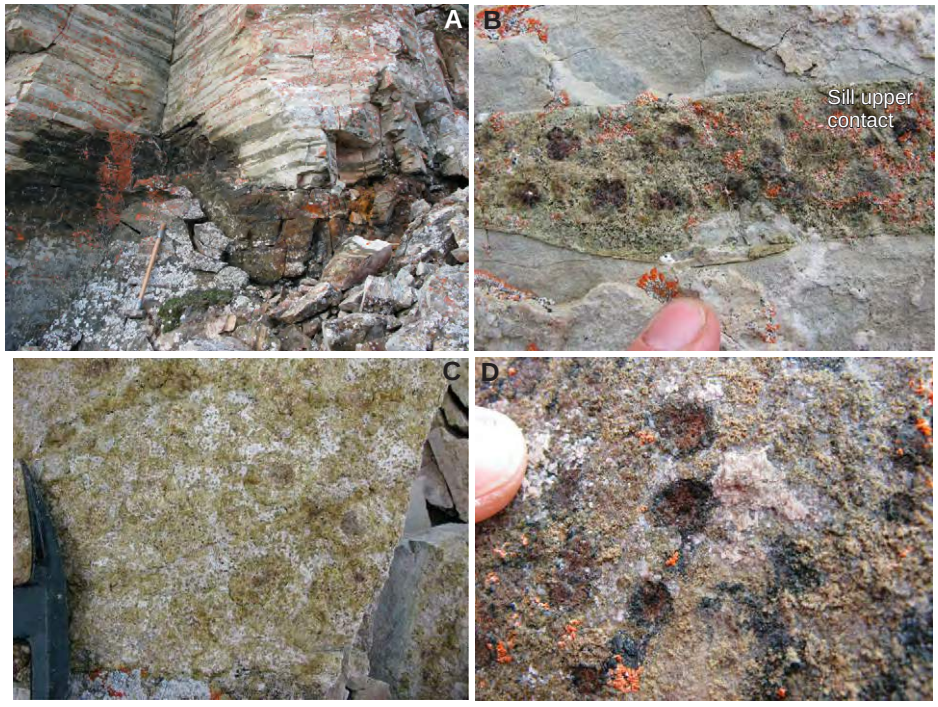

Figure 8. (A) View of contact-metamorphosed bedded limestone with silty layers of the Jago Bay Formation (domain A looking west). The silty layers contain prominent garnet and vesuvianite porphyroblasts (Figs. 8B and 8C). The black patch just above the sledgehammer (1 m long) is massive Fe-oxide skarn. The oxide-rich material preferentially seeps laterally along silty layers and forms coronas on garnet (Fig. 8D). Photo was taken from the skarn immediately to the right of the box showing the location of Figure 5 on the map in Figure 4. (B) Close-up of garnet porphyroblasts in a silty layer. (C) Close-up of vesuvianite coronas on garnet porphyroblasts. Hammer head for scale. (D) Close-up of magnetite coronas on garnet porphyroblasts; this image is located close to the massive skarn zone.

ing fault scarp, where it is markedly lower than the upper contact on the western side. Since there does not seem to be a large fault within domain A, this implies an overall dip of ~25° to the upper intrusive contact. The upper sill contact on the NE-facing scarp is characterized by the development of contact-metamorphic calc-silicate assemblages in the silty dolostone beds (Fig. 8), with more massive marble in the purer carbonates. Garnet porphyroblasts commonly have vesuvianite overgrowths (Fig. 8C). The calc-silicate rocks are replaced by oxide-rich (80% magnetite + minor pyrite and chalcopyrite) skarns (Fig. 8A). The oxide-rich assemblages preferentially extend along-strike in silty layers, and magnetite coronas are developed on garnet porphyroblasts (Fig. 8D). Individual oxide-skarn pods extend along-strike for up to 30 m, can be up to 3–4 m thick, and are developed discontinuously all along this upper sill-limestone contact (Fig. 4).

The next domain to the SE (domain 3) is dominated by olivine-rich gabbro near the base and gabbro and diabase near the top, but contact relationships are not preserved. These gabbros represent either a downdropped block or a discordant magma conduit.

The next domain to the NE (domain B) is dominated by flat-bedded dolostone and limestone with silty interbeds. It is at the same altitude as gabbros of domain 3, and it is interpreted to represent a downdropped panel of roof material. Thin dikes are common along the southwestern trailing edges of domain B, and their morphology closely resembles that of the dikes on the SW edge of domain A.

A prominent ridge to the east (domains 4 and C) exposes the sill upper contact on both sides (foreground of Fig. 6A; Fig. 6D). The roof carbonates are brecciated and injected by dikes (Fig. 7B), suggesting that magma exploited mechanical weaknesses. Host rocks above sill contacts are intensely metamorphosed and replaced by calc-silicate and oxide + sulfide-rich skarns over tens of meters. Dike contacts are also decorated by zoned garnet-vesuvianite porphyroblasts. The sill contact breaches the surface of the limestone on the SW face (Fig. 6D), but it is at least 20 m lower on the east face of this ridge (Fig. 6A), implying westward-upward transgression of the intrusive contact.

Horst Block

In the high-standing Horst Block (Figs. 4 and 6A), the normal sill stratigraphy is well developed in the west (domain 5), with a concordant lower contact against carbonate rocks of the Jago Bay Formation (domain E). Metamorphosed, impure limestones to the east (domain F) appear to be downdropped along the same NNW-trending contact that separates domains A and 2 in the Main Block. The SW face of this ridge is characterized by lobate, scalloped, steeply east-dipping intrusive contacts between underlying sill (domain 6) and contact-metamorphosed dolostone. A narrow band of calc-silicate rocks with relict gabbroic textures separates limestone from fresher diabase to the east (domain 7). Meter-scale pods of oxide-rich skarn are developed in laminated carbonate rocks a few meters above the calc-silicate rocks. Domain 7 is com-

Geological Society of America Bulletin, published online on 6 February 2012 as doi:10.1130/B30450.1

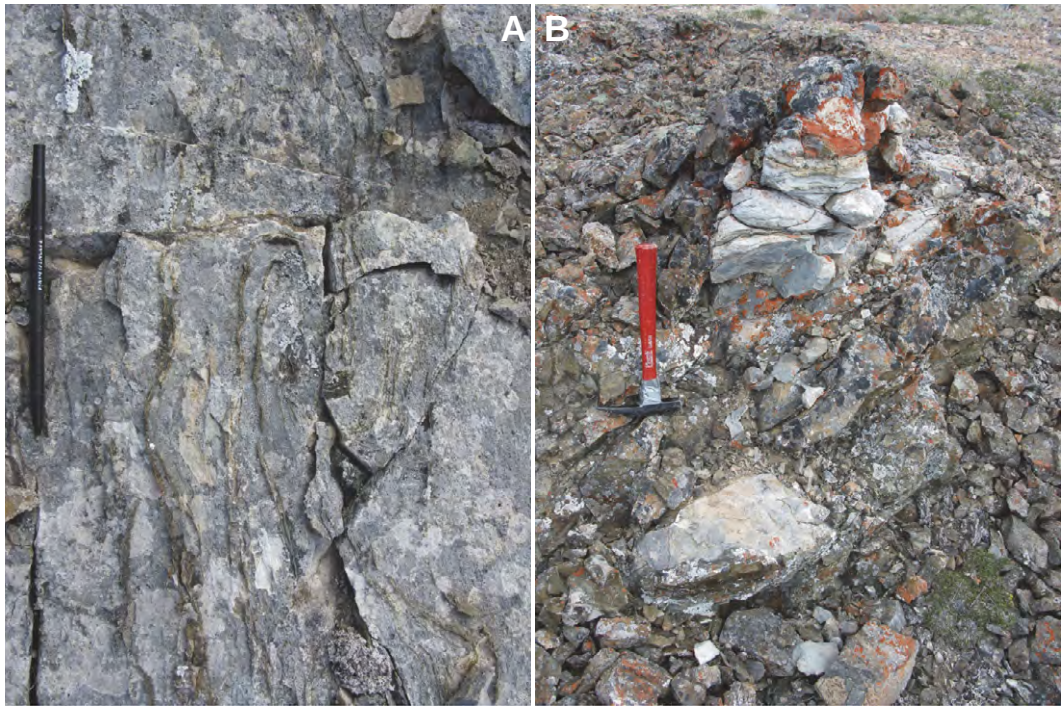

Figure 9. (A) Ductile fold in contact zone of limestone (domain G). The dominant bedding orientation is parallel to the pen and is nearly vertical here. An isoclinal closure is highlighted by the silty layers in the middle of the photo, implying ductile behavior. The sill contact is ~1 m to the left of the image. (B) Intrusive breccia at upper contact of sill, located close to photo in A.

posed of medium-grained gabbroic rocks, and neither the uppermost gabbro nor the olivine cumulate zone is exposed.

Northern Block

The rocks here are almost identical to the contact between domains 2 and A of the Main Block, and domains 6 and F of the Horst Block, and this is probably the northward extension of the same contact exposed at a different structural level. Rocks on the SW side of the contact (domain 8) are upper zone gabbroic rocks. The subhorizontal upper chilled margin against flat-bedded limestone (top left corner of Fig. 4) is preserved. The rocks on the NE side of the fault are mostly flat-bedded limestones (domain G). Near the domain 8-G contact, limestone is studded with dikelets, magmatic breccias (Fig. 9B), and small oxide-rich skarn zones. In many places, the contact zone is characterized by dikes and partly detached slivers of limestone up to 20 m long. The limestone nearest to the sill contact is intensely metamorphosed and appears to have been ductile, as attested by the presence of vertically dipping bedding and minor drag folds (Fig. 9A). This suggests that the limestone near the contact was sheared synchronously with magmatic emplacement.

DISCUSSION AND INTERPRETATION

The geological relationships described here suggest that in this part of Victoria Island, melt moved up-section along east-dipping faults, many of which correspond to prominent regional magnetic anomalies (Fig. 2B), suggesting that the melt-filled conduits may extend to some depth. It is not known if these are deep feeder dikes extending to the mantle, or if they simply represent anomalous thicknesses of basalt corresponding to up-section jogs. The dominant recorded motions and lithological offsets on many of these NNW-trending faults suggest they were east-dipping normal faults (~45°–70°), and the field evidence implies that the faults guided ascent of magma. It could instead be argued that the faulting is a consequence of sill emplacement (e.g., Pollard and Johnson, 1973; Thomson, 2007). However, theoretical arguments and experimental data (Rubin, 1995; Maaløe, 1998; Galland et al., 2008, 2009) imply that the propagation front of a dike or sill should be curved, and so structures resulting from sill propagation and inflation should also be curved. The straightness and lateral extent (up to 50 km) of these NNW-trending lineaments (Kiss and Oneschuk, 2010), together with the fact that all are parallel, suggest to us that these faults were not caused by sill inflation during horizontal propagation but were related to regional-scale tectonic extension and began to develop prior to the emplacement of the Franklin sills.

The most common emplacement pattern for Franklin sills is lateral propagation of magma parallel to bedding in the host rock. We can trace individual Franklin sills for tens of kilometers, with no obvious changes in thickness or stratigraphic level. Our field data, as discussed already, imply that sill propagation proceeded until a favorably dipping fault was encountered (Fig. 10A). Thereafter, lateral migration of melt halted because it was probably easier for melt to lift the roof and ascend the fault plane through this opening conduit. It seems inescapable that during inflation, the Franklin sills must either have lifted their roof strata, or depressed the floor strata, or both (Petford et al., 2000; Acocella and Rossetti, 2002). Seismic data (Hansen and Cartwright, 2006) and experiments (Acocella et al., 2004; Galland et al., 2008, 2009) suggest that in the absence of a preexisting structural control, the end points of roof uplift zones will be accommodated by reverse faults into which magmas could intrude (e.g., Fig. 10A). As pointed out already, the uniform and regionally extensive linearity of the NNW-trending normal faults on Victoria Island suggests to us that these faults developed prior to sill emplacement. If a propagating sill intercepts a fault that dips toward it, then sill inflation should lift the roof clear of the footwall (Fig. 10B). Since there is no fault-parallel slip, there would be no shear along the fault to generate observable structures recording reverse motion. With this type of geometry (Fig. 10B), sill inflation would widen the up-flow conduit, facilitating melt ascent to a higher stratigraphic level.

Field observations suggest the contact-metamorphic aureoles in the roof zone near the junctions between sills and dikes, and beneath the Uhuk Massif's westward extension, are wider than those that surround most of the dia-

Geological Society of America Bulletin, published online on 6 February 2012 as doi:10.1130/B30450.1

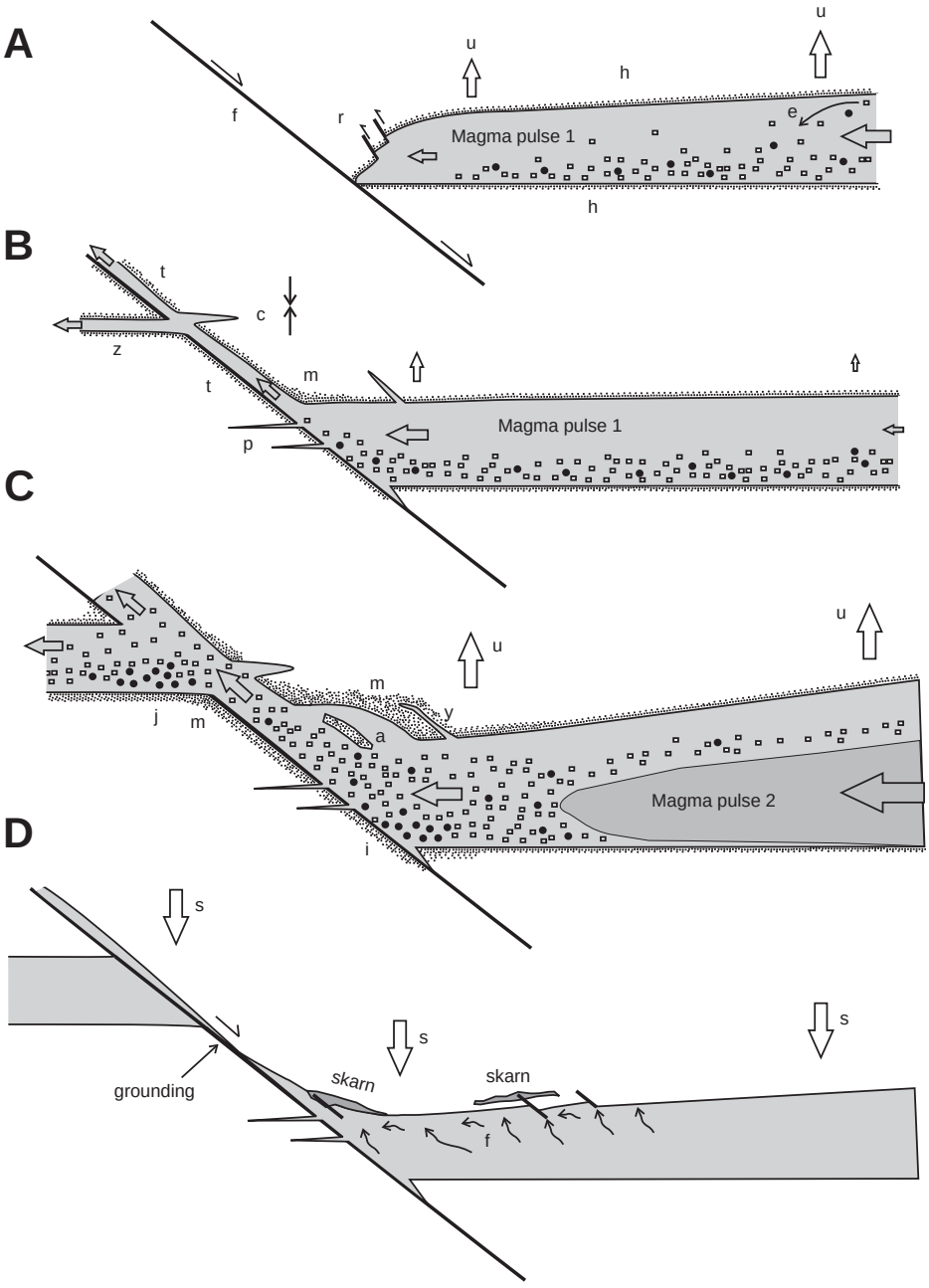

Figure 10. Cartoon showing possible scenario for ephemeral fault-mediated melt transfer, slurry emplacement, and possible metallogenetic consequences. (A) As magma spreads laterally parallel to bedding (open arrows), and the roof is raised (u), a compressional stress field is developed at the propagator tip (r). This represents a possible mechanism to develop reverse faults along which melt could jump up-section (Menand et al., 2008). Previously entrained or newly formed crystals (open boxes, mostly olivine + minor chromite) and immiscible sulfide (black circles) are deposited, forming a cumulate layer. The thermal aureole (h) is thin here. Eventually, the sill encounters a preexisting normal fault (f). (B) Magma preferentially ascends the fault, rather than continuing onward, although minor splays may develop in the footwall (p). The melt moves up the fault until a favorable horizon is reached (z), at which juncture a new sill begins to form. The newly nucleated sill preferentially transgresses in the footwall of the fault (z), because magmatic overpressure makes the hanging wall unfavorable (c). A wider metamorphic aureole is developed in the corner region (m). Because the transgressive conduit is narrow, cumulus crystals are unlikely to be entrained. (C) A new pulse of magma arrives (dark-gray arrow), remobilizing previously deposited, unconsolidated cumulates and sulfides. The new pulse increases the internal pressure, raising the roof (u). This widens the transgressive conduit, allowing large amounts of magma to ascend and enter the upper sill, and also allows remobilized cumulates and sulfides to be emplaced higher in the conduit system. Sulfides and cumulates would preferentially concentrate at the lower corner region where flow is disturbed (i) and at the hydraulic jump (j) where the upper sill is fed. Because of the enhanced magmatic flux through the conduit, the metamorphic aureoles in corner regions and around the conduit are widened (m). This is accentuated by dikes (y) in the roof zone that detach blocks (cf. Figs. 5, 6B, 7A, and 9B). Completely detached blocks rotate into subparallelism with the fault plane (a) as in the southern feeder dike (Fig. 3D). (D) When the magmatic overpressure associated with the new magma pulse wanes and decreases to less than the lithostatic load, the roof subsides (s). Roof subsidence would potentially be accommodated by expulsion of magma from the lower to the upper sill, continuing until the roof zone grounds against the footwall of the fault, as seen in the northern feeder dike. Alternatively, if the lower sill has largely crystallized prior to roof subsidence, then small amounts of fluid-enriched residual melt (f) may be expelled, to concentrate in favorable structural or porosity traps to form oxide-sulfide skarns (Uhuk Massif; Fig. 8A).

basic sills in the area. This inference needs to be confirmed with microscopic and other data, and to be compared with thermal models, but if correct, it implies that considerable volumes of magma may have passed through these channels (Huppert and Sparks, 1988; Holness and Humphreys, 2003).

The scenario for sill transgression outlined here has implications for the emplacement and remobilization of crystal slurries and magmatic sulfides. Late emplacement of olivine or pyroxene-rich slurries into previously developed sills is not uncommon (e.g., Simkin, 1967; Bédard et al., 1988; Husch, 1990; Larsen and Pedersen, 2000; Marsh, 2004; Gibb and Henderson, 2006;

Geological Society of America Bulletin, published online on 6 February 2012 as doi:10.1130/B30450.1

Bédard et al., 2007), and there are Nd isotopic data (Hulbert, 1998, unpublished report) suggesting that the olivine-enriched bases of some Franklin sills are not cumulates produced by local "in situ" crystallization, but represent late emplacement of isotopically distinct olivine slurries instead. Emplacement of crystal-charged slurries requires a period of crystallization and crystal concentration in a holding chamber, followed by remobilization of the crystal mush. Remobilization of immiscible Ni-sulfide accumulations is an economically important facet of the same problem. However, there are few constraints on the triggers or controls of slurry mobilization and emplacement. Inflation of a fault-terminated sill, as discussed here, represents a possible mechanism to modulate slurry emplacement (Fig. 10C).

In this model, a set of sills develops and begins to crystallize. If magmas are primitive (like some of the Franklin sills), olivine-rich cumulates would likely develop. Magmatic sulfides may also have formed and accumulated at the base of the largest, most primitive sills. Minute pentlandite-pyrrhotite globules occur in many olivine-rich Franklin sills (Bédard et al., 2009b), indicating that sulfide immiscibility occurred at some stage. We infer that the magma pressure in the Franklin conduit system increased markedly when new batches of magma arrived from the mantle (e.g., Lister and Kerr, 1991; Gerya and Burg, 2007). This could have led to rupture of the roof (e.g., Pollard and Johnson, 1973), or reactivation of preexisting faults, lifting the sill roof and opening the sloping conduit (fault), and allowing penetration of magma to higher levels. In its early stages, the dipping conduit would have been too narrow to allow large volumes of melt to ascend, and only small amounts of crystal-poor melt would have been able to seep out (Fig. 10B). Attempts to evacuate crystal-rich melts (or melt enriched in sulfide globules) would probably have clogged the channel, leading to a further buildup of magma pressure. We suggest that it was the sudden widening of ascent channels when the roof lifted in response to increases in magmatic pressure that allowed accumulated slurries to be evacuated in a catastrophic pulse, and that this could potentially also have remobilized early-formed sulfides (Fig. 10C). In terms of Ni-sulfide exploration (Naldrett et al., 1995; Li et al., 2001; Naldrett, 2005), the most favorable locations for deposit formation would be just below the junction with the transfer conduit ("I" in Fig. 10C, an entrapment zone), or where the fast-moving magma entered a more quiescent upper sill ("j" in Fig. 10C, hydraulic jump). Since the wide contact-metamorphic haloes are consistent with considerable magmatic throughflow, accumulations of sulfide could potentially be exposed to larger volumes of silicate melt as at Noril'sk, thus increasing the amount of melt seen by the deposited sulfides, and boosting platinum group element grades. The prominent magnetic lineaments at Uhuk and the southern feeder dike suggest that the conduit systems may be large, and that such lineaments may be favorable exploration targets.

At some stage, the magmatic pulse would wane, and so the pressure in the conduit system would decrease. When the magmatic pressure decreased to values less than the lithostatic load (1–4 km of metasedimentary rock, 1–2 km of congealed basaltic sills, and over 1 km of basaltic lava), the roof would have subsided (Fig. 10D) by expelling whatever magma remained in the lower sill. Roof subsidence may also have pressed out evolved, volatile-enriched residual melts enriched in precious and base metals from a near-rigid, crystal framework (filter-pressing). In the Uhuk Massif, the late oxide-sulfide skarns that overprint the contact-metamorphic aureole are developed all along the roof contact zone (Figs. 4 and 8). It seems reasonable to postulate that these skarns formed from late-magmatic or deuteric fluids pressed out from the underlying, partly crystallized, Fe-rich tholeiitic sills. We suggest that the fluids were focused by a sloping upper contact, guided by favorable structures (breccias, faults), and then ponded against a relatively "impermeable" meta-limestone cap. We are testing this hypothesis with geochemical and isotopic data.

As the hanging-wall panel descended, it would tend to close the dipping, dike-like conduit (Fig. 10D). An intermediate stage may be preserved in the northern feeder dike, where the lateral variation in dike thickness may indicate that subsidence of the roof rock was asymmetric, such that the southern edge became "grounded" against the footwall rocks, jamming the dike partly open (Fig. 3A). If the movement had been smoother and more orthogonal, the feeder dike might have been nearly obliterated, obscuring the record of this event. Thus, dike-like feeder systems developed along dipping faults may be ephemeral. They would widen during periods when the magmatic flux peaked and melts were overpressured, and close during waning stages, so as to become geophysically invisible and geologically negligible. Closure is unlikely to be complete, but if outcrop quality is poor, then the thin dikes and chilled margins that might remain may be missed, or be considered insignificant. Furthermore, anastomosing composite fault systems could excise or obliterate relics of a collapsed feeder dike.

This interpretation suggests a possible explanation for the rarity of dikes observed in some sill-dominated feeder systems. Fluctuations of magmatic pressure should lead to alternating phases of sill inflation and deflation as melt is transferred from lower to upper sills along fault-guided conduits. Subsidence of roof rock as magmatic pressure decreases would lead to deflation of the lower sills and close up many fault-dike conduits. The ephemeral nature of the steep conduits implies that fault-guided melt transfer zones might also exist elsewhere, but they have not been observed, either because exceptional exposures are required for their recognition, or because closure of the feeder dike-faults may have been virtually complete.

CONCLUSIONS

The sill-dominated feeder system for the Franklin event is characterized by fault-guided transfer zones that allowed magma to jump up-section to feed higher-level intrusions. The sill-dike junctions appear to be characterized by unusually wide and intense contact-metamorphic haloes, in part due to the development of skarn, possibly coupled with magmatic throughflow. The geometric constraints suggest that the conduits may have opened episodically when new magma pulses arrived from the mantle, generating magmatic overpressure. These events may also have been associated with remobilization of crystal slurries, and may also have played a role in localizing or enriching Ni-sulfide orebodies. In this and other systems, the conduits might be ephemeral, closing when magma pressure wanes. Roof subsidence during the deflation stage may press out evolved metal-rich fluids and play a role in generating mineralization.

ACKNOWLEDGMENTS

The manuscript was greatly improved by the constructive comments of Agust Gudmundsson, Olivier Galland, and Associate Editor Andrew Hynes. Thanks are due to Technical Field and Support Services of Natural Resources Canada (TFSS) for handling our equipment needs; to our support staff in Québec, Calgary, and Ottawa who helped with all the prefield contracting and travel arrangements; to Frank Kiss for getting the aeromagnetic maps to us in time; to the students and visiting scientists who participated in the mapping; to Discovery Mining and Expediting, the Ulukhaktok Development Corporation, and the Polar Continental Shelf Project for logistical support; to the pilots and mechanics of Borek Air, Summit Air, First Air, Héli-Transport, and Trinity, who got us there; to the Ulukhaktok Community Corporation, the Hamlet of Ulukhaktok, the Inuvialuit Land Administration, and the Olokhaktokmuit Hunters and Trappers Committee for access to the area and support personnel; to Sharon Brown and Susie Menogama, who made camp life a bowl of cherries; and especially to Nuna, who gave us great weather and kept us safe. This is Geological Survey of Canada (Earth Sciences Sector of Natural Resources Canada) contribution 20110030.

REFERENCES CITED

Acocella, V., and Rossetti, F., 2002, The role of extensional tectonics at different crustal levels on granite ascent and emplacement: An example from Tuscany (Italy): Tectonophysics, v. 354, p. 71–83, doi:10.1016/S0040-1951(02)00290-1.

Acocella, V., Funiciello, R., Marotta, E., Orsi, G., and de-Vita, S., 2004, The role of extensional structures on experimental calderas and resurgence: Journal of Volcanology and Geothermal Research, v. 129, p. 199–217, doi:10.1016/S0377-0273(03)00240-3.

Baragar, W.R.A., 1976, The Natkusiak Basalts, Victoria Island, District of Franklin, *in* Report of Activities: Geological Survey of Canada Paper 76–1A, p. 347–352.

Bédard, J.H., 1991, Cumulate recycling and crustal evolution in the Bay of Islands ophiolite: The Journal of Geology, v. 99, p. 225–249, doi:10.1086/629486.

Bédard, J.H., Francis, D.M., Hynes, A.J., and Nadeau, S., 1984, Fractionation in the feeder system at a Proterozoic rifted margin: Canadian Journal of Earth Sciences, v. 21, p. 489–499, doi:10.1139/e84-052.

Bédard, J.H., Sparks, R.S.J., Renner, R., Cheadle, M.J., and Hallworth, M.A., 1988, Peridotite sills and metasomatic gabbros in the Eastern Layered Series of the Rhum complex: Journal of the Geological Society of London, v. 25, p. 207224.

Bédard, J.H., Marsh, B.D., Hersum, T.G., Naslund, H.R., and Mukasa, S.B., 2007, Large-scale mechanical redistribution of orthopyroxene and plagioclase in the basement sill, Ferrar dolerites, McMurdo Dry Valleys, Antarctica: Petrological, mineral-chemical and field evidence for channelized movement of crystals and melt: Journal of Petrology, v. 48, p. 2289–2326, doi:10.1093/petrology/egm060.

Bédard, J.H., Leclerc, F., Harris, L., and Goulet, N., 2009a, Intra-sill magmatic evolution in the Cummings complex, Abitibi greenstone belt: Tholeiitic to calc-alkaline magmatism recorded in a subvolcanic conduit system: Lithos, v. 111, p. 47–71, doi:10.1016/j.lithos.2009.03.013.

Bédard, J.H., Naslund, H.R., Morgan, D., and Montjoie, R., 2009b, Geochemical and mineral-chemical systematics from a picritic Franklin sill on Victoria Island, N.W.T.; insights on internal fractionation processes [abs.], *in* Yellowknife Geoscience Forum Technical Program: Northwest Territories Geoscience Office, Canada.

Bryan, S.E., and Ernst, R.E., 2008, Revised definition of large igneous provinces (LIPs): Earth-Science Reviews, v. 86, p. 175–202, doi:10.1016/j.earscirev.2007.08.008.

Chevallier, L., and Woodford, A., 1999, Morph-tectonics and mechanism of emplacement of the dolerite rings and sills of the western Karoo, South Africa: South African Journal of Geology, v. 102, p. 43–54.

Cox, K.G., 1980, A model for flood basalt vulcanism: Journal of Petrology, v. 21, p. 629–650.

Denyszyn, S.W., Davis, D.W., and Halls, H.C., 2009, Paleomagnetism and U-Pb geochronology of the Clarence Head dykes, Arctic Canada: Orthogonal emplacement of mafic dykes in a large igneous province: Canadian Journal of Earth Sciences, v. 46, p. 155–167, doi:10.1139/E09-011.

Dick, H.J.B., Natland, J.H., Alt, J.C., Bach, W., Bideau, D., Gee, J.S., Haggas, S., Hertogen, J.G.H., Hirth, G., Holm, P.M., Ildefonse, B., Iturrino, G.J., John, B.E., Kelley, D.S., Kikawa, E., Kingdon, A., LeRoux, P.J., Maeda, J., Meyer, P.S., Miller, D.J., Naslund, H.R., Niu, Y.L., Robinson, P.T., Snow, J., Stephen, R.A., Trimby, P.W., Worm, H.U., and Yoshinobu, A., 2000, A long in situ section of the lower ocean crust: Results of ODP Leg 176 drilling at the Southwest Indian Ridge: Earth and Planetary Science Letters, v. 179, p. 31–51, doi:10.1016/S0012-821X(00)00102-3.

Dostal, J., and Dupuy, C., 1984, Geochemistry of the North Mountain Basalts (Nova Scotia, Canada): Chemical Geology, v. 45, p. 245–261, doi:10.1016/0009-2541(84)90040-8.

Dostal, J., Baragar, W.R.A., and Dupuy, C., 1986, Petrogenesis of the Natkusiak continental basalts, Victoria Island, Northwest Territories, Canada: Canadian Journal of Earth Sciences, v. 23, p. 622–632, doi:10.1139/e86-064.

Dupuy, C., Michard, A., Dostal, J., Dautel, D., and Baragar, W.R.A., 1995, Isotope and trace-element geochemistry of Proterozoic Natkusiak flood basalts from the northwestern Canadian Shield: Chemical Geology, v. 120, p. 15–25, doi:10.1016/0009-2541(94)00128-U.

Durbano, A., Pratt, B.R., Hadlari, T., and Dewing, K., 2010, Sedimentology and stratigraphy of the Lower Clastic Unit of the Cambrian, Northwest Victoria Island, *in* 38th Annual Yellowknife Geoscience Forum, Abstracts Volume: Northwest Territories Geoscience Office, p. 73–74.

Elliot, D.H., and Fleming, T.H., 2004, Occurrence and dispersal of magmas in the Jurassic Ferrar large igneous province, Antarctica: Gondwana Research, v. 7, p. 223–237, doi:10.1016/S1342-937X(05)70322-1.

Ernst, R.E., Buchan, K.L., and Palmer, H.C., 1995, Giant radiating dyke swarms: Characteristics, distribution and geotectonic applications, *in* Baer, G., and Heimann, A., eds., Physics and Chemistry of Dykes: Rotterdam, Netherlands, Balkema, p. 3–21.

Fahrig, W.F., 1987, The tectonic settings of continental mafic dyke swarms: Failed arm and early passive margin, *in* Halls, H.C., and Fahrig, W.F., eds., Mafic Dyke Swarms: Geological Association of Canada Special Paper 34, p. 331–348.

Fialko, Y., 2001, On origin of near-axis volcanism and faulting at fast spreading mid-ocean ridges: Earth and Planetary Science Letters, v. 190, p. 31–39, doi:10.1016/S0012-821X(01)00376-4.

Francis, E.H., and Walker, B.H., 1986, Emplacement of alkali-dolerite sills relative to extrusive volcanism and sedimentary basins in the Carboniferous of Fife, Scotland: Transactions of the Royal Society of Edinburgh, v. 77, p. 309–323.

Galerne, C.Y., Neumann, E.R., and Planke, S., 2008, Emplacement mechanisms of sill complexes: Information from the geochemical architecture of the Golden Valley Sill Complex, South Africa: Journal of Volcanology and Geothermal Research, v. 177, p. 425–440, doi:10.1016/j.jvolgeores.2008.06.004.

Galland, O., Cobbold, P.R., Hallot, E., and d'Ars, J.D., 2008, Magma-controlled tectonics in compressional settings: Insights from geological examples and experimental modelling: Bollettino della Societa Geologica Italiana, v. 127, p. 205–208.

Galland, O., Planke, S., Neumann, E.R., and Malthe-Sørenssen, A., 2009, Experimental modelling of shallow magma emplacement: Application to saucer-shaped intrusions: Earth and Planetary Science Letters, v. 277, p. 373–383, doi:10.1016/j.epsl.2008.11.003.

Gerya, T.V., and Burg, J.P., 2007, Intrusion of ultramafic magmatic bodies into the continental crust: Numerical simulation: Physics of the Earth and Planetary Interiors, v. 160, p. 124–142, doi:10.1016/j.pepi.2006.10.004.

Gibb, F.G.F., and Henderson, C.M.B., 2006, Chemistry of the Shiant Isles Main Sill, NW Scotland, and wider implications for the petrogenesis of mafic sills: Journal of Petrology, v. 47, p. 191–230, doi:10.1093/petrology/egi072.

Gudmundsson, A., 2011, Deflection of dykes into sills at discontinuities and magma-chamber formation: Tectonophysics, v. 500, p. 50–64, doi:10.1016/j.tecto.2009.10.015.

Gudmundsson, A., and Brenner, S.L., 2001, How hydrofractures become arrested: Terra Nova, v. 13, p. 456–462, doi:10.1046/j.1365-3121.2001.00380.x.

Gudmundsson, A., Friese, N., Galindo, I., and Philipp, S.L., 2008, Dike-induced reverse faulting in a graben: Geology, v. 36, p. 123–126, doi:10.1130/G24185A.1.

Hadlari, T., and Bédard, J.H., 2008, Reconnaissance fieldwork on Cambrian siliciclastic rocks, Victoria island, NT, *in* Yellowknife Geoscience Forum, Abstract Volume: Northwest Territories Geoscience Office.

Hansen, D.M., and Cartwright, J., 2006, Saucer-shaped sill with lobate morphology revealed by 3D seismic data: Implications for resolving a shallow-level sill emplacement mechanism: Journal of the Geological Society of London, v. 163, p. 509–523, doi:10.1144/0016-764905-073.

Hawkesworth, C.J., Lightfoot, P.C., Fedorenko, V.A., Blake, S., Naldrett, A.J., Doherty, W., and Gorbachev, N.S., 1995, Magma differentiation and mineralisation in the Siberian continental flood basalts: Lithos, v. 34, p. 61–88.

Heaman, L.M., LeCheminant, A.N., and Rainbird, R.H., 1992, Nature and timing of Franklin igneous events, Canada: Implications for a Late Proterozoic mantle plume and the break-up of Laurentia: Earth and Planetary Science Letters, v. 109, p. 117–131, doi:10.1016/0012-821X(92)90078-A.

Holness, M.B., and Humphreys, M.C.S., 2003, The Traigh Bhŕan na Sgůrra Sill, Isle of Mull: Flow localization in a major magma conduit: Journal of Petrology, v. 44, p. 1961–1976, doi:10.1093/petrology/egg066.

Hooper, P.R., and Hawkesworth, C.J., 1993, Isotopic and geochemical constraints on the origin and evolution of the Columbia River basalt: Journal of Petrology, v. 34, p. 1203–1246.

Hulbert, L., 1998, Mineralogical and Chemostratigraphic Investigation of Ultramafic-Bearing Sills on Ground Held by Aber Resources in the Wynniatt Bay–Glenelg Bay–Kilian Lake Area, Victoria Island: Northwest Territories Geoscience Office, 41 p.

Hulbert, L.J., Rainbird, R.W., Jefferson, C.W., and Friske, P., 2005, Map of mafic and ultramafic bodies related to the Franklin magmatic event, Minto Inlier, Victoria Island: Geological Survey of Canada Open-File Map 4928, map sheet scale 1:1,000,000 + CD-ROM.

Huppert, H.E., and Sparks, R.S.J., 1988, The generation of granitic magmas by intrusion of basalt into continental crust: Journal of Petrology, v. 29, p. 599–624.

Husch, J.M., 1990, Palisades sill: Origin of the olivine zone by separate magmatic injection rather than gravity settling: Geology, v. 18, p. 699–702, doi:10.1130/0091-7613(1990)018<0699:PSOOTO>2.3.CO;2.

Hutton, D.H.W., and Ingram, G.M., 1992, The Great Tonalite Sill of southeastern Alaska and British Columbia—Emplacement into an active contractional high angle reverse shear zone: Transactions of the Royal Society of Edinburgh–Earth Sciences, v. 83, p. 383–386.

Jefferson, C.W., 1985, Uppermost Shaler Group and its contact with the Natkusiak Basalts, Victoria Island, District of Franklin, *in* Current Research Part A: Geological Survey of Canada Paper 85–1A, p. 103–110.

Jefferson, C.W., Nelson, W.E., Kirkham, R.V., Reedman, J.H., and Scoates, R.F.J., 1985, Geology and copper occurrences of the Natkusiak Basalts, Victoria Island, District of Franklin, *in* Current Research Part A: Geological Survey of Canada Paper 85–1A, p. 203–214.

Jefferson, C.W., Hulbert, L.J., Rainbird, R.H., Hall, G.E.M., Gregoire, D.C., and Grinenko, L.I., 1994, Mineral Resource Assessment of the Neoproterozoic Franklin Igneous Events of Arctic Canada: Comparison with the Permo-Triassic Noril'sk-Talnakh Ni-Cu-PGE Deposits of Russia: Geological Survey of Canada Open-File Report 2789, 48 p.

Jourdan, F., Bertrand, H., Schärer, U., Blichert-Toft, J., Féraud, G., and Kampunzu, A.B., 2007, Major and trace element and Sr, Nd, Hf and Pb isotope compositions of the Karoo large igneous province, Botswana-Zimbabwe: Lithosphere vs. mantle plume contribution: Journal of Petrology, v. 48, p. 1043–1077, doi:10.1093/petrology/egm010.

Kerr, A.C., Tarney, J., Nivia, A., Marriner, G.F., and Saunders, A.D., 1998, The internal structure of oceanic plateaus: Inferences from obducted Cretaceous terranes in western Colombia and the Caribbean: Tectonophysics, v. 292, p. 173–188, doi:10.1016/S0040-1951(98)00067-5.

Kiss, F., and Oneschuk, D., 2010, First Vertical Derivative of the Magnetic Field, Minto Inlier Aeromagnetic Survey, Victoria Island, NTS 87 G/SE and Parts of 87 G/NW, 88 B/SE and 88 B/SW, Northwest Territories: Geological Survey of Canada Open-File Map 6705, scale 1:100,000.

Larsen, L.M., and Pedersen, A.K., 2000, Processes in high-Mg, high-*T* magmas: Evidence from olivine, chromite and glass in Palaeogene picrites from West Greenland: Journal of Petrology, v. 41, p. 1071–1098, doi:10.1093/petrology/41.7.1071.

Larsen, L.M., and Pedersen, A.K., 2009, Petrology of the Paleocene picrites and flood basalts on Disko and Nuussuaq, West Greenland: Journal of Petrology, v. 50, p. 1667–1711, doi:10.1093/petrology/egp048.

Li, C., Naldrett, A.J., and Ripley, E.M., 2001, Critical factors for the formation of a nickel-copper deposit in an

evolved magma system: Lessons from a comparison of the Pants Lake and Voisey's Bay sulfide occurrences in Labrador, Canada: Mineralium Deposita, v. 36, p. 85–92, doi:10.1007/s001260050288.

Lissenberg, C.J., Bédard, J.H., and van Staal, C.R., 2004, The structure and geochemistry of the gabbro zone of the Annieopsquotch ophiolite, Newfoundland: Implications for lower crustal accretion at spreading ridges: Earth and Planetary Science Letters, v. 229, p. 105–123, doi:10.1016/j.epsl.2004.10.029.

Lister, J.R., and Kerr, R.C., 1991, Fluid-mechanical models of crack propagation and their application to magma transport in dykes: Journal of Geophysical Research, v. 96, p. 10,049–10,077, doi:10.1029/91JB00600.

Maaløe, S., 1998, Shape of ascending feeder dikes, and ascent modes of magma: Journal of Volcanology and Geothermal Research, v. 81, p. 207–214, doi:10.1016/S0377-0273(98)00008-0.

Malthe-Sørenssen, A., Planke, S., Svensen, H., and Jamveit, B., 2004, Formation of saucer-shaped sills, *in* Breitkreuz, C., and Petford, N., eds., Physical Geology of High-Level Magmatic Systems: Geological Society of London Special Publication 234, p. 215–277.

Marsh, B.A., 2004, Magmatic mush column Rosetta Stone: The McMurdo Dry Valleys of Antarctica: Eos (Transactions, American Geophysical Union), v. 85, no. 47, p. 497, doi:10.1029/2004EO470001.

May, P.R., 1971, Pattern of Triassic-Jurassic diabase dikes around the North Atlantic in the context of pre-drift positions of the continents: Geological Society of America Bulletin, v. 82, p. 1285–1292, doi:10.1130/0016-7606(1971)82[1285:POTDDA]2.0.CO;2.

McHone, J.G., Anderson, D.L., Beutel, E.K., and Fialko, Y.A., 2005, Giant dikes, rifts, flood basalts, and plate tectonics: A contention of mantle models, *in* Foulger, G.R., Natland, J.H., and Anderson, D.L., eds., Plates, Plumes and Paradigms: Geological Society of America Special Paper 388, p. 401–420.

Menand, T., 2008, The mechanics and dynamics of sills in layered elastic rocks and their implications for the growth of laccoliths and other igneous complexes: Earth and Planetary Science Letters, v. 267, p. 93–99, doi:10.1016/j.epsl.2007.11.043.

Naldrett, A.J., 2005, A history of our understanding of magmatic Ni-Cu sulfide deposits: Canadian Mineralogist, v. 43, p. 2069–2098, doi:10.2113/gscanmin.43.6.2069.

Naldrett, A.J., Fedorenko, V.A., Lightfoot, P.C., Kunilov, V.I., Gorbachev, N.S., Doherty, W., and Johan, Z., 1995, Ni-Cu-PGE deposits of Noril'sk region, Siberia: Their formation in conduits for flood basalt volcanism: Transactions of the Institution of Mining and Metallurgy, Section B, Applied Earth Science, v. 104, p. B18–B36.

Paterson, S.R., and Tobisch, O.T., 1992, Rates of processes in magmatic arcs—Implications for the timing and nature of pluton emplacement and wall rock deformation: Journal of Structural Geology, v. 14, p. 291–300, doi:10.1016/0191-8141(92)90087-D.

Pehrsson, S.J., and Buchan, K.L., 1999, Borden dykes of Baffin Island, Northwest Territories: A Franklin U-Pb baddeleyite age and a paleomagnetic reinterpretation: Canadian Journal of Earth Sciences, v. 36, p. 65–73, doi:10.1139/e98-091.

Petford, N., Cruden, A.R., McCaffrey, K.J.W., and Vigneresse, J.L., 2000, Granite magma formation, transport and emplacement in the Earth's crust: Nature, v. 408, p. 669–673, doi:10.1038/35047000.

Pollard, D.D., and Johnson, A.M., 1973, Mechanics of growth of some laccolithic intrusions in the Henry Mountains, Utah: II. Bending and failure of overburden layers and sill formation: Tectonophysics, v. 18, p. 311–354, doi:10.1016/0040-1951(73)90051-6.

Pollard, D.D., and Segall, P., 1987, Theoretical displacements and stresses near fractures in rock: With applications to faults, joints, veins, dikes, and solution surfaces, *in* Atkinson, B.K., ed., Fracture Mechanics of Rock: London, Academic Press, p. 277–349.

Polteau, S., Mazzini, A., Galland, O., Planke, S., and Malthe-Sørenssen, A., 2008, Saucer-shaped intrusions: Occurrences, emplacement and implications: Earth and Planetary Science Letters, v. 266, p. 195–204, doi:10.1016/j.epsl.2007.11.015.

Rainbird, R.H., 1993, The sedimentary record of mantle plume uplift preceding eruption of the Neoproterozoic Natkusiak flood basalt: The Journal of Geology, v. 101, p. 305–318, doi:10.1086/648225.

Rainbird, R.H., Hodgson, D.A., Darch, W., and Lustwerk, R., 1994, Bedrock and surficial geology of northeast Minto Inlier, Victoria Island, NTS 76B7: Geological Survey of Canada Open-File Map 2781, scale 1:50,000.

Rainbird, R.H., LeCheminant, A.N., and Lawyer, J.I., 1996, The Duke of York and related Neoproterozoic inliers of southern Victoria Island, District of Franklin, Northwest Territories, *in* Current Research: Geological Survey of Canada Paper 1996-E, p. 125–134.

Rainbird, R.H., Bédard, J., Dewing, K., Hadlari, T., Kiss, Miles, W. Ootes, L., 2010, Victoria Island GEM Project: Results from 2010 field mapping and thematic studies, *in* Palmer, E. (compiler), 38th Annual Yellowknife Geoscience Forum, Abstracts Volume, p. 50–51.

Rocchi, S., Mazzotti, A., Marroni, M., Pandolfi, L., Constantini, P., Giuseppe, B., Biase, D., Federici, F., and Lo, P.G., 2007, Detection of Miocene saucer-shaped sills (offshore Senegal) via integrated interpretation of seismic, magnetic and gravity data: Terra Nova, v. 19, p. 232–239, doi:10.1111/j.1365-3121.2007.00740.x.

Rubin, A.M., 1995, Propagation of magma-filled cracks: Annual Review of Earth and Planetary Sciences, v. 23, p. 287–336, doi:10.1146/annurev.ea.23.050195.001443.

Shellnutt, J.G., Dostal, J., and Keppie, J.D., 2004, Petrogenesis of the 723 Ma Coronation sills, Amundsen basin, Arctic Canada: Implications for the break-up of Rodinia: Precambrian Research, v. 129, p. 309–324, doi:10.1016/j.precamres.2003.10.006.

Simkin, T., 1967, Flow differentiation in the picritic sills of North Skye, *in* Wyllie, P.J., ed., Ultramafic and Related Rocks: Hoboken, New Jersey, John Wiley, p. 64–69.

Sykes, L.R., 1978, Intraplate seismicity, reactivation of preexisting zones of weakness, alkaline magmatism, and other tectonism predating continental fragmentation: Reviews of Geophysics and Space Physics, v. 16, p. 621–688, doi:10.1029/RG016i004p00621.

Thomson, K., 2007, Determining magma flow in sills, dykes and laccoliths and their implications for sill emplacement mechanisms: Bulletin of Volcanology, v. 70, p. 183–201, doi:10.1007/s00445-007-0131-8.

Thomson, K., and Hutton, D., 2004, Geometry and growth of sill complexes: Insights using 3D seismic from the North Rockall Trough: Bulletin of Volcanology, v. 66, p. 364–375, doi:10.1007/s00445-003-0320-z.

Thorsteinsson, R., and Tozer, E.T., 1962, Banks, Victoria and Stefansson Islands, Arctic Archipelago: Geological Survey of Canada Memoir 330, 85 p.

Vigneresse, J.L., Tikoff, B., and Ameglio, L., 1999, Modification of the regional stress field by magma intrusion and formation of tabular granitic plutons: Tectonophysics, v. 302, p. 203–224, doi:10.1016/S0040-1951(98)00285-6.

Watanabe, T., Koyaguchi, T., and Seno, T., 1999, Tectonic stress controls on ascent and emplacement of magmas: Journal of Volcanology and Geothermal Research, v. 91, p. 65–78, doi:10.1016/S0377-0273(99)00054-2.

White, R.S., Smith, L.K., Roberts, A.W., Christie, P.A.F., Kusznir, N.J., and the iSIMM Team, 2008, Lower-crustal intrusion on the North Atlantic continental margin: Nature, v. 452, p. 460–464, doi:10.1038/nature06687.

Young, G.M., 1981, The Amundson Embayment, Northwest Territories: Relevance to the Upper Proterozoic evolution of North America, *in* Campbell, F.H.A., ed., Proterozoic Basins of Canada: Geological Survey of Canada Paper 81–10, p. 203–211.

Science Editor: A. Hope Jahren
Associate Editor: Andrew Hynes

Manuscript Received 17 November 2010
Revised Manuscript Received 21 April 2011
Manuscript Accepted 19 May 2011

Printed in the USA

Journal of
METAMORPHIC GEOLOGY

J. metamorphic Geol., 2013, **31,** 205–220 doi:10.1111/jmg.12015

Short-duration contact metamorphism of calcareous sedimentary rocks by Neoproterozoic Franklin gabbro sills and dykes on Victoria Island, Canada

P. I. NABELEK,[1] J. H. BÉDARD,[2] M. HRYCIUK[3] AND B. HAYES[4]
[1]*Department of Geological Sciences, University of Missouri, Columbia, MO 65211, USA (nabelekp@missouri.edu)*
[2]*Geological Survey of Canada, 490, rue de la Couronne, Quebec City, QC G1K9A9, Canada*
[3]*Department of Earth and Planetary Sciences, McGill University, 3450 University, St. Montreal, QC H3A 2A7, Canada*
[4]*School of Earth and Ocean Sciences, Cardiff University, Cardiff, CF10 3AT Wales, UK*

ABSTRACT This contribution addresses contact metamorphism and fluid flow in calcareous rocks of the Neoproterozoic Shaler Supergroup on Victoria Island, Arctic Canada. These processes occurred due to intrusion of gabbroic sills and dykes at *c.* 720 Ma during the Franklin magmatic event, which was associated with the break-up of Rodinia. The intrusive sheets (sills and dykes) are a few metres to ~50 m thick. Metasedimentary rocks were examined in three locations with very good exposures of vertical dykes feeding horizontal sills, the Northern Feeder Dyke (NFD) complex, the Southern Feeder Dyke (SFD) complex and the Uhuk Massif. In the NFD and SFD complexes, protoliths were limestones and dolostones with minor silicates, and at the Uhuk Massif, the protoliths were silty dolostones. At the time of magma emplacement, these locations were at depths of 1–4 km. The widths of contact aureoles are only several decametres wide, commensurate with thicknesses of the dykes and sills. Splays of tremolite mark incipient metamorphism. Highest grade rocks in the NFD and SFD complexes contain the prograde assemblage diopside + phlogopite whereas at Uhuk they contain the assemblage vesuvianite + garnet + diopside. The assemblages are successfully modelled with T–$X(CO_2)^{fluid}$ pseudosections that suggest achievement of CO_2-rich fluid compositions due to early decarbonation reactions, followed by influx of aqueous fluids after peak metamorphism. Rapid heating of host rocks and short near-peak temperature intervals are demonstrated by the prevalent morphology of diopside as radial splays of acicular crystals that appear to pseudomorph tremolite and by incomplete recrystallization of calcite in marbles. Calcsilicates in the roof of one sill at Uhuk experienced metasomatic influx of Fe that is evidenced by nearly pure andradite rims on grossular garnet. Vesuvianite, which overgrew the grossular portions of garnet, also contains ferric iron. Vesuvianite was partially consumed during retrograde growth of serpentine and andradite. The occurrence of serpentine in high-grade portions of aureoles is consistent with eventual levelling-off of temperatures between 350 and 400 °C, an inference that is supported by modelled conductive heat transfer from the cooling magma sheets. Focused fluid flow near intrusion-wall rock contacts is demonstrated by narrow zones of anomalously low $\delta^{13}C$ and $\delta^{18}O$ values of carbonate minerals. Although the up to 5‰ decrease of both $\delta^{13}C$ and $\delta^{18}O$ values from sedimentary values is much smaller than is typical for calcsilicate aureoles around large plutons, it is greater than what could have been achieved by decarbonation alone. The decrease in $\delta^{13}C$ is attributed to fluid-mediated exchange with organic low-^{13}C carbon that is dispersed through the unmetamorphosed rocks and the decrease in $\delta^{18}O$ is attributed to fluid-mediated isotopic exchange with the gabbroic intrusive sheets. This study shows that when gabbroic sills and dykes intrude a sedimentary basin, (i) contact aureoles are likely to be narrow, only on the scale of several decametres; (ii) short high-temperature regimes prevent achievement of equilibrium metamorphic textures; and (iii) T–$X(CO_2)^{fluid}$ paths in calcareous contact aureoles are likely to be complex, reflecting a transition from prograde decarbonation reactions to influx of aqueous fluids during cooling.

Key words: contact metamorphism; fluid flow; gabbroic sills; stable isotopes; Victoria Island.

INTRODUCTION

A consequence of magma intrusion into the upper crust is heat transfer to the surrounding rocks and generation of hydrothermal systems. Most previous studies of contact metamorphic systems have focused on aureoles that surround large plutons, where hydrothermal systems can operate for tens of thousands of years or much longer, depending on sizes of plutons and durations of magmatic system (Norton &

Taylor, 1979; Cathles, 1981; Norton, 1984; Fournier, 1989; Cook *et al.*, 1997; Cui *et al.*, 2001, 2002; Nabelek, 2009; Nabelek & Morgan, 2012). On the other hand, metamorphism by individual, tens of metres thick sheet intrusions (dykes and sills) occurs only on short time scales, with near-peak temperatures lasting only tens to hundreds of years, depending on the distance from an intrusion (Nabelek *et al.*, 2012). On these time scales, disequilibrium metamorphic features, including heterogeneous metamorphic textures, can be expected. However, in a large igneous province where magmatism can last for millions of years, hydrothermal systems surrounding sills and dykes can potentially exist on time scales that are orders of magnitude longer than individual heat pulses from invading sheet intrusions. Therefore, retrograde hydrothermal features can potentially develop and be preserved in metamorphosed rocks.

The purpose of this contribution is to describe short-duration metamorphism that was driven by emplacement of mafic sills and dykes into the sedimentary rocks of the Neoproterozoic Shaler Supergroup, which is exposed within the Minto Inlier in central Victoria Island, Arctic Canada (Fig. 1). The Shaler Supergroup was deposited into a shallow epeiric sea, referred to as the Amundsen Basin (Rainbird *et al.*, 1996). After lithification, strata were invaded *c.* 720 Ma ago by gabbro dykes and sills and were overlain by Natkusiak flood basalts during the Franklin magmatic event (Dostal *et al.*, 1986; Heaman *et al.*, 1992). The Franklin magmatic event is widespread across the Arctic region and can be correlated with mafic magmatism in Greenland and Siberia. It is interpreted as being related to the break-up of Rodinia (Heaman *et al.*, 1992). Shallow marine limestones and dolostones, which are interbedded with restricted-basin evaporites in the upper part of the stratigraphic section, dominate the Shaler Supergroup (Rainbird *et al.*, 1994, 1996). Subordinate units include sandstones and organic-rich shales, all of which were invaded by the sills. This contribution focuses on three separate localities within the Minto Inlier where the local magmatic plumbing systems are better understood (Bédard *et al.*, 2012). The localities contain remnant, fault-guided feeder dykes that fed prominent sills. These localities present an opportunity to examine metamorphism caused by invasion of mafic sheet intrusions in a large igneous province.

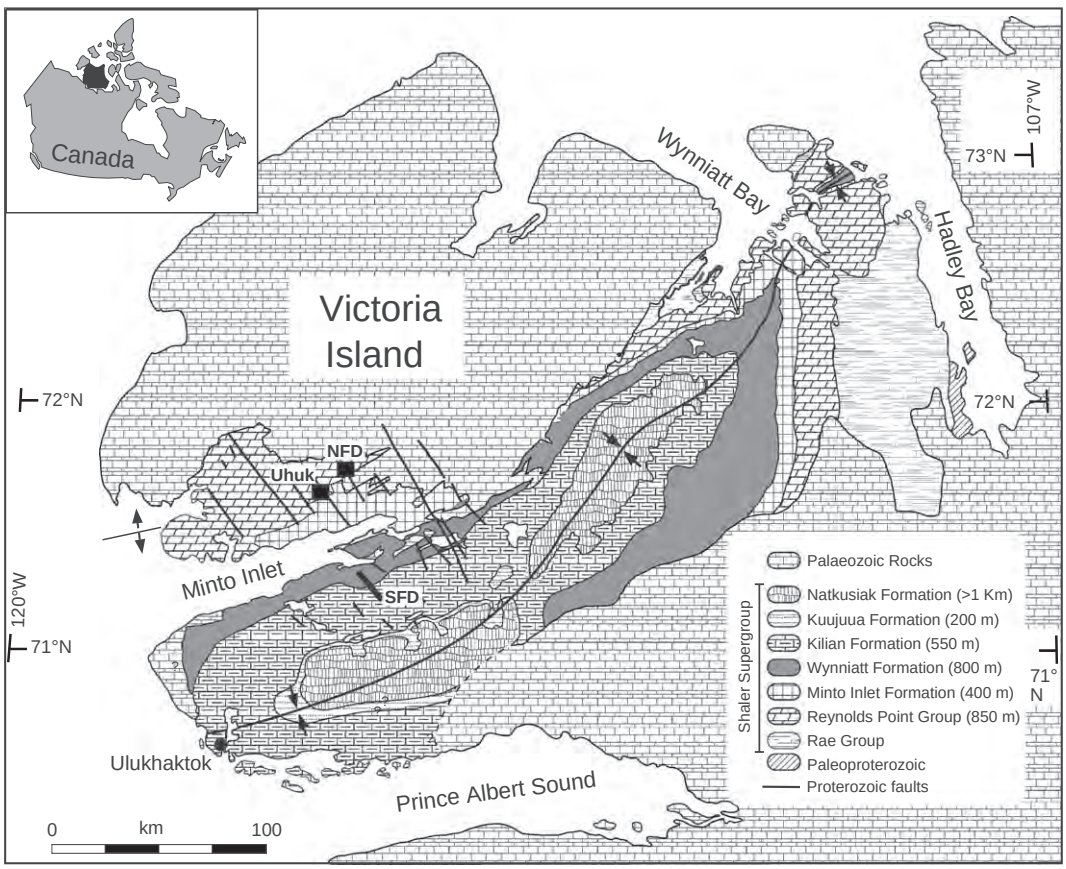

Fig. 1. Geological map of Victoria Island showing the major units of the Shaler Supergroup and the overlying Palaeozoic rocks (after Hulbert *et al.*, 2005; Bédard *et al.*, 2012). Heavy northwest-trending lines show Proterozoic vertical faults that have guided emplacement of sill-feeding dykes (not shown) into the Shaler Supergroup.

Metamorphism of the calcareous rocks and compositions of attending fluids are evaluated by employing calculated pseudosections and by stable isotope compositions of carbonate minerals. The data provide information on the development of mineral assemblages and the textural equilibration in contact aureoles of the gabbroic intrusive sheets, on the heat flow surrounding the crystallizing melts, and on the duration of related hydrothermal systems.

GEOLOGICAL SETTING

The Shaler Supergroup developed an open anticlinal–synclinal structure with shallowly plunging axes trending to the east–northeast (Fig. 1). The Supergroup is dominated by shallow-water marine carbonates and siliciclastic rocks with subordinate restricted-basin sulphate evaporites (Rainbird, 1993; Rainbird *et al*., 1996). In the study area, around Minto Inlet, the oldest unit is the Reynolds Point Group, which is dominated by carbonates, except near the top where it is more silty. Overlying this group is the Minto Inlet Formation, which contains thick, gypsum-dominated evaporites interbedded with carbonates. To the south of and overlying the Minto Inlet Formation are thick exposures of shallow marine carbonate rocks and deeper marine shales of the Wynniatt Formation. Overlying the Wynniatt Formation is the Kilian Formation, which includes interbedded carbonates, siliciclastics and sulphate evaporites. The top of the sedimentary sequence is the quartzarenite-dominated Kuujjua Formation. The sedimentary rocks are overlain conformably to uncomformably by the Natkusiak flood basalts. Cambrian to Devonian platform rocks uncomformably overlay the Natkusiak flood basalts.

The three areas in which contact metamorphism was examined in detail include: (i) the Northern Feeder Dyke (NFD) complex; (ii) the Southern Feeder Dyke (SFD) complex; and (iii) the Uhuk Massif (Fig. 1). Magmatism in all three areas was localized by northwest-trending Proterozoic faults. The NFD complex (Fig. 2a) occurs within the Boot Inlet Formation of the Reynolds Point Group (Rainbird *et al*., 1994, 1996). The formation is mostly a limestone, but the proportion of clay increases upwards. The complex includes a lower diabase sill (>20 m thick) that terminates to the SW against limestones on the footwall of one of the Proterozoic faults. A subvertical feeder dyke trends from this sill towards a younger, $\sim$50 m thick sill that caps the mesa at this locality (Bédard *et al*., 2012). Upslope from the lower sill there are windows with exposures of the apparently quite uneven upper surface of this particular sill. The stratigraphic distance between the two sills is at least 50 m, based on the current elevation difference between the sill windows and the upper sill. Bédard *et al*. (2012) showed that the exposed fault-guided dyke might have served as a conduit for upflowing magma. Anisotropy of magnetic susceptibility data, indicating a steep palaeodip of the magnetic lineation, is consistent with this interpretation (MacDonald *et al*., 2012). The palaeodepth of the NFD complex is estimated to have been 3–4 km based on the stratigraphy. Samples were collected with the aim of determining the 3D structure of metamorphism, extending from the roof of the lower sill at its lower exposure and the sill windows toward the base of the mesa-capping upper sill. Samples were also collected across the feeder dyke, and along several traverses perpendicular to the feeder dyke.

Northwest-trending dykes characterize the SFD complex (Fig. 2). Its palaeodepth during metamorphism is estimated to have been 1–2 km (Bédard *et al*., 2012). Metamorphism is discussed here for zones A and D of the complex. Zone D is $\sim$6 km to the northwest (downsection) of zone A. The dyke–sill system exposed in the intervening zones B and C is less well preserved. Along the trend of these zones is a set of prominent magnetic lineaments that suggests that the feeder dykes represent parts of a fault-related magmatic feeder zone (Bédard *et al*., 2012). The wall rocks of the feeder dyke(s) in zone A (Fig. 2b) belong to the Kilian Formation and include limestones with variable proportions of detrital silicates and remnants of evaporite beds. The dyke in zone A is $\sim$20 m wide and dips steeply to the west. To the south, it feeds into a sill that forms a prominent bench. In zone A, the shallowly dipping bedding in the host rocks shows a marked downward deflection on the east side and upward deflection on the west side of the dyke, suggesting that these are fault-related drag folds and that dyke ascent was fault guided. Within a metres-wide zone next to the dyke, some limestone beds are brecciated with conchoidal fractures filled by calcite ($\pm$pyrite). Samples include a marble from the intersection of the dyke with the capping sill at the highest sampled stratigraphic level, from a lower massive, partially graphitic limestone ledge that is brecciated near the dyke, and from the next lower limestone ledge, which has an evident skarn near the dyke. Calcsilicate samples interbedded with evaporites were collected $\sim$200 m further to the north (station 63).

Zone SFD-D is within dolostones of the Wynniatt Formation (Fig. 2c). The dolostones were deposited in subtidal and intertidal settings as evidenced by the presence of mudcracks, ooids and stromatolites (Rainbird *et al*., 1994). The dolostones, particularly in stromatolite horizons, are now fairly graphitic. A feature of the SFD-D zone is an irregular dyke-like mafic body, $\sim$50 m wide, that trends in the northwesterly direction and that may be related to a larger sill that makes up the mesa to the southwest. On the eastern side of the dyke-like body, the dolostone bedding was rotated up into parallelism with the mafic body and now has an $\sim$45° dip to the northeast (Bédard *et al*., 2012). Elsewhere in the SFD-D zone, the beds are near their original, near-horizontal orientation, but their dip increases somewhat towards the western margin of the mafic body, with a geometry that suggests an origin

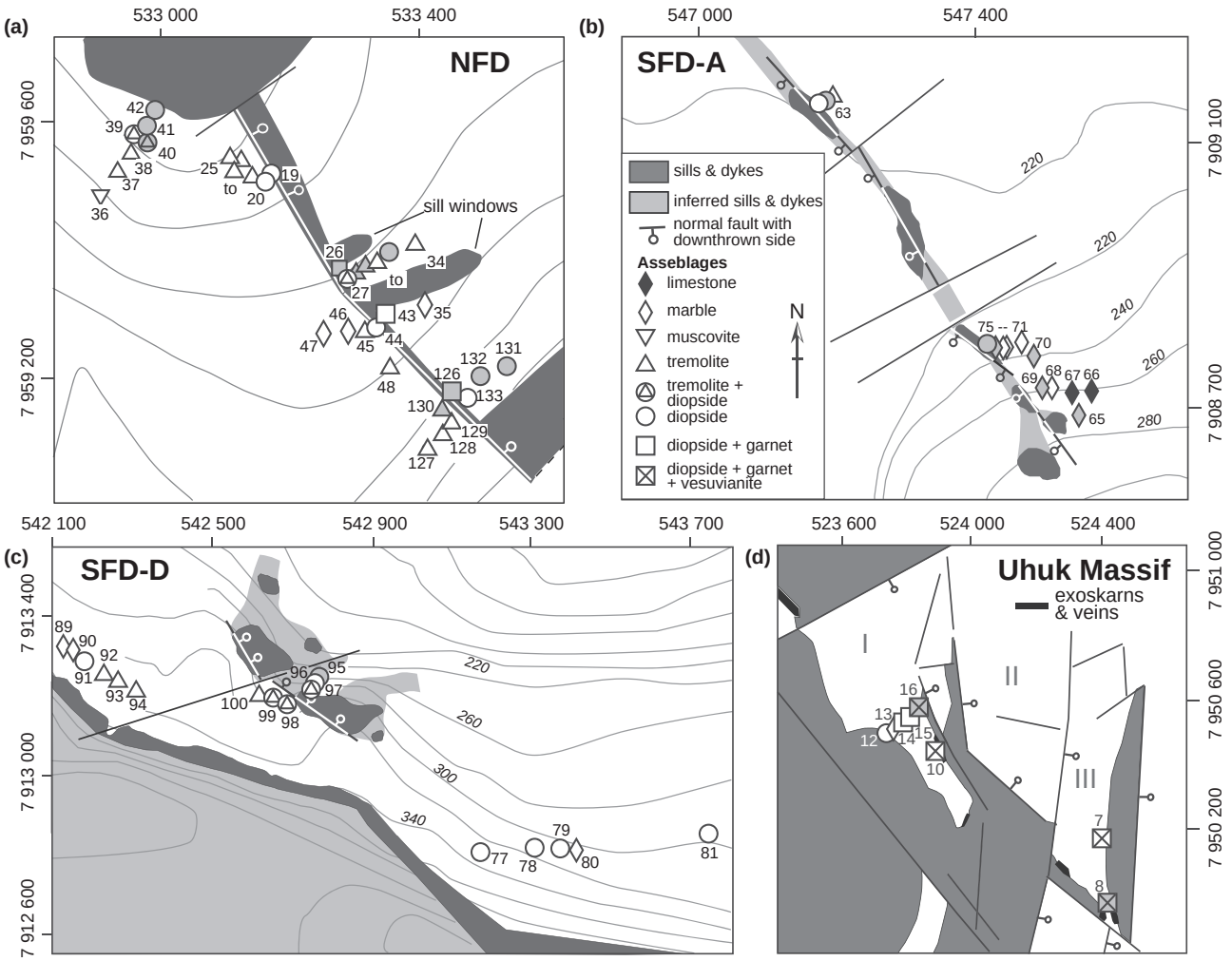

Fig. 2. Geological maps of (a) the Northern Feeder Dyke complex, (b) zone A of the Southern Feeder Dyke complex, (c) zone D of the Southern Feeder Dyke complex and (d) the eastern edge of the Uhuk Massif (after the more complete map of Bédard *et al.*, 2012). Station symbols denote characteristic minerals or rock types. Shaded symbols show occurrences of serpentine, chlorite or epidote. Contours, where shown, have 20 m interval. UTM coordinates for zone 11W are shown along margins. Northwest-trending faults are typically Proterozoic, coeval with magma emplacement; northeast-trending faults are typically post-Palaeozoic and dismembered the Proterozoic geology. Locations of exoskarns and skarn veins at the Uhuk Massif are shown.

as drag folds due to downward motion of the northeastern block. Samples were collected from ledges between the mesa-forming sill and the smaller dyke-like mafic body with the rotated sedimentary beds. Multiple samples with different morphologies and/or mineral contents were collected at some locations in the SFD-D zone.

The Uhuk massif contains on its eastern side a series of down-dropped blocks of a large primitive sill and its roof rocks, with normal motion along north–northwest-trending, northeast-dipping faults (Fig. 2d; Bédard *et al.*, 2012). Ascending magma actively intruded and brecciated the roof and then appears to have formed a sill to the west. A prominent northwest-trending magnetic lineament suggests that the Proterozoic faults guided magma ascent (Bédard *et al.*, 2012). Further dismemberment of the massif occurred by post-Palaeozoic faulting. The host rocks to the intrusions belong to the Jago Bay Formation (uppermost Reynolds Point Group; Rainbird *et al.*, 1994, 1996), which is characterized by yellow-weathering silty dolostone. Exoskarns produced by variable amounts of metasomatism of calcsilicates occur in several places above sill exposures. Samples were collected along two vertical traverses through the calcsilicates above the sill in block III and from the roof of the sill in block I. Station 8 occurs near massive skarns and where small gabbroic dykes have penetrated the overlying calcsilicates.

METHODS

Mineralogy and mineral chemistry of the metamorphic rocks were determined by petrography, semi-quantitative energy-dispersive analysis (EDA) using a Quanta 600 scanning electron microscope (SEM;

University of Missouri, Columbia, MO, USA), and in selected samples were determined by quantitative electron probe microanalysis (EPMA; Washington University, St. Louis, MO, USA). Carbonate minerals were analysed for oxygen and carbon isotope ratios by a dual-inlet Finnigan Delta Plus mass spectrometer with an automated Kiel acid reaction device at the University of Missouri. The carbonate minerals were extracted from billets that were left from thin-section preparation using a fine drill. Values are reported relative to the standard VSMOW for oxygen and the standard VPDB for carbon.

Garnet on Victoria Island is dominantly a grossular–andradite mixture, but also has variable concentrations of Ti (Table 1; mineral symbols are from Kretz, 1983). High-Ti garnet has been reported in hornfelses elsewhere (e.g. Labotka, 1995). One substitution mechanism is $2Ti^{4+}$ for $2Si^{4+}$ in andradite, which leads to the schorlomite (sch) end-member ($Ca_3Ti_2Fe_2^{3+}SiO_{12}$), and another mechanism is $Fe^{2+}Ti^{4+}$ for $2Fe^{3+}$, which leads to the morimotoite (mor) end-member ($Ca_3Fe^{2+}Ti^{4+}Si_3O_{12}$; Armbruster *et al.*, 1998). The morimotoite substitution may also involve incorporation of hydrogen into garnet, which, however, we did not characterize in this study. Proportions of garnet end-members (Table 1) were calculated from EPMA analysis by a least-squares regression. The maximum residual sum of squares for all spot analysis was 0.02.

MINERALOGY

Northern Feeder Dyke complex

Mineralogy of the NFD complex is dominated by calcite that can contain up to 4% dolomite component. In unmetamorphosed or weakly metamorphosed rocks, detrital quartz occurs in variable proportions, from none to tens of percent. It is generally absent from metamorphosed rocks near the mafic intrusive rocks. In these calcite-dominated rocks, dolomite was not petrographically identified and we did not come across it during EDA or EPMA analysis. It is therefore possible that magnesian calcite is the main Mg-bearing mineral in the unmetamorphosed rocks and was the source of Mg for metamorphic Mg-silicates. Muscovite is the main aluminium-bearing mineral, but its proportion is very small. The calcite (±quartz)-dominated mineralogy in the NFD complex reflects the CaO-dominated compositions of the rocks (Table 2).

Table 1. Representative analyses of silicate minerals.[a]

	Di 40-1	Di 7-12	Phl 40-1	Srp 40-1	Srp 8-1A	Epid 26-1	Vsv 7-12	Vsv 8-1A	Grt 26-1	Grt core 7-12	Grt rim 7-12	[b]Grt spot "A" 8-1A	[b]Grt spot "B" 8-1A	[b]Grt spot "C" 8-1A	[b]Grt spot "D" 8-1A
wt.%															
SiO_2	54.42	52.93	42.11	40.48	41.18	38.64	36.33	36.88	36.52	40.18	39.37	35.78	38.07	36.27	36.32
TiO_2	0.1	0.76	0.54	0.07	0	0.03	1.01	0.68	3.56	0.27	1.69	6.25	1.7	0.13	0.09
Al_2O_3	1.2	2.54	14.7	1.86	2.94	27.72	14.95	14.55	13.81	20.55	19.22	11.55	11.03	1.76	1.62
FeO	2.71	5.44	1.24	3.07	0.44	7.62	4.6	3.86	9.82	4.35	4.02	8.96	12.32	25.51	25.45
MnO	0.08	0.11	0.04	0.08	0.1	0.03	0.09	0.05	0.16	0.2	0.14	0.1	0.04	0	0.06
MgO	18.05	14.46	26.66	38.46	39.42	0	3.98	4.41	0.79	0.51	0.28	1.3	0.68	0.26	0.47
CaO	23.86	24.66	0.18	0.14	0.15	23.91	35.5	36.23	34.75	35.63	36.37	35.31	35.96	33.94	34.21
Na_2O	0.07	0.18	0.39	0.03	0.06	0.02	0.1	0.05							
K_2O	0.01	0.03	10.08	0.02	0.01	0.03	0.01	0							
F	nd	nd	1.26	nd	nd	nd	0.5	0.28							
Cl	nd	nd	0.09	0.41	0.09	nd	0.01	0.02							
Sum	100.51	101.11	97.3	84.63	84.39	98.01	97.07	97.02	99.42	101.68	101.08	99.25	99.81	97.88	98.22
Atoms/formula															
Si	1.97	1.93	2.92	1.86	1.86	2.99	17.7	17.87	2.86	2.99	2.97	2.82	2.98	3.01	3
Al	0.05	0.11	1.2	0.1	0.16	2.53	8.59	8.31	1.27	1.81	1.71	1.07	1.02	0.17	0.16
Ti	0	0.02	0.03	0	0	0	0.37	0.25	0.21	0.02	0.1	0.37	0.1	0.01	0.01
Fe^{3+}	0	0	0	0	0	0.43	1.38	1.56	0.59	0.18	0.17	0.54	0.81	1.77	1.76
Fe^{2+}	0.08	0.17	0.07	0.12	0.02	0.07	0.49	0	0.05	0.1	0.09	0.05	0	0	0
Mn	0	0	0	0	0	0	0.04	0.02	0.01	0.01	0.01	0.01	0	0	0
Mg	0.97	0.79	2.75	2.64	2.66	0	2.89	3.19	0.09	0.06	0.03	0.15	0.08	0.03	0.06
Ca	0.92	0.97	0.01	0.01	0.01	1.98	18.54	18.81	2.91	2.85	2.94	2.98	3.02	3.01	3.02
Na	0	0	0.05	0	0.01	0	0	0							
K	0	0	0.89	0	0	0	0	0							
F	nd	nd	0.28	nd	nd	nd	0.38	0.22							
Cl	nd	nd	0.01	0.02	0	nd	0	0.01							
Minera components															
% En	49	41													
% Fs	4	9													
% Wo	47	50													
% Prp									3	3	1	4	2	0	1
% Grs									61	86	83	53	51	9	8
% Adr									23	8	7	19	40	89	89
% Mor									6	3	7	15	6	2	2
% Sch									7	0	1	11	1	0	0

[a]Normalizations: diopside to 6 oxygen; phlogopite to 11 oxygen; serpetinite to 7 oxygen and 5 cations; epidote to 15 oxygen and 16 cations; garnet to 12 oxygen and 8 cations; vesuvianite to 73.5 oxygen and 50 cations; nd, not detected.
[b]Spots 'A-D' refer to analysis locations in Fig.4.

Incipient metamorphism is identified by the appearance of radial tremolite (Fig. 3b). Tremolite occurs in rocks as close as 30 m from the feeder dyke and the capping sill and in most samples between the windows to the lower sill (Fig. 2a). Diopside occurs only very close to the gabbroic sheets. In contrast to the typical equant shape of diopside in contact aureoles around large plutons (e.g., Berger *et al*., 2010; Nabelek & Morgan, 2012), diopside in these carbonates from Victoria Island typically occurs as radial splays of acicular crystals that resemble the common morphology of tremolite (Fig. 3c). Petrographically it is distinguished from tremolite by its larger extinction angle. Its morphology suggests that it pseudomorphs tremolite and that there was not a sufficient amount of time for it to equilibrate texturally. Phlogopite is common in more aluminous rocks and occurs together with both tremolite and diopside. A feature of many diopside-bearing rocks is the occurrence of serpentine (Fig. 3d; the specific form of serpentine was not determined).

Only locally, at the intersections of the dyke with the lower sill and near the sill window (stations 26–29 & 126), is there evidence for metasomatism. Samples from these locations contain variable amounts of garnet ($\sim Prp_3Grs_{61}Adr_{23}Mor_6Sch_7$), Fe^{3+}-bearing epidote (Table 1), chlorite and titanite, in addition to tremolite or diopside as metamorphic minerals. A sample located ~2 m above the lower sill (132-1) and one above the sill window (31-1) contain veinlets of

Table 2. Representative compositions of rocks used to compute pseudosections.

	Northern Feeder Dyke and Southern Feeder Dyke carbonates	Uhuk silty dolostones
SiO_2	1.53	25.30
TiO_2	0.02	0.25
Al_2O_3	0.44	4.49
FeO	0.37	9.50
MnO	0.01	0.06
MgO	0.91	4.19
CaO	54.63	29.04
Na_2O	0.02	0.00
K_2O	0.09	0.00
CO_2	43.02	24.70
Sum	101.04	97.50

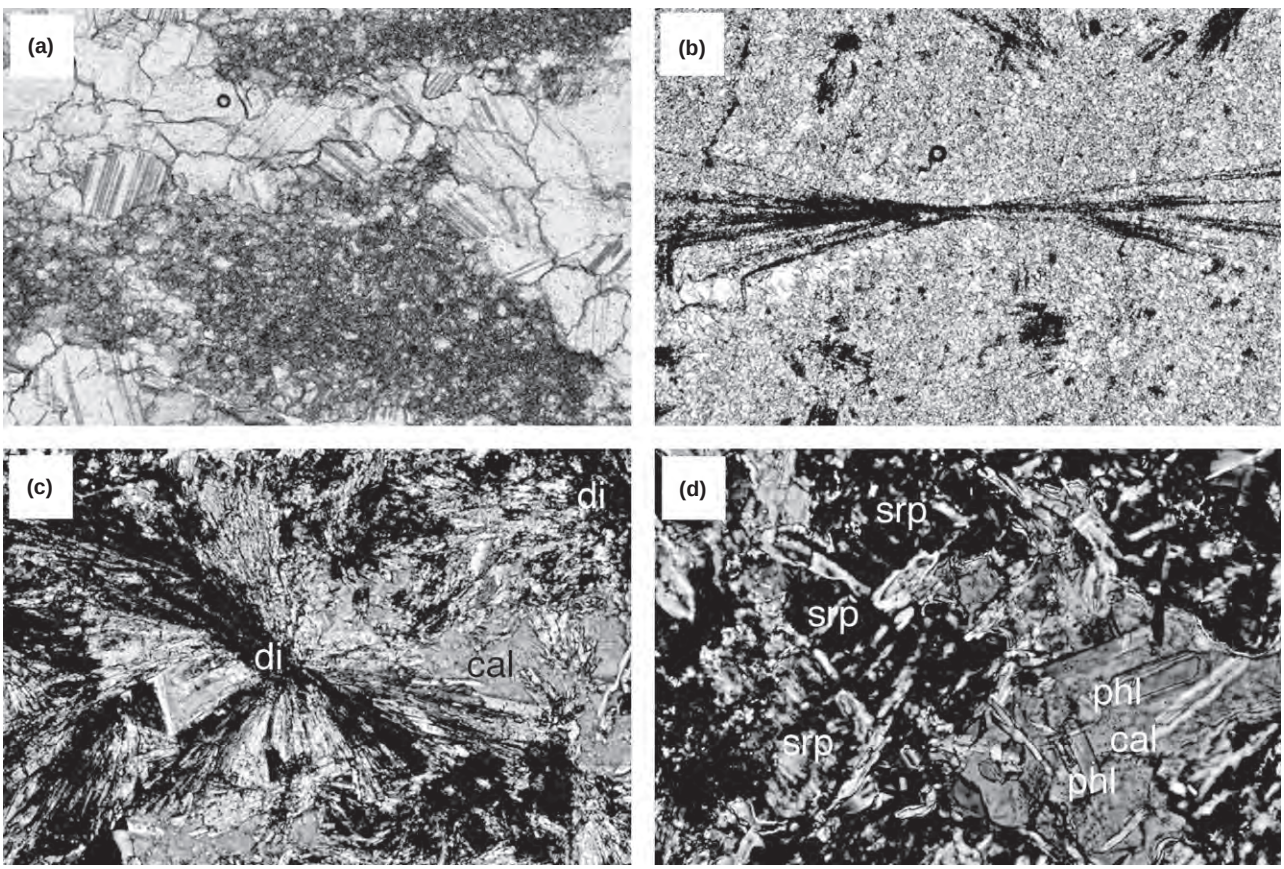

Fig. 3. (a) Variably recrystallized marble at the Southern Feeder Dyke (SFD)-D (field of view (fov) = 2 mm); (b) tremolite splay at the SFD-D complex (fov = 2 mm); (c) splay of acicular and bladed diopside in the Northern Feeder Dyke (NFD) complex (fov = 0.5 mm); (d) serpentine surrounding a recrystallized or newly formed pokioblastic calcite containing phlogopite in the NFD complex (fov = 0.5 mm).

anhydrite and the latter sample, unsurprisingly, also contains scapolite.

In high-grade contact aureoles around large plutons, calcite is usually highly recrystallized (annealed), even in rocks that apparently remained closed to external fluids (e.g. Nabelek *et al.*, 1984; Nabelek & Morgan, 2012). On Victoria Island, the calcite in unmetamorphosed and incipiently metamorphosed rocks is a fine-grained micrite (~5–10 μm) that becomes variably coarser (up to ~50 μm) next to mafic intrusions (Fig. 3a). In skarns and breccia-filling veins, calcite crystals can be on a millimetre scale. Neoformed calcite grains in skarns are typically poikiloblastic, enclosing metamorphic silicate minerals, whereas in calcite-dominated rocks, silicate minerals typically occur at calcite triple junctions, with the exception of some tremolite splays that overgrow micritic calcite.

In the NFD complex, the carbonate and silicate minerals are Fe poor (Table 1), except in the local skarns. This indicates that most of the Fe in the rocks is sequestered by pyrite and pyrrhotite. Pyrrhotite occurs in increasing proportions towards the mafic rocks, consistent with increasing temperature (Toulmin & Barton, 1964).

Southern Feeder Dyke complex

Metamorphic mineralogy in the SFD complex is similar to that in the NFD complex. In the SFD-A zone, massive limestone ledges below the capping sill are essentially monomineralic with micritic calcite and graphitic material; however, some samples contain detrital quartz. Near the dyke, calcite grain size is variable and triple junctions are more abundant. Marbles are commonly brecciated at contacts with the dyke with fractures filled by coarse calcite veins. Some of the marbles contain interstitial serpentine, showing the presence of Mg and Si in addition to the calcite components. The skarn in the lowest massive limestone ledge next to the dyke contains garnet, epidote and chlorite. At station 63, 10 m from the dyke there is tremolite, calcite and detrital quartz, and 2 m from the dyke, there is diopside enclosed in variably recrystallized calcite (~50 μm) and minor anhydrite. Fifty centimetres from the dyke there is a rare occurrence of wollastonite, due to a large amount of detrital quartz, in addition to diopside and neoformed, recrystallized calcite. Thus, next to the dyke in the SFD-A zone, the high-grade aureole, defined as having diopside, is very narrow.

The dominant outcrops in the SFD-D zone are variably recrystallized marble ledges. Those that have fossil stromatolites are fairly graphitic. Index metamorphic minerals are tremolite and diopside. Tremolite overgrowing a micritic matrix (Fig. 3b) occurs on a ledge approximately half way between the mesa-capping sill and the smaller mafic dyke-like body (Fig. 2c). Diopside is confined to close proximities of the mafic bodies, except in the eastern ledge (stations 77–81) where it occurs as much as ~200 m horizontally from the current edge of the upper sill, suggesting that a mafic body capped this ledge in the past, or that an unexposed intrusive apophysis may be present beneath.

Uhuk Massif

The metamorphic mineralogy at the Uhuk Massif is distinguished from that in the NFD and SFD complexes by containing the frequent assemblage of garnet + diopside. Garnet is stable due to elevated Al concentrations in the dolomitic Jago Bay Formation (Table 2). These two minerals plus vesuvianite occur throughout the whole 10 m vertical traverse above the lowermost exposure of the down-dropped sill at station 8 and through at least the first 5 m at station 7 (section III of Fig. 2d). The silty beds are interbedded with variably recrystallized marbles containing conchodial fractures filled by calcite. Diopside is nearly always acicular and together with some small calcite grains, also occurs as inclusions in garnet. In the matrix, calcite typically occurs as large recrystallized grains. Vesuvianite is always poikiloblastic, enclosing all other minerals. This indicates that vesuvianite was the last mineral that grew in the rocks during prograde metamorphism. Andradite and some diopside in the matrix appear to be intimately associated with retrograde serpentine. Mineralogy of calcsilicates in the sill's roof in section I of the Uhuk map (stations 10–17; Fig. 2d) is similar, although vesuvianite was found only in sample 16. Scapolite was found in samples 7-20 and 15-1. Magnetite, pyrite and pyrrhotite occur in various proportions. The sulphides occur as separate grains or as two-phase grains with lamellae of pyrrhotite in pyrite.

Metasomatism

The compositions of garnet and vesuvianite (Table 1) potentially record variable additions of Fe to the rocks by metasomatism and high oxidation conditions. For example, in sample 7–12 that came from 1 m above the sill, garnet is fairly homogeneous, dominated by the grossular component, but also contains significant andradite component ($Grs_{86}Adr_8Mor_3$ – $Grs_{83}Adr_7Mor_7$). Most Fe in vesuvianite in 7–12 is also apparently ferric. It is possible to grow these minerals from the bulk composition in Table 2 (see below), but there had to be oxidation of Fe in the rocks before or during mineral growth. In several samples at station 8, all Fe in vesuvianite appears to be ferric. The presence of ferric Fe indicates that these minerals grew at a fairly high fO_2.

The composition of garnet is particularly interesting in sample 8-1A (Table 1; Fig. 4). Core of a larger garnet is $grs_{62}adr_{34}$. Another brighter zone in the larger garnet in the BSE image of Fig. 4 is $grs_{54}adr_{44}$. This zone is surrounded by vesuvianite, which suggests that there was an influx of some oxidized, Fe-bearing fluid at this stage of metamorphism. The most Fe-enriched fluid

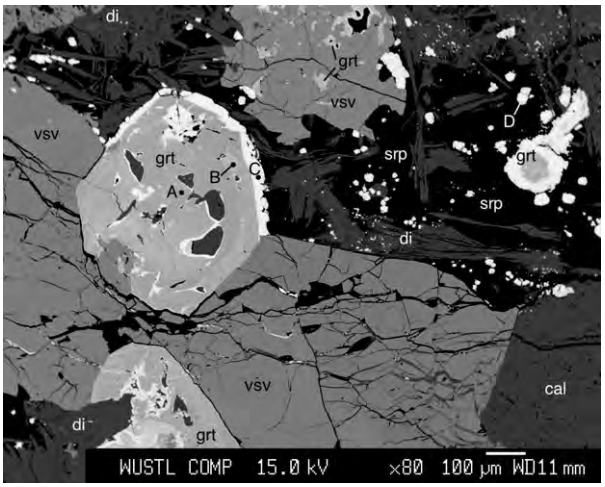

Fig. 4. A back-scatter electron image of a portion of sample 8-1A showing an assemblage of garnet, vesuvianite, calcite, diopside and serpentine. The bright rim on the larger garnet and small microgarnet are nearly pure andradite. Note that the andradite rim grew after vesuvianite and the small andradite crystals occur within serpentine-containing fractures in vesuvianite. Spots labelled by letters correspond to microprobe analyses in Table 1.

appears to have arrived after the growth of vesuvianite. It is indicated by a bright grs_9adr_{89} rim on the garnet that occurs only within a patch of serpentine with small-bladed diopside crystals. There are also small, ~10 μm andradite crystals (seen as brightest crystals in the BSE image) within the serpentine and within serpentine-filled cracks inside vesuvianite. The coexistence of these minerals suggests that assemblage andradite + serpentine + diopside was stable at the prevailing oxidizing conditions. Serpentine-filled embayments and cracks within vesuvianite suggest that it was consumed during formation of the three-phase assemblage, with ferric iron from vesuvianite used to stabilize andradite. Fe metasomatism at Uhuk is also clearly evidenced by occurrences of massive magnetite-rich exoskarns at other locations above the sill. At the locations discussed in this article, Fe metasomatism was more subtle but clearly evident in the mineral chemistry.

PHASE EQUILIBRIA CONSTRAINTS ON METAMORPHIC CONDITIONS

Temperature-$X(CO_2)^{fluid}$ pseudosections, showing theoretical mineral assemblages in the calcite-dominated rocks in the NFD and SFD complexes and the calcsilicates at Uhuk, were constructed using the THERIAK/DOMINO software (De Capitani & Petrakakis, 2010). An updated version (db55, 2007) of the activity models and thermodynamic database of Holland & Powell (1998) was used in the calculations. The pseudosections were calculated for 250 bar, appropriate for a hydrostatic pressure regime in the sedimentary rocks. With increasing pressure, the topology of the diagrams stays essentially intact, but the assemblage boundaries move to higher temperatures because nearly all reactions are volatile producing.

Northern Feeder Dyke and Southern Feeder Dyke zones

Assemblages in the calcite-dominated rocks (Fig. 5a,b) were modelled using a representative composition (Table 2), but without Fe. A Fe-absent composition is appropriate because almost all Fe in the NFD and SFD complexes is sequestered in sulphides or magnetite, and the silicate minerals contain very little Fe (Table 1). The composition used is one with the highest molar $CO_2/(CaO + MgO)$ ratio (0.98) of all the analysed rocks from the NFD complex (unpublished data), meaning that it is the least decarbonated. Except for some rocks that had abundant detrital quartz, most reactions were quartz absent because quartz was consumed early by incipient reactions. The pseudosection has a swath of tremolite-bearing assemblages that extends from CO_2-absent conditions to $X(CO_2)^{fluid} = 0.7$. In terms of temperature, the permissible tremolite-present field is fairly narrow. Tremolite was probably formed continuously on the univariant reaction:

$$5\,Dol + 8\,Qtz + H_2O \rightarrow Tr + 3\,Cal + 7\,CO_2, \qquad (1)$$

so that the interstitial fluid became CO_2-bearing. However, given the apparent paucity of dolomite in the NFD rocks, it is possible that Reaction 1 involved a dolomite component in calcite instead of dolomite as a separate phase. Initial univariant, closed-system behaviour is predicted for the onset of decarbonation reactions because the locally generated fluid pressure typically exceeds the background hydrostatic pressure, thus preventing influx of an external H_2O that would make the reaction discontinuous (Nabelek, 2007, 2009). Observed brecciation of rocks near dykes and sills demonstrates that fluid pressure sometimes exceeded the local lithostatic pressure. The pseudosection predicts an extremely small field for talc (Fig. 5b), which explains the apparent absence of talc from the metamorphosed rocks on Victoria Island.

Rocks containing the assemblage diopside + phlogopite occur directly above sills and near dykes. Indeed, these two minerals are predicted to coexist above 400 °C across most of the range of $X(CO_2)^{fluid}$. The typically acicular, radial morphology of diopside on Victoria Island suggests that most of it replaced previously formed tremolite by the reaction:

$$Tr + 3\,Cal \rightarrow 4\,Di + Dol_{ss} + CO_2 + H_2O, \qquad (2)$$

which has the dolomite component in calcite (Dol_{ss}) as the product. The solubility of dolomite into calcite increases with temperature along the surface of the solvus between the two minerals (Goldsmith & Newton, 1969). However, if quartz was still present and if $X(CO_2)^{fluid}$ reached more than ~0.7, diopside could have formed by the reaction

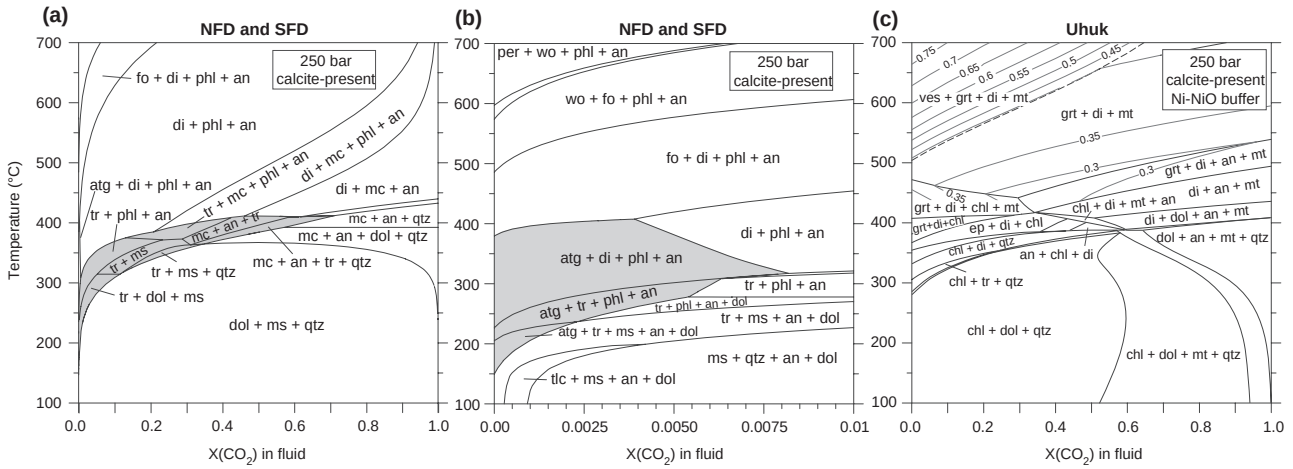

Fig. 5. Temperature-$X(CO_2)^{fluid}$ pseudosections showing stable mineral assemblages in metamorphosed rocks. The pseudosections were calculated using the THERIAK/DOMINO computer program (De Capitani & Petrakakis, 2010). Some narrow, low-variance assemblage fields are not labelled. (a) Pseudosection for rocks in Northern Feeder Dyke and Southern Feeder Dyke complexes showing assemblages across the full range of $X(CO_2)^{fluid}$ with the tremolite-present field highlighted. (b) Pseudosection for the same rocks highlighting the extent of serpentine (antigorite) stability in the $X(CO_2)^{fluid}$ range from 0 to 0.01. (c) Pseudosection for rocks at Uhuk calculated assuming the Ni-NiO buffer. Thin lines show fraction of andradite in garnet. The vesuvianite-present field is approximate due to a possible incompatibility between the thermodynamic data of Ogorodova *et al*. (2011) for Fe-vesuvianite and the db55 (2007) version of the thermodynamic database of Holland & Powell (1998).

$$Dol_{ss} + 2\,Qtz \rightarrow Di + CO_2. \quad (3)$$

Reactions 2 and 3 may have occurred at the same time if Reaction 2 was thermally overstepped, which would have effectively cancelled out the involvement of dol_{ss}. Phlogopite most likely formed by the reaction:

$$3\,Dol_{ss} + Mc + H_2O \rightarrow Phl + 3\,Cal + 3\,CO_2. \quad (4)$$

The restriction of the diopside + phlogopite assemblage to close proximities of the intrusive sheets, in spite of its large T–$X(CO_2)^{fluid}$ stability range, points to steep thermal gradients in the contact aureoles. Reaction 4 involves the addition of H_2O, which indicates that the rocks were invaded by H_2O after decarbonation reactions that produced diopside ceased. The reaction would have also produced new, probably relatively coarse calcite in the presence of H_2O.

Many rocks that contain diopside, and a few that contain tremolite, have serpentine. Forsterite, which is predicted to occur above 400 °C in H_2O-rich conditions was not found in the rocks. Serpentine-bearing assemblages were modelled using the thermodynamic data for antigorite ($Mg_{48}Si_{34}O_{147}H_{62}$) in the db55 database. (Using chrysotile instead of antigorite affects the assemblage boundaries only little). The antigorite field extends only to $X(CO_2)^{fluid}$ of 0.008 (Fig. 5b), which shows that the CO_2 that was generated by prograde decarbonation reactions in the serpentine-bearing high-grade rocks must eventually have been flushed away and that magnesian silicates (diopside and perhaps forsterite, if present) reacted to serpentine. The pseudosection suggests the following hydration reactions:

$$14\,Fo + 10\,Di + 10\,Dol_{ss} + 31\,H_2O \rightarrow Ant + 20\,Cal \quad (5)$$

or

$$17\,Di + 31\,Dol_{ss} + 31\,H_2O \rightarrow Ant + 48\,Cal + 14\,CO_2 \quad (6)$$

These reactions also produce calcite that is likely to be fairly coarse due to the presence of H_2O.

Scapolite (not analysed and not included in the pseudosection) that occurs in some samples in the NFD complex and at the Uhuk Massif, with or without anhydrite veinlets, probably records influx of a salty fluid:

$$An + Cal + NaCl_{aq} + CaSO_{4,aq} \rightarrow (Ca,\ Na)_4(Si,Al)_{12}O_{24}(CO_3, SO_4, Cl). \quad (7)$$

Uhuk Massif

The calcsilicate rocks at the Uhuk Massif include Fe-bearing silicate minerals, including diopside, garnet and vesuvianite, that require the incorporation of Fe in the construction of a pseudosection (Fig. 5c). The whole-rock composition chosen has the highest CO_2 concentration and among the lowest Fe concentrations of all analysed rocks (unpublished data) from the massif (Table 2). Because all the analysed rocks from the Uhuk Massif were decarbonated to various extents during metamorphism, CO_2 was added to the composition to make its molar proportion equal to the proportion of CaO + MgO, under the assumption that before metamorphism, both of these oxides were contained only in calcite and dolomite. There is no evidence in the protoliths for detrital plagioclase that would have also contained calcium.

Fe-bearing vesuvianite is a frequent mineral in metamorphosed Uhuk rocks. However, the db55 thermodynamic database does not include data for Fe-vesuvianite (one with two Fe atoms per formula unit). Therefore, thermodynamic data were taken from measurements on a natural Fe-vesuvianite by Ogorodova *et al.* (2011). The composition of vesuvianite is very close to $Mg_2Ca_{19}Fe_2Al_9Si_{18}O_{78}H_9$ in which all Fe is ferric and it corresponds closely to the composition of vesuvianite at Uhuk (Table 1). Because the activity-composition relationship between Fe-vesuvianite and Al-vesuvianite ($Mg_2Ca_{19}Al_{11}Si_{18}O_{78}H_9$) is unknown, the solution was assumed ideal.

The oxygen fugacity was constrained to the Ni–NiO buffer so that both ferrous and ferric iron could be present. This constraint agrees with magmatic oxygen fugacities of the mafic dykes and sills on Victoria Island, which were about two orders of magnitude higher than the quartz–fayalite–magnetite (QFM) buffer, as revealed by Fe-Ti-oxide oxybarometry (J. H. Bédard, unpublished data). A pseudosection calculated assuming the QFM buffer does not produce vesuvianite or andradite garnet. Ti in garnet was not considered in calculating the pseudosection.

The pseudosection for the Uhuk rocks (Fig. 5c) reproduces well the observed assemblages. However, because it is for a single composition, it does not address Fe metasomatism that was discussed above. All assemblages in the pseudosection include calcite. In unmetamorphosed rocks, the assemblage includes chlorite as the Fe-bearing silicate mineral. The ubiquitously coexisting diopside + garnet + magnetite in the high-grade rocks at Uhuk spans the full range of $X(CO_2)^{fluid}$ above 400 °C, and so provides no constraints on $X(CO_2)^{fluid}$. Diopside was most likely produced by a reaction similar to Reaction 2, but with magnetite as the source of Fe and, instead of using the dolomite component in calcite, it used dolomite that is common at Uhuk. Garnet probably initially formed by the reaction:

$$0.702\,Cpx(Di_{59}Hd_{41}) + 0.779\,Cal(Cal_{96.4}Dol_{3.6}) + 1.505\,An + 0.104\,Mt \rightarrow Grt(Grs_{70}Adr_{30}) + 0.807\,CO_2. \quad (8)$$

The reaction is based on compositions of the reactants before the onset of the reaction and of garnet at the reaction boundary as predicted by THERIAK output at $X(CO_2)^{fluid} = 0.5$. Elsewhere on the reaction boundary, the coefficients and compositions of solutions would be slightly different. The predicted garnet composition corresponds closely to compositions of garnet cores at Uhuk (Table 1). As shown by the contours in Fig. 5c, andradite component increases with temperature, particularly in the vesuvianite-present field, which is consistent with the andradite-dominated garnet in vesuvianite-present rocks. Equilibrium diopside becomes more magnesian with increasing temperature, reaching nearly pure diopside in the vesuvianite-present field, in agreement with the composition of diopside in vesuvianite-present rocks (Table 1). Reaction 8 is also consistent with the occurrence of both diopside and calcite as inclusions in garnet at Uhuk.

The vesuvianite-present field in the pseudosection occurs only above 500 °C and low $X(CO_2)^{fluid}$. Due to the poor constraint on the activity relationship between Al and Fe-vesuvianite, the location of the vesuvianite-present field is only approximate. Nevertheless, its confinement to low $X(CO_2)^{fluid}$ is consistent with a location of the vesuvianite-in reaction at $X(CO_2)^{fluid} \approx 0.003$ in an Fe-absent system (Nabelek & Morgan, 2012). The model predicts a nearly pure Fe-vesuvianite, in accord with composition of vesuvianite in Uhuk rocks (Table 1). The growth of vesuvianite involved the consumption of garnet + diopside and hydration by the approximate reaction:

$$2.85\,Grt(Grs_{60}Adr_{40)} + 1.935\,Cpx(Di_{93}Hd_7) + 5.725\,Cal(Cal_{96.5}Dol_{3.5)} + 2.79\,An + 4.5\,H_2O \rightarrow Fe\text{-}Ves + 0.138\,Mt + 5.926\,CO_2. \quad (9)$$

Thus, the presence of vesuvianite in the highest grade calcsilicate rocks demonstrates that the CO_2 that was produced earlier by decarbonation reactions was flushed away by H_2O, allowing vesuvianite to grow. A late crystallization of vesuvianite in the paragenetic sequence of minerals is consistent with its occurrence as a poikiloblastic phase that encloses all other phases in the rocks, except for serpentine.

Notable also is the confinement of chlorite and epidote-present fields to CO_2-poor conditions (Fig. 5c). This shows that the fluids that were responsible for the formation of epidote and chlorite-bearing skarns at several locations on Victoria Island must have been H_2O-dominated.

OXYGEN AND CARBON ISOTOPE RATIOS

Figure 6 shows summary plots for covariances of $\delta^{13}C$ and $\delta^{18}O$ values for carbonate minerals in metamorphosed rocks on Victoria Island (Table S1). The values fall within ranges of previously published data of Jones *et al.* (2010) for each of the examined formations. $\delta^{13}C$ and $\delta^{18}O$ values in the SFD-D zone are tightly clustered with ~2‰ ranges for both. Exceptions to the clustering are samples collected within several metres of the dyke at the locality (highlighted in Fig. 6c). Both $\delta^{18}O$ and $\delta^{13}C$ are lower by ~2‰ from the cluster in these rocks. Similar isotope ratio systematics are seen in the SFD-A zone. There are apparently two trends for the furthest samples from the dyke, with $\delta^{18}O$ more elevated in the middle limestone ledge. The difference probably reflects an original variability related to stratigraphy (Jones *et al.*, 2010). There seems to be a slight positive correlation between $\delta^{13}C$ and $\delta^{18}O$ in both trends. As in the SFD-D zone, highlighted

samples with lower $\delta^{13}C$ values in Fig. 6b came from within a few metres of the dyke. The lowest $\delta^{13}C$ values occur in samples that contain serpentine and/or garnet with epidote and have recrystallized calcite. Only one sample has an anomalously low $\delta^{18}O$ by ~3‰ and it contains a large proportion of chlorite. Overall, $\delta^{18}O$ values are more elevated in the dolomitic Wynniatt Formation in the SFD-D zone than in Killian Formation limestones in the SFD-A zone. Dolomitization typically elevates $\delta^{18}O$ due to the larger oxygen isotope fractionation between dolomite and H_2O ($\Delta^{18}O_{Dol\text{-}H_2O}$) than between calcite and H_2O ($\Delta^{18}O_{Cal\text{-}H_2O}$).

Isotope ratio shifts are especially well developed at Uhuk (Fig. 6d). All but one sample from the roof of

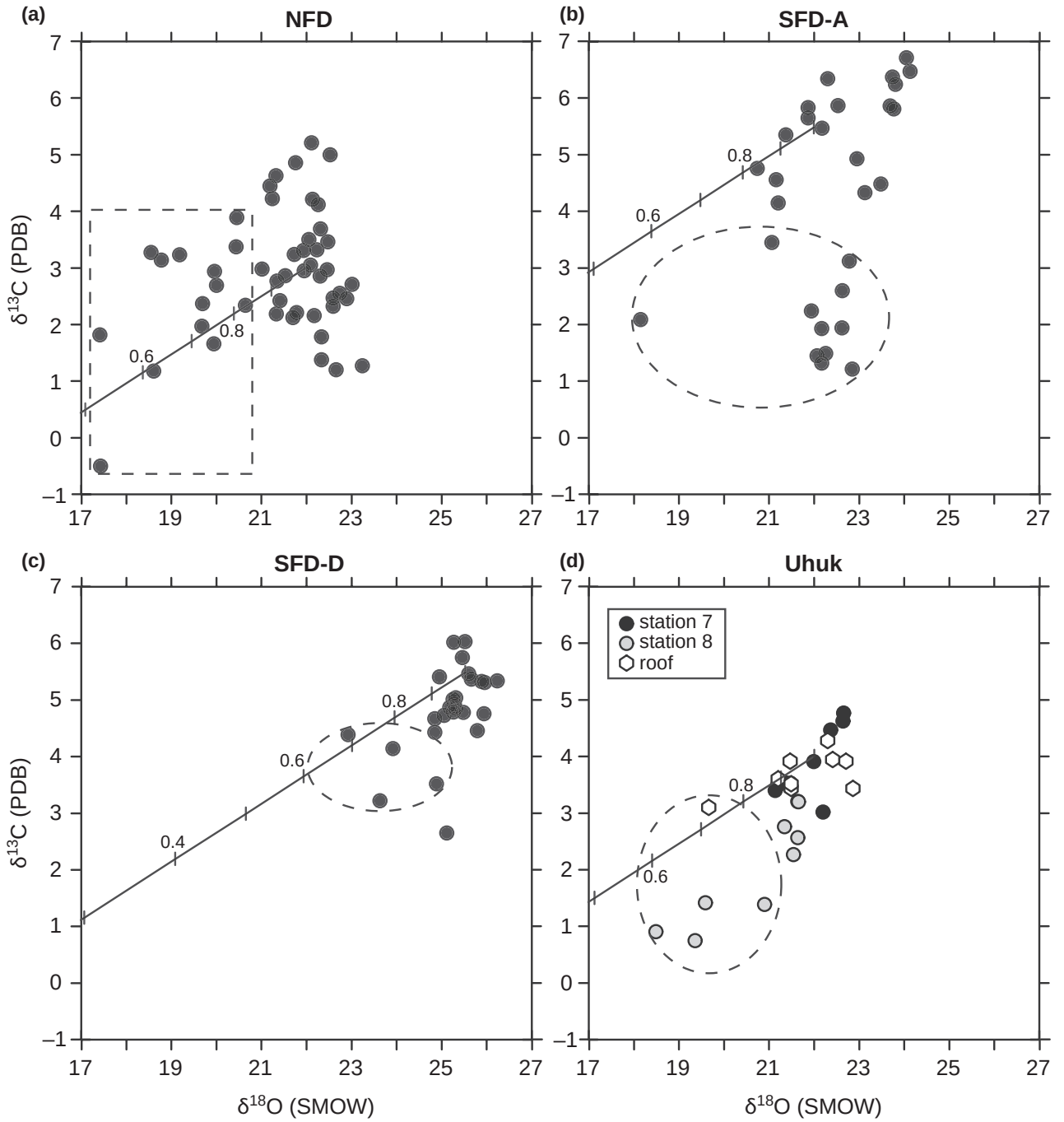

Fig. 6. Plots showing $\delta^{13}C$ and $\delta^{18}O$ values of carbonate minerals in metamorphosed rocks. Samples highlighted by dashed lines were collected very near gabbroic dykes and sills. Lines show predicted effect of Rayleigh decarbonation on the $\delta^{13}C$ and $\delta^{18}O$ of remaining calcite in the rocks. Tick marks on the lines show the fraction of the original carbonate mineral remaining. The metamorphic rocks on Victoria Island probably did not lose more than 20% of calcite by calcsilicate reactions.

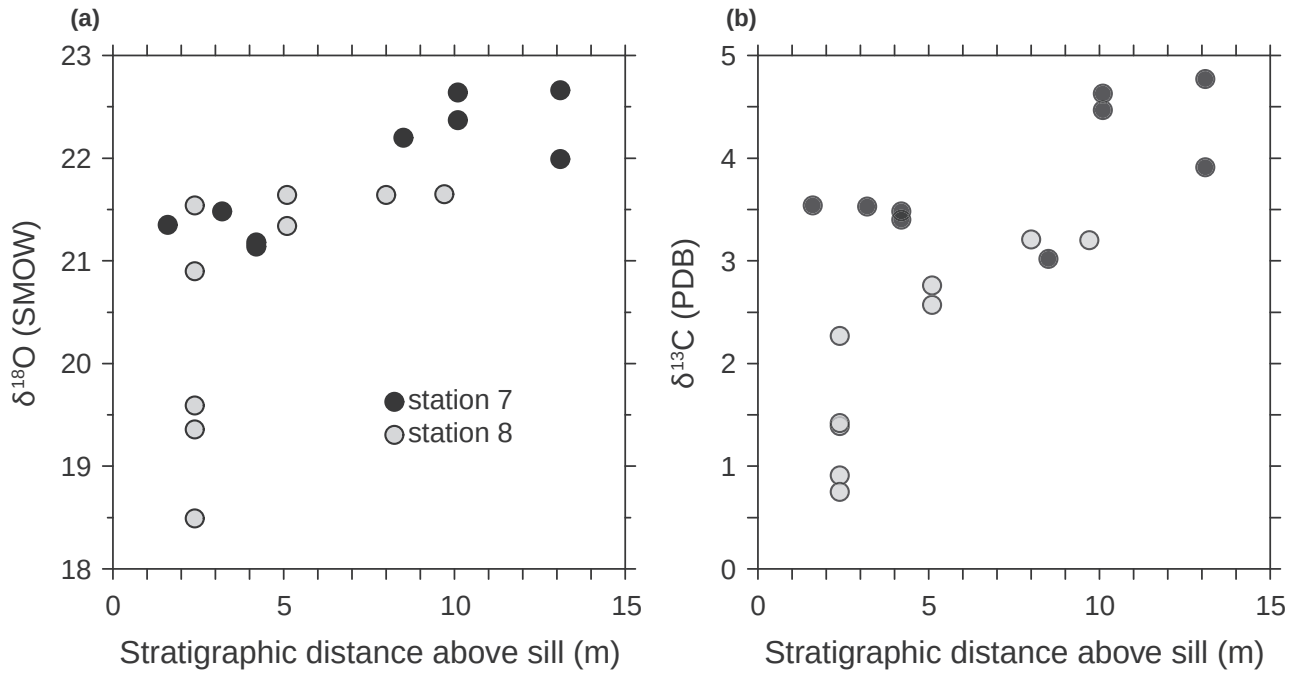

Fig. 7. Vertical profiles of δ^{13}C and δ^{18}O above a sill at the Uhuk Massif at stations 7 and 8.

the sill and the vertical profile at station 7 define a tight, 2‰ cluster of δ^{13}C and δ^{18}O. One skarn sample with the assemblage garnet + vesuvianite + diopside has a lower δ^{18}O by ~2‰ than the cluster. Details of the vertical profiles at stations 7 and 8 are shown in Fig. 7. There is a trend of decreasing δ^{13}C toward the sill, particularly at station 8 that has andradite garnet together with vesuvianite and diopside throughout. Even a sample 10 m above the sill has a lower δ^{13}C than most other samples at Uhuk. Trends for δ^{18}O are analogous, giving a positive correlation between the two isotope ratios at station 8 (Fig. 6d). Station 8 samples within 3 m of the sill have the lowest δ^{13}C and δ^{18}O values. Such extents of heavy isotope depletions are not seen at station 7 or in the roof samples.

The largest spread of δ^{13}C and δ^{18}O occurs in the NFD complex with ranges of ~5‰ for both (Fig. 6a). It is notable that most rocks with δ^{18}O values of < 20‰, highlighted in Fig. 6, occur directly above the lower sill and the sill windows on the east side of the dyke (down-thrown side of the dyke-guiding fault), whereas on the west side of the dyke, most samples have δ^{18}O values that appear unchanged from the primary δ^{18}O values of the Boot Inlet Formation (Fig. 8). Many of the ^{18}O-depleted rocks contain serpentine or chlorite, and the lowest δ^{18}O values occur in epidote-bearing skarns at the intersection of the sill window and the dyke.

The systematics of the δ^{13}C variation (Fig. 6a) are harder to unravel. Part of the range may be related to a primary stratigraphic variation, as suggested by different average values of sample traverses. However, analogously to the other locations, the lowest δ^{13}C values occur close to the dyke and below the capping sill, indicating a causal relationship.

DISCUSSION

Fluids

The lowest δ^{13}C and δ^{18}O values in each studied locality occur within a few metres of dykes and sills in each traverse. Although the lowest δ^{18}O values occur right next to mafic bodies, they are still significantly higher than the probable primary δ^{18}O of the intru-

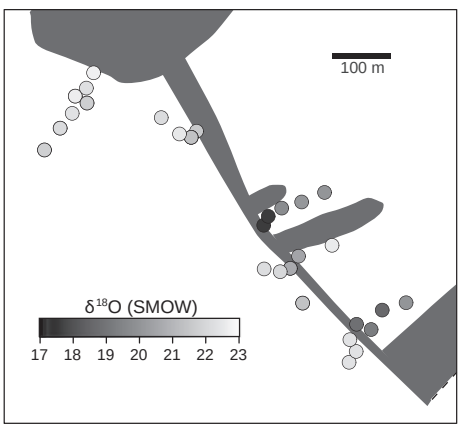

Fig. 8. Map distribution of δ^{18}O in calcite in the Northern Feeder Dyke complex. Dark areas are sills and dykes (see Fig. 2a). Where more than one sample per station was analysed, the lowest value is shown.

sions and flood basalts on Victoria Island, which should be 5–9‰ based on analysis of continental basalts elsewhere (Harmon & Hoefs, 1995). Clearly, there was only a limited oxygen isotope transfer from the mafic intrusions to the wall rocks, which contrasts with the frequent approach of oxygen isotope ratios of wall rocks to those of large granitic intrusions due to fluid expulsion from magmas (Valley, 1986; Nabelek, 1991; Baumgartner & Valley, 2001). Many metamorphic rocks near the mafic bodies on Victoria Island are ^{18}O-depleted beyond what can be explained by decarbonation. Calculated effects of Rayleigh decarbonation on $\delta^{18}O$ and $\delta^{13}C$ are superimposed on observed data in Fig. 6. They were calculated using isotopic fractionations between CO_2 and calcite at 400 °C, the approximate temperature at which most decarbonation reactions occurred (Fig. 5). The $\mathbf{\Delta}^{18}O_{(CO_2\text{-Cal})}$ is 7‰ and $\mathbf{\Delta}^{13}C_{(CO_2\text{-Cal})}$ is 3.6‰ (Chacko *et al.*, 1991). Rayleigh decarbonation implies instantaneous removal of CO_2 from the rock and therefore leads to greater isotopic depletion than batch decarbonation in which generated CO_2 stays in the rock (Nabelek, 1991). Due to the limited amount of silicates in the examined metamorphic rocks, a maximum of ~20% carbonate minerals were lost by metamorphic reactions. This implies the maximum of ~2‰ decrease in $\delta^{18}O$ by decarbonation. Thus, another mechanism must account for the excess ^{18}O depletion in the highlighted high-grade rocks in Fig. 6. The most likely mechanism was a fluid-mediated isotopic exchange with the proximal mafic sheets while calcite in the wall rocks was undergoing recrystallization or was produced by metamorphic reactions (e.g. Reactions 4 and 6).

The oxygen isotope systematics in the NFD complex (Fig. 8) present a particularly good illustration for the influence of mafic sheets on oxygen isotope depletion and they speak to the geometry of syn-metamorphic fluid flow. On the west side of the dyke, the largely unshifted $\delta^{18}O$ values indicate little isotopic exchange between the dyke and wall rocks. This suggests that fluid flow there was mostly vertical, parallel to the dyke. In contrast, the evident ^{18}O depletion in the wall rocks on the east side of the dyke points to a more vigorous isotopic exchange with the mafic sheets, particularly the sills. The sills show a fair amount of chloritization of mafic minerals and the wall rocks have serpentine, chlorite or epidote, all of which point to flow of aqueous fluids through all the rocks on the east side of the fault while the rocks were hot. While the sills were still partially molten, hence impermeable, early fluid flow was probably convective between the sills. Upon solidification, the sills apparently became more permeable due to shrinking, and therefore were invaded by aqueous fluids.

Pore fluids from within the sedimentary basin probably dominated the aqueous fluids near the intrusive sheets, at least during the retrograde stages of metamorphism when serpentine grew. However, during early stages of metamorphism, after fluid pressure next to the mafic sheets dropped, magmatic water emanating from the crystallizing mafic magma, sills especially, may have invaded the wall rocks. Mafic melts can contain as much as 3 wt% water at 1 kbar (Dixon *et al.*, 1995), and this amount of exsolved water may have caused some, if not all, of the ^{18}O depletion in the wall rocks. Expulsion of water from sills is consistent with the development of Fe-enriched skarns that typically occur above sills, especially at Uhuk Massif. There is no evidence for influx of meteoric water into the basin during the mafic magmatism. If meteoric waters invaded the basin, the evidence for their presence must have been erased by isotopic exchange with the host rocks. Alternatively, because isotopic exchange of minerals with fluids typically occurs during recrystallization (Nabelek *et al.*, 1992; Roselle *et al.*, 1999), flow of sedimentary and meteoric fluids may not have been registered by unrecrystallized carbonate minerals.

There are three mechanisms by which $\delta^{13}C$ in carbonate minerals can decrease from primary sedimentary values during metamorphism: (i) decarbonation; (ii) influx of low-^{13}C carbon from a nearby magma; and (iii) exchange with organic carbon. $\delta^{13}C$ values in host rocks proximal to the intrusions in the SFD-A and SFD-D zones and at Uhuk Massif are clearly lowered beyond what could have been accomplished by decarbonation (Fig. 6). Although a continental flood basalt magma can contain some CO_2, the amount is unlikely to influence $\delta^{13}C$ of carbon-dominated wall rocks. Assuming CO_2 saturation at 1 kbar (3 km depth), the basaltic melts would have contained no more than ~500 ppm CO_2 (Dixon *et al.*, 1995). Exchange with local low-^{13}C organic carbon was probably the main mechanism by which $\delta^{13}C$ values in carbonate minerals were decreased. $\delta^{13}C$ of organic carbon ranges from −19 to −28‰ (D. Thompson, personal communication). During metamorphic recrystallization of carbonates, $\delta^{13}C$ of carbonate minerals commonly decreases due to exchange with organic material and can mimic apparent climatic $\delta^{13}C$ excursions (Bergfeld *et al.*, 1996; Labotka *et al.*, 2000). Because the diffusion of carbon in carbonate minerals is very slow, $\sim 10^{-21}$ m^2 s^{-1} over the full range of $X(CO_2)^{fluid}$ (Labotka *et al.*, 2011), carbon isotope exchange in Victoria Island metamorphic rocks must have occurred during recrystallization of calcite in the presence of carbon-bearing fluids. Indeed, in samples with anomalously ^{13}C-depleted carbon, calcite has been recrystallized and is typically poikiloblastic. Recrystallization to a larger grain size itself implies the presence of an aqueous fluid component.

Overall, the carbon and oxygen isotope data and mineralogy point to focused fluid flow through narrow zones at the interfaces between the sheet intrusions and their wall rocks. The focusing may have been guided by a relative impermeability of the intrusions and by creation of reaction-enhanced permeability in the wall rocks due to a decrease in the

volume of the solid assemblages by reactions (e.g., Rumble *et al.*, 1982; Nabelek *et al.*, 1984; Nabelek, 2009). Moreover, high fluid pressures generated by heating of pore fluids and by early metamorphic decarbonation reactions may have driven fluid flow near the intrusions. Reaction-enhanced permeability and high transient fluid pressures would have been particularly important at Uhuk Massif due to the high proportion of silicates in the protoliths. They probably promoted the evident Fe metasomatism, the development of skarns and the brecciation of the sill's roof at Uhuk. Syn-intrusion faulting and junctions between sills and dykes may also have enhanced fluid flow near the mafic sheets.

Duration of metamorphism

Rapid heating and a short duration of elevated temperature regimes in contact aureoles of the gabbroic sheets on Victoria Island is implied by the prevalent acicular morphology of diopside and the variable recrystallization of calcite in thick marble horizons (Fig. 3). The morphology differs from the usual equant morphology of diopside and coarse marbles in aureoles of large intrusions (Berger *et al.*, 2010), where elevated temperature regimes can prevail for tens of thousands of years due to large pluton sizes and long durations of pluton growth (Annen, 2011; Nabelek *et al.*, 2012). Around large plutons, rock textures have a greater chance of annealing. On Victoria Island, rapid emplacement and much smaller thicknesses of gabbroic sheet intrusions limited the time that the wall rocks spent at elevated temperatures. However, an extended period of retrograde, H_2O-present metamorphism is evident in the frequent occurrence of hydrous minerals, including serpentine, chlorite and epidote.

Calculated temperature–time (T–t) paths of the aureole rocks support the occurrence of a short-duration elevated temperature regime, followed by an extended period of a retrograde regime in the contact aureoles on Victoria Island (Fig. 9). The profiles were calculated following the method of Nabelek *et al.* (2012) that employs temperature-dependent thermal diffusivity of crystallizing melts and aureole rocks (Whittington *et al.*, 2009). The necessary liquidus and solidus temperatures, 1150 and 840 °C, respectively, were obtained with the program MELTS (Ghiorso & Sack, 1995) for compositions of the Victoria Island sills (Dostal *et al.*, 1980). The initial temperature of the wall rocks was assumed to be 80 °C, which is appropriate for magma emplacement depth of ~3 km. A 50 m thick gabbroic sheet intrusion and heat transfer only by conduction were assumed.

The T–t paths for a rock 5 m from the sheet intrusion show a rapid temperature increase into a temperature regime in which diopside and phlogopite coexist in metamorphic rocks of the NFD and SFD complexes and in which vesuvianite, garnet and diopside coexist in Uhuk rock compositions (Fig. 5). The rapid temperature increase is consistent with prograde growth of acicular diopside splays. Irrespective how thick a sheet intrusion is, temperature will always increase rapidly in rocks right next to it, although the maximum temperature that will be reached will vary. Rocks 25 m from the model sheet intrusion reach diopside-present fields, but *c.* 60 years later. Rocks 50 m from the sheet intrusion barely reach the tremolite present field, if at all. Notable is the convergence after *c.* 150 years of the three illustrated T–t paths onto the 350–400 °C temperature range in which serpentine, chlorite and epidote are stable (Fig. 5). The calculations suggest that this temperature regime remained active around individual intrusive sheets for an extended period of time, giving an opportunity for these retrograde hydrous minerals to grow in the presence of convecting aqueous fluids.

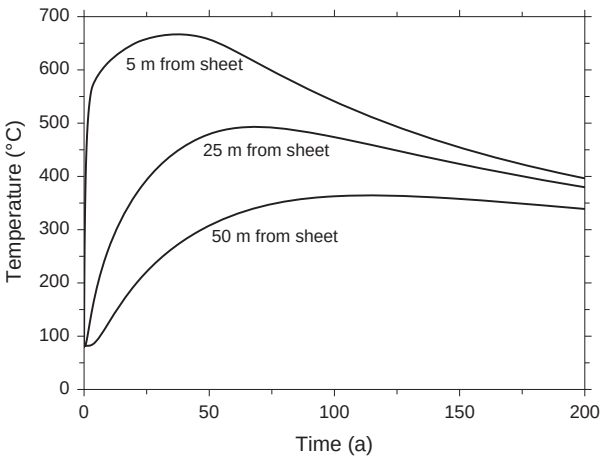

Fig. 9. Calculated conductive temperature–time paths surrounding a 50 m thick intrusive sheet. Liquidus and solidus temperatures, 1150 and 840 °C, respectively, were obtained with the program MELTS (Ghiorso & Sack, 1995) for compositions of the Victoria Island sills (Dostal *et al.*, 1980). The initial temperature of the wall rocks was assumed to be 80 °C. Note that 150 years after emplacement of a sheet intrusion, there is a convergence of temperatures onto the 300–400 °C range, in which retrograde serpentine, chlorite and epidote are predicted to be stable in the metamorphic rocks on Victoria Island (Fig. 5).

The Shaler Supergroup has numerous sills throughout its exposed stratigraphy. There are at least two geochemically distinct populations of dykes, sills and flood basalt that, based on field relationships, may represent different phases of the Franklin magmatic event (Williamson *et al.*, 2012). This would suggest that magmatism in the region occurred over a time period that was several orders of magnitude longer than the time it took to inject one dyke or one sill into the Shaler Supergroup. The narrow contact aureoles around the intrusive sheets are consistent with a long duration of the Franklin magmatic event on Victoria Island, because they point to only a limited heat input into the sedimentary basin by injected mafic magma at any one time.

ACKNOWLEDGEMENTS

This research is part of and was supported by a project led by the Geological Survey of Canada under the Geomapping for Energy and Minerals Program of Natural Resources Canada (contribution no. 20120192). Other funding sources include the U.S. National Science Foundation grant No. EAR-0911116, and by the University of Missouri Research Board grant No. RB-09-31. Y. Chen prepared samples for thin sections and drilled-out carbonate minerals. W.W. Ritts helped with SEM analysis, P. Carpenter helped with electron microprobe analysis, and S. Haynes ran stable isotope analysis. R. Rainbird, D. Thompson and L. Corriveau provided helpful comments on the manuscript. Thanks also go to all who have provided logistical and transportation support and good company on Victoria Island during two field seasons. L. Baumgartner and A. Berger provided constructive critiques of the manuscript and D. Whitney had important editorial suggestions.

REFERENCES

Annen, C., 2011. Implications of incremental emplacement of magma bodies for magma differentiation, thermal aureole dimensions and plutonism-volcanism relationships. *Tectonophysics*, **500,** 3–10.

Armbruster, T., Birrer, J., Libowitzky, E. & Beran, A., 1998. Crystal chemistry of Ti-bearing andradites. *European Journal of Mineralogy*, **10,** 907–921.

Baumgartner, L.P. & Valley, J.W., 2001. Stable isotope transport and contact metamorphic fluid flow. *Reviews in Mineralogy and Geochemistry*, **43,** 415–467.

Bédard, J.H., Naslund, H.R., Nabelek, P. *et al*., 2012. Fault-mediated melt ascent in a Neoproterozoic continental flood basalt province, the Franklin sills, Victoria Island, Canada. *Geological Society of America Bulletin*, **124,** 723–736.

Berger, A., Brodhag, S.H. & Herwegh, M., 2010. Reaction-induced nucleation and growth v. grain coarsening in contact metamorphic, impure carbonates. *Journal of Metamorphic Geology*, **28,** 809–824.

Bergfeld, D., Nabelek, P.I. & Labotka, T.C., 1996. Carbon isotope exchange during polymetamorphism in the Panamint Mountains, California. *Journal of Metamorphic Geology*, **14,** 199–212.

Cathles, L.M., 1981. Fluid flow and genesis of hydrothermal ore deposits. *Economic Geology*, **75th Anniversary Volume,** 424–457.

Chacko, T., Mayeda, T.K., Clayton, R.N. & Goldsmith, J.R., 1991. Oxygen and carbon isotope fractionations between CO_2 and calcite. *Geochimica et Cosmochimica Acta*, **55,** 2867–2882.

Cook, S.J., Bowman, J.R. & Forster, C.B., 1997. Contact metamorphism surrounding the Alta stock: finite element model simulation of heat- and $^{18}O/^{16}O$ mass-transport during prograde metamorphism. *American Journal of Science*, **297,** 1–55.

Cui, X., Nabelek, P.I. & Liu, M., 2001. Heat and fluid flow in contact metamorphic aureoles with layered and transient permeability, with application to the Notch Peak aureole, Utah. *Journal of Geophysical Research*, **106,** 6477–6491.

Cui, X., Nabelek, P.I. & Liu, M., 2002. Numerical modeling of fluid flow and oxygen isotope exchange in the Notch Peak contact-metamorphic aureole, Utah. *Geological Society of America Bulletin*, **114,** 869–882.

De Capitani, C. & Petrakakis, K., 2010. The computation of equilibrium assemblage diagrams with Theriak/Domino software. *American Mineralogist*, **95,** 1006–1016.

Dixon, J.E., Stolper, E.M. & Holloway, J.R., 1995. An experimental study of water and carbon dioxide solubilities in mid-ocean ridge basaltic liquids. *Part I: Calibration and solubility models*. *Journal of Petrology*, **36,** 1607–1631.

Dostal, J., Dupuy, C. & Leyreloup, A., 1980. Geochemistry and petrology of meta-igneous granulitic xenoliths in Neogene volcanic rocks of the Massif Central, France – implications for the lower crust. *Earth and Planetary Science Letters*, **50,** 31–40.

Dostal, J., Baragar, W.R.A. & Dupuy, C., 1986. Petrogenesis of the Natkusiak continental basalts, Victoria Island, Northwest Territories, Canada. *Canadian Journal of Earth Sciences*, **23,** 622–632.

Fournier, R.O., 1989. Geochemistry and dynamics of the Yellostone National Park hydrothermal system. *Annual Reviews of Earth and Planetary Sciences*, **17,** 13–53.

Ghiorso, M.S. & Sack, R.O., 1995. Chemical mass transfer in magmatic processes. IV. A revised and internally consistent thermodynamic model for the interpolation and extrapolation of liquid-solid equilibria in magmatic systems at elevated temperatures and pressures. *Contributions to Mineralogy and Petrology*, **119,** 197–212.

Goldsmith, J.R. & Newton, R.C., 1969. P-T-X relations in the system $CaCO_3$-$MgCO_3$ at high temperatures and pressures. *American Journal of Science*, **267-A,** 160–190.

Harmon, R.S. & Hoefs, J., 1995. Oxygen isotope heterogeneity of the mantle deduced from global ^{18}O systematics of basalts from different tectonic settings. *Contributions to Mineralogy and Petrology*, **120,** 95–114.

Heaman, L., Lecheminant, A. & Rainbird, R., 1992. Nature and timing of Franklin igneous events, Canada: implications for a Late Proterozoic mantle plume and the break-up of Laurentia. *Earth and Planetary Science Letters*, **109,** 117–131.

Holland, T.J.B. & Powell, R., 1998. An internally consistent thermodynamic data set for phases of petrological interest. *Journal of Metamorphic Geology*, **16,** 309–343.

Hulbert, L.J., Rainbird, R.W., Jefferson, C.W. & Friske, P., 2005. *Map of Mafic and Ultramafic Bodies Related to the Franklin Magmatic Event, Minto Inlier*. Geological Survey of Canada, Victoria Island.

Jones, D.S., Maloof, A.C., Hurtgen, M.T., Rainbird, R.H. & Schrag, D.P., 2010. Regional and global chemostratigraphic correlation of the early Neoproterozoic Shaler Supergroup, Victoria Island, Northwestern Canada. *Precambrian Research*, **181,** 43–63.

Kretz, R., 1983. Symbols for rock-forming minerals. *American Mineralogist*, **68,** 277–279.

Labotka, T.C., 1995. Evidence for immiscibility in Ti-rich garnet in a calc-silicate hornfels from northeastern Minnesota. *American Mineralogist*, **80,** 1026–1030.

Labotka, T.C., Bergfeld, D. & Nabelek, P.I., 2000. Two diamictites, two cap carbonates, two $\delta^{13}C$ excursions, two rifts: the Neoproterozoic Kingston Peak Formation, Death Valley, California: comment and Reply. *Geology*, **28,** 191–192.

Labotka, T.C., Cole, D.R., Fayek, M.J. & Chacko, T., 2011. An experimental study of the diffusion of C and O in calcite in mixed CO_2-H_2O fluid. *American Mineralogist*, **96,** 1262–1269.

MacDonald, W.D., Bédard, J., Hayes, B., Naslund, H.R., Carpenter, J. & Steigerwaldt, K., 2012. AMS magnetofabrics and emplacement of Franklin Dykes, Victoria Island, Arctic Canada. *Geological Association of Canada – Mineralogical Association of Canada annual meeting, Program with Abstracts*, **35,** 82.

Nabelek, P.I., 1991. Stable isotope monitors. *Reviews in Mineralogy*, **26,** 395–435.

Nabelek, P.I., 2007. Fluid evolution and kinetics of metamorphic reactions in calc-silicate contact aureoles – From H_2O to CO_2 and back. *Geology*, **35,** 927–930.

Nabelek, P.I., 2009. Numerical simulation of kinetically-controlled calc-silicate reactions and fluid flow with transient

permeability around crystallizing plutons. *American Journal of Science*, **309,** 517–548.
Nabelek, P.I. & Morgan, S.S., 2012. Metamorphism and fluid flow in the contact aureole of the Eureka Valley-Joshua Flat-Beer Creek pluton, California. *Geological Society of America Bulletin*, **124,** 228–239.
Nabelek, P.I., Labotka, T.C., O'Neil, J.R. & Papike, J.J., 1984. Contrasting fluid/rock interaction between the Notch Peak granitic intrusion and argillites and limestones in western Utah: evidence from stable isotopes and phase assemblages. *Contributions to Mineralogy and Petrology*, **86,** 25–34.
Nabelek, P.I., Labotka, T.C. & Russ-Nabelek, C., 1992. Stable isotope evidence for the role of diffusion, infiltration and local structure on contact metamorphism of calc-silicate rocks at Notch Peak, Utah. *Journal of Petrology*, **33,** 557–583.
Nabelek, P.I., Hofmeister, A.M. & Whittington, A.G., 2012. The influence of temperature-dependent thermal diffusivity on the conductive cooling rates of plutons and temperature-time paths in contact aureoles. *Earth and Planetary Science Letters, 317*, **318,** 157–164.
Norton, D.L., 1984. Theory of hydrothermal systems. *Annual Review of Earth and Planetary Sciences*, **12,** 155–177.
Norton, D.L. & Taylor, H.P., 1979. Quantitative simulation of the hydrothermal systems of crystallizing magmas on the basis of transport theory and oxygen isotope data: an analysis of the Skaergaard Intrusion. *Journal of Petrology*, **20,** 421–486.
Ogorodova, L.P., Kiseleva, I.A., Melchakova, L.V. & Spiridonov, E.M., 2011. Thermodynamic characteristics of minerals of the vesuvianite group. *Geochemistry International*, **49,** 191–195.
Rainbird, R.H., 1993. The sedimentary record of mantle plume uplift preceding eruption of the Neoproterozoic Natkusiak flood basalt. *The Journal of Geology*, **101,** 305–318.
Rainbird, R.H., Jefferson, C.W., Hildebrand, R.S. & Worth, J.K., 1994. The Shaler Supergroup and revision of Neoproterozoic stratigraphy in Amundsen Basin, Northwest Territories. *Current Research 1994-C, Geological Survey of Canada*, 61–70.
Rainbird, R., Jefferson, C. & Young, G., 1996. The early Neoproterozoic sedimentary Succession B of northwestern Laurentia: correlations and paleogeographic significance. *Geological Society of America Bulletin*, **108,** 454–470.
Roselle, G.T., Baumgartner, L.P. & Valley, J.W., 1999. Stable isotope evidence of heterogeneous fluid infiltration at the Ubehebe Peak contact aureole, Death Valley National Park, California. *American Journal of Science*, **299,** 93–138.
Rumble, D., Ferry, J.M., Hoering, T.C. & Boucot, A.J., 1982. Fluid flow during metamorphism at the Beaver Brook Fossil Locality, New Hampshire. *American Journal of Science*, **282,** 886–919.
Toulmin, P. & Barton, P.B., 1964. A thermodynamic study of pyrite and pyrrhotite. *Geochmica et Cosmochimica Acta*, **28,** 641–671.
Valley, J.W., 1986. Stable isotope geochemistry of metamorphic rocks. *Review in Mineralogy*, **16,** 445–489.
Whittington, A.G., Hofmeister, A.M. & Nabelek, P.I., 2009. Temperature-dependent thermal diffusivity of Earth's crust and implications for magmatism. *Nature*, **458,** 319–321.
Williamson, N., Cousens, B., Ootes, L., Bédard, J., Rainbird, R. & Dell'Oro, T., 2012. Volcano-stratigraphy and major element geochemistry of the Southern Lobe of the Natkusiak Formation Flood Basalts of Victoria Island: insights into the initiation of the Neoproterozoic Franklin Magmatic Event. *Geological Association of Canada – Mineralogical Association of Canada annual meeting, Program with Abstracts*, **35,** 152.

SUPPORTING INFORMATION

Additional Supporting Information may be found in the online version of this article at the publisher's web-site:

Table S1. δ13C and δ18O values of carbonate minerals in metamorphosed Victoria Island rocks.

Received 14 June 2010; revision accepted 11 October 2012.

Appendix C – electron microprobe methods for mineral species analysed

The following methods were used for all mineral chemical data presented in this thesis.

Olivine compositions. Analyses were done at 20 nA at 15 kV. Detection limits are *ca.* 0.01 wt% for all elements. Background values were counted for ½ the time counted at the peak. Spectrometer 1: LIF crystal, Mn-Kα, 20 seconds, standard = busx. Fe-Kα, 20 seconds, standard = haematite. Spectrometer 2: LLIF crystal, Cr-Kα, 20 seconds, standard = chromite. Na-Kα, 20 seconds, standard = nickel metal. Spectrometer 3: LPET crystal, Ca-Kα, 20 seconds, standard = diopside. Ti-Kα, 20 seconds, standard = rutile. Spectrometer 4: TAP crystal, Si-Kα, 20 seconds, standard = olvx (olivine). Mg-Kα, 20 seconds, standard = olvx. Spectrometer 5: TAP crystal, Al-Kα, 20 seconds, standard = plagvz (plagioclase). Not analyzed: O. Number of Oxygen's = 4. Number of H2O = 0.

Pyroxene compositions. Analyses were done at 20 nA at 15 kV. Detection limits are *ca.* 0.01 wt% for all elements. Background values were counted for ½ the time counted at the peak. Spectrometer 1: LIF crystal, Fe-Kα, 15 seconds, standard = haematite. Cr-Kα, 15 seconds, standard = chromite. Ti-Kα, 15 seconds, standard = rutile. Spectrometer 2: LLIF crystal, Ni-Kα, 20 seconds, standard = nickel metal. Mn-Kα, 20 seconds, standard = busx. Spectrometer 3: LPET crystal, K-Kα, 20 seconds, standard = orthoclase. Ca-Kα, 20 seconds, standard = diopside. Spectrometer 4: TAP crystal, Si-Kα, 20 seconds, standard = gzvz. Mg-Kα, 20 seconds, standard = olvx. Spectrometer 5: TAP crystal, Na-Kα, 20 seconds, standard = albite. Al-Kα, 20 seconds, standard = cor. Not analyzed: O. Number of Oxygen's = 6. Number of H2O = 0. Same method used for both clinopyroxene and orthopyroxene.

Plagioclase compositions. Analyses were done at 20 nA at 15 kV. Detection limits are *ca.* 0.01 wt% for all elements. Background values were counted for ½ the time counted at the peak. Spectrometer 1: LIF crystal, Ti-Kα, 20 seconds, standard = rutile. Mn-Kα, 20 seconds, standard = busx. Spectrometer 2: LIFF crystal, Fe-Kα, 20

seconds, standard = haematite. Ba-Kα, 20 seconds, standard = barite. Spectrometer 3: LPET crystal, Ca-Kα, 20 seconds, standard = diopside. K-Kα, 15 seconds, standard = orthoclase. Sr-Lα, 15 seconds, standard = celestite. Spectrometer 4: TAP crystal, Si-Kα, 20 seconds, standard = plagvz. Mg-Kα, 20 seconds, standard = olvx. Spectrometer 5: Na-Kα, 20 seconds, standard = albite. Al-Kα, 20 seconds, standard = cor. Not analyzed: O. Number of Oxygen's = 8. Number of H2O = 0.

Spinel compositions. Analyses were done at 20 nA at 15 kV. Detection limits are *ca.* 0.01 wt% for all elements. Background values were counted for ½ the time counted at the peak. Spectrometer 1: LIF crystal, Co-Kα, 15 seconds, standard = ATX-Co. Fe-Kα, 15 seconds, standard = haematite. Mn-Kα, 15 seconds, standard = busx. Spectrometer 2: LLIF crystal, Zn-Kα, 15 seconds, standard = sphalerite. Ni-Kα, 15 seconds, standard = nickel metal. Cr-Kα, 15 seconds, standard = chromite. Spectrometer 3: LPET crystal, Ca-Kα, 20 seconds, standard = diopside. Ti-Kα, 20 seconds, standard = rutile. Spectrometer 4: TAP crystal, Si-Kα, 20 seconds, standard = gzvz. Na-Kα, 20 seconds, standard = albite. Spectrometer 5: Al-Kα, 20 seconds, standard = plagvz. Mg-Kα, 20 seconds, standard = olvx. Not analyzed: H. Not analyzed: O. Number of Oxygen's = 32. Number of H2O = 0.

Appendix D1 – Franklin liquid line of descent

Jean Bédard, co-supervisor of this PhD thesis, carried out much of the Franklin magma liquid line of descent (LLD) modelling. Jean constructed and organised the Victoria Island geochemical database and modelled the magma suites to find the best-fit liquid line of decent to the two suites of magma (Franklin Type-1 and Type-2). Below is a summary of the geochemical database and justifications for the model parameters.

The major element distributions of the Type-1 versus Type-2 suites were examined using simple Harker plots. The database was culled to remove obvious olivine and clinopyroxene cumulates, as well as obvious hybrids with limestone. The culled database includes samples classed as lavas (v), chilled margins (+) and diabasic facies (x). It is probable that many of these compositions are perturbed by a) post emplacement alteration, b) metasomatism or exchange with wallrocks and/or c) pre-, syn- or post-emplacement accumulation of phases. Although the most obvious olivine cumulates were excluded, it is probable that some of the higher-MgO analyses from the database (many with no corresponding petrographic data) contain 'cumulus' olivine. This will be tested using the PELE modelling. Some of the diabasic samples may represent 2- or 3-phase cumulates (cpx+plag+olivine, cpx+plag+pigeonite, plag+cpx+magnetite…), principally reflecting loss of pore melt during solidification. This would mainly act to decrease incompatible element contents (TiO2, K2O, P2O5..), shift bulk compositions back along the cotectic Fe-enrichment trend, and possible cause enrichment of Al2O3 and CaO above the true LLD.

There are obvious differences in the distributions of the two suites of Franklin magmas (Type-1 versus Type-2), which imply they should be modelled separately. Magmas of the Type-1 suite extend to higher MgO contents than those of the Type-2 suite. Although much of the Type-1 high-MgO tail is probably an accumulation effect, the almost complete lack of such a tail for the Type-2 suite implies that these magmas did not experience a long olivine-only crystallisation history after emplacement in the crust. Furthermore, Type-1 sills contain relatively little ferrogabbro with high FeO/MgO, in contrast with the Type-2 sills, which do. As a result, most sills related to the Type-1 suite show a clear Fe-enrichment trend, but rarely 'turn the corner' towards an Fe-depletion/SiO2 enrichment trend that indicates abundant extraction of magnetite. This contrasts with sills of Type-2 suite, that show more extended evolution towards low FeO and higher SiO2. The overall

trend of geochemical evolution also differs between the two suites. The Type-1 suite shows a trajectory at a slightly lower FeO and TiO2, and a slightly higher SiO2 content for a given MgO value, and starts its FeO-TiO2-enrichment trend at a slightly lower MgO content than the Type-2 sills. Thus, the FeO-TiO2-enrichment trends of the two suites are offset one from the other. Additionally, Type-1 magmas show a slightly higher K2O content, but the two suites have similar Na2O contents.

Since many of the most detailed studies were done on sills emplaced near the Fort Collinson Formation, pressures for Type-1 magma differentiation were estimated from the height of this overlying stratigraphic column, ~2.5 km, which translates to ~0.8 kbar. All simulations were done at this pressure. Preliminary QUILF calculations by Bédard et al (2008) on Type-1 magmas suggest QFM +1 to +2, so calculations were done at QFM +1 and +2, bracketing observed fO2 conditions. The gabbroic segment of the PELE models cannot exactly mimic the observed trends, however, because the PELE code does not include pigeonite, which is observed near the base of the gabbroic sequence in several Type-1 sills.

Trace hornblende and biotite occur as rims on higher-temperature silicates in many sills, suggesting that some magmas were not entirely dry, such that extended in-situ fractional crystallization locally caused water contents to build up to the point where these phases were stabilized. An initial water content of 0.2% was assumed for some models, since 95% crystallization of such a starting point will yield the 4% H2O content needed to stabilize hornblende. Of course, F and Cl will stabilize these phases even at lower H2O contents. Limited data show that Hb and biotite in Franklin sills do indeed contain significant Cl and F-contents (up to 1-1.5 wt% combined F+Cl), but some water may also be present. There is no direct analytical data on H in these phases to constrain this at present. Melt CO2 solubilities are very low at these pressures, and initial staring contents were assumed to be ca 0.2% also. These values were varied.

Typical S-contents of Franklin magmas are ca 0.04%, with some chilled margins recording higher values (up to ca 0.15%). Small Ni-Fe sulphide blebs in chills and olivine cumulates suggest early, small-scale sulphide immiscibility may be common. Even though PELE does not consider the effects of Cu and Ni on sulphide immiscibility, early Fe-sulphide melt exsolution is commonly observed in models that assumed higher initial S contents of

ca 0.12%, and small amounts of sulphide exsolves intermittently throughout the model crystallization history. The amounts are always small, however, in keeping with the small amount of initial S in the melt. More evolved ferrogabbroic rocks typically contain Cu-Fe sulphide blebs. Models that assumed low initial S contents of ca 0.04% only showed immiscibility in the later crystallization history, often after cosaturation of magnetite. This suggests that the sharp decrease in FeO caused by magnetite crystallization often triggers immiscibility by lowering S-solubility in the melt, which is strongly dependent on FeO content (Mavrogenes?). These results and observations imply that the v0 melts were probably very close to sulphide saturation, but that S contents were probably too low to create sulphide orebodies during closed-system crystallization. On the other hand, even minor assimilation of S-rich limestone or sulphates would probably trigger immiscible sulphide separation, with the amount of sulphide produced correlating directly to S-input.

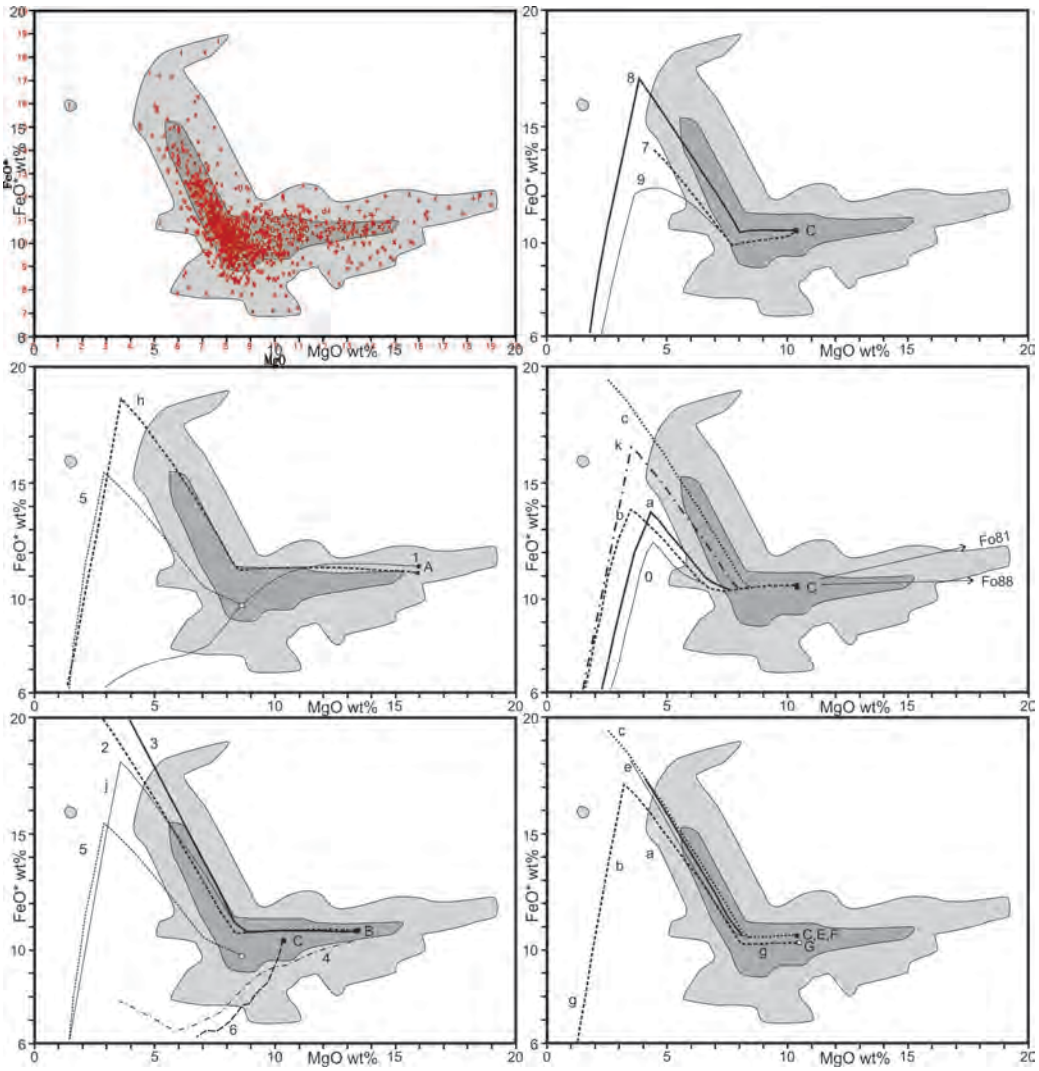

A final ‘optimized’ model K was run with slightly lower CaO, water (0.1%) and CO2 (0.1%), and higher Al2O3 and SiO2 the initial Uhuk chill model (C), and yields an optimal fit to the data. Na2O is probably very slightly too high, since mixing lines with plausible olivine compositions do not fit the accumulative high-MgO tail of the data. This presupposes that these compositions are primary, however. This model hits the solidus at about 1240C, initially crystallizing Fo 88 olivine. About 7.5% olivine is extracted prior to feldspar cosaturation at ca 1175C. At these conditions Fo85 olivine and An79 plagioclase form, compositions very similar to the observed data. Only a short interval of ol+plag crystallization is allowed before cpx joins the assemblage below 1165C at SiO2 ca 51.7 and MgO 7.3%, in accord with the absence of thick wehrlitic cumulate sequences. The 3-phase assemblage crystallizes between 1160C and 1060 C, with an average proportion of Ol:Cpx:plag of 16:37:47. Magnetite joins the assemblage at SiO2 >54%, FeO*>16.6%, TiO2 >2.25% and MgO <3%, with an initial pulse of 3.5%/10C crystallization at 1060C, also triggering minor sulphide immiscibility. Thereafter, the proportion decreases to 0.8% and then to 0.5, 0.4, and 0.3 at 1050, 1040 and 1030C. After 1030C, orthopyroxene joins the assemblage. Ilmenite is absent, however. The subsequent evolutionary path is probably not realistic.

I compared the LLD derived from PELE that best fits the Franklin Type-1 suite to MELTS. Below are simple excel plots showing the LLDs from PELE (green triangles) and MELTS (red squares) run at the same parameters (high Ce/Yb family in blue diamonds refers to the Type-1 Franklin magma suite). Fe-enrichment starts earlier in the PELE model. The PELE model has Fe-depletion beginning at 4% MgO (after reaching a maximum of 16% FeO). MELTS reaches 13% FeO at a slightly higher MgO (5-6%). MELTS has CaO decreasing at 9% MgO (cpx in). PELE has CaO decreasing at 7% MgO. MELTS has Al2O3 increasing at 9% MgO (cpx in) and then decreasing at 7.5% MgO (plag in). Al2O3 in the PELE model decreases earlier and thus matches the high Ce/Yb family liquid line of descent much better.

The plots below show the LLD derived from PELE is a better fit to the Type-1 Franklin magma suite.

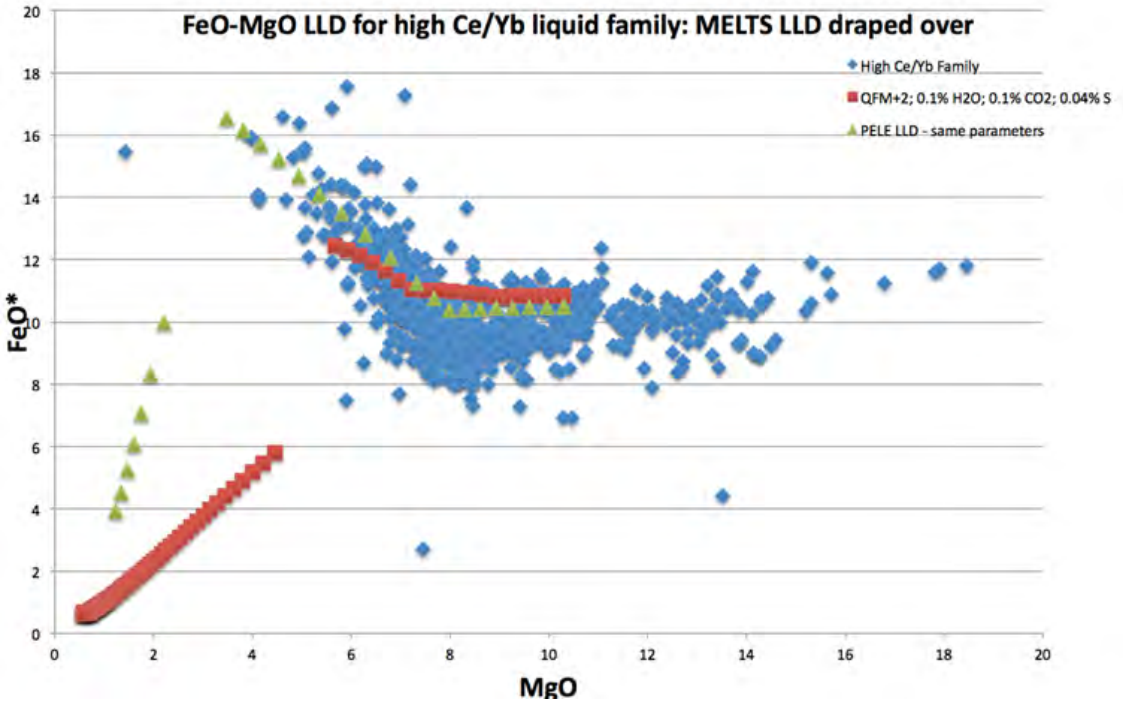
FeO-MgO LLD for high Ce/Yb liquid family: MELTS LLD draped over
High Ce/Yb Family
QFM+2; 0.1% H2O; 0.1% CO2; 0.04% S
PELE LLD - same parameters
FeO*
MgO
0
2
4
6
8
10
12
14
16
18
20

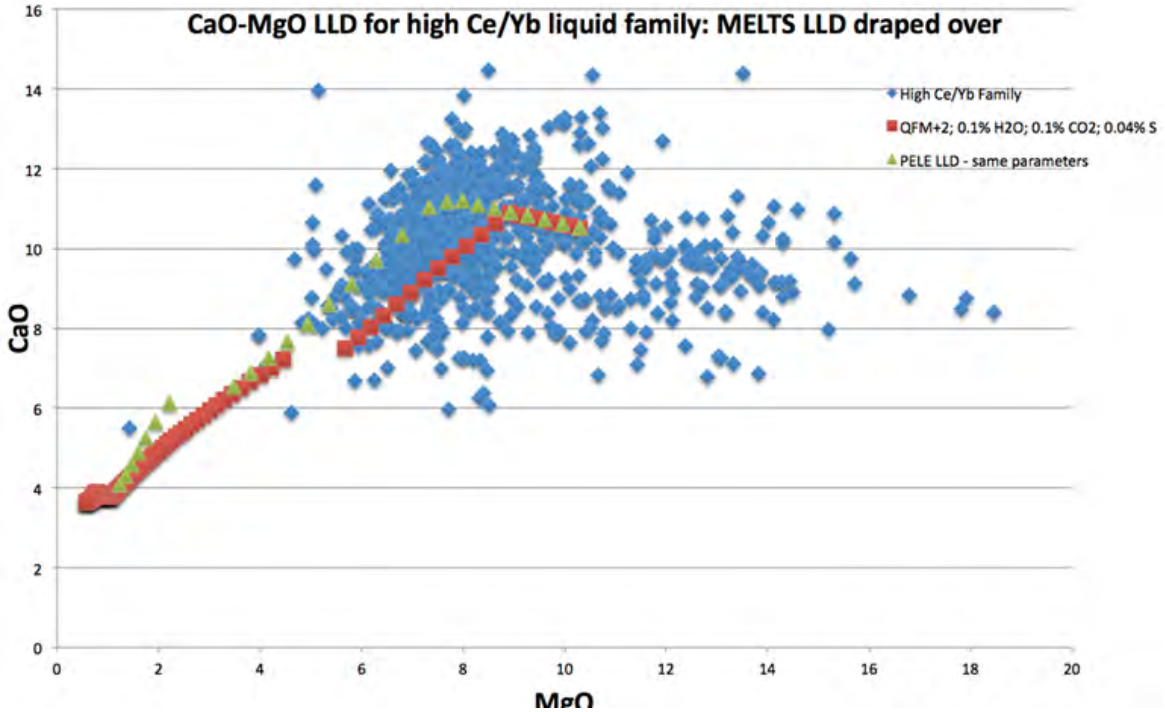
CaO-MgO LLD for high Ce/Yb liquid family: MELTS LLD draped over
High Ce/Yb Family
QFM+2; 0.1% H2O; 0.1% CO2; 0.04% S
PELE LLD - same parameters
CaO
MgO
0
2
4
6
8
10
12
14
16
18
20

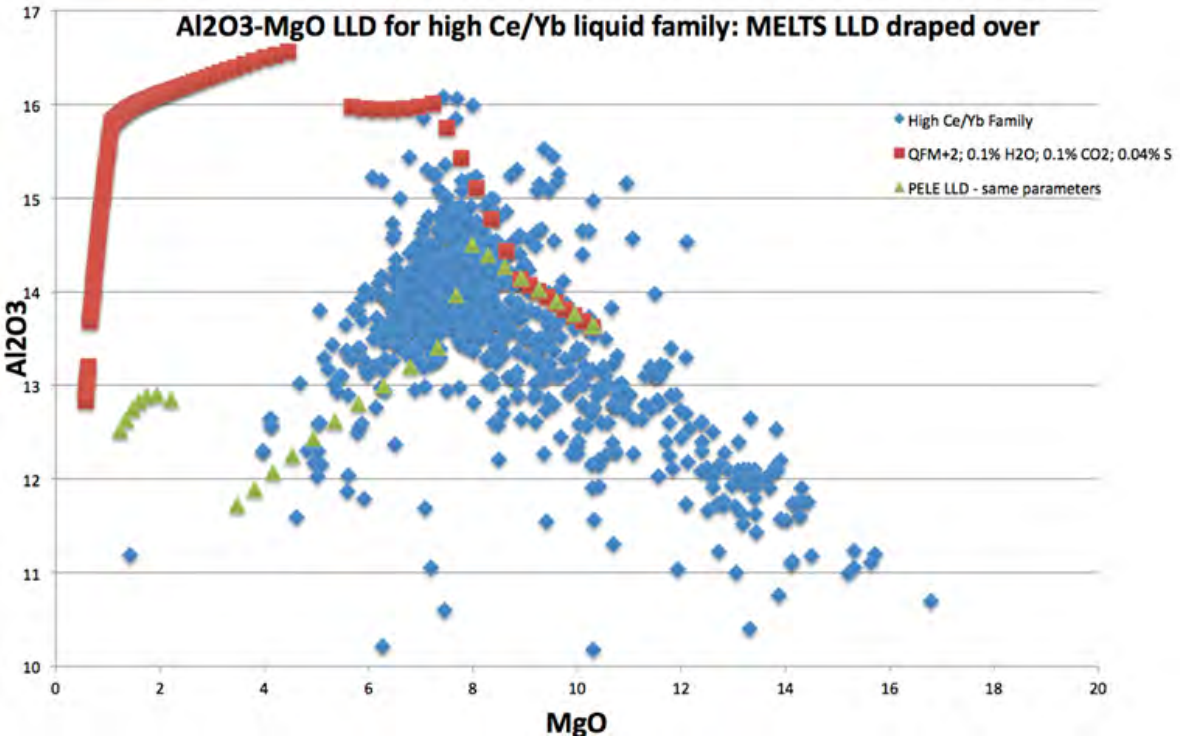

Below are other LLDs calculated from MELTS for other parameters. These plots concur with the above plots, showing that the LLD calculated from PELE is the best-fit model to the data.

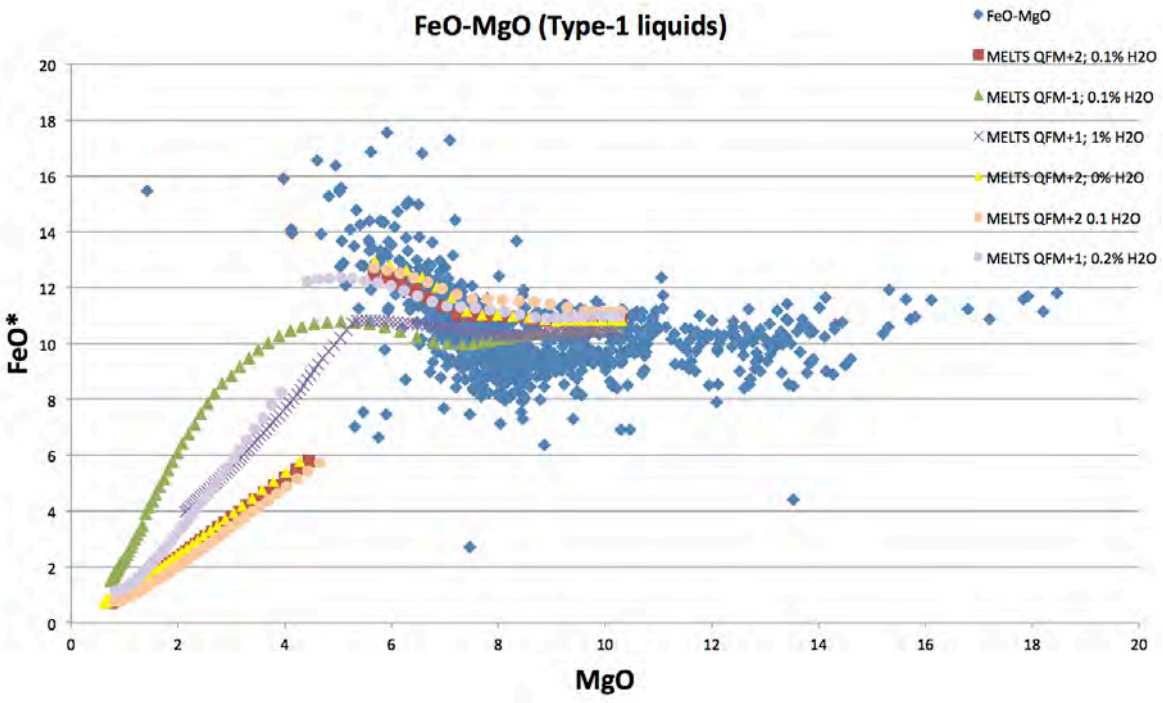

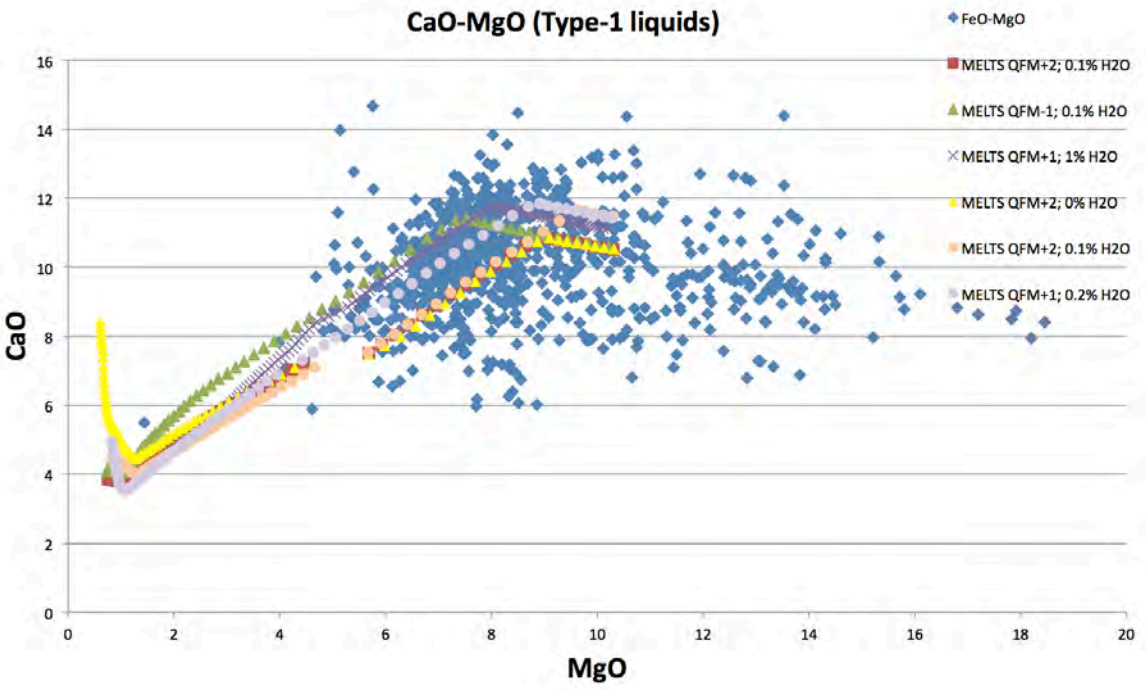
CaO-MgO (Type-1 liquids)
FeO-MgO
MELTS QFM+2; 0.1% H2O
MELTS QFM-1; 0.1% H2O
MELTS QFM+1; 1% H2O
MELTS QFM+2; 0% H2O
MELTS QFM+2; 0.1% H2O
MELTS QFM+1; 0.2% H2O
CaO
MgO
0
2
4
6
8
10
12
14
16
18
20

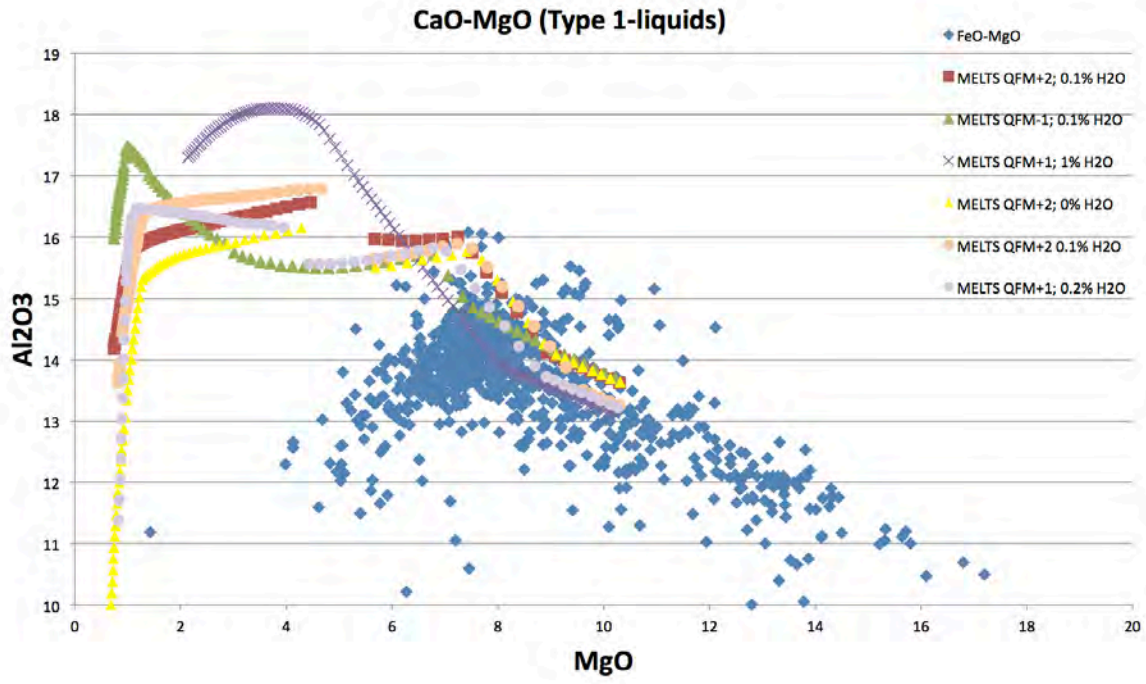
CaO-MgO (Type 1-liquids)
FeO-MgO
MELTS QFM+2; 0.1% H2O
MELTS QFM-1; 0.1% H2O
MELTS QFM+1; 1% H2O
MELTS QFM+2; 0% H2O
MELTS QFM+2 0.1% H2O
MELTS QFM+1; 0.2% H2O
Al2O3
MgO
10
11
12
13
14
15
16
17
18
19
0
2
4
6
8
10
12
14
16
18
20

Appendix D2 – Model melt parameterisations for mineral chemistry

Below are simple excel plots showing Fe/Mg versus MgO and FeO that were used to calculate the model melt compositions in equilibrium with olivine and clinopyroxene. The plots include Type-1 Franklin liquid compositions from the Victoria Island database.

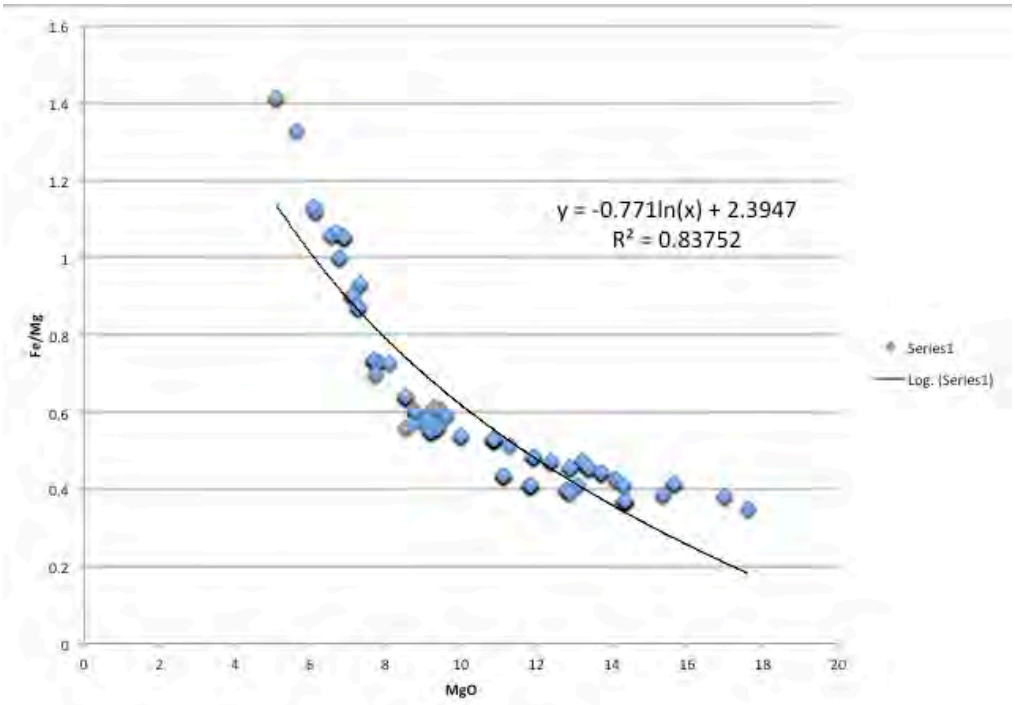

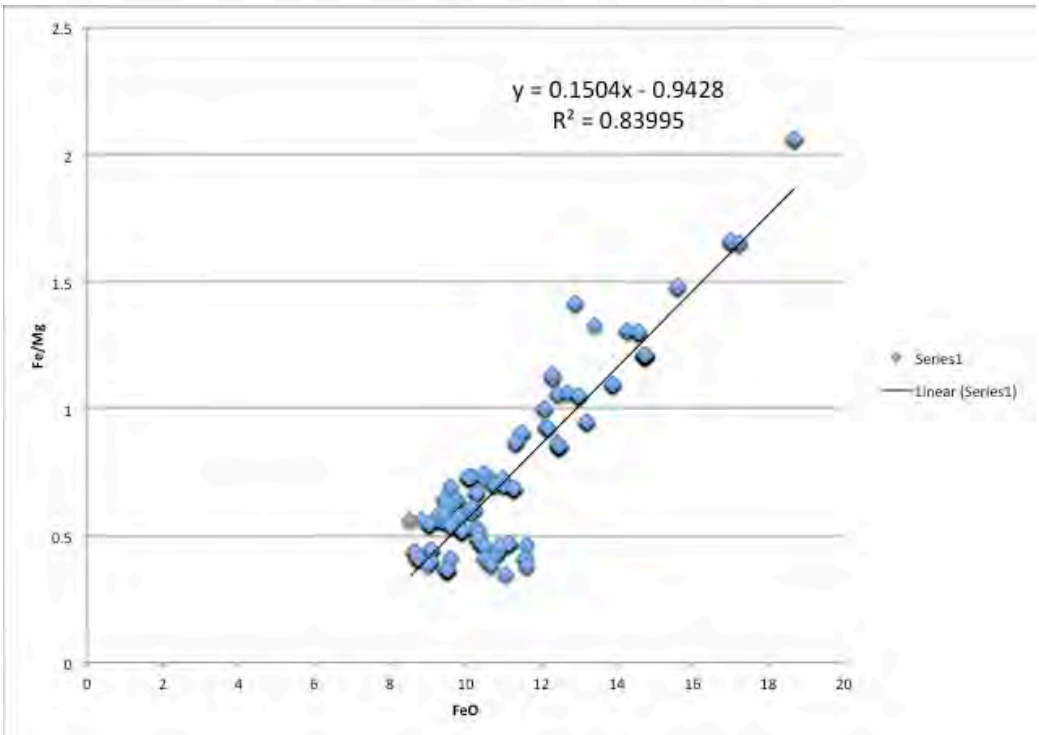

Appendix E1 – LPS whole-rock chemistry

Sample	10JB327 B1	10BH166 A2	10BH166 A3	11BH311 B2	10BH166 A4	10BH166 A5	10BH167 A1	10BH167 A2
Zone	LCM	LBZ	LBZ	LOZ	LOZ	LOZ	LOZ	MOZ
SiO_2	48.28	46.47	45.07	44.36	44.01	44.49	43.66	42.39
TiO_2	1.02	0.92	0.8	0.79	0.72	0.73	0.7	0.58
Al_2O_3	12.76	11.23	9.49	9.65	8.95	9	8.83	6.68
Fe_2O_3T	11.13	13.25	13.28	13.49	13.4	13.46	13.68	14.83
FeOT	10.01	11.91	11.94	12.12	12.05	12.1	12.3	13.33
MnO	0.15	0.19	0.19	0.2	0.19	0.2	0.18	0.2
MgO	10.74	15.32	17.84	19.64	20.69	19.95	21.42	23.52
CaO	12.25	10.16	9.65	9.33	8.92	8.81	7.97	6.47
Na_2O	1.53	1.33	1.31	0.54	1.01	0.97	0.96	0.31
K_2O	0.56	0.52	0.45	0.38	0.46	0.41	0.36	0.27
P_2O_5	0.09	0.07	0.07	0.07	0.06	0.06	0.06	0.05
S	0.11							
LOI	1.4	1.55	1.39	1.57	1.64	1.92	2.23	5.78
Total	100.3	101.02	99.55	100	100.06	100.01	100.05	101.09
Cs	1.32	0.91	0.81	0.55	0.59	0.79	0.77	1.21
K	4621.83	5214.31	4542.21	3751.91	4581.02	4140.43	3627.98	2745.24
Rb	4	20.4	17	10.4	15.3	16.1	13.6	10.3
Ba	133	96.5	58.5	95.9	131.1	68.7	53.2	53.3
Th	0.6	1.4	1.36	0.87	1.17	1.31	1.23	0.69
U	0.21	0.27	0.26	0.2	0.24	0.24	0.26	0.14
Nb	4.6	3.63	3.5	2.21	2.78	2.97	3.08	1.97
Ta	<0.3	0.24	0.25	0.17	0.21	0.21	0.21	0.13
La	6.8	6.61	6.39	4.53	5.66	5.57	5.71	3.48
Ce	16.3	15.34	14.3	10.45	12.96	12.63	12.93	8.01
Pr	2.5	2.09	1.93	1.41	1.76	1.76	1.72	1.13
Pb	1.51	2.83	3.09	1.71	3.27	4.38	2.98	2.19
P	381.63	729.04	679.89	651.94	608.74	627.9	600.75	522.92
Sr	140	143.9	106.2	104.8	110.1	101.5	98.1	60.1
Nd	10.7	9.09	8.55	6.16	7.67	7.45	7.32	4.95
Sm	2.7	2.38	2.15	1.68	1.96	2.07	1.86	1.3
Zr	72	65.8	67.7	49.6	51.4	81.	62.8	49.5
Hf	1.87	1.77	1.72	1.05	1.39	1.9	1.52	0.96
Eu	0.87	0.77	0.74	0.55	0.65	0.63	0.62	0.44
Gd	3.18	2.65	2.48	1.79	2.19	2.16	2.06	1.39
Tb	0.54	0.43	0.43	0.3	0.36	0.34	0.34	0.25
Dy	3.2	2.83	2.73	2.01	2.32	2.35	2.3	1.6
Y	19	17.6	15.9	13.9	14.1	12.5	13.5	8.8
Ho	0.68	0.5	0.5	0.36	0.43	0.43	0.44	0.28
Er	1.84	1.55	1.45	1.03	1.26	1.27	1.27	0.83
Tm	0.26	0.24	0.24	0.17	0.21	0.2	0.19	0.14
Yb	1.75	1.53	1.46	1.05	1.25	1.22	1.25	0.87
Lu	0.26	0.24	0.23	0.17	0.2	0.19	0.19	0.14
Co	45	66.5	61.8	60.1	62.8	63.2	65.8	64.5
Cr	660	788.6	1030.2	1096.2	1364.4	1345.9	1314.8	1490
Cu	133	93.5	89.7	83	80.7	104	91.1	64.9
Ni	219	325.4	403.4	451.2	723.2	453.8	536	640.9
Sc	38.9	37.3	32.1	33	31.3	30.6	29.5	25.5
V	299	291.1	229.8	230.1	224.7	214.8	230.6	180.7
Zn	43	71.6	76.9	76.4	77.1	82	76.3	58.9

Sample	10BH167 A3	10BH167 A4	11BH311 B3	11BH311 B4	10BH167 A5	10BH167 A6	10BH167 A7	10BH167 A8
Zone	MOZ	UOZ	UOZ	CPZ	CPZ	DZ	DZ	DZ
SiO_2	41.61	42.72	43.95	49.94	48.63	47.85	47.45	48.1
TiO_2	0.55	0.69	0.64	0.9	0.94	1.02	1.05	0.96
Al_2O_3	6.56	8.07	7.9	10.55	12.08	13.59	14.12	14.39
Fe_2O_3T	14.14	13.99	14.43	10.11	11	11.96	12.03	10.71
FeOT	12.71	12.58	12.97	9.09	9.89	10.75	10.81	9.63
MnO	0.2	0.19	0.2	0.17	0.16	0.19	0.17	0.17
MgO	25.43	21.83	20.52	11.45	10.56	8.63	8.58	8.63
CaO	6.21	8.17	8.36	14.11	12.09	11.65	11.54	10.82
Na_2O	0.4	0.81	0.78	1.26	1.51	1.84	1.76	1.83
K_2O	0.27	0.31	0.26	0.85	1.02	1.04	1.35	1.98
P_2O_5	0.05	0.06	0.05	0.06	0.07	0.07	0.08	0.08
S								
LOI	5.53	2.82	3.08	1.9	2.01	2.7	2.2	3.31
Total	100.95	99.67	100.17	101.31	100.08	100.56	100.33	100.98
Cs	1.32	0.77	0.71	0.68	0.77	0.8	0.7	0.58
K	2698.49	3061.85	2596.98	8474.67	10277.55	10444.53	13523.71	19766.51
Rb	11.8	12.7	9.4	23.8	28.1	31.4	37.4	70.8
Ba	30	87.4	4.6	105.1	81.9	79.5	221.9	179.5
Th	0.79	0.95	0.81	1.25	1.31	1.42	1.56	1.45
U	0.16	0.2	0.17	0.24	0.28	0.28	0.34	0.3
Nb	1.78	2.64	1.81	3.26	3.67	3.86	3.89	4.06
Ta	0.14	0.17	0.15	0.22	0.25	0.27	0.29	0.27
La	3.68	4.88	3.99	5.83	6.22	6.59	7.46	6.9
Ce	8.38	11.24	9.11	13.93	14.59	15.26	17.44	16.27
Pr	1.16	1.56	1.25	1.89	2.01	2.08	2.4	2.22
Pb	1.87	2.77	1.77	1.85	1.96	2.76	2.4	2.21
P	514.89	639.41	516.62	640.06	671.02	718.88	841.73	758.71
Sr	58.7	91.2	80.4	166.6	206.2	234.9	305.3	318.7
Nd	5.14	6.75	5.49	8.42	8.82	9.11	10.39	9.66
Sm	1.43	1.85	1.39	2.29	2.35	2.5	2.74	2.46
Zr	42.9	54.9	46.9	68.8	79.9	76.2	82.4	80.7
Hf	1.02	1.33	0.94	1.68	1.76	2.05	2.22	2.01
Eu	0.45	0.59	0.49	0.72	0.79	0.97	0.89	0.85
Gd	1.46	1.96	1.64	2.49	2.6	2.74	3.01	2.71
Tb	0.25	0.31	0.26	0.45	0.44	0.48	0.53	0.46
Dy	1.68	2.14	1.86	2.88	2.9	3.19	3.25	3.11
Y	8.8	11.6	10.5	18.1	18.6	18.2	21	18.9
Ho	0.3	0.39	0.34	0.54	0.57	0.59	0.59	0.57
Er	0.92	1.21	0.98	1.59	1.65	1.72	1.81	1.68
Tm	0.14	0.19	0.15	0.25	0.24	0.26	0.28	0.26
Yb	0.87	1.19	1.04	1.51	1.57	1.68	1.72	1.66
Lu	0.15	0.18	0.16	0.25	0.25	0.26	0.27	0.26
Co	64.6	64.6	61.5	49.6	50.9	58.9	55.1	50.4
Cr	1591.6	1244.9	1704.8	1945.7	1023.8	324.9	269	292.9
Cu	89	92.1	64	87.7	95.8	104.6	108.4	91
Ni	622.8	513	562.2	124.7	80.9	56.4	87.4	68.1
Sc	24.1	30.3	31.5	56.4	49.5	42.6	41.4	40.7
V	167	205.7	201	363.7	342.6	346.7	343.4	321.2
Zn	119.3	123.8	55.9	54	80.3	61.4	75.5	43.1

Sample	10BH167 A9	11BH311 B6	10BH167 A10	10BH167 A10	10BH167 A11-1	10BH167 A12	10BH167 A14	11BH311 B7
Zone	DZ	DZ	DZ	DZ	DZ	DZ	UBZ	UCM
SiO_2	46.59	47.88	46.62	46.62	47.95	47.15	48.61	48.34
TiO_2	1.24	1.18	1.17	1.17	1.03	1.07	1.02	1.08
Al_2O_3	13.36	14.24	13.51	13.51	12.88	13.07	12.87	13.08
Fe_2O_3T	13.81	12.21	11.68	11.68	12.29	12.26	12.56	12.21
FeOT	12.41	10.98	10.5	10.5	11.05	11.02	11.29	10.97
MnO	0.18	0.18	0.17	0.17	0.2	0.18	0.19	0.19
MgO	8.01	8.46	7.92	7.92	8.85	8.81	9.18	8.68
CaO	9.81	11.26	11.29	11.29	10.26	11.03	12.06	12.04
Na_2O	2.4	1.78	2.01	2.01	1.67	1.52	1.6	1.63
K_2O	1.17	1.26	1.07	1.07	1.61	1.55	0.98	1.13
P_2O_5	0.09	0.09	0.09	0.09	0.08	0.09	0.09	0.09
S								
LOI	4.09	2.2	3.52	3.52	3.13	2.61	2.04	2.39
Total	100.74	100.76	99.06	99.06	99.95	99.33	101.19	100.86
Cs	0.36	1.11	0.37	0.37	0.84	1.28	1.81	0.54
K	11704.8	12584.77	10.655.67	10655.67	16124.63	15465.69	9834.86	11313.22
Rb	39.8	37.2	35.4	35.4	52.5	40.8	34.3	27.2
Ba	140.9	143.1	112.7	112.7	211.5	161.3	125.3	174.3
Th	1.63	1.72	1.85	1.85	1.56	1.43	1.69	1.7
U	0.35	0.35	0.37	0.37	0.31	0.32	0.37	0.34
Nb	4.44	4	4.8	4.8	4.32	3.92	3.55	4.29
Ta	0.3	0.32	0.35	0.35	0.28	0.26	0.29	0.31
La	7.55	7.94	7.97	7.97	7.64	7.53	7.92	8
Ce	17.34	18.34	19.1	19.1	17.6	17.15	17.84	18.53
Pr	2.34	2.51	2.59	2.59	2.42	2.33	2.41	2.54
Pb	1.56	1.74	1.72	1.72	1.61	1.3	2.63	2.43
P	896.02	853.7	896.2	896.2	836.12	890.75	854.83	861.78
Sr	240.9	261.4	247.2	247.2	224.4	232.3	231.1	226.1
Nd	10.33	10.64	11.51	11.51	10.5	10.37	10.4	10.78
Sm	2.88	2.82	2.94	2.94	2.74	2.74	2.78	2.81
Zr	81.2	81.1	92.4	92.4	88.9	73.8	77.3	75.6
Hf	2.19	2.08	2.39	2.39	2.07	2.03	1.9	2.03
Eu	1.13	1.02	1.03	1.03	0.93	0.91	0.9	0.96
Gd	2.98	3.25	3.37	3.37	3.06	2.98	2.98	3.04
Tb	0.53	0.53	0.62	0.62	0.5	0.52	0.5	0.54
Dy	3.34	3.52	3.72	3.72	3.26	3.32	3.24	3.45
Y	21	21.4	21.5	21.5	18.2	18.9	18.3	19.2
Ho	0.63	0.66	0.69	0.69	0.59	0.6	0.58	0.61
Er	1.87	1.9	2	2	1.8	1.79	1.75	1.84
Tm	0.3	0.29	0.31	0.31	0.28	0.28	0.28	0.29
Yb	1.89	1.8	2.04	2.04	1.85	1.73	1.76	1.81
Lu	0.29	0.3	0.31	0.31	0.28	0.29	0.27	0.28
Co	66.1	57.1	57.5	57.5	54.5	55.3	58.4	52.5
Cr	153.5	266.2	211.5	211.5	147.4	172.2	615.4	609.5
Cu	102.9	108.2	152.6	152.6	96	104.1	128.1	122.4
Ni	80.7	61.5	75.3	75.3	66.1	62.5	91.3	81.4
Sc	40.4	41.3	39.9	39.9	41.1	41	41.2	42.1
V	407.4	372.7	346.3	346.3	298.2	311.7	328.1	317.7
Zn	48	116.8	44.1	44.1	39.2	54.5	76.4	28.3

Sample	10JB328 B1	Standard 1 JB1-a	Certified JB1-a		Standard 2 NIM-g	Certified NIM-g	
Zone	UCM						
SiO_2	48	52.14	52.16		75.5	75.7	
TiO_2	1.05	1.29	1.3		0.08	0.09	
Al_2O_3	12.78	14.26	14.51		12.25	12.08	
Fe_2O_3T	11.33	9.27	9.1		2.23	2.02	
FeOT	10.18						
MnO	0.15	0.15	0.15		0.02	0.02	
MgO	10.32	7.92	7.75		0.03	0.06	
CaO	10.16	9.28	9.23		0.86	0.78	
Na_2O	2.45	2.7	2.74		3.32	3.36	
K_2O	0.5	1.43	1.42		5.08	4.99	
P_2O_5	0.09	0.26	0.27		0	0.01	
S	0.08						
LOI	2.7	0.78	0.78		0.55	0.51	
Total	99.8	99.47	99.39		99.93	99.62	
Cs	0.6	1.10	1.2		0.76	1	
K	4149.85						
Rb	13.3	40.6	41		313.8	320	
Ba	109	502.7	497		113.6	120	
Th	0.7	8.74	8.8		48.97	50	
U	0.2	1.61	1.6		15.66	15	
Nb	4.58	26.12	27		50.36	53	
Ta	0.3	1.63	2		4.5	4.5	
La	6.4	36.72	38.1		105.41	109	
Ce	16.1	64.56	66.1		189.58	195	
Pr	2.4	7.01	7.3		19.59		
Pb	1.06	7.33	7.2		28.24	40	
P	403.1						
Sr	252	450.6	443		10.6	10	
Nd	10.5	24.23	25.5		69.92	72	
Sm	2.8	4.93	5.02		14.95	15.8	
Zr	65	143.9	146		311.4	300	
Hf	1.79	3.4	3.48		12.27	12	
Eu	0.77	1.44	1.47		0.32	0.35	
Gd	3.11	4.82	4.54		14.52	14	
Tb	0.52	0.7	0.69		2.68	3	
Dy	3.2	3.98	4.19		16.73	17	
Y	19	23.9	24		154.3	143	
Ho	0.65	0.72	0.72		3.41		
Er	1.86	2.09	2.18		11.26		
Tm	0.26	0.32	0.31		1.95	2	
Yb	1.74	1.99	2.10		13.68	14.2	
Lu	0.25	0.32	0.32		1.99	2	
Co	52	42.2	39.5		3.9	4	
Cr	689	421.9	415		7.0	12	
Cu	149	58.8	55		16.2	12	
Ni	201	142.3	134		2.8	8	
Sc	39.5	29.9	27.9		0.3	1	
V	306	216.2	206		4.7	2	
Zn	52	84.7	82		48.2	50	

Appendix E2 – LPS Olivine mineral chemistry & inverse melt compositions

Sample	10BH166 A1	10BH166 A1	10BH166 A1	10BH166 A1	10BH166 A1	10BH166 A1	10BH166 A1
Zone	LCM	LCM	LCM	LCM	LCM	LCM	LCM
X Region	1 Core	2 Rimw	3 Rim	4 Core	5 Rimw	6 Rim	10 Core
SiO2	40.861	40.531	39.982	40.411	40.316	39.750	39.613
TiO2	0	0	0	0	0	0	0
Al2O3	0.082	0.078	0.060	0.102	0.084	0.035	0.038
Cr2O3	0.081	0.037	0.051	0.057	0.068	0.052	0.024
FeO	12.136	11.798	16.214	11.951	12.051	14.627	13.099
MnO	0.168	0.136	0.198	0.142	0.168	0.150	0.202
MgO	47.411	47.048	43.920	47.320	47.272	45.013	46.862
CaO	0.289	0.280	0.229	0.274	0.270	0.290	0.264
NiO	0.333	0.365	0.307	0.338	0.379	0.321	0.302
Total	101.361	100.273	100.961	100.595	100.608	100.238	100.404
Fo (mole %)	87.440	87.664	82.839	87.587	87.485	84.577	86.441
Melt MgO	12.909	13.054	10.131	13.004	12.938	11.137	12.275
Melt FeO	9.077	9.020	10.319	9.040	9.066	9.834	9.336

Sample	10BH166 A1	10BH166 A1	10BH166 A1	10BH166 A1	10BH166 A1	10BH166 A1	10BH166 A1
Zone	LCM	LCM	LCM	LCM	LCM	LCM	LCM
X Region	11 Rimw	12 Rim	14 Core	15 Rimw	16 Rim	18 Core	19 Rim
SiO2	39.577	39.483	40.024	40.191	39.157	39.846	37.780
TiO2	0	0	0.001	0	0	0	0.011
Al2O3	0.059	0.036	0.047	0.017	0.059	0.036	0.032
Cr2O3	0.056	0.019	0.058	0.046	0.037	0.056	0.023
FeO	13.317	15.284	12.404	12.062	14.313	13.597	22.654
MnO	0.199	0.144	0.208	0.209	0.147	0.173	0.278
MgO	46.819	45.491	47.045	47.281	45.460	45.983	38.931
CaO	0.276	0.250	0.191	0.194	0.301	0.238	0.209
NiO	0.355	0.262	0.348	0.352	0.292	0.278	0.236
Total	100.658	100.969	100.325	100.352	99.766	100.207	100.153
Fo (mole %)	86.235	84.137	87.111	87.477	84.985	85.768	75.384
Melt MgO	12.146	10.877	12.699	12.933	11.381	11.857	6.425
Melt FeO	9.390	9.955	9.162	9.068	9.723	9.513	12.654

Sample	10BH166 A2	10BH166 A2	10BH166 A2	10BH166 A2	10BH166 A2	10BH166 A2	10BH166 A2
Zone	LBZ	LBZ	LBZ	LBZ	LBZ	LBZ	LBZ
X Region	1 Core	2 Rimw	3 Rimw	4 Rimw	5 Rim	6 Core	7 Rimw
SiO2	38.628	39.362	39.252	39.350	36.954	39.758	38.949
TiO2	0	0	0	0.005	0	0	0
Al2O3	0.406	0.045	0.035	0.060	0.033	0.058	0.037
Cr2O3	0.525	0.048	0.063	0.072	0.017	0.047	0.015
FeO	13.812	13.372	13.282	13.272	25.216	14.175	16.254
MnO	0.124	0.162	0.199	0.156	0.234	0.288	0.209
MgO	44.690	46.684	46.531	46.213	35.895	46.051	44.556
CaO	1.148	0.283	0.257	0.286	0.240	0.258	0.245
NiO	0.323	0.320	0.301	0.320	0.259	0.297	0.287
Total	99.656	100.276	99.920	99.734	98.848	100.932	100.552
Fo (mole %)	85.220	86.152	86.193	86.121	71.725	85.271	83.007
Melt MgO	11.523	12.094	12.120	12.075	4.963	11.553	10.227
Melt FeO	9.660	9.411	9.401	9.420	13.977	9.646	10.271

Sample	10BH166 A2	10BH166 A2	10BH166 A2	10BH166 A2	10BH166 A3	10BH166 A3	10BH166 A3
Zone	LBZ	LBZ	LBZ	LBZ	LBZ	LBZ	LBZ
X Region	8 Rim	24 Core	25 Rimw	26 Rim	9 Core	10 Rimw	11 Rim
SiO2	37.195	39.989	39.625	39.787	37.520	37.341	37.640
TiO2	0	0	0	0	0.011	0	0.019
Al2O3	0.038	0.046	0.168	0.041	0.061	0.032	0.048

Cr2O3	0.023	0.051	0.220	0.053	0.012	0	0
FeO	25.707	14.915	15.355	18.019	23.174	22.858	24.282
MnO	0.282	0.181	0.181	0.335	0.249	0.308	0.373
MgO	36.612	45.097	44.040	43.266	38.123	37.944	36.920
CaO	0.258	0.247	0.658	0.265	0.244	0.268	0.156
NiO	0.215	0.257	0.266	0.284	0.208	0.244	0.205
Total	100.330	100.783	100.513	102.050	99.602	98.995	99.643
Fo (mole %)	71.735	84.346	83.636	81.056	74.565	74.735	73.042
Melt MgO	4.967	11.000	10.586	9.156	6.077	6.149	5.463
Melt FeO	13.974	9.898	10.094	10.838	12.939	12.879	13.486

Sample	10BH166 A3	10BH166 A3	10BH166 A3	10BH166 A3	11BH311 B2	11BH311 B2	11BH311 B2
Zone	LBZ	LBZ	LBZ	LBZ	LOZ	LOZ	LOZ
X Region	21 Core	22 Rim	23 Core	24 Rim	125 Core	126 Rim	128 Core
SiO2	37.042	36.796	37.151	37.654	38.867	38.874	39.294
TiO2	0	0.029	0	0.013	0.002	0.006	0.006
Al2O3	0.055	0	0.029	0.009	0.013	0.029	0.044
Cr2O3	0.013	0.015	0.025	0.019	0.027	0.003	0.023
FeO	22.935	24.553	22.542	22.521	18.680	24.400	19.286
MnO	0.238	0.347	0.399	0.297	0.226	0.299	0.343
MgO	38.177	36.293	38.059	38.421	42.022	37.602	41.754
CaO	0.278	0.202	0.261	0.188	0.256	0.233	0.229
NiO	0.229	0.176	0.206	0.258	0.247	0.169	0.216
Total	98.967	98.411	98.672	99.380	100.340	101.615	101.195
Fo (mole %)	74.787	72.483	75.054	75.248	80.035	73.306	79.415
Melt MgO	6.171	5.247	6.284	6.367	8.622	5.566	8.307
Melt FeO	12.861	13.692	12.768	12.701	11.146	13.389	11.337

Sample	11BH311 B2	11BH311 B2	11BH311 B2	10BH166 A4	10BH166 A4	10BH166 A4	10BH166 A4
Zone	LOZ	LOZ	LOZ	LOZ	LOZ	LOZ	LOZ
X Region	129 Rim	133 Core	134 Rim	7 Core	8 Rim	12 Core	13 Rim
SiO2	38.394	38.347	37.917	38.105	38.3	39.727	39.702
TiO2	0	0.005	0.009	0	0.006	0	0
Al2O3	0.117	0.042	0.034	0.043	0.043	0.047	0.028
Cr2O3	0.050	0.029	0.023	0.011	0.029	0.040	0.053
FeO	21.462	17.318	23.053	17.324	17.447	16.813	16.070
MnO	0.274	0.227	0.244	0.260	0.335	0.324	0.144
MgO	39.935	43.594	38.526	42.571	42.730	43.532	44.104
CaO	0.168	0.238	0.199	0.164	0.239	0.208	0.212
NiO	0.186	0.284	0.215	0.225	0.192	0.202	0.241
Total	100.586	100.084	100.220	98.703	99.321	100.893	100.554
Fo (mole %)	76.829	81.771	74.862	81.409	81.358	82.187	83.024
Melt MgO	7.067	9.540	6.202	9.344	9.317	9.768	10.236
Melt FeO	12.166	10.628	12.835	10.734	10.749	10.507	10.267

Sample	10BH166 A4	10BH166 A4	10BH166 A4	10BH166 A4	10BH166 A4	10BH166 A4	10BH166 A4
Zone	LOZ	LOZ	LOZ	LOZ	LOZ	LOZ	LOZ
X Region	14 Core	15 Rim	19 Core	20 Rimw	21 Rim	24 Core	25 Rimw
SiO2	39.569	39.398	38.942	38.632	38.207	40.179	40.157
TiO2	0	0.005	0	0.008	0	0	0
Al2O3	0.060	0.042	0.042	0.042	0.061	0.059	0.049
Cr2O3	0.045	0.017	0.039	0.039	0.056	0.034	0.055
FeO	16.535	16.496	16.712	16.376	22.495	12.944	14.534
MnO	0.264	0.293	0.246	0.235	0.306	0.139	0.181
MgO	43.738	43.459	43.034	43.446	38.386	46.354	45.750
CaO	0.260	0.210	0.220	0.216	0.234	0.258	0.263
NiO	0.294	0.228	0.316	0.307	0.240	0.330	0.321
Total	100.765	100.148	99.551	99.301	99.985	100.297	101.310
Fo (mole %)	82.498	82.440	82.107	82.541	75.253	86.453	84.870
Melt MgO	9.941	9.908	9.724	9.964	6.369	12.282	11.312
Melt FeO	10.417	10.434	10.530	10.405	12.699	9.333	9.754

Sample	10BH166 A4	10BH166 A5	10BH166 A5	10BH166 A5	10BH166 A5	10BH166 A5	10BH166 A5
Zone	LOZ	LOZ	LOZ	LOZ	LOZ	LOZ	LOZ
X Region	26 Rim	6 Core	7 Rimw	8 Rim	15 Core	16 Rimw	17 Rimw
SiO2	38.471	38.269	38.451	38.270	39.837	39.770	39.391
TiO2	0	0	0	0.013	0	0	0
Al2O3	0.075	0.053	0.044	0.052	0.055	0.060	0.048
Cr2O3	0.070	0.019	0.061	0.048	0.038	0.074	0.078
FeO	20.387	21.408	21.632	21.137	11.500	11.636	11.290
MnO	0.322	0.315	0.301	0.307	0.185	0.283	0.177
MgO	40.140	39.211	39.637	39.623	47.678	47.432	47.638
CaO	0.198	0.279	0.288	0.208	0.302	0.286	0.251
NiO	0.293	0.215	0.194	0.184	0.376	0.405	0.358
Total	99.956	99.769	100.608	99.842	99.971	99.946	99.231
Fo (mole %)	77.820	76.547	76.554	76.961	88.078	87.899	88.262
Melt MgO	7.528	6.939	6.942	7.127	13.324	13.207	13.445
Melt FeO	11.842	12.260	12.257	12.122	8.915	8.960	8.869

Sample	10BH166 A5	10BH166 A5	10BH167 A1	10BH167 A1	10BH167 A1	10BH167 A1	10BH167 A1
Zone	LOZ	LOZ	LOZ	LOZ	LOZ	LOZ	LOZ
X Region	18 Rimw	19 Rim	7 Core	8 Rim	16 Core	17 Rim	9 Core
SiO2	38.929	37.659	39.760	38.484	39.768	38.327	39.071
TiO2	0.007	0	0.002	0	0	0.009	0
Al2O3	0.049	0.032	0.153	0.024	0.057	0.026	0.036
Cr2O3	0.046	0.006	0.221	0	0.054	0.019	0.037
FeO	14.322	19.870	16.317	22.165	14.457	21.130	15.603
MnO	0.245	0.328	0.163	0.258	0.253	0.261	0.192
MgO	45.491	40.880	43.403	38.590	45.191	40.147	44.162
CaO	0.268	0.206	0.482	0.232	0.260	0.225	0.250
NiO	0.324	0.213	0.297	0.266	0.298	0.229	0.245
Total	99.681	99.194	100.798	100.019	100.338	100.373	99.596
Fo (mole %)	84.985	78.569	82.579	75.625	84.780	77.199	83.454
Melt MgO	11.381	7.888	9.985	6.529	10.481	10.483	11.258
Melt FeO	9.723	11.602	10.394	12.571	10.145	10.144	9.779

Sample	10BH167 A1	10BH167 A2	10BH167 A2	10BH167 A2	10BH167 A2	10BH167 A2	10BH167 A2
Zone	LOZ	MOZ	MOZ	MOZ	MOZ	MOZ	MOZ
X Region	10 Rim	1 Core	2 Rimw	3 Rim	12 Core	13 Rim	14 Core
SiO2	39.642	38.633	39.057	39.102	38.424	38.946	38.273
TiO2	0.003	0	0	0	0	0	0
Al2O3	0.073	0.037	0.037	0.030	0.043	0.036	0.057
Cr2O3	0.015	0.063	0	0	0.029	0.012	0.025
FeO	15.597	17.164	18.997	20.044	16.414	16.292	17.634
MnO	0.198	0.232	0.217	0.307	0.163	0.169	0.203
MgO	44.156	42.727	41.648	41.064	43.322	42.907	41.625
CaO	0.167	0.297	0.283	0.202	0.264	0.221	0.292
NiO	0.205	0.226	0.248	0.252	0.262	0.281	0.212
Total	100.056	99.379	100.487	101.001	98.921	98.864	98.321
Fo (mole %)	83.457	81.604	79.620	78.498	82.466	82.435	80.793
Melt MgO	7.237	9.449	8.410	7.854	9.923	9.905	9.016
Melt FeO	12.044	10.677	11.274	11.625	10.426	10.435	10.917

Sample	10BH167 A2	10BH167 A3	10BH167A 3	10BH167 A3	10BH167 A3	10BH167 A3	10BH167 A3
Zone	MOZ	MOZ	MOZ	MOZ	MOZ	MOZ	MOZ
X Region	15 Rim	1 Core	2 Rim	8 Core	9 Rim	18 Core	19 Rim
SiO2	38.899	38.860	38.636	39.167	38.994	38.182	38.351
TiO2	0	0.002	0.003	0	0	0	0
Al2O3	0.046	0.033	0.029	0.044	0.035	0.036	0.027
Cr2O3	0.050	0.035	0.054	0.023	0.039	0.013	0.026
FeO	17.921	19.525	20.328	18.111	17.074	19.481	18.845

MnO	0.237	0.225	0.270	0.169	0.197	0.262	0.248
MgO	42.645	41.049	40.454	42.396	42.600	40.425	41.748
CaO	0.293	0.237	0.199	0.297	0.278	0.258	0.244
NiO	0.235	0.226	0.226	0.244	0.269	0.185	0.188
Total	100.326	100.192	100.199	100.451	99.486	98.842	99.677
Fo (mole %)	80.918	78.932	78.004	80.663	81.638	78.714	79.789
Melt MgO	9.082	8.066	7.616	8.948	9.468	7.959	8.496
Melt FeO	10.880	11.488	11.783	10.956	10.667	11.557	11.222

Sample	10BH167 A3	10BH167 A3	10BH167 A4	10BH167 A4	10BH167 A4	10BH167 A4	10BH167 A4
Zone	MOZ	MOZ	UOZ	UOZ	UOZ	UOZ	UOZ
X Region	23 Rep	24 Rep	4 Core	5 Rimw	6 Rim	7 Rimw	8 Rim
SiO2	38.887	38.251	38.754	37.594	38.332	38.105	37.382
TiO2	0	0	0	0.023	0	0.002	0.004
Al2O3	0.048	0.032	0	0.048	0.042	0.028	0.019
Cr2O3	0.040	0.025	0.034	0	0.026	0.025	0.004
FeO	17.318	17.877	20.306	24.617	21.751	23.537	27.056
MnO	0.232	0.240	0.247	0.316	0.317	0.342	0.362
MgO	43.492	42.671	40.352	36.728	39.444	37.548	34.962
CaO	0.225	0.230	0.285	0.151	0.244	0.251	0.133
NiO	0.249	0.235	0.197	0.165	0.211	0.134	0.167
Total	100.491	99.561	100.175	99.642	100.367	99.972	100.089
Fo (mole %)	81.736	80.965	77.979	72.668	76.368	73.977	69.722
Melt MgO	9.521	9.107	7.604	5.318	6.858	5.836	4.260
Melt FeO	10.638	10.866	11.791	13.623	12.320	13.147	14.761

Sample	10BH167 A4	10BH167 A4	10BH167 A4	10BH167 A4	11BH311 B3	11BH311 B3	11BH311 B3
Zone	UOZ	UOZ	UOZ	UOZ	UOZ	UOZ	UOZ
X Region	19 Core	20 Rim	26 Core	27 Rim	13 Rim	14 Rimw	15 Rimw
SiO2	38.600	38.423	37.243	38.144	39.378	38.573	38.540
TiO2	0.001	0	0.011	0.006	0	0.002	0
Al2O3	0.051	0.032	0.030	0.037	0.037	0.026	0.015
Cr2O3	0.044	0.028	0.025	0.039	0.021	0.038	0.004
FeO	19.578	24.323	22.739	19.862	20.973	21.200	21.868
MnO	0.310	0.293	0.421	0.296	0.314	0.369	0.293
MgO	41.471	37.350	38.558	41.324	39.894	39.475	39.003
CaO	0.281	0.265	0.222	0.282	0.239	0.251	0.231
NiO	0.185	0.184	0.190	0.227	0.222	0.225	0.214
Total	100.521	100.898	99.439	100.217	101.078	100.159	100.168
Fo (mole %)	79.056	73.236	75.135	78.757	77.219	76.842	76.067
Melt MgO	8.128	5.539	6.318	7.980	7.246	7.073	6.724
Melt FeO	11.449	13.415	12.740	11.543	12.037	12.162	12.421

Sample	11BH311B 3	11BH311 B3	11BH311B 3	11BH311 B3	11BH311 B3	11BH311 B3	11BH311 B3
Zone	UOZ	UOZ	UOZ	UOZ	UOZ	UOZ	UOZ
X Region	16 Core	17 Rimw	19 Rim	20 Rim	21 Core	22 Rimw	23 Rim
SiO2	38.012	37.842	38.028	38.343	38.179	38.242	38.970
TiO2	0.012	0.002	0	0.010	0	0	0
Al2O3	0.017	0.015	0.041	0.019	0.040	0.039	0.021
Cr2O3	0	0.001	0.019	0	0.039	0.022	0.014
FeO	22.844	22.459	22.573	22.059	21.714	21.053	20.908
MnO	0.330	0.321	0.298	0.342	0.342	0.299	0.314
MgO	38.685	38.594	38.559	39.216	39.331	39.527	39.619
CaO	0.213	0.218	0.174	0.144	0.226	0.228	0.247
NiO	0.193	0.133	0.229	0.206	0.186	0.206	0.195
Total	100.306	99.585	99.921	100.339	100.057	99.616	100.288
Fo (mole %)	75.110	75.383	75.272	76.008	76.347	76.989	77.152
Melt MgO	6.308	6.425	6.377	6.698	6.849	7.140	7.215
Melt FeO	12.748	12.654	12.692	12.441	12.327	12.113	12.059

Sample	11BH311B3	11BH311B3	11BH311B3	11BH311B3	11BH311B3	11BH311B3	11BH311B3
Zone	UOZ	UOZ	UOZ	UOZ	UOZ	UOZ	UOZ
X Region	25 Core	26 Rimw	27 Rim	48 Core	49 Rim	50 Core	51 Rim
SiO2	39.041	38.529	38.218	39.003	39.194	39.677	39.689
TiO2	0	0.004	0.018	0.016	0	0	0
Al2O3	0.035	0.044	0.020	0.034	1.097	0.045	0.030
Cr2O3	0.009	0.035	0.048	0.034	0.015	0.062	0.046
FeO	23.508	23.240	23.614	20.830	18.951	20.215	18.997
MnO	0.341	0.374	0.295	0.311	0.271	0.276	0.344
MgO	37.933	38.231	38.350	40.556	41.327	40.522	41.601
CaO	0.215	0.223	0.219	0.249	0.244	0.263	0.239
NiO	0.161	0.174	0.209	0.197	0.215	0.211	0.184
Total	101.243	100.854	100.991	101.230	101.314	101.271	101.130
Fo (mole %)	74.197	74.564	74.320	77.626	79.534	78.128	79.602
Melt MgO	5.925	6.077	5.976	7.437	8.367	7.675	8.401
Melt FeO	13.069	12.939	13.025	11.905	11.300	11.743	11.279

Sample	11BH311B3	11BH311B3	11BH311B3	11BH311B3
Zone	UOZ	UOZ	UOZ	UOZ
X Region	57 Core	58 Rimw	59 Rimw	60 Rim
SiO2	38.742	38.899	39.347	39.585
TiO2	0	0.007	0	0.012
Al2O3	0.052	0.042	0.033	0.021
Cr2O3	0	0.046	0.012	0.024
FeO	20.701	19.642	19.391	18.848
MnO	0.311	0.282	0.236	0.206
MgO	39.971	41.107	41.620	41.558
CaO	0.242	0.260	0.264	0.172
NiO	0.215	0.161	0.187	0.230
Total	100.234	100.446	101.090	100.656
Fo (mole %)	77.482	78.856	79.274	79.712
Melt MgO	7.369	8.029	8.236	8.457
Melt FeO	11.952	11.512	11.381	11.245

Appendix E1-A – Point counting results and error

Count #1		**%**				
Sample #	**Zone**	**Ol**	**Plag**	**Cpx**	**Fe-Ti**	**Gm**
166A1	LCM	3	0	0	0	97
166A2	LBZ	17	0	0	5	78
166A3	OZ	49	24	25	2	0
166A4	OZ	47	26	19	8	0
166A5	OZ	43	21	29	7	0
167A1	OZ	44	26	24	6	0
167A2	OZ	56	24	16	4	0
167A3	OZ	52	25	18	5	0
167A4	OZ	40	31	23	6	0
167A5	CPZ	3	33	59	5	0
167A6	DZ	0	44	45	11	0
167A7	DZ	0	41	46	13	0
167A8	DZ	0	40	52	8	0
167A9	DZ	0	48	40	12	0
167A10	DZ	0	43	42	15	0
167A11	DZ	0	51	47	2	0
167A12	DZ	0	43	47	10	0
167A14	UBZ	0	0	4	4	92
167A15	UCM	6	0	0	2	92
Count #2		**%**				
Sample #	**Zone**	**Ol**	**Plag**	**Cpx**	**Fe-Ti**	**Gm**
166A1	LCM	5	0	0	2	93
166A2	LBZ	13	0	0	3	84
166A3	OZ	45	23	26	6	0
166A4	OZ	49	25	20	6	0
166A5	OZ	42	24	28	6	0
167A1	OZ	47	22	23	8	0
167A2	OZ	52	24	18	6	0
167A3	OZ	55	19	23	3	0
167A4	OZ	44	32	18	6	0
167A5	CPZ	4	31	62	3	0
167A6	DZ	0	48	44	8	0
167A7	DZ	0	39	42	19	0
167A8	DZ	0	41	50	9	0
167A9	DZ	0	47	43	10	0
167A10	DZ	0	42	44	14	0
167A11	DZ	0	51	45	4	0
167A12	DZ	0	44	47	9	0
167A14	UBZ	0	0	4	5	91
167A15	UCM	3	0	0	2	95

Error – 1 standard deviation

		1sig-Ol	**1sig-Plag**	**1sig-Cpx**	**1sig-Fe-Ti**	**1sig-Gm**
166A1	LCM	1.414	0.000	0.000	1.414	2.828
166A2	LBZ	2.828	0.000	0.000	1.414	4.243
166A3	OZ	2.828	0.707	0.707	2.828	0.000

166A4	OZ	1.414	0.707	0.707	1.414	0.000
166A5	OZ	0.707	2.121	0.707	0.707	0.000
167A1	OZ	2.121	2.828	0.707	1.414	0.000
167A2	OZ	2.828	0.000	1.414	1.414	0.000
167A3	OZ	2.121	4.243	3.536	1.414	0.000
167A4	OZ	2.828	0.707	3.536	0.000	0.000
167A5	CPZ	0.707	1.414	2.121	1.414	0.000
167A6	DZ	0.000	2.828	0.707	2.121	0.000
167A7	DZ	0.000	1.414	2.828	4.243	0.000
167A8	DZ	0.000	0.707	1.414	0.707	0.000
167A9	DZ	0.000	0.707	2.121	1.414	0.000
167A10	DZ	0.000	0.707	1.414	0.707	0.000
167A11	DZ	0.000	0.000	1.414	1.414	0.000
167A12	DZ	0.000	0.707	0.000	0.707	0.000
167A14	UBZ	0.000	0.000	0.000	0.707	0.707
167A15	UCM	2.121	0.000	0.000	0.000	2.121

Appendix E1-B – LPS whole-rock plots and descriptions

Major Elements

SiO2: Consistently around 45 wt% through the sill, with LCM and UCM showing good similarities. There is a slight increase in SiO2 between the LCM and the LBZ. There is a slight trend of decreasing SiO2 from the LBZ through the OZ. The highest SiO2 values preserved in the sill are within the CPZ. There is very little variation in SiO2 through the DZ.

TiO2: Overall, a Z-style profile. Both LCM and the UCM show a reasonable fit with a slightly higher TiO2 value in the UCM. There is a decreasing trend in TiO2 from the LCM, through the LBZ and OZ. The UOZ (Upper OZ) shows an increase in TiO2 leading towards the CPZ. There is a sudden jump in TiO2 in the CPZ from 0.65 to 0.95 wt% (values similar to the LCM). Then there appears to be two cycles in TiO2 in the DZ, with higher values in the upper cycle, which decrease from 1.2 to 1 wt%. The UBZ and UCM have values around 1.05 wt% compared within 0.9 wt% at the LCM.

Al2O3: Overall, a Z-style profile. Values decrease from the LCM up through the LBZ and OZ. They begin to increase in the roof of the OZ (much like TiO2) with a jump up to 8 wt% from 6.5 wt% and then another jump to 12 wt% in the CPZ. The highest values are in the DZ, typically around 14 wt%. They steadily decrease towards the UBZ/UCM (~13 wt%) but these are slightly higher than at the LCM.

Fe2O3 (total iron expressed as Fe2O3): There appears to be two separate trends for Fe2O3. The LCM value is 13 wt%, which increases slightly into the LBZ, through the OZ. Midway through the OZ, the value jumps to 15 wt% and then back to 14 wt% for the upper part of the OZ. Then the second trend starts within the CPZ at values of 10 wt%. Values increase back up to ~14 wt% in the DZ, but are consistently ~12 wt% through the DZ and the UBZ/UCM (which incidentally are lower than the LCM/LBZ).

MnO: The MnO profile is similar in appearance to the Fe2O3 profile with two trends visible. MnO increases from the LCM (0.18 wt%) to the LBZ (0.19 wt%) and is constantly around 0.19-0.2 wt% for the OZ. There is a decrease at the CPZ from 0.19 wt% to 0.16 wt%. MnO values are around 0.15-0.17 wt% for the DZ. The UBZ and LBZ are very similar. The UCM contains slightly less MnO than the LCM.

MgO: Almost shows a ‘traditional’ S-shaped curve, but there isn’t a big enough increase in the UBZ and UCM to create symmetry with the LCM-LBZ. The LCM value (frozen liquid) is 13 wt%, with an increase through the LBZ (15 to 17 wt%), and an increase through the OZ to a highest value of 25 wt%. It decreases to around 21 wt% in the UOZ and then shows a big decrease from 21 to 11 wt% in the CPZ. The value drops again, to <10 wt% and remains consistently so through the DZ. The UBZ replicates this, and the UCM shows a slight decrease to values >10 wt% – similar to the LCM.

CaO: Appears to show two broad trends. CaO decreases from 11 wt% in the LCM, through the LBZ to 6 wt% at the middle OZ (MOZ). There is a slight increase in CaO in the UOZ to 8-9 wt%. There is a sudden increase at the CPZ to 14-15 wt%, and then the value is consistently ~11 wt% in the DZ, similar to the UBZ. The UCM shows good fit with the LCM, with ~11 wt% CaO.

Na2O: Na2O shows a Z-style curve but with much higher values at the UBZ, and especially the UCM. There is a decrease in Na2O from the LCM (1.55 wt%) through the LBZ to the

lower olivine zone (LOZ; values of 0.5 wt%). There is an increase in Na2O just above the LOZ to values of 1, followed by a decrease to values of ~0.35 wt%, followed by an increase to 0.75 wt% in the UOZ. Values increase to 1.4-1.5 wt% in the CPZ as well as in the lower DZ (1.8-1.9 wt%). There is a decreasing trend in the DZ, including some peaks (up to ~2.5 wt%). The UBZ (1.6 wt%) is similar to the LCM, and the UCM shows values (2.35 wt%) similar to the DZ, as opposed to the LCM.

K2O: Again, two 'cycles' are visible. There is a slight decrease in K2O from the LCM (0.50 wt%) up through the LBZ and OZ (to as low as ~0.25 wt%). There is a sudden increase in K2O at the boundary of the CPZ to 1.4-1.5 wt%. There is a consistent value (~1.4 wt%) through the DZ with elevations up to 2 wt% in one sample. The UBZ and UCM have greater K2O contents compared to the LBZ and LCM (~1 wt%).

P2O5: Roughly a Z-style curve, with a LCM value of 0.08 wt% decreasing through the LBZ and the OZ (to ~0.05 wt%). The UOZ has a slightly higher value and starts the increasing trend up through the CPZ and DZ to values of ~0.09 wt%. The UBZ contains more P2O5 than the LBZ, however, the LCM and UCM are similar.

FeO* (FeO* calculated from Fe2O3 with the proportion of Fe2+ to Fe3+ set at 0.9): Identical to Fe2O3 trend.

LOI: There is a rough trend indicating an increase in LOI values up-section through the LPS. The MOZ has elevated LOI values (up to 5.6-5.7 wt% compared with 1.3 wt% for the LCM). The UCM shows a higher LOI value compared with the LCM.

Trace Elements:

ICP-OES

Sc: A 'two-cycle trend', with a LCM value of 38 ppm decreasing through the LBZ and OZ, until the UOZ where it climbs to 33 ppm. Then there is a big jump to 57 ppm within the CPZ, and then the DZ consistently contains ~43 ppm, including the UBZ and UCM (both higher than the LBZ and LCM, respectively).

V: Similar to Sc. LCM values are at 320 ppm, which decrease through the LBZ and OZ to the lowest value in the LPS of 165 ppm. There is an increase in the UOZ to 210 ppm, and then a jump to >350 ppm in the CPZ. Then there appears to be two cycles in the DZ, both decreasing upwards, but generally with high V contents than the lower half of the LPS. The UBZ and UCM are roughly similar to the LCM.

Cr: Cr displays a S-shaped curve, with LCM values of 750 ppm, increasing through the LBZ and OZ. The CPZ at the contact with the OZ contains 2000 ppm, the highest value in the LPS. This decreases in the next CPZ sample, and into the DZ, to a value of <500 ppm, and then stays around the same throughout the DZ. The UBZ and UCM crudely correlate with the LCM (750 ppm).

Co: Weak trends, with a steady increase from the LCM through the LBZ and OZ, followed by a sharp decrease in the CPZ. There are possibly two cycles in the DZ. The UBZ and UCM crudely correlate with the LCM.

Ni: An asymmetric S-shape. The LCM has a value of 230 ppm, followed by a increase through the LBZ and the OZ (highest value of ~720 ppm). The UOZ begins to show a

decrease in comparison to the MOZ, followed by a sharp decrease at the CPZ to values of <100 ppm. Values are ~90 ppm in the DZ, with a slight increase in the UBZ to ~100 ppm. The UCM is roughly similar to the LCM (200 ppm).

Cu: LCM values are at 100 ppm, with a decrease through the LBZ and in the LOZ. There is a slight increase in the MOZ before a decrease in the UOZ. Cu is at 90 ppm in the CPZ and stays roughly around 100 ppm throughout the DZ except for one sample where a value of ~160 ppm is observed. The UBZ and UCM have higher Cu values than the LCM/LBZ.

Zn: There may be two cycles in Zn through the LPS. The LCM has a value of ~80 ppm, with decreases through the LBZ, and there is a slight increase LOZ, before a decrease in the MOZ and then an increase in the UOZ. The CPZ has a higher value, leading to a decreasing trend in the DZ, except for two values, which show an increase (up to 120 ppm). The UBZ shows some scatter, and the UCM is similar to the LCM.

Sr: An asymmetric Z-shape curve. The LCM has a value of 150 ppm, which decreases through the LBZ and OZ, until the UOZ where it begins to increase, leading into the CPZ with values of 160-200 ppm. Sr increases in the DZ to ~300 ppm. The UBZ and UCM are similar, but with higher values compared with the LCM/LBZ, respectively.

Y: A ‘two-cycle trend’. LCM values are at 17 ppm, which decrease through the LBZ and OZ, but begin to increase in the UOZ, eventually increasing to 17 ppm in the CPZ. They increase slightly through the DZ before decreasing in the upper DZ. The UBZ/UCM values fit well, and correlate with the LCM.

Zr: A weak ‘two-cycle trend’. The LCM has a value of 70 ppm, which decreases through the LBZ (decreasing TMF?). Values increase in the LOZ with a further increase in the MOZ, before decreasing in the UOZ. The CPZ has values similar to the LCM, and they stay constant through the DZ, with the UBZ and UCM showing similar values, that corresponds with the LCM.

Ba: A weak ‘two-cycle trend’? The LCM has values of 130 ppm, which decrease through the LBZ. They jump up slightly in the LOZ, but decrease again in the MOZ. Values increase in the UOZ and increase again in the CPZ to LCM-like values. The lower DZ is similar to the CPZ, before values increase to >200 ppm followed by a decreasing trend upward through the rest of the DZ. Values increase slightly at the very top of the DZ. The UBZ and UCM roughly correlate with the LCM.

ICP-MS:

Co: There is an almost S-shaped curve for Co, with both LCM and UCM values very similar. The LCM has a value of ~60 ppm, with increases in the first LBZ sample and then decreasing towards the top of the LBZ and into the LOZ. Co increases in the MOZ (~70 ppm) and then decreases slightly in the UOZ (~60 ppm) and into the base of the CPZ (~50 ppm– lowest values in the sill). Values increase slightly in the next CPZ sample (~55 ppm) and then are fairly consistent through the DZ (~55 ppm) apart from one sample which has a value of ~70 ppm in the mid-DZ. The UBZ value increases slightly from the DZ mean value.

Ga: Smooth asymmetrical Z-shaped trend. The LCM has a value of ~14 ppm, increasing in the first LBZ sample and then decreasing in the next LBZ sample and into the LOZ. The Ga content shows a slight decrease before increasing slightly in the UOZ and the CPZ (~14-15 ppm). Ga shows a further increase in the DZ. The value of Ga may increase slightly up

through the DZ, but values are all between 16-17 ppm, with the UBZ and UCM being similar, with both higher than the LCM and LBZ.

Rb: Rb displays almost two separate trends but it is quite a smooth ‘weak’ Z-shape overall. There is an increase in Rb from ~18 to 20 ppm in the first LBZ sample but then it decreases slightly in the higher LBZ sample. Similar increases are seen in the LOZ, but then it says consistently the same in the rest of the OZ towards the UOZ. There is a sudden increase to ~28 ppm in the CPZ and it increases again slightly at the bottom of the DZ with an increase up to ~72 ppm. It begins to decrease again in the upper DZ, continuing in the UBZ and finally the UCM (~15 ppm), which is lower than the LCM.

P: A good Z-shape curve is produced. The P value is ~800 ppm at the LCM, and then it decreases through the LBZ and the OZ (there may be a slight increase in P in the LOZ). P values start to increase in the UOZ and into the CPZ. It continues to increase through the DZ with P values greater the LCM value. The UBZ is similar to the mean value of the DZ, before decreasing slightly into the UCM, which has almost the same P value as the LCM.

Nb: An asymmetrical Z-shape profile. Values increase from the LCM into the LBZ, and then decrease in the next LBZ sample and into the LOZ. There is a slight increase in the LOZ, before the trend decreases again, before an increase in the UOZ. This is continued into the CPZ, with an increasing trend in the base and middle parts of the DZ. Values fluctuate slightly through the upper DZ, UBZ and then UCM preserves a higher Nb concentration than the LCM.

Sn: Sn decreases from the LCM and through the LBZ and into the OZ. One sample shows an increase in the LOZ but then the trend generally decreases through the OZ, before UOZ where an increase is observed. This is continued into the CPZ, with a range of values in the base of the DZ, before a smooth decreasing trend is observed towards the UBZ. The UBZ shows a recovery, with values greater than the LBZ, but the UCM has a value less than the LCM.

Cs: A decreasing trend through the LBZ and into the LOZ. Values increase in the MOZ before decreasing in the UOZ. The CPZ shows a slightly increasing trend, which leads into the base of the DZ, followed by fluctuating values in the middle/upper parts of the DZ. The UBZ shows a range of values, before the UCM, which has a value less than the LCM.

Ba: Ba shows a decreasing trend from the LCM and through the LBZ. There is a slight increase in the LOZ, before values decrease in the MOZ, which is followed by a slight increase in the UOZ, which leads into the CPZ. The mid/upper DZ is then detached from the basal DZ/CPZ by a separate decreasing trend up-sill. The UBZ shows a slight skew in values, before the UCM seems to preserve a value close to that of the LCM.

La: A weak Z-shape is displayed. There is a decreasing trend through the LBZ from the LCM and into the OZ. The basal OZ bulge is seen again, before it decreases again. The roof of the OZ hints at a partial recovery, which steps up into the CPZ, followed by a slight increasing trend in the basal regions of the DZ, which values remain fairly consistently, as does the UBZ, which have higher values than the LBZ. The UCM and LCM are very similar.

REE (Ce/Pr/Nd/Sm/Gd/Tb/Dy/Ho/Er/Tm/Yb/Lu): All behave, generally, the same as La. However, the difference between the UOZ and CPZ becomes greater towards the HREE end of the REE spectrum.

Eu: Eu behaves similarly to the other REE, however, more complex behaviour is seen through the DZ and UBZ, with two decreasing cycles separated by an increase in Eu values mid way through the DZ.

Hf: Similar to the REE but a more less pronounced jump from the roof of the OZ to the CPZ with good symmetry between the LCM and UCM.

Ta: Ta behaves much like the REE, but with a less pronounced increase between the OZ and CPZ.

Pb: Pb shows more complex behaviour in comparison to the REE. There is an increase in Pb from the LCM, through the LBZ; a decrease in the LOZ, followed by a sharp increase to the highest values in the sill (OZ sample 10BH1665A5); followed by a decrease through the MOZ and UOZ. Pb values decrease in the CPZ before increasing in the basal DZ, followed by a smooth decreasing trend all through the DZ. The UBZ has Pb values similar to the LCM, much like the UCM.

Th: The LCM and LBZ values remain fairly constant before a sharp decrease in the LOZ, followed by an increase in sample 10BH166A5. Th values decrease through the MOZ and into the UOZ, before a slight increase in the sample immediately beneath the CPZ. Th values increase in the CPZ, before increasing through the DZ. Th values decrease in the upper DZ. Th values increase in the UCM and UBZ, with both showing higher values than the LCM and LBZ, respectively.

U: U behaves like Th, but with a less pronounced increase in sample 10BH166A5; a less pronounced increase in the CPZ.

LREE enrichment ratios

La/Yb: A slight decrease from the LCM to the UOZ (a slight increase in the LOZ – sample 10BH166A5). The La/Yb is consistently the same throughout the DZ and is the same in the UBZ. The UBZ and DZ has a La/Yb similar to the LCM. The UCM La/Yb ratio is slightly lower than the LCM.

Ce/Yb: Behaves the same as La/Yb.

La/Sm: Behaves like La/Yb and Ce/Yb, however, the LOZ increase (10BH166A5) is more pronounced.

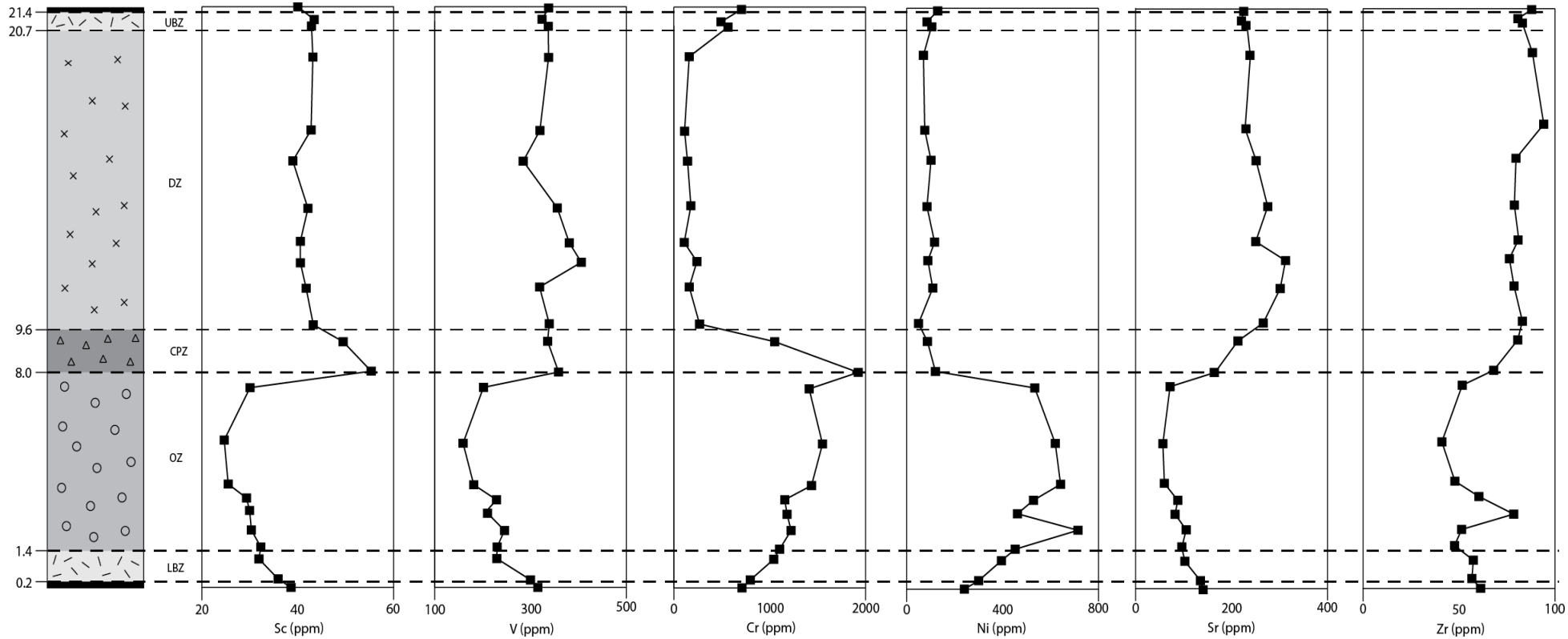
21.4
20.7
9.6
8.0
1.4
0.2
UBZ
DZ
CPZ
OZ
LBZ
20
40
60
Sc (ppm)
100
300
500
V (ppm)
0
1000
2000
Cr (ppm)
0
400
800
Ni (ppm)
0
200
400
Sr (ppm)
0
50
100
Zr (ppm)

Appendix E3 – LPS Clinopyroxene mineral chemistry & inverse melt compositions

Zone	Sample code	SiO_2	Al_2O_3	FeO*	TiO_2	Cr_2O_3	MgO	MnO	CaO	NiO	Na_2O	K_2O	Total	Womol%	Enmol%	Fsmol%	Mgmol%	Melt MgO	Melt FeO
LBZ	10BH166 A2 9	50.900	3.000	9.800	0.800	0.300	16.500	0.200	18.300	0.000	0.200	0.000	100.100	39.083	42.363	18.554	0.750	4.166	14.876
	10BH166 A2 10	50.000	4.000	8.800	0.700	0.400	15.800	0.300	19.100	0.000	0.300	0.000	99.400	41.616	41.386	16.997	0.762	4.849	14.097
	10BH166 A2 11	52.400	1.700	12.800	0.500	0.200	19.200	0.300	13.200	0.000	0.100	0.000	100.500	27.714	48.462	23.823	0.728	3.580	15.652
	10BH166 A2 9-11 av	51.100	2.900	10.467	0.667	0.300	17.167	0.267	16.867	0.000	0.200	0.000	100.000	36.053	44.114	19.833	0.745	4.119	14.934
	10BH166 A2 21	53.000	1.300	16.500	0.200	0.200	24.400	0.400	3.700	0.000	0.100	0.000	99.800	7.763	61.547	30.690	0.725	4.809	14.140
	10BH166 A2 22	53.300	0.800	16.200	0.200	0.100	24.800	0.400	3.400	0.000	0.100	0.000	99.300	7.147	62.668	30.186	0.732	4.952	13.990
	10BH166 A2 23	52.700	1.300	14.100	0.300	0.200	23.300	0.300	7.200	0.000	0.200	0.000	99.600	15.091	58.711	26.198	0.746	5.365	13.579
	10BH166 A2 21-23 av	53.000	1.133	15.600	0.233	0.167	24.167	0.367	4.767	0.000	0.133	0.000	99.567	10.004	60.973	29.023	0.734	5.024	13.916
LBZ	10BH166 A3 1	50.300	4.100	5.500	0.400	0.800	16.600	0.100	20.900	0.000	0.200	0.000	99.000	45.701	43.638	10.661	0.843	9.098	10.871
	10BH166 A3 2	51.500	3.200	5.800	0.400	0.600	17.700	0.100	19.900	0.000	0.200	0.000	99.400	42.962	45.938	11.100	0.845	9.004	10.925
	10BH166 A3 3	51.500	2.400	5.600	0.300	0.400	18.100	0.200	19.700	0.000	0.200	0.000	98.300	42.435	46.872	10.693	0.852	9.343	10.735
	10BH166 A3 4	50.300	4.400	6.400	0.400	0.900	16.800	0.100	20.300	0.000	0.200	0.000	99.700	43.968	43.744	12.288	0.824	8.194	11.408
	10BH166 A3 5	51.100	3.600	6.600	0.500	0.500	17.300	0.100	19.500	0.000	0.200	0.000	99.500	42.255	45.067	12.678	0.824	7.828	11.643
	10BH166 A3 1-5 av	50.940	3.540	5.980	0.400	0.640	17.300	0.120	20.060	0.000	0.200	0.000	99.180	43.459	45.057	11.484	0.838	8.680	11.113
	10BH166 A3 6	52.200	2.100	15.400	0.600	0.100	26.200	0.300	2.200	0.100	0.000	0.000	99.100	4.646	66.522	28.832	0.752	6.621	12.501
	10BH166 A3 7	52.500	2.000	15.500	0.600	0.100	26.100	0.300	2.100	0.100	0.000	0.000	99.300	4.448	66.452	29.100	0.750	6.423	12.656
	10BH166 A3 8	52.500	1.800	15.600	0.600	0.000	25.900	0.300	2.000	0.100	0.100	0.000	98.900	4.258	66.297	29.445	0.747	6.245	12.800
	10BH166 A3 6-8 av	52.400	1.967	15.500	0.600	0.067	26.067	0.300	2.100	0.100	0.033	0.000	99.100	4.451	66.424	29.125	0.750	6.430	12.651
	10BH166 A3 12	49.900	4.600	6.000	0.600	0.800	16.700	0.100	20.400	0.000	0.200	0.000	99.300	44.546	43.840	11.614	0.832	8.773	11.058
	10BH166 A3 13	50.700	4.000	5.600	0.500	0.600	16.800	0.100	20.900	0.000	0.200	0.000	99.500	45.375	43.848	10.778	0.842	9.003	10.925
	10BH166 A3 14	50.400	3.000	7.100	0.400	0.300	16.800	0.200	19.300	0.100	0.200	0.000	97.800	42.148	44.107	13.745	0.808	6.760	12.394
	10BH166 A3 12-14 av	50.850	3.392	8.550	0.525	0.442	19.092	0.175	15.675	0.050	0.158	0.000	98.925	33.924	49.673	16.403	0.799	7.163	12.098
	10BH166 A3 33	50.100	4.400	5.400	0.500	0.800	16.200	0.100	21.200	0.000	0.200	0.000	99.000	46.632	42.838	10.529	0.842	9.033	10.908
	10BH166 A3 34	50.700	4.600	6.000	0.400	1.000	16.700	0.100	20.100	0.000	0.200	0.000	99.900	44.180	44.129	11.691	0.832	8.502	11.219
	10BH166 A3 35	52.500	1.900	8.800	0.400	0.300	18.000	0.200	17.400	0.000	0.200	0.000	99.700	37.148	46.198	16.654	0.785	5.261	13.680
	10BH166 A3 33-35 av	51.100	3.633	6.733	0.433	0.700	16.967	0.133	19.567	0.000	0.200	0.000	99.533	42.599	44.406	12.995	0.818	7.396	11.933
LOZ	BH311 B2 124	50.539	2.353	9.768	1.195	0.104	16.280	0.191	19.613	0.027	0.301	0.012	100.383	40.994	40.907	18.099	0.748	4.190	14.846
	BH311 B2 124	51.254	2.215	8.956	0.690	0.389	17.694	0.234	17.705	0.030	0.268	0.003	99.438	37.738	45.340	16.922	0.779	5.487	13.464
	BH311 B2 124	52.484	2.044	7.410	0.371	0.678	18.515	0.171	18.314	0.042	0.221	0.011	100.261	38.849	47.217	13.934	0.817	7.205	12.068
	BH311 B2 124	51.404	2.772	6.255	0.329	0.702	18.062	0.177	18.983	0.052	0.198	0.031	98.965	41.052	46.957	11.991	0.837	8.607	11.156

Appendix E3 – LPS Clinopyroxene mineral chemistry & inverse melt compositions

Zone	Sample code	SiO_2	Al_2O_3	FeO*	TiO_2	Cr_2O_3	MgO	MnO	CaO	NiO	Na_2O	K_2O	Total	Womol%	Enmol%	Fsmol%	Mgmol%	Melt MgO	Melt FeO
	BH311 B2 124	51.500	2.909	6.354	0.387	0.741	18.351	0.161	18.992	0.010	0.205	0.010	99.620	40.680	47.255	12.065	0.837	8.797	11.044
	BH311 B2 124	51.324	2.915	5.920	0.308	0.668	18.396	0.135	19.233	0.080	0.215	0.008	99.202	41.276	47.462	11.262	0.847	9.432	10.687
	BH311 B2 124	51.421	3.136	5.997	0.265	0.667	17.910	0.138	19.710	0.050	0.215	0.003	99.512	42.335	46.246	11.419	0.842	8.961	10.950
	BH311 B2 124	51.551	2.625	5.324	0.395	0.669	17.712	0.123	20.899	0.051	0.167	0.002	99.518	44.550	45.390	10.061	0.856	9.622	10.584
	BH311 B2 124	50.625	4.081	6.098	0.516	0.885	17.438	0.151	19.724	0.023	0.201	0.007	99.749	42.791	45.481	11.728	0.836	8.954	10.953
	BH311 B2 124	49.804	4.111	5.970	0.602	0.781	16.801	0.116	20.798	0.019	0.212	0.010	99.224	44.932	43.635	11.433	0.834	8.876	10.998
	BH311 B2 124	50.400	4.039	5.716	0.495	0.598	16.942	0.125	20.564	0.084	0.196	0.007	99.166	44.706	44.278	11.016	0.841	9.061	10.892
	BH311 B2 124	50.743	3.998	5.767	0.366	0.804	16.740	0.117	20.695	0.054	0.233	0.019	99.536	45.056	43.814	11.130	0.838	8.739	11.078
	BH311 B2 124	49.939	4.059	5.754	0.530	0.803	16.993	0.133	20.406	0.066	0.198	0.007	98.888	44.423	44.473	11.104	0.840	9.222	10.802
	BH311 B2 124	50.310	3.883	5.915	0.387	0.746	16.943	0.120	20.526	0.041	0.218	0.006	99.095	44.488	44.147	11.365	0.836	8.799	11.043
	BH311 B2 124	50.001	3.370	7.709	0.413	0.654	22.083	0.101	13.128	0.074	0.165	0.025	97.723	28.226	57.080	14.693	0.836	10.323	10.224
	BH311 B2 124	54.102	3.350	6.595	0.429	0.688	17.048	0.189	19.664	0.032	0.197	0.007	102.301	42.743	44.549	12.708	0.822	6.664	12.468
	BH311 B2 124	37.336	1.898	7.614	0.884	0.480	18.460	0.205	20.140	0.000	0.143	0.017	87.177	41.033	45.215	13.752	0.812	11.042	9.879
	BH311 B2 124	49.677	3.004	8.690	1.019	0.212	16.108	0.254	19.208	0.065	0.286	0.015	98.538	41.507	41.846	16.647	0.768	5.076	13.863
	BH311 B2 124	50.611	2.361	8.885	0.799	0.017	15.560	0.235	20.358	0.050	0.376	0.004	99.256	43.370	39.851	16.779	0.757	4.119	14.934
	BH311 B2 124	50.207	2.441	8.800	0.869	0.169	16.925	0.246	18.307	0.022	0.250	0.007	98.243	39.408	43.799	16.792	0.774	5.282	13.659
	BH311 B2 124 av	50.262	3.078	6.975	0.562	0.573	17.548	0.166	19.348	0.044	0.223	0.011	98.790	41.508	45.247	13.245	0.818	7.827	11.643
	BH311 B2 127	50.689	2.514	6.869	0.165	0.448	18.068	0.256	19.510	0.045	0.144	0.000	98.708	41.230	45.902	12.868	0.824	8.026	11.514
	BH311 B2 127	52.906	2.433	6.027	0.380	0.694	18.152	0.155	19.999	0.015	0.202	0.001	100.964	42.403	46.269	11.328	0.843	8.576	11.175
	BH311 B2 127	52.530	2.530	6.242	0.294	0.493	18.814	0.165	19.143	0.055	0.182	0.011	100.459	40.476	47.824	11.700	0.843	8.915	10.976
	BH311 B2 127	51.205	4.123	5.848	0.516	0.978	16.792	0.174	20.451	0.006	0.204	0.009	100.306	44.631	44.055	11.313	0.837	8.594	11.164
	BH311 B2 127	51.762	4.125	5.951	0.502	0.816	17.070	0.125	20.647	0.060	0.222	0.008	101.288	44.456	44.185	11.359	0.836	8.599	11.161
	BH311 B2 127	51.660	4.170	5.645	0.466	0.812	17.059	0.152	20.521	0.064	0.209	0.016	100.774	44.579	44.551	10.871	0.843	8.994	10.931
	BH311 B2 127	51.322	4.225	5.871	0.387	0.847	17.087	0.124	20.525	0.080	0.225	0.005	100.698	44.358	44.394	11.248	0.838	8.843	11.018
	BH311 B2 127	51.346	4.192	5.943	0.566	0.825	17.007	0.145	20.568	0.031	0.224	0.008	100.855	44.441	44.176	11.383	0.836	8.686	11.109
	BH311 B2 127	51.247	4.176	6.079	0.516	0.977	17.126	0.153	20.083	0.000	0.214	0.012	100.583	43.601	44.699	11.700	0.834	8.598	11.162
	BH311 B2 127	51.420	4.267	5.620	0.631	0.926	16.830	0.172	20.464	0.045	0.235	0.007	100.617	44.800	44.294	10.907	0.842	8.953	10.954
	BH311 B2 127	51.717	4.244	5.696	0.445	0.983	16.870	0.129	20.764	0.040	0.211	0.011	101.110	45.047	43.999	10.954	0.841	8.798	11.044
	BH311 B2 127	51.411	4.221	5.556	0.416	0.826	16.780	0.117	20.932	0.013	0.187	0.006	100.465	45.475	43.825	10.700	0.843	8.933	10.965
	BH311 B2 127	51.800	4.176	5.866	0.573	0.917	16.531	0.199	21.365	0.019	0.220	0.008	101.674	46.007	42.795	11.198	0.834	8.306	11.338
	BH311 B2 127	51.068	4.176	5.417	0.438	0.778	16.548	0.131	21.319	0.070	0.198	0.006	100.149	46.331	43.233	10.436	0.845	9.047	10.900
	BH311 B2 127	51.408	4.196	5.461	0.502	0.883	16.544	0.164	21.515	0.050	0.224	0.005	100.952	46.524	43.008	10.468	0.844	8.977	10.940

Appendix E3 – LPS Clinopyroxene mineral chemistry & inverse melt compositions

Zone	Sample code	SiO_2	Al_2O_3	FeO*	TiO_2	Cr_2O_3	MgO	MnO	CaO	NiO	Na_2O	K_2O	Total	Womol%	Enmol%	Fsmol%	Mgmol%	Melt MgO	Melt FeO
	BH311 B2 127	51.308	4.213	5.377	0.423	1.027	16.432	0.131	21.501	0.023	0.219	0.006	100.660	46.719	42.924	10.357	0.845	9.006	10.924
	BH311 B2 127	51.449	4.288	5.732	0.524	0.992	16.456	0.081	21.250	0.000	0.236	0.006	101.014	46.081	42.900	11.019	0.836	8.505	11.217
	BH311 B2 127	51.528	4.286	5.707	0.516	1.040	16.711	0.119	20.959	0.023	0.220	0.001	101.110	45.457	43.571	10.972	0.839	8.740	11.077
	BH311 B2 127	50.226	4.846	6.761	0.550	0.900	16.629	0.152	19.620	0.053	0.185	0.001	99.923	43.022	43.836	13.142	0.814	7.704	11.724
	BH311 B2 127	53.278	5.799	6.009	0.366	0.554	17.997	0.162	20.105	0.041	0.189	0.000	104.500	42.715	45.967	11.317	0.842	9.313	10.752
	BH311 B2 127 av	51.564	4.060	5.884	0.459	0.836	17.075	0.150	20.562	0.037	0.208	0.006	100.840	44.418	44.320	11.262	0.838	8.695	11.104
	BH311 B2 135	51.711	1.937	9.216	0.697	0.285	17.802	0.259	17.409	0.005	0.239	0.005	99.565	37.056	45.554	17.390	0.775	5.119	13.819
	BH311 B2 135	50.522	2.089	8.787	0.548	0.302	20.190	0.232	15.984	0.027	0.213	0.017	98.911	33.268	50.519	16.213	0.804	7.742	11.699
	BH311 B2 135	51.079	1.879	7.699	0.443	0.456	17.516	0.204	19.975	0.052	0.203	0.011	99.517	41.739	44.000	14.261	0.802	6.533	12.570
	BH311 B2 135	51.752	2.647	7.451	0.464	0.434	18.893	0.208	17.118	0.055	0.208	0.022	99.252	36.864	48.912	14.224	0.819	7.718	11.715
	BH311 B2 135	52.183	1.923	6.648	0.508	0.575	18.357	0.166	18.740	0.016	0.208	0.018	99.342	40.127	47.254	12.619	0.831	7.928	11.578
	BH311 B2 135	52.153	2.499	5.690	0.287	0.516	18.255	0.179	19.753	0.001	0.199	0.000	99.532	42.259	46.950	10.791	0.851	9.245	10.789
	BH311 B2 135	50.652	4.361	6.322	0.579	1.080	17.168	0.118	19.338	0.053	0.229	0.010	99.910	42.425	45.280	12.295	0.829	8.507	11.216
	BH311 B2 135	51.685	3.118	6.170	0.358	0.728	18.139	0.215	18.909	0.066	0.193	0.005	99.586	40.942	47.215	11.843	0.840	8.806	11.039
	BH311 B2 135	53.048	2.360	6.149	0.351	0.624	18.945	0.155	18.784	0.014	0.176	0.010	100.616	39.957	48.448	11.595	0.846	8.915	10.976
	BH311 B2 135	52.467	2.217	5.810	0.423	0.616	18.808	0.160	19.025	0.025	0.185	0.006	99.742	40.664	48.328	11.008	0.852	9.379	10.716
	BH311 B2 135	50.219	4.427	5.682	0.559	1.140	16.394	0.126	20.933	0.043	0.213	0.012	99.748	45.827	43.146	11.027	0.837	8.892	10.989
	BH311 B2 135	50.672	4.306	5.709	0.696	0.795	16.569	0.140	20.927	0.057	0.197	0.013	100.081	45.586	43.390	11.024	0.838	8.823	11.029
	BH311 B2 135	50.802	4.312	5.764	0.531	0.830	16.677	0.168	20.699	0.020	0.210	0.012	100.025	45.138	43.720	11.142	0.838	8.775	11.057
	BH311 B2 135	48.533	4.070	6.891	0.485	0.947	17.998	0.161	18.033	0.041	0.207	0.027	97.393	39.392	47.264	13.344	0.823	8.943	10.960
	BH311 B2 135	51.048	4.252	5.588	0.660	0.852	16.488	0.109	20.937	0.086	0.245	0.012	100.277	45.802	43.362	10.836	0.840	8.815	11.034
	BH311 B2 135	50.332	3.971	5.569	0.688	0.838	17.074	0.119	19.607	0.064	0.254	0.031	98.547	43.504	45.543	10.954	0.845	9.369	10.721
	BH311 B2 135	48.625	4.001	6.019	0.529	0.967	17.630	0.170	19.056	0.043	0.216	0.004	97.260	41.802	46.493	11.705	0.839	9.701	10.543
	BH311 B2 135	50.703	3.905	6.472	0.529	0.810	17.574	0.141	18.920	0.039	0.213	0.014	99.320	41.324	46.145	12.531	0.829	8.460	11.244
	BH311 B2 135	52.056	2.681	7.912	0.378	0.590	18.204	0.212	18.052	0.033	0.267	0.007	100.392	38.449	46.612	14.939	0.804	6.747	12.404
	BH311 B2 135 av	51.839	2.437	9.272	0.569	0.406	18.941	0.237	15.948	0.022	0.211	0.014	99.896	33.977	48.512	17.511	0.784	6.025	12.984
	BH311 B2 136	51.104	3.170	6.741	0.514	0.690	17.881	0.174	18.907	0.038	0.214	0.013	99.446	40.805	46.332	12.863	0.826	8.118	11.456
	BH311 B2 136	51.787	2.405	7.472	0.372	0.439	17.952	0.210	18.892	0.012	0.223	0.022	99.786	40.113	45.823	14.064	0.811	6.953	12.250
	BH311 B2 136	49.102	2.884	5.915	0.351	0.737	17.846	0.170	19.928	0.000	0.206	0.013	97.152	42.740	46.014	11.246	0.843	9.637	10.577
	BH311 B2 136	53.065	2.707	5.952	0.401	0.672	18.059	0.156	19.882	0.044	0.199	0.003	101.140	42.421	46.322	11.258	0.844	8.597	11.162
	BH311 B2 136	52.628	2.516	5.850	0.402	0.638	18.604	0.114	19.632	0.011	0.225	0.009	100.629	41.608	47.401	10.991	0.850	9.293	10.763
	BH311 B2 136	53.075	2.395	5.673	0.416	0.730	18.355	0.182	19.696	0.052	0.179	0.000	100.753	42.094	47.159	10.748	0.852	9.120	10.859

Appendix E3 – LPS Clinopyroxene mineral chemistry & inverse melt compositions

Zone	Sample code	SiO_2	Al_2O_3	FeO*	TiO_2	Cr_2O_3	MgO	MnO	CaO	NiO	Na_2O	K_2O	Total	Womol%	Enmol%	Fsmol%	Mgmol%	Melt MgO	Melt FeO
	BH311 B2 136	49.485	2.390	6.074	0.351	0.702	18.589	0.167	19.658	0.041	0.174	0.006	97.637	41.482	47.157	11.362	0.845	9.828	10.476
	BH311 B2 136	52.968	2.729	6.171	0.330	0.611	18.363	0.158	19.266	0.090	0.185	0.012	100.883	41.156	47.158	11.686	0.841	8.549	11.190
	BH311 B2 136	52.625	2.753	5.828	0.308	0.716	17.962	0.173	19.979	0.034	0.177	0.020	100.575	42.746	46.200	11.054	0.846	8.795	11.045
	BH311 B2 136	52.575	3.075	6.378	0.408	0.571	17.704	0.160	20.008	0.023	0.199	0.008	101.109	42.620	45.337	12.044	0.832	7.992	11.536
	BH311 B2 136	52.803	3.036	5.984	0.387	0.672	17.590	0.167	20.193	0.026	0.210	0.006	101.074	43.292	45.336	11.373	0.840	8.317	11.331
	BH311 B2 136	52.463	2.619	6.809	0.308	0.653	17.483	0.218	19.940	0.037	0.235	0.023	100.788	42.431	44.725	12.844	0.821	7.218	12.058
	BH311 B2 136	51.023	3.367	7.663	0.929	0.569	16.201	0.208	20.096	0.061	0.326	0.014	100.457	43.343	42.007	14.651	0.790	5.923	13.072
	BH311 B2 136	52.825	2.872	6.035	0.151	0.624	17.987	0.177	20.022	0.034	0.209	0.000	100.936	42.604	46.012	11.384	0.842	8.519	11.209
	BH311 B2 136	52.768	2.531	5.792	0.394	0.751	18.211	0.174	19.799	0.024	0.222	0.004	100.670	42.282	46.753	10.965	0.849	9.003	10.925
	BH311 B2 136	53.218	2.407	5.912	0.229	0.712	18.278	0.131	19.848	0.056	0.201	0.008	101.000	42.174	46.690	11.136	0.846	8.695	11.104
	BH311 B2 136	52.964	2.589	5.864	0.394	0.616	17.955	0.187	19.867	0.059	0.188	0.020	100.703	42.587	46.270	11.143	0.845	8.583	11.170
	BH311 B2 136	52.781	2.768	5.628	0.309	0.677	17.768	0.178	19.882	0.079	0.205	0.018	100.293	43.005	46.203	10.791	0.849	8.818	11.032
	BH311 B2 136	52.919	2.128	6.817	0.380	0.222	18.472	0.200	19.077	0.051	0.180	0.003	100.449	40.309	46.922	12.769	0.828	7.652	11.759
	BH311 B2 136	52.086	3.067	6.757	0.401	0.362	17.371	0.158	19.731	0.045	0.230	0.021	100.229	42.338	44.810	12.853	0.821	7.317	11.988
	BH311 B2 136	53.214	1.780	6.596	0.358	0.283	18.418	0.196	18.947	0.039	0.188	0.007	100.026	40.368	47.174	12.458	0.833	7.617	11.782
	BH311 B2 136 av	52.319	2.651	6.259	0.379	0.598	17.958	0.174	19.717	0.041	0.208	0.011	100.314	42.086	46.074	11.841	0.836	8.298	11.343
LOZ	10BH166 A4 1	52.600	2.500	6.000	0.200	0.500	18.700	0.200	19.000	0.000	0.200	0.000	99.900	40.599	48.036	11.365	0.847	9.029	10.910
	10BH166 A4 2	51.500	2.600	6.400	0.500	0.600	17.600	0.200	19.700	0.000	0.200	0.000	99.200	42.337	45.471	12.193	0.831	8.005	11.528
	10BH166 A4 3	50.200	2.900	9.000	1.100	0.000	15.600	0.200	20.100	0.000	0.300	0.000	99.400	42.919	40.045	17.036	0.755	4.284	14.733
	10BH166 A4 1-3 av	51.433	2.667	7.133	0.600	0.367	17.300	0.200	19.600	0.000	0.233	0.000	99.500	41.951	44.515	13.534	0.812	6.942	12.258
	10BH166 A4 4	49.700	4.200	5.900	0.500	1.100	17.100	0.100	19.800	0.000	0.200	0.000	98.800	43.433	45.094	11.473	0.838	9.190	10.820
	10BH166 A4 5	49.600	4.200	6.000	0.600	1.100	16.800	0.200	19.900	0.000	0.200	0.000	98.600	43.818	44.471	11.711	0.833	8.849	11.014
	10BH166 A4 6	49.800	2.700	9.000	1.000	0.100	16.600	0.200	18.700	0.100	0.300	0.000	98.400	40.099	42.793	17.108	0.767	5.120	13.819
	10BH166 A4 4-6 av	49.700	3.700	6.967	0.700	0.767	16.833	0.167	19.467	0.033	0.233	0.000	98.600	42.430	44.109	13.461	0.812	7.529	11.842
	10BH166 A4 9	49.900	3.700	5.600	0.400	0.900	16.900	0.100	20.500	0.100	0.200	0.000	98.200	44.778	44.378	10.843	0.843	9.246	10.789
	10BH166 A4 10	49.500	3.800	5.500	0.300	0.900	16.400	0.100	20.800	0.100	0.200	0.000	97.700	45.824	43.435	10.741	0.842	9.041	10.904
	10BH166 A4 11	51.100	2.300	6.200	0.400	0.500	17.200	0.200	20.200	0.100	0.200	0.000	98.300	43.559	44.589	11.852	0.832	7.908	11.590
	10BH166 A4 9-11 av	50.167	3.267	5.767	0.367	0.767	16.833	0.133	20.500	0.100	0.200	0.000	98.067	44.712	44.138	11.150	0.839	8.727	11.085
LOZ	10BH166 A5 1	53.100	2.100	5.800	0.200	0.600	18.900	0.200	18.400	0.000	0.200	0.000	99.500	39.773	49.113	11.114	0.853	9.120	10.859
	10BH166 A5 2	50.300	4.400	5.500	0.400	1.000	16.700	0.100	19.700	0.000	0.200	0.000	98.300	44.119	44.962	10.919	0.844	9.142	10.847
	10BH166 A5 3	51.000	3.300	6.600	0.600	0.800	16.600	0.200	19.300	0.000	0.200	0.000	98.600	42.787	44.242	12.971	0.818	7.103	12.141
	10BH166 A5 4	50.700	3.000	8.300	0.800	0.300	16.600	0.200	18.600	0.000	0.300	0.000	98.800	40.511	43.464	16.025	0.781	5.438	13.509

Appendix E3 – LPS Clinopyroxene mineral chemistry & inverse melt compositions

Zone	Sample code	SiO_2	Al_2O_3	FeO*	TiO_2	Cr_2O_3	MgO	MnO	CaO	NiO	Na_2O	K_2O	Total	Womol%	Enmol%	Fsmol%	Mgmol%	Melt MgO	Melt FeO
	10BH166 A5 5	50.500	2.900	8.500	0.800	0.300	16.200	0.200	18.600	0.000	0.300	0.000	98.300	40.780	42.699	16.520	0.773	4.914	14.029
	10BH166 A5 1-5 av	51.120	3.140	6.940	0.560	0.600	17.000	0.180	18.920	0.000	0.240	0.000	98.700	41.574	44.908	13.518	0.814	6.998	12.217
	10BH166 A5 25	50.200	4.400	5.800	0.600	1.200	16.900	0.200	19.600	0.000	0.200	0.000	99.100	43.499	45.090	11.411	0.839	9.063	10.891
	10BH166 A5 26	49.600	4.500	6.300	0.500	0.900	16.700	0.200	19.700	0.000	0.200	0.000	98.500	43.429	44.259	12.312	0.825	8.387	11.289
	10BH166 A5 27	35.700	5.000	11.100	0.400	0.400	16.400	0.300	17.300	0.000	0.100	0.100	86.800	36.922	42.078	21.000	0.725	7.305	11.997
	10BH166 A5 25-27 av	45.167	4.633	7.733	0.500	0.833	16.667	0.233	18.867	0.000	0.167	0.033	94.800	41.231	43.787	14.982	0.793	7.967	11.552
	10BH166 A5 28	52.800	1.500	15.000	0.600	0.100	26.600	0.300	2.000	0.100	0.000	0.000	98.900	4.231	67.642	28.127	0.760	6.767	12.389
	10BH166 A5 29	52.500	1.600	15.600	0.700	0.000	26.400	0.300	1.900	0.100	0.000	0.000	99.100	4.003	66.863	29.134	0.751	6.469	12.620
	10BH166 A5 30	53.800	1.100	15.800	0.500	0.000	26.800	0.300	1.700	0.100	0.000	0.000	100.200	3.547	67.227	29.225	0.751	6.208	12.831
	10BH166 A5 28-30 av	53.033	1.400	15.467	0.600	0.033	26.600	0.300	1.867	0.100	0.000	0.000	99.400	3.925	67.244	28.831	0.754	6.479	12.612
LOZ	10BH167 A1 1	51.300	3.900	5.500	0.500	0.800	16.600	0.100	20.700	0.100	0.200	0.000	99.800	45.463	43.829	10.708	0.843	8.750	11.072
	10BH167 A1 2	51.300	3.900	5.500	0.400	1.000	17.100	0.200	19.900	0.100	0.200	0.000	99.500	43.897	45.347	10.755	0.847	9.184	10.823
	10BH167 A1 3	50.400	3.000	9.000	1.400	0.100	15.800	0.300	18.900	0.000	0.300	0.000	99.100	41.201	41.407	17.392	0.758	4.369	14.631
	10BH167 A1 1-3 av	51.000	3.600	6.667	0.767	0.633	16.500	0.200	19.833	0.067	0.233	0.000	99.467	43.514	43.520	12.966	0.815	7.148	12.108
	10BH167 A1 11	51.000	3.800	6.200	0.400	1.000	17.900	0.200	18.600	0.000	0.200	0.000	99.300	40.776	47.175	12.049	0.837	8.937	10.963
	10BH167 A1 12	51.300	3.700	5.400	0.400	0.900	17.300	0.100	19.800	0.000	0.200	0.000	99.000	43.627	45.825	10.547	0.851	9.383	10.713
	10BH167 A1 13	51.600	3.400	6.800	0.600	0.600	17.200	0.200	19.200	0.000	0.200	0.000	99.800	41.825	45.044	13.131	0.818	7.315	11.989
	10BH167 A1 11-13 av	51.300	3.633	6.133	0.467	0.833	17.467	0.167	19.200	0.000	0.200	0.000	99.367	42.073	46.013	11.914	0.835	8.513	11.212
	10BH167 A1 21	53.500	1.900	15.300	0.700	0.100	26.200	0.300	2.500	0.000	0.000	0.000	100.500	5.256	66.226	28.518	0.753	6.360	12.707
	10BH167 A1 22	53.200	2.000	14.400	0.600	0.200	26.500	0.300	2.500	0.100	0.100	0.000	99.800	5.305	67.606	27.089	0.766	7.108	12.137
	10BH167 A1 21-22 av	53.350	1.950	14.850	0.650	0.150	26.350	0.300	2.500	0.050	0.050	0.000	100.150	5.281	66.913	27.807	0.760	6.729	12.418
MOZ	10BH167 A2 4	52.300	1.900	12.300	0.500	0.300	28.000	0.300	2.400	0.100	0.100	0.000	98.200	5.110	71.673	23.217	0.802	9.284	10.768
	10BH167 A2 5	54.900	1.100	12.300	0.200	0.300	28.900	0.300	2.200	0.100	0.000	0.000	100.300	4.598	72.613	22.789	0.807	8.995	10.930
	10BH167 A2 4-5 av	53.600	1.500	12.300	0.350	0.300	28.450	0.300	2.300	0.100	0.050	0.000	99.250	4.852	72.148	23.001	0.805	9.142	10.847
	10BH167 A2 9	51.100	2.400	5.400	0.500	0.700	18.100	0.100	20.500	0.000	0.200	0.000	99.000	43.574	46.251	10.175	0.857	9.933	10.422
	10BH167 A2 10	51.800	2.500	5.200	0.300	0.700	17.700	0.100	20.300	0.000	0.200	0.000	98.700	43.951	46.069	9.980	0.858	9.566	10.614
	10BH167 A2 11	51.700	3.100	6.700	0.600	0.600	17.500	0.100	19.500	0.000	0.200	0.000	100.200	41.956	45.265	12.779	0.823	7.634	11.771
	10BH167 A2 9-11 av	51.533	2.667	5.767	0.467	0.667	17.767	0.100	20.100	0.000	0.200	0.000	99.300	43.160	45.863	10.977	0.846	8.999	10.928
MOZ	10BH167 A3 5	51.600	3.600	5.300	0.400	0.600	17.200	0.100	20.700	0.000	0.200	0.000	99.700	44.926	44.877	10.197	0.853	9.386	10.712
	10BH167 A3 6	51.000	4.000	5.500	0.600	1.100	17.100	0.100	20.300	0.000	0.200	0.000	100.000	44.388	44.951	10.661	0.847	9.379	10.716

Appendix E3 – LPS Clinopyroxene mineral chemistry & inverse melt compositions

Zone	Sample code	SiO_2	Al_2O_3	FeO*	TiO_2	Cr_2O_3	MgO	MnO	CaO	NiO	Na_2O	K_2O	Total	Womol%	Enmol%	Fsmol%	Mgmol%	Melt MgO	Melt FeO
	10BH167 A3 7	49.500	3.800	8.200	0.600	0.500	17.900	0.300	17.400	0.000	0.200	0.000	98.500	37.672	46.590	15.738	0.795	7.127	12.123
	10BH167 A3 5-7 av	50.700	3.800	6.333	0.533	0.733	17.400	0.167	19.467	0.000	0.200	0.000	99.400	42.320	45.475	12.205	0.830	8.467	11.240
	10BH167 A3 10	52.400	2.400	5.800	0.300	0.600	18.500	0.100	19.400	0.100	0.200	0.000	99.800	41.469	47.541	10.990	0.850	9.212	10.808
	10BH167 A3 11	52.100	2.900	5.800	0.500	0.700	18.300	0.100	19.100	0.000	0.200	0.000	99.800	41.305	47.576	11.119	0.849	9.248	10.788
	10BH167 A3 12	52.400	2.200	6.900	0.500	0.500	18.400	0.200	18.100	0.000	0.200	0.000	99.400	39.062	47.738	13.200	0.826	7.598	11.795
	10BH167 A3 10-12 av	52.300	2.500	6.167	0.433	0.600	18.400	0.133	18.867	0.033	0.200	0.000	99.667	40.614	47.618	11.768	0.842	8.659	11.125
	10BH167 A3 20	51.000	4.300	5.600	0.400	1.200	17.200	0.100	19.800	0.100	0.200	0.000	99.800	43.572	45.503	10.924	0.846	9.359	10.726
	10BH167 A3 21	53.100	2.400	5.500	0.400	0.700	18.500	0.200	19.400	0.000	0.200	0.000	100.300	41.706	47.812	10.482	0.857	9.437	10.684
	10BH167 A3 22	52.200	2.400	7.600	1.200	0.400	17.600	0.200	18.800	0.000	0.300	0.000	100.700	40.261	45.311	14.428	0.805	6.549	12.557
	10BH167 A3 20-22 av	52.100	3.033	6.233	0.667	0.767	17.767	0.167	19.333	0.033	0.233	0.000	100.267	41.831	46.213	11.956	0.836	8.360	11.305
UOZ	10BH167 A4 13	51.600	3.300	5.600	0.300	1.200	17.500	0.100	20.100	0.000	0.300	0.000	100.100	43.599	45.634	10.768	0.848	9.276	10.772
	10BH167 A4 14	52.300	2.500	6.200	0.300	0.700	17.900	0.200	19.300	0.000	0.200	0.000	99.600	41.671	46.462	11.867	0.837	8.186	11.413
	10BH167 A4 15	51.900	2.500	8.900	0.900	0.100	16.800	0.200	18.600	0.000	0.300	0.000	100.300	39.840	43.260	16.899	0.771	4.696	14.262
	10BH167 A4 13-15 av	51.933	2.767	6.900	0.500	0.667	17.400	0.167	19.333	0.000	0.267	0.000	100.000	41.695	45.113	13.192	0.818	7.182	12.084
	10BH167 A4 16	53.600	1.900	14.500	0.700	0.100	27.100	0.300	2.100	0.000	0.100	0.000	100.400	4.418	68.540	27.042	0.769	7.295	12.004
	10BH167 A4 17	53.600	1.900	14.800	0.600	0.200	27.000	0.300	2.300	0.100	0.000	0.000	100.800	4.804	67.794	27.402	0.765	7.068	12.166
	10BH167 A4 18	53.400	1.600	15.300	0.800	0.000	26.500	0.300	1.900	0.000	0.100	0.000	100.000	4.015	67.323	28.662	0.755	6.522	12.578
	10BH167 A4 16-18 av	53.533	1.800	14.867	0.700	0.100	26.867	0.300	2.100	0.033	0.067	0.000	100.400	4.414	67.886	27.700	0.763	6.959	12.245
	10BH167 A4 23	52.900	2.500	5.600	0.300	0.900	18.300	0.100	19.800	0.000	0.200	0.000	100.700	42.340	47.044	10.615	0.853	9.262	10.780
	10BH167 A4 24	51.900	3.300	5.900	0.300	1.100	17.700	0.100	19.500	0.000	0.200	0.000	100.000	42.383	46.249	11.368	0.842	8.812	11.035
	10BH167 A4 25	52.700	1.900	6.600	0.300	0.700	18.400	0.200	19.100	0.000	0.200	0.000	100.200	40.577	46.993	12.430	0.832	7.897	11.597
	10BH167 A4 23-25 av	52.500	2.567	6.033	0.300	0.900	18.133	0.133	19.467	0.000	0.200	0.000	100.300	41.761	46.766	11.474	0.843	8.640	11.136
UOZ	BH311 B3 28	51.746	2.573	9.000	1.060	0.026	15.888	0.195	20.233	0.053	0.351	0.009	100.091	42.720	40.328	16.952	0.759	4.127	14.924
	BH311 B3 28	51.076	2.956	9.045	1.457	0.043	16.360	0.220	19.284	0.080	0.345	0.012	100.878	41.056	41.873	17.071	0.763	4.774	14.177
	BH311 B3 28	51.296	2.923	8.453	1.008	0.352	16.771	0.238	19.002	0.060	0.272	0.003	100.378	40.727	43.213	16.060	0.780	5.410	13.536
	BH311 B3 28	51.464	2.798	7.952	0.866	0.448	16.656	0.227	19.070	0.015	0.269	0.018	99.783	41.328	43.395	15.277	0.789	5.600	13.360
	BH311 B3 28	51.640	3.027	8.444	0.665	0.534	17.255	0.196	18.500	0.032	0.279	0.018	100.590	39.590	44.391	16.019	0.785	5.720	13.251
	BH311 B3 28	51.973	2.932	7.874	0.637	0.626	17.149	0.248	18.705	0.039	0.269	0.000	100.452	40.398	44.526	15.075	0.795	5.998	13.007
	BH311 B3 28	51.611	2.870	7.526	0.695	0.632	17.319	0.223	19.039	0.042	0.235	0.010	100.202	40.917	44.745	14.338	0.804	6.601	12.516
	BH311 B3 28	51.863	3.158	7.482	0.437	0.880	17.319	0.184	18.993	0.000	0.258	0.007	100.581	40.893	44.827	14.280	0.805	6.649	12.479

Appendix E3 – LPS Clinopyroxene mineral chemistry & inverse melt compositions

Zone	Sample code	SiO_2	Al_2O_3	FeO*	TiO_2	Cr_2O_3	MgO	MnO	CaO	NiO	Na_2O	K_2O	Total	Womol%	Enmol%	Fsmol%	Mgmol%	Melt MgO	Melt FeO
	BH311 B3 28	52.170	3.115	6.935	0.624	0.781	17.017	0.170	19.713	0.067	0.260	0.005	100.857	42.560	44.167	13.273	0.814	6.911	12.281
	BH311 B3 28	51.816	3.308	7.114	0.552	0.924	16.915	0.166	19.879	0.049	0.234	0.007	100.964	42.732	43.712	13.556	0.809	6.807	12.359
	BH311 B3 28	51.965	3.248	6.957	0.552	0.868	16.963	0.194	19.904	0.037	0.272	0.014	100.974	42.838	43.889	13.273	0.813	6.980	12.230
	BH311 B3 28	52.017	3.302	6.310	0.546	0.918	16.856	0.151	20.061	0.001	0.257	0.009	100.428	43.688	44.130	12.182	0.826	7.574	11.812
	BH311 B3 28	51.228	4.146	6.933	0.544	0.898	17.213	0.122	18.098	0.001	0.399	0.119	99.701	40.274	46.049	13.677	0.816	7.582	11.806
	BH311 B3 28	51.757	3.378	6.591	0.416	1.070	17.032	0.162	20.324	0.035	0.226	0.009	101.000	43.574	43.899	12.527	0.822	7.578	11.809
	BH311 B3 28	51.481	4.018	6.076	0.359	1.242	16.726	0.142	20.647	0.040	0.264	0.021	101.016	44.748	43.579	11.673	0.831	8.235	11.382
	BH311 B3 28	52.439	3.244	5.489	0.310	0.978	17.122	0.156	20.684	0.021	0.247	0.011	100.701	44.835	44.618	10.547	0.848	8.801	11.042
	BH311 B3 28	52.323	3.067	5.724	0.360	0.924	17.103	0.132	20.820	0.007	0.253	0.017	100.730	44.817	44.260	10.923	0.842	8.470	11.238
	BH311 B3 28	52.503	2.984	5.485	0.324	0.952	17.387	0.158	20.587	0.053	0.227	0.006	100.666	44.415	45.095	10.490	0.850	8.952	10.955
	BH311 B3 28	52.541	2.969	5.744	0.360	0.845	17.459	0.166	20.239	0.038	0.244	0.002	100.607	43.694	45.313	10.993	0.844	8.607	11.156
	BH311 B3 28	52.364	3.060	5.681	0.331	0.933	17.464	0.162	20.223	0.064	0.239	0.005	100.526	43.722	45.391	10.888	0.846	8.787	11.050
	BH311 B3 28	52.458	3.036	5.907	0.374	0.889	17.548	0.164	20.119	0.023	0.238	0.003	100.759	43.312	45.415	11.273	0.841	8.523	11.206
	BH311 B3 28	52.777	2.869	6.212	0.316	0.835	17.489	0.167	19.881	0.051	0.256	0.017	100.870	42.835	45.300	11.865	0.834	7.908	11.590
	BH311 B3 28	52.334	2.814	6.134	0.352	0.788	17.681	0.171	19.691	0.019	0.225	0.013	100.222	42.452	45.825	11.723	0.837	8.247	11.375
	BH311 B3 28	52.620	2.556	6.412	0.424	0.813	17.877	0.156	19.540	0.039	0.261	0.003	100.701	41.828	46.005	12.167	0.832	7.981	11.543
	BH311 B3 28	52.965	2.477	6.440	0.395	0.822	17.895	0.183	19.244	0.043	0.248	0.015	100.727	41.415	46.299	12.286	0.832	7.786	11.670
	BH311 B3 28	52.912	2.407	7.034	0.380	0.794	17.972	0.223	18.971	0.017	0.248	0.013	100.971	40.526	46.154	13.320	0.820	7.177	12.088
	BH311 B3 28	52.606	2.458	7.572	0.494	0.740	17.782	0.174	18.604	0.039	0.247	0.015	100.731	39.843	45.782	14.375	0.807	6.523	12.578
	BH311 B3 28	52.386	2.459	8.423	0.686	0.482	17.612	0.228	18.343	0.000	0.266	0.008	100.893	39.042	45.065	15.893	0.788	5.665	13.300
	BH311 B3 28	52.289	2.592	7.001	0.395	0.314	17.484	0.204	18.375	0.026	0.428	0.047	99.155	40.296	46.094	13.610	0.817	6.910	12.282
	BH311 B3 28	51.211	2.939	8.958	1.043	0.299	16.787	0.196	18.821	0.029	0.317	0.018	100.618	40.093	42.990	16.916	0.770	5.078	13.861
	BH311 B3 28 av	52.061	2.989	7.030	0.565	0.722	17.203	0.183	19.520	0.034	0.271	0.015	100.559	42.039	44.544	13.417	0.814	6.952	12.251
	BH311 B3 29	50.752	2.728	8.403	1.051	0.269	16.582	0.225	19.330	0.000	0.317	0.008	99.665	41.380	42.674	15.946	0.779	5.418	13.529
	BH311 B3 29	51.337	2.719	8.218	0.823	0.439	16.991	0.189	19.364	0.000	0.266	0.005	100.351	41.134	43.391	15.475	0.787	5.752	13.222
	BH311 B3 29	51.372	2.730	7.433	0.767	0.562	17.101	0.174	19.347	0.013	0.276	0.027	99.802	41.611	44.217	14.172	0.804	6.561	12.547
	BH311 B3 29	51.289	3.427	6.512	0.294	1.066	16.974	0.145	20.275	0.059	0.232	0.012	100.285	43.646	43.927	12.427	0.823	7.732	11.706
	BH311 B3 29	51.501	3.687	5.493	0.453	1.087	16.950	0.122	20.719	0.005	0.220	0.021	100.258	45.075	44.331	10.594	0.846	9.061	10.892
	BH311 B3 29	51.373	3.380	4.878	0.295	1.212	16.668	0.130	21.611	0.000	0.155	0.005	99.707	47.008	43.586	9.406	0.859	9.680	10.554
	BH311 B3 29	50.629	3.699	5.318	0.338	1.193	16.917	0.153	20.710	0.031	0.234	0.013	99.235	45.256	44.442	10.302	0.850	9.542	10.627
	BH311 B3 29	52.422	2.271	4.778	0.224	1.059	16.540	0.170	22.827	0.042	0.149	0.008	100.490	48.623	42.355	9.022	0.861	9.200	10.815
	BH311 B3 29	47.376	5.618	8.880	0.249	0.964	16.638	0.227	16.119	0.039	0.172	0.024	96.306	36.640	45.466	17.894	0.770	6.279	12.773

Appendix E3 – LPS Clinopyroxene mineral chemistry & inverse melt compositions

Zone	Sample code	SiO_2	Al_2O_3	FeO*	TiO_2	Cr_2O_3	MgO	MnO	CaO	NiO	Na_2O	K_2O	Total	Womol%	Enmol%	Fsmol%	Mgmol%	Melt MgO	Melt FeO
	BH311 B3 29	51.288	3.555	5.767	0.201	1.235	17.133	0.152	20.381	0.000	0.242	0.007	99.961	44.220	44.688	11.092	0.841	8.856	11.010
	BH311 B3 29	51.010	3.519	5.622	0.359	1.183	17.349	0.170	20.394	0.024	0.203	0.012	99.845	44.110	45.111	10.779	0.846	9.333	10.741
	BH311 B3 29	51.186	3.463	5.371	0.417	1.236	17.346	0.153	20.495	0.001	0.210	0.012	99.890	44.449	45.225	10.326	0.852	9.635	10.578
	BH311 B3 29	51.163	3.408	5.399	0.410	1.241	17.304	0.099	20.534	0.049	0.233	0.000	99.840	44.520	45.103	10.377	0.851	9.563	10.616
	BH311 B3 29	51.885	2.805	6.073	0.366	0.893	17.953	0.164	19.719	0.000	0.234	0.009	100.101	42.238	46.230	11.532	0.840	8.756	11.068
	BH311 B3 29	51.466	2.946	5.313	0.151	1.175	17.655	0.136	20.447	0.022	0.223	0.002	99.536	44.085	45.761	10.155	0.856	9.725	10.530
	BH311 B3 29	51.960	2.695	5.413	0.360	1.039	17.700	0.091	20.511	0.000	0.223	0.006	99.998	44.026	45.674	10.300	0.854	9.423	10.692
	BH311 B3 29	51.763	2.789	5.475	0.367	0.987	17.666	0.109	20.412	0.066	0.226	0.010	99.870	43.894	45.669	10.437	0.852	9.388	10.711
	BH311 B3 29	52.072	2.836	5.633	0.309	0.789	17.564	0.120	20.475	0.034	0.241	0.002	100.075	43.953	45.327	10.719	0.847	8.961	10.950
	BH311 B3 29	51.957	2.935	5.676	0.360	0.876	17.655	0.153	20.525	0.026	0.211	0.003	100.377	43.875	45.370	10.756	0.847	9.081	10.881
	BH311 B3 29	51.463	2.887	5.519	0.374	0.798	17.356	0.138	20.501	0.034	0.240	0.009	99.319	44.318	45.105	10.576	0.849	9.119	10.860
	BH311 B3 29	51.894	2.645	5.765	0.425	0.631	17.573	0.143	20.229	0.006	0.216	0.001	99.528	43.536	45.466	10.998	0.845	8.719	11.090
	BH311 B3 29	51.670	2.686	6.686	0.495	0.930	17.511	0.159	19.879	0.031	0.213	0.000	100.260	42.425	44.927	12.649	0.824	7.680	11.740
	BH311 B3 29	52.079	2.427	6.697	0.330	0.690	17.715	0.181	19.304	0.000	0.226	0.011	99.660	41.481	45.763	12.757	0.825	7.507	11.857
	BH311 B3 29	47.406	2.019	8.747	5.162	0.472	15.070	0.323	19.311	0.031	0.122	0.012	98.675	42.741	40.098	17.162	0.754	5.029	13.911
	BH311 B3 29	52.184	2.163	7.292	0.366	0.549	18.016	0.173	18.866	0.018	0.229	0.006	99.862	40.150	46.093	13.757	0.815	7.005	12.212
	BH311 B3 29	52.136	2.144	7.507	0.552	0.462	18.273	0.226	18.413	0.000	0.238	0.007	99.958	39.147	46.704	14.148	0.813	7.029	12.194
	BH311 B3 29	48.513	3.696	9.751	1.096	0.328	16.395	0.307	17.313	0.049	0.311	0.019	97.778	37.912	43.160	18.928	0.750	4.932	14.010
	BH311 B3 29	46.944	4.493	10.090	1.187	0.203	16.826	0.280	16.504	0.031	0.266	0.290	97.114	36.132	44.285	19.582	0.748	5.633	13.329
	BH311 B3 29	51.229	2.435	8.629	0.951	0.295	16.985	0.221	18.894	0.084	0.287	0.009	100.019	40.232	43.480	16.288	0.778	5.341	13.602
	BH311 B3 29	51.008	2.545	8.301	1.130	0.222	16.551	0.216	19.277	0.034	0.289	0.007	99.580	41.427	42.760	15.814	0.780	5.321	13.622
	BH311 B3 29 av	51.011	3.045	6.688	0.662	0.803	17.165	0.175	19.756	0.024	0.230	0.019	99.578	42.641	44.546	12.812	0.821	7.627	11.776
	BH311 B3 31	50.007	3.086	9.123	1.457	0.238	16.494	0.222	18.993	0.018	0.299	0.009	99.946	40.489	42.271	17.240	0.763	5.120	13.819
	BH311 B3 32	50.927	2.449	8.128	1.131	0.222	16.361	0.211	19.834	0.063	0.329	0.013	99.668	42.464	42.110	15.426	0.782	5.383	13.562
	BH311 B3 31-32 av	50.467	2.768	8.626	1.294	0.230	16.428	0.217	19.414	0.041	0.314	0.011	99.807	41.476	42.190	16.333	0.773	5.244	13.696
	BH311 B3 33	50.708	2.506	8.366	1.045	0.196	16.925	0.192	19.047	0.076	0.263	0.002	99.326	40.690	43.467	15.843	0.783	5.642	13.321
	BH311 B3 33	52.028	2.046	7.601	0.480	0.318	18.383	0.216	17.892	0.000	0.221	0.004	99.189	38.288	47.293	14.419	0.812	6.908	12.283
	BH311 B3 33	52.222	2.168	7.188	0.531	0.375	18.589	0.193	18.608	0.037	0.232	0.020	100.163	39.318	47.219	13.464	0.822	7.638	11.768
	BH311 B3 33	52.018	2.234	6.621	0.581	0.559	18.329	0.170	19.052	0.034	0.214	0.001	99.813	40.574	46.926	12.500	0.831	8.143	11.440
	BH311 B3 33	51.962	2.318	6.164	0.230	0.704	18.050	0.170	19.198	0.000	0.214	0.000	99.010	41.409	46.805	11.786	0.839	8.399	11.282
	BH311 B3 33	51.557	2.735	6.289	0.410	0.796	17.833	0.160	19.601	0.000	0.226	0.008	99.615	42.049	45.991	11.960	0.835	8.416	11.271
	BH311 B3 33	51.625	2.898	5.785	0.230	0.915	17.726	0.169	20.217	0.034	0.198	0.000	99.797	43.333	45.675	10.992	0.845	9.024	10.913

Appendix E3 – LPS Clinopyroxene mineral chemistry & inverse melt compositions

Zone	Sample code	SiO_2	Al_2O_3	FeO*	TiO_2	Cr_2O_3	MgO	MnO	CaO	NiO	Na_2O	K_2O	Total	Womol%	Enmol%	Fsmol%	Mgmol%	Melt MgO	Melt FeO
	BH311 B3 33	51.653	2.570	5.545	0.273	0.973	17.465	0.156	20.350	0.022	0.202	0.009	99.218	43.989	45.386	10.625	0.849	9.002	10.926
	BH311 B3 33	51.692	2.810	5.299	0.424	1.171	17.635	0.149	20.447	0.035	0.204	0.015	99.881	44.119	45.745	10.136	0.856	9.665	10.561
	BH311 B3 33	51.478	3.100	5.538	0.209	1.201	17.824	0.167	20.513	0.055	0.209	0.008	100.302	43.784	45.737	10.479	0.852	9.659	10.565
	BH311 B3 33	49.243	7.202	6.749	0.688	0.637	13.973	0.181	19.290	0.003	0.745	0.027	98.738	45.851	39.928	14.221	0.787	6.178	12.856
	BH311 B3 33	51.364	3.535	5.618	0.273	1.008	17.517	0.158	19.913	0.046	0.206	0.000	99.638	43.335	45.828	10.838	0.847	9.284	10.768
	BH311 B3 33	51.476	3.509	5.805	0.338	1.204	17.981	0.110	19.509	0.047	0.202	0.004	100.185	42.162	46.717	11.121	0.847	9.437	10.684
	BH311 B3 33	51.190	3.322	5.656	0.338	1.165	17.888	0.126	19.647	0.055	0.217	0.014	99.618	42.558	46.582	10.861	0.849	9.596	10.598
	BH311 B3 33	51.939	2.881	5.387	0.230	1.092	18.074	0.135	19.653	0.064	0.202	0.000	99.657	42.579	47.075	10.346	0.857	9.745	10.519
	BH311 B3 33	51.737	2.525	5.762	0.309	0.867	17.795	0.136	20.286	0.000	0.224	0.004	99.645	43.358	45.724	10.917	0.846	8.999	10.927
	BH311 B3 33	51.826	3.045	5.692	0.295	0.854	17.630	0.152	20.168	0.029	0.220	0.004	99.915	43.458	45.670	10.873	0.847	9.039	10.905
	BH311 B3 33	51.685	2.517	7.012	0.330	0.598	17.801	0.171	19.015	0.063	0.230	0.006	99.428	40.778	45.892	13.330	0.819	7.360	11.959
	BH311 B3 33	52.260	2.427	7.651	0.409	0.383	18.050	0.189	18.359	0.000	0.203	0.004	99.935	39.194	46.326	14.480	0.808	6.637	12.489
	BH311 B3 33	50.850	2.532	8.316	0.866	0.296	16.723	0.172	19.470	0.000	0.284	0.008	99.517	41.473	42.824	15.703	0.782	5.497	13.454
	BH311 B3 33 av	51.526	2.944	6.402	0.424	0.766	17.610	0.164	19.512	0.030	0.246	0.007	99.630	42.115	45.640	12.245	0.831	8.131	11.448
	BH311 B3 37	51.780	3.821	5.857	0.618	1.029	16.824	0.133	20.582	0.038	0.229	0.004	100.915	44.744	43.969	11.287	0.837	8.423	11.267
	BH311 B3 37	51.605	3.770	5.738	0.345	1.170	16.918	0.150	20.883	0.000	0.226	0.006	100.811	45.096	43.920	10.984	0.840	8.727	11.085
	BH311 B3 37	51.610	3.391	5.637	0.381	1.035	17.091	0.126	20.928	0.050	0.231	0.000	100.480	45.034	44.213	10.753	0.844	8.914	10.976
	BH311 B3 37	51.416	3.247	5.477	0.410	1.056	17.675	0.121	20.007	0.017	0.194	0.008	99.628	43.389	46.082	10.529	0.852	9.557	10.619
	BH311 B3 37	52.000	3.174	5.172	0.194	1.290	17.128	0.103	20.802	0.048	0.270	0.017	100.198	45.244	44.785	9.972	0.855	9.434	10.686
	BH311 B3 37	51.658	3.489	5.548	0.209	1.275	17.280	0.157	20.255	0.030	0.257	0.004	100.162	44.084	45.212	10.704	0.847	9.172	10.830
	BH311 B3 37	51.308	2.934	5.207	0.345	1.338	17.136	0.158	21.048	0.021	0.195	0.010	99.700	45.495	44.528	9.977	0.854	9.547	10.624
	BH311 B3 37	51.669	3.412	5.196	0.446	1.431	17.150	0.141	20.765	0.067	0.248	0.005	100.530	45.153	44.832	10.016	0.855	9.655	10.567
	BH311 B3 37	51.479	3.458	5.239	0.338	1.416	17.431	0.156	20.378	0.011	0.228	0.008	100.142	44.322	45.577	10.101	0.856	9.836	10.472
	BH311 B3 37	52.832	1.505	6.029	0.115	1.304	15.767	0.167	22.182	0.061	0.326	0.008	100.296	47.722	40.779	11.498	0.823	6.270	12.780
	BH311 B3 37	52.381	2.718	5.420	0.381	1.018	18.055	0.145	19.857	0.021	0.213	0.003	100.212	42.826	46.812	10.362	0.856	9.554	10.621
	BH311 B3 37	51.531	3.143	6.434	0.323	0.786	18.707	0.198	18.223	0.025	0.229	0.034	99.633	39.260	48.452	12.288	0.838	9.025	10.913
	BH311 B3 37	50.896	3.669	6.279	0.381	0.813	16.425	0.208	20.431	0.019	0.313	0.012	99.446	44.665	43.167	12.168	0.823	7.672	11.746
	BH311 B3 37	51.641	3.481	5.813	0.547	0.902	16.346	0.188	21.140	0.099	0.283	0.003	100.443	46.013	42.771	11.216	0.834	8.026	11.514
	BH311 B3 37	51.390	3.104	5.748	0.295	1.160	17.790	0.158	19.664	0.045	0.258	0.022	99.634	42.612	46.346	11.042	0.847	9.293	10.763
	BH311 B3 37	52.256	2.980	5.855	0.360	1.064	18.118	0.145	19.900	0.019	0.208	0.004	100.909	42.457	46.470	11.073	0.846	9.173	10.829
	BH311 B3 37	50.564	4.802	6.670	0.552	0.948	16.354	0.147	19.950	0.000	0.236	0.000	100.223	43.824	43.188	12.988	0.814	7.497	11.864
	BH311 B3 37	51.972	3.286	5.591	0.302	1.210	17.502	0.141	20.231	0.030	0.252	0.006	100.523	43.764	45.515	10.721	0.848	9.181	10.825

Appendix E3 – LPS Clinopyroxene mineral chemistry & inverse melt compositions

Zone	Sample code	SiO_2	Al_2O_3	FeO*	TiO_2	Cr_2O_3	MgO	MnO	CaO	NiO	Na_2O	K_2O	Total	Womol%	Enmol%	Fsmol%	Mgmol%	Melt MgO	Melt FeO
	BH311 B3 37	51.526	3.417	5.855	0.431	1.243	17.544	0.125	19.920	0.071	0.244	0.004	100.380	43.116	45.650	11.234	0.842	9.031	10.910
	BH311 B3 37	51.590	3.345	5.805	0.431	1.143	17.150	0.313	20.128	0.048	0.231	0.005	100.189	43.860	44.927	11.213	0.840	8.694	11.105
	BH311 B3 37	51.405	3.482	5.768	0.388	1.222	17.593	0.155	19.881	0.047	0.245	0.001	100.187	43.085	45.835	11.081	0.845	9.226	10.800
	BH311 B3 37	51.542	3.567	5.940	0.302	1.274	17.487	0.166	19.873	0.006	0.236	0.012	100.405	43.051	45.542	11.407	0.840	8.874	10.999
	BH311 B3 37	52.237	3.014	5.596	0.446	0.938	17.639	0.139	20.222	0.042	0.228	0.000	100.501	43.593	45.713	10.694	0.849	9.104	10.868
	BH311 B3 37	52.567	2.731	5.373	0.346	0.974	17.570	0.165	20.545	0.034	0.209	0.009	100.523	44.249	45.493	10.258	0.854	9.180	10.826
	BH311 B3 37	52.202	2.596	5.682	0.389	0.780	17.784	0.131	20.208	0.000	0.208	0.010	99.990	43.342	45.855	10.803	0.848	8.948	10.957
	BH311 B3 37	52.399	2.504	6.050	0.345	0.727	18.080	0.160	19.877	0.004	0.229	0.010	100.385	42.313	46.270	11.417	0.842	8.651	11.130
	BH311 B3 37	52.711	2.304	6.252	0.424	0.608	18.163	0.163	19.380	0.011	0.219	0.007	100.242	41.448	46.699	11.853	0.838	8.239	11.380
	BH311 B3 37	51.581	2.302	6.994	0.186	0.580	17.933	0.207	17.167	0.051	0.271	0.010	97.282	38.212	47.988	13.800	0.820	7.177	12.088
	BH311 B3 37	52.763	2.187	6.891	0.402	0.633	18.615	0.174	18.861	0.026	0.245	0.002	100.799	39.835	47.264	12.902	0.828	7.880	11.609
	BH311 B3 37	52.725	2.135	6.843	0.259	0.590	18.369	0.218	19.433	0.044	0.219	0.000	100.835	40.841	46.410	12.749	0.827	7.727	11.709
	BH311 B3 37 av	51.841	3.099	5.865	0.363	1.032	17.454	0.162	20.091	0.033	0.239	0.007	100.187	43.422	45.342	11.236	0.841	8.706	11.097
	BH311 B3 45	54.036	1.802	13.535	0.532	0.216	27.431	0.318	2.123	0.052	0.048	0.007	100.100	4.508	70.017	25.475	0.783	7.827	11.643
	BH311 B3 46	51.385	2.305	14.287	0.580	0.164	26.515	0.296	1.863	0.045	0.053	0.013	97.506	4.015	68.692	27.293	0.768	7.544	11.832
	BH311 B3 47	53.881	1.538	14.189	0.629	0.004	27.410	0.312	1.887	0.031	0.047	0.013	99.941	3.980	69.494	26.527	0.775	7.431	11.909
	BH311 B3 45-47 av		1.882	14.004	0.580	0.128	27.119	0.309	1.958	0.043	0.049	0.011	99.182	4.167	69.401	26.432	0.775	7.598	11.795
CPZ	BH311 B4 1	50.879	2.618	13.019	0.698	0.213	15.154	0.274	16.504	0.000	0.246	0.025	99.630	35.674	39.379	24.946	0.675	1.615	19.734
	BH311 B4 1	52.109	3.347	5.636	0.408	0.973	17.753	0.138	19.675	0.056	0.230	0.010	100.335	42.759	46.383	10.858	0.849	9.226	10.800
	BH311 B4 1	52.395	2.997	5.310	0.301	0.910	17.887	0.160	20.071	0.042	0.208	0.009	100.290	43.367	46.462	10.171	0.857	9.622	10.585
	BH311 B4 1	52.478	2.847	6.669	0.279	0.470	17.556	0.153	19.492	0.036	0.202	0.006	100.188	41.910	45.379	12.711	0.824	7.341	11.971
	BH311 B4 1	51.603	3.443	6.271	0.437	0.745	17.757	0.160	19.468	0.012	0.197	0.000	100.093	41.980	46.032	11.987	0.835	8.514	11.212
	BH311 B4 1 av	51.893	3.050	7.381	0.425	0.662	17.221	0.177	19.042	0.029	0.217	0.010	100.107	41.138	44.727	14.135	0.808	6.503	12.593
	BH311 B4 2	52.254	2.401	8.906	0.456	0.195	16.864	0.243	18.827	0.005	0.186	0.010	100.347	40.061	43.139	16.799	0.771	4.523	14.454
	BH311 B4 3	52.822	2.698	7.658	0.415	0.221	17.246	0.183	19.703	0.043	0.213	0.000	101.202	41.722	43.903	14.375	0.801	5.936	13.060
	BH311 B4 4	52.727	2.788	7.277	0.508	0.209	16.957	0.191	19.184	0.000	0.241	0.005	100.087	41.686	44.297	14.017	0.806	5.978	13.025
	BH311 B4 2-4 av	52.601	2.629	7.947	0.460	0.208	17.022	0.206	19.238	0.016	0.213	0.005	100.545	41.156	43.780	15.064	0.793	5.436	13.512
	BH311 B4 11	52.081	3.272	5.594	0.365	1.297	17.720	0.164	19.934	0.024	0.217	0.001	100.669	43.151	46.114	10.735	0.850	9.318	10.749
	BH311 B4 12	52.571	3.233	6.648	0.321	1.188	18.976	0.156	17.640	0.030	0.222	0.003	100.988	38.062	49.223	12.716	0.836	8.750	11.072
	BH311 B4 13	52.868	2.275	6.116	0.287	0.467	17.681	0.164	20.177	0.007	0.193	0.009	100.244	43.063	45.366	11.571	0.837	7.896	11.598
	BH311 B4 11-13 av	52.507	2.927	6.119	0.324	0.984	18.126	0.161	19.250	0.020	0.211	0.004	100.634	41.425	46.901	11.674	0.841	8.650	11.131
	BH311 B4 14	53.839	1.933	6.127	0.229	0.654	18.923	0.162	19.437	0.023	0.198	0.007	101.532	40.819	47.774	11.406	0.846	8.661	11.124

Appendix E3 – LPS Clinopyroxene mineral chemistry & inverse melt compositions

Zone	Sample code	SiO_2	Al_2O_3	FeO*	TiO_2	Cr_2O_3	MgO	MnO	CaO	NiO	Na_2O	K_2O	Total	Womol%	Enmol%	Fsmol%	Mgmol%	Melt MgO	Melt FeO
	BH311 B4 15	53.830	2.240	6.264	0.193	0.754	19.173	0.173	18.651	0.005	0.208	0.012	101.503	39.470	48.779	11.751	0.845	8.741	11.077
	BH311 B4 16	49.354	2.542	12.374	0.558	0.120	14.752	0.304	18.776	0.047	0.226	0.009	99.062	39.545	37.352	23.103	0.680	1.955	18.754
	BH311 B4 14-16 av	52.341	2.238	8.255	0.327	0.509	17.616	0.213	18.955	0.025	0.211	0.009	100.699	39.945	44.635	15.420	0.790	5.651	13.312
	BH311 B4 17	53.276	2.090	5.946	0.258	0.782	17.636	0.147	20.608	0.014	0.216	0.004	100.977	43.772	45.033	11.196	0.841	8.022	11.517
	BH311 B4 18	52.161	3.450	5.530	0.401	1.232	17.618	0.164	20.116	0.039	0.216	0.008	100.935	43.543	45.846	10.611	0.850	9.359	10.727
	BH311 B4 19	52.596	2.206	9.654	0.512	0.073	16.992	0.244	18.320	0.056	0.191	0.000	100.844	38.727	43.182	18.091	0.758	3.960	15.136
	BH311 B4 17-19 av	52.678	2.582	7.043	0.390	0.696	17.415	0.185	19.681	0.036	0.208	0.004	100.919	42.014	44.687	13.299	0.816	6.775	12.383
	BH311 B4 22	53.539	2.046	5.837	0.158	0.808	19.034	0.134	18.802	0.036	0.205	0.001	100.600	40.125	48.833	11.042	0.853	9.161	10.836
	BH311 B4 23	51.453	2.063	13.831	0.747	0.038	14.411	0.350	17.729	0.023	0.249	0.000	100.894	37.471	36.616	25.913	0.650	0.979	22.301
	BH311 B4 22-23 av	52.496	2.055	9.834	0.453	0.423	16.723	0.242	18.266	0.030	0.227	0.001	100.747	38.798	42.724	18.478	0.752	3.612	15.607
	BH311 B4 24	53.468	1.967	7.014	0.186	0.726	20.060	0.182	16.527	0.041	0.167	0.004	100.342	35.269	51.463	13.269	0.836	8.429	11.263
	BH311 B4 25	53.824	1.860	6.006	0.186	0.746	19.302	0.161	18.305	0.051	0.184	0.001	100.626	39.085	49.547	11.368	0.851	8.975	10.941
	BH311 B4 26	52.353	2.931	5.971	0.380	0.524	17.101	0.155	20.124	0.012	0.200	0.008	99.759	43.771	44.716	11.513	0.836	7.857	11.623
	BH311 B4 24-26 av	53.215	2.253	6.330	0.251	0.665	18.821	0.166	18.319	0.035	0.184	0.004	100.242	39.375	48.575	12.050	0.841	8.418	11.270
	BH311 B4 33	54.047	1.891	7.009	0.214	0.561	20.641	0.193	15.911	0.035	0.162	0.008	100.672	33.898	52.865	13.237	0.840	8.664	11.122
	BH311 B4 34	52.895	2.486	6.529	0.344	0.414	17.727	0.175	19.915	0.025	0.187	0.002	100.699	42.360	45.329	12.311	0.829	7.490	11.869
	BH311 B4 35	50.706	0.839	27.473	0.468	0.016	14.185	0.666	5.492	0.000	0.082	0.000	99.927	11.710	36.361	51.929	0.479	0.058	36.789
	BH311 B4 36	52.502	3.468	6.275	0.322	0.684	18.115	0.147	18.985	0.026	0.215	0.001	100.740	40.982	47.010	12.008	0.837	8.519	11.209
	BH311 B4 37	52.927	2.633	6.920	0.458	0.279	17.827	0.189	19.317	0.024	0.204	0.006	100.784	41.203	45.713	13.085	0.821	7.129	12.122
	BH311 B4 38	52.495	2.642	7.134	0.415	0.257	17.457	0.170	19.798	0.033	0.179	0.004	100.584	42.026	44.549	13.424	0.813	6.709	12.433
	BH311 B4 37-38 av	52.711	2.638	7.027	0.437	0.268	17.642	0.180	19.558	0.029	0.192	0.005	100.684	41.615	45.131	13.254	0.817	6.918	12.276
	BH311 B4 36-RIMAV	52.607	3.053	6.651	0.379	0.476	17.879	0.163	19.271	0.027	0.203	0.003	100.712	41.298	46.071	12.631	0.827	7.705	11.723
CPZ	10BH167 A5 1	51.300	3.900	6.800	0.600	0.900	17.300	0.100	19.100	0.000	0.200	0.000	100.200	41.589	45.286	13.126	0.819	7.682	11.739
	10BH167 A5 2	52.400	2.900	7.000	0.200	0.600	18.300	0.200	18.700	0.000	0.200	0.000	100.500	39.868	46.903	13.229	0.823	7.674	11.744
	10BH167 A5 3	51.400	3.500	7.100	0.400	0.700	17.600	0.100	19.000	0.000	0.200	0.000	100.000	40.902	45.549	13.549	0.815	7.431	11.909
	10BH167 A5 1-3 av	51.700	3.433	6.967	0.400	0.733	17.733	0.133	18.933	0.000	0.200	0.000	100.233	40.780	45.918	13.302	0.819	7.597	11.796
	10BH167 A5 8	51.500	2.000	7.200	0.200	0.600	17.500	0.200	19.300	0.000	0.200	0.000	98.600	41.309	45.030	13.661	0.812	6.743	12.407
	10BH167 A5 9	50.800	2.200	6.900	0.300	0.600	18.400	0.100	18.800	0.100	0.200	0.000	98.400	39.969	47.027	13.004	0.826	8.159	11.430
	10BH167 A5 10	51.000	2.100	9.500	0.400	0.100	17.200	0.200	18.500	0.000	0.200	0.000	99.100	38.866	43.441	17.693	0.763	4.637	14.326
	10BH167 A5 8-10 av	51.100	2.100	7.867	0.300	0.433	17.700	0.167	18.867	0.033	0.200	0.000	98.700	40.041	45.159	14.800	0.800	6.402	12.673
	10BH167 A5 23	50.200	3.600	6.400	0.400	0.900	16.900	0.200	19.800	0.000	0.200	0.000	98.600	43.241	44.369	12.390	0.825	8.036	11.508

Appendix E3 – LPS Clinopyroxene mineral chemistry & inverse melt compositions

Zone	Sample code	SiO_2	Al_2O_3	FeO*	TiO_2	Cr_2O_3	MgO	MnO	CaO	NiO	Na_2O	K_2O	Total	Womol%	Enmol%	Fsmol%	Mgmol%	Melt MgO	Melt FeO
	10BH167 A5 24	50.100	3.400	6.400	0.300	0.800	17.200	0.100	19.700	0.000	0.200	0.000	98.400	42.779	44.901	12.320	0.827	8.235	11.382
	10BH167 A5 25	52.000	2.400	8.600	0.400	0.100	17.300	0.200	19.100	0.000	0.200	0.000	100.400	40.192	43.765	16.043	0.782	5.242	13.698
	10BH167 A5 26	49.400	1.800	18.900	0.700	0.100	14.100	0.400	14.700	0.000	0.200	0.000	100.300	30.369	35.019	34.613	0.571	0.440	26.398
	10BH167 A5 27	48.200	1.500	22.900	0.600	0.000	11.700	0.500	14.300	0.000	0.200	0.000	99.800	29.384	28.902	41.713	0.477	0.050	37.552
	10BH167 A5 23-27 av	49.980	2.540	12.640	0.480	0.380	15.440	0.280	17.520	0.000	0.200	0.000	99.500	37.051	39.254	23.696	0.685	2.109	18.365
	10BH167 A5 48	50.200	3.100	10.800	0.600	0.000	15.900	0.200	18.000	0.000	0.200	0.000	99.100	38.553	40.941	20.506	0.724	3.204	16.222
	10BH167 A5 49	50.100	2.000	9.100	0.400	0.100	17.900	0.200	17.900	0.000	0.200	0.000	97.800	37.695	45.317	16.988	0.778	5.692	13.276
	10BH167 A5 50	51.000	2.000	9.200	0.400	0.100	17.700	0.200	18.000	0.000	0.200	0.000	98.600	37.947	44.859	17.193	0.774	5.199	13.740
	10BH167 A5 48-50 av	50.433	2.367	9.700	0.467	0.067	17.167	0.200	17.967	0.000	0.200	0.000	98.500	38.063	43.721	18.217	0.759	4.640	14.324
	10BH167 A5 51	49.400	3.600	8.000	0.400	0.400	18.300	0.200	17.500	0.000	0.200	0.000	98.100	37.560	47.219	15.221	0.803	7.588	11.802
	10BH167 A5 52	47.900	2.200	8.600	0.300	0.400	15.600	0.200	20.300	0.100	0.200	0.000	95.700	43.490	40.178	16.333	0.764	4.904	14.040
	10BH167 A5 53	49.600	2.300	7.700	0.300	0.300	17.300	0.200	18.500	0.000	0.200	0.000	96.300	40.110	45.091	14.799	0.800	6.562	12.546
	10BH167 A5 54	48.400	2.500	7.800	0.300	0.400	16.900	0.200	19.100	0.000	0.200	0.000	95.900	41.225	43.851	14.924	0.794	6.596	12.520
	10BH167 A5 55	49.600	2.600	7.000	0.300	0.500	17.300	0.100	19.600	0.100	0.200	0.000	97.200	42.057	44.627	13.315	0.815	7.538	11.836
	10BH167 A5 56	49.200	2.200	8.600	0.400	0.200	17.400	0.200	18.800	0.000	0.200	0.000	97.100	39.711	44.185	16.103	0.783	6.045	12.968
	10BH167 A5 57	50.000	2.100	9.300	0.300	0.000	17.000	0.200	18.300	0.000	0.200	0.000	97.400	38.952	43.501	17.548	0.765	4.781	14.170
	10BH167 A5 58	50.100	2.000	10.700	0.400	0.000	17.000	0.200	17.400	0.000	0.200	0.000	98.000	36.769	43.187	20.044	0.739	3.828	15.310
	10BH167 A5 59	48.200	2.300	15.500	0.600	0.000	14.400	0.300	16.700	0.000	0.200	0.000	98.300	34.973	36.253	28.774	0.623	1.078	21.804
	10BH167 A5 60	45.900	1.100	27.500	0.500	0.100	7.700	0.600	15.200	0.000	0.200	0.000	98.800	31.125	18.955	49.919	0.333	0.000	70.717
	10BH167 A5 51-60 av	48.830	2.290	11.070	0.380	0.230	15.890	0.240	18.140	0.020	0.200	0.000	97.280	38.550	40.596	20.854	0.719	3.233	16.176
	10BH167 A5 64	51.100	2.100	7.200	0.200	0.400	17.800	0.200	19.200	0.100	0.200	0.000	98.300	40.867	45.547	13.585	0.815	7.165	12.096
	10BH167 A5 65	50.600	2.100	8.400	0.300	0.100	17.700	0.200	18.600	0.000	0.200	0.000	98.200	39.303	44.963	15.734	0.790	5.997	13.008
	10BH167 A5 66	47.500	1.800	17.800	1.000	0.100	13.400	0.400	16.300	0.000	0.200	0.000	98.500	33.826	33.430	32.745	0.573	0.519	25.551
	10BH167 A5 64-66 av	49.733	2.000	11.133	0.500	0.200	16.300	0.267	18.033	0.033	0.200	0.000	98.333	37.966	41.255	20.778	0.723	3.271	16.115
	10BH167 A5 67	48.900	3.400	6.600	0.400	0.700	17.000	0.200	19.600	0.000	0.200	0.000	97.000	42.713	44.537	12.750	0.821	8.161	11.429
	10BH167 A5 68	50.100	3.400	6.700	0.400	0.800	17.400	0.100	19.500	0.000	0.200	0.000	98.600	42.065	45.123	12.812	0.822	8.090	11.474
	10BH167 A5 69	51.000	2.700	6.600	0.300	0.500	17.600	0.100	19.500	0.000	0.200	0.000	98.600	41.927	45.493	12.580	0.826	7.846	11.630
	10BH167 A5 70	50.100	2.200	12.400	0.500	0.100	15.700	0.200	17.700	0.000	0.200	0.000	99.100	37.211	39.680	23.109	0.693	2.241	18.055
	10BH167 A5 67-70 av	50.025	2.925	8.075	0.400	0.525	16.925	0.150	19.075	0.000	0.200	0.000	98.325	40.951	43.682	15.368	0.789	6.070	12.946
	10BH167 A5 93	49.500	1.400	25.600	0.500	0.000	15.200	0.500	7.000	0.000	0.100	0.100	99.900	14.593	38.095	47.311	0.514	0.230	29.733

Appendix E3 – LPS Clinopyroxene mineral chemistry & inverse melt compositions

Zone	Sample code	SiO_2	Al_2O_3	FeO*	TiO_2	Cr_2O_3	MgO	MnO	CaO	NiO	Na_2O	K_2O	Total	Womol%	Enmol%	Fsmol%	Mgmol%	Melt MgO	Melt FeO
	10BH167 A5 94	49.500	0.900	29.700	0.400	0.000	14.800	0.600	5.000	0.000	0.100	0.000	101.100	10.179	36.222	53.599	0.470	0.103	33.833
	10BH167 A5 95	46.900	0.900	34.200	0.400	0.000	10.400	0.700	6.700	0.000	0.100	0.000	100.300	13.530	25.248	61.222	0.351	0.002	54.661
	10BH167 A5 93-95 av	48.633	1.067	29.833	0.433	0.000	13.467	0.600	6.233	0.000	0.100	0.033	100.433	12.755	33.128	54.117	0.446	0.050	37.538
DZ	10BH167 A6 1	49.900	3.300	8.700	0.300	0.600	15.400	0.200	20.200	0.100	0.200	0.000	98.800	43.510	39.878	16.612	0.759	4.412	14.582
	10BH167 A6 2	51.400	2.400	7.100	0.200	0.400	18.000	0.200	18.800	0.000	0.200	0.000	98.800	40.228	46.304	13.468	0.819	7.384	11.941
	10BH167 A6 3	51.100	2.200	6.900	0.300	0.300	17.600	0.200	18.900	0.100	0.200	0.000	97.700	40.931	45.822	13.247	0.820	7.240	12.043
	10BH167 A6 4	52.600	2.200	7.600	0.200	0.300	18.300	0.200	18.600	0.100	0.200	0.000	100.300	39.293	46.475	14.232	0.811	6.761	12.394
	10BH167 A6 5	49.700	1.900	10.000	0.300	0.100	17.200	0.300	17.900	0.000	0.200	0.000	97.600	37.730	43.585	18.685	0.754	4.545	14.429
	10BH167 A6 6	49.400	1.900	11.600	0.500	0.000	16.500	0.200	17.300	0.000	0.200	0.000	97.600	36.483	41.831	21.685	0.717	3.154	16.302
	10BH167 A6 1-6 av	50.683	2.317	8.650	0.300	0.283	17.167	0.217	18.617	0.050	0.200	0.000	98.467	39.676	43.982	16.342	0.780	5.379	13.566
	10BH167 A6 7	49.300	1.600	21.300	0.700	0.000	14.100	0.400	12.500	0.000	0.200	0.000	100.100	25.862	35.071	39.066	0.541	0.280	28.717
	10BH167 A6 19	45.200	7.300	13.400	1.300	0.000	15.100	0.200	11.000	0.000	2.000	0.300	95.800	26.809	44.241	28.950	0.668	3.873	15.249
	10BH167 A6 20	43.800	9.400	14.500	0.800	0.000	14.400	0.300	10.500	0.000	2.100	0.300	96.200	25.821	42.571	31.609	0.639	3.487	15.788
	10BH167 A6 21	48.000	5.000	19.500	0.400	0.000	11.800	0.200	11.000	0.000	0.900	0.100	97.000	25.899	33.400	40.700	0.519	0.193	30.637
	10BH167 A6 19-21 av	45.667	7.233	15.800	0.833	0.000	13.767	0.233	10.833	0.000	1.667	0.233	96.333	26.174	39.986	33.840	0.608	1.906	18.885
	10BH167 A6 22	48.900	2.100	7.900	0.300	0.400	15.100	0.200	21.500	0.000	0.200	0.000	96.600	46.082	38.908	15.010	0.773	4.771	14.181
	10BH167 A6 23	49.700	2.900	5.300	0.300	0.600	15.600	0.100	22.700	0.000	0.100	0.000	97.400	49.185	40.635	10.180	0.840	8.267	11.363
	10BH167 A6 24	49.600	3.700	7.000	0.500	0.700	16.900	0.200	19.400	0.000	0.200	0.000	98.100	42.245	44.242	13.513	0.811	7.506	11.857
	10BH167 A6 25	49.600	2.400	10.500	0.500	0.100	15.800	0.200	18.300	0.000	0.200	0.000	97.500	39.268	40.759	19.973	0.728	3.263	16.128
	10BH167 A6 26	47.500	2.400	15.200	0.700	0.000	14.000	0.300	17.600	0.000	0.200	0.000	98.000	36.739	35.133	28.127	0.621	1.098	21.710
	10BH167 A6 22-26 av	49.060	2.700	9.180	0.460	0.360	15.480	0.200	19.900	0.000	0.180	0.000	97.520	42.660	39.894	17.445	0.750	4.145	14.901
	10BH167 A6 27	50.000	1.900	8.100	0.300	0.300	14.600	0.200	21.800	0.000	0.300	0.000	97.400	46.849	37.720	15.431	0.763	3.830	15.307
	10BH167 A6 28	49.600	2.000	7.700	0.300	0.400	15.300	0.200	21.300	0.100	0.200	0.000	97.100	45.788	39.539	14.673	0.780	4.890	14.054
	10BH167 A6 29	51.000	2.200	7.900	0.400	0.200	17.700	0.200	18.900	0.000	0.200	0.000	98.600	40.058	45.099	14.843	0.800	6.411	12.666
	10BH167 A6 30	49.700	2.100	11.300	0.500	0.100	16.300	0.300	17.200	0.000	0.200	0.000	97.600	36.742	41.860	21.398	0.720	3.114	16.368
	10BH167 A6 31	50.000	2.400	13.900	0.600	0.000	15.200	0.300	17.100	0.000	0.200	0.000	99.700	35.853	38.312	25.835	0.661	1.554	19.931
	10BH167 A6 27-31 av	50.060	2.120	9.780	0.420	0.200	15.820	0.240	19.260	0.020	0.220	0.000	98.080	41.024	40.510	18.466	0.742	3.610	15.610
DZ	10BH167 A8 1	51.500	2.100	9.900	0.200	0.000	17.000	0.300	17.700	0.000	0.200	0.000	98.800	37.729	43.564	18.707	0.754	3.936	15.168
	10BH167 A8 2	52.700	1.900	6.800	0.300	0.200	18.200	0.200	19.300	0.000	0.200	0.000	99.700	40.883	46.348	12.769	0.827	7.404	11.928
	10BH167 A8 3	52.000	2.100	5.800	0.300	0.300	18.000	0.200	19.900	0.000	0.200	0.000	98.700	42.630	46.356	11.014	0.847	8.750	11.071

Appendix E3 – LPS Clinopyroxene mineral chemistry & inverse melt compositions

Zone	Sample code	SiO_2	Al_2O_3	FeO*	TiO_2	Cr_2O_3	MgO	MnO	CaO	NiO	Na_2O	K_2O	Total	Womol%	Enmol%	Fsmol%	Mgmol%	Melt MgO	Melt FeO
	10BH167 A8 4	51.900	2.700	8.500	0.500	0.100	17.200	0.200	18.200	0.100	0.200	0.000	99.600	39.214	44.552	16.235	0.783	5.236	13.704
	10BH167 A8 1-4 av	52.025	2.200	7.750	0.325	0.150	17.600	0.225	18.775	0.025	0.200	0.000	99.200	40.114	45.207	14.679	0.802	6.102	12.919
	10BH167 A8 7	51.100	1.900	14.700	0.500	0.000	14.700	0.400	16.200	0.000	0.200	0.000	99.800	34.539	37.678	27.783	0.641	0.877	22.864
	10BH167 A8 8	52.100	2.800	7.900	0.500	0.200	16.700	0.200	19.700	0.000	0.200	0.000	100.400	42.112	42.917	14.970	0.790	5.411	13.535
	10BH167 A8 9	51.900	1.900	11.500	0.500	0.000	16.300	0.300	17.200	0.000	0.200	0.000	99.700	36.604	41.702	21.695	0.716	2.478	17.539
	10BH167 A8 7-9 av	51.700	2.200	11.367	0.500	0.067	15.900	0.300	17.700	0.000	0.200	0.000	99.967	37.747	40.764	21.489	0.714	2.402	17.698
DZ	10BH167 A9 5	49.300	1.800	20.500	0.700	0.000	11.800	0.400	16.300	0.000	0.200	0.000	101.000	33.499	29.154	37.347	0.506	0.075	35.479
	10BH167 A9 6	49.100	2.400	14.200	0.600	0.100	14.700	0.300	17.500	0.000	0.200	0.000	99.100	36.642	37.002	26.357	0.648	1.394	20.487
	10BH167 A9 7	48.900	2.000	18.700	0.700	0.000	12.800	0.400	16.500	0.000	0.200	0.000	100.200	34.045	31.751	34.204	0.550	0.253	29.238
	10BH167 A9 5-7 av	49.100	2.067	17.800	0.667	0.033	13.100	0.367	16.767	0.000	0.200	0.000	100.100	34.718	32.610	32.673	0.567	0.347	27.619
	10BH167 A9 11	46.900	2.000	13.100	0.700	0.000	13.400	0.200	19.900	0.000	0.200	0.000	96.500	41.787	33.827	24.385	0.646	1.326	20.746
	10BH167 A9 12	48.000	2.800	8.900	0.300	0.100	18.100	0.200	17.700	0.000	0.200	0.000	96.300	37.382	45.955	16.663	0.784	6.776	12.382
	10BH167 A9 13	48.000	2.800	8.000	0.300	0.200	17.400	0.200	18.600	0.000	0.200	0.000	95.800	39.906	44.879	15.215	0.795	7.000	12.215
	10BH167 A9 14	48.900	2.200	9.000	0.300	0.000	14.900	0.200	21.600	0.000	0.200	0.000	97.400	45.483	37.718	16.800	0.747	3.777	15.378
	10BH167 A9 11-14 av	47.950	2.450	9.750	0.400	0.075	15.950	0.200	19.450	0.000	0.200	0.000	96.500	41.148	40.566	18.285	0.745	4.359	14.644
DZ	BH311 B6 62	51.758	2.390	9.739	0.671	0.000	16.428	0.205	18.785	0.000	0.212	0.008	100.196	39.826	41.871	18.303	0.750	3.748	15.417
	BH311 B6 62	52.014	2.425	8.595	0.516	0.000	16.728	0.213	19.083	0.032	0.211	0.007	99.824	40.765	42.959	16.276	0.776	4.705	14.253
	BH311 B6 62	52.147	2.415	9.626	0.443	0.017	17.788	0.257	17.123	0.030	0.194	0.011	100.051	36.400	45.460	18.140	0.767	4.697	14.261
	BH311 B6 62	52.839	1.877	9.404	0.364	0.026	18.302	0.283	17.114	0.006	0.192	0.021	100.428	36.065	46.367	17.568	0.776	4.954	13.987
	BH311 B6 62	53.036	1.788	9.476	0.386	0.030	18.234	0.253	17.317	0.024	0.194	0.005	100.743	36.351	46.015	17.633	0.774	4.794	14.156
	BH311 B6 62	52.841	1.732	10.039	0.399	0.043	18.061	0.268	16.905	0.010	0.206	0.000	100.504	35.577	45.695	18.729	0.762	4.292	14.723
	BH311 B6 62 av	52.439	2.105	9.480	0.463	0.019	17.590	0.247	17.721	0.017	0.202	0.009	100.291	37.497	44.728	17.775	0.768	4.523	14.455
	BH311 B6 65	50.547	1.761	15.640	0.780	0.008	13.990	0.326	16.334	0.006	0.211	0.016	99.619	34.741	35.771	29.488	0.614	0.582	24.966
	BH311 B6 65	50.727	2.410	13.091	0.742	0.013	15.148	0.294	17.041	0.000	0.230	0.016	99.712	36.369	38.865	24.767	0.673	1.606	19.764
	BH311 B6 65	50.747	2.398	12.670	0.708	0.000	14.631	0.320	18.323	0.010	0.243	0.007	100.057	38.866	37.310	23.824	0.673	1.497	20.123
	BH311 B6 65 av	50.674	2.190	13.800	0.743	0.007	14.590	0.313	17.233	0.005	0.228	0.013	99.796	36.659	37.315	26.026	0.654	1.142	21.509
	BH311 B6 67	49.903	2.064	15.940	0.653	0.000	14.998	0.370	14.984	0.000	0.209	0.010	99.131	31.783	38.245	29.972	0.626	0.962	22.388
	BH311 B6 67	50.884	2.196	10.125	0.577	0.000	16.639	0.256	18.029	0.000	0.291	0.058	99.055	38.353	42.553	19.094	0.745	3.861	15.266
	BH311 B6 67	49.274	3.096	15.788	0.350	0.080	16.030	0.293	12.049	0.057	0.173	0.052	97.242	26.589	42.526	30.885	0.644	1.498	20.121
	BH311 B6 67 av	50.020	2.452	13.951	0.527	0.027	15.889	0.306	15.021	0.019	0.224	0.040	98.476	32.242	41.108	26.650	0.672	1.802	19.172
	BH311 B6 68	49.996	1.497	16.231	0.695	0.000	13.935	0.358	16.193	0.043	0.297	0.004	99.249	34.210	35.392	30.398	0.605	0.555	25.208

Appendix E3 – LPS Clinopyroxene mineral chemistry & inverse melt compositions

Zone	Sample code	SiO_2	Al_2O_3	FeO*	TiO_2	Cr_2O_3	MgO	MnO	CaO	NiO	Na_2O	K_2O	Total	Womol%	Enmol%	Fsmol%	Mgmol%	Melt MgO	Melt FeO
	BH311 B6 69	50.351	2.194	15.287	0.697	0.017	13.273	0.417	17.587	0.000	0.276	0.024	100.123	37.344	33.882	28.775	0.607	0.509	25.656
	BH311 B6 69	50.264	2.525	13.157	0.849	0.000	13.655	0.316	18.527	0.006	0.327	0.016	99.642	39.752	35.222	25.025	0.649	1.020	22.092
	BH311 B6 69	50.708	1.907	17.069	0.637	0.029	14.719	0.381	14.062	0.007	0.210	0.006	99.735	29.991	37.739	32.271	0.606	0.605	24.771
	BH311 B6 69 av	50.441	2.209	15.171	0.728	0.015	13.882	0.371	16.725	0.004	0.271	0.015	99.833	35.696	35.614	28.690	0.621	0.677	24.188
	BH311 B6 71	51.969	2.468	8.079	0.559	0.061	17.370	0.185	19.330	0.000	0.214	0.005	100.240	40.803	44.079	15.118	0.793	5.813	13.168
	BH311 B6 71	48.095	6.130	16.229	0.295	0.475	15.909	0.193	16.286	0.071	0.176	0.027	103.886	32.704	38.406	28.890	0.636	2.279	17.969
	BH311 B6 71	53.499	1.882	6.963	0.215	0.328	20.253	0.206	16.899	0.061	0.173	0.013	100.492	35.637	51.346	13.017	0.838	8.623	11.147
	BH311 B6 71	52.683	2.193	6.377	0.446	0.368	18.655	0.194	19.080	0.076	0.186	0.009	100.267	40.458	47.555	11.987	0.839	8.462	11.243
	BH311 B6 71	50.635	1.953	13.216	0.800	0.000	15.009	0.318	17.339	0.038	0.237	0.003	99.548	36.815	38.311	24.875	0.669	1.470	20.217
	BH311 B6 71 av	51.376	2.925	10.173	0.463	0.246	17.439	0.219	17.787	0.049	0.197	0.011	100.887	37.284	43.939	18.777	0.755	4.521	14.457
	BH311 B6 72	50.421	0.582	21.544	0.035	0.050	7.736	0.519	19.661	0.000	0.241	0.001	100.790	40.910	19.351	39.739	0.390	0.000	83.836
	BH311 B6 72	31.440	13.311	27.961	0.013	0.000	13.324	0.208	1.634	0.000	0.072	0.095	88.058	3.850	37.744	58.406	0.459	1.415	20.413
	BH311 B6 72	49.413	1.272	24.134	0.566	0.000	9.785	0.560	14.373	0.000	0.204	0.009	100.316	30.240	24.749	45.011	0.419	0.002	54.996
	BH311 B6 72 av	43.758	5.055	24.546	0.205	0.017	10.282	0.429	11.889	0.000	0.172	0.035	96.388	25.000	27.281	47.719	0.423	0.060	36.595
DZ	10BH167 A10 7	51.700	2.100	14.000	0.500	0.000	16.600	0.300	15.000	0.000	0.200	0.000	100.600	31.668	42.131	26.201	0.679	1.841	19.062
	10BH167 A10 8	50.800	2.000	16.100	0.600	0.000	13.800	0.400	16.100	0.000	0.200	0.000	100.000	34.283	35.326	30.391	0.604	0.469	26.071
	10BH167 A10 9	50.700	1.300	15.200	0.200	0.000	10.100	0.300	20.200	0.000	0.200	0.000	98.400	44.089	26.502	29.409	0.542	0.015	43.888
	10BH167 A10 10	50.900	2.100	14.100	0.500	0.000	15.600	0.300	15.500	0.000	0.200	0.000	99.400	33.153	40.113	26.734	0.663	1.409	20.434
	10BH167 A10 7-10 av	51.025	1.875	14.850	0.450	0.000	14.025	0.325	16.700	0.000	0.200	0.000	99.600	35.741	36.085	28.174	0.627	0.617	24.663
	10BH167 A10 11	50.600	1.700	14.500	0.600	0.000	14.600	0.300	16.800	0.000	0.200	0.000	99.400	35.589	37.182	27.229	0.642	0.930	22.563
	10BH167 A10 12	50.000	2.300	14.100	0.800	0.000	14.000	0.300	17.200	0.000	0.200	0.000	99.000	36.966	36.172	26.863	0.639	0.906	22.695
	10BH167 A10 13	50.200	1.700	16.700	0.600	0.000	11.800	0.400	18.000	0.000	0.200	0.000	99.700	38.306	30.189	31.505	0.557	0.116	33.217
	10BH167 A10 11-13 av	50.267	1.900	15.100	0.667	0.000	13.467	0.333	17.333	0.000	0.200	0.000	99.367	36.951	34.513	28.536	0.614	0.525	25.494
	10BH167 A10 14	48.700	2.500	18.300	0.300	0.000	9.400	0.400	17.500	0.000	0.200	0.100	97.300	38.869	25.099	36.031	0.478	0.007	48.000
	10BH167 A10 15	48.700	4.300	23.000	0.200	0.000	8.400	0.300	11.700	0.000	0.400	0.100	97.200	27.734	23.937	48.329	0.394	0.000	63.483
	10BH167 A10 16	44.800	5.900	23.800	1.400	0.000	7.800	0.300	10.200	0.000	1.800	0.800	96.800	25.077	23.054	51.870	0.369	0.007	47.447
	10BH167 A10 14-16 av	47.400	4.233	21.700	0.633	0.000	8.533	0.333	13.133	0.000	0.800	0.333	97.100	30.809	24.065	45.126	0.412	0.003	51.752
	10BH167 A10 17	52.400	2.400	9.500	0.500	0.000	16.800	0.200	18.200	0.000	0.200	0.000	100.200	38.874	43.139	17.988	0.759	3.930	15.175
	10BH167 A10 18	52.600	2.700	9.200	0.600	0.100	17.200	0.200	18.300	0.000	0.200	0.000	101.100	38.826	43.871	17.303	0.769	4.574	14.397
	10BH167 A10 19	51.800	1.600	12.200	0.600	0.000	12.900	0.300	20.600	0.000	0.200	0.000	100.400	43.902	33.050	23.048	0.653	0.581	24.977

Appendix E3 – LPS Clinopyroxene mineral chemistry & inverse melt compositions

Zone	Sample code	SiO_2	Al_2O_3	FeO*	TiO_2	Cr_2O_3	MgO	MnO	CaO	NiO	Na_2O	K_2O	Total	Womol%	Enmol%	Fsmol%	Mgmol%	Melt MgO	Melt FeO
	10BH167 A10 17-19 av	52.267	2.233	10.300	0.567	0.033	15.633	0.233	19.033	0.000	0.200	0.000	100.567	40.533	40.023	19.444	0.730	2.635	17.223
	10BH167 A10 20	53.100	1.900	7.700	0.400	0.200	17.700	0.200	18.900	0.000	0.200	0.000	100.300	40.209	45.269	14.522	0.804	5.864	13.123
	10BH167 A10 21	53.400	1.900	7.600	0.300	0.200	18.000	0.200	18.900	0.000	0.200	0.000	100.700	39.978	45.772	14.251	0.808	6.148	12.881
	10BH167 A10 22	51.800	2.400	9.300	0.600	0.000	16.300	0.200	18.900	0.000	0.200	0.000	99.700	40.437	41.925	17.638	0.757	3.859	15.268
	10BH167 A10 20-22 av	52.767	2.067	8.200	0.433	0.133	17.333	0.200	18.900	0.000	0.200	0.000	100.233	40.207	44.329	15.464	0.790	5.231	13.709
	10BH167 A10 31	52.600	2.600	7.100	0.400	0.200	17.300	0.200	19.000	0.000	0.200	0.000	99.500	41.222	45.123	13.655	0.813	6.393	12.681
	10BH167 A10 32	52.700	2.500	8.300	0.400	0.100	17.100	0.200	17.900	0.000	0.200	0.000	99.400	39.070	44.870	16.060	0.786	4.898	14.046
	10BH167 A10 33	51.500	2.300	10.000	0.400	0.100	16.000	0.300	17.700	0.000	0.200	0.000	98.400	38.647	41.998	19.355	0.740	3.097	16.396
	10BH167 A10 34	51.400	2.300	12.500	0.600	0.100	14.900	0.300	16.700	0.000	0.200	0.000	99.000	36.548	39.202	24.250	0.680	1.397	20.476
	10BH167 A10 35	50.600	2.000	18.400	0.600	0.000	11.700	0.500	15.200	0.000	0.200	0.000	99.300	33.350	30.861	35.788	0.531	0.054	37.159
	10BH167 A10 31-35 av	51.760	2.340	11.260	0.480	0.100	15.400	0.300	17.300	0.000	0.200	0.000	99.120	37.777	40.427	21.796	0.709	2.037	18.543
DZ	10BH167 A11-1 4	50.000	2.200	10.300	0.400	0.100	19.200	0.200	14.600	0.000	0.200	0.000	97.300	31.188	49.307	19.505	0.769	5.715	13.255
	10BH167 A11-1 5	49.000	2.300	12.600	0.300	0.000	18.000	0.300	14.800	0.000	0.200	0.000	97.500	31.087	45.452	23.461	0.718	3.828	15.310
	10BH167 A11-1 6	49.400	2.100	13.700	0.500	0.000	17.900	0.300	14.400	0.000	0.200	0.000	98.600	29.960	44.772	25.268	0.700	3.196	16.234
	10BH167 A11-1 4-6 av	49.467	2.200	12.200	0.400	0.033	18.367	0.267	14.600	0.000	0.200	0.000	97.800	30.740	46.489	22.771	0.728	4.149	14.896
	10BH167 A11-1 11	48.100	3.000	10.500	0.400	0.000	16.100	0.200	18.300	0.000	0.200	0.000	96.800	38.967	41.214	19.820	0.732	4.013	15.068
	10BH167 A11-1 12	48.000	2.800	11.600	0.700	0.100	16.100	0.200	17.700	0.000	0.200	0.000	97.500	37.391	40.887	21.723	0.712	3.453	15.838
	10BH167 A11-1 13	48.900	2.700	13.400	0.800	0.000	15.300	0.300	17.800	0.000	0.200	0.000	99.400	37.028	38.262	24.710	0.670	2.056	18.497
	10BH167 A11-1 14	48.400	1.800	19.200	0.500	0.000	11.600	0.400	17.200	0.000	0.200	0.000	99.300	35.710	28.953	35.337	0.518	0.097	34.126
	10BH167 A11-1 11-14 av	48.350	2.575	13.675	0.600	0.025	14.775	0.275	17.750	0.000	0.200	0.000	98.250	37.263	37.288	25.449	0.658	1.701	19.466
	10BH167 A11-1 20	50.700	2.800	11.600	0.600	0.000	16.200	0.200	18.600	0.000	0.200	0.000	100.900	38.463	40.273	21.264	0.713	2.998	16.562
	10BH167 A11-1 21	50.100	3.000	13.500	0.700	0.000	15.700	0.300	17.300	0.000	0.300	0.000	100.700	35.936	39.206	24.859	0.675	2.120	18.338
	10BH167 A11-1 22	49.100	1.700	22.000	0.500	0.100	13.900	0.500	13.000	0.000	0.200	0.000	100.900	26.416	33.955	39.629	0.530	0.253	29.245
	10BH167 A11-1 20-22 av	49.967	2.500	15.700	0.600	0.033	15.267	0.333	16.300	0.000	0.233	0.000	100.833	33.559	37.787	28.654	0.634	1.253	21.035
	10BH167 A11-1 23	48.600	2.400	11.700	0.400	0.100	14.100	0.300	19.500	0.100	0.200	0.000	97.300	41.647	36.202	22.151	0.682	1.853	19.028
	10BH167 A11-1 24	49.200	2.500	13.000	0.500	0.000	16.700	0.300	15.900	0.000	0.200	0.000	98.300	33.473	42.266	24.261	0.696	2.834	16.850
	10BH167 A11-1 25	47.300	1.800	21.000	0.600	0.100	13.600	0.500	13.600	0.000	0.200	0.000	98.600	28.003	33.665	38.331	0.536	0.335	27.794
	10BH167 A11-1 23-25 av	48.367	2.233	15.233	0.500	0.067	14.800	0.367	16.333	0.033	0.200	0.000	98.067	34.292	37.356	28.352	0.634	1.264	20.988
	10BH167 A11-1 31	49.000	1.900	21.900	0.800	0.000	13.300	0.400	13.900	0.000	0.200	0.000	101.300	28.193	32.430	39.376	0.520	0.195	30.569

Appendix E3 – LPS Clinopyroxene mineral chemistry & inverse melt compositions

Zone	Sample code	SiO_2	Al_2O_3	FeO*	TiO_2	Cr_2O_3	MgO	MnO	CaO	NiO	Na_2O	K_2O	Total	Womol%	Enmol%	Fsmol%	Mgmol%	Melt MgO	Melt FeO
	10BH167 A11-1 32	48.600	2.100	18.900	0.600	0.000	12.400	0.400	16.700	0.000	0.200	0.000	99.900	34.532	30.824	34.644	0.539	0.199	30.466
	10BH167 A11-1 33	47.600	2.100	21.100	0.900	0.000	12.000	0.400	15.100	0.000	0.200	0.000	99.400	31.308	29.911	38.781	0.503	0.120	33.043
	10BH167 A11-1 31-33 av	48.400	2.033	20.633	0.767	0.000	12.567	0.400	15.233	0.000	0.200	0.000	100.200	31.324	31.065	37.611	0.520	0.168	31.347
DZ	10BH167 A11-2 5	49.500	2.000	16.300	0.600	0.000	14.600	0.400	14.900	0.000	0.200	0.000	98.600	31.769	37.423	30.808	0.615	0.788	23.412
	10BH167 A11-2 6	50.900	2.600	11.200	0.600	0.000	16.900	0.300	16.600	0.000	0.200	0.000	99.200	35.436	43.370	21.194	0.729	3.419	15.889
	10BH167 A11-2 7	50.400	2.300	13.400	0.500	0.000	15.300	0.300	16.000	0.000	0.200	0.000	98.500	34.578	39.751	25.671	0.670	1.529	20.015
	10BH167 A11-2 5-7 av	50.267	2.300	13.633	0.567	0.000	15.600	0.333	15.833	0.000	0.200	0.000	98.767	33.924	40.182	25.894	0.671	1.680	19.533
DZ	10BH167 A12 1	49.400	1.300	24.500	0.500	0.000	11.000	0.600	10.800	0.000	0.100	0.000	98.300	23.610	28.910	47.480	0.444	0.006	48.654
	10BH167 A12 2	50.800	2.400	15.900	0.600	0.000	15.100	0.300	13.600	0.000	0.300	0.000	99.000	29.663	39.594	30.743	0.629	0.884	22.825
	10BH167 A12 3	52.100	2.100	10.400	0.400	0.000	17.600	0.200	15.000	0.000	0.200	0.000	98.000	33.056	46.627	20.317	0.751	3.694	15.492
	10BH167 A12 4	50.400	2.700	8.400	0.600	0.000	15.600	0.200	19.100	0.100	0.200	0.000	97.400	42.163	41.399	16.438	0.768	4.269	14.751
	10BH167 A12 5	50.100	2.300	13.900	0.600	0.000	16.800	0.300	13.400	0.000	0.200	0.000	97.700	29.182	43.984	26.834	0.683	2.190	18.172
	10BH167 A12 6	50.000	2.800	17.000	0.600	0.000	15.000	0.400	12.900	0.000	0.200	0.000	98.900	28.042	39.199	32.759	0.611	0.809	23.278
	10BH167 A12 1-6 av	50.467	2.267	15.017	0.550	0.000	15.183	0.333	14.133	0.017	0.200	0.000	98.217	30.927	39.943	29.130	0.643	1.049	21.946
	10BH167 A12 11	44.600	5.900	24.900	0.200	0.000	10.700	0.400	6.200	0.000	0.400	0.100	93.300	15.072	31.270	53.658	0.434	0.051	37.415
	10BH167 A12 13	44.500	4.800	26.000	1.200	0.000	7.000	0.400	9.100	0.000	1.800	0.600	95.500	22.434	20.746	56.820	0.324	0.001	59.665
	10BH167 A12 21	43.100	6.400	28.300	0.900	0.000	4.900	0.400	10.100	0.000	1.700	0.900	96.600	24.588	14.340	61.072	0.236	0.000	88.177
	10BH167 A12 22	50.600	2.300	14.600	0.500	0.000	16.500	0.300	14.300	0.100	0.200	0.000	99.400	30.375	42.134	27.491	0.668	1.828	19.099
	10BH167 A12 23	50.200	3.900	14.600	0.700	0.000	17.000	0.300	13.800	0.000	0.200	0.000	100.600	29.250	43.318	27.432	0.675	2.477	17.541
	10BH167 A12 24	42.200	6.400	29.900	1.300	0.000	4.100	0.400	9.400	0.000	1.900	0.700	96.300	23.020	12.071	64.910	0.196	0.000	107.020
	10BH167 A12 21-24 av	46.525	4.750	21.850	0.850	0.000	10.625	0.350	11.900	0.025	1.000	0.400	98.225	27.019	29.002	43.979	0.464	0.089	34.619
UBZ	10BH167 A14 1	52.000	4.100	6.900	0.400	0.500	17.800	0.200	17.200	0.000	0.200	0.000	99.200	38.465	47.856	13.679	0.821	7.552	11.826
	10BH167 A14 2	51.800	3.900	6.600	0.400	0.600	17.500	0.200	18.500	0.100	0.200	0.000	99.800	40.759	46.351	12.890	0.825	7.806	11.657
	10BH167 A14 3	52.700	1.100	19.200	0.400	0.100	21.300	0.400	4.600	0.000	0.100	0.000	99.800	9.740	54.220	36.039	0.664	2.333	17.849
	10BH167 A14 1-3 av	52.167	3.033	10.900	0.400	0.400	18.867	0.267	13.433	0.033	0.167	0.000	99.600	29.345	49.547	21.108	0.755	4.660	14.301
	10BH167 A14 10	51.900	2.900	9.900	0.500	0.300	18.000	0.200	15.200	0.000	0.200	0.000	99.200	33.322	47.439	19.239	0.764	4.714	14.243
	10BH167 A14 11	50.500	4.700	6.600	0.500	0.700	16.700	0.200	18.300	0.000	0.200	0.000	98.400	41.377	45.394	13.229	0.818	7.597	11.796
	10BH167 A14 12	50.300	2.300	13.900	0.800	0.200	14.300	0.300	16.500	0.000	0.200	0.000	98.800	35.859	37.362	26.779	0.647	1.007	22.154
	10BH167 A14 13	51.300	2.300	11.600	0.500	0.000	15.300	0.300	17.300	0.000	0.200	0.000	98.900	37.628	40.006	22.366	0.702	1.935	18.808
	10BH167 A14 14	51.500	3.800	7.000	0.400	0.300	16.600	0.200	19.600	0.000	0.200	0.000	99.500	42.831	43.609	13.560	0.809	6.599	12.518

Appendix E3 – LPS Clinopyroxene mineral chemistry & inverse melt compositions

Zone	Sample code	SiO_2	Al_2O_3	FeO*	TiO_2	Cr_2O_3	MgO	MnO	CaO	NiO	Na_2O	K_2O	Total	Womol%	Enmol%	Fsmol%	Mgmol%	Melt MgO	Melt FeO
	10BH167 A14 15	51.400	5.000	6.600	0.300	0.500	16.600	0.100	19.300	0.000	0.200	0.000	100.000	42.787	44.242	12.971	0.818	7.372	11.950
	10BH167 A14 16	50.700	3.300	12.200	0.500	0.300	15.200	0.300	16.800	0.000	0.200	0.000	99.600	36.611	39.821	23.568	0.689	2.007	18.619
	10BH167 A14 17	51.000	4.300	7.000	0.600	0.700	17.000	0.200	18.100	0.000	0.200	0.000	99.100	40.454	45.677	13.869	0.812	7.205	12.068
	10BH167 A14 18	51.200	4.300	7.100	0.400	0.500	16.900	0.200	18.000	0.000	0.200	0.000	98.800	40.349	45.543	14.109	0.809	6.846	12.329
	10BH167 A14 19	51.200	4.200	6.700	0.600	0.400	16.800	0.200	18.500	0.000	0.200	0.000	98.700	41.446	45.247	13.306	0.817	7.219	12.058
	10BH167 A14 20	51.400	4.100	7.300	0.600	0.500	16.800	0.200	18.000	0.100	0.200	0.000	99.100	40.297	45.215	14.487	0.804	6.488	12.605
	10BH167 A14 10-20 av	51.127	3.745	8.718	0.518	0.400	16.382	0.218	17.782	0.009	0.200	0.000	99.100	39.337	43.567	17.097	0.770	4.788	14.162
	10BH167 A14 27	50.900	4.700	6.400	0.400	0.600	16.900	0.100	18.700	0.000	0.200	0.000	99.000	41.844	45.462	12.695	0.825	7.910	11.589
	10BH167 A14 28	51.000	3.400	8.300	0.300	0.200	17.100	0.200	16.900	0.100	0.200	0.000	97.700	37.711	45.872	16.418	0.786	5.542	13.412
	10BH167 A14 29	49.200	4.500	16.100	0.700	0.000	13.800	0.300	10.900	0.000	0.900	0.100	96.700	26.100	39.725	34.175	0.604	0.819	23.217
	10BH167 A14 27-29 av	50.367	4.200	10.267	0.467	0.267	15.933	0.200	15.500	0.033	0.433	0.033	97.800	35.424	43.776	20.800	0.734	3.606	15.616
	10BH167 A14 30	50.900	2.300	12.900	0.700	0.000	14.900	0.300	16.300	0.000	0.200	0.000	98.600	35.708	39.241	25.051	0.673	1.361	20.609
	10BH167 A14 31	50.800	2.600	12.800	0.700	0.000	15.000	0.200	16.300	0.000	0.200	0.000	98.600	35.683	39.477	24.840	0.676	1.499	20.116
	10BH167 A14 32	50.300	2.200	12.800	0.600	0.100	14.400	0.300	16.800	0.000	0.200	0.000	97.700	36.957	38.082	24.961	0.667	1.216	21.190
	10BH167 A14 30-32 av	50.667	2.367	12.833	0.667	0.033	14.767	0.267	16.467	0.000	0.200	0.000	98.300	36.115	38.934	24.951	0.672	1.357	20.627

Appendix E4 – LPS Plagioclase compositions

Zone	Sample code	SiO2	TiO2	Al2O3	MgO	CaO	MnO	FeO	Na2O	K2O	BaO	SrO	Total	Anmol%
LCM	10BH166 A1 20	51.240	0.076	29.739	0.274	13.994	0.000	1.119	3.619	0.199	0.000	0.066	100.326	67.344
	10BH166 A1 21	51.767	0.027	29.624	0.117	13.144	0.018	0.965	4.188	0.287	0.053	0.028	100.218	62.343
	10BH166 A1 20-21 av	51.504	0.052	29.682	0.196	13.569	0.009	1.042	3.904	0.243	0.027	0.047	100.272	64.825
LBZ	10BH166 A2 12	50.807	0.049	30.277	0.214	13.945	0.018	1.061	3.768	0.189	0.000	0.052	100.380	66.441
	10BH166 A2 13	51.358	0.000	29.807	0.208	13.427	0.071	1.014	4.052	0.232	0.000	0.000	100.169	63.830
	10BH166 A2 12-13 av	51.083	0.025	30.042	0.211	13.686	0.045	1.038	3.910	0.211	0.000	0.026	100.275	65.134
	10BH166 A2 14	49.594	0.022	30.764	0.308	14.978	0.012	0.709	3.210	0.096	0.000	0.073	99.766	71.662
	10BH166 A2 15	50.859	0.005	30.383	0.210	14.363	0.041	0.781	3.576	0.150	0.000	0.021	100.389	68.354
	10BH166 A2 16	50.990	0.092	29.723	0.130	13.543	0.000	0.982	3.863	0.239	0.000	0.105	99.667	65.055
	10BH166 A2 14-16 av	50.481	0.040	30.290	0.216	14.295	0.018	0.824	3.550	0.162	0.000	0.066	99.941	68.361
	10BH166 A2 17	50.011	0.000	30.531	0.453	14.454	0.000	1.150	3.335	0.135	0.007	0.056	100.132	69.988
	10BH166 A2 18	50.167	0.049	30.989	0.275	14.874	0.041	0.855	3.346	0.120	0.000	0.049	100.765	70.588
	10BH166 A2 19	52.400	0.038	29.555	0.143	13.206	0.000	1.118	4.134	0.247	0.000	0.042	100.883	62.943
	10BH166 A2 17-19 av	50.859	0.029	30.358	0.290	14.178	0.014	1.041	3.605	0.167	0.002	0.049	100.593	67.832
LBZ	10BH166 A3 15	49.557	0.027	30.476	0.232	14.527	0.000	0.715	3.432	0.130	0.000	0.084	99.180	69.533
	10BH166 A3 16	46.214	0.069	29.926	1.075	11.648	0.195	5.650	3.179	0.134	0.020	0.074	98.184	66.304
	10BH166 A3 17	49.912	0.000	31.083	0.148	14.735	0.000	0.845	3.256	0.147	0.000	0.049	100.175	70.835
	10BH166 A3 15-17 av	48.561	0.032	30.495	0.485	13.637	0.065	2.403	3.289	0.137	0.007	0.069	99.180	69.033
	10BH166 A3 18	50.204	0.108	30.506	0.285	14.439	0.000	0.697	3.531	0.136	0.000	0.035	99.941	68.788
	10BH166 A3 19	49.908	0.114	30.681	0.231	14.642	0.000	0.767	3.364	0.132	0.000	0.056	99.895	70.103
	10BH166 A3 20	52.337	0.027	29.218	0.071	12.246	0.000	0.778	4.640	0.253	0.000	0.063	99.633	58.471
	10BH166 A3 18-20 av	50.816	0.083	30.135	0.196	13.776	0.000	0.747	3.845	0.174	0.000	0.051	99.823	65.786
	10BH166 A3 27	49.680	0.032	30.650	0.202	14.521	0.000	0.787	3.513	0.142	0.000	0.115	99.642	68.993
	10BH166 A3 28	48.615	0.092	31.106	0.109	14.930	0.050	0.922	3.207	0.154	0.000	0.080	99.265	71.379
	10BH166 A3 29	49.744	0.065	30.453	0.144	14.146	0.000	0.950	3.470	0.206	0.000	0.052	99.230	68.436
	10BH166 A3 30	49.346	0.063	30.736	0.152	14.532	0.017	0.886	3.397	0.167	0.000	0.082	99.379	69.606
	10BH166 A3 36	49.826	0.087	30.933	0.253	14.891	0.000	0.595	3.265	0.130	0.000	0.003	99.892	71.065
	10BH166 A3 37	48.971	0.000	30.760	0.247	14.941	0.000	0.646	3.264	0.130	0.000	0.000	98.959	71.140
	10BH166 A3 38	49.355	0.000	30.599	0.276	14.608	0.000	0.669	3.464	0.153	0.000	0.084	99.208	69.369

Appendix E4 – LPS Plagioclase compositions

Zone	Sample code	SiO2	TiO2	Al2O3	MgO	CaO	MnO	FeO	Na2O	K2O	BaO	SrO	Total	Anmol%
	10BH166 A3 36-38 av	49.384	0.029	30.764	0.259	14.813	0.000	0.637	3.331	0.138	0.000	0.029	99.353	70.523
LOZ	BH311 B2 130	49.219	0.103	30.421	0.346	14.850	0.000	0.761	3.206	0.116	0.000	0.000	99.022	71.430
	BH311 B2 131	49.557	0.038	30.440	0.221	14.601	0.000	0.645	3.269	0.134	0.000	0.080	98.985	70.618
	BH311 B2 132	49.882	0.114	30.285	0.174	14.239	0.000	0.880	3.553	0.178	0.000	0.000	99.305	68.193
	BH311 B2 130-132 av	49.553	0.085	30.382	0.247	14.563	0.000	0.762	3.343	0.143	0.000	0.027	99.104	70.081
LOZ	10BH166 A4 16	50.602	0.027	30.590	0.204	14.632	0.000	0.687	3.313	0.178	0.000	0.035	100.268	70.214
	10BH166 A4 17	49.675	0.000	30.726	0.273	14.742	0.000	0.607	3.171	0.112	0.009	0.024	99.339	71.505
	10BH166 A4 18	50.591	0.049	30.752	0.173	14.612	0.021	0.795	3.492	0.156	0.002	0.031	100.674	69.194
	10BH166 A4 16-18 av	50.289	0.025	30.689	0.217	14.662	0.007	0.696	3.325	0.149	0.004	0.030	100.094	70.295
	10BH166 A4 29	51.425	0.043	30.361	0.175	13.915	0.009	0.776	3.832	0.191	0.000	0.031	100.758	66.021
	10BH166 A4 30	50.890	0.076	30.543	0.188	14.133	0.024	0.750	3.679	0.177	0.013	0.035	100.508	67.281
	10BH166 A4 31	50.615	0.097	30.440	0.137	13.608	0.000	0.917	3.874	0.212	0.000	0.035	99.935	65.202
	10BH166 A4 29-31 av	50.977	0.072	30.448	0.167	13.885	0.011	0.814	3.795	0.193	0.004	0.034	100.400	66.170
LOZ	10BH166 A5 9	50.044	0.054	30.492	0.211	14.369	0.006	0.868	3.522	0.151	0.002	0.105	99.824	68.676
	10BH166 A5 10	50.534	0.059	30.283	0.200	14.110	0.000	0.710	3.622	0.161	0.000	0.031	99.710	67.655
	10BH166 A5 11	50.854	0.000	30.049	0.172	13.880	0.000	0.707	3.715	0.186	0.000	0.059	99.622	66.654
	10BH166 A5 9-11 av	50.477	0.038	30.275	0.194	14.120	0.002	0.762	3.620	0.166	0.001	0.065	99.719	67.663
	10BH166 A5 12	47.763	0.043	29.055	0.148	15.794	0.000	0.769	3.339	0.160	0.007	0.021	97.099	71.696
	10BH166 A5 13	49.438	0.108	27.718	2.462	11.771	0.035	2.516	3.884	0.540	0.005	0.011	98.488	60.538
	10BH166 A5 12-13 av	48.601	0.076	28.387	1.305	13.783	0.018	1.643	3.612	0.350	0.006	0.016	97.794	66.464
	10BH166 A5 22	50.286	0.016	30.654	0.209	14.311	0.009	0.631	3.505	0.149	0.000	0.056	99.826	68.701
	10BH166 A5 23	50.319	0.049	30.265	0.219	14.189	0.032	0.743	3.626	0.164	0.000	0.066	99.672	67.742
	10BH166 A5 24	50.725	0.140	30.794	0.170	13.276	0.006	0.841	4.134	0.256	0.000	0.035	100.377	63.034
	10BH166 A5 22-24 av	50.443	0.068	30.571	0.199	13.925	0.016	0.738	3.755	0.190	0.000	0.052	99.958	66.482
LOZ	10BH167 A1 5	51.035	0.054	30.269	0.277	14.238	0.000	0.755	3.506	0.181	0.000	0.035	100.350	68.459
	10BH167 A1 6	52.840	0.086	29.272	0.219	12.502	0.026	0.936	4.453	0.342	0.000	0.195	100.871	59.627
	10BH167 A1 5-6 av	51.938	0.070	29.771	0.248	13.370	0.013	0.846	3.980	0.262	0.000	0.115	100.611	64.025
	10BH167 A1 14	50.482	0.049	30.346	0.201	14.060	0.000	0.742	3.681	0.179	0.000	0.105	99.845	67.163

Appendix E4 – LPS Plagioclase compositions

Zone	Sample code	SiO2	TiO2	Al2O3	MgO	CaO	MnO	FeO	Na2O	K2O	BaO	SrO	Total	Anmol%
	10BH167 A1 15	51.149	0.016	30.324	0.173	14.118	0.000	0.798	3.673	0.206	0.000	0.014	100.471	67.197
	10BH167 A1 14-15 av	50.816	0.033	30.335	0.187	14.089	0.000	0.770	3.677	0.193	0.000	0.060	100.158	67.180
	10BH167 A1 18	50.441	0.038	30.771	0.229	14.639	0.015	0.691	3.461	0.155	0.000	0.070	100.510	69.424
	10BH167 A1 19	48.812	0.070	28.858	2.494	12.778	0.000	2.817	3.131	0.178	0.000	0.011	99.149	68.494
	10BH167 A1 20	51.174	0.054	29.897	0.137	13.704	0.000	0.888	3.912	0.215	0.018	0.059	100.058	65.116
	10BH167 A1 18-20 av	50.142	0.054	29.842	0.953	13.707	0.005	1.465	3.501	0.183	0.006	0.047	99.906	67.647
MOZ	10BH167 A2 6	49.667	0.059	30.653	0.250	14.633	0.018	0.809	3.335	0.131	0.000	0.070	99.625	70.270
	10BH167 A2 7	49.833	0.130	31.264	0.221	15.141	0.009	0.578	3.175	0.126	0.000	0.084	100.561	71.975
	10BH167 A2 8	50.118	0.022	30.824	0.231	14.893	0.012	0.616	3.229	0.097	0.007	0.066	100.115	71.415
	10BH167 A2 6-8 av	49.873	0.070	30.914	0.234	14.889	0.013	0.668	3.246	0.118	0.002	0.073	100.100	71.223
	10BH167 A2 16	51.160	0.113	29.877	0.122	13.289	0.000	0.769	4.255	0.241	0.027	0.024	99.877	62.432
	10BH167 A2 17	50.045	0.043	28.319	2.590	11.844	0.059	2.599	3.647	0.227	0.000	0.049	99.422	63.290
	10BH167 A2 18	51.373	0.151	29.766	0.182	13.329	0.035	0.957	4.077	0.245	0.000	0.080	100.195	63.477
	10BH167 A2 16-18 av	50.859	0.102	29.321	0.965	12.821	0.031	1.442	3.993	0.238	0.009	0.051	99.831	63.055
	10BH167 A2 19	50.090	0.027	30.897	0.278	14.961	0.009	0.597	3.247	0.109	0.031	0.017	100.263	71.318
	10BH167 A2 20	50.296	0.000	30.860	0.299	14.925	0.000	0.608	3.309	0.102	0.000	0.056	100.455	70.956
	10BH167 A2 21	49.867	0.070	31.144	0.229	15.160	0.044	0.765	3.130	0.095	0.000	0.066	100.570	72.408
	10BH167 A2 19-21 av	50.084	0.032	30.967	0.269	15.015	0.018	0.657	3.229	0.102	0.010	0.046	100.429	71.559
MOZ	10BH167 A3 13	49.893	0.076	30.608	0.168	14.194	0.000	0.686	3.635	0.155	0.000	0.077	99.492	67.731
	10BH167 A3 14	50.869	0.005	30.672	0.146	14.091	0.000	0.799	3.636	0.220	0.000	0.000	100.438	67.316
	10BH167 A3 13-14 av	50.381	0.041	30.640	0.157	14.143	0.000	0.743	3.636	0.188	0.000	0.039	99.965	67.524
	10BH167 A3 15	49.970	0.022	30.688	0.203	14.390	0.000	0.598	3.646	0.147	0.000	0.063	99.727	67.997
	10BH167 A3 16	51.467	0.081	29.787	0.181	13.354	0.000	0.681	4.128	0.230	0.033	0.063	100.005	63.260
	10BH167 A3 17	51.674	0.124	29.881	0.147	13.036	0.006	0.731	4.261	0.237	0.000	0.108	100.205	61.991
	10BH167 A3 15-17 av	51.037	0.076	30.119	0.177	13.593	0.002	0.670	4.012	0.205	0.011	0.078	99.979	64.422
	10BH167 A3 25	49.886	0.092	30.822	0.220	14.577	0.000	0.713	3.464	0.135	0.000	0.000	99.909	69.394
	10BH167 A3 26	49.320	0.054	30.410	0.809	14.430	0.021	1.365	3.321	0.147	0.000	0.056	99.933	69.999
	10BH167 A3 25-26 av	49.603	0.073	30.616	0.515	14.504	0.011	1.039	3.393	0.141	0.000	0.028	99.921	69.694

Appendix E4 – LPS Plagioclase compositions

Zone	Sample code	SiO2	TiO2	Al2O3	MgO	CaO	MnO	FeO	Na2O	K2O	BaO	SrO	Total	Anmol%
UOZ	10BH167 A4 1	49.766	0.097	30.649	0.269	14.802	0.000	0.539	3.254	0.127	0.014	0.045	99.562	71.004
	10BH167 A4 2	50.794	0.000	30.804	0.218	14.647	0.018	0.562	3.456	0.131	0.000	0.073	100.703	69.559
	10BH167 A4 3	52.097	0.167	29.628	0.150	13.183	0.041	0.839	4.184	0.249	0.000	0.014	100.552	62.625
	10BH167 A4 1-3 av	50.886	0.088	30.360	0.212	14.211	0.020	0.647	3.631	0.169	0.005	0.044	100.272	67.719
	10BH167 A4 28	49.596	0.005	31.509	0.215	15.312	0.032	0.704	3.017	0.094	0.005	0.073	100.562	73.315
	10BH167 A4 29	49.766	0.097	30.649	0.269	14.802	0.000	0.539	3.254	0.127	0.014	0.045	99.562	71.004
	10BH167 A4 28-29 av	49.681	0.051	31.079	0.242	15.057	0.016	0.622	3.136	0.111	0.010	0.059	100.062	72.161
UOZ	BH311 B3 24	50.548	0.054	29.870	0.661	13.567	0.027	1.145	3.609	0.171	0.000	0.000	99.652	66.828
	BH311 B3 24	50.851	0.098	29.610	0.605	13.892	0.000	0.848	3.659	0.188	0.014	0.094	99.859	66.975
	BH311 B3 24	50.646	0.049	29.962	0.233	14.167	0.024	0.667	3.703	0.163	0.000	0.010	99.624	67.264
	BH311 B3 24	49.542	0.098	29.672	1.099	13.703	0.006	1.099	3.376	0.137	0.007	0.000	98.739	68.591
	BH311 B3 24	51.237	0.049	30.294	0.200	14.371	0.015	0.633	3.577	0.155	0.000	0.021	100.552	68.341
	BH311 B3 24	50.531	0.043	30.150	0.244	14.230	0.024	0.671	3.582	0.149	0.000	0.042	99.666	68.121
	BH311 B3 24	50.600	0.087	30.213	0.304	14.307	0.052	0.711	3.502	0.143	0.000	0.115	100.034	68.736
	BH311 B3 24	50.716	0.000	30.345	0.280	14.425	0.000	0.656	3.479	0.144	0.000	0.031	100.076	69.046
	BH311 B3 24	50.861	0.060	30.427	0.219	14.377	0.000	0.632	3.485	0.147	0.000	0.031	100.239	68.927
	BH311 B3 24	51.039	0.027	30.454	0.245	14.381	0.018	0.617	3.402	0.158	0.000	0.010	100.351	69.389
	BH311 B3 24	50.618	0.119	30.581	0.229	14.462	0.000	0.598	3.495	0.134	0.047	0.073	100.356	68.988
	BH311 B3 24	51.173	0.000	30.477	0.208	14.622	0.027	0.573	3.420	0.150	0.000	0.052	100.702	69.664
	BH311 B3 24	50.246	0.000	30.709	0.207	14.547	0.000	0.583	3.455	0.149	0.000	0.031	99.927	69.349
	BH311 B3 24	50.250	0.005	30.544	0.200	14.590	0.000	0.587	3.404	0.124	0.000	0.035	99.739	69.817
	BH311 B3 24	49.828	0.065	30.637	0.241	14.561	0.000	0.658	3.314	0.131	0.000	0.098	99.533	70.296
	BH311 B3 24	51.067	0.049	30.609	0.206	14.442	0.039	0.625	3.513	0.144	0.000	0.024	100.718	68.868
	BH311 B3 24	50.898	0.049	30.314	0.218	14.102	0.039	0.646	3.654	0.154	0.000	0.070	100.144	67.482
	BH311 B3 24	51.176	0.043	30.015	0.204	13.989	0.000	0.720	3.695	0.171	0.004	0.052	100.069	66.996
	BH311 B3 24	50.537	0.022	28.792	1.627	12.356	0.061	2.085	3.702	0.164	0.000	0.056	99.402	64.186
	BH311 B3 24	41.020	0.085	22.175	10.754	5.743	0.143	10.021	1.959	0.180	0.000	0.000	92.080	60.438
	BH311 B3 24 av	50.169	0.050	29.793	0.909	13.742	0.024	1.239	3.449	0.153	0.004	0.042	99.573	67.915
	BH311 B3 34	50.215	0.060	30.126	0.199	14.264	0.058	0.586	3.498	0.120	0.051	0.028	99.205	68.724
	BH311 B3 35	50.166	0.087	30.216	0.209	14.625	0.027	0.602	3.411	0.114	0.000	0.038	99.495	69.865
	BH311 B3 36	50.565	0.076	29.819	0.173	14.000	0.000	0.725	3.729	0.169	0.025	0.056	99.337	66.800

Appendix E4 – LPS Plagioclase compositions

Zone	Sample code	SiO2	TiO2	Al2O3	MgO	CaO	MnO	FeO	Na2O	K2O	BaO	SrO	Total	Anmol%
	BH311 B3 34-36 av	50.315	0.074	30.054	0.194	14.296	0.028	0.638	3.546	0.134	0.025	0.041	99.346	68.463
	BH311 B3 41	48.452	0.027	30.565	0.209	15.202	0.000	0.655	2.961	0.108	0.005	0.000	98.184	73.473
	BH311 B3 42	49.579	0.109	30.498	0.199	14.942	0.000	0.633	3.105	0.129	0.011	0.000	99.205	72.120
	BH311 B3 43	50.083	0.022	30.251	0.172	14.353	0.012	0.783	3.476	0.200	0.000	0.035	99.387	68.737
	BH311 B3 41-43 av	49.371	0.053	30.438	0.193	14.832	0.004	0.690	3.181	0.146	0.005	0.012	98.925	71.443
	BH311 B3 44	50.161	0.043	30.427	0.130	14.500	0.000	0.850	3.323	0.203	0.002	0.080	99.719	69.861
	BH311 B3 44	44.634	0.071	27.581	1.402	18.125	0.279	1.601	2.667	0.060	0.007	0.049	96.476	78.718
	BH311 B3 44	49.957	0.000	30.551	0.238	14.662	0.082	0.599	3.257	0.131	0.020	0.080	99.577	70.766
	BH311 B3 44	50.239	0.000	30.320	0.252	14.645	0.052	0.543	3.335	0.146	0.000	0.073	99.605	70.227
	BH311 B3 44	49.690	0.000	30.519	0.271	14.818	0.009	0.561	3.151	0.122	0.000	0.105	99.246	71.705
	BH311 B3 44	49.080	0.038	30.490	0.402	14.850	0.000	0.682	3.133	0.114	0.000	0.045	98.834	71.895
	BH311 B3 44	44.358	0.037	26.349	2.669	10.981	0.314	9.214	2.332	0.097	0.000	0.106	96.457	71.694
	BH311 B3 44	46.609	0.059	28.369	1.689	12.418	0.319	5.787	2.879	0.128	0.004	0.035	98.296	69.836
	BH311 B3 44	50.280	0.000	30.664	0.324	14.972	0.000	0.633	3.131	0.124	0.000	0.010	100.138	72.031
	BH311 B3 44	46.985	0.032	28.366	4.385	12.424	0.082	2.888	2.625	0.114	0.000	0.032	97.933	71.774
	BH311 B3 44	49.491	0.016	30.676	0.230	14.919	0.000	0.624	3.204	0.125	0.018	0.024	99.327	71.478
	BH311 B3 44	44.942	0.124	26.448	5.831	11.232	0.386	4.755	2.191	0.137	0.011	0.021	96.078	73.107
	BH311 B3 44	48.722	0.103	30.770	0.223	14.974	0.024	0.717	3.187	0.136	0.014	0.147	99.017	71.618
	BH311 B3 44	50.018	0.000	30.602	0.218	14.825	0.055	0.776	3.161	0.128	0.000	0.045	99.828	71.627
	BH311 B3 44	50.114	0.049	30.536	0.191	14.633	0.000	0.649	3.315	0.148	0.000	0.035	99.670	70.324
	BH311 B3 44	49.733	0.000	29.926	1.035	14.127	0.055	0.833	3.355	0.155	0.000	0.049	99.268	69.309
	BH311 B3 44	47.933	0.092	27.599	4.018	12.094	0.012	3.219	2.908	0.211	0.000	0.018	98.104	68.687
	BH311 B3 44	50.157	0.027	30.308	0.211	14.238	0.000	0.726	3.514	0.161	0.033	0.035	99.410	68.450
	BH311 B3 44	50.857	0.130	29.873	0.288	14.065	0.000	0.853	3.615	0.168	0.000	0.108	99.957	67.599
	BH311 B3 44	51.018	0.157	30.258	0.160	14.130	0.036	0.833	3.599	0.188	0.000	0.077	100.456	67.716
	BH311 B3 44 av	48.749	0.049	29.532	1.208	14.082	0.085	1.867	3.094	0.140	0.005	0.059	98.870	70.921
	BH311 B3 53	52.352	0.103	29.940	0.172	13.494	0.015	0.868	4.035	0.218	0.000	0.122	101.319	64.089
	BH311 B3 53	52.539	0.065	29.689	0.190	13.225	0.000	0.673	4.028	0.224	0.000	0.076	100.709	63.641
	BH311 B3 53	52.802	0.071	29.630	0.172	13.281	0.000	0.694	4.018	0.208	0.000	0.069	100.945	63.853
	BH311 B3 53	52.524	0.060	29.892	0.171	13.644	0.015	0.671	3.868	0.192	0.033	0.035	101.105	65.332
	BH311 B3 53	51.885	0.136	29.800	0.163	13.579	0.043	0.660	3.908	0.184	0.005	0.101	100.464	65.060
	BH311 B3 53	52.052	0.054	30.042	0.145	13.611	0.000	0.689	3.943	0.199	0.027	0.077	100.839	64.836

Appendix E4 – LPS Plagioclase compositions

Zone	Sample code	SiO2	TiO2	Al2O3	MgO	CaO	MnO	FeO	Na2O	K2O	BaO	SrO	Total	Anmol%
	BH311 B3 53	52.132	0.119	29.741	0.160	13.513	0.000	0.735	3.993	0.221	0.000	0.136	100.750	64.342
	BH311 B3 53	52.226	0.038	29.500	0.138	13.147	0.000	0.737	4.155	0.212	0.000	0.101	100.254	62.850
	BH311 B3 53	52.335	0.141	29.476	0.127	12.862	0.094	0.769	4.209	0.261	0.005	0.097	100.376	61.863
	BH311 B3 53	53.210	0.087	28.865	0.095	11.988	0.009	0.712	4.700	0.352	0.000	0.090	100.108	57.326
	BH311 B3 53 av	52.406	0.087	29.658	0.153	13.234	0.018	0.721	4.086	0.227	0.007	0.090	100.687	63.319
CPZ	BH311 B4 6	50.365	0.081	31.131	0.188	14.650	0.000	0.815	3.459	0.148	0.000	0.042	100.879	69.479
	BH311 B4 7	50.652	0.016	30.624	0.230	14.757	0.000	0.686	3.295	0.155	0.000	0.128	100.543	70.594
	BH311 B4 6-7 av	50.509	0.049	30.878	0.209	14.704	0.000	0.751	3.377	0.152	0.000	0.085	100.711	70.037
	BH311 B4 8	51.277	0.043	30.701	0.169	14.683	0.054	0.758	3.286	0.141	0.016	0.083	101.211	70.581
	BH311 B4 9	49.979	0.043	31.061	0.196	15.045	0.000	0.605	3.137	0.126	0.007	0.024	100.223	72.075
	BH311 B4 10	50.365	0.092	31.157	0.220	14.988	0.000	0.718	3.228	0.135	0.052	0.063	101.018	71.341
	BH311 B4 8-10 av	50.540	0.059	30.973	0.195	14.905	0.018	0.694	3.217	0.134	0.025	0.057	100.817	71.332
	BH311 B4 21	51.797	0.087	29.651	0.109	13.266	0.003	0.746	4.094	0.228	0.000	0.076	100.057	63.335
	BH311 B4 21	51.921	0.000	29.647	0.132	13.336	0.000	0.794	3.949	0.231	0.011	0.059	100.080	64.236
	BH311 B4 21	51.956	0.060	29.705	0.133	13.388	0.003	0.809	4.090	0.221	0.000	0.007	100.372	63.594
	BH311 B4 21	57.107	0.065	27.261	0.040	9.774	0.064	0.508	5.937	0.378	0.047	0.062	101.243	46.577
	BH311 B4 21 av	53.195	0.053	29.066	0.104	12.441	0.018	0.714	4.518	0.265	0.015	0.051	100.438	59.435
	BH311 B4 27	51.790	0.022	30.200	0.156	13.874	0.048	0.785	3.719	0.163	0.000	0.080	100.837	66.709
	BH311 B4 28	51.932	0.016	30.441	0.155	14.139	0.000	0.735	3.602	0.176	0.002	0.000	101.198	67.757
	BH311 B4 29	54.161	0.032	28.989	0.108	12.482	0.000	0.774	4.469	0.265	0.000	0.166	101.446	59.767
	BH311 B4 27-29 av	52.628	0.023	29.877	0.140	13.498	0.016	0.765	3.930	0.201	0.001	0.082	101.160	64.744
	BH311 B4 30	50.537	0.060	30.986	0.186	14.930	0.042	0.675	3.269	0.129	0.013	0.090	100.917	71.082
	BH311 B4 31	51.298	0.016	29.309	0.708	13.168	0.042	1.823	3.461	0.267	0.000	0.121	100.213	66.678
	BH311 B4 32	53.800	0.124	28.989	0.090	12.070	0.067	0.779	4.691	0.300	0.000	0.052	100.962	57.707
	BH311 B4 30-32 av	51.878	0.067	29.761	0.328	13.389	0.050	1.092	3.807	0.232	0.004	0.088	100.697	65.156
CPZ	10BH167 A5 11	51.539	0.011	29.111	0.104	12.915	0.106	0.773	4.231	0.207	0.000	0.059	99.056	62.039
	10BH167 A5 12	50.635	0.000	29.524	0.103	13.361	0.032	0.804	3.980	0.191	0.023	0.017	98.670	64.239
	10BH167 A5 13	50.249	0.000	29.700	0.120	13.313	0.000	0.921	4.029	0.193	0.014	0.073	98.612	63.886
	10BH167 A5 14	54.892	0.011	26.702	0.030	9.409	0.026	0.598	6.154	0.393	0.002	0.041	98.258	44.776
	10BH167 A5 15	98.067	0.000	0.074	0.013	0.036	0.006	0.258	0.002	0.008	0.000	0.000	98.464	73.254
	10BH167 A5 11-15 av	61.076	0.004	23.022	0.074	9.807	0.034	0.671	3.679	0.198	0.008	0.038	98.612	58.711

Appendix E4 – LPS Plagioclase compositions

Zone	Sample code	SiO2	TiO2	Al2O3	MgO	CaO	MnO	FeO	Na2O	K2O	BaO	SrO	Total	Anmol%
	10BH167 A5 16	48.337	0.022	30.850	0.201	14.978	0.000	0.644	3.093	0.111	0.013	0.080	98.329	72.316
	10BH167 A5 17	49.522	0.097	30.910	0.196	14.751	0.032	0.662	3.316	0.125	0.000	0.000	99.611	70.578
	10BH167 A5 18	49.194	0.097	30.548	0.206	14.856	0.006	0.714	3.131	0.108	0.007	0.066	98.933	71.932
	10BH167 A5 19	49.307	0.000	30.531	0.188	14.701	0.000	0.657	3.259	0.138	0.000	0.010	98.791	70.805
	10BH167 A5 20	48.551	0.081	30.323	0.178	14.398	0.047	0.708	3.445	0.135	0.000	0.024	97.890	69.246
	10BH167 A5 21	49.350	0.027	30.151	0.129	14.087	0.000	0.668	3.746	0.135	0.007	0.132	98.432	66.989
	10BH167 A5 22	50.472	0.011	30.173	0.150	14.001	0.000	0.800	3.606	0.150	0.000	0.076	99.439	67.622
	10BH167 A5 26-22 av	49.248	0.048	30.498	0.178	14.539	0.012	0.693	3.371	0.129	0.004	0.055	98.775	69.920
	10BH167 A5 34	48.740	0.070	30.703	0.172	14.798	0.000	0.676	3.213	0.112	0.000	0.059	98.543	71.331
	10BH167 A5 35	49.099	0.059	30.512	0.153	14.507	0.015	0.719	3.317	0.127	0.000	0.042	98.550	70.216
	10BH167 A5 36	49.612	0.054	30.174	0.152	14.249	0.000	0.775	3.483	0.126	0.000	0.132	98.757	68.830
	10BH167 A5 37	50.164	0.032	29.521	0.139	13.370	0.026	0.840	3.851	0.198	0.000	0.090	98.231	64.984
	10BH167 A5 38	49.630	0.005	29.533	0.116	13.203	0.000	0.901	3.996	0.203	0.000	0.083	97.670	63.858
	10BH167 A5 39	49.998	0.081	28.947	0.093	12.694	0.000	0.759	4.229	0.204	0.005	0.031	97.041	61.647
	10BH167 A5 40	50.930	0.102	28.639	0.084	12.037	0.000	0.765	4.628	0.255	0.000	0.073	97.513	58.107
	10BH167 A5 41	52.928	0.059	27.960	0.048	11.120	0.000	0.888	5.120	0.288	0.000	0.042	98.453	53.648
	10BH167 A5 34-41 av	50.138	0.058	29.499	0.120	13.247	0.005	0.790	3.980	0.189	0.001	0.069	98.095	64.077
	10BH167 A5 71	49.039	0.070	31.381	0.183	15.094	0.000	0.743	3.004	0.134	0.000	0.070	99.718	72.955
	10BH167 A5 72	48.838	0.022	31.164	0.136	14.965	0.000	0.821	3.129	0.131	0.000	0.052	99.258	72.006
	10BH167 A5 73	51.080	0.054	29.505	0.116	13.058	0.000	0.810	4.181	0.199	0.013	0.014	99.030	62.582
	10BH167 A5 74	56.958	0.081	26.337	0.015	8.632	0.044	0.562	6.630	0.438	0.023	0.172	99.892	40.795
	10BH167 A5 71-74 av	51.479	0.057	29.597	0.113	12.937	0.011	0.734	4.236	0.226	0.009	0.077	99.475	61.977
	10BH167 A5 84	48.324	0.022	31.788	0.208	15.958	0.000	0.587	2.670	0.096	0.000	0.056	99.709	76.340
	10BH167 A5 85	46.703	0.086	31.733	0.200	15.580	0.015	0.622	2.708	0.102	0.000	0.105	97.854	75.625
	10BH167 A5 86	47.501	0.005	31.694	0.200	15.669	0.000	0.636	2.789	0.082	0.025	0.052	98.653	75.250
	10BH167 A5 87	47.179	0.059	31.190	0.161	15.156	0.000	0.752	3.019	0.113	0.000	0.042	97.671	73.028
	10BH167 A5 88	47.441	0.000	30.924	0.154	14.906	0.000	0.986	3.219	0.127	0.000	0.031	97.788	71.381
	10BH167 A5 84-88 av	47.430	0.034	31.466	0.185	15.454	0.003	0.717	2.881	0.104	0.005	0.057	98.335	74.323
	10BH167 A5 90	49.573	0.000	31.342	0.327	15.109	0.044	0.755	2.773	0.188	0.000	0.000	100.111	74.243
	10BH167 A5 91	50.088	0.000	30.628	0.157	14.469	0.018	0.783	3.432	0.140	0.000	0.000	99.715	69.409

Appendix E4 – LPS Plagioclase compositions

Zone	Sample code	SiO2	TiO2	Al2O3	MgO	CaO	MnO	FeO	Na2O	K2O	BaO	SrO	Total	Anmol%
	10BH167 A5 92	59.567	0.000	24.508	0.009	6.448	0.000	0.321	7.801	0.585	0.070	0.058	99.367	30.292
	10BH167 A5 90-92 av	53.076	0.000	28.826	0.164	12.009	0.021	0.620	4.669	0.304	0.023	0.019	99.731	57.657
DZ	10BH167 A6 12	46.672	0.005	31.563	0.211	15.482	0.000	0.613	2.735	0.106	0.000	0.024	97.411	75.311
	10BH167 A6 13	48.142	0.000	30.901	0.272	14.456	0.000	0.732	3.024	0.173	0.023	0.000	97.723	71.769
	10BH167 A6 14	49.179	0.011	30.338	0.162	14.354	0.070	0.709	3.421	0.144	0.000	0.021	98.409	69.290
	10BH167 A6 15	49.598	0.022	30.085	0.158	13.997	0.000	0.878	3.617	0.157	0.000	0.070	98.582	67.523
	10BH167 A6 12-15 av	48.398	0.010	30.722	0.201	14.572	0.018	0.733	3.199	0.145	0.006	0.029	98.031	70.959
	10BH167 A6 32	49.692	0.065	30.040	0.138	13.915	0.088	0.865	3.659	0.153	0.000	0.080	98.695	67.163
	10BH167 A6 33	49.701	0.000	29.810	0.122	13.856	0.000	0.836	3.650	0.162	0.000	0.014	98.151	67.087
	10BH167 A6 34	48.706	0.065	30.085	0.143	13.945	0.023	0.931	3.664	0.165	0.063	0.031	97.821	67.060
	10BH167 A6 32-34 av	49.366	0.043	29.978	0.134	13.905	0.037	0.877	3.658	0.160	0.021	0.042	98.222	67.103
	10BH167 A6 35	47.872	0.022	30.893	0.228	15.148	0.015	0.574	2.866	0.119	0.000	0.070	97.807	73.980
	10BH167 A6 36	48.132	0.016	31.063	0.230	15.194	0.026	0.689	2.964	0.106	0.000	0.105	98.525	73.459
	10BH167 A6 37	48.149	0.049	31.150	0.205	15.074	0.000	0.735	2.957	0.115	0.000	0.000	98.434	73.311
	10BH167 A6 38	47.152	0.081	30.526	0.296	14.865	0.021	0.824	3.073	0.120	0.000	0.052	97.010	72.270
	10BH167 A6 35-38 av	47.826	0.042	30.908	0.240	15.070	0.016	0.706	2.965	0.115	0.000	0.057	97.944	73.254
	10BH167 A6 39	50.550	0.124	29.403	0.144	13.424	0.026	0.824	3.827	0.182	0.000	0.049	98.553	65.273
	10BH167 A6 40	50.153	0.048	29.634	0.129	13.595	0.000	0.819	3.697	0.165	0.045	0.080	98.365	66.324
	10BH167 A6 39-40 av	50.352	0.086	29.519	0.137	13.510	0.013	0.822	3.762	0.174	0.023	0.065	98.459	65.798
	10BH167 A6 44	53.108	0.113	28.552	0.088	12.051	0.000	0.687	4.654	0.230	0.000	0.076	99.559	58.087
	10BH167 A6 45	54.593	0.038	28.167	0.070	11.311	0.009	0.603	5.016	0.285	0.000	0.176	100.268	54.571
	10BH167 A6 46	55.847	0.000	26.694	0.021	9.055	0.082	0.539	6.380	0.380	0.061	0.124	99.183	42.966
	10BH167 A6 44-46 av	54.516	0.050	27.804	0.060	10.806	0.030	0.610	5.350	0.298	0.020	0.125	99.670	51.827
DZ	10BH167 A8 10	52.432	0.086	29.548	0.140	13.260	0.000	1.024	4.085	0.190	0.005	0.062	100.832	63.505
	10BH167 A8 11	50.622	0.075	30.161	0.158	14.304	0.000	0.912	3.632	0.149	0.043	0.035	100.091	67.890
	10BH167 A8 12	53.479	0.027	28.784	0.105	11.666	0.000	0.867	4.727	0.406	0.000	0.000	100.061	56.349
	10BH167 A8 13	53.638	0.091	28.522	0.069	11.774	0.018	0.870	4.934	0.244	0.000	0.080	100.240	56.086
	10BH167 A8 10-13 av	52.543	0.070	29.254	0.118	12.751	0.005	0.918	4.345	0.247	0.012	0.044	100.306	60.976

Appendix E4 – LPS Plagioclase compositions

Zone	Sample code	SiO2	TiO2	Al2O3	MgO	CaO	MnO	FeO	Na2O	K2O	BaO	SrO	Total	Anmol%
DZ	10BH167 A9 1	51.604	0.054	29.529	0.124	13.239	0.032	0.846	4.088	0.201	0.000	0.052	99.769	63.418
	10BH167 A9 2	51.060	0.016	29.538	0.124	13.364	0.000	0.817	3.934	0.205	0.002	0.000	99.060	64.474
	10BH167 A9 3	50.714	0.140	29.469	0.125	13.148	0.047	0.818	4.116	0.201	0.000	0.101	98.879	63.104
	10BH167 A9 4	55.391	0.054	27.344	0.018	10.117	0.000	0.542	5.755	0.336	0.043	0.041	99.641	48.299
	10BH167 A9 1-4 av	52.192	0.066	28.970	0.098	12.467	0.020	0.756	4.473	0.236	0.011	0.049	99.337	59.804
	10BH167 A9 16	49.194	0.097	29.348	0.113	12.893	0.000	0.915	4.168	0.275	0.000	0.063	97.066	62.097
	10BH167 A9 17	50.116	0.000	29.567	0.128	13.256	0.029	0.861	4.074	0.201	0.000	0.059	98.291	63.525
	10BH167 A9 16-17 av	49.655	0.049	29.458	0.121	13.075	0.015	0.888	4.121	0.238	0.000	0.061	97.679	62.813
DZ	BH311 B6 61	48.888	0.043	31.706	0.220	16.226	0.070	0.546	2.461	0.088	0.063	0.049	100.360	77.983
	BH311 B6 61	49.335	0.071	31.500	0.242	16.062	0.000	0.559	2.431	0.080	0.000	0.028	100.308	78.137
	BH311 B6 61	49.270	0.038	31.345	0.234	15.791	0.009	0.554	2.605	0.098	0.000	0.035	99.979	76.575
	BH311 B6 61	49.537	0.033	31.302	0.219	15.520	0.000	0.556	2.733	0.092	0.000	0.066	100.058	75.431
	BH311 B6 61	51.682	0.011	29.555	0.209	13.350	0.012	0.657	3.670	0.342	0.027	0.038	99.553	65.415
	BH311 B6 61 av	49.742	0.039	31.082	0.225	15.390	0.018	0.574	2.780	0.140	0.018	0.043	100.052	74.708
	BH311 B6 70	49.980	0.000	31.386	0.171	15.349	0.033	0.753	2.888	0.116	0.000	0.118	100.794	74.103
	BH311 B6 70	51.314	0.011	30.631	0.222	14.665	0.079	0.663	3.391	0.138	0.000	0.066	101.180	69.948
	BH311 B6 70	52.898	0.087	29.378	0.143	13.181	0.000	0.783	4.089	0.211	0.000	0.010	100.780	63.274
	BH311 B6 70	53.849	0.103	28.866	0.122	12.312	0.058	0.855	4.605	0.292	0.000	0.097	101.159	58.649
	BH311 B6 70 av	52.010	0.050	30.065	0.165	13.877	0.043	0.764	3.743	0.189	0.000	0.073	100.978	66.494
	BH311 B6 77	50.236	0.027	29.906	0.170	14.297	0.000	0.778	3.425	0.129	0.000	0.087	99.055	69.240
	BH311 B6 78	51.392	0.022	29.470	0.167	13.980	0.006	0.746	3.647	0.151	0.027	0.014	99.622	67.311
	BH311 B6 77-78 av	50.814	0.025	29.688	0.169	14.139	0.003	0.762	3.536	0.140	0.014	0.051	99.339	68.276
DZ	10BH167 A10 1	52.773	0.011	29.263	0.107	13.221	0.026	0.843	4.145	0.204	0.000	0.035	100.628	63.064
	10BH167 A10 2	51.973	0.000	29.674	0.149	13.319	0.000	0.845	3.972	0.199	0.000	0.031	100.162	64.208
	10BH167 A10 3	57.179	0.005	26.792	0.022	9.487	0.000	0.500	6.126	0.388	0.000	0.062	100.561	45.102
	10BH167 A10 1-3 av	53.975	0.005	28.576	0.093	12.009	0.009	0.729	4.748	0.264	0.000	0.043	100.450	57.421
	10BH167 A10 4	51.961	0.022	29.425	0.143	13.204	0.012	0.836	4.130	0.199	0.000	0.007	99.939	63.133
	10BH167 A10 5	52.048	0.011	29.794	0.138	13.630	0.050	0.795	3.896	0.175	0.000	0.000	100.537	65.252
	10BH167 A10 6	51.187	0.086	30.110	0.138	13.950	0.000	0.809	3.808	0.172	0.000	0.111	100.371	66.285
	10BH167 A10 4-6 av	51.732	0.040	29.776	0.140	13.595	0.021	0.813	3.945	0.182	0.000	0.039	100.282	64.893

Appendix E4 – LPS Plagioclase compositions

Zone	Sample code	SiO2	TiO2	Al2O3	MgO	CaO	MnO	FeO	Na2O	K2O	BaO	SrO	Total	Anmol%
	10BH167 A10 23	52.731	0.005	29.026	0.131	11.670	0.000	0.993	4.672	0.548	0.040	0.038	99.854	56.129
	10BH167 A10 24	52.344	0.054	29.420	0.124	13.186	0.021	0.911	4.212	0.212	0.000	0.083	100.567	62.611
	10BH167 A10 25	55.616	0.000	27.732	0.032	10.342	0.044	0.819	5.860	0.318	0.034	0.128	100.925	48.470
	10BH167 A10 23-25 av	53.564	0.020	28.726	0.096	11.733	0.022	0.908	4.915	0.359	0.025	0.083	100.449	55.703
	10BH167 A10 26	51.435	0.043	30.128	0.162	13.990	0.000	0.775	3.511	0.299	0.000	0.059	100.402	67.587
	10BH167 A10 27	51.368	0.000	30.178	0.163	13.945	0.000	0.756	3.484	0.477	0.000	0.069	100.440	66.987
	10BH167 A10 28	50.534	0.043	30.603	0.155	14.556	0.029	0.772	3.316	0.132	0.049	0.038	100.227	70.212
	10BH167 A10 29	52.038	0.016	29.718	0.143	13.653	0.000	0.818	3.887	0.176	0.000	0.003	100.452	65.337
	10BH167 A10 30	53.792	0.097	28.710	0.097	12.233	0.000	0.725	4.619	0.242	0.000	0.035	100.550	58.589
	10BH167 A10 26-30 av	51.833	0.040	29.867	0.144	13.675	0.006	0.769	3.763	0.265	0.010	0.041	100.414	65.732
DZ	10BH167 A11-1 1	49.580	0.059	30.513	0.186	14.321	0.047	0.679	3.501	0.144	0.000	0.031	99.061	68.759
	10BH167 A11-1 2	50.147	0.048	30.026	0.158	13.796	0.044	0.766	3.724	0.188	0.023	0.028	98.948	66.432
	10BH167 A11-1 3	54.111	0.000	27.345	0.030	10.140	0.026	0.727	5.732	0.368	0.005	0.087	98.571	48.395
	10BH167 A11-1 1-3 av	51.279	0.036	29.295	0.125	12.752	0.039	0.724	4.319	0.233	0.009	0.049	98.860	61.165
	10BH167 A11-1 15	49.778	0.070	30.090	0.147	13.583	0.000	0.752	3.882	0.172	0.000	0.021	98.495	65.264
	10BH167 A11-1 16	50.439	0.059	29.772	0.132	13.307	0.012	0.783	4.009	0.215	0.000	0.017	98.745	63.922
	10BH167 A11-1 15-16 av	50.109	0.065	29.931	0.140	13.445	0.006	0.768	3.946	0.194	0.000	0.019	98.620	64.593
	10BH167 A11-1 19	95.481	0.065	0.122	0.011	0.000	0.000	0.076	0.039	0.008	0.000	0.018	95.820	0.000
	10BH167 A11-1 26	66.239	0.011	20.024	0.065	0.136	0.000	0.462	11.862	0.099	0.022	0.079	98.999	0.626
DZ	10BH167 A11-2 1	52.082	0.087	29.300	0.119	13.241	0.015	0.761	3.962	0.209	0.000	0.066	99.842	64.092
	10BH167 A11-2 2	52.626	0.060	29.420	0.112	13.172	0.000	0.874	4.085	0.235	0.000	0.056	100.640	63.194
	10BH167 A11-2 3	53.637	0.043	28.376	0.094	11.500	0.000	0.966	5.015	0.299	0.000	0.024	99.954	54.943
	10BH167 A11-2 1-3 av	52.782	0.063	29.032	0.108	12.638	0.005	0.867	4.354	0.248	0.000	0.049	100.145	60.725
	10BH167 A11-2 9	51.974	0.043	29.713	0.127	13.204	0.000	0.887	4.112	0.215	0.033	0.119	100.427	63.138
	10BH167 A11-2 10	53.016	0.000	28.519	0.093	11.916	0.000	0.668	4.798	0.279	0.016	0.035	99.340	56.915
	10BH167 A11-2 9-10 av	52.495	0.022	29.116	0.110	12.560	0.000	0.778	4.455	0.247	0.025	0.077	99.884	60.025
	10BH167 A11-2 13	80.034	0.000	10.958	0.414	3.876	0.042	0.973	3.119	0.147	0.024	0.016	99.603	39.943
	10BH167 A11-2 14	53.397	0.103	28.689	0.071	11.760	0.000	0.919	4.934	0.283	0.020	0.056	100.232	55.913
DZ	10BH167 A12 7	57.379	0.065	26.288	0.036	8.680	0.029	0.456	6.641	0.328	0.000	0.000	99.902	41.161

Appendix E4 – LPS Plagioclase compositions

Zone	Sample code	SiO2	TiO2	Al2O3	MgO	CaO	MnO	FeO	Na2O	K2O	BaO	SrO	Total	Anmol%
	10BH167 A12 8	54.994	0.113	28.220	0.066	11.193	0.000	0.591	5.155	0.356	0.000	0.145	100.833	53.440
	10BH167 A12 9	54.404	0.081	28.359	0.084	11.417	0.000	0.547	5.119	0.299	0.018	0.045	100.373	54.256
	10BH167 A12 10	53.312	0.016	28.855	0.093	12.218	0.000	0.622	4.657	0.257	0.000	0.066	100.096	58.317
	10BH167 A12 7-10 av	55.022	0.069	27.931	0.070	10.877	0.007	0.554	5.393	0.310	0.005	0.064	100.301	51.779
	10BH167 A12 14	49.869	0.005	30.423	0.167	14.142	0.000	0.696	3.599	0.160	0.000	0.077	99.138	67.843
	10BH167 A12 15	50.333	0.065	29.881	0.136	13.718	0.035	0.784	3.836	0.206	0.022	0.077	99.093	65.596
	10BH167 A12 16	52.320	0.059	29.398	0.118	12.829	0.000	0.690	4.360	0.250	0.007	0.073	100.104	61.036
	10BH167 A12 17	56.179	0.000	27.224	0.041	9.888	0.076	0.610	5.954	0.449	0.036	0.055	100.512	46.620
	10BH167 A12 14-17 av	52.175	0.032	29.232	0.116	12.644	0.028	0.695	4.437	0.266	0.016	0.071	99.712	60.220
	10BH167 A12 18	52.462	0.022	29.201	0.119	12.813	0.003	0.731	4.356	0.242	0.000	0.052	100.001	61.062
	10BH167 A12 19	54.116	0.005	28.550	0.080	11.839	0.000	0.618	4.827	0.327	0.070	0.062	100.494	56.407
	10BH167 A12 20	56.282	0.000	27.315	0.031	10.164	0.053	0.623	5.792	0.416	0.083	0.000	100.759	48.010
	10BH167 A12 18-20 av	54.287	0.009	28.355	0.077	11.605	0.019	0.657	4.992	0.328	0.051	0.038	100.418	55.138
UBZ	10BH167 A14 4	50.772	0.043	30.420	0.136	14.363	0.000	1.029	3.464	0.237	0.000	0.070	100.534	68.678
	10BH167 A14 5	51.167	0.000	30.320	0.145	14.411	0.000	0.954	3.521	0.232	0.000	0.049	100.799	68.433
	10BH167 A14 6	50.966	0.048	30.603	0.172	14.660	0.000	1.001	3.389	0.222	0.031	0.066	101.158	69.583
	10BH167 A14 4-6 av	50.968	0.030	30.448	0.151	14.478	0.000	0.995	3.458	0.230	0.010	0.062	100.830	68.899
	10BH167 A14 7	51.527	0.000	30.425	0.141	14.159	0.006	1.063	3.641	0.172	0.000	0.049	101.183	67.577
	10BH167 A14 8	50.776	0.097	30.441	0.125	14.332	0.021	0.978	3.516	0.163	0.000	0.000	100.449	68.612
	10BH167 A14 9	50.620	0.038	30.686	0.134	14.625	0.021	1.014	3.304	0.201	0.005	0.049	100.697	70.161
	10BH167 A14 7-9 av	50.974	0.045	30.517	0.133	14.372	0.016	1.018	3.487	0.179	0.002	0.033	100.776	68.781
	10BH167 A14 21	50.856	0.016	30.378	0.149	14.233	0.000	0.789	3.466	0.184	0.000	0.066	100.137	68.679
	10BH167 A14 22	50.713	0.016	30.763	0.135	14.519	0.000	0.875	3.345	0.172	0.047	0.024	100.609	69.823
	10BH167 A14 23	50.262	0.043	31.191	0.102	15.024	0.000	0.970	3.056	0.176	0.000	0.000	100.824	72.358
	10BH167 A14 21-23 av	50.610	0.025	30.777	0.129	14.592	0.000	0.878	3.289	0.177	0.016	0.030	100.523	70.287
	10BH167 A14 24	51.030	0.000	30.276	0.142	14.408	0.038	0.991	3.477	0.182	0.049	0.017	100.610	68.824
	10BH167 A14 25	51.214	0.054	30.287	0.156	14.399	0.000	0.946	3.494	0.174	0.000	0.153	100.877	68.800
	10BH167 A14 26	50.781	0.011	30.288	0.117	14.318	0.000	1.039	3.518	0.165	0.000	0.024	100.261	68.571
	10BH167 A14 33	50.688	0.000	30.280	0.123	14.497	0.035	1.046	3.736	0.207	0.000	0.007	100.619	67.415

Appendix E4 – LPS Plagioclase compositions

Zone	Sample code	SiO2	TiO2	Al2O3	MgO	CaO	MnO	FeO	Na2O	K2O	BaO	SrO	Total	Anmol%
	10BH167 A14 34	50.181	0.065	31.336	0.117	15.088	0.023	0.982	3.192	0.144	0.000	0.052	101.180	71.726
	10BH167 A14 35	50.030	0.000	30.762	0.128	14.529	0.000	0.939	3.442	0.171	0.000	0.028	100.029	69.314
	10BH167 A14 33-35 av	50.300	0.022	30.793	0.123	14.705	0.019	0.989	3.457	0.174	0.000	0.029	100.609	69.470

Appendix E5 – LPS Cr-spinel compositions

Zone	Sample code	SiO2	TiO2	Al2O3	Cr2O3	Fe2O3	MgO	CaO	MnO	FeO	CoO	NiO	ZnO	Na2O	Total	Cr#	Fe3#	Fe2#
LCM	166 A1 7	0.091	0.695	19.937	41.393	7.865	8.783	0.000	0.000	21.658	0.000	0.096	0.073	0.021	100.614	58.208	9.525	58.041
	166 A1 8	0.105	0.365	25.879	38.491	6.696	14.219	0.000	0.000	13.933	0.050	0.253	0.049	0.025	100.065	50.161	7.607	35.471
	166 A1 9	0.089	0.391	25.851	38.249	6.616	13.556	0.000	0.000	14.965	0.043	0.241	0.064	0.018	100.083	49.814	7.579	38.244
	166 A1 13	0.069	0.765	23.695	37.931	9.384	13.001	0.000	0.000	15.686	0.071	0.294	0.024	0.000	100.919	51.781	10.867	40.363
LBZ	166_A3 25	0.197	2.030	10.917	28.695	25.882	4.056	0.063	0.000	26.271	0.077	0.101	0.169	0.013	98.471	63.812	35.394	78.418
	166_A3 26	4.422	1.704	10.962	27.678	28.870	12.006	0.009	0.000	15.235	0.161	0.208	0.179	0.020	101.454	62.876	38.431	41.587
LOZ	166_A4 22	0.073	1.483	20.449	33.048	14.321	8.821	0.000	0.000	20.976	0.094	0.205	0.223	0.000	99.693	52.018	17.663	57.152
	166_A4 23	0.041	11.308	3.753	8.610	45.093	2.729	0.000	0.144	26.846	0.021	0.169	0.082	0.000	98.796	60.615	75.137	84.665
	166_A4 27	0.077	0.540	21.024	36.647	10.243	8.748	0.003	0.000	20.904	0.107	0.177	0.231	0.023	98.724	53.903	12.539	57.274
	166_A4 28	0.066	0.545	21.681	38.113	8.833	9.697	0.000	0.000	19.807	0.077	0.210	0.140	0.025	99.194	54.113	10.662	53.403
LOZ	166_A5 14	0.066	6.317	1.235	1.586	57.351	0.371	0.021	0.680	28.588	0.000	0.205	0.084	0.028	96.532	46.292	94.091	97.734
	166_A5 20	0.054	7.544	5.110	21.458	34.350	3.690	0.001	0.000	25.733	0.080	0.177	0.073	0.000	98.270	73.801	52.927	79.640
	166_A5 21	0.068	1.945	10.004	41.377	15.526	5.302	0.000	0.000	24.768	0.005	0.048	0.165	0.040	99.248	73.507	20.791	72.384
	166_A5 31	0.066	6.298	3.915	1.553	51.921	0.000	0.047	0.295	29.065	0.000	0.295	0.000	0.007	93.462	21.024	86.993	100.000
MOZ	167_A3 3	0.049	0.391	11.133	35.522	20.343	5.159	0.027	0.000	24.444	0.000	0.184	0.128	0.012	97.392	68.158	27.089	72.666
	167_A3 4	0.697	5.585	3.674	20.112	37.447	3.147	0.021	0.000	25.856	0.000	0.218	0.113	0.030	96.900	78.595	58.207	82.170
UOZ	167_A4 9	0.037	5.894	6.133	27.590	28.712	3.559	0.004	0.000	26.350	0.006	0.140	0.107	0.008	98.540	75.109	42.659	80.591
	167_A4 10	0.059	2.932	9.578	33.344	22.665	5.481	0.027	0.000	24.018	0.018	0.105	0.109	0.011	98.347	70.022	31.175	71.087
	167_A4 11	0.044	11.147	3.772	7.857	46.477	3.078	0.000	0.079	26.403	0.101	0.186	0.059	0.009	99.212	58.281	76.640	82.798
UOZ	BH311 B3 1	0.040	8.803	3.408	6.726	48.223	2.277	0.008	0.102	28.501	0.082	0.220	0.016	0.027	102.149	56.974	79.542	87.538
	BH311 B3 2	0.019	8.048	4.583	18.321	35.51	3.544	0.000	0.000	28.8	0.000	0.198	0.032	0.000	101.212	72.83	57.33	82.041

Appendix E5 – LPS Cr-spinel compositions

						0				47						5	4	
	BH311 B3 4	0.042	8.436	3.653	18.648	35.201	3.454	0.000	0.000	28.371	0.039	0.150	0.092	0.031	101.086	77.402	58.167	82.162
	BH311 B3 6	0.050	0.950	4.995	40.857	4.148	10.511	0.178	0.000	22.824	0.033	0.078	0.043	0.017	100.660	60.367	5.515	54.917
	BH311 B3 7	0.050	1.033	18.701	39.676	4.812	10.623	0.161	0.000	22.809	0.064	0.126	0.071	0.009	101.045	58.734	6.348	54.640
	BH311 B3 8	0.052	0.972	17.970	40.804	4.540	10.585	0.129	0.000	22.594	0.045	0.116	0.142	0.023	100.616	60.369	6.010	54.490
	BH311 B3 9	0.462	1.268	17.041	39.106	6.605	10.467	0.205	0.000	22.587	0.011	0.107	0.037	0.039	101.441	60.622	8.884	54.760
	BH311 B3 10	0.040	2.017	12.677	35.675	13.173	6.495	0.191	0.000	27.460	0.042	0.063	0.051	0.041	100.254	65.373	18.683	70.349
	BH311 B3 11	0.041	3.168	9.496	33.634	17.098	5.359	0.092	0.000	28.219	0.046	0.134	0.150	0.004	100.948	70.380	25.400	74.706
	BH311 B3 12	0.010	10.701	4.337	10.623	42.366	4.341	0.031	0.000	26.306	0.069	0.187	0.126	0.022	101.413	62.165	70.237	77.274
	BH311 B3 55	0.029	9.152	4.226	12.993	41.003	3.166	0.000	0.000	28.699	0.000	0.222	0.076	0.004	100.686	67.351	66.915	83.567
	BH311 B3 56	0.033	8.518	4.732	17.134	36.779	3.991	0.000	0.000	28.140	0.045	0.196	0.030	0.000	101.280	70.833	59.133	79.824
CPZ	167 A5 98	0.037	50.168	0.049	0.028	19.987	0.018	0.006	1.744	29.743	0.023	0.000	0.000	0.020	101.823	28.571	99.459	99.891
DZ	BH311 B6 76	0.027	51.277	0.046	0.006	18.500	0.019	0.059	1.694	29.595	0.002	0.000	0.000	0.014	101.292	6.667	99.583	99.890

Appendix E6 – PELE model results

					Liq Comp	Liq Comp	Liq Comp	Liq Comp	Liq Comp	Liq Comp	Liq Comp	Liq Comp	Liq Comp	Liq Comp	Liq Comp	Liq Comp	Liq Comp	Liq Comp	Liq Comp
Step	TC	LogfO2	LogfS2	Liq Mass	SiO2	TiO2	Al2O3	Fe2O3	Cr2O3	FeO	FeO*	MgO	CaO	Na2O	K2O	P2O5	H2O	CO2	S
5	1305	-6.43	-0.21	99.96	50.22	0.91	13.26	2.16	0.05	8.34	10.28	10.31	11.23	1.97	1.17	0.08	0.20	0.01	0.11
10	1255	-6.94	-0.25	99.89	50.25	0.91	13.27	2.20	0.05	8.27	10.24	10.31	11.24	1.97	1.17	0.08	0.20	0.01	0.09
11	1245	-7.04	-0.26	99.56	50.29	0.91	13.31	2.21	0.05	8.25	10.23	10.19	11.27	1.98	1.17	0.08	0.20	0.01	0.09
12	1235	-7.13	-0.26	98.59	50.39	0.92	13.44	2.23	0.05	8.19	10.20	9.84	11.39	1.99	1.18	0.08	0.21	0.01	0.08
13	1225	-7.23	-0.28	97.65	50.49	0.93	13.57	2.25	0.05	8.15	10.17	9.48	11.50	2.01	1.19	0.08	0.21	0.01	0.08
14	1215	-7.34	-0.30	96.73	50.60	0.94	13.70	2.26	0.05	8.11	10.13	9.14	11.60	2.03	1.20	0.08	0.21	0.01	0.08
15	1205	-7.45	-0.32	95.85	50.70	0.94	13.83	2.27	0.05	8.06	10.09	8.80	11.71	2.05	1.22	0.08	0.21	0.01	0.07
16	1195	-7.56	-0.33	94.99	50.80	0.95	13.95	2.28	0.05	8.00	10.05	8.48	11.82	2.07	1.23	0.08	0.21	0.01	0.07
17	1185	-7.68	-0.35	94.17	50.90	0.96	14.07	2.28	0.05	7.95	10.00	8.16	11.92	2.09	1.24	0.08	0.21	0.01	0.07
18	1175	-7.79	-0.37	93.37	51.00	0.97	14.19	2.29	0.05	7.89	9.95	7.85	12.02	2.11	1.25	0.09	0.22	0.02	0.07
18b	1170	-7.80	-0.34	92.97	51.05	0.97	14.25	2.33	0.05	7.81	9.90	7.71	12.07	2.12	1.25	0.09	0.22	0.02	0.07
19	1165	-7.88	-0.33	88.66	51.18	1.02	14.09	2.38	0.05	8.05	10.19	7.47	11.89	2.16	1.31	0.09	0.23	0.02	0.07
19b	1160	-7.91	-0.26	83.34	51.28	1.09	14.02	2.49	0.06	8.35	10.59	7.17	11.51	2.23	1.40	0.10	0.24	0.02	0.07
20	1155	-7.96	-0.22	78.69	51.38	1.15	13.94	2.57	0.06	8.67	10.97	6.87	11.15	2.29	1.48	0.10	0.26	0.02	0.07
21	1145	-7.98	-0.04	71.04	51.53	1.27	13.78	2.81	0.07	9.19	11.72	6.35	10.46	2.40	1.64	0.11	0.28	0.02	0.08
22	1135	-8.10	0.04	64.86	51.71	1.40	13.63	2.95	0.07	9.73	12.38	5.83	9.85	2.50	1.80	0.12	0.31	0.02	0.08
23	1125	-8.22	0.11	59.82	51.89	1.51	13.49	3.07	0.08	10.21	12.97	5.35	9.29	2.59	1.95	0.13	0.34	0.02	0.09
24	1115	-8.35	0.19	55.61	52.06	1.63	13.34	3.18	0.09	10.66	13.52	4.90	8.77	2.67	2.10	0.14	0.36	0.02	0.09
25	1105	-8.47	0.25	52.04	52.24	1.74	13.19	3.29	0.09	11.06	14.01	4.48	8.29	2.74	2.24	0.15	0.39	0.03	0.09

Appendix E6-1 (accompanying chapter 4) - PELE modelling

PELE modeling – justification for environmental conditions: since many of the most detailed studies were done on sills emplaced near the Fort Collinson Fm, pressures for V0 differentiation were estimated from the height of this overlying stratigraphic column, ca. 2.5 km, which translates to ca. 0.8 kb. All simulations were done at this pressure. Preliminary QUILF calculations by Bédard et al 2008 (Yellowknife geoscience forum poster) on v0 sills suggest QFM +1 t +2, so calculations were done at QFM+1 and +2, bracketing observed fO2 conditions. The gabbroic segment of the PELE models cannot exactly mimic the observed trends, however, because the PELE code does not include pigeonite, which is observed near the base of the gabbroic sequence in several V0 sills. Trace hornblende and biotite occur as rims on higher-temperature silicates in many sills, suggesting that some magmas were not entirely dry, such that extended in-situ fractional crystallization locally caused water contents to build up to the point where these phases were stabilized. An initial water content of 0.2% was assumed for some models, since 95% crystallization of such a starting point will yield the 4% H2O content needed to stabilize hornblende. Of course, F and Cl will stabilize these phases even at lower H2O contents. Limited data show that Hb and biotite in Franklin sills do indeed contain significant Cl and F-contents (up to 1-1.5 wt% combined F+Cl), but some water may also be present. There is no direct analytical data on H in these phases to constrain this at present. Melt CO2 solubilities are very low at these pressures, and initial staring contents were assumed to be ca 0.2% also. These values were varied. Typical S-contents of Franklin magmas are ca 0.04%, with some chilled margins recording higher values (up to ca 0.15%). Small Ni-Fe sulphide blebs in chills and olivine cumulates suggest early, small-scale sulphide immiscibility may be common. Even though PELE does not consider the effects of Cu and Ni on sulphide immiscibility, early Fe-sulfide melt exsolution is commonly observed in models that assumed higher initial S contents of ca 0.12%, and small amounts of sulfide exsolves intermittently throughout the model crystallization history. The amounts are always small, however, in keeping with the small amount of initial S in the melt. More evolved ferrogabbroic rocks typically contain Cu-Fe sulphide blebs. Models that assumed low initial S contents of ca 0.04% only showed immiscibility in the later crystallization history, often after cosaturation of magnetite. This suggests that the sharp decrease in FeO caused by magnetite crystallization often

triggers immiscibility by lowering S-solubility in the melt, which is strongly dependent on FeO content (Mavrogenes?). These results and observations imply that the v0 melts were probably very close to sulfide saturation, but that S contents were probably too low to create sulphide orebodies during closed-system crystallization. On the other hand, even minor assimilation of S-rich limestone or sulfates would probably trigger immiscible sulfide separation, with the amount of sulphide produced correlating directly to S-input.

Optimal PELE model run - A 3rd starting composition (C), attempted to mimic evolution of the Uhuk/P-Sill/LPS system using (initially) the average composition of the chilled margin and roof-dyke apophyses from the Uhuk massif, which have ca. 10.3 wt% MgO and 0.12 % S. In retrospect, the high S is probably the result of minor wallrock assimilation or exchange, and is probably higher than the magmatic value. V0 model D2, Uhuk2 #7 is used in the manuscript.

Appendix E7-2 – Element map descriptions and interpretations (accompanying Chapter 4)

1) 10RAT-BH166A03 – LBZ – a rare orthopyroxene (opx) crystal. BSE: euhedral orthopyroxene with co-crystallized plagioclase. Plagioclase is interstitial to olivine. Some olivine may be partially enclosed by the opx. Fe: twins are visible in the orthopyroxene. Enclosed olivines have less Fe than groundmass/interstitial olivine. Magnetite is visible in the groundmass and in fractured olivine. Cr: a Cr-rich band across the centre of the orthopyroxene crystal. Clinopyroxene to the left that is interstitial may also be sector-zoned? Minimal subhedral chromites in the groundmass. Ti: Ti pattern in the orthopyroxene is very similar to Cr. The northern rim of the orthopyroxene is Ti-enriched. Ilmenite is present in the groundmass. Al: Twinning in orthopyroxene is prominent. Interstitial plagioclase around the groundmass is dendritic-looking. Mg: Orthopyroxene crystal doesn't appear to show twinning in Mg. Chadacrystic olivines are more Mg-rich than groundmass olivines. Olivine in lower right of image appears to be partially intergrown with clinopyroxene.

2) 11RAT-BH311B02 – LOZ – zoned clinopyroxene crystal. BSE: Euhedral clinopyroxene crystal with a fine-grained olivine chadacryst in its core. Rim of the clinopyroxene is slightly irregular because of plagioclase impingement. Ti: hint of Ti-enrichment on clinopyroxene rim. Trace amounts of ilmenite may be visible? Cr: the western half of the clinopyroxene crystal is enriched in Cr. Possibly a broken crystal/xenocryst? A clinopyroxene crystal in the top left of the image shows sector-zoning. Ca: Ca shows the same behaviour as Cr. Some calcite/carbonate cement in the groundmass? Mg: Clinopyroxene crystal shows similar zoning pattern to Cr and Ca, though area rich in Mg is relatively depleted in Cr and Ca. Olivine is prominent, with some showing partial co-crystallization textures with both clinopyroxene and plagioclase. Al: Al behaves like Cr and Ca in the clinopyroxene crystal. Sector-zoned in the top left clinopyroxene is visible. The interstitial texture of plagioclase is prominent.

3) 11RAT-BH311B03 – UOZ – euhedral clinopyroxene crystal. BSE: a euhedral, cumulus-looking clinopyroxene crystal with a euhedral chromite and tabular olivine

inclusion. Ti: hint of Ti-enrichment in the rim of the clinopyroxene. Cr: clinopyroxene core is depleted, with a 'depleted-halo' surrounding the chromite crystal. Trace amounts of chromite visible in olivine and groundmass. Ca: Ca shows similar behaviour to Cr, though may be more convoluted. There appears to be a Ca-depleted core, a Ca-enriched mantle and Ca-depleted rim in the clinopyroxene crystal. Rim may wider in Ca than it appears in Cr. Mg: there are hints of a patchy Mg-enriched mantle in the clinopyroxene. The clinopyroxene rim appears depleted in Mg. Tabular olivine inclusion is visible, as well as surrounding skeletal olivines. Al: Al pattern in clinopyroxene is very complex; Al-enriched core with a radiating pattern of Al-enrichment and Al-depletion in the mantle/rim of the clinopyroxene.

4) 11RAT-BH311B03 – UOZ – a skeletal olivine crystal. BSE: a skeletal olivine with magnetite filled fractures, residing in interstitial plagioclase. Ti: local, fine-grained ilmenite crystals are present – usually associated with magnetite-filled fractures in olivine. Possible hint of Ti-enriched rims on clinopyroxene? Cr: euhedral clinopyroxene in the image are enriched in Cr with normal zoning. A clinopyroxene near the top of the image may have a Cr-depleted/xenocrystic core? Ca: Ca shows similar behaviour to Cr, with euhedral (cumulus?) clinopyroxene enriched in Ca. Mg: Olivine is prominent in the image. Euhedral clinopyroxene crystals are enriched. Some minor clinopyroxene inclusions in skeletal olivines? Al: The clinopyroxene at the top of the image has Al-behaviour resembling Cr, with prominent zoning (concentric zoning?). Interstitial plagioclase is clearly visible.

5) 11RAT-BH311B04 – CPZ – sector-zoned clinopyroxene crystal. BSE: a euhedral clinopyroxene crystal. Interstitial plagioclase (partly altered to albite?) also visible in the BSE image. Ti: hint of a Ti-enriched rim on the clinopyroxene. Minor ilmenite associated with the rims of clinopyroxene are visible. Cr: prominent sector-zoned is visible in the euhedral clinopyroxene. Sector-zoning is also discernable in other cpx crystals. Mg: faint sector-zoning visible in Mg but more complex? Sometimes Mg-high's correspond to Cr-high's and Cr-low's. Al: Al behaviour is coupled with Cr. Interstitial plagioclase is clearly visible, surrounding the sector-zoned clinopyroxene crystals. 6) 10RAT-BH167A05 – CPZ – subhedral clinopyroxene crystal. BSE: a subhedral clinopyroxene crystal with normal zoning. Fe: clinopyroxene is normally zoned with an Fe-enriched rim. Local alteration at the rim with Fe-enrichment

(magnetite?)? Cr: similar behaviour to Fe. Finer-grained cpx crystals either side of the larger cpx (synneusis?) appear to have Cr-rich rims; broken grains or resorbed? Ti: banded-like Ti-zoning in the large cpx crystal? Rims of Ti-enriched with ilmenite adjacent to these rims. Al: banded-like (or sector-zoned?) zoning resembling Cr. Interstitial (some partially intergrown with cpx?) plagioclase is visible. Mg: unclear, but possibly banded-like zoning similar to Cr/Al but with inverse enrichment.

7) 11RAT-BH311B06 – DZ – acicular clinopyroxene crystal. BSE: euhedral and twinned clinopyroxene crystal. Other more interstitial-looking cpx may be intergrown with interstitial plagioclase. Ti: hint of Ti-enrichment along the northern rim of the cpx crystal; with adjacent ilmenite crystals. Cr: southern rim of the cpx crystal is enriched in Cr (indicating growth direction towards the LPS upper contact). Ca: Ca behaves like Cr. Interstitial plagioclase alteration is visible. Mg: Mg is depleted at the northern rim of the cpx crystal with similar levels of enrichment in the rest of the cpx crystal. Al: similar behaviour to Cr/Ca, with Al-enrichment at the southern rim, and Al-depletion at the northern rim of the cpx crystal. Subhedral/interstitial cpx at the top left shows irregular Al-zoning. Interstitial plagioclase is prominent in the image with co-crystallization textures with interstitial cpx.

8) 10RAT-BH167A14 – UBZ – coarse clinopyroxene crystal amongst dendritic border zone groundmass. BSE: euhedral clinopyroxene showing normal zoning and co-plagioclase-crystallization textures at its rims. Fe: cpx is normally zoned with an Fe-enriched rim. Groundmass cpx is also Fe-enriched. Cr: homogeneous Cr-enrichment in the core of the cpx with a depleted rim (the inverse of Fe). Groundmass cpx shows no Cr-enrichment. Ti: Ti behaviour is closely related to Fe. Cpx rim shows Ti-enrichment. Groundmass cpx also shows Ti-enrichment. Minor ilmenite is present in the groundmass. Al: Al-behaviour in cpx appears to be very similar to Cr. Plagioclase impingement in the rims of the cpx are visible as are the habits of plagioclase dendrites/cpx dendrites. Mg: cpx is crudely normally zoned in Mg (similar behaviour to Cr-Ti-Al-Fe). Groundmass olivine is more depleted in Mg.

Appendix E7-1 – Element maps (accompanying Chapter 4)

1) 10RAT-BH166A03 - LBZ

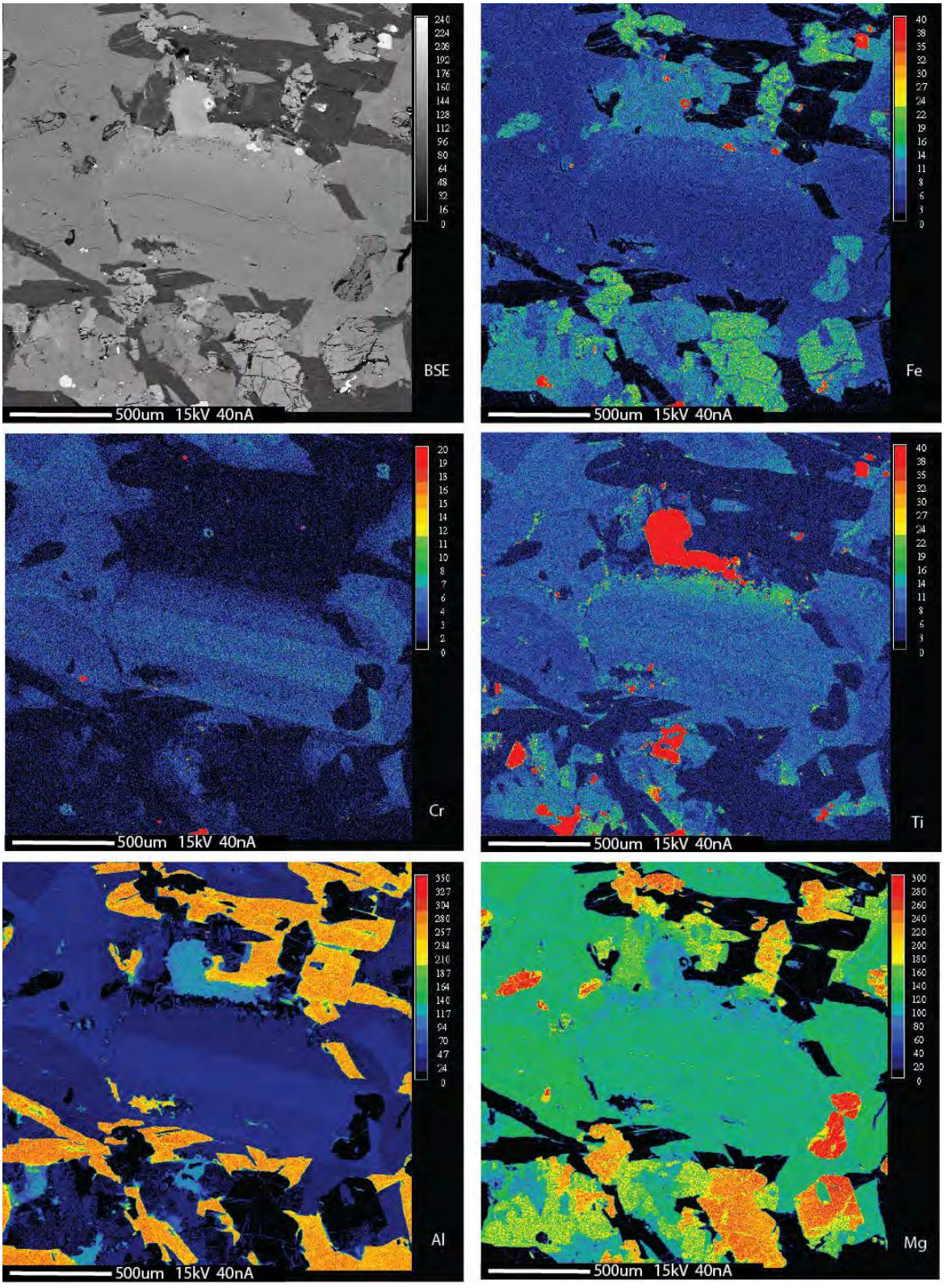

2) 11RAT-BH311B02 – LOZ

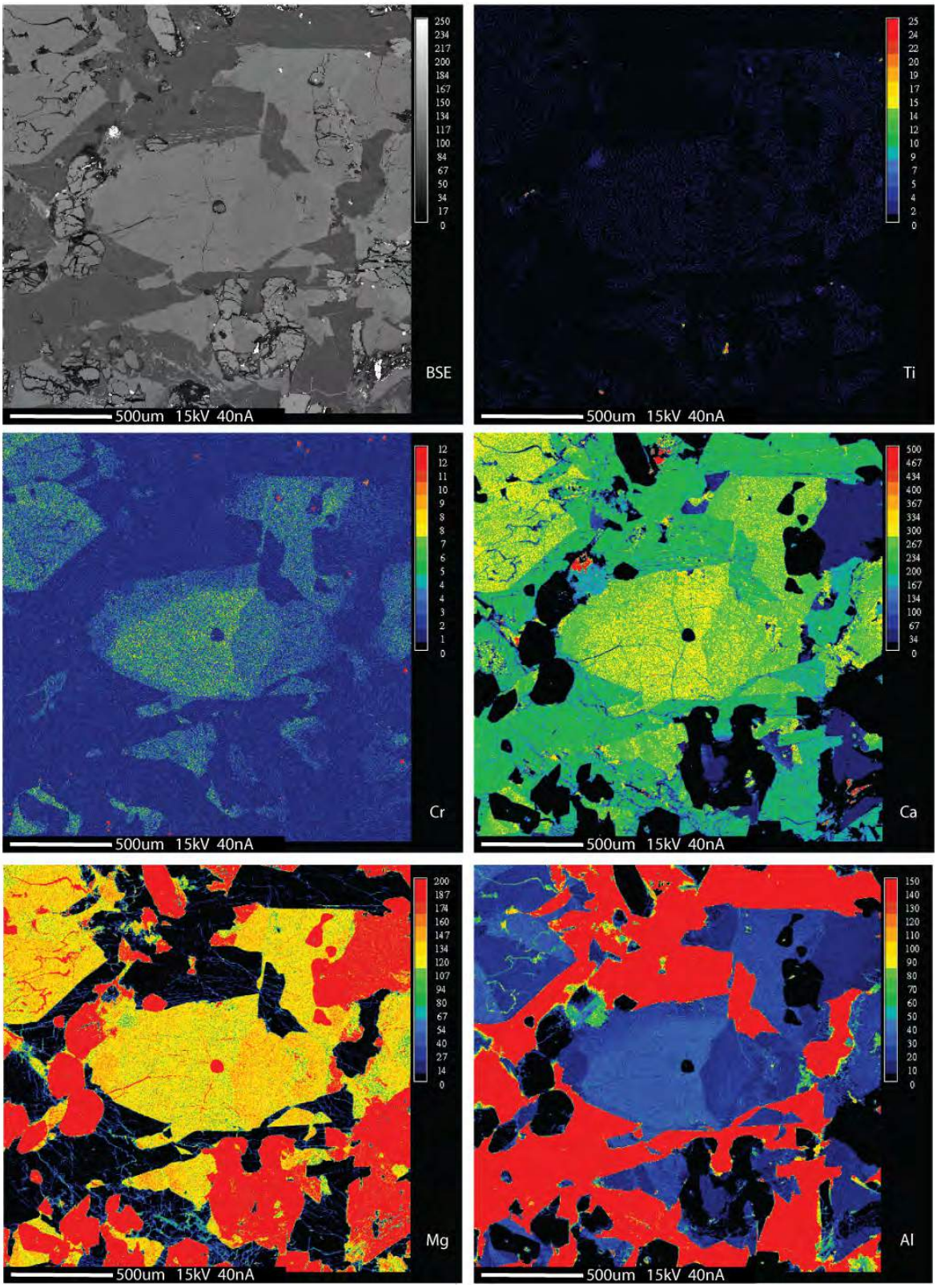

3) 11RAT-BH311B03 – UOZ

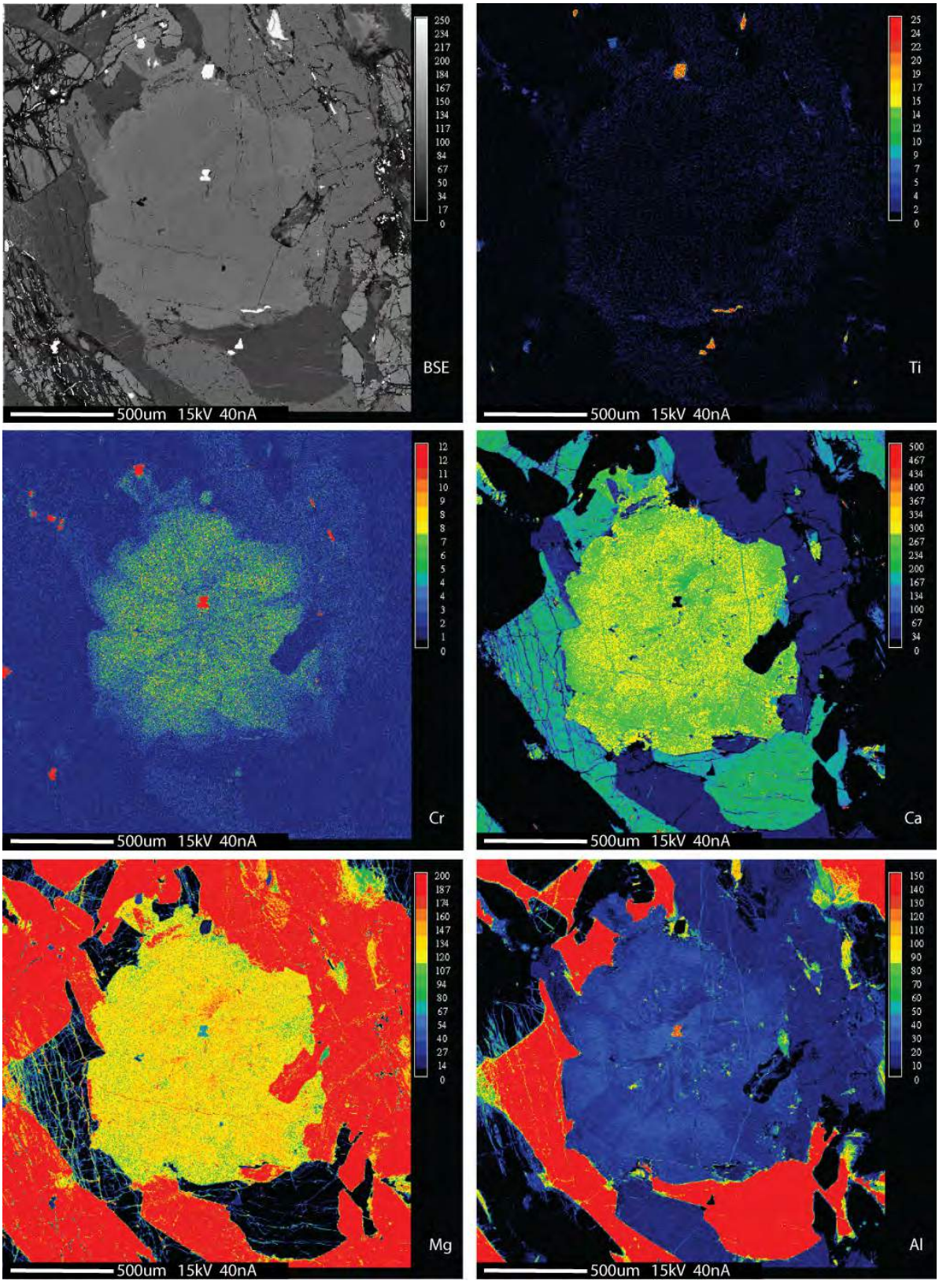

4) 11RAT-BH311B03 – UOZ

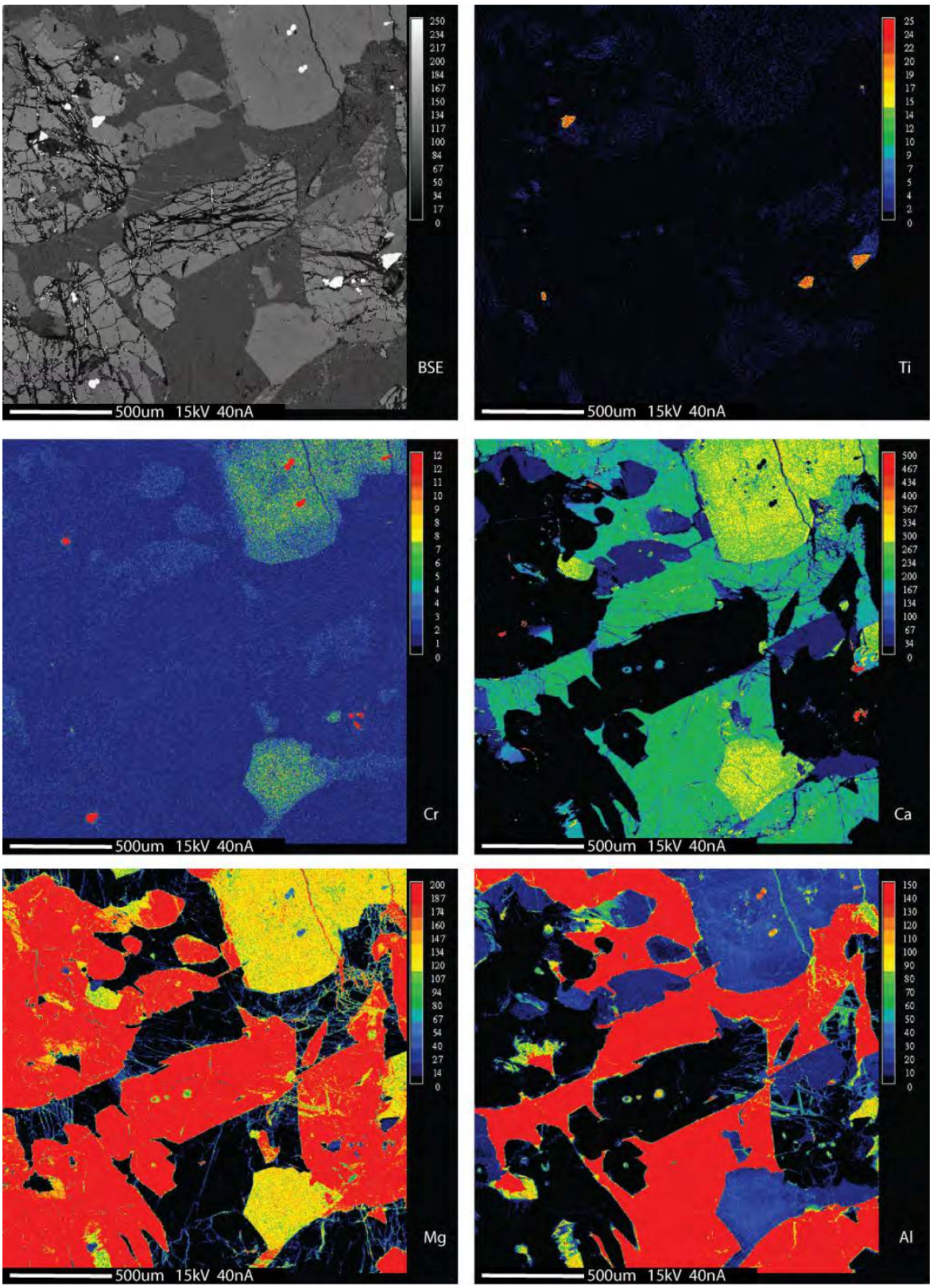

5) 11RAT-BH311B04 – CPZ

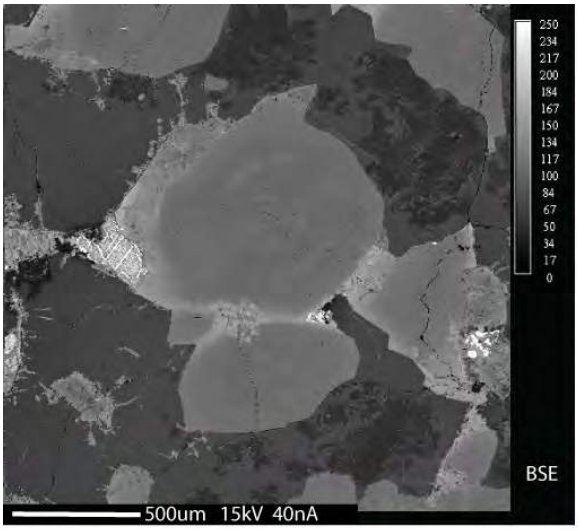

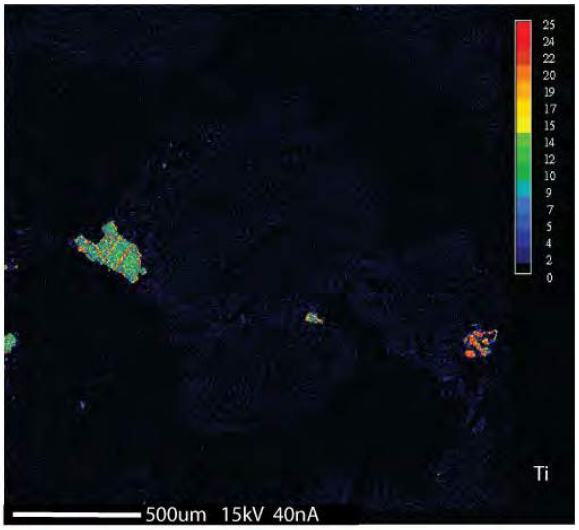

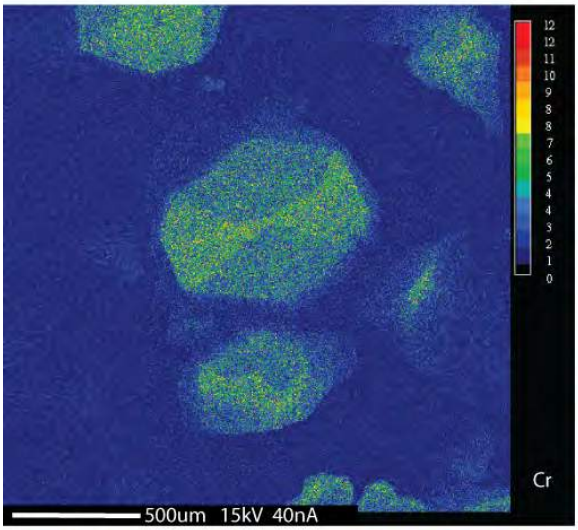

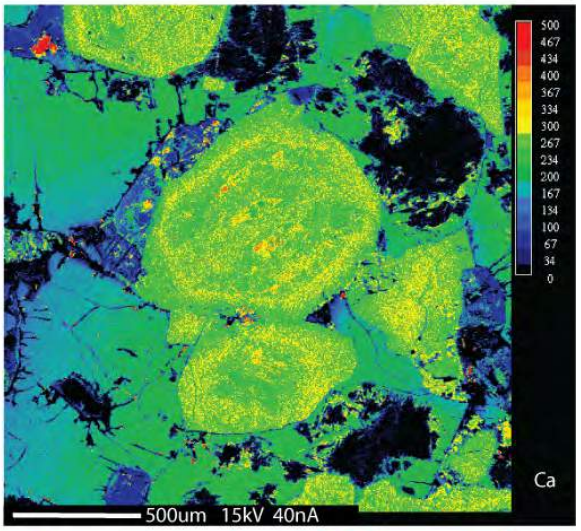

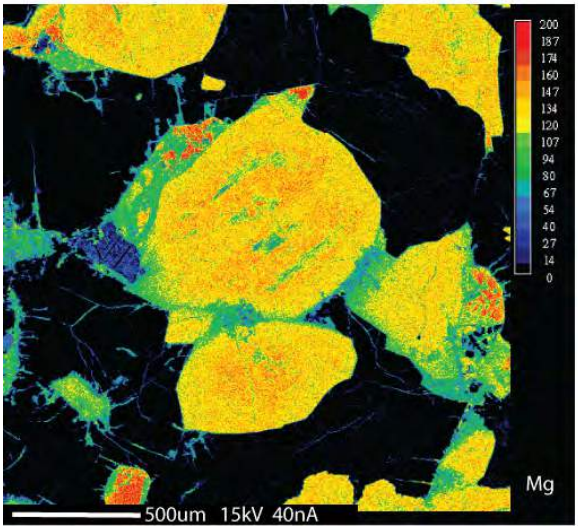

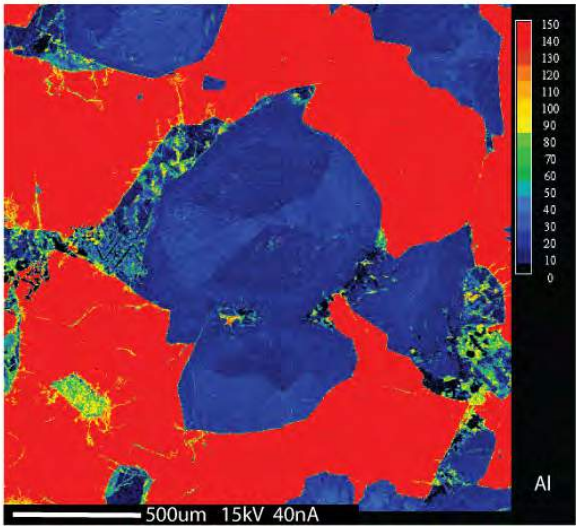

6) 10RAT-BH167A05 - CPZ

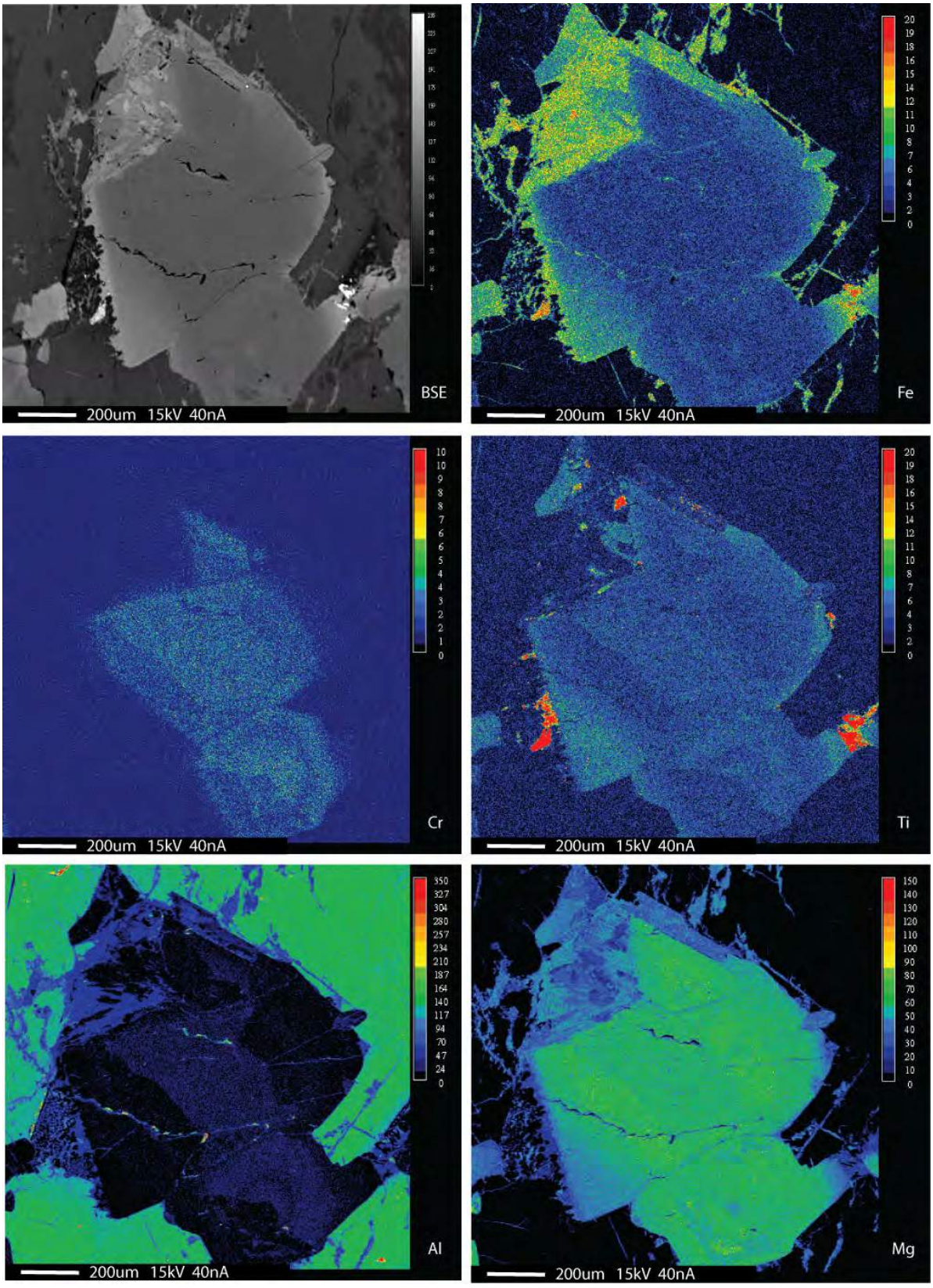

7) 11RAT-BH311B06 – DZ

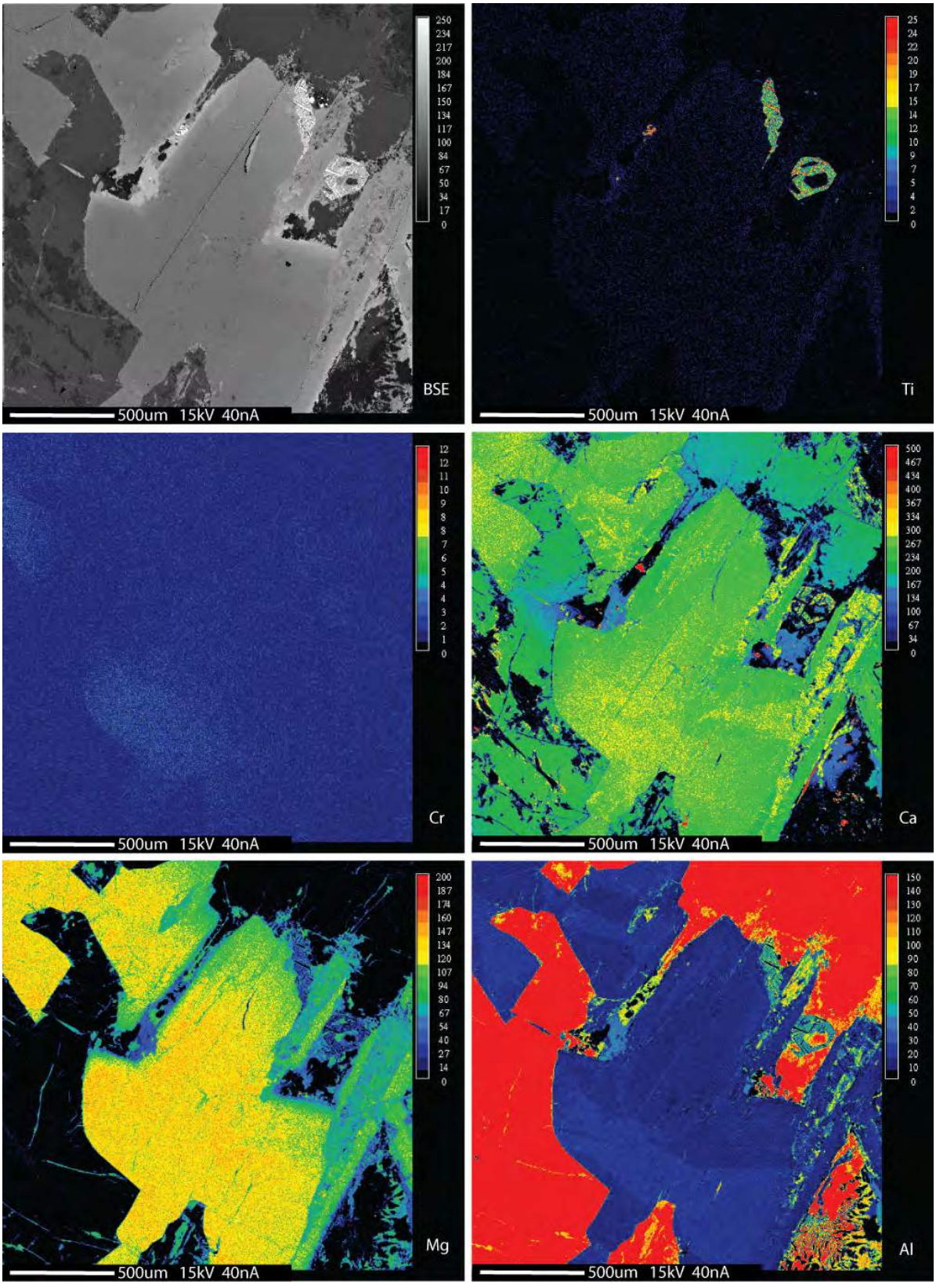

8) 10RAT-BH167A14 – UBZ

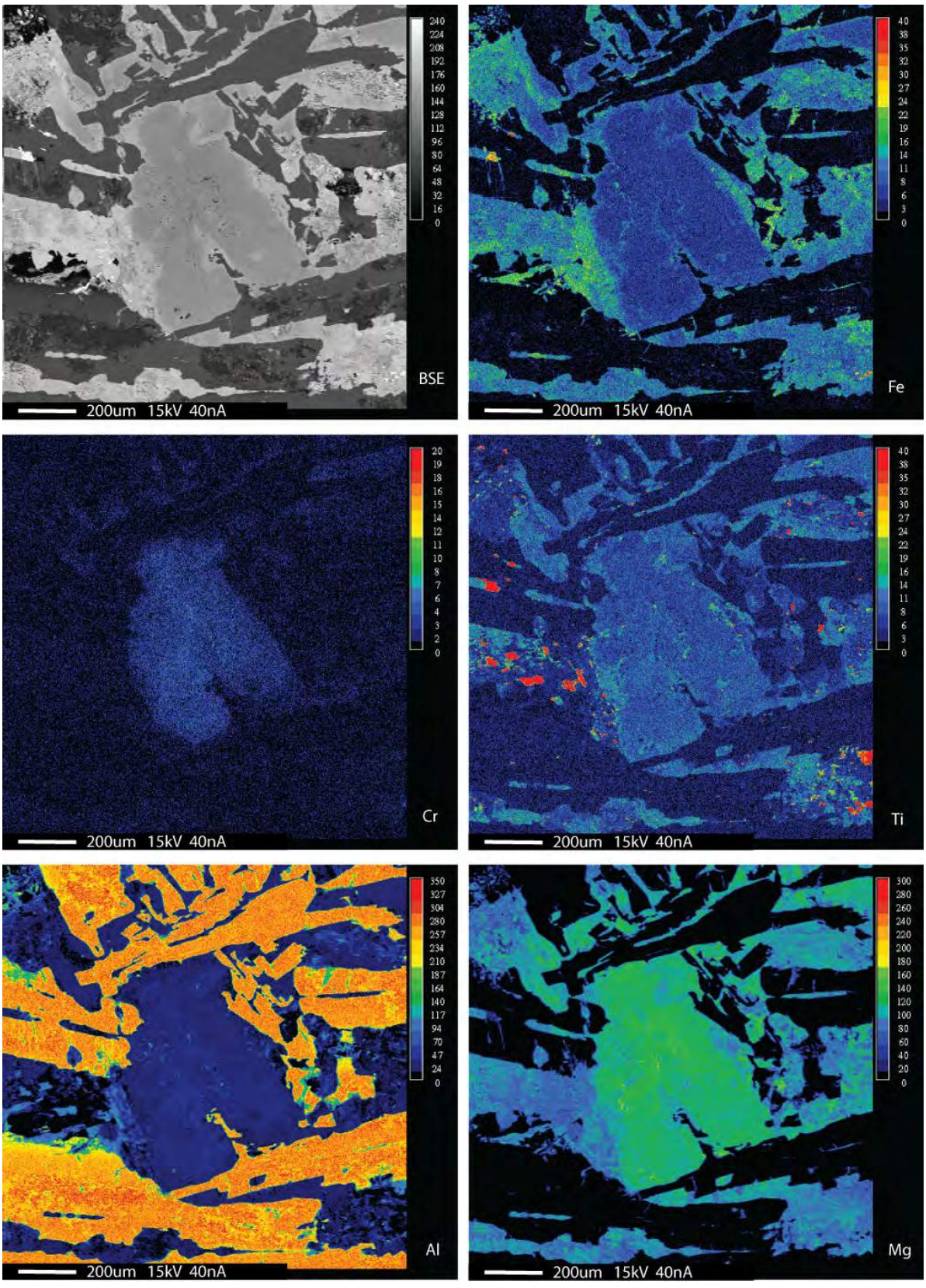

Appendix F1 – FCSC whole-rock data

INTRUSION	**LPS**	**LPS**	**LPS**	**LPS**	**LPS**	**LPS**	**LPS**
ZONE	LBZ	LBZ	OZ	OZ	OZ	OZ	OZ
LITHOLOGY	ol-gabbro	ol-gabbro	ol-gabbro	ol-gabbro	ol-gabbro	ol-gabbro	ol-gabbro
HEIGHT (m)	0.200	1.020	1.400	1.790	2.720	2.810	3.640
SAMPLE I.D.	**10BH166A2**	**10BH166A3**	**11BH311B2**	**10BH166A4**	**10BH166A5**	**10BH167A1**	**10BH167A2**
Lab	Cardiff	Cardiff	Cardiff	Cardiff	Cardiff	Cardiff	Cardiff
SiO2	46.471	45.073	44.357	44.006	44.491	43.659	42.389
TiO2	0.919	0.803	0.792	0.721	0.733	0.704	0.576
Al2O3	11.234	9.492	9.650	8.953	8.997	8.827	6.683
Fe2O3T	13.250	13.278	13.485	13.399	13.461	13.680	14.832
FeO*	11.912	11.937	12.123	12.046	12.101	12.299	13.334
Fe2O3*	1.338	1.341	1.362	1.353	1.360	1.382	1.498
MnO	0.189	0.188	0.196	0.191	0.197	0.185	0.204
MgO	15.321	17.841	19.643	20.688	19.950	21.418	23.519
CaO	10.162	9.649	9.327	8.921	8.811	7.966	6.473
Na2O	1.329	1.311	0.544	1.013	0.971	0.962	0.311
K2O	0.521	0.454	0.375	0.458	0.414	0.363	0.275
P2O5	0.073	0.068	0.065	0.061	0.063	0.060	0.052
LOI	1.546	1.391	1.565	1.644	1.925	2.230	5.776
SUM	101.016	99.547	100.000	100.056	100.011	100.054	101.090
ICP-OES (ppm)							
Sc	37.338	32.112	32.985	31.315	30.609	29.491	25.489
V	301.203	229.759	230.126	248.462	214.833	230.551	180.719
Cr	801.270	1039.579	1096.210	1364.362	1345.936	1314.779	1489.962
Co	63.429	61.791	61.894	62.755	63.185	65.824	64.520
Ni	325.367	403.375	451.197	723.231	453.780	536.045	640.872
Cu	98.701	91.309	83.047	80.678	103.995	91.063	64.891
Zn	74.591	72.214	76.352	82.765	82.037	76.284	58.904
Sr	143.942	106.225	104.842	110.067	96.208	98.102	60.147
Y	17.628	15.873	13.869	14.129	12.480	13.466	8.832
Zr	65.767	67.654	49.649	51.378	80.964	62.820	49.540
Ba	96.519	58.493	95.924	131.089	68.693	53.199	18.348
ICP-MS							
Ti	0.902	0.807	0.763	0.697	0.759	0.711	0.564
V	291.100	239.400	206.000	224.700	242.800	226.000	187.300
Cr	788.600	1030.200	1056.500	1371.500	1343.500	1278.300	1558.300
Co	66.500	59.100	60.100	58.900	63.700	65.100	67.800
Ni	287.000	390.500	430.800	717.300	442.400	526.800	626.800
Cu	93.500	89.700	74.800	72.100	101.000	80.800	66.600
Zn	71.600	76.900	60.600	77.100	86.400	67.400	75.300
Rb	20.400	17.000	10.400	15.300	16.100	13.600	10.300
K	5214.310	4542.210	3751.910	4581.020	4140.430	3627.980	2745.240
Sr	133.800	113.700	94.200	104.000	101.500	94.300	56.900
P	729.037	679.891	651.937	608.736	627.897	600.748	522.919
Y	18.100	16.500	11.600	14.100	14.000	13.600	9.700
Zr	69.700	69.900	51.100	59.300	81.400	62.800	45.400
Nb	3.630	3.500	2.210	2.780	2.970	3.080	1.970
Sn	0.690	0.800	0.710	1.270	0.720	0.850	0.560
Cs	0.910	0.810	0.550	0.590	0.790	0.770	1.210
Ba	108.900	71.600	88.900	137.500	80.200	67.200	53.300
La	6.610	6.390	4.530	5.660	5.570	5.710	3.480
Ce	15.340	14.300	10.450	12.960	12.630	12.930	8.010
Pr	2.090	1.930	1.410	1.760	1.760	1.720	1.130
Nd	9.090	8.550	6.160	7.670	7.450	7.320	4.950
Sm	2.380	2.150	1.680	1.960	2.070	1.860	1.300
Eu	0.770	0.740	0.550	0.650	0.630	0.620	0.440
Gd	2.650	2.480	1.790	2.190	2.160	2.060	1.390
Tb	0.430	0.430	0.300	0.360	0.340	0.340	0.250
Dy	2.830	2.730	2.010	2.320	2.350	2.300	1.600
Ho	0.500	0.500	0.360	0.430	0.430	0.440	0.280
Er	1.550	1.450	1.030	1.260	1.270	1.270	0.830
Tm	0.240	0.240	0.170	0.210	0.200	0.190	0.140
Yb	1.530	1.460	1.050	1.250	1.220	1.250	0.870

Lu	0.240	0.230	0.170	0.200	0.190	0.190	0.140
Hf	1.770	1.720	1.050	1.390	1.900	1.520	0.960
Ta	0.240	0.250	0.170	0.210	0.210	0.210	0.130
Pb	2.830	3.090	1.710	3.270	4.380	2.980	2.190
Th	1.400	1.360	0.870	1.170	1.310	1.230	0.690
U	0.270	0.260	0.200	0.240	0.240	0.260	0.140
Inversion models							
Fitted to MgO (wt %) of >	8.000	8.000	8.000	8.000	8.000	8.000	8.000
Th			1.569	1.790	2.005	1.941	1.700
Nb			4.012	4.272	4.564	4.883	4.910
Ta			0.300	0.317	0.317	0.327	0.309
La			8.216	8.694	8.555	9.048	8.661
Ce			18.938	19.896	19.389	20.476	19.906
Pr			2.553	2.700	2.700	2.722	2.804
P			1173.815	930.504	959.794	946.896	1284.183
Nd			11.109	11.737	11.400	11.551	12.192
Sm			3.005	2.983	3.151	2.918	3.155
Zr			91.413	90.259	123.896	98.525	110.194
Hf			1.878	2.116	2.892	2.385	2.330
Ti			1.364	1.061	1.156	1.115	1.368
Eu			0.984	0.989	0.959	0.973	1.068
Gd			3.177	3.316	3.270	3.213	3.325
Tb			0.530	0.544	0.513	0.529	0.594
Dy			3.556	3.505	3.550	3.579	3.806
Y			20.536	21.314	21.162	21.177	23.106
Ho			0.635	0.649	0.649	0.684	0.663
Er			1.813	1.898	1.913	1.970	1.958
Tm			0.299	0.316	0.301	0.295	0.330
Yb			1.834	1.873	1.828	1.928	2.023
Lu			0.297	0.300	0.285	0.293	0.326
Cr			949.663	1261.149	1235.402	1170.069	1355.043
Sc			48.471	41.670	40.730	39.999	44.405
Rb			18.817	23.463	24.689	21.511	25.520
Ba			160.325	210.406	122.724	106.044	131.281
U			0.361	0.367	0.367	0.410	0.345
Sr			170.159	159.314	155.484	148.983	140.563
Residual modes							
TMF			0.550	0.650	0.650	0.630	0.400
Olivine			0.450	0.350	0.350	0.370	0.600

INTRUSION	**LPS**	**LPS**	**LPS**	**LPS**	**LPS**	**LPS**	**LPS**	**LPS**
ZONE	OZ	OZ ROOF-1	OZ ROOF-2	CPZ	CPZ	DZ	DZ	DZ
LITHOLOGY	ol-gabbro	ol-gabbro	ol-gabbro	cpx-rich	cpx-rich	diabase	diabase	diabase
HEIGHT (m)	5.450	7.280	7.280	8.000	8.970	9.570	11.110	12.070
SAMPLE I.D.	**10BH167A3**	**10BH167A4**	**11BH311B3**	**11BH311B4**	**10BH167A5**	**10BH167A6**	**10BH167A7**	**10BH167A8**
Lab	Cardiff	Cardiff	Cardiff	Cardiff	Cardiff	Cardiff	Cardiff	Cardiff
SiO2	41.605	42.723	43.952	49.942	48.634	47.851	47.446	48.105
TiO2	0.549	0.693	0.637	0.902	0.944	1.023	1.052	0.964
Al2O3	6.563	8.070	7.897	10.551	12.075	13.590	14.118	14.386
Fe2O3T	14.137	13.992	14.431	10.109	11.002	11.962	12.025	10.712
FeO*	12.709	12.579	12.973	9.088	9.891	10.754	10.811	9.630
Fe2O3*	1.428	1.413	1.458	1.021	1.111	1.208	1.215	1.082
MnO	0.197	0.193	0.202	0.167	0.164	0.193	0.169	0.167
MgO	25.433	21.827	20.523	11.453	10.565	8.632	8.579	8.625
CaO	6.209	8.167	8.355	14.110	12.088	11.647	11.542	10.824
Na2O	0.405	0.812	0.781	1.264	1.506	1.841	1.758	1.831
K2O	0.270	0.306	0.260	0.847	1.023	1.044	1.352	1.977
P2O5	0.051	0.064	0.052	0.064	0.067	0.072	0.084	0.076
LOI	5.527	2.820	3.085	1.901	2.012	2.701	2.204	3.311
SUM	100.947	99.668	100.174	101.311	100.079	100.558	100.330	100.979

ICP-OES (ppm)								
Sc	24.136	30.251	31.452	56.368	49.546	42.598	41.397	40.741
V	166.999	205.681	200.964	363.709	342.559	346.740	343.431	321.218
Cr	1591.642	1244.937	1704.769	1945.740	1023.784	324.874	268.965	292.890
Co	64.578	64.637	61.531	49.618	50.940	58.931	55.089	50.374
Ni	622.833	512.994	562.236	124.712	80.923	56.405	87.370	68.101
Cu	89.048	92.100	63.983	87.659	95.804	104.588	108.387	91.037
Zn	119.319	123.834	55.870	54.004	80.284	61.370	75.458	43.058
Sr	58.729	91.154	80.446	166.629	206.172	234.867	305.276	318.651
Y	8.764	11.556	10.462	18.379	18.535	18.238	21.050	18.858
Zr	42.879	54.872	46.906	68.792	79.921	76.238	82.355	80.722
Ba	30.026	87.394	4.585	105.062	81.940	79.461	221.917	179.504
ICP-MS								
Ti	0.549	0.718	0.674	0.894	0.941	1.033	1.037	0.998
V	169.400	215.700	203.000	345.300	327.700	336.100	330.700	301.200
Cr	1618.300	1233.900	1655.900	1988.700	992.200	328.800	263.400	276.800
Co	68.400	63.600	58.500	50.300	55.900	54.100	52.200	51.400
Ni	621.300	513.600	579.300	114.300	79.000	55.600	85.400	64.500
Cu	62.200	86.900	57.800	86.500	91.600	106.400	105.300	90.600
Zn	128.500	137.300	73.600	49.600	80.300	58.800	67.200	38.800
Rb	11.800	12.700	9.400	23.800	28.100	31.400	37.400	70.800
K	2698.490	3061.850	2596.980	8474.670	10227.550	10444.530	13523.710	19766.510
Sr	59.300	92.100	75.200	166.700	200.100	228.400	277.700	302.300
P	514.886	639.414	516.623	640.057	671.018	718.881	841.732	758.709
Y	9.900	13.300	11.200	18.100	18.600	19.000	20.200	19.200
Zr	45.300	57.900	42.200	69.000	75.900	78.800	80.000	80.100
Nb	1.780	2.640	1.810	3.260	3.670	3.860	3.890	4.060
Sn	0.350	0.910	0.220	0.930	0.790	1.080	1.840	0.550
Cs	1.320	0.770	0.710	0.680	0.770	0.800	0.700	0.580
Ba	41.700	93.900	40.600	121.000	95.500	91.000	231.100	187.400
La	3.680	4.880	3.990	5.830	6.220	6.590	7.460	6.900
Ce	8.380	11.240	9.110	13.930	14.590	15.260	17.440	16.270
Pr	1.160	1.560	1.250	1.890	2.010	2.080	2.400	2.220
Nd	5.140	6.750	5.490	8.420	8.820	9.110	10.390	9.660
Sm	1.430	1.850	1.390	2.290	2.350	2.500	2.740	2.460
Eu	0.450	0.590	0.490	0.720	0.790	0.970	0.890	0.850
Gd	1.460	1.960	1.640	2.490	2.600	2.740	3.010	2.710
Tb	0.250	0.310	0.260	0.450	0.440	0.480	0.530	0.460
Dy	1.680	2.140	1.860	2.880	2.900	3.190	3.250	3.110
Ho	0.300	0.390	0.340	0.540	0.570	0.590	0.590	0.570
Er	0.920	1.210	0.980	1.590	1.650	1.720	1.810	1.680
Tm	0.140	0.190	0.150	0.250	0.240	0.260	0.280	0.260
Yb	0.870	1.190	1.040	1.510	1.570	1.680	1.720	1.660
Lu	0.150	0.180	0.160	0.250	0.250	0.260	0.270	0.260
Hf	1.020	1.330	0.940	1.680	1.760	2.050	2.220	2.010
Ta	0.140	0.170	0.150	0.220	0.250	0.270	0.290	0.270
Pb	1.870	2.770	1.770	1.850	1.960	2.760	2.400	2.210
Th	0.790	0.950	0.810	1.250	1.310	1.420	1.560	1.450
U	0.160	0.200	0.170	0.240	0.280	0.280	0.340	0.300
Inversion models								
Fitted to MgO (wt %) of >	8.000	8.000	8.000					
Model melts in ppm								
Th	1.946	1.573	1.604					
Nb	4.437	4.394	3.613					
Ta	0.333	0.277	0.290					
La	9.159	8.117	7.956					
Ce	20.825	18.684	18.147					
Pr	2.878	2.591	2.488					
P	1264.455	1057.231	1020.994					
Nd	12.660	11.175	10.871					
Sm	3.471	3.043	2.725					
Zr	109.951	95.230	82.745					
Hf	2.476	2.188	1.843					
Ti	1.334	1.181	1.321					

Eu	1.092	0.970	0.961					
Gd	3.493	3.203	3.184					
Tb	0.594	0.505	0.502					
Dy	3.996	3.488	3.598					
Y	23.583	21.689	21.684					
Ho	0.711	0.634	0.656					
Er	2.170	1.964	1.885					
Tm	0.330	0.308	0.288					
Yb	2.023	1.919	1.981					
Lu	0.349	0.290	0.305					
Cr	1407.217	1121.727	1471.911					
Sc	42.048	42.250	48.762					
Rb	29.237	21.082	18.688					
Ba	102.709	155.464	80.396					
U	0.394	0.331	0.337					
Sr	146.492	152.686	149.206					
Residual modes								
TMF	0.400	0.600	0.500					
Olivine	0.600	0.400	0.500					

INTRUSION	**LPS**	**LPS**	**LPS**	**LPS**	**LPS**	**LPS**	**LPS**	**LPS**
ZONE	DZ	DZ	DZ	DZ	DZ	UBZ	UBZ	UCZ-1
LITHOLOGY	diabase	diabase	diabase	diabase	diabase	fg diabase	fg diabase	aphanitic
HEIGHT (m)	12.710	14.000	15.700	16.880	19.700	20.680	20.880	21.430
SAMPLE I.D.	**10BH167A9**	**11BH311B6**	**10BH167A10**	**10BH167A11**	**10BH167A12**	**10BH167A14**	**11BH311B7**	**10BH167A15**
Lab	Cardiff	Cardiff	Cardiff	Cardiff	Cardiff	Cardiff	Cardiff	Cardiff
SiO2	46.588	47.884	46.621	47.954	47.146	48.608	48.341	45.701
TiO2	1.237	1.184	1.172	1.026	1.067	1.022	1.079	1.007
Al2O3	13.362	14.243	13.506	12.884	13.068	12.871	13.084	12.240
Fe2O3T	13.809	12.215	11.680	12.291	12.258	12.561	12.206	12.274
FeO*	12.414	10.981	10.501	11.049	11.020	11.292	10.973	11.034
Fe2O3*	1.395	1.234	1.180	1.241	1.238	1.269	1.233	1.240
MnO	0.178	0.185	0.172	0.195	0.185	0.189	0.187	0.190
MgO	8.011	8.460	7.922	8.852	8.812	9.178	8.681	10.491
CaO	9.813	11.261	11.291	10.265	11.031	12.058	12.036	11.510
Na2O	2.398	1.778	2.014	1.665	1.516	1.601	1.635	1.901
K2O	1.170	1.258	1.066	1.612	1.547	0.983	1.131	0.877
P2O5	0.090	0.085	0.090	0.084	0.089	0.085	0.086	0.083
LOI	4.087	2.203	3.525	3.125	2.613	2.036	2.395	2.721
SUM	100.742	100.756	99.060	99.953	99.332	101.193	100.861	111.270
Sc	40.415	41.333	39.927	41.081	40.976	41.233	42.139	39.586
V	407.444	372.683	346.257	298.195	311.704	328.094	317.668	332.612
Cr	153.473	266.179	211.518	147.432	172.221	615.423	609.521	782.803
Co	66.124	57.052	57.519	54.510	55.329	58.376	52.496	59.896
Ni	80.701	61.527	75.320	66.057	62.455	91.307	81.361	132.918
Cu	102.888	108.183	152.625	95.982	104.134	128.052	122.438	112.439
Zn	48.001	116.808	44.137	39.167	54.472	76.399	28.256	59.533
Sr	240.897	261.357	247.229	224.427	232.326	231.139	226.091	203.720
Y	20.961	21.448	21.537	18.249	18.882	18.286	19.160	19.067
Zr	81.169	81.136	92.382	88.942	73.837	77.295	75.579	87.164
Ba	140.940	143.081	112.716	211.527	161.288	125.344	174.296	109.987
Ti	1.268	1.192	1.178	1.052	1.037	1.055	1.058	0.982
V	390.800	350.200	333.100	309.500	318.800	347.200	315.900	319.300
Cr	157.100	249.300	211.700	148.300	162.100	590.500	586.300	779.900
Co	70.300	55.600	53.100	56.000	54.500	58.700	56.800	60.100
Ni	75.800	62.800	73.900	61.100	65.900	85.700	83.600	128.100
Cu	96.900	108.500	152.200	107.200	110.000	133.500	124.100	119.200
Zn	47.900	124.600	37.300	36.900	54.200	75.500	51.300	57.300
Rb	39.800	37.200	35.400	52.500	40.800	34.300	27.200	9.900
K	11704.800	12584.770	10655.670	16124.630	15465.690	9834.860	11313.220	8774.260

Sr	222.400	254.400	242.300	232.300	234.700	232.000	229.900	209.100
P	896.020	853.701	896.202	836.117	890.748	854.826	861.778	828.765
Y	21.000	21.900	22.700	21.200	20.200	20.000	21.300	20.400
Zr	85.300	81.300	90.000	86.500	79.300	77.600	80.500	85.900
Nb	4.440	4.000	4.800	4.320	3.920	3.550	4.290	3.960
Sn	1.010	0.990	0.940	0.830	0.630	1.210	1.070	1.230
Cs	0.360	1.110	0.370	0.840	1.280	1.810	0.540	0.370
Ba	146.500	157.000	121.600	211.800	157.400	127.900	195.000	126.200
La	7.550	7.940	7.970	7.640	7.530	7.920	8.000	7.330
Ce	17.340	18.340	19.100	17.600	17.150	17.840	18.530	17.280
Pr	2.340	2.510	2.590	2.420	2.330	2.410	2.540	2.340
Nd	10.330	10.640	11.510	10.500	10.370	10.400	10.780	10.410
Sm	2.880	2.820	2.940	2.740	2.740	2.780	2.810	2.850
Eu	1.130	1.020	1.030	0.930	0.910	0.910	0.960	0.880
Gd	2.980	3.250	3.370	3.060	2.980	2.980	3.040	3.050
Tb	0.530	0.530	0.620	0.500	0.520	0.500	0.540	0.530
Dy	3.430	3.520	3.720	3.260	3.320	3.240	3.450	3.390
Ho	0.630	0.660	0.690	0.590	0.600	0.580	0.610	0.610
Er	1.870	1.900	2.000	1.800	1.790	1.750	1.840	1.780
Tm	0.300	0.290	0.310	0.280	0.280	0.280	0.290	0.280
Yb	1.890	1.800	2.040	1.850	1.730	1.760	1.810	1.750
Lu	0.290	0.300	0.310	0.280	0.290	0.270	0.280	0.270
Hf	2.190	2.080	2.390	2.070	2.030	1.900	2.030	2.180
Ta	0.300	0.320	0.350	0.280	0.260	0.290	0.310	0.290
Pb	1.560	1.740	1.720	1.610	1.300	2.630	2.430	3.350
Th	1.630	1.720	1.850	1.560	1.430	1.690	1.700	1.800
U	0.350	0.350	0.370	0.310	0.320	0.370	0.340	0.360

INTRUSION	**LPS**	**LPS**	**LPS**	**WUS**	**WUS**	**UHUK MASSIF**	**UHUK MASSIF**
ZONE	UCZ-2	LCZ	UCZ				
LITHOLOGY	aphanitic	aphanitic	aphanitic	chill	chill	small dike	small dike
HEIGHT (m)	21.430	0.000	0.000				
SAMPLE I.D.	**11BH311B8**	**11JB327B1**	**11JB328B1**	**10NW037C1**	**10NW038A1**	**10JB160B1**	**10JB160B2**
Lab	Cardiff	INRS, Quebec	INRS, Quebec	INRS, Quebec	INRS, Quebec	INRS, Quebec	INRS, Quebec
SiO2	46.081	48.278	48.000	48.259	47.823	48.083	47.476
TiO2	1.020	1.023	1.048	0.989	0.931	0.989	0.972
Al2O3	12.529	12.763	12.776	13.144	12.956	13.219	13.078
Fe2O3T	11.983	11.135	11.329	11.812	12.161	11.153	11.091
FeO*	10.773	10.010	10.185	10.619	10.932	10.027	9.971
Fe2O3*	1.210	1.125	1.144	1.193	1.228	1.126	1.120
MnO	0.151	0.147	0.152	0.158	0.169	0.149	0.145
MgO	10.883	10.743	10.323	10.465	10.515	9.413	9.413
CaO	10.263	12.255	10.159	11.193	12.067	12.287	11.707
Na2O	2.569	1.526	2.451	1.806	1.647	1.921	2.029
K2O	0.603	0.557	0.500	1.097	0.632	1.059	1.548
P2O5	0.083	0.087	0.092	0.081	0.068	0.079	0.082
LOI	2.965	1.443	2.673	1.818	1.513	1.204	2.131
SUM	111.113	100.254	99.777	101.178	100.942	99.841	100.159
ICP-OES (ppm)							
Sc	41.232	38.906	39.497	37.374	37.969	37.621	37.191
V	335.438	299.460	306.207			279.057	278.312
Cr	734.756	660.194	688.506			511.276	506.349
Co	55.411	45.109	52.274			40.414	46.505
Ni	260.662	218.871	200.659			148.769	157.283
Cu	120.053	133.257	148.530			78.401	82.513
Zn	98.873	42.689	52.096			56.134	48.260
Sr	273.861	140.284	251.900			462.455	1024.056
Y	20.095	19.000	19.000			20.000	18.000
Zr	82.760	72.000	65.000			66.200	102.000
Ba	88.756	132.823	109.494			182.506	357.273
ICP-MS							

Ti	1.032	#REF!	#REF!	#REF!	#REF!	#REF!	#REF!
V	336.300	299.460	306.207	278.632	283.854		
Cr	723.500	660.194	688.506	672.582	696.834		
Co	60.100	45.109	52.274	43.390	52.983		
Ni	246.800	218.871	200.659	212.890	230.816		
Cu	125.200	133.257	148.530	75.519	135.193		
Zn	95.400	42.689	52.096	55.387	85.043		
Rb	15.100	24.000	13.300	28.000	20.700	36.600	44.200
K	6034.240	4621.826	4149.848	9110.821	5247.524	8795.409	12850.823
Sr	252.100	140.284	251.900	477.476	311.910	462.455	1024.056
P	826.519	381.632	403.103	353.054	296.195	4916.171	4888.903
Y	19.900	19.000	19.000	17.800	16.700	20.000	18.000
Zr	82.900	72.000	65.000	60.500	52.000	66.200	102.000
Nb	4.190	4.600	4.580	4.510	4.160	5.140	5.030
Sn	0.940						
Cs	0.600	1.320	0.600	1.490	1.210	2.100	8.900
Ba	103.000	132.823	109.494	290.650	130.420	182.506	357.273
La	6.800	6.800	6.400	7.200	6.700	8.400	7.200
Ce	16.330	16.300	16.100	15.500	13.900	17.200	17.100
Pr	2.250	2.500	2.400	2.300	2.000	2.600	2.500
Nd	9.990	10.700	10.500	10.400	10.200	12.200	10.600
Sm	2.750	2.700	2.800	3.000	2.500	3.000	2.800
Eu	0.740	0.870	0.770	0.820	0.780	0.970	0.790
Gd	2.950	3.180	3.110	2.810	2.510	3.050	2.980
Tb	0.510	0.540	0.520	0.530	0.470	0.560	0.530
Dy	3.260	3.200	3.200	3.030	3.130	3.520	3.100
Ho	0.590	0.680	0.650	0.600	0.560	0.700	0.630
Er	1.710	1.840	1.860	1.680	1.700	1.960	1.860
Tm	0.270	0.260	0.260	0.250	0.220	0.280	0.250
Yb	1.750	1.750	1.740	1.700	1.610	1.810	1.720
Lu	0.270	0.260	0.250	0.230	0.230	0.270	0.250
Hf	2.040	1.870	1.790	1.790	1.600	1.860	2.610
Ta	0.280	<0.3	0.300	< 0.3	< 0.3	0.330	0.350
Pb	1.730	1.510	1.060	2.000	3.620	3.250	4.500
Th	1.560	0.600	0.700	1.620	1.300	2.000	< 0.7
U	0.340	0.210	0.200	0.270	0.190	0.450	0.400

INTRUSION	**PS**	**PS**	**PS**	**PS**	**PS**	**PS**	**PS**
ZONE	LBZ	LBZ	LBZ	OZ	OZ	OZ	OZ
LITHOLOGY							
HEIGHT (m)							
SAMPLE I.D.	**10JB287A1**	**10JB367A1**	**10JB367B1**	**10JB367C1**	**10JB367E1**	**10JB367G1**	**10JB367H1**
Lab	INRS, Quebec	INRS, Quebec	INRS, Quebec	INRS, Quebec	INRS, Quebec	INRS, Quebec	INRS, Quebec
SiO2	46.709	46.815	45.891	46.265	44.798	45.248	44.889
TiO2	0.761	0.861	0.776	0.781	0.677	0.699	0.656
Al2O3	9.974	11.111	9.780	9.629	8.673	8.664	8.528
Fe2O3T	12.900	12.875	13.023	13.144	13.075	13.368	13.291
FeO*	11.597	11.575	11.708	11.816	11.754	12.017	11.948
Fe2O3*	1.303	1.300	1.315	1.327	1.321	1.350	1.342
MnO	0.189	0.188	0.187	0.188	0.185	0.189	0.190
MgO	17.827	15.637	17.911	18.460	20.759	21.581	22.083
CaO	8.488	9.746	8.748	8.410	7.455	7.661	7.646
Na2O	1.110	1.120	1.001	0.997	0.872	0.809	0.750
K2O	0.480	0.470	0.448	0.422	0.368	0.283	0.280
P2O5	0.064	0.061	0.063	0.061	0.049	0.053	0.054
LOI	1.940	1.498	2.104	2.260	2.633	2.353	2.552
SUM	100.724	100.660	100.216	100.902	99.814	101.201	101.258
ICP-OES (ppm)							
Sc	30.049	33.213	30.189	29.959	26.980	27.686	27.543
V							
Cr							
Co							
Ni							

Cu							
Zn							
Sr							
Y							
Zr							
Ba							
ICP-MS							
Ti	0.761	0.861	0.776	0.782	0.677	0.700	0.656
V	220.529	249.049	231.223	229.306	194.702	206.674	206.186
Cr	976.403	874.433	1033.881	1019.141	888.763	1206.526	1520.895
Co	67.746	61.931	72.595	72.723	77.503	81.584	85.347
Ni	511.649	549.269	525.578	566.507	671.256	685.003	732.561
Cu	105.870	121.532	120.388	103.780	100.425	94.949	116.600
Zn	82.583	90.330	69.791	91.370	93.100	64.989	69.587
Rb	18.500	17.700	14.700	14.600	12.400	9.400	9.500
K	3988.100	3902.579	3715.648	3501.683	3058.421	2350.845	2324.680
Sr	115.942	126.808	112.429	106.760	94.352	90.789	87.993
P	277.716	268.193	275.032	267.844	215.876	231.351	234.740
Y	15.000	14.600	14.300	15.000	11.600	12.500	12.500
Zr	51.000	52.000	58.000	62.000	47.000	43.000	42.000
Nb	3.660	3.690	3.650	4.000	3.170	2.860	2.920
Sn							
Cs	1.130	0.500	0.700	0.500	0.130	1.260	0.400
Ba	86.832	85.240	80.287	81.807	70.184	59.686	55.531
La	7.000	6.400	6.500	7.100	5.700	5.000	4.900
Ce	14.700	13.200	14.000	15.600	11.500	10.900	10.800
Pr	2.000	2.000	1.900	2.000	1.730	1.510	1.530
Nd	9.400	9.600	8.040	8.540	8.180	7.300	6.490
Sm	2.300	2.500	2.100	2.200	2.000	1.900	1.720
Eu	0.740	0.820	0.670	0.720	0.660	0.590	0.620
Gd	2.370	2.480	2.430	2.530	1.980	1.890	2.110
Tb	0.410	0.410	0.410	0.430	0.330	0.340	0.350
Dy	2.680	2.920	2.400	2.400	2.390	2.160	2.100
Ho	0.510	0.580	0.530	0.540	0.450	0.430	0.460
Er	1.480	1.600	1.490	1.540	1.280	1.260	1.300
Tm	0.220	0.230	0.210	0.210	0.190	0.175	0.177
Yb	1.360	1.510	1.370	1.430	1.210	1.090	1.230
Lu	0.200	0.220	0.200	0.220	0.180	0.168	0.180
Hf	1.470	1.470	1.610	1.740	1.330	1.210	1.260
Ta	< 0.3	< 0.3	<0.3	<0.3	< 0.3	< 0.3	<0.3
Pb	3.400	2.100	1.570	1.760	1.900	1.900	1.080
Th	1.620	1.470	0.800	0.900	1.200	1.000	1.100
U	0.250	0.240	0.260	0.310	0.210	0.131	0.210

INTRUSION	**PS**	**PS**	**PS**	**PS**	**PS**	**PS**	**PS**	**PS**
ZONE	DZ!	OZ	OZ	OZ	CPZ	DZ	DZ	DZ
LITHOLOGY								
HEIGHT (m)								
SAMPLE I.D.	**10JB367J1**	**10JB368A1**	**10JB368B1**	**10JB368G1**	**10JB368D1**	**10JB290A1**	**10JB367I1**	**10JB369A1**
Lab	INRS, Quebec	INRS, Quebec	INRS, Quebec	INRS, Quebec	INRS, Quebec	INRS, Quebec	INRS, Quebec	INRS, Quebec
SiO2	49.063	43.495	43.499	43.900	49.124	49.882	43.433	48.644
TiO2	1.179	0.616	0.702	0.681	0.880	1.215	0.606	1.259
Al2O3	14.513	8.028	8.339	8.410	11.006	14.243	7.723	15.219
Fe2O3T	12.457	13.238	13.470	13.677	10.353	13.218	13.279	13.087
FeO*	11.199	11.901	12.110	12.295	9.307	11.883	11.938	11.765
Fe2O3*	1.258	1.337	1.360	1.381	1.046	1.335	1.341	1.322
MnO	0.177	0.186	0.195	0.197	0.183	0.197	0.187	0.185
MgO	7.023	23.150	20.424	20.806	11.375	7.270	23.336	6.077
CaO	10.355	7.081	7.577	7.732	13.263	10.799	6.869	9.395
Na2O	1.748	0.645	0.793	0.801	1.183	1.740	0.456	1.887
K2O	1.537	0.314	0.417	0.386	1.071	1.335	0.354	1.470

P2O5	0.097	0.045	0.058	0.055	0.062	0.104	0.042	0.109
LOI	2.176	3.470	4.251	3.477	1.815	1.448	4.005	2.689
SUM	100.545	100.756	100.084	100.483	100.640	101.637	100.798	100.253
ICP-OES (ppm)								
Sc	37.406	25.140	28.660	28.823	50.667	38.651	25.057	31.949
V								
Cr								
Co								
Ni								
Cu								
Zn								
Sr								
Y								
Zr								
Ba								
ICP-MS								
Ti	1.179	0.616	0.702	0.681	0.881	1.215	0.606	1.259
V	308.835	196.651	205.289	208.894	295.776	333.911	196.506	309.452
Cr	123.766	3126.391	1965.958	1973.188	1516.208	80.726	3203.112	55.127
Co	41.882	77.016	78.664	81.629	41.239	41.447	88.282	48.340
Ni	74.149	726.957	548.652	541.335	143.339	82.241	778.038	82.955
Cu	155.524	89.884	99.502	96.979	118.320	171.616	89.036	193.099
Zn	82.465	78.038	93.744	68.003	164.731	101.142	84.678	78.185
Rb	47.300	9.800	11.900	10.900	25.900	41.000	12.200	47.400
K	12757.895	2609.399	3458.906	3203.613	8892.019	11083.326	2940.067	12201.306
Sr	325.433	82.457	90.970	87.649	201.929	235.502	84.111	325.847
P	424.789	197.764	255.153	240.710	269.191	452.342	185.145	477.326
Y	22.100	10.900	11.800	12.600	15.400	21.000	10.400	24.000
Zr	81.300	37.000	43.000	44.000	52.000	82.000	38.000	91.000
Nb	5.600	2.420	2.990	2.780	3.500	4.910	2.600	5.850
Sn								
Cs	0.980	0.640	0.260	0.980	< 0.12	1.540	0.600	0.910
Ba	193.346	51.210	58.603	56.110	135.817	159.652	54.158	189.377
La	9.500	3.800	5.000	4.800	5.900	8.600	4.100	10.500
Ce	19.900	8.620	10.100	10.800	12.300	20.200	9.400	22.200
Pr	3.000	1.250	1.560	1.510	1.900	2.800	1.290	3.200
Nd	14.000	6.040	7.460	7.030	9.400	12.200	5.510	14.900
Sm	3.500	1.550	1.900	1.800	2.400	3.100	1.500	3.800
Eu	1.130	0.560	0.640	0.610	0.800	0.970	0.510	1.200
Gd	3.630	1.590	1.920	1.870	2.510	3.430	1.770	3.830
Tb	0.650	0.300	0.330	0.340	0.430	0.580	0.300	0.690
Dy	4.180	1.850	2.340	2.170	3.060	3.500	1.770	4.210
Ho	0.830	0.370	0.460	0.430	0.600	0.740	0.380	0.830
Er	2.300	1.050	1.290	1.220	1.720	2.060	1.020	2.390
Tm	0.340	0.154	0.180	0.178	0.250	0.290	0.141	0.340
Yb	2.170	0.950	1.180	1.160	1.540	1.970	0.970	2.240
Lu	0.310	0.140	0.174	0.164	0.230	0.280	0.157	0.330
Hf	2.260	0.950	1.240	1.210	1.490	2.220	1.120	2.470
Ta	0.300	< 0.3	< 0.3	< 0.3	< 0.3	0.300	<0.3	0.300
Pb	1.340	3.300	1.560	1.470	0.730	2.800	1.680	2.100
Th	2.100	1.000	1.100	1.000	1.100	< 0.7	< 0.7	2.100
U	0.330	0.125	0.161	0.120	0.200	0.220	0.152	0.330

INTRUSION	**WUS**	**WUS**	**WUS**	**WUS**	**WUS**	**WUS**	**WUS**	**WUS**
ZONE	LBZ	LBZ	LBZ	LBZ	LBZ	LBZ	OZ	OZ
LITHOLOGY								
HEIGHT (m)								
SAMPLE I.D.	**0723A001**	**0723A002**	**0723A002**	**0726A008 C**	**0726A008 D**	**0726A008 E**	**0723A003**	**0723A004**
Lab	INRS, Quebec	INRS, Quebec	INRS, Quebec	INRS, Quebec	INRS, Quebec	INRS, Quebec	INRS, Quebec	INRS, Quebec
SiO2	45.500	45.680	45.680	46.920	45.220	46.380	44.460	42.590
TiO2	0.710	0.720	0.720	0.730	0.680	0.640	0.620	0.520
Al2O3	9.640	9.920	9.920	10.080	9.190	8.960	8.550	7.500

Fe2O3T	12.610	12.370	12.370	12.430	12.640	13.800	12.350	12.920
FeO*	11.336	11.121	11.121	11.175	11.363	12.406	11.103	11.615
Fe2O3*	1.274	1.249	1.249	1.255	1.277	1.394	1.247	1.305
MnO	0.180	0.170	0.170	0.170	0.170	0.180	0.170	0.180
MgO	19.720	18.430	18.430	17.210	18.620	19.190	20.710	23.070
CaO	8.250	8.240	8.240	8.310	7.920	7.880	7.130	6.210
Na2O	1.090	1.100	1.100	1.130	1.190	1.070	0.920	0.800
K2O	0.310	0.470	0.470	0.320	0.270	0.250	0.420	0.260
P2O5	0.060	0.060	0.060	0.070	0.060	0.060	0.060	0.050
LOI	1.600	2.500	2.500	2.200	3.700	1.200	4.200	5.500
SUM	100.010	99.980	99.980	99.850	100.000	100.000	99.980	100.010
ICP-OES (ppm)								
Sc	27.000	28.000	28.000	30.000	26.000	29.000	25.000	22.000
V	203.000	209.000	209.000	221.000	204.000	213.000	183.000	155.000
Cr	1505.355	1382.189	1382.189	1375.347	1649.047	2032.229	1655.890	1751.685
Co	92.800	89.000	89.000	85.600	90.300	91.600	105.100	106.600
Ni	628.300	589.800	589.800	463.600	504.100	499.700	793.400	903.700
Cu	93.400	89.700	89.700	88.000	65.000	74.300	77.600	69.500
Zn	47.000	45.000	45.000	44.000	43.000	47.000	50.000	53.000
Sr	140.200	167.100	167.100	118.700	115.700	105.500	135.200	90.700
Y	13.500	14.500	14.500	14.300	12.200	12.100	13.000	10.100
Zr	44.700	48.900	48.900	50.700	43.100	39.900	43.000	32.900
Ba	81.800	101.300	101.300	78.900	69.900	57.200	93.000	187.200
ICP-MS								
Ti	1.090	1.100	1.100	1.130	1.190	1.070	0.920	0.800
V	203.000	209.000	209.000	221.000	204.000	213.000	183.000	155.000
Cr	1505.355	1382.189	1382.189	1375.347	1649.047	2032.229	1655.890	1751.685
Co	92.800	89.000	89.000	85.600	90.300	91.600	105.100	106.600
Ni	628.300	589.800	589.800	463.600	504.100	499.700	793.400	903.700
Cu	93.400	89.700	89.700	88.000	65.000	74.300	77.600	69.500
Zn	47.000	45.000	45.000	44.000	43.000	47.000	50.000	53.000
Rb	10.800	13.700	13.700	13.100	12.100	9.100	14.100	9.500
K	2573.461	3901.699	3901.699	2656.476	2241.401	2075.372	3486.624	2158.386
Sr	140.200	167.100	167.100	118.700	115.700	105.500	135.200	90.700
P	261.853	261.853	261.853	305.495	261.853	261.853	261.853	218.211
Y	13.500	14.500	14.500	14.300	12.200	12.100	13.000	10.100
Zr	44.700	48.900	48.900	50.700	43.100	39.900	43.000	32.900
Nb	3.300	3.200	3.200	3.400	3.300	2.600	2.700	2.300
Sn								
Cs	0.900	1.300	1.300	1.200	2.600	0.900	1.300	1.100
Ba	81.800	101.300	101.300	78.900	69.900	57.200	93.000	187.200
La	6.100	6.400	6.400	6.200	5.000	4.700	5.900	4.200
Ce	14.600	15.200	15.200	14.900	11.400	11.200	13.400	10.700
Pr	1.790	1.980	1.980	1.940	1.540	1.450	1.600	1.290
Nd	7.000	8.000	8.000	8.000	6.400	6.700	7.500	5.800
Sm	2.000	2.200	2.200	2.400	2.000	1.900	1.900	1.300
Eu	0.740	0.760	0.760	0.720	0.650	0.630	0.490	0.460
Gd	2.150	2.550	2.550	2.410	2.100	1.890	1.970	1.740
Tb	0.330	0.430	0.430	0.430	0.360	0.340	0.350	0.260
Dy	2.200	2.530	2.530	2.600	2.060	2.290	2.070	1.790
Ho	0.480	0.480	0.480	0.510	0.420	0.430	0.420	0.360
Er	1.390	1.540	1.540	1.520	1.290	1.150	1.270	1.110
Tm	0.210	0.230	0.230	0.200	0.190	0.190	0.190	0.180
Yb	1.250	1.280	1.280	1.380	1.170	1.210	1.060	1.080
Lu	0.180	0.180	0.180	0.210	0.200	0.180	0.190	0.130
Hf	1.300	1.800	1.800	1.700	1.400	1.400	1.100	1.000
Ta	0.200	0.200	0.200	0.200	0.200	0.100	0.200	0.300
Pb	6.900	3.700	3.700	3.200	2.400	2.200	4.000	3.800
Th	1.500	1.900	1.900	1.000	0.900	1.000	1.300	1.100
U	0.400	0.400	0.400	0.300	0.200	0.200	0.300	0.300
Inversion models								
Fitted to MgO (wt %) of >	10.000	10.000	10.000	10.000	10.000	10.000	10.000	10.000
Model melts in ppm								
Th	2.140	1.900	1.900	1.000	0.900	1.000	1.998	1.998

Nb	4.724	3.200	3.200	3.400	3.300	2.600	4.168	4.205
Ta	0.282	0.200	0.200	0.200	0.200	0.100	0.303	0.534
La	8.728	6.400	6.400	6.200	5.000	4.700	9.104	7.673
Ce	20.881	15.200	15.200	14.900	11.400	11.200	20.666	19.533
Pr	2.559	1.980	1.980	1.940	1.540	1.450	2.466	2.353
P	373.222	261.853	261.853	305.495	261.853	261.853	402.107	395.738
Nd	9.986	8.000	8.000	8.000	6.400	6.700	11.530	10.536
Sm	2.841	2.200	2.200	2.400	2.000	1.900	2.905	2.342
Zr	63.492	48.900	48.900	50.700	43.100	39.900	65.745	59.273
Hf	1.846	1.800	1.800	1.700	1.400	1.400	1.681	1.800
Ti	1.548	1.100	1.100	1.130	1.190	1.070	1.406	1.441
Eu	1.051	0.760	0.760	0.720	0.650	0.630	0.749	0.829
Gd	3.041	2.550	2.550	2.410	2.100	1.890	2.996	3.110
Tb	0.466	0.430	0.430	0.430	0.360	0.340	0.531	0.463
Dy	3.106	2.530	2.530	2.600	2.060	2.290	3.142	3.189
Y	19.070	14.500	14.500	14.300	12.200	12.100	19.740	18.008
Ho	0.677	0.480	0.480	0.510	0.420	0.430	0.636	0.640
Er	1.958	1.540	1.540	1.520	1.290	1.150	1.921	1.968
Tm	0.296	0.230	0.230	0.200	0.190	0.190	0.287	0.319
Yb	1.753	1.280	1.280	1.380	1.170	1.210	1.595	1.900
Lu	0.252	0.180	0.180	0.210	0.200	0.180	0.286	0.229
Cr	726.172	1382.189	1382.189	1375.347	1649.047	2032.229	640.700	563.515
Sc	34.386	28.000	28.000	30.000	26.000	29.000	33.387	32.501
Rb	15.433	13.700	13.700	13.100	12.100	9.100	21.722	17.314
Ba	116.690	101.300	101.300	78.900	69.900	57.200	142.967	340.053
U	0.571	0.400	0.400	0.300	0.200	0.200	0.461	0.545
Sr	200.171	167.100	167.100	118.700	115.700	105.500	208.063	165.028
Residual modes								
TMF	0.698	1.000	1.000	1.000	1.000	1.000	0.647	0.546
Olivine	0.300	0.000	0.000	0.000	0.000	0.000	0.350	0.450

INTRUSION	**WUS**	**WUS**	**WUS**	**WUS**	**WUS**	**WUS**	**WUS**
ZONE	OZ	OZ	OZ	OZ	OZ	OZ	OZ
LITHOLOGY							
HEIGHT (m)							
SAMPLE I.D.	**0723A005**	**0723A008**	**0723A014**	**0723A015**	**0726A001**	**0726A002**	**0726A003**
Lab	INRS, Quebec	INRS, Quebec	INRS, Quebec	INRS, Quebec	INRS, Quebec	INRS, Quebec	INRS, Quebec
SiO2	41.410	40.640	41.850	42.710	41.910	44.060	44.780
TiO2	0.550	0.380	0.470	0.500	0.450	0.530	0.620
Al2O3	7.440	6.100	6.610	6.950	6.640	7.620	8.440
Fe2O3T	13.410	12.810	13.270	12.720	13.060	12.710	11.670
FeO*	12.056	11.516	11.930	11.435	11.741	11.426	10.491
Fe2O3*	1.354	1.294	1.340	1.285	1.319	1.284	1.179
MnO	0.190	0.170	0.170	0.170	0.180	0.170	0.150
MgO	22.640	26.010	23.090	23.490	24.080	22.840	20.180
CaO	5.880	5.200	5.540	5.750	5.580	6.300	8.030
Na2O	0.880	0.510	0.690	0.670	0.570	0.700	0.910
K2O	0.290	0.270	0.350	0.260	0.310	0.250	0.320
P2O5	0.060	0.040	0.040	0.040	0.040	0.060	0.040
LOI	6.800	7.500	7.400	6.200	6.600	4.300	4.400
SUM	100.000	100.020	99.870	99.860	99.860	99.860	99.860
ICP-OES (ppm)							
Sc	23.000	18.000	20.000	21.000	20.000	23.000	25.000
V	166.000	114.000	146.000	157.000	137.000	153.000	172.000
Cr	2244.347	1395.874	1676.418	1655.890	2039.071	1245.339	1300.079
Co	107.700	114.900	102.800	99.200	105.900	96.600	84.900
Ni	729.900	1029.400	805.600	907.400	889.600	821.300	676.100
Cu	71.000	47.200	66.100	53.500	53.300	60.300	52.800
Zn	59.000	59.000	62.000	52.000	56.000	52.000	42.000
Sr	87.900	79.200	116.100	117.400	87.800	94.700	116.300
Y	10.800	7.200	8.600	9.200	8.500	10.200	11.600
Zr	34.700	25.000	32.000	33.800	29.700	35.100	41.900

Ba	76.100	43.800	54.600	71.200	54.800	60.100	71.100
ICP-MS							
Ti	0.880	0.510	0.690	0.670	0.570	0.700	0.910
V	166.000	114.000	146.000	157.000	137.000	153.000	172.000
Cr	2244.347	1395.874	1676.418	1655.890	2039.071	1245.339	1300.079
Co	107.700	114.900	102.800	99.200	105.900	96.600	84.900
Ni	729.900	1029.400	805.600	907.400	889.600	821.300	676.100
Cu	71.000	47.200	66.100	53.500	53.300	60.300	52.800
Zn	59.000	59.000	62.000	52.000	56.000	52.000	42.000
Rb	10.200	8.700	8.700	8.900	8.600	8.900	10.000
K	2407.431	2241.401	2905.520	2158.386	2573.461	2075.372	2656.476
Sr	87.900	79.200	116.100	117.400	87.800	94.700	116.300
P	261.853	174.569	174.569	174.569	174.569	261.853	174.569
Y	10.800	7.200	8.600	9.200	8.500	10.200	11.600
Zr	34.700	25.000	32.000	33.800	29.700	35.100	41.900
Nb	2.500	1.800	1.600	1.600	1.200	2.400	2.200
Sn							
Cs	2.100	0.700	1.400	1.200	0.900	1.100	1.600
Ba	76.100	43.800	54.600	71.200	54.800	60.100	71.100
La	4.400	3.200	4.000	4.200	3.700	4.700	5.100
Ce	10.700	7.400	9.300	9.600	8.900	10.600	11.600
Pr	1.330	0.980	1.180	1.250	1.220	1.390	1.490
Nd	5.400	4.100	4.800	5.500	5.400	6.100	6.500
Sm	1.500	1.100	1.200	1.400	1.300	1.500	1.800
Eu	0.560	0.390	0.450	0.490	0.390	0.530	0.600
Gd	1.650	1.130	1.450	1.680	1.560	1.720	1.880
Tb	0.340	0.180	0.280	0.310	0.240	0.320	0.320
Dy	1.920	1.240	1.650	1.620	1.550	1.760	2.060
Ho	0.370	0.280	0.330	0.340	0.320	0.390	0.430
Er	1.070	0.800	0.970	0.990	0.920	1.110	1.200
Tm	0.180	0.110	0.120	0.130	0.130	0.140	0.170
Yb	1.080	0.650	0.950	1.010	0.950	1.110	1.190
Lu	0.140	0.100	0.110	0.140	0.110	0.150	0.160
Hf	1.200	1.000	1.000	1.100	0.900	1.100	1.300
Ta	0.200	0.100	0.200	0.200	0.200	0.100	0.200
Pb	4.400	2.300	3.600	4.600	5.700	4.000	2.300
Th	0.900	0.600	0.500	0.900	0.500	0.900	0.800
U	0.300	0.100	0.200	0.200	0.200	0.200	0.200
Inversion models							
Fitted to MgO (wt %) of >	10.000	10.000	101.000	10.000	10.000	10.000	10.000
Model melts in ppm							
Th	1.638	1.048	0.996	1.632	1.039	1.546	1.228
Nb	4.579	3.164	3.213	2.920	2.515	4.146	3.391
Ta	0.357	0.172	0.389	0.355	0.405	0.169	0.303
La	8.053	5.621	8.024	7.659	7.748	8.114	7.858
Ce	19.568	12.989	18.637	17.493	18.616	18.286	17.863
Pr	2.430	1.719	2.362	2.276	2.549	2.396	2.293
P	475.747	304.571	347.053	316.017	361.993	449.115	267.661
Nd	9.827	7.164	9.562	9.973	11.222	10.477	9.977
Sm	2.708	1.908	2.367	2.518	2.673	2.558	2.748
Zr	62.627	43.355	63.111	60.786	61.053	59.854	63.967
Hf	2.164	1.734	1.971	1.977	1.848	1.875	1.984
Ti	1.587	0.884	1.360	1.205	1.171	1.194	1.389
Eu	1.011	0.676	0.888	0.881	0.802	0.904	0.916
Gd	2.954	1.945	2.832	2.997	3.173	2.912	2.855
Tb	0.606	0.309	0.544	0.551	0.486	0.540	0.485
Dy	3.427	2.128	3.210	2.881	3.140	2.972	3.122
Y	19.291	12.367	16.748	16.374	17.236	17.234	17.588
Ho	0.659	0.480	0.640	0.603	0.646	0.657	0.651
Er	1.900	1.367	1.876	1.752	1.852	1.866	1.813
Tm	0.320	0.188	0.232	0.230	0.262	0.235	0.257
Yb	1.903	1.103	1.820	1.773	1.892	1.853	1.788
Lu	0.247	0.170	0.211	0.246	0.219	0.250	0.240
Cr	622.134	662.966	639.366	634.562	652.294	592.173	623.390
Sc	34.024	25.978	31.138	30.983	31.888	32.857	33.347

Rb	18.623	15.248	17.400	16.191	17.950	15.331	15.382
Ba	138.489	76.533	108.765	129.102	113.881	103.229	109.133
U	0.546	0.175	0.398	0.363	0.416	0.344	0.307
Sr	160.225	138.597	231.736	213.221	182.855	162.894	178.703
Residual modes							
TMF	0.545	0.568	0.497	0.547	0.476	0.578	0.648
Olivine	0.450	0.430	0.500	0.450	0.520	0.420	0.350

INTRUSION	**WUS**	**WUS**	**WUS**	**WUS**	**WUS**	**WUS**	**WUS**
ZONE	OZ	OZ	DZ	DZ	DZ	DZ	DZ
LITHOLOGY							
HEIGHT (m)							
SAMPLE I.D.	**0726A004**	**10KS095A6**	**10JB156B2**	**10HY062A1**	**10HY062A2**	**10HY062A3**	**10KS095A15**
Lab	INRS, Quebec	INRS, Quebec	INRS, Quebec	INRS, Quebec	INRS, Quebec	INRS, Quebec	INRS, Quebec
SiO2	45.430	40.175	48.192	50.522	50.266	50.924	47.379
TiO2	0.610	0.428	1.166	0.928	1.170	1.260	0.923
Al2O3	8.460	6.045	13.458	14.930	13.916	14.264	13.564
Fe2O3T	12.830	12.247	12.623	10.272	12.823	12.690	10.238
FeO*	11.534	11.010	11.348	9.235	11.528	11.409	9.204
Fe2O3*	1.296	1.237	1.275	1.038	1.295	1.282	1.034
MnO	0.170	0.162	0.135	0.149	0.177	0.173	0.153
MgO	20.870	23.331	7.038	8.261	7.213	6.911	7.272
CaO	7.230	5.507	10.644	10.939	9.830	9.844	9.779
Na2O	0.940	0.718	2.489	1.771	1.878	1.874	2.300
K2O	0.300	0.173	1.827	1.271	1.298	1.288	1.126
P2O5	0.060	0.035	0.109	0.059	0.071	0.094	0.080
LOI	2.600	6.558	2.501	1.409	1.559	1.588	2.447
SUM	99.850	95.630	100.492	100.572	100.283	100.994	95.367
ICP-OES (ppm)							
Sc	26.000	19.993	36.957	37.573	41.455	38.341	34.685
V	182.000	124.591	328.279	271.841	364.848	331.975	247.192
Cr	1484.827	1213.669	76.500	265.265	13.506	49.195	70.504
Co	91.700	94.596	26.156	39.669	47.881	45.662	42.151
Ni	720.700	911.732	80.325	129.038	88.139	91.190	88.802
Cu	71.300	58.365	139.789	103.929	183.807	156.483	132.777
Zn	50.000	75.901	< 40	83.119	91.711	103.441	61.340
Sr	98.500	100.000	746.485	237.289	234.915	220.129	359.000
Y	11.600	8.200	20.000	13.400	20.000	22.000	20.000
Zr	39.000	32.000	78.200	72.000	89.000	105.000	70.000
Ba	72.200	50.100	279.372	114.507	122.750	163.649	186.000
ICP-MS							
Ti	0.940	0.718	2.490	1.771	1.878	1.874	2.301
V	182.000	124.591	328.279	271.841	364.848	331.975	247.192
Cr	1484.827	1213.669	76.500	265.265	13.506	49.195	70.504
Co	91.700	94.596	26.156	39.669	47.881	45.662	42.151
Ni	720.700	911.732	80.325	129.038	88.139	91.190	88.802
Cu	71.300	58.365	139.789	103.929	183.807	156.483	132.777
Zn	50.000	75.901	< 40	83.119	91.711	103.441	61.340
Rb	9.100	7.300	29.600	26.000	33.900	34.300	34.400
K	2490.446	1434.383	15166.978	10555.051	10777.409	10690.636	9350.536
Sr	98.500	100.000	746.485	237.289	234.915	220.129	359.000
P	261.853	154.287	475.123	259.397	309.167	411.462	347.542
Y	11.600	8.200	20.000	13.400	20.000	22.000	20.000
Zr	39.000	32.000	78.200	72.000	89.000	105.000	70.000
Nb	2.700	2.040	6.210	4.230	5.380	6.390	4.820
Sn							
Cs	0.600	1.650	1.900	0.600	0.600	1.000	0.400
Ba	72.200	50.100	279.372	114.507	122.750	163.649	186.000
La	5.200	3.500	9.200	7.300	9.200	11.200	7.800
Ce	12.500	8.010	18.600	16.800	21.400	26.000	18.500
Pr	1.650	1.020	2.800	2.100	2.700	3.300	2.300

Nd	6.900	4.550	13.000	9.800	12.300	14.500	10.500
Sm	2.000	1.210	3.300	2.500	3.100	3.800	2.700
Eu	0.610	0.390	1.050	0.810	1.030	1.150	0.900
Gd	2.030	1.310	3.320	2.740	3.420	4.030	3.180
Tb	0.360	0.240	0.580	0.450	0.580	0.680	0.520
Dy	2.040	1.420	3.670	2.900	3.500	4.220	3.310
Ho	0.450	0.280	0.730	0.610	0.750	0.880	0.670
Er	1.250	0.848	2.050	1.760	2.150	2.500	1.920
Tm	0.190	0.121	0.300	0.260	0.310	0.370	0.290
Yb	1.120	0.769	1.830	1.640	1.950	2.260	1.770
Lu	0.190	0.118	0.280	0.240	0.300	0.350	0.270
Hf	1.200	0.796	2.120	1.930	2.290	2.700	1.900
Ta	0.300	0.130	0.350	0.300	0.350	0.400	0.310
Pb	3.500	62.300	2.300	3.000	6.100	8.650	25.400
Th	1.200	0.900	1.900	1.400	1.100	2.400	2.000
U	0.300	0.156	0.650	0.310	0.400	0.470	0.360
Inversion models							
Fitted to MgO (wt %) of >	10.000	10.000					
Model melts in ppm							
Th	1.842	1.980					
Nb	4.162	4.532					
Ta	0.454	0.278					
La	8.012	7.767					
Ce	19.249	17.753					
Pr	2.539	2.258					
P	401.491	338.646					
Nd	10.591	10.011					
Sm	3.053	2.630					
Zr	59.539	69.563					
Hf	1.831	1.730					
Ti	1.435	1.561					
Eu	0.931	0.848					
Gd	3.083	2.814					
Tb	0.545	0.513					
Dy	3.091	3.036					
Y	17.588	17.553					
Ho	0.681	0.597					
Er	1.888	1.800					
Tm	0.287	0.257					
Yb	1.683	1.614					
Lu	0.285	0.248					
Cr	711.977	741.625					
Sc	34.681	32.851					
Rb	13.998	16.140					
Ba	110.821	110.231					
U	0.460	0.343					
Sr	151.352	220.556					
Residual modes							
TMF	0.648	0.449					
Olivine	0.350	0.550					

INTRUSION	**WUS**	**WUS**	**WUS**	**WUS**	**FCSC**
ZONE	DZ	DZ	UCM	lower chill	
LITHOLOGY					
HEIGHT (m)					
SAMPLE I.D.	**10JB155A1**	**10JB155C1**	**10HY062A4**	**10AW054B1**	**av chill**
Lab	INRS, Quebec	INRS, Quebec	INRS, Quebec	INRS, Quebec	
SiO2	36.247	34.763	49.204	48.780	48.057
TiO2	0.401	0.467	0.976	0.970	0.990

Al2O3	7.160	7.531	12.691	12.937	12.918
Fe2O3T	10.087	8.357	11.206	12.202	11.665
FeO*	9.068	7.513	10.074	10.970	10.487
Fe2O3*	1.019	0.844	1.132	1.232	1.178
MnO	0.089	0.109	0.119	0.186	0.160
MgO	4.714	5.268	10.273	10.898	10.328
CaO	31.751	36.845	9.317	11.461	11.170
Na2O	0.518	< 0.07	2.426	1.490	1.891
K2O	1.052	< 0.08	1.028	0.565	1.026
P2O5	0.163	0.229	0.063	0.085	0.080
LOI	7.988	7.129	3.723	0.612	1.639
SUM	100.833	101.033	101.078	100.457	101.561
ICP-OES (ppm)					
Sc	6.663	7.643	35.727	37.468	38.204
V	87.217	84.817	275.439	280.116	290.731
Cr	29.759	33.366	731.167	644.611	607.268
Co	32.360	9.484	42.640	47.692	47.064
Ni	25.712	25.594	226.309	211.648	184.990
Cu	239.772	16.120	28.023	132.485	106.992
Zn	< 40	< 40	140.232	63.087	72.822
Sr	214.201	130.842	252.722	179.948	441.285
Y	20.000	18.000	15.400	18.000	18.416
Zr	93.000	106.000	74.000	69.000	72.314
Ba	219.648	< 6	134.090	113.764	193.100
ICP-MS					
Ti	0.518	#VALUE!	2.427	1.490	0.000
V	87.217	84.817	275.439	280.116	290.272
Cr	29.759	33.366	731.167	644.611	628.370
Co	32.360	9.484	42.640	47.692	47.961
Ni	25.712	25.594	226.309	211.648	192.426
Cu	239.772	16.120	28.023	132.485	110.848
Zn	< 40	< 40	140.232	63.087	74.844
Rb	25.300	0.200	22.000	21.000	28.261
K	8735.618	-dl	8536.621	4689.708	8653.266
Sr	214.201	130.842	252.722	179.948	435.198
P	713.116	997.605	273.601	368.814	417.700
Y	20.000	18.000	15.400	18.000	18.350
Zr	93.000	106.000	74.000	69.000	70.467
Nb	6.410	5.690	4.810	4.950	4.721
Sn					1.085
Cs	0.620	< 0.13	< 0.26	7.600	2.614
Ba	219.648	< 6	134.090	113.764	196.729
La	8.300	31.700	6.700	7.800	7.379
Ce	22.200	42.100	17.000	17.900	16.412
Pr	3.600	4.800	2.200	2.500	2.383
Nd	16.000	17.800	10.500	10.700	10.889
Sm	3.000	3.300	2.700	2.800	2.817
Eu	0.910	0.880	0.770	0.890	0.846
Gd	2.680	2.910	2.990	3.020	2.922
Tb	0.440	0.440	0.500	0.500	0.519
Dy	2.760	2.780	3.200	3.200	3.244
Ho	0.580	0.560	0.660	0.650	0.634
Er	1.790	1.690	1.860	1.850	1.821
Tm	0.280	0.260	0.290	0.250	0.261
Yb	1.790	1.560	1.700	1.680	1.712
Lu	0.260	0.230	0.260	0.250	0.250
Hf	2.230	2.840	1.960	1.940	1.917
Ta	0.400	0.400	0.300	<0.3	0.323
Pb	0.650	1.150	10.000	3.900	3.002
Th	4.900	3.800	1.600	0.700	1.434
U	1.620	4.990	0.340	0.300	0.303

Appendix F2 – FCSC olivine mineral chemistry

Sample code	Sill	SiO2	TiO2	Al2O3	Cr2O3	FeO	MnO	MgO	CaO	NiO	Total	Fo
JB367C 46	PS	40.50	0.00	0.03	0.05	11.72	0.17	47.09	0.30	0.37	100.23	0.88
JB367C 47	PS	40.38	0.00	0.07	0.05	11.79	0.21	46.82	0.28	0.37	99.97	0.88
JB367C 52	PS	39.74	0.00	0.03	0.02	17.72	0.24	41.95	0.11	0.29	100.07	0.81
JB367C 54	PS	40.40	0.01	0.01	0.01	13.36	0.21	45.35	0.28	0.30	99.92	0.86
JB367C 59	PS	40.28	0.01	0.04	0.06	12.23	0.20	46.16	0.26	0.36	99.58	0.87
JB367C 60	PS	40.16	0.00	0.03	0.03	12.72	0.14	46.59	0.26	0.30	100.23	0.87
JB367C 62	PS	41.44	0.00	0.04	0.02	11.52	0.12	44.94	0.23	0.31	98.61	0.87
av JB367C ol cores	PS	40.41	0.00	0.03	0.03	13.01	0.18	45.56	0.24	0.33	99.80	0.86
JB367C 63	PS	38.09	0.00	0.02	0.02	25.07	0.37	35.70	0.21	0.21	99.68	0.72
JB367C 61	PS	38.78	0.00	0.00	0.03	18.51	0.26	41.37	0.22	0.24	99.41	0.80
JB367C 48	PS	53.48	0.45	1.21	0.02	17.23	0.38	24.69	1.89	0.06	99.42	0.72
JB367C 53	PS	38.96	0.01	0.00	0.00	21.80	0.31	37.92	0.19	0.22	99.41	0.76
JB367C 55	PS	39.26	0.00	0.02	0.03	19.02	0.28	40.84	0.21	0.28	99.93	0.79
av JB367C ol rims	PS	41.71	0.09	0.25	0.02	20.33	0.32	36.10	0.54	0.20	99.57	0.76
JB367H 66	PS	39.34	0.00	0.05	0.00	18.45	0.24	41.90	0.24	0.27	100.49	0.80
JB367H 67	PS	39.39	0.00	0.03	0.03	16.38	0.23	42.52	0.22	0.20	98.99	0.82
JB367H 75	PS	39.06	0.00	0.04	0.04	19.46	0.33	40.74	0.21	0.25	100.14	0.79
JB367H 76	PS	39.45	0.00	0.04	0.07	16.53	0.19	42.64	0.26	0.27	99.45	0.82
JB367H 77	PS	39.14	0.01	0.02	0.00	19.98	0.30	40.16	0.24	0.24	100.08	0.78
JB367H 78	PS	38.83	0.03	0.00	0.03	20.94	0.28	39.57	0.16	0.28	100.11	0.77
JB367H 79	PS	39.82	0.01	0.03	0.06	15.25	0.20	43.90	0.25	0.33	99.84	0.84
JB367H 80	PS	39.37	0.00	0.01	0.04	18.42	0.22	41.45	0.25	0.23	99.98	0.80
JB367H 68	PS	38.93	0.00	0.03	0.04	18.90	0.24	40.16	0.25	0.25	98.80	0.79
JB367H 87	PS	38.62	0.01	0.01	0.01	20.63	0.37	39.15	0.30	0.27	99.37	0.77
JB367H 88	PS	38.85	0.00	0.02	0.05	20.25	0.25	39.56	0.20	0.22	99.40	0.78
JB367H 74	PS	38.82	0.00	0.03	0.02	21.51	0.25	39.27	0.26	0.22	100.38	0.76
JB367H 72	PS	38.79	0.01	0.02	0.00	20.04	0.36	40.33	0.18	0.23	99.94	0.78
JB367H 73	PS	38.93	0.00	0.02	0.00	20.56	0.24	39.96	0.13	0.28	100.14	0.78
JB367H 85	PS	39.07	0.00	0.03	0.06	19.46	0.28	40.27	0.19	0.21	99.56	0.79
JB367H 86	PS	38.83	0.04	0.02	0.01	20.85	0.31	38.90	0.19	0.25	99.40	0.77
av 10JB367H olivines	PS	39.08	0.01	0.03	0.03	19.23	0.27	40.65	0.22	0.25	99.75	0.79
JB368B 107	PS	38.70	0.00	0.00	0.00	21.35	0.25	39.05	0.24	0.20	99.78	0.77
JB368B 108	PS	38.86	0.02	0.01	0.01	21.42	0.55	38.49	0.22	0.21	99.77	0.76
JB368B 109	PS	38.57	0.00	0.02	0.03	20.22	0.26	39.55	0.30	0.23	99.17	0.78
JB368B 110	PS	38.82	0.00	0.01	0.00	21.97	0.34	38.73	0.22	0.21	100.30	0.76
JB368B 114	PS	38.45	0.01	0.02	0.02	22.24	0.25	38.56	0.23	0.18	99.94	0.76
JB368B 115	PS	39.07	0.02	0.01	0.01	19.56	0.27	40.24	0.25	0.21	99.63	0.79
JB368B 116	PS	38.38	0.00	0.01	0.04	20.63	0.38	38.86	0.18	0.19	98.68	0.77
JB368B 117	PS	38.47	0.00	0.00	0.05	21.22	0.25	37.34	0.20	0.21	97.73	0.76
JB368B 118	PS	38.72	0.00	0.02	0.01	20.64	0.18	39.37	0.24	0.25	99.42	0.77
JB368B 119	PS	39.02	0.01	0.02	0.03	19.92	0.25	40.51	0.19	0.16	100.12	0.78
JB368B 120	PS	38.57	0.00	0.00	0.00	22.24	0.29	38.65	0.19	0.20	100.13	0.76
JB368B 121	PS	38.41	0.00	0.02	0.02	22.44	0.30	38.15	0.24	0.13	99.71	0.75
JB368B 122	PS	38.34	0.02	0.02	0.03	22.37	0.29	38.09	0.20	0.18	99.54	0.75
av 10JB368B oliv		38.64	0.01	0.01	0.02	21.25	0.30	38.89	0.22	0.20	99.53	0.77
10KS95 A7 b11	WUS	38.20	0.01	0.13	0.01	23.55	0.35	35.86	0.26	0.17	98.57	0.73
10KS95 A7 b12	WUS	37.73	0.01	0.14	0.00	24.02	0.28	36.06	0.27	0.11	98.62	0.73
10KS95 A7 b13	WUS	37.92	0.00	0.12	0.00	25.69	0.32	34.79	0.20	0.06	99.13	0.71
10KS95 A7 b24	WUS	38.91	0.01	0.15	0.01	21.21	0.26	38.64	0.28	0.14	99.61	0.76
10KS95 A7 b25	WUS	39.07	0.00	0.13	0.00	20.54	0.20	38.96	0.21	0.20	99.33	0.77
av 10ks95A7 ol	WUS	38.37	0.01	0.13	0.00	23.00	0.28	36.86	0.25	0.14	99.05	0.74
10KS95 A5 b4	WUS	39.27	0.00	0.15	0.00	18.38	0.26	40.84	0.21	0.26	99.40	0.80
10KS95 A5 b5	WUS	39.26	0.00	0.14	0.00	17.91	0.33	40.66	0.16	0.27	98.76	0.80
av 10ks95A5 olpheno?	WUS	39.27	0.00	0.14	0.00	18.14	0.30	40.75	0.19	0.27	99.08	0.80
10KS95 A5 a10	WUS	39.29	0.00	0.15	0.04	17.81	0.33	40.87	0.18	0.24	98.92	0.80
10KS95 A5 a11	WUS	39.40	0.01	0.14	0.01	16.98	0.24	41.80	0.13	0.27	98.97	0.81

Sample code	Sill	SiO2	TiO2	Al2O3	Cr2O3	FeO	MnO	MgO	CaO	NiO	Total	Fo
10KS95 A5 a12	WUS	40.83	0.00	0.12	0.03	16.10	0.24	41.97	0.17	0.23	99.70	0.82
10KS95 A5 b1	WUS	39.96	0.01	0.14	0.04	14.99	0.21	43.72	0.18	0.27	99.52	0.84
av 10ks95A5 ol incl	WUS	39.87	0.01	0.14	0.03	16.47	0.25	42.09	0.16	0.25	99.28	0.82
10JB367I a5	PS	39.57	0.00	0.13	0.05	16.36	0.23	42.48	0.23	0.26	99.32	0.82
10JB367I a7	PS	39.52	0.01	0.13	0.11	17.84	0.25	41.53	0.15	0.27	99.81	0.81
10JB367I b11	PS	39.36	0.01	0.15	0.02	18.22	0.21	41.45	0.23	0.27	99.92	0.80
10JB367I b12	PS	39.44	0.00	0.15	0.02	17.59	0.24	41.67	0.19	0.22	99.53	0.81
av 10jb367i ol incl	PS	39.47	0.00	0.14	0.05	17.50	0.23	41.78	0.20	0.25	99.64	0.81
10JB367J a1	PS	39.31	0.00	0.14	0.03	18.53	0.33	40.71	0.21	0.24	99.50	0.80
10JB367J a2	PS	39.49	0.01	0.14	0.04	16.85	0.24	41.87	0.27	0.23	99.16	0.82
10JB367J a4	PS	39.02	0.00	0.12	0.04	18.24	0.35	40.37	0.25	0.20	98.61	0.80
av 10jb367j ol incl	PS	39.28	0.00	0.14	0.04	17.87	0.31	40.98	0.24	0.22	99.09	0.80
10JB367J b11	PS	38.68	0.00	0.13	0.01	21.68	0.33	38.25	0.22	0.20	99.54	0.76
10JB367J c16	PS	38.86	0.00	0.13	0.03	20.53	0.24	38.66	0.28	0.17	98.91	0.77
10JB367J c17	PS	38.77	0.00	0.15	0.00	20.69	0.30	39.65	0.29	0.20	100.06	0.77
10JB367J c18	PS	38.94	0.00	0.12	0.02	19.94	0.30	39.27	0.17	0.21	98.99	0.78
10JB367J c19	PS	38.68	0.00	0.13	0.00	20.31	0.40	38.67	0.16	0.15	98.52	0.77
10JB367J d31	PS	38.63	0.00	0.13	0.00	19.85	0.35	39.19	0.27	0.16	98.61	0.78
10JB367J d32	PS	38.54	0.01	0.15	0.03	21.14	0.38	38.27	0.22	0.18	98.92	0.76
av 10jb367j ol int-dendritic	PS	38.73	0.00	0.13	0.01	20.59	0.33	38.85	0.23	0.18	99.08	0.77
10JB367G b1	PS	40.49	0.00	0.15	0.06	12.91	0.26	45.77	0.27	0.32	100.27	0.86
10JB367G a10	PS	39.65	0.00	0.13	0.04	14.59	0.17	44.04	0.24	0.28	99.14	0.84
10JB367G a11	PS	40.00	0.01	0.14	0.04	14.90	0.24	44.27	0.23	0.32	100.15	0.84
10JB367G a12	PS	39.79	0.00	0.14	0.02	14.43	0.21	44.27	0.24	0.35	99.46	0.85
av 10jb367g big ol pheno? - rim	PS	39.98	0.00	0.14	0.04	14.21	0.22	44.59	0.24	0.32	99.75	0.85
10JB367G b2	PS	39.69	0.02	0.12	0.04	16.85	0.24	42.68	0.22	0.33	100.22	0.82
10JB367G a16	PS	39.07	0.03	0.13	0.00	19.76	0.40	40.26	0.19	0.25	100.09	0.78
10JB367G b5	PS	39.02	0.01	0.14	0.05	19.76	0.28	40.04	0.23	0.29	99.81	0.78
10JB367G b6	PS	39.13	0.00	0.13	0.01	19.61	0.31	40.41	0.18	0.26	100.04	0.79
av 10jb367g ol gm, rims & in plag	PS	39.23	0.01	0.13	0.03	18.99	0.31	40.85	0.20	0.28	100.04	0.79
10JB367E c3	PS	40.47	0.00	0.14	0.06	12.44	0.16	45.54	0.26	0.32	99.42	0.87
10JB367E c4	PS	40.52	0.00	0.14	0.04	12.68	0.25	47.60	0.27	0.31	101.82	0.87
10JB367E b6	PS	41.00	0.00	0.15	0.05	11.79	0.21	46.76	0.27	0.36	100.62	0.88
10JB367E b7	PS	40.85	0.00	0.15	0.08	11.53	0.19	46.90	0.27	0.40	100.39	0.88
10JB367E a25	PS	40.94	0.01	0.23	0.05	11.00	0.15	46.87	0.63	0.37	100.24	0.88
av 10jb367e big ol pheno? Minus rim	PS	40.75	0.00	0.16	0.06	11.89	0.19	46.73	0.34	0.35	100.50	0.88
10JB367E b8	PS	39.60	0.00	0.14	0.05	17.44	0.22	42.05	0.24	0.30	100.10	0.81
10JB367E b12	PS	38.71	0.01	0.15	0.00	20.74	0.21	39.26	0.26	0.25	99.60	0.77
10JB367E b13	PS	38.78	0.00	0.15	0.04	21.99	0.31	38.24	0.22	0.26	99.99	0.76
10JB367E b14	PS	39.58	0.01	0.14	0.03	19.44	0.23	40.84	0.20	0.29	100.77	0.79
10JB367E b15	PS	39.41	0.00	0.14	0.00	17.23	0.24	41.65	0.24	0.26	99.20	0.81
10JB367E a20	PS	38.86	0.00	0.13	0.05	20.01	0.34	39.15	0.19	0.25	98.99	0.78
10JB367E a21	PS	38.97	0.00	0.14	0.04	19.27	0.29	39.45	0.20	0.22	98.60	0.78
10JB367E a22	PS	39.00	0.00	0.14	0.00	20.27	0.28	39.32	0.16	0.30	99.47	0.78
10JB367E a23	PS	39.59	0.00	0.15	0.02	16.56	0.14	42.73	0.16	0.29	99.63	0.82
av 10jb367e ragged looking ol & pheno rim	PS	39.17	0.00	0.14	0.03	19.22	0.25	40.30	0.21	0.27	99.59	0.79
JB367A 1	PS	39.50	0.00	0.02	0.04	13.54	0.22	45.67	0.29	0.33	99.62	0.86
JB367A 2	PS	39.96	0.00	0.05	0.04	13.21	0.18	45.54	0.28	0.30	99.56	0.86
10JB367A a3	PS	40.09	0.01	0.17	0.06	13.12	0.17	45.23	0.25	0.31	99.42	0.86
10JB367A a4	PS	40.43	0.01	0.15	0.05	13.15	0.10	45.27	0.28	0.33	99.77	0.86
JB367A 3	PS	39.23	0.00	0.06	0.13	13.59	0.30	45.76	0.30	0.31	99.69	0.86
JB367A 4	PS	39.06	0.00	0.04	0.05	13.22	0.26	45.06	0.25	0.34	98.28	0.86
10JB367A a5	PS	40.44	0.02	0.14	0.05	13.23	0.09	46.56	0.28	0.30	101.12	0.86
10JB367A a6	PS	40.49	0.01	0.14	0.09	13.76	0.11	45.19	0.32	0.30	100.41	0.85

Sample code	Sill	SiO2	TiO2	Al2 O3	Cr2O3	FeO	MnO	MgO	CaO	NiO	Total	Fo
10JB367A a1	PS	40.50	0.00	0.14	0.04	12.98	0.13	45.89	0.28	0.29	100.27	0.86
JB367A 6	PS	39.28	0.00	0.04	0.01	13.73	0.20	45.30	0.25	0.34	99.14	0.85
JB367A 7	PS	39.50	0.00	0.05	0.01	13.62	0.20	45.21	0.26	0.36	99.21	0.86
10JB367A b8	PS	40.58	0.01	0.14	0.07	13.18	0.21	45.77	0.27	0.27	100.51	0.86
JB367A 18	PS	39.13	0.01	0.07	0.08	13.64	0.16	44.98	0.33	0.30	98.68	0.85
10JB367A b10	PS	40.71	0.00	0.14	0.02	13.49	0.18	45.97	0.24	0.34	101.09	0.86
JB367A 19	PS	38.57	0.00	0.05	0.07	13.38	0.22	45.24	0.25	0.30	98.07	0.86
JB367A 20	PS	39.06	0.00	0.04	0.02	13.17	0.21	45.50	0.24	0.33	98.56	0.86
10JB367A b11	PS	40.79	0.00	0.13	0.02	13.77	0.17	45.42	0.23	0.33	100.86	0.85
JB367A 21	PS	38.34	0.00	0.07	0.07	13.40	0.19	44.76	0.39	0.30	97.51	0.86
JB367A 22	PS	39.13	0.00	0.06	0.04	14.46	0.20	44.75	0.26	0.33	99.22	0.85
10JB367B c1	PS	40.37	0.00	0.15	0.03	13.55	0.26	45.55	0.23	0.29	100.45	0.86
10JB367B c2	PS	40.15	0.00	0.15	0.04	13.58	0.24	45.58	0.23	0.30	100.30	0.86
10JB367B c9	PS	40.04	0.00	0.14	0.06	13.42	0.21	45.21	0.22	0.36	99.67	0.86
10JB367B b11	PS	41.33	0.02	0.14	0.05	10.59	0.15	48.55	0.13	0.41	101.38	0.89
10JB367B b12	PS	40.46	0.01	0.14	0.03	11.67	0.23	47.09	0.10	0.38	100.13	0.88
10JB367B a20	PS	40.63	0.00	0.15	0.09	10.31	0.14	48.55	0.25	0.37	100.51	0.89
10JB367B a21	PS	41.08	0.00	0.16	0.06	10.11	0.17	48.55	0.30	0.33	100.77	0.90
10JB367B a28	PS	47.39	0.01	0.17	0.03	9.78	0.16	36.71	0.16	0.13	94.59	0.87
10JB367B a29	PS	40.42	0.00	0.15	0.04	15.81	0.25	44.00	0.28	0.22	101.18	0.83
10JB367B c4	PS	39.91	0.00	0.15	0.04	15.27	0.19	43.70	0.21	0.27	99.74	0.84
10JB367B c6	PS	34.63	0.00	0.15	0.03	23.70	0.45	37.30	0.24	0.21	96.72	0.74
10JB367B b15	PS	38.23	0.00	0.13	0.01	24.37	0.24	36.60	0.21	0.20	100.03	0.73
10JB367B b18	PS	37.73	0.01	0.13	0.00	28.26	0.42	33.85	0.16	0.25	100.82	0.68
10JB367B a22	PS	39.87	0.00	0.16	0.05	16.15	0.25	43.49	0.24	0.28	100.55	0.83
10JB367B a23	PS	39.32	0.00	0.15	0.02	19.11	0.28	41.05	0.22	0.27	100.46	0.79
10JB367B c3	PS	39.20	0.00	0.15	0.03	18.98	0.24	41.22	0.25	0.24	100.32	0.79
10JB367B a26	PS	39.83	0.00	0.17	0.08	17.49	0.21	42.51	0.24	0.23	100.81	0.81
10KS95 A3 a1	WUS	39.77	0.01	0.14	0.00	16.38	0.22	43.63	0.15	0.25	100.57	0.83
10KS95 A3 a2	WUS	39.15	0.00	0.13	0.00	15.91	0.21	43.65	0.14	0.29	99.48	0.83
10KS95 A3 b16	WUS	40.28	0.00	0.13	0.03	13.10	0.25	45.59	0.22	0.34	99.94	0.86
10KS95 A3 b11	WUS	39.49	0.00	0.14	0.05	17.75	0.31	42.61	0.21	0.27	100.83	0.81
10KS95 A3 d35	WUS	40.01	0.00	0.12	0.04	17.09	0.22	42.92	0.20	0.34	100.93	0.82
10KS95 A3 d36	WUS	39.43	0.00	0.14	0.04	15.97	0.23	43.56	0.17	0.29	99.82	0.83
10KS95 A3 a6	WUS	39.28	0.00	0.13	0.00	18.71	0.28	41.84	0.21	0.24	100.70	0.80
10KS95 A3 a7	WUS	39.34	0.00	0.14	0.01	19.25	0.24	40.99	0.19	0.24	100.41	0.79
10KS95 A3 b17	WUS	39.44	0.01	0.15	0.04	18.65	0.28	41.65	0.28	0.27	100.77	0.80
10KS95 A3 b18	WUS	39.01	0.02	0.12	0.02	19.93	0.31	40.34	0.13	0.23	100.11	0.78
10KS95 A3 c19	WUS	38.73	0.00	0.12	0.02	20.75	0.31	40.19	0.16	0.24	100.54	0.78
10KS95 A3 c26	WUS	39.42	0.01	0.13	0.01	20.35	0.34	40.62	0.09	0.26	101.25	0.78
10KS95 A3 c29	WUS	39.13	0.00	0.14	0.02	18.31	0.31	41.43	0.11	0.25	99.70	0.80
10KS95 A1 c11	WUS	40.65	0.00	0.14	0.03	13.59	0.21	45.43	0.20	0.31	100.57	0.86
10KS95 A1 c12	WUS	40.24	0.00	0.13	0.07	13.47	0.16	45.61	0.20	0.32	100.21	0.86
10KS95 A1 c13	WUS	39.68	0.00	0.14	0.04	12.12	0.15	45.85	0.24	0.34	98.56	0.87
10KS95 A1 c14	WUS	39.95	0.02	0.14	0.03	13.72	0.08	45.50	0.23	0.29	99.96	0.86
10KS95 A1 b20	WUS	40.31	0.00	0.13	0.06	12.68	0.11	46.12	0.27	0.32	100.00	0.87
10KS95 A1 a34	WUS	40.12	0.00	0.13	0.05	13.51	0.25	45.65	0.27	0.24	100.23	0.86
10KS95 A1 a35	WUS	40.27	0.00	0.13	0.03	13.95	0.24	45.49	0.24	0.24	100.62	0.85

Sample code	Sill	SiO2	TiO2	Al2 O3	Cr2O3	FeO	MnO	MgO	CaO	NiO	Total	Fo
10KS95 A1 a36	WUS	40.00	0.00	0.14	0.03	15.70	0.22	43.75	0.24	0.27	100.36	0.83
10KS95 A1 a41	WUS	40.26	0.00	0.14	0.03	14.62	0.19	45.08	0.18	0.22	100.74	0.85
10KS95 A1 a42	WUS	41.10	0.00	0.14	0.05	13.69	0.21	45.38	0.22	0.21	101.00	0.86
av 10ks95A1 ol pheno	WUS	40.26	0.00	0.14	0.04	13.70	0.18	45.38	0.23	0.28	100.22	0.86
10KS95 A1 b22	WUS	39.90	0.01	0.15	0.03	15.42	0.30	44.47	0.14	0.33	100.75	0.84
10KS95 A1 b23	WUS	39.61	0.00	0.15	0.02	16.34	0.26	43.18	0.20	0.27	100.04	0.82

10KS95 A1 b24	WUS	39.17	0.00	0.14	0.06	16.04	0.23	42.78	0.19	0.22	98.84	0.83
av 10ks95A1 ol incl in skeletal cpx pheno	WUS	39.56	0.00	0.14	0.04	15.93	0.26	43.48	0.18	0.28	99.88	0.83
10KS95 A1 a43	WUS	39.15	0.00	0.13	0.07	18.90	0.27	40.96	0.10	0.26	99.84	0.79
10KS95 A1 b21	WUS	38.34	0.01	0.15	0.02	21.00	0.30	39.25	0.20	0.24	99.51	0.77
10KS95 A1 d1	WUS	38.79	0.00	0.14	0.02	19.65	0.28	40.53	0.25	0.20	99.85	0.79
10KS95 A1 d2	WUS	39.35	0.00	0.15	0.02	19.21	0.27	40.63	0.25	0.27	100.14	0.79
10KS95 A1 d3	WUS	38.87	0.00	0.13	0.02	21.68	0.35	39.00	0.22	0.23	100.50	0.76
10KS95 A1 d5	WUS	39.44	0.00	0.14	0.03	18.43	0.24	41.81	0.14	0.28	100.51	0.80
av 10ks95A1 skeletal ol & pheno rims	WUS	38.99	0.00	0.14	0.03	19.81	0.28	40.36	0.19	0.25	100.06	0.78
10JB368A a1	PS	39.17	0.00	0.14	0.03	17.98	0.31	41.98	0.28	0.29	100.19	0.81
10JB368A a2	PS	39.11	0.02	0.15	0.01	18.86	0.25	41.06	0.23	0.26	99.96	0.80
10JB368A a3	PS	39.22	0.00	0.15	0.01	19.28	0.34	40.82	0.18	0.24	100.25	0.79
10JB368A a10	PS	38.73	0.01	0.14	0.02	19.30	0.31	40.57	0.18	0.25	99.51	0.79
10JB368A b21	PS	39.20	0.00	0.13	0.03	17.89	0.28	41.69	0.17	0.25	99.64	0.81
10JB368A b22	PS	38.81	0.00	0.14	0.06	18.34	0.20	41.64	0.16	0.29	99.64	0.80
10JB368A b23	PS	39.09	0.00	0.14	0.04	19.23	0.25	40.65	0.23	0.22	99.86	0.79
10JB368A b25	PS	39.32	0.00	0.13	0.00	19.40	0.22	40.62	0.24	0.24	100.19	0.79
av 10jb368a ol pheno, crown & gm	PS	39.08	0.00	0.14	0.02	18.78	0.27	41.13	0.21	0.26	99.90	0.80
10JB368A c27	PS	39.89	0.00	0.14	0.02	15.52	0.18	44.09	0.28	0.24	100.35	0.84
10JB368A c28	PS	39.78	0.00	0.15	0.05	14.73	0.12	44.28	0.21	0.23	99.57	0.84
10JB368A c35	PS	39.35	0.00	0.15	0.04	17.18	0.32	42.37	0.21	0.27	99.87	0.81
10JB368A c36	PS	39.21	0.02	0.15	0.07	16.53	0.10	43.03	0.16	0.28	99.55	0.82
av 10jb368a ol incl in px oiks	PS	39.55	0.01	0.14	0.04	15.99	0.18	43.44	0.21	0.25	99.83	0.83
NW38A 15	WUS	36.76	0.02	0.01	0.00	30.99	0.43	30.81	0.18	0.17	99.38	0.64
NW38A 16	WUS	36.93	0.00	0.00	0.03	31.72	0.41	30.64	0.12	0.12	99.97	0.63
NW38A 17	WUS	36.67	0.00	0.07	0.14	31.20	0.41	30.68	0.11	0.13	99.42	0.64
NW38A 18	WUS	36.81	0.03	0.00	0.01	31.67	0.43	30.14	0.12	0.11	99.31	0.63
NW38A 19	WUS	36.88	0.01	0.04	0.00	31.19	0.42	30.74	0.21	0.15	99.64	0.64
NW38A 20	WUS	36.56	0.01	0.00	0.00	31.69	0.33	30.18	0.14	0.10	99.04	0.63
NW38A 21	WUS	36.60	0.00	0.03	0.00	32.04	0.46	31.10	0.17	0.11	100.50	0.63
NW38A 22	WUS	36.68	0.04	0.05	0.02	32.08	0.49	30.10	0.35	0.15	99.96	0.63
av NW38A ol phenos	WUS	36.74	0.01	0.03	0.03	31.57	0.42	30.55	0.17	0.13	99.65	0.63
AW54B1 23	WUS	40.32	0.01	0.03	0.05	12.83	0.08	45.89	0.28	0.35	99.83	0.86
AW54B1 25	WUS	40.24	0.00	0.02	0.05	13.61	0.15	44.97	0.23	0.24	99.52	0.85
AW54B1 26	WUS	40.12	0.00	0.03	0.08	13.72	0.19	44.92	0.29	0.30	99.66	0.85
AW54B1 28	WUS	40.20	0.00	0.01	0.04	13.75	0.23	44.63	0.22	0.24	99.34	0.85
AW54B1 30	WUS	40.33	0.00	0.02	0.09	13.54	0.12	44.96	0.25	0.30	99.62	0.86
AW54B1 31	WUS	40.21	0.01	0.11	0.10	13.09	0.19	44.74	0.43	0.37	99.27	0.86
AW54B1 32	WUS	40.10	0.00	0.03	0.03	14.14	0.19	44.99	0.28	0.30	100.08	0.85
AW54B1 34	WUS	39.98	0.02	0.03	0.08	13.73	0.16	45.32	0.23	0.28	99.86	0.85
AW54B1 37	WUS	39.92	0.00	0.06	0.07	13.32	0.20	45.67	0.31	0.31	99.90	0.86
AW54B1 39	WUS	39.83	0.00	0.07	0.15	12.47	0.16	46.01	0.33	0.30	99.34	0.87
av AW54B1 ol cores	WUS	40.13	0.01	0.04	0.07	13.42	0.17	45.21	0.28	0.30	99.64	0.86
AW54B1 24	WUS	39.54	0.00	0.03	0.05	16.56	0.24	42.59	0.15	0.30	99.46	0.82
AW54B1 29	WUS	39.44	0.02	0.03	0.05	17.24	0.22	41.86	0.28	0.24	99.37	0.81
AW54B1 33	WUS	38.74	0.01	0.05	0.05	19.76	0.24	40.17	0.27	0.23	99.53	0.78

Appendix F3 – FCSC sulphur isotope data

Sulphur isotopes were analysed at McGill University, Montreal - details of methods are included in Hryciuk et al (In Prep)					
SILL	**SAMPLE ID**	**LITHOLOGY**	**HEIGHT FROM BASE (m)**	**δ^{34}S (VCDT)**	**S (wt %)**
LPS	10BH166 A1	LCZ	0.00	3.69	0.03
LPS	10BH166 A5	OZ	2.72	3.96	0.03
LPS	10BH167 A2	OZ	3.64	4.10	0.02
LPS	10BH167 A4	OZ	7.28	3.72	0.03
LPS	10BH167 A5	CPZ	8.97	4.07	0.05
LPS	10BH167 A8	DZ	12.07	6.66	0.17
LPS	10BH167 A11	DZ	16.88	5.73	0.03
LPS	11BH311 B8	UCZ	21.43	6.94	0.13
PS	10RAT-JB287A01	LCZ	0.00	5.79	0.05
PS	10RAT-JB367A01	LBZ	3.00	3.77	0.05
PS	10RAT-JB367E01	LBZ	4.00	4.84	0.03
PS	10RAT-JB367G01	OZ	7.00	3.27	0.03
PS	10RAT-JB368B01	OZ	9.00	3.57	0.03
PS	10RAT-JB368D01	DZ	12.00	8.02	0.05
PS	10RAT-JB368G01	DZ	16.00	3.53	0.04
PS	10RAT-JB369A01	DZ	18.00	5.12	0.08

Appendix F5 – Dolostone whole-rock data

SAMPLE ID	SiO2	TiO2	Al2O3	Fe2O3	FeOt	FeOt	MnO	MgO	CaO	Na2O	K2O	P2O5	Cr2O3	S wt%	LOI	H2OT	CO2T	TOT
2388-2	1.18	0.02	0.39	1.87	1.68		0.27	8.09	46.74	0.03	0.05	0.04	0.01		41.40			100.10
87RAR-5B-10	16.40	0.05	0.80	1.30	1.17	1.40	0.08	17.30	24.30	0.01	0.21	0.01		0.01		0.70	38.40	99.60
92RAT-M104	20.90	0.18	2.50	2.80	2.52	2.70	0.10	13.20	23.70	0.01	0.83	0.03				0.80	34.80	99.90
93RAT-10	9.70	0.11	1.70	1.00	0.90	1.10	0.06	18.00	26.40	0.01	0.80	0.03		<dl		0.60	41.30	99.70
0730A011	9.76	0.04	0.57	1.24	1.11		0.04	17.86	28.13	0.03	0.26	0.01	0.00	0.12	42.00			99.94
HDB-2005-100																		
GNME-06-04/009	16.46	0.16	2.88	2.62	2.36		0.03	10.37	38.07	0.25	0.09	0.06	0.00	0.05	29.00		7.32	99.99
GNME-06-04/010	18.41	0.17	2.98	2.45	2.20		0.03	10.28	37.21	0.24	0.06	0.06	0.00	0.25	28.10		7.35	99.99
GNME-06-04/121	14.62	0.05	0.99	1.11	1.00		0.03	18.82	31.45	0.01	0.02	0.01	0.00	0.12	32.90		7.27	99.99
GNME-06-04/122	14.85	0.14	2.49	1.60	1.44		0.04	19.74	30.56	0.01	0.24	0.02	0.00	0.77	30.30		6.40	99.99
GNME-06-05/005	14.83	0.12	1.92	1.04	0.93		0.02	10.90	38.03	0.11	0.32	0.02	0.00	0.16	32.60		8.58	99.91
GNME-06-05/032	14.62	0.07	1.49	3.18	2.86		0.02	22.08	26.99	0.01	0.02	0.01	0.00	0.07	31.40		6.19	99.87
GNME-06-05/033	13.44	0.07	1.28	1.27	1.14		0.03	23.03	27.45	0.01	0.02	0.03	0.00	0.01	33.30		6.43	99.92
GNME-06-05/129	10.35	0.06	1.00	0.70	0.63		0.02	19.57	32.78	0.01	0.02	0.02	0.00	0.14	35.40		8.80	99.93
GNME-06-05/130	8.17	0.07	1.13	0.83	0.75		0.01	19.27	36.95	0.02	0.04	0.03	0.00	3.00	32.60		8.35	99.12
GNME-06-05/131	12.28	0.06	1.11	0.67	0.60		0.03	20.66	31.16	0.01	0.09	0.04	0.00	0.13	33.80		7.84	99.91
10RAT-RR197B01	2.39	0.01	0.19	0.55	0.50		0.10	19.08	29.05	< 0.07	< 0.08	< 0.03		0.07	45.70			97.20
10RAT-HY074A01b	16.69	0.17	3.08	1.32	1.19		0.04	17.15	27.04	0.14	0.67	0.04		0.38	33.20			99.90
10RAT-HY074A02b	12.92	0.16	2.80	1.53	1.37		0.04	18.20	29.43	0.09	0.85	0.04		0.42	34.30			100.80
11-RAT-BH188A1	7.10	0.02	0.50	0.38	0.34		0.01	19.60	31.00	< 0,05	0.09	0.01		0.18	39.23			98.00
11-RAT-BH367A1	1.50	0.01	0.10	0.98	0.88		0.03	17.40	32.00	< 0,05	< 0,007	< 0,01		0.43	44.17			97.00
11-RAT-BH369A1	1.50	0.01	0.20	0.68	0.61		0.03	22.00	35.60	0.14	< 0,007	0.01		0.26	38.81			99.00
Dolostone average	11.34	0.08	1.43	1.39	1.25	1.73	0.05	17.27	31.62	0.06	0.26	0.03	0.00	0.36	35.46	0.70	14.54	99.51

Appendix G1 – SFDC whole-rock data

ZONE	D	D	D	D	D	D	D	D
LITHOLOGY	dyke core	dyke core	dyke	dyke core	dyke core	dyke chill	capping sill	dyke core
			internal chill					
SAMPLE I.D.	**11MH123B2**	**11BH296A1**	**11BH268A2**	**11BH270A2**	**11BH266A2**	**11MH126A2**	**11MH128A2**	**11BH264A2**
Lab	Cardiff	Cardiff	Cardiff	Cardiff	Cardiff	Cardiff	Cardiff	Cardiff
SiO2	47.85	47.21	48.75	47.92	47.80	47.06	46.91	46.99
TiO2	1.23	1.90	1.56	1.32	1.38	1.29	1.07	1.96
Al2O3	13.39	11.92	12.60	12.76	13.17	13.11	13.90	10.84
Fe2O3T	13.88	17.72	15.46	12.40	14.52	13.90	12.57	19.36
FeO*	12.48	15.93	13.90	11.15	13.05	12.49	11.30	17.41
Fe2O3*	1.40	1.79	1.56	1.25	1.47	1.40	1.27	1.96
MnO	0.20	0.23	0.22	0.18	0.20	0.20	0.19	0.26
MgO	8.19	5.63	7.09	7.45	7.71	8.47	8.43	5.57
CaO	11.22	9.92	11.66	11.66	12.25	11.67	13.53	9.77
Na2O	2.03	1.95	2.36	2.21	2.08	2.07	1.65	2.59
K2O	0.49	1.77	0.72	1.31	0.52	0.83	0.47	0.79
P2O5	0.11	0.17	0.12	0.11	0.12	0.09	0.09	0.21
LOI	0.79	0.71	0.79	1.57	1.04	0.82	0.87	1.18
TOTAL	99.37	116.85	101.34	98.89	100.78	113.41	99.66	99.53
Sc	40.48	41.80	44.98	44.45	44.22	42.11	42.62	40.68
V	367.20	464.97	462.38	401.62	427.53	415.06	298.90	474.13
Cr	237.27	5.00	56.76	228.72	197.49	211.54	304.43	5.78
Co	66.48	83.35	75.74	58.67	69.21	66.35	56.16	90.57
Ni	193.65	7.45	30.08	73.22	50.38	64.61	95.52	39.53
Cu	122.08	207.33	147.31	117.08	133.78	135.47	104.30	166.74
Zn	93.99	111.66	80.52	115.53	89.23	83.14	74.79	123.49
Sr	205.85	407.41	262.77	425.98	217.09	270.42	172.07	304.64
Y	22.05	32.53	27.06	23.95	25.26	23.25	18.70	35.60
Zr	58.37	133.91	97.34	65.35	96.16	86.36	63.41	140.64
Ba	184.80	244.08	107.74	155.74	100.80	201.41	81.76	149.62
Ti	1.23	1.95	1.49	1.30	1.36	1.28	1.08	1.96
V	337.80	497.70	416.00	338.00	378.60	398.20	323.40	479.50
Cr	222.30	4.00	63.10	220.80	189.60	208.30	283.80	9.70
Co	65.10	79.20	75.70	54.50	64.70	65.90	55.40	87.80
Ni	192.60	11.80	34.40	77.20	50.70	60.00	81.80	41.90
Cu	119.60	227.00	143.10	111.70	131.70	129.30	107.80	177.50
Zn	87.00	117.50	77.50	108.10	84.90	80.20	78.70	123.30
Rb	11.10	50.40	21.50	37.20	12.80	22.10	13.80	22.30
K	4946.76	17668.01	7213.11	13093.01	5191.70	8271.14	4652.79	7942.05
Sr	194.10	411.70	261.90	419.40	206.50	3333.00	174.20	303.30
P	1056.73	1682.99	1246.97	1078.19	1177.46	940.65	862.70	2139.32
Y	21.40	36.30	26.90	20.60	25.40	23.40	19.90	38.00
Zr	73.00	133.50	96.70	66.80	95.00	89.40	66.60	134.70
Nb	3.39	6.29	4.82	2.95	4.69	4.01	2.80	6.52
Sn	1.72	1.19	0.99	1.95	0.82	1.00	1.44	0.83
Cs	0.55	0.92	1.51	2.02	0.81	0.95	0.95	0.62
Ba	176.40	237.20	110.70	143.40	107.40	206.00	86.00	145.50
La	5.53	8.49	6.73	5.51	6.97	5.96	4.94	10.63
Ce	13.56	20.84	16.66	13.30	16.87	14.47	11.96	25.58
Pr	1.96	3.08	2.43	1.93	2.38	2.13	1.75	3.72
Nd	9.25	14.30	11.54	8.90	11.15	9.68	8.07	17.29
Sm	2.62	4.10	3.41	2.60	3.26	2.84	2.47	4.89
Eu	0.99	1.38	1.16	0.97	1.11	1.04	0.86	1.52
Gd	3.21	4.91	3.88	2.89	3.62	3.34	2.88	5.55
Tb	0.55	0.91	0.69	0.52	0.67	0.61	0.49	0.94
Dy	3.63	5.52	4.41	3.44	4.21	3.94	3.24	6.00
Ho	0.64	1.07	0.78	0.64	0.77	0.71	0.59	1.05
Er	1.89	3.06	2.32	1.85	2.24	2.07	1.75	3.12
Tm	0.30	0.47	0.37	0.29	0.36	0.32	0.27	0.51
Yb	1.81	3.03	2.32	1.83	2.18	2.03	1.75	3.17
Lu	0.29	0.47	0.35	0.29	0.34	0.31	0.26	0.46
Hf	1.82	3.52	2.50	1.65	2.50	2.24	1.63	3.45
Ta	0.26	0.41	0.32	0.22	0.31	0.27	0.20	0.45

Pb	1.92	7.50	1.58	1.44	1.67	1.90	2.85	1.96
Th	0.76	1.39	0.98	0.76	0.97	0.82	0.71	1.46
U	0.18	0.30	0.20	0.17	0.23	0.18	0.15	0.34
Os	0.21	<0.03	0.07			0.06		
Ir	0.44	0.17	0.04			0.04		
Ru	0.83	0.30	0.44			0.37		
Rh	1.01	0.80	0.65			0.42		
Pt	17.7	9.07	10.7			6.51		
Pd	22.4	16.6	24.9			16.4		
Au	4.38	4.17	3.26			2.22		

ZONE	D	D	D	D	C	C	C	C
LITHOLOGY	dyke core	dyke core	dyke core	dyke core	dyke core	dyke core	small dyke	dyke chill
SAMPLE I.D.	**11MH124B2**	**11MH271A2**	**11MH125A2**	**11BH269A2**	**11MH129A2**	**11BH239A2**	**11MH131A2**	**11MH130A2**
Lab	Cardiff	Cardiff	Cardiff	Cardiff	Cardiff	Cardiff	Cardiff	Cardiff
SiO2	47.09	47.05	47.80	48.40	47.72	48.32	47.27	47.64
TiO2	1.26	1.34	1.27	1.42	1.16	1.81	1.21	1.38
Al2O3	12.81	13.05	12.83	13.10	13.25	12.96	12.80	13.12
Fe2O3T	14.01	12.86	14.20	14.12	14.08	17.05	13.46	14.09
FeO*	12.59	11.56	12.76	12.69	12.66	15.32	12.10	12.67
Fe2O3*	1.41	1.30	1.43	1.43	1.42	1.72	1.36	1.42
MnO	0.21	0.18	0.22	0.21	0.21	0.24	0.20	0.21
MgO	8.09	8.21	7.93	7.58	9.00	4.96	8.06	7.20
CaO	12.04	13.55	13.20	10.48	11.85	10.04	13.72	12.35
Na2O	1.64	1.99	1.77	2.34	2.04	2.43	1.66	1.88
K2O	0.59	1.06	0.44	1.49	0.43	1.37	1.32	0.57
P2O5	0.11	0.11	0.09	0.11	0.09	0.15	0.09	0.11
LOI	1.16	1.30	0.90	1.91	0.81	0.66	1.07	0.56
TOTAL	98.99	100.71	100.64	101.16	114.72	99.99	100.86	99.13
Sc	40.44	43.27	44.86	45.56	42.41	43.04	43.23	42.09
V	350.44	369.14	364.94	390.46	383.52	475.33	346.74	377.42
Cr	230.11	208.64	181.31	215.34	306.85	35.19	196.59	132.81
Co	64.15	59.82	66.27	66.58	68.68	82.45	62.58	66.89
Ni	129.41	61.42	63.92	57.12	491.27	48.80	67.33	44.49
Cu	135.10	109.78	117.83	128.49	116.96	181.65	129.50	145.96
Zn	92.27	57.62	86.66	60.36	71.15	101.22	63.16	100.42
Sr	203.44	300.27	206.74	435.94	209.83	388.06	592.23	204.63
Y	21.10	21.58	19.17	22.37	21.24	34.61	19.52	20.99
Zr	76.96	82.58	71.78	92.63	68.79	119.59	73.77	85.27
Ba	97.15	271.18	420.29	191.78	128.66	243.95	344.47	143.44
Ti	1.32	1.37	1.24	1.41	1.14	1.79	1.19	1.42
V	357.20	374.00	372.70	401.80	378.00	471.40	353.00	380.20
Cr	217.90	198.40	171.60	209.00	306.80	43.20	187.30	132.10
Co	61.20	54.20	62.20	63.10	66.20	86.80	57.90	66.80
Ni	109.30	60.00	52.70	54.30	461.20	52.90	63.50	44.90
Cu	148.30	118.10	128.30	135.10	107.40	204.60	138.40	151.60
Zn	103.00	55.30	88.70	61.10	72.00	106.90	64.30	105.60
Rb	19.10	45.40	14.10	53.00	11.40	40.10	37.20	16.70
K	5901.90	10597.21	4373.96	14867.85	4322.78	13655.46	13156.67	5734.03
Sr	212.90	319.70	217.00	458.90	191.10	376.70	609.30	215.30
P	1073.12	1094.31	892.00	1124.10	928.05	1540.67	917.28	1122.32
Y	23.70	24.10	21.70	25.50	19.60	34.70	22.60	24.90
Zr	83.40	88.20	73.10	94.10	64.60	114.30	76.90	90.90
Nb	3.90	4.47	3.36	4.25	2.76	5.40	3.45	4.55
Sn	1.36	1.44	1.52	1.15	0.89	2.23	0.84	1.66
Cs	0.97	2.66	0.73	1.32	0.56	0.56	1.89	0.98
Ba	107.40	271.30	398.00	191.90	124.80	251.70	332.00	148.70
La	6.92	6.18	4.91	6.44	4.69	8.58	5.14	6.49
Ce	16.10	15.04	11.86	15.45	11.65	20.93	12.43	15.46
Pr	2.28	2.24	1.79	2.27	1.75	3.01	1.84	2.30

Nd	10.58	10.37	8.41	10.83	7.98	14.07	8.72	10.60
Sm	2.95	3.00	2.52	3.10	2.25	4.05	2.61	3.08
Eu	1.09	1.10	0.98	1.19	0.89	1.39	0.92	1.13
Gd	3.52	3.38	2.94	3.64	2.80	4.69	2.95	3.58
Tb	0.66	0.64	0.54	0.67	0.52	0.87	0.56	0.66
Dy	3.93	3.91	3.57	4.05	3.31	5.18	3.47	4.04
Ho	0.74	0.72	0.65	0.77	0.62	0.95	0.65	0.74
Er	2.10	2.17	1.90	2.21	1.81	2.88	1.96	2.15
Tm	0.33	0.34	0.30	0.34	0.28	0.45	0.30	0.33
Yb	2.04	2.04	1.84	2.10	1.78	2.78	1.88	2.10
Lu	0.33	0.33	0.29	0.34	0.29	0.44	0.29	0.34
Hf	2.27	2.27	1.89	2.55	1.65	3.09	1.97	2.47
Ta	0.28	0.29	0.22	0.31	0.21	0.38	0.23	0.30
Pb	2.18	1.03	2.36	1.04	1.50	2.10	3.09	3.55
Th	0.85	0.89	0.77	0.89	0.68	1.25	0.70	0.86
U	0.18	0.24	0.16	0.21	0.16	0.31	0.17	0.20
Os					<0.03		0.10	
Ir					<0.03		0.03	
Ru					0.22		0.30	
Rh					0.47		0.49	
Pt					6.41		9.07	
Pd					15.1		17.0	
Au					2.67		2.21	

ZONE	C/D	B	B	B	B	B	B	B	B
LITHOLOGY	dyke core	dyke	dyke	dyke	connecting	connecting	dyke	connecting	dyke
		prop tip	propr tip	prop tip	dyke	dyke	prop tip	dyke	prop tip
SAMPLE I.D.	**11BH292 A1**	**11BH185 A2**	**11BH197 A4**	**11BH185 A2**	**11BH207 A1**	**11BH209 A1**	**11BH185 A1**	**11BH210 A1**	**11JB105 C2**
Lab	Cardiff	Cardiff	Cardiff	Cardiff	Cardiff	Cardiff	Cardiff	Cardiff	INRS
SiO2	47.46	45.36	42.65	45.36	49.66	49.05	48.53	49.60	47.28
TiO2	1.17	1.19	0.94	1.19	1.00	0.99	1.15	1.02	1.08
Al2O3	13.34	13.13	10.66	13.13	13.00	12.85	13.95	13.16	13.73
Fe2O3T	13.79	11.46	5.57	11.46	9.43	9.12	10.17	7.69	11.70
FeO*	12.40	10.30	5.01	10.30	8.48	8.20	9.14	6.91	10.52
Fe2O3*	1.39	1.16	0.56	1.16	0.95	0.92	1.03	0.78	1.18
MnO	0.21	0.13	0.08	0.13	0.11	0.11	0.15	0.09	0.14
MgO	7.45	8.60	9.11	8.60	10.13	9.44	8.39	10.29	7.38
CaO	12.86	13.81	18.45	13.81	10.35	11.61	11.66	11.30	12.04
Na2O	1.93	1.59	2.33	1.59	0.98	1.23	1.82	0.86	1.38
K2O	0.55	1.91	1.85	1.91	3.74	3.10	2.55	3.64	2.18
P2O5	0.08	0.08	0.05	0.08	0.10	0.09	0.10	0.10	0.08
LOI	0.50	2.44	9.36	2.44	1.74	1.46	2.99	2.16	2.88
TOTAL	99.36	99.71	106.63	111.17	100.24	99.07	101.46	99.90	100.02
Sc	46.31	43.60	33.06	43.56	39.37	37.97	44.24	38.61	
V	380.10	376.30	285.36	376.32	317.35	308.35	337.87	275.80	
Cr	93.01	199.20	151.42	199.24	518.30	477.83	207.69	440.31	
Co	68.22	55.00	24.72	55.03	42.64	43.79	46.70	34.72	
Ni	36.46	67.60	33.11	67.59	116.17	116.54	58.91	153.19	
Cu	135.35	104.30	108.99	104.31	22.44	18.14	85.87	18.30	
Zn	94.31	38.20	89.67	38.19	14.24	20.13	36.37	17.84	
Sr	225.35	602.90	346.54	602.95	1267.76	970.20	707.70	1479.68	
Y	21.77	22.50	19.79	22.50	22.71	22.08	20.14	20.21	
Zr	68.17	86.00	70.43	86.02	115.44	97.87	76.93	108.39	
Ba	182.55	325.10	800.25	325.11	1440.85	521.80	284.50	1448.70	
Ti	1.16	1.15	0.93	1.15	0.98	0.95	1.17	0.99	0.00
V	356.70	366.40	276.80	366.40	299.60	288.60	334.40	291.50	31.00
Cr	100.60	195.80	148.10	195.80	471.90	456.70	201.20	431.30	4.00
Co	66.90	49.90	22.20	49.90	38.60	40.10	44.20	37.30	72.00
Ni	43.90	73.90	33.50	73.90	109.70	103.60	57.00	142.70	13.00
Cu	144.70	110.80	116.40	110.80	18.50	17.60	90.60	17.80	< 7
Zn	100.40	31.30	98.30	31.30	12.60	18.60	35.00	13.40	< 6

Rb	16.40	58.40	68.20	58.40	123.70	93.50	77.60	131.60	0.13
K	5497.20	19100.00	18496.46	19111.44	37363.39	30951.48	25547.07	36356.64	
Sr	215.40	591.80	330.10	591.80	1247.30	983.00	719.40	1398.10	111.00
P	812.31	800.00	537.76	799.53	988.82	933.79	959.27	953.97	203.59
Y	21.10	22.80	19.60	22.80	22.10	22.30	21.90	21.60	9.40
Zr	67.80	87.50	75.20	87.50	115.20	104.20	78.80	106.60	1.70
Nb	3.17	3.92	4.17	3.92	5.54	5.61	3.44	5.67	0.43
Sn	1.06	1.58	1.65	1.58	0.91	1.20	1.10	0.78	< 0.5
Cs	0.45	0.55	0.37	0.55	1.65	2.04	0.71	2.32	<0.1
Ba	187.70	340.20	804.40	340.20	1386.00	507.30	272.30	1319.40	3.60
La	4.96	5.61	6.10	5.61	7.86	14.11	5.15	8.16	13.00
Ce	11.99	13.58	14.53	13.58	20.08	28.24	12.79	18.78	22.50
Pr	1.75	1.99	2.03	1.99	2.85	3.48	1.90	2.61	2.60
Nd	8.50	9.16	9.08	9.16	11.97	13.95	8.72	11.61	9.20
Sm	2.48	2.65	2.49	2.65	3.18	3.27	2.52	3.00	2.00
Eu	0.98	1.15	0.86	1.15	1.04	1.04	1.07	1.04	1.13
Gd	2.99	3.21	2.93	3.21	3.32	3.47	3.01	3.24	1.88
Tb	0.54	0.58	0.55	0.58	0.55	0.62	0.55	0.56	0.34
Dy	3.46	3.76	3.33	3.76	3.45	3.71	3.53	3.47	1.79
Ho	0.62	0.68	0.60	0.68	0.62	0.68	0.66	0.63	0.35
Er	1.87	2.03	1.74	2.03	1.94	2.03	1.86	1.88	0.80
Tm	0.30	0.30	0.28	0.30	0.31	0.31	0.31	0.32	0.11
Yb	1.79	1.92	1.72	1.92	1.97	2.04	1.80	1.92	0.59
Lu	0.28	0.32	0.27	0.32	0.30	0.32	0.29	0.32	0.06
Hf	1.75	2.21	1.83	2.21	3.05	2.63	1.86	2.63	0.02
Ta	0.22	0.25	0.28	0.25	0.40	0.43	0.23	0.40	<0.024
Pb	1.43	2.60	6.86	2.60	2.56	1.90	1.43	1.50	0.29
Th	0.75	0.79	1.34	0.79	3.12	3.30	0.77	2.99	<0.24
U	0.16	0.27	0.68	0.27	0.74	0.75	0.20	0.70	0.23
		<0.03							
Os		<0.03					0.20	0.14	
Ir		0.26					0.16	0.15	
Ru		0.44					0.34	0.33	
Rh		21.8					0.42	0.22	
Pt		13.6					13.6	9.36	
Pd		1.77					11.1	5.24	
Au							1.77	0.50	

ZONE	B	A	A	A	A	A	E	E
LITHOLOGY	dyke	dyke chill	small dyke	dyke core	dyke core	dyke chill	dyke chill	dyke core
	prop tip		apophysis					
SAMPLE I.D.	**11JB109B1**	**11BH154A3**	**11BH154A2**	**11BH175A1**	**11BH167A4**	**11BH167A2**	**11BH366B1**	**11BH372A1**
Lab	INRS	Cardiff	Cardiff	Cardiff	Cardiff	Cardiff	Cardiff	Cardiff
SiO2	50.82	47.37	47.35	46.71	47.01	46.37	46.60	48.16
TiO2	0.98	1.29	1.43	1.09	1.27	1.19	1.18	1.50
Al2O3	13.48	13.79	12.79	13.42	13.03	12.91	13.71	12.27
Fe2O3T	10.28	12.61	13.60	12.68	14.31	13.61	12.90	15.98
FeO*	9.24	11.33	12.23	11.40	12.86	12.24	11.60	14.37
Fe2O3*	1.04	1.27	1.37	1.28	1.45	1.38	1.30	1.61
MnO	0.16	0.17	0.19	0.19	0.22	0.20	0.19	0.24
MgO	8.51	7.90	6.80	8.62	7.49	8.06	8.12	6.70
CaO	9.79	9.39	11.37	12.57	11.22	10.33	12.08	9.74
Na2O	1.26	2.35	2.34	1.11	1.76	1.00	1.63	1.80
K2O	2.58	2.83	2.29	2.99	2.32	3.24	2.26	1.74
P2O5	0.09	0.09	0.11	0.10	0.10	0.09	0.09	0.13
LOI	1.22	2.49	1.90	1.53	1.68	1.83	1.44	1.42
TOTAL	99.30	100.28	100.18	101.02	100.41	112.46	100.19	99.68
Sc		46.90	46.12	45.99	43.81	42.54	46.5	43.7
V		399.83	425.50	346.17	428.11	405.52	380.8	398.7
Cr		196.66	59.38	248.07	146.11	192.95	217.3	27.3
Co		59.71	66.62	61.23	66.96	64.65	62.2	73.7
Ni		76.58	35.62	90.82	50.69	56.54	74.2	44.5
Cu		113.01	126.56	114.49	138.55	131.39	111.1	150.8

Zn		46.35	52.41	79.39	136.83	107.65	99.5	90.7
Sr		473.09	518.36	571.81	336.42	610.24	456.0	297.3
Y		24.65	27.49	21.41	23.53	21.57	22.2	25.7
Zr		90.32	91.33	66.95	79.75	75.88	72.3	97.7
Ba		1199.84	847.44	675.50	124.84	493.43	513.7	199.9
Ti	1.08	1.25	1.43	1.10	1.27	1.17	1.2	1.5
V	316.00	386.30	426.30	329.80	400.70	396.00	372.2	423.1
Cr	203.00	200.60	61.10	239.60	141.60	188.60	209.8	38.0
Co	47.00	55.80	64.00	62.10	66.00	65.20	59.7	70.2
Ni	100.00	73.20	39.30	90.70	51.00	54.50	70.3	43.7
Cu	156.00	117.80	132.20	114.80	148.50	131.40	105.4	154.6
Zn	71.00	42.20	55.00	74.60	141.90	114.60	107.8	90.2
Rb	57.20	120.50	95.60	85.50	76.40	83.10	52.7	48.0
K	18067.50	28326.50	22855.16	29883.01	23221.78	32421.48	22601.50	17391.98
Sr	781.00	454.70	507.90	565.10	325.60	584.10	442.60	308.20
P	358.78	913.86	1121.59	973.52	1009.35	931.94	881.69	1280.08
Y	19.00	23.70	27.10	20.60	24.40	22.10	21.1	28.1
Zr	61.00	89.00	95.50	69.20	83.30	77.90	70.1	98.5
Nb	3.32	3.86	4.42	2.92	3.88	3.49	2.82	4.44
Sn	1.10	1.51	0.99	0.80	1.14	0.79	0.94	1.60
Cs	1.09	1.46	1.02	1.09	0.73	0.72	0.80	0.90
Ba	214.00	1298.00	884.80	651.70	134.80	477.80	511.8	185.7
La	4.80	5.47	6.12	4.88	6.02	5.18	4.86	6.81
Ce	11.50	13.70	15.42	12.02	14.61	12.54	12.03	16.59
Pr	1.74	2.02	2.31	1.80	2.12	1.87	1.77	2.47
Nd	8.08	9.57	10.68	8.38	9.82	8.67	8.25	11.36
Sm	2.40	2.79	3.26	2.46	3.03	2.61	2.49	3.44
Eu	0.99	1.20	1.21	0.92	1.08	1.07	0.97	1.22
Gd	2.82	3.29	3.72	2.80	3.42	3.07	2.94	4.00
Tb	0.57	0.60	0.67	0.50	0.64	0.56	0.54	0.69
Dy	3.30	3.77	4.18	3.18	4.09	3.69	3.36	4.56
Ho	0.74	0.68	0.77	0.58	0.74	0.68	0.60	0.83
Er	1.95	2.12	2.30	1.73	2.18	1.94	1.84	2.48
Tm	0.29	0.32	0.36	0.27	0.35	0.32	0.27	0.39
Yb	1.93	2.01	2.26	1.72	2.16	1.92	1.78	2.47
Lu	0.27	0.31	0.35	0.27	0.32	0.31	0.29	0.36
Hf	1.86	2.42	2.54	1.72	2.21	2.04	1.79	2.59
Ta	0.23	0.25	0.29	0.20	0.27	0.23	0.21	0.31
Pb	3.00	4.03	1.58	2.09	4.08	2.32	2.85	1.36
Th	0.80	0.80	0.94	0.67	0.87	0.76	0.70	1.02
U	0.18	0.18	0.21	0.16	0.20	0.18	0.16	0.23
Os		0.04	<0.03		<0.03		<0.03	
Ir		0.03	<0.03		<0.03		<0.03	
Ru		0.24	0.17		0.20		0.38	
Rh		0.34	0.38		0.48		0.73	
Pt		7.47	15.7		6.85		38.7	
Pd		12.9	15.7		21.6		17.3	
Au		1.33	1.85		2.45		3.30	

Appendix G2 – SFDC olivine mineral chemistry

ZONE	SAMPLE ID	X Region	SiO2	TiO2	Al2O3	Cr2O3	FeO	MnO	MgO	CaO	NiO	Total	Fo (mol %)
D	MH123 B2 46	core	37.72	0.00	0.05	0.02	24.33	0.30	37.63	0.30	0.19	100.55	0.73
	MH123 B2 47	rimward	37.66	0.00	0.03	0.00	25.76	0.33	36.08	0.25	0.15	100.26	0.71
	MH123 B2 48	rimward	37.15	0.00	0.01	0.03	29.13	0.42	33.17	0.29	0.11	100.30	0.67
	MH123 B2 49	rim	34.30	0.02	0.03	0.02	35.46	0.56	27.97	0.23	0.05	98.64	0.58
	MH123 B2 46-49	average	36.71	0.01	0.03	0.02	28.67	0.40	33.71	0.27	0.13	99.94	0.68
	MH123 B2 50	core	37.30	0.00	0.04	0.01	25.92	0.34	36.20	0.29	0.16	100.26	0.71
	MH123 B2 51	rim	35.34	0.02	0.00	0.02	35.04	0.47	28.70	0.21	0.10	99.90	0.59
	MH123 B2 50-51	average	36.32	0.01	0.02	0.01	30.48	0.41	32.45	0.25	0.13	100.08	0.65
	MH123 B2 52	core	36.93	0.00	0.05	0.00	24.73	0.37	36.75	0.30	0.16	99.28	0.73
	MH123 B2 53	rim	37.14	0.01	0.04	0.02	23.79	0.32	37.37	0.19	0.14	99.02	0.74
	MH123 B2 52-53	average	37.03	0.01	0.05	0.01	24.26	0.34	37.06	0.24	0.15	99.15	0.73
	MH123 B2 65	core	37.68	0.01	0.03	0.04	21.32	0.25	39.22	0.33	0.16	99.03	0.77
	MH123 B2 66	rimward	37.13	0.00	0.04	0.00	22.26	0.33	39.04	0.32	0.12	99.24	0.76
	MH123 B2 67	rimward	37.19	0.00	0.05	0.00	23.64	0.24	37.98	0.30	0.17	99.58	0.74
	MH123 B2 68	rimward	34.99	0.01	0.04	0.00	34.75	0.59	28.33	0.24	0.13	99.05	0.59
	MH123 B2 69	rim	33.82	0.01	0.01	0.01	40.81	0.67	22.87	0.26	0.12	98.58	0.50
	MH123 B2 65-69	average	36.16	0.00	0.03	0.01	28.56	0.41	33.49	0.29	0.14	99.10	0.67
	MH123 B2 92	rep	34.48	0.00	0.02	0.02	32.35	0.35	29.86	0.25	0.11	97.42	0.62
	MH123 B2 93	core	33.16	0.00	0.03	0.03	37.88	0.60	25.19	0.26	0.08	97.23	0.54
	MH123 B2 94	rim	35.10	0.00	0.03	0.00	35.74	0.42	27.22	0.25	0.16	98.91	0.58
	MH123 B2 93-94	average	34.13	0.00	0.03	0.01	36.81	0.51	26.21	0.26	0.12	98.07	0.56
	MH126 A2 32	core	39.55	0.00	0.43	0.02	19.87	0.25	40.41	0.27	0.17	100.96	0.78
	MH126 A2 33	rim	39.92	0.01	0.10	0.02	19.27	0.37	41.01	0.31	0.24	101.26	0.79
	MH126 A2 34	rim2	39.06	0.00	0.13	0.03	24.72	0.26	36.61	0.30	0.15	101.26	0.73
	MH126 A2 33-34	rim average	39.51	0.00	0.22	0.02	21.29	0.30	39.34	0.29	0.19	101.16	0.77
	MH126 A2 32-34	average (incl A384)	39.53	0.00	0.33	0.02	20.58	0.28	39.87	0.28	0.18	101.06	0.78
	MH126 A2 36	core	39.88	0.03	0.58	0.25	19.35	0.26	39.50	1.27	0.16	101.25	0.78
	MH126 A2 37	rim	38.89	0.00	0.05	0.00	26.21	0.30	35.22	0.28	0.16	101.12	0.71
	MH126 A2 36-37	average	39.38	0.02	0.31	0.13	22.78	0.28	37.36	0.77	0.16	101.18	0.74
	MH126 A2 38	core	38.99	0.00	0.06	0.02	18.49	0.26	42.07	0.30	0.19	100.39	0.80
	MH126 A2 39	rim	37.64	0.01	0.07	0.02	24.57	0.39	37.27	0.29	0.20	100.44	0.73
	MH126 A2 38-39	average	38.32	0.00	0.06	0.02	21.53	0.33	39.67	0.29	0.20	100.41	0.77
	MH126 A2 40	core	38.91	0.00	0.08	0.03	18.70	0.31	42.03	0.35	0.18	100.61	0.80
	MH126 A2 41	rim	36.25	0.01	0.00	0.00	33.05	0.45	30.13	0.12	0.13	100.14	0.62
	MH126 A2 40-41	average	37.58	0.00	0.04	0.01	25.88	0.38	36.08	0.24	0.16	100.38	0.71
	MH126 A2 42	core	39.94	0.02	0.06	0.02	19.07	0.26	42.12	0.30	0.24	102.02	0.80
	MH126 A2 43	rim	38.23	0.00	0.05	0.03	24.06	0.30	37.22	0.27	0.22	100.38	0.73
	MH126 A2 42-43	average	39.09	0.01	0.05	0.02	21.57	0.28	39.67	0.28	0.23	101.20	0.77
C	MH129 A2 136	core	34.93	0.02	0.03	0.00	41.46	0.57	23.31	0.24	0.08	100.64	0.50

	MH129 A2 137	rimwards	34.24	0.02	0.05	0.00	41.19	0.57	23.22	0.24	0.06	99.59	0.50
	MH129 A2 138	rim	33.94	0.04	0.01	0.02	40.63	0.50	23.50	0.19	0.07	98.89	0.51
	MH129 A2 136-138	average	34.37	0.03	0.03	0.01	41.09	0.55	23.35	0.22	0.07	99.70	0.50
	MH129 A2 139	rep	34.48	0.03	0.02	0.00	42.17	0.51	22.85	0.19	0.07	100.31	0.49
	MH129 A2 140	core	33.90	0.03	0.03	0.01	41.23	0.58	22.99	0.20	0.07	99.03	0.50
	MH129 A2 141	rim	34.57	0.00	0.01	0.00	42.22	0.52	22.96	0.17	0.08	100.53	0.49
	MH129 A2 140-141	average	34.24	0.01	0.02	0.00	41.72	0.55	22.97	0.19	0.08	99.78	0.50
	MH129 A2 142	rep	34.52	0.02	0.03	0.00	40.41	0.52	23.72	0.20	0.06	99.48	0.51
	MH129 A2 143	rep	34.33	0.03	0.02	0.02	41.19	0.62	24.02	0.17	0.03	100.43	0.51
	MH129 A2 149	core	34.36	0.00	0.01	0.00	41.80	0.50	22.30	0.22	0.07	99.26	0.49
	MH129 A2 150	rim	34.11	0.00	0.09	0.00	42.44	0.71	21.83	0.21	0.05	99.43	0.48
	MH129 A2 149-150	average	34.24	0.00	0.05	0.00	42.12	0.60	22.07	0.21	0.06	99.35	0.48
	MH129 A2 173	rep	34.50	0.00	0.02	0.00	42.29	0.58	22.56	0.21	0.05	100.21	0.49
	MH129 A2 174	rep	34.76	0.01	0.01	0.00	41.87	0.65	22.69	0.22	0.02	100.23	0.49
E	BH366 B1 72	core	38.65	0.00	0.09	0.02	23.65	0.30	38.36	0.16	0.16	101.39	0.50
	BH366 B1 73	rimwards	38.27	0.00	0.07	0.00	26.35	0.35	35.89	0.16	0.16	101.24	0.50
	BH366 B1 74	rim	38.44	0.00	0.07	0.00	25.81	0.32	35.71	0.14	0.14	100.64	0.51
	BH366 B1 72-74	average	38.45	0.00	0.08	0.01	25.27	0.32	36.65	0.15	0.15	101.09	0.50
	BH366 B1 75	rep	38.19	0.01	0.22	0.09	26.80	0.38	34.38	0.67	0.10	100.83	0.49
	BH366 B1 76	core	39.54	0.00	0.03	0.00	20.93	0.29	40.26	0.20	0.15	101.39	0.50
	BH366 B1 77	rim	37.68	0.00	0.07	0.00	28.58	0.40	33.20	0.22	0.14	100.29	0.49
	BH366 B1 76-77	average	38.61	0.00	0.05	0.00	24.75	0.35	36.73	0.21	0.15	100.84	0.50
	BH366 B1 83	core	39.98	0.00	0.03	0.03	18.20	0.29	42.06	0.29	0.21	101.07	0.51
	BH366 B1 84	rimwards	39.10	0.00	0.07	0.01	22.23	0.31	38.78	0.30	0.19	100.99	0.51
	BH366 B1 85	rim	38.38	0.01	0.03	0.00	26.02	0.41	36.05	0.11	0.12	101.13	0.49
	BH366 B1 83-85	average	39.15	0.00	0.04	0.01	22.15	0.33	38.96	0.23	0.17	101.06	0.48
	BH366 B1 89	core	38.64	0.01	2.66	0.03	21.45	0.34	39.15	0.30	0.20	102.77	0.48
	BH366 B1 90	rim	37.27	0.03	0.03	0.02	28.61	0.38	33.81	0.13	0.14	100.42	0.49
	BH366 B1 89-90	average	37.95	0.02	1.35	0.03	25.03	0.36	36.48	0.22	0.17	101.60	0.49
	BH366 B1 91	core	37.90	0.00	0.04	0.02	26.08	0.47	35.99	0.22	0.15	100.85	#VALUE!
	BH366 B1 92	rim	37.49	0.01	0.08	0.00	27.59	0.32	34.48	0.13	0.11	100.21	#VALUE!
	BH366 B1 91-92	average	37.69	0.00	0.06	0.01	26.84	0.39	35.23	0.17	0.13	100.53	#VALUE!
A	BH154 A2 73	core	38.19	0.00	0.01	0.00	22.49	0.31	38.27	0.27	0.16	99.70	0.75
	BH154 A2 74	rimwards	38.82	0.00	0.00	0.00	22.68	0.39	38.57	0.33	0.13	100.91	0.75
	BH154 A2 75	rimwards	39.43	0.01	0.03	0.00	22.86	0.31	38.65	0.34	0.15	101.76	0.75
	BH154 A2 76	rimwards	38.96	0.00	0.05	0.00	22.57	0.37	38.99	0.33	0.11	101.38	0.75
	BH154 A2 77	rim	39.13	0.01	0.03	0.00	23.25	0.37	38.58	0.35	0.15	101.87	0.75
	BH154 A2 73-77	average	38.91	0.00	0.02	0.00	22.77	0.35	38.61	0.32	0.14	101.12	0.75
	BH167 A4 1	core	38.86	0.00	0.03	0.04	21.11	0.23	39.83	0.35	0.16	100.60	0.77
	BH167 A4 2	rimwards	38.36	0.00	0.04	0.00	21.46	0.40	39.35	0.32	0.15	100.08	0.77
	BH167 A4 3	rim	39.21	0.01	0.04	0.00	19.91	0.31	40.14	0.29	0.17	100.08	0.78
	BH167 A4 1-3	average	38.81	0.00	0.03	0.01	20.83	0.31	39.77	0.32	0.16	100.25	0.77

	BH167 A4 4	rim	36.47	0.00	0.04	0.00	31.79	0.52	30.75	0.33	0.09	99.99	0.63
	BH167 A4 5	core	38.74	0.01	0.04	0.00	20.80	0.27	40.21	0.33	0.15	100.56	0.78
	BH167 A4 6	rimwards	38.55	0.01	0.02	0.03	22.49	0.39	38.70	0.34	0.15	100.68	0.75
	BH167 A4 7	rim	35.56	0.00	0.05	0.01	37.53	0.46	26.79	0.29	0.06	100.74	0.56
	BH167 A4 5-7	average	37.62	0.01	0.03	0.01	26.94	0.37	35.23	0.32	0.12	100.66	0.70
	BH167 A4 13	core	39.09	0.01	0.03	0.04	22.10	0.35	38.84	0.30	0.13	100.89	0.76
	BH167 A4 14	rim	38.90	0.01	0.02	0.03	23.25	0.32	37.21	0.30	0.21	100.24	0.74
	BH167 A4 13-14	average	38.99	0.01	0.03	0.04	22.68	0.34	38.03	0.30	0.17	100.56	0.75
	BH167 A4 54	rep	37.94	0.00	0.02	0.00	25.56	0.37	35.87	0.33	0.11	100.21	0.71
	BH175 A1 76	core	38.25	0.00	0.04	0.01	19.64	0.25	41.22	0.32	0.19	99.90	0.79
	BH175 A1 77	rimwards	38.33	0.00	0.04	0.01	18.89	0.28	41.86	0.36	0.13	99.91	0.80
	BH175 A1 78	rim	37.19	0.00	0.04	0.01	20.73	0.32	39.95	0.35	0.18	98.77	0.77
	BH175 A1 76-78	average	37.92	0.00	0.04	0.01	19.75	0.28	41.01	0.34	0.16	99.53	0.79
	BH175 A1 80	core	37.15	0.00	0.17	0.03	18.20	0.32	41.81	0.43	0.22	98.32	0.80
	BH175 A1 81	rimwards	37.38	0.02	0.05	0.01	18.72	0.17	42.01	0.34	0.19	98.90	0.80
	BH175 A1 82	rim	37.13	0.00	0.02	0.01	21.45	0.28	39.67	0.35	0.16	99.08	0.77
	BH175 A1 80-82	average	37.22	0.01	0.08	0.02	19.46	0.26	41.16	0.37	0.19	98.76	0.79
	BH175 A1 84	core	38.79	0.01	0.03	0.01	19.23	0.32	41.72	0.34	0.17	100.62	0.79
	BH175 A1 85	rim	37.16	0.00	0.04	0.00	23.42	0.27	38.16	0.34	0.16	99.56	0.74
	BH175 A1 84-85	average	37.97	0.01	0.04	0.00	21.33	0.30	39.94	0.34	0.17	100.09	0.77
	BH175 A1 90	core	38.65	0.00	0.02	0.03	18.67	0.30	41.64	0.36	0.20	99.86	0.80
	BH175 A1 91	rimwards	38.97	0.00	0.03	0.03	18.84	0.32	41.95	0.36	0.19	100.67	0.80
	BH175 A1 92	rimwards	38.88	0.00	0.04	0.02	18.97	0.38	41.95	0.37	0.18	100.80	0.80
	BH175 A1 93	rim	37.18	0.00	0.10	0.02	20.35	0.33	40.16	0.49	0.17	98.81	0.78
	BH175 A1 90-93	average	38.42	0.00	0.05	0.02	19.21	0.33	41.43	0.40	0.18	100.04	0.79
	BH175 A1 94	core	37.63	0.02	0.03	0.03	18.32	0.21	41.86	0.35	0.20	98.64	0.80
	BH175 A1 95	rimwards	38.78	0.01	0.03	0.01	18.70	0.37	41.82	0.37	0.14	100.22	0.80
	BH175 A1 96	rim	38.14	0.00	0.03	0.01	20.97	0.26	39.76	0.34	0.17	99.68	0.77
	BH175 A1 94-96	average	38.18	0.01	0.03	0.01	19.33	0.28	41.15	0.35	0.17	99.51	0.79
	BH175 A1 111	core	37.67	0.00	0.04	0.04	18.41	0.36	41.81	0.34	0.18	98.84	0.80
	BH175 A1 112	rimwards	38.14	0.01	0.04	0.02	18.85	0.33	41.71	0.35	0.23	99.67	0.80
	BH175 A1 113	rimwards	37.76	0.00	0.09	0.04	18.56	0.25	41.72	0.39	0.18	98.98	0.80
	BH175 A1 114	rim	37.01	0.00	0.04	0.01	20.77	0.29	39.76	0.35	0.15	98.38	0.77
	BH175 A1 111-114	average	37.64	0.00	0.05	0.03	19.15	0.31	41.25	0.36	0.18	98.97	0.79
	BH175 A1 115	core	38.72	0.00	0.04	0.00	18.57	0.29	41.50	0.34	0.21	99.65	0.80
	BH175 A1 116	rim	37.93	0.02	0.02	0.04	22.99	0.33	38.44	0.35	0.20	100.31	0.75
	BH175 A1 115-116	average	38.32	0.01	0.03	0.02	20.78	0.31	39.97	0.34	0.20	99.98	0.77
	BH175 A1 126	core	37.99	0.00	0.02	0.02	18.98	0.25	41.54	0.36	0.16	99.33	0.80
	BH175 A1 127	rim	36.68	0.00	0.12	0.04	25.32	0.34	35.87	0.48	0.17	99.02	0.72
	BH175 A1 126-127	average	37.34	0.00	0.07	0.03	22.15	0.30	38.71	0.42	0.17	99.18	0.76

Appendix G3 – SFDC clinopyroxene mineral chemistry

ZD	SAMPLE ID	X REGION	SiO2	Al2O3	FeO*	TiO2	Cr2O3	MgO	MnO	CaO	NiO	Na2O	K2O	Total	mg#
	BH268 A2 1	core	52.59	2.10	7.62	0.51	0.20	17.10	0.22	20.02	0.00	0.20	0.01	100.56	79.99
	BH268 A2 2	rimwards	51.81	3.09	7.87	0.52	0.37	16.47	0.22	20.24	0.04	0.23	0.00	100.86	78.85
	BH268 A2 3	rim	51.49	3.14	7.81	0.66	0.27	16.68	0.18	19.57	0.01	0.23	0.00	100.04	79.18
	BH268 A2 1-3	average	51.96	2.78	7.77	0.56	0.28	16.75	0.21	19.94	0.02	0.22	0.00	100.49	79.34
	BH268 A2 8	core	52.30	3.06	8.86	0.41	0.16	16.95	0.23	18.97	0.00	0.23	0.00	101.15	77.33
	BH268 A2 9	rimwards	53.51	1.55	9.46	0.33	0.18	18.98	0.27	16.65	0.04	0.16	0.01	101.13	78.15
	BH268 A2 10	rim	53.59	1.80	8.91	0.34	0.10	18.14	0.28	17.71	0.02	0.16	0.02	101.09	78.39
	BH268 A2 8-10	average	53.13	2.14	9.08	0.36	0.15	18.03	0.26	17.78	0.02	0.18	0.01	101.12	77.95
	BH268 A2 15	ground rep	49.98	2.53	18.14	1.04	0.01	12.90	0.37	15.39	0.00	0.25	0.00	100.60	55.89
	BH268 A2 16	core	53.78	1.69	8.18	0.34	0.29	18.60	0.23	17.81	0.04	0.16	0.01	101.12	80.21
	BH268 A2 17	rimwards	51.85	3.11	9.61	0.49	0.19	17.17	0.23	17.99	0.02	0.21	0.00	100.87	76.10
	BH268 A2 18	rim	52.99	1.77	10.68	0.35	0.10	18.42	0.30	15.47	0.04	0.13	0.00	100.26	75.46
	BH268 A2 16-18	average	52.87	2.19	9.49	0.39	0.19	18.06	0.25	17.09	0.03	0.17	0.00	100.75	77.26
	BH268 A2 21	core	52.20	3.09	6.68	0.58	0.62	16.49	0.12	20.83	0.02	0.22	0.00	100.85	81.48
	BH268 A2 22	rim	52.17	3.08	7.89	0.64	0.25	16.72	0.21	19.57	0.00	0.22	0.00	100.74	79.06
	BH268 A2 21-22	average	52.19	3.08	7.28	0.61	0.44	16.61	0.16	20.20	0.01	0.22	0.00	100.79	80.27
	BH268 A2 23	core	53.13	1.70	7.95	0.36	0.19	17.98	0.23	18.50	0.05	0.17	0.00	100.26	80.11
	BH268 A2 24	rimwards	53.13	1.82	7.82	0.27	0.22	17.44	0.24	19.56	0.01	0.21	0.00	100.72	79.89
	BH268 A2 25	rim	50.58	4.04	10.08	0.86	0.05	16.27	0.24	17.95	0.03	0.22	0.00	100.33	74.20
	BH268 A2 23-25	average	52.28	2.52	8.62	0.50	0.15	17.23	0.24	18.67	0.03	0.20	0.00	100.44	78.07
	BH268 A2 26	ground rep	51.71	2.48	22.05	0.18	0.00	13.75	0.22	3.12	0.01	0.23	0.06	93.80	52.63
	MH126 A2 29	core	53.12	2.04	6.61	0.46	0.64	17.76	0.17	19.75	0.00	0.23	0.00	100.76	82.71
	MH126 A2 30	rimwards	53.12	2.16	6.47	0.32	0.61	17.62	0.15	20.02	0.02	0.23	0.00	100.71	82.91
	MH126 A2 31	rim	53.62	2.05	8.29	0.50	0.49	19.17	0.25	16.92	0.04	0.22	0.00	101.54	80.47
	MH126 A2 29-31	average	53.29	2.08	7.12	0.43	0.58	18.18	0.19	18.89	0.02	0.23	0.00	101.00	82.03
	MH126 A2 45	ground rep	49.73	5.13	8.72	0.84	0.28	15.00	0.18	20.24	0.01	0.20	0.00	100.32	75.41
	BH296 A1 19	core	51.60	1.92	13.12	0.58	0.00	15.05	0.28	17.40	0.04	0.36	0.02	100.37	67.14
	BH296 A1 19	rimwards	51.90	2.00	12.91	0.54	0.00	15.19	0.32	17.60	0.00	0.24	0.00	100.69	67.70
	BH296 A1 19	rimwards	51.86	2.02	12.73	0.64	0.00	15.02	0.30	17.80	0.00	0.25	0.00	100.63	67.76
	BH296 A1 19	rimwards	51.90	1.96	12.79	0.58	0.00	15.15	0.28	18.16	0.04	0.26	0.01	101.12	67.86
	BH296 A1 19	rimwards	49.16	2.92	15.46	0.63	0.04	14.30	0.34	15.61	0.01	0.22	0.00	98.68	62.24
	BH296 A1 19	rimwards	51.65	1.86	14.81	0.63	0.06	15.01	0.33	16.39	0.03	0.23	0.00	100.99	64.36
	BH296 A1 19	rimwards	53.03	0.99	21.73	0.30	0.00	18.60	0.46	4.83	0.02	0.12	0.01	100.08	60.40
	BH296 A1 19	rimwards	52.00	1.21	21.64	0.43	0.05	18.05	0.52	6.34	0.00	0.09	0.00	100.30	59.78
	BH296 A1 19	rimwards	51.98	0.94	23.69	0.35	0.00	17.31	0.54	5.29	0.00	0.08	0.01	100.19	56.57
	BH296 A1 19	rim	50.93	1.10	25.7	0.45	0.00	14.6	0.62	6.70	0.0	0.13	0.00	100.3	50.3

					3			4			0			1	5
	BH296 A1 19	x average	51.60	1.69	17.46	0.51	0.01	15.83	0.40	12.61	0.01	0.20	0.01	100.33	62.42
	BH296 A1 21	rim	51.73	1.84	13.31	0.48	0.04	14.95	0.34	17.41	0.00	0.20	0.00	100.30	66.68
	BH296 A1 21	rimward	52.40	1.93	11.48	0.61	0.00	15.75	0.32	18.09	0.01	0.23	0.00	100.81	70.97
	BH296 A1 21	rimward	52.23	1.92	12.05	0.55	0.00	15.40	0.29	17.97	0.06	0.24	0.00	100.70	69.49
	BH296 A1 21	rimward	51.83	1.96	12.52	0.71	0.04	15.00	0.31	17.84	0.03	0.26	0.02	100.51	68.09
	BH296 A1 21	rimward	51.17	2.09	12.73	0.95	0.02	14.97	0.31	17.76	0.00	0.25	0.01	100.25	67.70
	BH296 A1 21	rimward	52.10	2.00	11.27	0.60	0.07	15.52	0.26	18.49	0.03	0.23	0.01	100.57	71.04
	BH296 A1 21	rimward	51.64	2.09	10.73	0.68	0.00	15.48	0.27	18.61	0.00	0.22	0.01	99.74	71.99
	BH296 A1 21	rimward	51.45	2.33	10.92	0.70	0.00	15.43	0.26	18.60	0.00	0.24	0.01	99.93	71.58
	BH296 A1 21	rimward	51.42	2.43	11.27	0.74	0.06	15.40	0.32	18.59	0.00	0.22	0.00	100.43	70.89
	BH296 A1 21	core	51.58	2.33	11.41	0.63	0.00	15.37	0.25	18.47	0.02	0.25	0.00	100.31	70.59
	BH296 A1 21	core	51.59	2.36	11.34	0.69	0.02	15.23	0.29	18.51	0.05	0.23	0.01	100.31	70.54
	BH296 A1 21	rimward	51.32	2.47	11.75	0.64	0.03	15.22	0.28	18.59	0.02	0.24	0.00	100.55	69.77
	BH296 A1 21	rimward	51.00	2.47	11.19	0.82	0.05	14.89	0.26	18.40	0.02	0.24	0.03	99.35	70.34
	BH296 A1 21	rimward	51.23	2.43	11.28	0.77	0.00	15.29	0.26	18.45	0.00	0.27	0.00	99.98	70.71
	BH296 A1 21	rimward	51.19	2.40	11.71	0.74	0.02	15.27	0.25	18.16	0.00	0.24	0.01	99.98	69.91
	BH296 A1 21	rimward	51.26	2.41	11.78	0.58	0.01	15.43	0.26	18.12	0.02	0.25	0.01	100.12	70.00
	BH296 A1 21	rimward	50.64	3.72	11.76	0.96	0.07	14.58	0.24	17.16	0.04	0.51	0.13	99.81	68.85
	BH296 A1 21	rimward	52.50	2.21	9.81	0.25	0.00	13.93	0.31	21.14	0.04	0.38	0.00	100.57	71.69
	BH296 A1 21	rimward	51.22	2.48	12.03	0.69	0.00	15.59	0.28	17.09	0.04	0.22	0.00	99.63	69.78
	BH296 A1 21	rim	51.97	1.96	13.09	0.57	0.00	14.72	0.28	18.07	0.01	0.19	0.00	100.88	66.70
	BH296 A1 21	x average	51.57	2.29	11.67	0.67	0.02	15.17	0.28	18.28	0.02	0.25	0.01	100.24	69.87
	BH296 A1 31	core	51.50	1.49	17.33	0.68	0.00	14.19	0.40	14.39	0.02	0.19	0.00	100.18	59.33
	BH296 A1 31	rimwards	51.27	1.52	16.15	0.73	0.00	13.53	0.39	15.85	0.00	0.20	0.00	99.64	59.89
	BH296 A1 31	rimwards	51.22	1.62	15.84	0.79	0.00	13.21	0.37	17.19	0.02	0.23	0.01	100.49	59.78
	BH296 A1 31	rimwards	51.15	1.50	16.83	0.66	0.04	13.50	0.40	15.76	0.04	0.21	0.02	100.10	58.85
	BH296 A1 31	rimwards	51.91	1.68	17.14	0.45	0.00	12.95	0.32	13.81	0.01	0.30	0.01	98.57	57.37
	BH296 A1 31	rimwards	51.62	0.82	25.66	0.43	0.00	16.12	0.58	5.36	0.02	0.08	0.00	100.69	52.82
	BH296 A1 31	rimwards	50.98	0.97	25.13	0.55	0.00	15.82	0.64	5.78	0.00	0.09	0.00	99.95	52.86
	BH296 A1 31	rim	48.04	2.16	26.70	0.43	0.00	13.26	0.59	5.96	0.01	0.10	0.02	97.27	46.95
	BH296 A1 31	x average	50.96	1.47	20.10	0.59	0.01	14.07	0.46	11.76	0.01	0.17	0.01	99.61	55.98
	BH296 A1 32	core	51.16	1.60	16.72	0.64	0.00	13.84	0.38	15.63	0.00	0.25	0.00	100.23	59.60
	BH296 A1 32	rimwards	51.39	1.66	15.55	0.67	0.00	13.80	0.40	16.17	0.00	0.22	0.00	99.84	61.26
	BH296 A1 32	rimwards	51.27	1.65	15.95	0.57	0.00	13.89	0.38	16.24	0.00	0.22	0.00	100.16	60.82
	BH296 A1 32	rimwards	50.19	2.22	17.70	0.64	0.02	13.95	0.38	14.05	0.01	0.21	0.04	99.41	58.42
	BH296 A1 32	rimwards	50.20	1.70	20.23	0.56	0.02	12.23	0.47	14.32	0.00	0.20	0.00	99.92	51.85
	BH296 A1 32	rimwards	50.33	1.03	22.71	0.62	0.01	10.54	0.56	14.35	0.00	0.20	0.00	100.35	45.27
	BH296 A1 32	rimwards	50.34	1.18	23.3	0.73	0.00	11.1	0.56	12.8	0.0	0.15	0.00	100.3	46.0

					5			7		7	0			5	2
	BH296 A1 32	rim	50.83	1.19	20.05	0.54	0.07	11.62	0.49	15.11	0.00	0.17	0.00	100.07	50.81
	BH296 A1 32	x average	50.71	1.53	19.03	0.62	0.01	12.63	0.45	14.84	0.00	0.20	0.01	100.04	54.26
	BH296 A1 33	core	53.36	1.69	12.52	0.49	0.03	15.28	0.17	15.25	0.00	0.20	0.13	99.13	68.50
	BH296 A1 33	rimwards	52.81	1.67	9.91	0.43	0.03	15.45	0.22	19.69	0.03	0.18	0.01	100.42	73.52
	BH296 A1 33	rimwards	52.50	1.94	10.13	0.46	0.01	15.88	0.28	18.93	0.01	0.19	0.01	100.34	73.63
	BH296 A1 33	rimwards	52.24	1.91	10.36	0.50	0.03	15.95	0.29	18.44	0.02	0.20	0.00	99.94	73.30
	BH296 A1 33	rimwards	52.53	2.07	11.66	0.52	0.06	15.89	0.32	17.87	0.04	0.22	0.00	101.17	70.83
	BH296 A1 33	rimwards	52.44	1.99	12.60	0.57	0.00	15.13	0.33	17.69	0.02	0.23	0.00	101.00	68.15
	BH296 A1 33	rimwards	51.34	1.62	17.56	0.63	0.06	14.00	0.42	14.91	0.03	0.21	0.00	100.77	58.68
	BH296 A1 33	rim	49.94	1.08	26.31	0.44	0.01	9.97	0.62	11.44	0.00	0.21	0.00	100.02	40.31
	BH296 A1 33	x average	52.15	1.75	13.88	0.50	0.03	14.69	0.33	16.78	0.02	0.20	0.02	100.35	65.86
	BH296 A1 34	core	52.04	2.10	11.59	0.55	0.08	15.13	0.28	18.23	0.01	0.21	0.01	100.20	69.95
	BH296 A1 34	rimwards	52.57	1.72	11.47	0.38	0.01	15.87	0.26	17.85	0.01	0.22	0.01	100.36	71.15
	BH296 A1 34	rimwards	52.47	1.87	12.01	0.54	0.09	15.39	0.28	17.91	0.04	0.23	0.00	100.83	69.55
	BH296 A1 34	rimwards	52.15	2.32	11.63	0.84	0.00	14.74	0.29	18.61	0.05	0.30	0.01	100.93	69.31
	BH296 A1 34	rimwards	52.12	1.92	12.09	0.56	0.01	15.21	0.29	18.20	0.00	0.21	0.02	100.61	69.15
	BH296 A1 34	rimwards	51.61	1.82	15.34	0.65	0.06	14.17	0.39	16.57	0.01	0.18	0.01	100.81	62.21
	BH296 A1 34	rimwards	51.21	1.87	16.17	0.86	0.06	13.55	0.36	16.89	0.00	0.23	0.01	101.20	59.90
	BH296 A1 34	rimwards	51.32	1.62	16.08	0.79	0.00	13.26	0.39	16.47	0.00	0.24	0.02	100.18	59.50
	BH296 A1 34	rimwards	51.11	1.47	17.03	0.64	0.03	12.50	0.39	16.56	0.01	0.23	0.01	99.97	56.67
	BH296 A1 34	rim	49.68	1.89	19.33	0.61	0.00	11.06	0.41	15.98	0.05	0.23	0.00	99.23	50.50
	BH296 A1 34	x average	51.63	1.86	14.27	0.64	0.03	14.09	0.33	17.33	0.02	0.23	0.01	100.43	63.79
	BH296 A1 35	core	52.98	1.65	11.30	0.39	0.03	16.21	0.29	18.09	0.00	0.18	0.01	101.12	71.88
	BH296 A1 35	rimwards	52.35	2.06	11.26	0.45	0.02	15.45	0.32	17.82	0.03	0.20	0.01	99.98	70.97
	BH296 A1 35	rimwards	52.47	1.89	10.49	0.44	0.00	15.58	0.26	19.35	0.01	0.21	0.00	100.70	72.58
	BH296 A1 35	rimwards	52.37	1.91	10.68	0.42	0.06	15.96	0.29	18.65	0.01	0.22	0.01	100.57	72.69
	BH296 A1 35	rimwards	52.67	1.88	11.48	0.50	0.05	15.78	0.29	18.22	0.02	0.22	0.00	101.10	71.01
	BH296 A1 35	rimwards	51.94	1.92	12.89	0.64	0.00	15.01	0.32	17.61	0.04	0.20	0.00	100.57	67.48
	BH296 A1 35	rimwards	51.44	1.89	15.54	0.60	0.00	14.26	0.39	16.35	0.00	0.21	0.00	100.68	62.05
	BH296 A1 35	rim	51.27	1.58	16.56	0.51	0.00	13.25	0.43	16.13	0.00	0.20	0.01	99.94	58.76
	BH296 A1 35	x average	52.19	1.85	12.53	0.49	0.02	15.19	0.32	17.78	0.01	0.20	0.01	100.58	68.43
	BH296 A1 45	core	50.50	1.19	22.48	0.48	0.10	10.20	0.52	14.35	0.00	0.17	0.00	99.98	44.72
	BH296 A1 45	rimwards	50.20	1.15	22.18	0.68	0.00	9.92	0.47	15.28	0.00	0.18	0.00	100.08	44.36
	BH296 A1 45	rimwards	49.51	1.45	21.93	0.66	0.03	9.75	0.51	15.13	0.00	0.23	0.00	99.20	44.19
	BH296 A1 45	rimwards	49.80	1.18	22.34	0.68	0.00	9.62	0.51	15.61	0.00	0.20	0.00	99.94	43.42
	BH296 A1 45	rimwards	49.74	1.16	22.42	0.69	0.03	9.53	0.53	15.53	0.03	0.20	0.01	99.85	43.09
	BH296 A1 45	rim	49.80	1.13	22.98	0.66	0.00	8.96	0.53	15.87	0.00	0.19	0.01	100.14	40.99
	BH296 A1 45	x average	49.92	1.21	22.3	0.64	0.03	9.66	0.51	15.3	0.0	0.20	0.00	99.86	43.4

					9					0	1				6
	MH123 B2 58	rep	50.77	2.12	14.71	1.00	0.05	14.28	0.40	16.52	0.00	0.18	0.00	100.02	63.37
	MH123 B2 61	core	52.23	2.64	8.47	0.43	0.04	16.66	0.18	19.17	0.05	0.21	0.00	100.07	77.80
	MH123 B2 62	rim	52.34	2.74	8.49	0.53	0.13	16.35	0.23	19.53	0.00	0.24	0.00	100.58	77.44
	MH123 B2 58-62	average	51.78	2.50	10.55	0.65	0.07	15.76	0.27	18.41	0.02	0.21	0.00	100.22	72.87
	MH123 B2 76	core	53.16	0.81	20.67	0.34	0.08	20.76	0.46	4.41	0.01	0.07	0.01	100.78	64.15
	MH123 B2 77	rimward	51.29	1.85	17.15	0.82	0.01	15.56	0.42	13.30	0.05	0.19	0.01	100.63	61.80
	MH123 B2 78	rim	50.55	1.05	26.36	0.68	0.00	12.95	0.59	8.31	0.02	0.12	0.00	100.62	46.69
	MH123 B2 76-78	average	51.66	1.24	21.39	0.61	0.03	16.42	0.49	8.67	0.03	0.13	0.01	100.68	57.54
	MH123 B2 81	rim	50.40	1.12	21.07	0.40	0.01	10.87	0.46	15.15	0.02	0.19	0.00	99.69	47.90
	MH123 B2 82	core	52.47	1.53	13.29	0.45	0.00	16.82	0.34	15.24	0.01	0.20	0.00	100.36	69.27
	MH123 B2 83	core	52.87	1.56	10.99	0.41	0.06	16.73	0.27	17.50	0.04	0.17	0.01	100.61	73.06
	MH123 B2 84	rim	52.36	1.62	12.66	0.60	0.00	16.44	0.34	16.55	0.04	0.21	0.01	100.83	69.83
	MH123 B2 81-84	average	52.03	1.46	14.50	0.46	0.02	15.22	0.35	16.11	0.02	0.19	0.01	100.37	65.01
	MH123 B2 85	core	50.83	2.26	13.49	0.85	0.06	14.14	0.32	17.41	0.05	0.26	0.02	99.69	65.12
	MH123 B2 86	rimward	51.10	2.35	13.67	0.83	0.01	14.94	0.34	16.66	0.00	0.23	0.01	100.14	66.07
	MH123 B2 87	rim	51.36	2.37	11.10	0.65	0.02	15.65	0.28	17.83	0.00	0.24	0.02	99.52	71.54
	MH123 B2 85-87	average	51.10	2.33	12.75	0.78	0.03	14.91	0.31	17.30	0.02	0.24	0.01	99.78	67.58
	MH123 B2 91	core	52.09	2.09	12.97	0.63	0.00	16.58	0.37	15.17	0.00	0.18	0.01	100.09	69.49
	MH123 B2 91	rimward	51.99	2.10	13.55	0.73	0.00	16.63	0.33	15.02	0.04	0.28	0.02	100.68	68.62
	MH123 B2 91	rimward	51.82	2.09	14.08	0.66	0.06	16.54	0.37	14.89	0.00	0.21	0.01	100.73	67.67
	MH123 B2 91	rimward	51.59	2.04	13.81	0.72	0.05	16.46	0.40	14.63	0.02	0.24	0.02	99.98	68.00
	MH123 B2 91	rim	51.69	1.98	14.70	0.52	0.00	16.48	0.38	14.15	0.02	0.20	0.01	100.12	66.64
	MH123 B2 91	x average	51.84	2.06	13.82	0.65	0.02	16.54	0.37	14.77	0.02	0.22	0.01	100.32	68.08
	MH123 B2 99	rim	51.22	1.11	18.81	0.45	0.04	12.32	0.44	15.66	0.01	0.22	0.00	100.27	53.86
	MH123 B2 99	rimward	51.23	1.37	16.39	0.51	0.04	13.87	0.38	16.01	0.00	0.22	0.01	100.04	60.13
	MH123 B2 99	rimward	51.55	1.48	15.50	0.53	0.00	15.31	0.41	14.97	0.03	0.22	0.02	100.01	63.77
	MH123 B2 99	rimward	52.03	1.60	12.61	0.63	0.04	15.72	0.33	16.38	0.02	0.21	0.02	99.58	68.95
	MH123 B2 99	core	51.37	2.51	11.49	0.68	0.02	15.47	0.26	17.86	0.03	0.24	0.02	99.95	70.59
	MH123 B2 99	core	51.45	2.84	10.92	0.75	0.03	15.47	0.26	18.11	0.01	0.26	0.04	100.13	71.63
	MH123 B2 99	rimward	51.45	2.66	9.61	0.69	0.10	15.61	0.21	18.62	0.01	0.24	0.03	99.21	74.33
	MH123 B2 99	rimward	51.92	2.75	9.35	0.52	0.01	16.04	0.22	18.94	0.01	0.25	0.01	100.01	75.36
	MH123 B2 99	rimward	52.99	1.62	9.27	0.39	0.05	16.92	0.24	18.68	0.02	0.22	0.02	100.40	76.48
	MH123 B2 99	rim	53.11	1.65	9.16	0.29	0.06	16.96	0.25	18.58	0.03	0.20	0.01	100.28	76.75
	MH123 B2 99	x average	51.83	1.96	12.31	0.54	0.04	15.37	0.30	17.38	0.02	0.23	0.02	99.99	69.18
	MH123 B2 101	core	53.40	1.59	8.51	0.34	0.07	17.14	0.25	18.95	0.06	0.17	0.01	100.49	78.20
	MH123 B2 102	rimward	51.71	2.89	7.99	0.53	0.23	16.16	0.23	19.45	0.00	0.22	0.00	99.41	78.27
	MH123 B2 103	rim	51.81	2.80	8.55	0.61	0.12	16.56	0.20	19.08	0.04	0.23	0.01	100.01	77.53
	MH123 B2 101-	average	52.31	2.43	8.35	0.49	0.14	16.6	0.23	19.1	0.0	0.21	0.01	99.97	78.0

	103							2		6	3				0
	MH123 B2 104	core	50.68	1.98	14.60	0.84	0.00	14.19	0.35	16.49	0.01	0.24	0.00	99.38	63.40
	MH123 B2 105	rim	44.47	7.31	23.24	1.13	0.00	10.23	0.21	5.76	0.05	0.22	4.46	97.08	43.96
	MH123 B2 104-105	average	47.58	4.64	18.92	0.98	0.00	12.21	0.28	11.12	0.03	0.23	2.23	98.23	53.68
C	MH129 A2 125	core	52.13	2.90	7.95	0.59	0.22	16.64	0.17	19.59	0.04	0.22	0.00	100.45	78.86
	MH129 A2 126	rimward	52.40	2.62	7.92	0.54	0.17	16.66	0.21	19.76	0.04	0.20	0.00	100.52	78.95
	MH129 A2 127	rim	51.17	1.25	17.48	0.71	0.05	12.66	0.40	16.28	0.05	0.24	0.01	100.29	56.34
	MH129 A2 125-127	average	51.90	2.26	11.12	0.61	0.15	15.32	0.26	18.54	0.04	0.22	0.00	100.42	71.39
	MH129 A2 132	core	51.89	0.71	23.73	0.44	0.00	17.96	0.53	4.75	0.01	0.07	0.00	100.09	57.43
	MH129 A2 133	rim	51.70	0.47	17.39	0.16	0.00	10.47	0.35	19.82	0.01	0.18	0.00	100.54	51.77
	MH129 A2 132-133	average	51.80	0.59	20.56	0.30	0.00	14.22	0.44	12.28	0.01	0.12	0.00	100.32	54.60
	MH129 A2 151	rep	51.29	1.26	22.45	0.62	0.00	17.51	0.53	6.17	0.01	0.10	0.00	99.95	58.16
	MH129 A2 152	core	52.04	1.02	22.27	0.50	0.02	18.28	0.44	5.85	0.06	0.08	0.00	100.55	59.40
	MH129 A2 152	rimwards	52.38	1.00	21.45	0.49	0.00	19.14	0.44	4.85	0.03	0.09	0.01	99.88	61.39
	MH129 A2 152	rimwards	52.48	1.06	21.29	0.39	0.01	19.67	0.54	4.27	0.05	0.08	0.01	99.84	62.22
	MH129 A2 152	rimwards	51.92	1.20	22.19	0.37	0.00	19.63	0.47	3.36	0.06	0.06	0.01	99.28	61.19
	MH129 A2 152	rimwards	52.41	1.00	22.99	0.42	0.00	19.17	0.51	4.08	0.05	0.09	0.00	100.72	59.78
	MH129 A2 152	rimwards	52.20	1.22	20.85	0.58	0.04	18.11	0.46	7.13	0.01	0.10	0.01	100.71	60.75
	MH129 A2 152	rimwards	51.40	0.94	24.15	0.36	0.00	17.29	0.50	4.34	0.03	0.10	0.01	99.12	56.06
	MH129 A2 152	rimwards	51.46	1.21	14.98	0.75	0.00	12.83	0.36	18.24	0.02	0.25	0.00	100.11	60.42
	MH129 A2 152	rimwards	52.04	1.84	11.79	0.58	0.00	15.59	0.32	17.57	0.00	0.22	0.01	99.97	70.22
	MH129 A2 152	rimwards	51.92	1.96	11.99	0.55	0.02	15.73	0.31	17.44	0.00	0.23	0.01	100.16	70.03
	MH129 A2 152	rimwards	52.16	1.94	11.68	0.52	0.03	15.53	0.34	17.88	0.03	0.23	0.00	100.34	70.32
	MH129 A2 152	rimwards	51.97	2.12	11.84	0.21	0.00	13.11	0.28	20.07	0.01	0.35	0.04	100.00	66.36
	MH129 A2 152	rimwards	52.45	2.11	9.24	0.62	0.13	16.12	0.22	19.47	0.00	0.21	0.01	100.58	75.67
	MH129 A2 152	rimwards	52.86	2.18	7.90	0.53	0.03	16.53	0.20	20.22	0.01	0.21	0.01	100.68	78.85
	MH129 A2 152	rim	52.45	2.01	10.46	0.33	0.07	15.15	0.24	19.71	0.02	0.21	0.02	100.65	72.07
	MH129 A2 152	x average	52.14	1.52	16.34	0.48	0.02	16.79	0.38	12.30	0.02	0.17	0.01	100.17	65.65
	MH129 A2 153	core	52.25	2.93	7.98	0.42	0.15	16.89	0.22	19.26	0.01	0.22	0.00	100.32	79.04
	MH129 A2 153	rimwards	52.44	2.92	8.06	0.47	0.28	17.24	0.20	18.60	0.06	0.18	0.00	100.43	79.22
	MH129 A2 153	rimwards	52.62	2.49	7.66	0.58	0.21	16.69	0.19	19.67	0.00	0.19	0.01	100.31	79.51
	MH129 A2 153	rimwards	52.24	2.18	9.28	0.49	0.06	15.93	0.22	19.52	0.01	0.23	0.01	100.16	75.37
	MH129 A2 153	rimwards	47.75	2.26	10.20	0.31	0.04	14.94	0.29	17.03	0.11	0.45	0.08	93.44	72.30
	MH129 A2 153	rimwards	52.07	1.01	23.14	0.51	0.00	18.20	0.54	4.95	0.01	0.08	0.00	100.51	58.36
	MH129 A2 153	rimwards	52.56	1.29	19.89	0.51	0.00	19.52	0.44	6.59	0.03	0.07	0.01	100.89	63.62
	MH129 A2 153	rimwards	52.68	1.07	19.78	0.35	0.00	20.02	0.45	5.93	0.02	0.10	0.01	100.41	64.33
	MH129 A2 153	rimwards	52.34	1.00	23.51	0.51	0.05	19.44	0.52	3.36	0.04	0.04	0.01	100.82	59.57
	MH129 A2 153	rim	52.20	1.12	22.97	0.32	0.00	18.98	0.48	4.73	0.00	0.07	0.00	100.88	59.55
	MH129 A2 153	x average	51.92	1.83	15.2	0.45	0.08	17.7	0.35	11.9	0.0	0.16	0.01	99.82	69.0

					5			8		6	3				9
	MH129 A2 154	core	53.13	1.97	7.75	0.36	0.14	17.37	0.23	19.45	0.03	0.20	0.01	100.63	79.97
	MH129 A2 155	rimwards	52.87	2.05	9.96	0.66	0.00	16.42	0.24	18.78	0.02	0.23	0.00	101.23	74.60
	MH129 A2 156	rim	52.23	1.07	22.32	0.41	0.07	19.17	0.50	5.03	0.00	0.09	0.00	100.90	60.48
	MH129 A2 154-156	average	52.75	1.69	13.35	0.48	0.07	17.65	0.32	14.42	0.02	0.17	0.00	100.92	71.68
	MH129 A2 163	core	52.20	2.03	11.92	0.58	0.03	15.54	0.29	18.42	0.00	0.23	0.01	101.25	69.91
	MH129 A2 164	rimward	52.54	2.21	8.78	0.56	0.07	16.56	0.21	19.92	0.00	0.22	0.00	101.07	77.07
	MH129 A2 165	rim	52.40	2.21	8.83	0.47	0.08	16.05	0.19	19.81	0.00	0.21	0.00	100.26	76.41
	MH129 A2 163-165	average	52.38	2.15	9.84	0.54	0.06	16.05	0.23	19.38	0.00	0.22	0.00	100.86	74.46
	MH129 A2 166	rep	51.52	2.28	12.92	0.55	0.01	14.71	0.30	18.00	0.00	0.24	0.01	100.56	66.99
	MH129 A2 167	core	52.14	3.12	8.01	0.52	0.17	16.72	0.19	19.24	0.07	0.21	0.01	100.39	78.82
	MH129 A2 168	rim	52.49	2.71	7.86	0.55	0.05	16.87	0.21	19.52	0.06	0.22	0.01	100.56	79.28
	MH129 A2 167-168	average	52.32	2.92	7.93	0.53	0.11	16.79	0.20	19.38	0.06	0.21	0.01	100.47	79.05
B	BH185 A2_1 39	core	52.75	2.44	7.34	0.42	0.57	17.89	0.19	18.79	0.02	0.25	0.00	100.66	81.29
	BH185 A2_1 40	rim	52.36	2.87	6.09	0.34	0.73	16.87	0.15	20.91	0.01	0.24	0.00	100.57	83.17
	BH185 A2_1 39-40	average	52.56	2.66	6.71	0.38	0.65	17.38	0.17	19.85	0.02	0.24	0.00	100.61	82.23
	BH185 A2_1 42	core	53.74	1.76	7.44	0.26	0.43	19.12	0.21	17.73	0.06	0.20	0.00	100.94	82.09
	BH185 A2_1 43	rim	52.57	2.71	6.13	0.44	0.64	16.91	0.15	20.96	0.07	0.20	0.01	100.78	83.10
	BH185 A2_1 42-43	average	53.15	2.24	6.78	0.35	0.53	18.02	0.18	19.34	0.06	0.20	0.01	100.86	82.60
	BH185 A2_1 49	core	51.97	3.14	6.99	0.47	0.46	16.83	0.19	20.35	0.02	0.22	0.00	100.64	81.10
	BH185 A2_1 50	rimwards	51.69	2.76	9.33	0.66	0.00	15.84	0.20	19.73	0.01	0.23	0.00	100.45	75.16
	BH185 A2_1 51	rim	50.91	2.55	12.97	0.86	0.00	14.30	0.30	18.28	0.00	0.28	0.01	100.45	66.27
	BH185 A2_1 49-51	average	51.52	2.82	9.76	0.66	0.15	15.66	0.23	19.45	0.01	0.24	0.00	100.51	74.18
	BH185 A2_2 47	core	53.24	1.63	7.51	0.46	0.12	17.68	0.22	19.32	0.01	0.20	0.00	100.40	80.74
	BH185 A2_2 48	rim	51.61	2.54	9.15	0.54	0.00	16.69	0.23	18.20	0.01	0.21	0.02	99.20	76.47
	BH185 A2_2 47-48	average	52.43	2.09	8.33	0.50	0.06	17.19	0.22	18.76	0.01	0.20	0.01	99.80	78.61
	BH185 A2_2 49	core	52.02	2.95	8.19	0.68	0.09	16.54	0.15	19.76	0.03	0.21	0.00	100.61	78.25
	BH185 A2_2 50	rim	52.23	2.62	8.60	0.58	0.07	16.38	0.27	19.28	0.04	0.24	0.01	100.34	77.24
	BH185 A2_2 49-50	average	52.13	2.79	8.40	0.63	0.08	16.46	0.21	19.52	0.03	0.22	0.01	100.47	77.74
	BH185 A2_2 52	core	52.23	2.20	10.19	0.35	0.04	17.01	0.20	17.77	0.03	0.20	0.02	100.22	74.83
	BH185 A2_2 53	rim	50.83	1.72	16.95	0.77	0.01	12.97	0.44	16.35	0.02	0.24	0.01	100.31	57.68
	BH185 A2_2 52-53	average	51.53	1.96	13.57	0.56	0.03	14.99	0.32	17.06	0.02	0.22	0.01	100.26	66.26
	BH185 A2_2 56	core	51.98	2.68	9.90	0.55	0.03	16.11	0.25	18.90	0.01	0.22	0.01	100.61	74.36
	BH185 A2_2 57	rim	52.29	2.43	8.90	0.59	0.08	17.22	0.20	18.38	0.01	0.23	0.01	100.32	77.52
	BH185 A2_2 56-57	average	52.13	2.55	9.40	0.57	0.06	16.66	0.22	18.64	0.01	0.22	0.01	100.47	75.94
	BH185 A2_2 58	rim (overgrowth)	53.11	1.68	8.47	0.43	0.01	16.97	0.22	19.44	0.03	0.19	0.01	100.57	78.11
	BH185 A2_2 59	core	52.83	2.26	5.98	0.39	0.48	17.31	0.16	20.70	0.01	0.20	0.01	100.32	83.75
	BH185 A2_2 60	rimwards	52.44	2.73	5.99	0.37	0.63	16.95	0.11	21.01	0.05	0.21	0.00	100.48	83.45

	BH185 A2_2 61	rim	53.16	2.18	5.67	0.36	0.55	17.36	0.16	21.01	0.00	0.23	0.01	100.69	84.51
	BH185 A2_2 59-61	average	52.81	2.39	5.88	0.37	0.55	17.20	0.14	20.91	0.02	0.21	0.01	100.50	83.90
	BH185 A2_2 62	ground rep	53.13	2.47	5.90	0.29	0.51	17.08	0.15	21.15	0.04	0.20	0.01	100.91	83.77
	BH185 A2_2 63	ground rep	49.29	3.78	10.62	0.49	0.24	13.69	0.27	19.93	0.06	0.22	0.13	98.72	69.67
	BH185 A2_2 65	core	52.45	2.74	6.30	0.40	0.59	16.94	0.13	20.88	0.00	0.22	0.00	100.65	82.75
	BH185 A2_2 66	rim	52.62	2.76	6.34	0.33	0.67	17.06	0.15	20.71	0.04	0.22	0.00	100.89	82.74
	BH185 A2_2 65-66	average	52.53	2.75	6.32	0.37	0.63	17.00	0.14	20.80	0.02	0.22	0.00	100.77	82.74
	BH185 A2_2 67	ground rep	51.00	4.59	8.63	0.72	0.36	16.87	0.19	17.62	0.05	0.24	0.01	100.28	77.69
	BH185 A2_2 69	core	51.24	4.09	6.49	0.39	0.88	16.29	0.12	20.61	0.04	0.24	0.01	100.38	81.73
	BH185 A2_2 70	rim	52.44	2.60	5.93	0.37	0.72	17.12	0.12	21.08	0.05	0.21	0.01	100.63	83.74
	BH185 A2_2 69-70	average	51.84	3.35	6.21	0.38	0.80	16.70	0.12	20.84	0.04	0.22	0.01	100.51	82.73
E	BH366 B1 78	core	51.53	3.66	7.66	0.72	0.23	16.52	0.21	19.29	0.03	0.21	0.01	100.06	79.35
	BH366 B1 79	rim	51.83	3.20	8.14	0.51	0.09	15.83	0.17	20.14	0.01	0.23	0.01	100.16	77.60
	BH366 B1 78-79	average	51.68	3.43	7.90	0.61	0.16	16.18	0.19	19.71	0.02	0.22	0.01	100.11	78.48
	BH366 B1 80	core	51.60	3.63	8.83	0.51	0.00	16.24	0.22	19.25	0.00	0.24	0.00	100.53	76.63
	BH366 B1 81	rim	51.01	1.29	20.52	0.53	0.06	13.65	0.51	11.85	0.02	0.16	0.00	99.59	54.23
	BH366 B1 80-81	average	51.31	2.46	14.68	0.52	0.03	14.95	0.36	15.55	0.01	0.20	0.00	100.06	65.43
	BH366 B1 88	rep	51.32	3.50	9.12	0.65	0.06	15.77	0.21	19.67	0.03	0.22	0.01	100.54	75.51
	BH366 B1 94	rep	51.93	3.24	8.76	0.62	0.12	16.37	0.24	19.20	0.04	0.20	0.00	100.73	76.90
	BH372 A1 106	core	51.37	2.83	10.29	0.79	0.08	15.93	0.28	18.18	0.03	0.22	0.00	99.98	73.40
	BH372 A1 106	rimward	51.80	2.31	9.40	0.61	0.14	16.09	0.23	18.99	0.05	0.21	0.00	99.83	75.32
	BH372 A1 106	rimward	52.01	2.20	9.90	0.66	0.06	15.71	0.27	18.96	0.02	0.22	0.00	100.01	73.88
	BH372 A1 106	rimward	51.69	2.12	11.61	0.60	0.00	15.16	0.30	18.11	0.00	0.22	0.00	99.81	69.94
	BH372 A1 106	rim	51.09	2.07	13.64	0.52	0.00	14.50	0.37	17.19	0.01	0.24	0.00	99.61	65.46
	BH372 A1 106	average	51.59	2.30	10.97	0.63	0.06	15.48	0.29	18.29	0.02	0.22	0.00	99.85	71.60
	BH372 A1 107	rim	50.69	1.77	16.50	0.78	0.00	12.75	0.38	16.83	0.00	0.24	0.00	99.93	57.94
	BH372 A1 107	rimward	51.21	1.93	15.51	0.86	0.01	13.75	0.37	17.00	0.08	0.25	0.00	100.95	61.23
	BH372 A1 107	rimward	50.84	2.27	12.93	0.54	0.03	14.51	0.29	17.26	0.01	0.28	0.01	98.95	66.66
	BH372 A1 107	rimward	52.48	1.88	11.08	0.31	0.06	15.67	0.30	18.70	0.02	0.22	0.01	100.72	71.59
	BH372 A1 107	core	52.49	1.97	11.08	0.61	0.00	15.73	0.27	18.61	0.00	0.21	0.00	100.98	71.68
	BH372 A1 107	core	52.40	1.89	10.71	0.60	0.00	15.77	0.26	18.51	0.02	0.24	0.01	100.39	72.41
	BH372 A1 107	rimward	52.33	1.98	11.19	0.50	0.00	15.73	0.27	18.58	0.02	0.22	0.00	100.82	71.48
	BH372 A1 107	rimward	52.42	1.88	10.26	0.41	0.04	15.86	0.29	18.97	0.00	0.18	0.00	100.31	73.36
	BH372 A1 107	rimward	52.55	1.34	8.88	0.57	0.00	14.34	0.23	22.88	0.05	0.07	0.00	100.91	74.22
	BH372 A1 107	rim	51.12	1.64	15.01	0.66	0.05	11.97	0.37	19.58	0.01	0.27	0.01	100.70	58.69
	BH372 A1 107	x average	51.85	1.85	12.31	0.58	0.02	14.61	0.30	18.69	0.02	0.22	0.00	100.47	67.93
	BH372 A1 108	rim	50.86	1.60	17.78	0.62	0.00	14.14	0.41	14.59	0.01	0.23	0.00	100.24	58.63
	BH372 A1 108	rimward	51.29	2.00	14.28	0.75	0.00	14.96	0.37	16.21	0.04	0.21	0.00	100.09	65.12

	BH372 A1 108	rimward	51.69	2.10	12.65	0.40	0.00	15.51	0.31	17.73	0.00	0.21	0.00	100.61	68.59
	BH372 A1 108	rimward	51.51	2.08	10.53	0.48	0.00	15.81	0.25	18.71	0.00	0.22	0.00	99.58	72.79
	BH372 A1 108	core	51.85	2.02	10.36	0.65	0.04	15.72	0.26	18.73	0.01	0.21	0.00	99.84	72.99
	BH372 A1 108	core	51.47	2.05	10.47	0.43	0.00	15.67	0.27	18.68	0.05	0.19	0.00	99.27	72.74
	BH372 A1 108	rimward	52.00	2.06	10.34	0.55	0.00	15.76	0.27	18.75	0.01	0.23	0.00	99.97	73.10
	BH372 A1 108	rimward	51.20	2.18	11.82	0.63	0.00	15.35	0.25	18.25	0.00	0.23	0.00	99.91	69.84
	BH372 A1 108	rimward	51.58	2.07	12.51	0.69	0.08	15.31	0.29	17.92	0.00	0.21	0.00	100.65	68.57
	BH372 A1 108	rim	51.22	2.29	11.71	0.44	0.01	13.76	0.33	20.05	0.03	0.21	0.01	100.06	67.68
	BH372 A1 108	x average	51.47	2.05	12.24	0.56	0.01	15.20	0.30	17.96	0.01	0.21	0.00	100.02	69.00
	BH372 A1 109	rim	51.91	2.27	13.31	0.57	0.00	13.65	0.31	16.95	0.06	0.44	0.11	99.59	64.63
	BH372 A1 109	rimward	52.20	1.92	12.03	0.60	0.05	15.00	0.28	18.33	0.00	0.22	0.00	100.60	68.96
	BH372 A1 109	rimward	52.07	2.04	10.81	0.48	0.03	15.84	0.31	18.31	0.00	0.23	0.00	100.12	72.31
	BH372 A1 109	rimward	52.28	2.14	11.03	0.55	0.00	15.46	0.28	18.76	0.00	0.20	0.00	100.71	71.41
	BH372 A1 109	core	51.86	2.22	11.51	0.63	0.02	15.57	0.27	18.32	0.03	0.23	0.00	100.65	70.68
	BH372 A1 109	core	51.51	1.98	11.89	0.66	0.00	14.69	0.29	18.77	0.03	0.23	0.00	100.04	68.78
	BH372 A1 109	rimward	51.49	2.06	14.13	0.66	0.00	14.13	0.30	17.60	0.00	0.24	0.01	100.61	64.06
	BH372 A1 109	rimward	50.82	1.78	15.60	0.77	0.02	13.14	0.38	17.45	0.00	0.24	0.00	100.19	60.02
	BH372 A1 109	rimward	50.54	1.59	16.76	0.81	0.00	12.51	0.38	17.01	0.00	0.24	0.00	99.83	57.08
	BH372 A1 109	rim	50.53	1.33	17.67	0.75	0.01	11.54	0.46	17.09	0.00	0.20	0.00	99.58	53.78
	BH372 A1 109	x average	51.52	1.93	13.47	0.65	0.01	14.15	0.33	17.86	0.01	0.25	0.01	100.19	65.17
	BH372 A1 114	rim	51.18	1.40	16.71	0.51	0.00	11.79	0.40	17.96	0.01	0.19	0.01	100.14	55.71
	BH372 A1 114	core	50.91	1.51	16.90	0.60	0.00	12.53	0.41	16.89	0.00	0.23	0.00	99.96	56.91
	BH372 A1 114	core	50.80	1.53	16.87	0.77	0.06	12.73	0.40	16.73	0.01	0.23	0.00	100.11	57.35
	BH372 A1 114	rim	49.69	0.82	24.13	0.44	0.03	6.98	0.64	16.94	0.00	0.17	0.00	99.84	34.03
	BH372 A1 114	x average	50.64	1.31	18.65	0.58	0.02	11.01	0.46	17.13	0.00	0.20	0.00	100.01	51.00
	BH372 A1 115	rim	50.45	3.07	11.24	0.48	0.06	14.69	0.23	18.18	0.03	0.25	0.01	98.70	69.95
	BH372 A1 115	rimward	51.35	2.77	9.30	0.60	0.04	15.76	0.23	19.06	0.02	0.21	0.00	99.34	75.13
	BH372 A1 115	rimward	52.67	1.67	9.61	0.41	0.04	16.66	0.25	18.38	0.00	0.18	0.00	99.86	75.55
	BH372 A1 115	rimward	51.67	2.59	9.62	0.61	0.05	15.86	0.22	19.28	0.02	0.22	0.00	100.13	74.60
	BH372 A1 115	core	51.50	2.36	9.84	0.53	0.06	16.06	0.23	18.21	0.03	0.22	0.00	99.03	74.42
	BH372 A1 115	core	49.91	3.27	11.55	0.48	0.06	16.10	0.23	16.51	0.01	0.19	0.03	98.34	71.30
	BH372 A1 115	rimward	52.26	1.92	9.77	0.54	0.04	15.84	0.27	19.04	0.00	0.19	0.00	99.88	74.28
	BH372 A1 115	rimward	51.04	2.46	10.12	0.44	0.00	15.77	0.24	18.15	0.00	0.24	0.01	98.46	73.53
	BH372 A1 115	rimward	52.35	2.13	10.25	0.61	0.05	15.92	0.28	18.83	0.02	0.19	0.00	100.62	73.47
	BH372 A1 115	rim	52.23	2.10	10.93	0.53	0.04	15.80	0.28	18.42	0.05	0.21	0.00	100.60	72.03
	BH372 A1 115	x average	51.54	2.43	10.22	0.52	0.04	15.85	0.25	18.41	0.02	0.21	0.01	99.50	73.43
	BH372 A1 116	rim	51.05	1.75	15.61	0.89	0.00	12.01	0.33	15.31	0.02	0.31	0.01	97.30	57.81
	BH372 A1 116	rimward	52.10	2.03	11.09	0.44	0.00	15.95	0.29	18.35	0.03	0.20	0.00	100.50	71.93

	BH372 A1 116	rimward	52.59	1.88	10.26	0.58	0.05	16.43	0.22	18.43	0.02	0.19	0.00	100.65	74.05
	BH372 A1 116	rimward	52.41	1.89	10.24	0.45	0.02	16.39	0.25	18.80	0.01	0.23	0.01	100.70	74.04
	BH372 A1 116	core	52.50	1.91	10.18	0.50	0.03	16.35	0.26	18.88	0.00	0.22	0.00	100.81	74.11
	BH372 A1 116	core	52.24	2.10	10.67	0.49	0.00	16.32	0.25	18.24	0.02	0.21	0.00	100.54	73.15
	BH372 A1 116	rimward	52.25	2.04	10.87	0.57	0.00	16.05	0.28	18.22	0.00	0.20	0.00	100.47	72.47
	BH372 A1 116	rimward	51.53	1.56	13.89	0.77	0.05	13.25	0.36	17.54	0.02	0.27	0.00	99.24	62.95
	BH372 A1 116	rimward	51.46	1.15	16.28	0.47	0.00	11.11	0.39	18.39	0.00	0.19	0.00	99.44	54.87
	BH372 A1 116	rim	43.50	3.90	27.16	0.29	0.02	7.13	0.48	11.60	0.00	0.25	0.03	94.36	31.87
	BH372 A1 116	x average	51.16	2.02	13.63	0.54	0.02	14.10	0.31	17.38	0.01	0.23	0.01	99.40	64.73
	BH372 A1 121	core	51.03	1.28	19.72	0.58	0.00	13.79	0.45	13.54	0.00	0.17	0.00	100.56	55.48
	BH372 A1 122	rimward	50.55	1.28	21.05	0.44	0.00	11.56	0.54	14.18	0.00	0.17	0.00	99.76	49.46
	BH372 A1 123	rim (very altered)	45.74	4.21	31.72	0.07	0.01	3.73	0.64	9.49	0.00	0.87	0.72	97.20	17.31
	BH372 A1 121-123	average	49.11	2.25	24.17	0.36	0.00	9.69	0.54	12.40	0.00	0.40	0.24	99.17	40.75
	BH372 A1 124	rim	40.81	9.78	27.36	0.24	0.00	8.44	0.10	0.15	0.00	0.13	6.46	93.48	35.48
	BH372 A1 124	core	51.01	2.38	17.65	0.45	0.02	10.90	0.30	15.18	0.01	0.26	0.06	98.21	52.38
	BH372 A1 124	core	52.44	2.04	10.97	0.56	0.00	16.00	0.25	18.26	0.02	0.20	0.00	100.75	72.22
	BH372 A1 124	core	52.37	1.91	10.65	0.39	0.02	16.10	0.24	18.30	0.03	0.20	0.00	100.22	72.93
	BH372 A1 124	rim	52.01	2.09	10.93	0.51	0.00	15.61	0.28	18.53	0.05	0.23	0.00	100.23	71.79
	BH372 A1 124	x average	49.73	3.64	15.51	0.43	0.01	13.41	0.23	14.09	0.02	0.21	1.30	98.58	60.96
A	BH154 A2 65	core	53.64	1.56	8.08	0.36	0.09	18.18	0.27	17.77	0.03	0.19	0.00	100.18	80.04
	BH154 A2 66	rimwards	52.54	2.57	7.75	0.42	0.18	16.53	0.17	20.27	0.00	0.22	0.00	100.65	79.17
	BH154 A2 67	rim	52.85	2.27	7.22	0.38	0.21	16.55	0.16	20.74	0.02	0.22	0.00	100.62	80.32
	BH154 A2 65-67	average	53.01	2.13	7.69	0.39	0.16	17.09	0.20	19.59	0.02	0.21	0.00	100.48	79.84
	BH154 A2 70	ground rep	50.67	2.81	15.13	0.82	0.02	13.49	0.34	16.98	0.00	0.29	0.01	100.55	61.38
	BH154 A2 71	core	52.53	2.35	7.18	0.51	0.29	16.88	0.19	20.34	0.01	0.22	0.00	100.50	80.73
	BH154 A2 72	rim	51.96	2.65	12.04	0.59	0.00	16.55	0.29	16.16	0.00	0.24	0.01	100.48	71.02
	BH154 A2 71-72	average	52.25	2.50	9.61	0.55	0.15	16.72	0.24	18.25	0.01	0.23	0.01	100.49	75.88
	BH154 A2 80	ground rep	51.45	2.07	16.44	0.47	0.00	14.12	0.40	15.43	0.00	0.26	0.01	100.63	60.48
	BH167 A2 57	core	51.63	3.27	9.16	0.76	0.10	16.39	0.26	18.54	0.03	0.23	0.00	100.36	76.12
	BH167 A2 58	rimwards	51.04	2.66	13.22	0.63	0.00	15.99	0.31	15.90	0.04	0.22	0.02	100.02	68.30
	BH167 A2 59	rim	42.80	7.11	27.55	0.40	0.04	7.40	0.34	7.95	0.01	0.24	2.74	96.56	32.36
	BH167 A2 57-59	average	48.49	4.34	16.64	0.60	0.05	13.26	0.30	14.13	0.02	0.23	0.92	98.98	58.93
	BH167 A2 61	core	53.69	1.79	7.82	0.31	0.23	18.50	0.23	18.06	0.03	0.17	0.00	100.83	80.83
	BH167 A2 62	rim	52.62	1.54	15.27	0.35	0.02	18.17	0.41	11.51	0.03	0.13	0.02	100.08	67.94
	BH167 A2 61-62	average	53.16	1.66	11.55	0.33	0.13	18.33	0.32	14.79	0.03	0.15	0.01	100.45	74.39
	BH167 A4 8	core	51.62	1.77	8.93	0.50	0.00	16.64	0.22	18.62	0.01	0.21	0.00	98.52	76.86
	BH167 A4 9	rimwards	52.56	1.60	8.44	0.43	0.00	17.33	0.25	18.77	0.03	0.19	0.00	99.60	78.54
	BH167 A4 10	rim	51.69	2.28	9.94	0.52	0.00	16.61	0.25	18.29	0.00	0.23	0.00	99.81	74.85

	BH167 A4 8-10	average	51.96	1.88	9.10	0.48	0.00	16.86	0.24	18.56	0.01	0.21	0.00	99.31	76.75
	BH167 A4 11	rim (same x, next to ol)	51.42	1.67	11.39	0.64	0.06	15.87	0.29	17.87	0.00	0.28	0.00	99.49	71.28
	BH167 A4 25	rim	49.86	2.65	12.52	0.90	0.00	13.87	0.30	18.71	0.01	0.27	0.01	99.10	66.38
	BH167 A4 26	rimward	50.25	2.75	12.96	0.72	0.09	15.00	0.32	17.12	0.00	0.25	0.01	99.48	67.35
	BH167 A4 27	rimward	50.57	2.66	12.99	1.02	0.00	14.91	0.30	17.23	0.00	0.26	0.01	99.95	67.16
	BH167 A4 28	rimward	50.07	2.76	13.26	0.92	0.00	14.88	0.35	17.11	0.03	0.27	0.01	99.66	66.66
	BH167 A4 29	core	50.06	2.67	12.84	0.95	0.04	14.39	0.30	17.62	0.05	0.27	0.00	99.18	66.64
	BH167 A4 30	rimward	49.96	2.57	14.68	0.84	0.00	14.71	0.33	16.80	0.02	0.29	0.00	100.20	64.10
	BH167 A4 31	rimward	49.81	2.41	15.57	0.97	0.00	14.03	0.38	16.37	0.01	0.29	0.00	99.83	61.62
	BH167 A4 32	rimward	49.52	2.61	15.66	0.87	0.00	13.23	0.35	16.90	0.00	0.27	0.00	99.42	60.08
	BH167 A4 33	rim	50.01	2.30	16.96	1.07	0.00	13.57	0.41	15.29	0.01	0.23	0.00	99.83	58.78
	BH167 A4 34	core	49.97	2.28	17.38	0.96	0.00	13.10	0.44	15.80	0.00	0.24	0.00	100.16	57.31
	BH167 A4 35	rim	49.77	1.65	20.46	0.77	0.00	13.90	0.50	11.81	0.04	0.16	0.01	99.07	54.77
	BH167 A4 25-35	average	49.99	2.48	15.03	0.91	0.01	14.14	0.36	16.43	0.02	0.26	0.00	99.63	62.80
	BH167 A4 41	rim	52.11	2.91	8.25	0.42	0.26	17.36	0.20	18.94	0.04	0.26	0.00	100.75	78.94
	BH167 A4 42	rimward	52.13	2.83	7.86	0.54	0.17	17.34	0.19	19.23	0.03	0.27	0.01	100.60	79.71
	BH167 A4 43	rimward	52.44	2.73	8.00	0.48	0.10	17.32	0.24	19.20	0.04	0.24	0.01	100.79	79.41
	BH167 A4 44	rimward	52.50	2.75	7.71	0.55	0.19	17.35	0.20	19.15	0.08	0.26	0.01	100.73	80.05
	BH167 A4 45	core	52.29	2.70	7.57	0.41	0.16	17.37	0.21	19.09	0.01	0.25	0.01	100.07	80.35
	BH167 A4 46	rimward	53.10	1.66	7.60	0.26	0.10	17.60	0.22	19.32	0.02	0.22	0.01	100.10	80.49
	BH167 A4 47	rimward	53.00	1.53	8.41	0.43	0.05	17.41	0.22	18.81	0.02	0.33	0.01	100.21	78.67
	BH167 A4 48	rimward	52.97	1.53	9.94	0.33	0.03	17.75	0.28	17.62	0.02	0.21	0.01	100.66	76.09
	BH167 A4 49	rim	52.57	1.70	11.21	0.60	0.06	16.91	0.31	17.30	0.02	0.22	0.01	100.90	72.88
	BH167 A4 41-49	average	52.57	2.26	8.51	0.45	0.12	17.38	0.23	18.74	0.03	0.25	0.01	100.53	78.51
	BH167 A4 55	rim	50.27	1.33	19.68	0.62	0.00	13.08	0.48	14.74	0.05	0.20	0.00	100.44	54.22
	BH167 A4 56	core	49.21	2.63	14.40	0.93	0.00	13.16	0.25	17.77	0.00	0.32	0.01	98.67	61.95
	BH167 A4 57	core	49.71	2.45	15.48	0.85	0.01	14.04	0.38	16.19	0.00	0.24	0.01	99.36	61.79
	BH167 A4 58	rim	50.01	1.73	18.56	0.61	0.01	12.91	0.42	15.17	0.01	0.24	0.00	99.66	55.35
	BH167 A4 55-58	average	49.80	2.04	17.03	0.75	0.01	13.30	0.38	15.97	0.02	0.25	0.01	99.53	58.33
	BH167 A4 59	cpx overgrowth rep	49.62	1.68	19.92	0.73	0.01	11.70	0.48	15.59	0.00	0.22	0.00	99.93	51.14
	BH167 A4 69	core	50.59	2.06	16.57	0.63	0.00	16.81	0.40	12.47	0.04	0.19	0.00	99.76	64.39
	BH167 A4 70	rim	50.97	1.37	14.48	0.48	0.00	16.80	0.38	13.75	0.03	0.22	0.03	98.51	67.39
	BH167 A4 69-70	average	50.78	1.72	15.52	0.56	0.00	16.81	0.39	13.11	0.03	0.21	0.01	99.13	65.89
	BH167 A4 72	rim	54.86	3.38	7.69	0.51	0.42	17.64	0.22	18.25	0.01	0.20	0.02	103.20	80.34
	BH167 A4 72	rimward	50.53	3.47	7.03	0.52	0.47	16.58	0.15	20.51	0.03	0.23	0.00	99.52	80.78
	BH167 A4 72	rimward	50.58	3.45	6.89	0.59	0.63	16.51	0.16	20.41	0.02	0.20	0.00	99.45	81.03
	BH167 A4 72	rimward	50.27	3.51	6.99	0.62	0.42	16.49	0.20	19.90	0.02	0.22	0.00	98.64	80.79

	BH167 A4 72	core	50.71	3.36	7.72	0.56	0.35	16.80	0.17	19.52	0.07	0.21	0.00	99.49	79.49
	BH167 A4 72	core	50.77	3.12	7.74	0.47	0.33	17.09	0.17	19.59	0.01	0.19	0.01	99.50	79.74
	BH167 A4 72	rimward	50.28	2.73	8.74	0.51	0.22	15.80	0.23	19.95	0.04	0.18	0.01	98.68	76.31
	BH167 A4 72	rimward	51.14	2.67	7.79	0.50	0.19	16.78	0.17	20.32	0.04	0.19	0.01	99.79	79.34
	BH167 A4 72	rimward	51.19	2.50	8.69	0.51	0.04	17.41	0.20	18.85	0.00	0.23	0.00	99.62	78.12
	BH167 A4 72	rim	49.10	0.77	19.32	0.29	0.00	8.29	0.61	20.01	0.00	0.15	0.05	98.59	43.33
	BH167 A4 72	x average	50.94	2.90	8.86	0.51	0.31	15.94	0.23	19.73	0.02	0.20	0.01	99.65	75.93
	BH167 A4 73	rim	52.29	1.50	10.32	0.44	0.00	17.00	0.27	18.28	0.00	0.21	0.00	100.31	74.58
	BH167 A4 73	rimward	51.95	1.48	10.66	0.51	0.08	17.15	0.30	17.42	0.00	0.18	0.00	99.71	74.14
	BH167 A4 73	rimward	51.79	1.48	11.25	0.42	0.04	17.20	0.30	17.00	0.02	0.21	0.00	99.70	73.15
	BH167 A4 73	rimward	52.18	1.39	11.52	0.52	0.03	17.00	0.33	16.94	0.00	0.23	0.01	100.15	72.45
	BH167 A4 73	rimward	52.25	1.44	12.39	0.37	0.00	17.30	0.33	16.04	0.02	0.22	0.00	100.36	71.33
	BH167 A4 73	rimward	51.93	1.43	12.63	0.41	0.04	17.31	0.31	15.76	0.03	0.19	0.01	100.04	70.95
	BH167 A4 73	rimward	52.22	1.41	13.26	0.39	0.04	17.38	0.33	15.35	0.02	0.21	0.01	100.61	70.03
	BH167 A4 73	core	52.00	1.43	13.41	0.33	0.03	17.30	0.40	14.85	0.03	0.18	0.00	99.97	69.68
	BH167 A4 73	rimward	52.36	1.41	14.26	0.38	0.03	17.44	0.38	14.08	0.00	0.18	0.00	100.53	68.55
	BH167 A4 73	rimward	43.86	1.59	19.45	7.17	0.05	15.05	0.51	7.87	0.16	0.29	0.04	96.04	57.96
	BH167 A4 73	rimward	50.16	2.01	16.29	0.72	0.03	16.00	0.38	13.38	0.00	0.23	0.01	99.20	63.65
	BH167 A4 73	rimward	49.75	2.01	18.22	0.79	0.00	15.14	0.42	13.09	0.00	0.20	0.00	99.61	59.69
	BH167 A4 73	rimward	50.38	1.87	18.02	0.77	0.00	14.04	0.48	14.00	0.07	0.21	0.02	99.86	58.13
	BH167 A4 73	rimward	49.67	1.34	18.23	0.84	0.00	12.19	0.42	16.30	0.02	0.23	0.01	99.26	54.38
	BH167 A4 73	rim	50.48	0.27	20.54	0.23	0.07	8.89	0.54	18.26	0.00	0.16	0.00	99.44	43.55
	BH167 A4 73	x average	50.88	1.47	14.70	0.95	0.03	15.76	0.38	15.24	0.02	0.21	0.01	99.65	65.48
	BH175 A1 87	ground rep	49.15	4.52	8.77	0.80	0.38	15.57	0.16	19.50	0.03	0.22	0.02	99.10	75.99
	BH175 A1 88	ground rep	48.02	2.52	16.97	1.13	0.00	12.33	0.36	16.98	0.00	0.25	0.03	98.60	56.43
	BH175 A1 101	core	51.47	2.52	6.12	0.31	0.67	17.35	0.14	20.45	0.07	0.18	0.01	99.28	83.49
	BH175 A1 102	rim	50.79	2.94	6.38	0.37	0.61	17.00	0.17	20.65	0.05	0.23	0.03	99.23	82.59
	BH175 A1 101-102	average	51.13	2.73	6.25	0.34	0.64	17.18	0.15	20.55	0.06	0.21	0.02	99.25	83.04
	BH175 A1 107	rim	52.90	1.90	6.80	0.22	0.42	17.81	0.20	19.85	0.05	0.19	0.02	100.36	82.35
	BH175 A1 107	rimward	52.11	2.38	5.74	0.36	0.50	17.04	0.14	21.02	0.04	0.22	0.02	99.55	84.10
	BH175 A1 107	rimward	52.16	2.42	6.06	0.42	0.66	17.06	0.14	21.01	0.03	0.21	0.00	100.16	83.38
	BH175 A1 107	core	52.30	2.29	6.18	0.37	0.53	17.46	0.15	20.28	0.06	0.20	0.01	99.82	83.43
	BH175 A1 107	core	51.90	2.41	5.93	0.27	0.48	17.07	0.16	21.00	0.06	0.23	0.01	99.50	83.70
	BH175 A1 107	rimward	51.68	2.81	6.33	0.27	0.77	16.93	0.15	20.84	0.01	0.21	0.00	99.98	82.65
	BH175 A1 107	rimward	50.17	3.78	7.06	0.51	0.67	16.29	0.11	20.17	0.04	0.21	0.05	99.06	80.44
	BH175 A1 107	rim	50.34	4.49	7.70	0.95	0.10	16.17	0.19	19.72	0.02	0.22	0.01	99.91	78.91
	BH175 A1 107	x average	51.69	2.81	6.47	0.42	0.52	16.98	0.16	20.49	0.04	0.21	0.01	99.79	82.37
	BH175 A1 108	rim	51.85	2.78	5.91	0.47	0.71	16.91	0.14	21.05	0.05	0.22	0.01	100.10	83.61

	BH175 A1 108	rimward	50.59	3.94	6.77	0.46	0.57	16.40	0.17	20.42	0.03	0.24	0.02	99.60	81.19
	BH175 A1 108	core	50.93	3.56	5.95	0.50	0.65	16.41	0.16	20.88	0.03	0.22	0.01	99.29	83.10
	BH175 A1 108	core	50.55	3.49	6.74	0.49	0.51	16.26	0.17	20.80	0.02	0.23	0.01	99.26	81.13
	BH175 A1 108	rimward	50.97	2.88	7.32	0.47	0.24	16.09	0.16	20.62	0.02	0.25	0.02	99.04	79.66
	BH175 A1 108	rim	50.87	3.15	7.45	0.64	0.17	16.40	0.19	20.36	0.04	0.19	0.03	99.49	79.69
	BH175 A1 108	x average	50.96	3.30	6.69	0.50	0.47	16.41	0.17	20.69	0.03	0.22	0.02	99.46	81.40
	BH175 A1 109	rim	52.04	2.73	5.80	0.42	0.55	16.96	0.15	21.02	0.05	0.23	0.01	99.97	83.89
	BH175 A1 109	rimward	50.41	8.34	8.31	0.37	0.62	15.08	0.13	15.50	0.05	0.23	1.03	100.06	76.38
	BH175 A1 109	rimward	50.78	3.73	6.15	0.40	0.88	16.39	0.11	20.73	0.02	0.24	0.01	99.42	82.61
	BH175 A1 109	rimward	54.50	3.45	6.50	0.44	0.69	16.65	0.17	20.71	0.03	0.26	0.01	103.41	82.02
	BH175 A1 109	rimward	51.49	3.46	6.38	0.47	0.73	16.26	0.17	20.60	0.03	0.32	0.16	100.09	81.97
	BH175 A1 109	core	51.31	3.47	6.36	0.50	0.82	16.81	0.14	20.27	0.05	0.23	0.01	99.96	82.49
	BH175 A1 109	rimward	51.02	3.82	6.68	0.44	0.80	16.55	0.15	20.33	0.06	0.24	0.01	100.10	81.53
	BH175 A1 109	rimward	51.14	3.44	6.35	0.42	0.55	16.70	0.12	20.62	0.00	0.26	0.03	99.62	82.41
	BH175 A1 109	rimward	52.09	2.47	5.57	0.37	0.49	17.01	0.15	20.92	0.03	0.22	0.05	99.34	84.48
	BH175 A1 109	rim	51.55	3.28	6.24	0.52	0.68	16.45	0.15	20.64	0.00	0.25	0.02	99.76	82.44
	BH175 A1 109	x average	51.63	3.82	6.43	0.43	0.68	16.49	0.14	20.13	0.03	0.25	0.13	100.17	82.02
	BH175 A1 119	ground rep	50.04	3.33	10.41	0.44	0.00	15.40	0.22	18.11	0.02	0.25	0.07	98.26	72.50
	BH175 A1 120	core	50.87	3.21	6.29	0.49	0.77	17.03	0.17	20.35	0.01	0.19	0.00	99.38	82.84
	BH175 A1 120	rimwards	51.06	3.40	6.32	0.41	0.63	16.67	0.14	20.68	0.00	0.22	0.01	99.55	82.45
	BH175 A1 120	rimwards	50.14	4.06	6.43	0.50	0.57	16.53	0.16	20.32	0.06	0.21	0.01	98.97	82.09
	BH175 A1 120	rimwards	50.14	3.99	6.49	0.45	0.71	16.61	0.16	20.12	0.04	0.25	0.02	98.99	82.01
	BH175 A1 120	rimwards	50.73	3.47	6.17	0.35	0.82	16.74	0.14	20.48	0.02	0.22	0.01	99.15	82.87
	BH175 A1 120	rimwards	50.73	3.52	7.02	0.44	0.63	17.13	0.16	19.97	0.06	0.22	0.01	99.88	81.31
	BH175 A1 120	rimwards	50.63	3.69	6.93	0.49	0.41	16.81	0.16	19.57	0.07	0.19	0.00	98.95	81.21
	BH175 A1 120	rim	50.99	3.05	6.65	0.49	0.43	17.27	0.17	19.80	0.05	0.19	0.02	99.12	82.23
	BH175 A1 120	x average	50.66	3.55	6.54	0.45	0.62	16.85	0.16	20.16	0.04	0.21	0.01	99.25	82.13
	BH175 A1 121	core	51.61	2.54	6.00	0.33	0.53	17.06	0.15	20.83	0.04	0.21	0.03	99.33	83.51
	BH175 A1 121	rimwards	53.90	2.24	6.41	0.42	0.27	17.76	0.15	19.77	0.04	0.19	0.01	101.16	83.15
	BH175 A1 121	rimwards	52.03	2.25	5.72	0.42	0.38	17.42	0.18	20.71	0.05	0.19	0.00	99.35	84.43
	BH175 A1 121	rimwards	52.39	2.41	6.15	0.46	0.50	17.48	0.14	20.42	0.03	0.18	0.01	100.15	83.52
	BH175 A1 121	rimwards	51.54	2.28	6.08	0.24	0.69	17.35	0.21	20.70	0.04	0.19	0.01	99.33	83.57
	BH175 A1 121	rimwards	52.21	2.07	6.12	0.24	0.53	17.67	0.15	20.24	0.03	0.21	0.01	99.47	83.73
	BH175 A1 121	rimwards	50.89	2.37	5.98	0.32	0.67	17.19	0.15	20.98	0.02	0.21	0.01	98.78	83.66
	BH175 A1 121	rim	51.77	2.38	8.09	0.56	0.16	17.86	0.20	18.44	0.05	0.15	0.02	99.67	79.74
	BH175 A1 121	x average	52.04	2.32	6.32	0.37	0.47	17.47	0.17	20.26	0.04	0.19	0.01	99.66	83.16
	BH175 A1 123	ground rep	49.10	4.00	14.15	0.33	0.16	15.23	0.28	15.06	0.04	0.18	0.22	98.74	65.74
	BH175 A1 125	core	52.03	2.83	6.28	0.39	0.72	17.35	0.20	20.17	0.00	0.22	0.02	100.22	83.12

	BH175 A1 125	rimwards	50.67	4.44	6.57	0.52	0.67	16.63	0.17	20.05	0.05	0.24	0.03	100.06	81.85
	BH175 A1 125	rimwards	52.16	2.46	5.83	0.41	0.60	16.96	0.16	20.98	0.02	0.22	0.00	99.78	83.84
	BH175 A1 125	rimwards	51.56	3.13	6.64	0.44	0.56	16.68	0.18	20.36	0.04	0.21	0.02	99.83	81.74
	BH175 A1 125	rimwards	52.08	2.80	6.18	0.50	0.66	17.02	0.15	20.67	0.02	0.23	0.00	100.32	83.07
	BH175 A1 125	rimwards	51.10	3.17	6.52	0.24	0.60	16.50	0.13	20.75	0.00	0.20	0.01	99.23	81.86
	BH175 A1 125	rimwards	52.59	2.40	6.28	0.33	0.55	17.40	0.15	20.85	0.01	0.20	0.00	100.77	83.16
	BH175 A1 125	rimwards	51.88	2.76	5.97	0.35	0.68	16.88	0.14	21.13	0.02	0.20	0.02	100.03	83.43
	BH175 A1 125	rimwards	52.17	2.72	5.92	0.37	0.64	16.90	0.11	21.18	0.00	0.20	0.01	100.21	83.56
	BH175 A1 125	rim	51.05	3.63	6.82	0.54	0.54	16.31	0.18	20.47	0.04	0.24	0.01	99.81	81.00
	BH175 A1 125	x average	51.73	3.03	6.30	0.41	0.62	16.86	0.16	20.66	0.02	0.22	0.01	100.03	82.66
	BH175 A1 130	ground rep	49.18	1.50	18.64	0.95	0.04	12.23	0.42	15.04	0.00	0.21	0.05	98.26	53.91

Appendix G4 – SFDC plagioclase mineral chemistry

ZONE	SAMPLE ID	X Region	SiO2	TiO2	Al2O3	MgO	CaO	MnO	FeO	Na2O	K2O	BaO	SrO	Total	An
D	BH268 A2 4	chad rep	48.58	0.03	30.31	0.24	14.58	0.02	0.84	3.36	0.08	0.04	0.06	98.12	70.19
	BH268 A2 5	chad rep	48.83	0.05	30.42	0.22	14.56	0.01	0.90	3.42	0.07	0.00	0.06	98.54	69.90
	BH268 A2 6	core	49.93	0.07	30.20	0.24	14.62	0.00	0.74	3.33	0.09	0.03	0.03	99.28	70.39
	BH268 A2 7	rim	51.14	0.00	29.81	0.23	14.07	0.00	0.80	3.42	0.34	0.00	0.08	99.88	68.09
	BH268 A2 6-7	average	50.53	0.04	30.00	0.24	14.34	0.00	0.77	3.38	0.21	0.01	0.06	99.58	69.24
	BH268 A2 11	chad rep	50.35	0.04	30.40	0.22	14.61	0.00	0.81	3.39	0.07	0.00	0.08	99.97	70.16
	BH268 A2 12	core	51.65	0.07	30.59	0.25	14.65	0.00	0.75	3.33	0.08	0.00	0.03	101.39	70.54
	BH268 A2 13	rim	51.15	0.02	30.89	0.23	14.85	0.03	0.76	3.18	0.07	0.00	0.08	101.25	71.80
	BH268 A2 12-13	average	51.40	0.04	30.74	0.24	14.75	0.02	0.75	3.25	0.07	0.00	0.05	101.32	71.17
	BH268 A2 14	ground (rep)	57.68	0.10	26.66	0.05	9.40	0.00	0.87	6.21	0.38	0.00	0.13	101.48	44.56
	BH268 A2 19	chad core	51.16	0.09	30.27	0.25	14.57	0.05	0.73	3.49	0.07	0.00	0.08	100.77	69.50
	BH268 A2 20	chad rim	52.11	0.07	30.14	0.20	13.85	0.00	0.88	3.82	0.10	0.00	0.06	101.23	66.35
	BH268 A2 19-20	chad average	51.64	0.08	30.20	0.23	14.21	0.03	0.81	3.65	0.08	0.00	0.07	101.00	67.92
	BH268 A2 27	ground (rep)	52.84	0.16	27.63	0.33	11.41	0.00	2.42	4.60	0.20	0.03	0.07	99.69	57.11
	BH268 A2 28	plag rep (near cpx)	52.81	0.08	29.25	0.32	13.71	0.00	1.09	3.91	0.09	0.02	0.06	101.32	65.62
	MH126 A2 44	ground (rep)	50.70	0.04	29.83	0.22	14.10	0.02	1.17	3.59	0.14	0.01	0.04	99.85	67.90
	BH296 A1 3	core	51.04	0.07	29.32	0.11	12.86	0.02	0.97	4.32	0.14	0.01	0.10	98.94	61.69
	BH296 A1 4	rimwards	52.36	0.07	29.33	0.11	12.78	0.03	0.89	4.48	0.13	0.02	0.07	100.26	60.73
	BH296 A1 5	rim	52.33	0.07	29.68	0.08	13.04	0.08	1.00	4.28	0.13	0.03	0.08	100.79	62.22
	BH296 A1 3-5	average	51.91	0.07	29.44	0.10	12.89	0.04	0.95	4.36	0.13	0.02	0.08	100.00	61.54
	BH296 A1 6	rep	52.73	0.07	29.52	0.11	12.77	0.05	0.87	4.49	0.13	0.00	0.08	100.83	60.65
	BH296 A1 7	core	53.25	0.04	29.15	0.05	11.99	0.03	0.58	4.49	0.70	0.00	0.04	100.32	57.22
	BH296 A1 8	rim	52.44	0.11	29.19	0.06	12.70	0.08	1.04	4.45	0.13	0.00	0.07	100.27	60.71
	BH296 A1 7-8	average	52.85	0.07	29.17	0.06	12.34	0.05	0.81	4.47	0.42	0.00	0.06	100.29	58.97
	BH296 A1 9	chad rep	52.78	0.10	29.05	0.08	12.38	0.00	1.07	4.65	0.17	0.00	0.00	100.26	58.99
	BH296 A1 10	core	53.31	0.09	28.09	0.06	11.24	0.03	0.82	5.30	0.25	0.00	0.00	99.19	53.22
	BH296 A1 11	rimwards	54.72	0.09	27.82	0.05	10.68	0.00	0.78	5.43	0.21	0.00	0.08	99.86	51.45
	BH296 A1 12	rim	55.58	0.03	26.90	0.05	9.81	0.00	0.84	5.88	0.31	0.00	0.07	99.47	47.13
	BH296 A1 10-12	average	54.54	0.07	27.61	0.05	10.58	0.01	0.81	5.53	0.26	0.00	0.05	99.51	50.60
	BH296 A1 13	chad core	55.29	0.12	27.28	0.06	9.89	0.00	0.92	5.89	0.27	0.01	0.07	99.80	47.36
	BH296 A1 14	chad rim	55.86	0.09	27.07	0.05	9.59	0.03	0.99	6.21	0.27	0.00	0.10	100.26	45.35
	BH296 A1 13-14	average	55.58	0.10	27.17	0.06	9.74	0.02	0.96	6.05	0.27	0.00	0.09	100.03	46.36
	BH296 A1 15	core	52.94	0.03	28.74	0.06	11.98	0.01	0.84	4.79	0.19	0.00	0.04	99.62	57.37
	BH296 A1 16	rimwards	53.79	0.01	27.97	0.06	10.87	0.05	0.73	5.31	0.24	0.00	0.15	99.16	52.37
	BH296 A1 17	rimwards	54.18	0.08	27.79	0.08	10.62	0.01	0.70	5.60	0.20	0.05	0.08	99.39	50.56
	BH296 A1 18	rim	56.0	0.08	27.15	0.04	9.62	0.00	0.8	6.02	0.28	0.02	0.0	100.1	46.1

			7						0				8	6	4
	BH296 A1 15-18	average	54.24	0.05	27.91	0.06	10.77	0.01	0.77	5.43	0.23	0.02	0.09	99.58	51.61
	BH296 A1 20	core	53.24	0.10	29.05	0.10	12.59	0.02	0.95	4.44	0.17	0.00	0.00	100.64	60.49
	BH296 A1 20	rimwards	54.40	0.05	28.57	0.11	11.96	0.01	0.88	4.88	0.18	0.01	0.03	101.08	56.96
	BH296 A1 20	rimwards	55.14	0.00	28.35	0.06	11.49	0.00	0.85	5.21	0.22	0.00	0.05	101.37	54.25
	BH296 A1 20	rimwards	55.59	0.04	28.01	0.08	11.06	0.05	0.81	5.31	0.23	0.00	0.09	101.26	52.80
	BH296 A1 20	rimwards	55.69	0.05	27.75	0.07	10.70	0.00	0.79	5.48	0.25	0.01	0.05	100.83	51.14
	BH296 A1 20	rimwards	55.74	0.04	27.57	0.06	10.45	0.00	0.85	5.62	0.28	0.00	0.13	100.75	49.86
	BH296 A1 20	rimwards	56.58	0.13	27.58	0.06	10.17	0.02	1.08	5.84	0.27	0.01	0.10	101.83	48.30
	BH296 A1 20	rim	54.49	0.21	27.21	0.10	9.63	0.00	2.16	5.90	0.16	0.00	0.03	99.89	46.96
	BH296 A1 20	x average	55.11	0.08	28.01	0.08	11.01	0.01	1.04	5.33	0.22	0.00	0.06	100.95	52.60
	BH296 A1 22	rim	55.67	0.02	26.60	0.04	9.04	0.06	0.65	6.27	0.32	0.00	0.01	98.67	43.55
	BH296 A1 22	rimward	51.79	0.06	23.22	0.95	6.99	0.42	7.28	5.18	0.99	0.05	0.02	96.95	39.81
	BH296 A1 22	rimward	55.59	0.04	26.96	0.04	9.51	0.01	0.64	6.04	0.28	0.07	0.07	99.24	45.70
	BH296 A1 22	rimward	55.31	0.05	27.08	0.07	9.69	0.07	0.61	5.98	0.24	0.01	0.11	99.21	46.58
	BH296 A1 22	rimward	54.71	0.09	27.25	0.08	9.95	0.09	0.66	5.94	0.23	0.00	0.09	99.07	47.43
	BH296 A1 22	rimward	54.72	0.05	27.21	0.06	10.13	0.01	0.67	5.88	0.19	0.00	0.09	99.01	48.27
	BH296 A1 22	rimward	54.65	0.00	27.18	0.08	10.30	0.00	0.65	5.66	0.20	0.00	0.08	98.81	49.55
	BH296 A1 22	rimward	54.53	0.02	27.57	0.06	10.40	0.00	0.67	5.58	0.17	0.00	0.06	99.07	50.23
	BH296 A1 22	rimward	53.87	0.15	27.45	0.08	10.56	0.05	0.74	5.45	0.19	0.00	0.05	98.58	51.17
	BH296 A1 22	core	54.20	0.11	27.64	0.14	10.45	0.02	0.83	5.30	0.37	0.01	0.03	99.10	51.02
	BH296 A1 22	core	53.86	0.05	27.68	0.07	10.53	0.00	0.74	5.49	0.17	0.00	0.04	98.64	50.97
	BH296 A1 22	rimward	54.35	0.07	27.58	0.08	10.31	0.00	0.69	5.74	0.19	0.00	0.10	99.10	49.29
	BH296 A1 22	rimward	54.47	0.05	27.46	0.06	10.04	0.02	0.64	5.83	0.20	0.00	0.11	98.88	48.19
	BH296 A1 22	rimward	54.41	0.07	27.10	0.06	9.95	0.00	0.68	5.80	0.21	0.00	0.00	98.29	48.06
	BH296 A1 22	rimward	54.20	0.04	27.27	0.06	9.80	0.00	0.65	5.99	0.21	0.00	0.06	98.28	46.90
	BH296 A1 22	rimward	54.77	0.11	27.03	0.07	9.60	0.05	0.63	6.07	0.21	0.05	0.11	98.70	46.03
	BH296 A1 22	rimward	55.04	0.08	27.07	0.07	9.44	0.00	0.66	6.16	0.23	0.00	0.08	98.81	45.27
	BH296 A1 22	rimward	55.30	0.08	26.74	0.04	9.21	0.01	0.67	6.13	0.29	0.05	0.07	98.60	44.56
	BH296 A1 22	rimward	55.37	0.01	26.64	0.04	9.18	0.00	0.65	6.37	0.26	0.00	0.02	98.52	43.70
	BH296 A1 22	rim	55.55	0.14	26.58	0.04	8.89	0.00	0.98	6.37	0.32	0.04	0.10	99.00	42.69
	BH296 A1 22	x average	54.62	0.06	26.96	0.11	9.70	0.04	1.02	5.86	0.27	0.01	0.07	98.73	46.95
	BH296 A1 25	core	54.35	0.06	27.24	0.07	10.21	0.00	0.66	5.71	0.20	0.01	0.07	98.56	49.14
	BH296 A1 26	rimward	52.73	0.07	28.60	0.05	11.54	0.00	0.77	5.04	0.19	0.00	0.07	99.05	55.29
	BH296 A1 27	rim	55.60	0.09	26.57	0.03	9.04	0.01	0.90	6.28	0.35	0.00	0.07	98.95	43.41
	BH296 A1 25-27	average	54.23	0.07	27.47	0.05	10.26	0.00	0.78	5.67	0.25	0.00	0.07	98.85	49.28
	BH296 A1 28	core	51.17	0.00	29.21	0.08	12.71	0.01	1.07	4.42	0.13	0.01	0.00	98.81	60.92
	BH296 A1 29	rimward	53.18	0.12	28.30	0.07	11.34	0.03	0.93	5.11	0.15	0.00	0.08	99.31	54.61
	BH296 A1 30	rim	53.9	0.12	27.90	0.07	10.8	0.04	1.0	5.43	0.19	0.00	0.0	99.64	51.9

			6				7		0				5		4
	BH296 A1 28-30	average	52.77	0.08	28.47	0.07	11.64	0.03	1.00	4.99	0.16	0.00	0.04	99.25	55.82
	BH296 A1 36	chad rep	50.98	0.07	29.18	0.10	12.49	0.00	0.93	4.51	0.13	0.00	0.06	98.45	60.04
	BH296 A1 37	chad rep	51.38	0.03	29.26	0.08	12.41	0.00	0.86	4.53	0.16	0.01	0.05	98.77	59.65
	BH296 A1 38	chad rep	51.27	0.00	29.09	0.06	12.36	0.01	1.01	4.55	0.13	0.01	0.07	98.54	59.58
	BH296 A1 41	chad rep	51.44	0.02	28.97	0.05	12.16	0.03	0.93	4.70	0.18	0.05	0.02	98.55	58.18
	BH296 A1 42	chad rep	50.97	0.08	30.47	0.05	12.94	0.00	0.79	4.19	0.13	0.01	0.09	99.72	62.57
	BH296 A1 43	chad rep	50.59	0.11	29.54	0.06	12.76	0.01	0.98	4.45	0.13	0.00	0.12	98.75	60.85
	BH296 A1 44	chad rep	53.10	0.03	27.84	0.04	10.82	0.00	0.84	5.44	0.16	0.00	0.09	98.37	51.85
	BH296 A1 36-44	chad average	51.39	0.05	29.19	0.06	12.28	0.01	0.91	4.62	0.15	0.01	0.07	98.73	58.96
	MH123 B2 56	core	49.60	0.01	29.71	0.12	13.13	0.00	0.95	4.21	0.18	0.00	0.01	97.91	62.65
	MH123 B2 57	rim	50.39	0.19	28.91	0.14	12.18	0.00	1.24	4.59	0.20	0.00	0.02	97.85	58.75
	MH123 B2 56-57	average	49.99	0.10	29.31	0.13	12.65	0.00	1.09	4.40	0.19	0.00	0.01	97.88	60.70
	MH123 B2 59	core	48.07	0.05	30.93	0.16	14.52	0.02	0.85	3.46	0.11	0.00	0.10	98.27	69.43
	MH123 B2 60	rim	48.53	0.03	31.00	0.27	14.83	0.03	1.57	3.01	0.10	0.00	0.04	99.40	72.71
	MH123 B2 59-60	average	48.30	0.04	30.96	0.21	14.68	0.02	1.21	3.23	0.11	0.00	0.07	98.84	71.07
	MH123 B2 63	core	46.49	0.00	32.05	0.14	15.82	0.03	0.69	2.60	0.06	0.00	0.00	97.89	76.79
	MH123 B2 64	rim	50.18	0.04	29.24	0.11	12.69	0.00	1.06	4.37	0.13	0.00	0.08	97.90	61.15
	MH123 B2 63-64	average	48.33	0.02	30.64	0.13	14.26	0.02	0.88	3.49	0.10	0.00	0.04	97.89	68.97
	MH123 B2 70	core	47.81	0.03	31.36	0.13	14.88	0.00	0.87	3.03	0.13	0.07	0.05	98.35	72.46
	MH123 B2 71	rimwards	47.52	0.04	31.29	0.10	14.99	0.00	0.92	3.02	0.11	0.01	0.13	98.13	72.81
	MH123 B2 72	rim	52.05	0.02	27.87	0.09	11.14	0.00	1.07	5.02	0.22	0.00	0.15	97.61	54.40
	MH123 B2 70-72	average	49.13	0.03	30.17	0.11	13.67	0.00	0.95	3.69	0.15	0.03	0.11	98.03	66.56
	MH123 B2 73	rep (impinging ol)	45.11	0.01	31.12	0.14	14.79	0.02	1.11	3.05	0.12	0.00	0.04	95.51	72.34
	MH123 B2 74	rim	53.23	0.05	27.86	0.11	10.89	0.00	0.89	5.31	0.20	0.00	0.07	98.61	52.53
	MH123 B2 74	rimward	51.72	0.00	29.30	0.17	12.76	0.00	0.86	4.23	0.15	0.00	0.04	99.23	61.98
	MH123 B2 74	rimward	50.55	0.03	29.64	0.17	13.36	0.00	0.82	3.93	0.12	0.00	0.04	98.65	64.82
	MH123 B2 74	rimward	49.29	0.06	29.86	0.20	13.68	0.03	0.78	3.69	0.11	0.00	0.02	97.73	66.76
	MH123 B2 74	core	48.63	0.04	30.52	0.21	14.27	0.00	0.76	3.53	0.08	0.00	0.01	98.04	68.76
	MH123 B2 74	core	48.44	0.12	30.66	0.18	14.61	0.05	0.77	3.27	0.08	0.03	0.03	98.23	70.79
	MH123 B2 74	rimward	48.68	0.10	30.78	0.19	14.65	0.00	0.76	3.23	0.08	0.00	0.07	98.54	71.15
	MH123 B2 74	rimward	48.88	0.03	30.66	0.37	14.35	0.01	0.99	3.40	0.12	0.00	0.05	98.86	69.49
	MH123 B2 74	rimward	49.32	0.01	30.67	0.17	14.43	0.00	0.88	3.33	0.09	0.01	0.04	98.94	70.14
	MH123 B2 74	rim	49.78	0.02	30.04	0.17	13.92	0.02	0.94	3.66	0.11	0.00	0.06	98.70	67.36
	MH123 B2 74	x average	49.85	0.05	30.00	0.19	13.69	0.01	0.84	3.76	0.11	0.01	0.04	98.55	66.38
	MH123 B2 79	core	50.84	0.04	30.05	0.17	13.62	0.03	0.88	3.91	0.10	0.00	0.02	99.65	65.42
	MH123 B2 80	rim	51.53	0.07	29.26	0.21	13.02	0.07	1.14	4.10	0.16	0.00	0.07	99.63	63.11
	MH123 B2 79-80	average	51.18	0.05	29.65	0.19	13.32	0.05	1.01	4.01	0.13	0.00	0.04	99.64	64.27
	MH123 B2 88	core	50.0	0.10	28.96	0.15	12.6	0.00	0.8	4.37	0.15	0.00	0.0	97.37	61.0

			7				7		3				8		6
	MH123 B2 89	rim	50.45	0.08	29.44	0.19	13.21	0.04	0.75	4.08	0.10	0.00	0.03	98.38	63.77
	MH123 B2 88-89	average	50.26	0.09	29.20	0.17	12.94	0.02	0.79	4.22	0.12	0.00	0.05	97.87	62.42
	MH123 B2 90	chad rep	50.90	0.07	29.72	0.19	13.71	0.00	0.82	3.87	0.11	0.00	0.01	99.39	65.81
	MH123 B2 95	rim	52.84	0.07	28.18	0.23	11.83	0.01	0.96	4.78	0.16	0.00	0.02	99.08	57.25
	MH123 B2 95	rimward	52.00	0.02	28.53	0.18	12.22	0.04	0.86	4.60	0.17	0.00	0.04	98.64	58.94
	MH123 B2 95	rimward	52.03	0.12	28.88	0.15	12.59	0.00	0.86	4.32	0.13	0.00	0.11	99.19	61.23
	MH123 B2 95	rimward	50.94	0.01	29.48	0.19	13.30	0.02	0.78	4.10	0.13	0.00	0.09	99.03	63.75
	MH123 B2 95	core	49.49	0.03	29.89	0.22	13.85	0.00	0.77	3.72	0.10	0.00	0.12	98.19	66.91
	MH123 B2 95	core	49.82	0.02	30.23	0.21	14.31	0.00	0.73	3.41	0.08	0.00	0.05	98.86	69.52
	MH123 B2 95	rimward	48.85	0.00	30.99	0.15	14.70	0.00	0.69	3.26	0.07	0.00	0.09	98.81	71.08
	MH123 B2 95	rimward	48.45	0.09	31.18	0.20	15.18	0.04	0.65	3.02	0.06	0.02	0.02	98.92	73.21
	MH123 B2 95	rimward	47.72	0.06	32.30	0.19	15.73	0.00	0.72	2.58	0.06	0.00	0.06	99.43	76.81
	MH123 B2 95	rim	47.72	0.08	30.65	0.46	14.50	0.00	1.50	3.05	0.09	0.00	0.06	98.09	72.05
	MH123 B2 95	x average	49.99	0.05	30.03	0.22	13.82	0.01	0.85	3.68	0.11	0.00	0.06	98.82	67.07
	MH123 B2 97	core	51.45	0.11	29.97	0.17	13.64	0.08	0.80	3.91	0.11	0.00	0.03	100.27	65.48
	MH123 B2 98	rim	51.74	0.00	30.00	0.19	13.83	0.00	0.84	3.75	0.10	0.00	0.06	100.50	66.70
	MH123 B2 97-98	average	51.59	0.05	29.99	0.18	13.74	0.04	0.82	3.83	0.10	0.00	0.04	100.39	66.09
	MH123 B2 100	chad rep	49.29	0.03	30.28	0.11	13.91	0.03	0.99	3.64	0.11	0.01	0.06	98.45	67.39
C	MH129 A2 128	chad rep	50.07	0.07	30.88	0.06	14.22	0.00	0.68	3.56	0.10	0.00	0.11	99.76	68.40
	MH129 A2 129	core	48.79	0.00	31.05	0.07	14.79	0.01	0.71	3.23	0.09	0.00	0.03	98.76	71.31
	MH129 A2 130	rim	49.97	0.04	30.82	0.09	14.60	0.02	0.80	3.33	0.09	0.00	0.00	99.77	70.41
	MH129 A2 129-130	average	49.38	0.02	30.94	0.08	14.69	0.02	0.76	3.28	0.09	0.00	0.02	99.26	70.86
	MH129 A2 131	chad rep	47.49	0.00	30.78	0.14	13.93	0.06	0.87	3.60	0.12	0.00	0.00	96.99	67.66
	MH129 A2 135	rim	50.93	0.09	28.62	0.08	12.00	0.04	0.85	4.70	0.18	0.00	0.02	97.51	57.92
	MH129 A2 135	rimward	50.51	0.12	29.27	0.10	12.78	0.02	0.84	4.24	0.14	0.00	0.05	98.06	62.00
	MH129 A2 135	rimward	48.50	0.06	30.23	0.10	13.76	0.08	0.85	3.79	0.12	0.00	0.08	97.56	66.27
	MH129 A2 135	rimward	46.95	0.00	30.73	0.09	14.51	0.05	0.80	3.24	0.09	0.00	0.06	96.51	70.84
	MH129 A2 135	core	45.98	0.10	28.42	2.04	12.39	0.00	4.07	2.98	0.14	0.00	0.00	96.12	69.08
	MH129 A2 135	core	48.12	0.00	31.00	0.07	14.68	0.00	0.71	3.18	0.08	0.00	0.07	97.91	71.47
	MH129 A2 135	rimward	48.19	0.00	30.58	0.07	13.99	0.00	0.55	3.55	0.10	0.00	0.01	97.04	68.17
	MH129 A2 135	rimward	49.15	0.04	29.67	0.13	13.20	0.00	0.72	3.87	0.16	0.00	0.07	97.00	64.74
	MH129 A2 135	rimward	49.01	0.11	30.44	0.06	13.64	0.05	0.64	3.71	0.12	0.00	0.09	97.87	66.54
	MH129 A2 135	rim	49.51	0.11	29.99	0.07	13.04	0.00	0.63	4.16	0.12	0.00	0.08	97.70	62.98
	MH129 A2 135	average	48.68	0.06	29.89	0.28	13.40	0.02	1.07	3.74	0.12	0.00	0.05	97.33	66.00
	MH129 A2 144	rim	51.17	0.07	30.00	0.07	13.08	0.02	0.62	4.18	0.20	0.00	0.08	99.48	62.62
	MH129 A2 144	rimward	50.73	0.09	31.02	0.08	14.12	0.00	0.54	3.58	0.19	0.04	0.05	100.44	67.76
	MH129 A2 144	rimward	50.23	0.07	30.95	0.06	14.21	0.00	0.49	3.57	0.15	0.00	0.06	99.79	68.15
	MH129 A2 144	rimward	51.6	0.03	29.63	0.10	12.9	0.00	0.6	4.10	0.23	0.02	0.0	99.35	62.7

			0				9		3				2		6
	MH129 A2 144	core	51.16	0.05	29.94	0.09	13.38	0.03	0.66	3.91	0.20	0.00	0.06	99.46	64.65
	MH129 A2 144	core	49.49	0.02	31.23	0.08	14.84	0.00	0.64	3.16	0.14	0.01	0.00	99.59	71.58
	MH129 A2 144	rimward	50.62	0.11	30.71	0.06	14.13	0.02	0.65	3.45	0.15	0.04	0.02	99.98	68.72
	MH129 A2 144	rimward	50.73	0.11	30.70	0.09	14.04	0.00	0.59	3.52	0.18	0.00	0.00	99.96	68.09
	MH129 A2 144	rimward	49.20	0.08	31.40	0.06	14.73	0.03	0.61	3.13	0.15	0.02	0.00	99.41	71.56
	MH129 A2 144	rim	52.80	0.10	29.33	0.09	12.60	0.00	0.72	4.27	0.28	0.00	0.07	100.25	61.02
	MH129 A2 144	x average	50.77	0.07	30.49	0.08	13.81	0.01	0.61	3.69	0.19	0.01	0.04	99.77	66.69
	MH129 A2 145	rep	50.01	0.08	31.23	0.06	14.54	0.00	0.84	3.34	0.15	0.00	0.08	100.31	70.06
	MH129 A2 146	rep	49.86	0.00	31.43	0.07	14.48	0.03	0.77	3.31	0.16	0.00	0.06	100.16	70.10
	MH129 A2 147	core	51.38	0.10	29.27	0.10	12.70	0.01	0.75	4.27	0.18	0.00	0.05	98.81	61.52
	MH129 A2 148	rim	52.74	0.10	28.59	0.11	11.79	0.00	0.92	4.84	0.20	0.00	0.10	99.38	56.71
	MH129 A2 147-148	average	52.06	0.10	28.93	0.11	12.24	0.00	0.83	4.56	0.19	0.00	0.07	99.10	59.12
	MH129 A2 157	core	53.77	0.10	28.12	0.08	10.96	0.04	0.58	5.31	0.20	0.00	0.04	99.19	52.70
	MH129 A2 158	rim	50.73	0.05	29.88	0.08	12.88	0.08	0.70	4.32	0.14	0.00	0.07	98.93	61.73
	MH129 A2 157-158	average	52.25	0.08	29.00	0.08	11.92	0.06	0.64	4.81	0.17	0.00	0.05	99.06	57.22
	MH129 A2 161	rim	53.85	0.13	28.69	0.06	11.59	0.00	0.79	5.05	0.23	0.00	0.01	100.39	55.18
	MH129 A2 161	rimward	50.32	0.09	30.69	0.08	14.32	0.03	0.80	3.53	0.12	0.00	0.07	100.04	68.70
	MH129 A2 161	rimward	49.96	0.08	30.75	0.09	14.42	0.01	0.85	3.47	0.10	0.02	0.14	99.87	69.21
	MH129 A2 161	rimward	49.99	0.03	30.80	0.08	13.97	0.00	0.68	3.55	0.13	0.00	0.11	99.32	68.00
	MH129 A2 161	core	50.45	0.04	30.86	0.09	14.26	0.00	0.69	3.52	0.12	0.00	0.07	100.08	68.68
	MH129 A2 161	core	50.66	0.13	30.48	0.09	14.10	0.08	0.80	3.52	0.11	0.00	0.08	100.04	68.45
	MH129 A2 161	rimward	50.25	0.04	30.95	0.13	14.45	0.00	0.80	3.38	0.15	0.00	0.06	100.22	69.63
	MH129 A2 161	rimward	50.92	0.04	30.66	0.08	14.07	0.00	0.75	3.66	0.12	0.00	0.06	100.36	67.52
	MH129 A2 161	rimward	50.33	0.07	31.01	0.05	14.59	0.02	0.78	3.37	0.10	0.00	0.03	100.34	70.09
	MH129 A2 161	rim	53.69	0.04	28.75	0.08	11.76	0.08	0.74	4.89	0.21	0.00	0.07	100.29	56.37
	MH129 A2 161	x average	51.04	0.07	30.36	0.08	13.75	0.02	0.77	3.79	0.14	0.00	0.07	100.09	66.18
	MH129 A2 169	chad rep	50.02	0.00	31.13	0.10	14.61	0.00	1.15	3.36	0.08	0.00	0.01	100.45	70.28
	MH129 A2 170	chad rep	53.25	0.00	29.15	0.12	12.26	0.02	0.80	4.76	0.18	0.01	0.00	100.55	58.13
	MH129 A2 171	rim	52.90	0.06	29.42	0.06	12.43	0.00	0.74	4.59	0.15	0.01	0.01	100.37	59.42
	MH129 A2 171	rimward	51.49	0.09	28.71	0.37	11.90	0.00	2.01	4.37	0.36	0.05	0.04	99.38	58.78
	MH129 A2 171	rimward	50.66	0.04	30.97	0.06	14.10	0.00	0.59	3.68	0.11	0.01	0.05	100.27	67.51
	MH129 A2 171	rimward	51.31	0.08	30.36	0.08	13.59	0.00	0.68	3.91	0.12	0.03	0.03	100.18	65.30
	MH129 A2 171	core	49.68	0.01	31.14	0.06	14.39	0.00	0.45	3.55	0.12	0.00	0.04	99.44	68.68
	MH129 A2 171	core	50.64	0.00	30.67	0.05	13.47	0.01	0.50	3.34	0.82	0.00	0.07	99.57	65.72
	MH129 A2 171	rimward	54.23	0.14	28.03	0.19	11.12	0.04	0.88	5.08	0.30	0.00	0.04	100.04	53.81
	MH129 A2 171	rimward	51.06	0.08	30.91	0.06	14.11	0.00	0.57	3.55	0.12	0.00	0.09	100.55	68.22
	MH129 A2 171	rimward	50.68	0.10	30.74	0.08	13.88	0.00	0.65	3.63	0.14	0.00	0.07	99.97	67.33
	MH129 A2 171	rim	51.2	0.06	30.60	0.07	13.7	0.02	0.6	3.75	0.14	0.00	0.0	100.3	66.4

			2				7		2				5	0	3
	MH129 A2 171	x average	51.39	0.07	30.16	0.11	13.28	0.01	0.77	3.94	0.24	0.01	0.05	100.01	64.12
B	BH185 A2_141	rep	64.61	0.00	19.10	0.03	0.41	0.00	0.30	0.66	14.73	0.26	0.11	100.20	2.11
	BH185 A2_144	rep	58.65	0.00	23.26	0.26	3.17	0.00	0.73	1.77	10.84	0.05	0.48	99.20	16.42
	BH185 A2_145	core	53.40	0.07	29.20	0.21	11.61	0.00	0.92	4.25	1.06	0.00	0.10	100.82	56.49
	BH185 A2_146	rim	55.84	0.06	27.62	0.11	10.67	0.08	0.86	5.40	0.46	0.03	0.11	101.24	50.83
	BH185 A2_145-46	average	54.62	0.06	28.41	0.16	11.14	0.04	0.89	4.82	0.76	0.02	0.11	101.03	53.66
	BH185 A2_147	core	52.92	0.03	29.74	0.16	13.49	0.05	0.88	4.13	0.13	0.02	0.06	101.59	63.86
	BH185 A2_148	rim	55.80	0.14	27.76	0.12	9.89	0.01	0.89	5.41	0.97	0.00	0.06	101.04	47.46
	BH185 A2_147-48	average	54.36	0.09	28.75	0.14	11.69	0.03	0.88	4.77	0.55	0.01	0.06	101.31	55.66
	BH185 A2_152	core	52.14	0.07	29.31	0.15	12.95	0.00	0.95	4.44	0.13	0.00	0.03	100.17	61.24
	BH185 A2_153	rim	53.49	0.05	28.69	0.15	12.63	0.00	1.04	4.59	0.16	0.00	0.04	100.84	59.82
	BH185 A2_152-53	average	52.82	0.06	29.00	0.15	12.79	0.00	0.99	4.51	0.14	0.00	0.03	100.50	60.53
	BH185 A2_251	rep	54.52	0.00	28.23	0.09	11.66	0.02	0.81	5.00	0.19	0.01	0.00	100.52	55.69
	BH185 A2_254	core	50.78	0.05	30.80	0.20	14.51	0.00	0.73	3.35	0.09	0.05	0.02	100.57	70.12
	BH185 A2_255	rim	51.79	0.02	30.47	0.18	14.10	0.07	0.82	3.68	0.14	0.00	0.00	101.26	67.40
	BH185 A2_254-55	average	51.28	0.04	30.64	0.19	14.30	0.04	0.77	3.51	0.11	0.03	0.01	100.92	68.76
	BH185 A2_264	rep	49.00	0.00	31.28	0.92	0.07	0.00	3.80	0.04	9.87	0.00	0.07	95.05	0.60
	BH185 A2_268	ground (rep)	53.49	0.13	28.27	0.28	11.67	0.04	1.40	4.92	0.20	0.00	0.00	100.39	56.09
E	BH366 B1 82	rep	53.20	0.10	29.02	0.07	12.65	0.00	1.23	4.25	0.29	0.00	0.03	100.82	61.19
	BH366 B1 86	rep	51.11	0.04	31.00	0.14	14.66	0.02	1.03	3.22	0.21	0.01	0.02	101.47	70.67
	BH366 B1 87	rep	50.70	0.00	31.04	0.04	14.78	0.01	0.98	3.22	0.15	0.00	0.04	100.95	71.13
	BH366 B1 93	rep	50.95	0.09	30.82	0.11	14.76	0.00	0.93	3.22	0.18	0.00	0.02	101.06	70.97
	BH366 B1 82-93	rep average	51.49	0.06	30.47	0.09	14.21	0.01	1.04	3.47	0.21	0.00	0.03	101.07	68.49
	BH372 A1 111	core	51.30	0.00	29.86	0.11	13.65	0.06	0.93	3.85	0.12	0.01	0.11	100.00	65.74
	BH372 A1 112	rimwards	51.62	0.07	28.94	0.30	4.99	0.01	1.62	2.44	6.08	0.02	0.11	96.19	29.97
	BH372 A1 113	rim	56.96	0.13	26.64	0.05	9.29	0.03	0.78	6.37	0.24	0.00	0.07	100.56	44.04
	BH372 A1 111-113	average	53.29	0.07	28.48	0.15	9.31	0.03	1.11	4.22	2.14	0.01	0.10	98.92	46.58
	BH372 A1 118	rep	55.22	0.07	26.25	0.03	8.66	0.04	0.62	6.60	0.25	0.00	0.11	97.84	41.45
	BH372 A1 119	core	52.61	0.10	28.53	0.23	9.46	0.00	1.04	4.31	1.61	0.01	0.08	97.98	49.34
	BH372 A1 120	rim	52.99	0.08	27.61	0.06	10.46	0.02	0.78	5.56	0.20	0.00	0.01	97.76	50.38
	BH372 A1 119-120	average	52.80	0.09	28.07	0.14	9.96	0.01	0.91	4.94	0.90	0.01	0.05	97.87	49.86
A	BH154 A2 68	chad rep	53.15	0.08	31.12	0.48	0.78	0.01	1.09	2.85	8.14	0.00	0.15	97.86	4.99
	BH154 A2 69	ground rep	52.45	0.08	29.53	0.14	11.93	0.00	1.24	3.89	1.16	0.07	0.06	100.55	58.54
	BH154 A2 79	ground rep	51.53	0.08	29.95	0.08	13.53	0.07	1.09	3.93	0.20	0.00	0.05	100.49	64.83
	BH167 A2 54	chad rep	53.19	0.04	29.68	0.16	13.22	0.00	1.01	4.29	0.14	0.00	0.01	101.73	62.55
	BH167 A2 55	core	50.20	0.04	31.65	0.15	1.28	0.06	1.42	0.12	11.25	0.00	0.25	96.41	8.57
	BH167 A2 56	rim	55.13	0.09	28.05	0.10	11.30	0.00	1.11	5.21	0.24	0.00	0.05	101.28	53.78
	BH167 A2 55-	average	52.6	0.07	29.85	0.12	6.29	0.03	1.2	2.67	5.75	0.00	0.1	98.84	31.1

	56		6						7				5		7
	BH167 A2 63	rep	53.47	0.12	29.48	0.29	0.20	0.02	1.32	0.42	12.29	0.16	0.22	97.99	1.28
	BH167 A2 64	rep	54.80	0.03	28.33	0.13	11.96	0.01	1.08	4.93	0.17	0.00	0.02	101.45	56.74
	BH167 A4 15	core	50.31	0.00	30.64	0.23	15.07	0.03	0.70	3.04	0.08	0.00	0.07	100.17	72.93
	BH167 A4 16	rim	53.96	0.00	28.17	0.14	12.09	0.07	1.08	4.56	0.16	0.00	0.04	100.26	58.90
	BH167 A4 15-16	average	52.14	0.00	29.41	0.18	13.58	0.05	0.89	3.80	0.12	0.00	0.05	100.21	65.92
	BH167 A4 17	rim	58.66	0.10	25.85	0.04	8.64	0.02	0.74	6.60	0.32	0.01	0.06	101.02	41.21
	BH167 A4 18	core	55.47	0.00	27.44	0.10	10.93	0.01	0.65	5.29	0.20	0.00	0.11	100.21	52.70
	BH167 A4 19	core	55.31	0.07	27.38	0.09	10.97	0.06	0.69	5.24	0.19	0.02	0.01	100.02	53.03
	BH167 A4 20	core	55.36	0.05	27.68	0.10	11.29	0.00	0.76	5.13	0.19	0.00	0.03	100.61	54.25
	BH167 A4 21	rim	55.13	0.09	27.68	0.08	11.29	0.00	0.77	5.04	0.18	0.00	0.02	100.29	54.74
	BH167 A4 17-21	average	55.98	0.06	27.21	0.08	10.62	0.02	0.72	5.46	0.22	0.01	0.05	100.43	51.19
	BH167 A4 22	chad core	54.53	0.07	28.07	0.13	11.95	0.00	1.02	4.80	0.16	0.03	0.08	100.83	57.35
	BH167 A4 23	chad rimwards	54.52	0.05	27.96	0.11	11.94	0.00	0.95	4.82	0.17	0.00	0.02	100.55	57.24
	BH167 A4 24	chad rim	54.95	0.02	27.47	0.11	10.81	0.00	1.10	5.16	0.48	0.00	0.01	100.10	52.18
	BH167 A4 22-24	average	54.66	0.05	27.83	0.12	11.57	0.00	1.02	4.92	0.27	0.01	0.04	100.49	55.59
	BH167 A4 36	rep	53.73	0.05	28.06	0.14	12.30	0.04	1.05	4.72	0.15	0.00	0.05	100.29	58.48
	BH167 A4 38	core	53.76	0.11	27.70	0.10	10.18	0.00	0.81	4.14	2.19	0.06	0.07	99.11	50.14
	BH167 A4 39	rimwards	55.83	0.11	27.29	0.11	10.88	0.03	0.79	5.37	0.18	0.00	0.05	100.64	52.28
	BH167 A4 40	rim	55.53	0.08	27.07	0.09	10.61	0.00	0.89	5.40	0.22	0.00	0.14	100.03	51.41
	BH167 A4 38-40	average	55.04	0.10	27.35	0.10	10.56	0.01	0.83	4.97	0.86	0.02	0.09	99.92	51.28
	BH167 A4 50	rim (fresh)	55.23	0.07	27.87	0.14	1.08	0.01	1.06	1.65	10.43	0.00	0.16	97.69	6.53
	BH167 A4 51	core	53.50	0.05	29.19	0.13	12.62	0.01	0.82	4.52	0.18	0.00	0.00	101.02	60.05
	BH167 A4 52	rim	56.50	0.07	27.22	0.06	10.19	0.05	0.81	5.70	0.22	0.03	0.09	100.92	49.04
	BH167 A4 51-52	average	55.00	0.06	28.20	0.09	11.41	0.03	0.82	5.11	0.20	0.01	0.04	100.97	54.55
	BH167 A4 60	rep	55.94	0.00	26.89	0.08	10.37	0.00	0.91	5.65	0.22	0.00	0.03	100.07	49.71
	BH167 A4 61	core	52.08	0.02	29.22	0.17	13.48	0.01	0.79	3.99	0.11	0.00	0.00	99.88	64.69
	BH167 A4 62	rimwards	54.99	0.01	27.63	0.10	11.35	0.00	0.86	5.18	0.19	0.00	0.04	100.36	54.16
	BH167 A4 63	rim	58.87	0.04	25.25	0.00	8.07	0.00	0.62	6.76	0.37	0.00	0.13	100.11	38.90
	BH167 A4 64	rim2	56.63	0.10	26.77	0.05	10.07	0.00	0.87	5.75	0.22	0.04	0.02	100.52	48.51
	BH167 A4 63-64	rim average	57.75	0.07	26.01	0.03	9.07	0.00	0.74	6.26	0.30	0.02	0.07	100.32	43.70
	BH167 A4 61-64	average (incl r757)	54.94	0.03	27.62	0.10	11.30	0.00	0.80	5.14	0.20	0.01	0.04	100.18	54.18
	BH167 A4 65	chad rep	54.06	0.05	27.79	0.13	11.94	0.00	1.11	4.88	0.17	0.00	0.09	100.22	56.95
	BH167 A4 66	core	56.03	0.00	26.63	0.07	10.13	0.00	0.67	5.65	0.24	0.01	0.01	99.43	49.07
	BH167 A4 67	rim	56.98	0.04	26.26	0.06	10.09	0.00	0.76	5.77	0.24	0.00	0.00	100.20	48.46
	BH167 A4 66-67	average	56.50	0.02	26.44	0.06	10.11	0.00	0.71	5.71	0.24	0.00	0.01	99.81	48.76
	BH167 A4 68	rim	58.56	0.06	25.17	0.02	8.08	0.04	0.63	6.77	0.34	0.04	0.08	99.79	38.95
	BH167 A4 68	rimward	56.68	0.03	26.73	0.08	10.20	0.00	0.71	5.75	0.22	0.05	0.14	100.60	48.83
	BH167 A4 68	rimward	55.2	0.07	27.30	0.08	11.1	0.00	0.8	5.32	0.20	0.00	0.0	100.1	53.0

			6				2		2				1	7	0
	BH167 A4 68	rimward	54.21	0.11	28.21	0.12	11.69	0.02	0.88	4.92	0.17	0.00	0.08	100.41	56.19
	BH167 A4 68	core	54.21	0.00	27.99	0.12	11.75	0.00	0.89	4.94	0.18	0.03	0.05	100.16	56.19
	BH167 A4 68	core	53.28	0.07	29.20	0.19	0.44	0.00	1.13	1.96	10.07	0.00	0.06	96.40	2.73
	BH167 A4 68	rimward	53.37	0.02	27.93	0.13	11.91	0.05	0.93	4.68	0.20	0.00	0.08	99.30	57.80
	BH167 A4 68	rimward	53.85	0.13	28.15	0.14	12.10	0.00	0.93	4.67	0.15	0.02	0.05	100.18	58.35
	BH167 A4 68	rimward	53.95	0.05	27.20	0.11	11.25	0.00	0.85	5.21	0.18	0.00	0.06	98.85	53.86
	BH167 A4 68	rim	55.74	0.09	26.77	0.07	10.44	0.04	0.76	5.59	0.22	0.00	0.05	99.76	50.17
	BH167 A4 68	x average	54.91	0.06	27.47	0.11	9.90	0.01	0.85	4.98	1.19	0.01	0.06	99.56	47.61
	BH167 A4 74	rep	49.51	0.02	30.80	0.23	0.21	0.04	0.79	0.30	11.55	0.00	0.27	93.72	1.43
	BH175 A1 83	rep	48.67	0.15	30.98	0.27	15.40	0.00	0.75	2.92	0.10	0.00	0.00	99.23	74.04
	BH175 A1 86	rep	48.92	0.03	30.78	0.26	14.97	0.00	0.84	3.11	0.08	0.01	0.04	99.03	72.36
	BH175 A1 89	ground (rep)	48.89	0.00	29.05	0.15	12.89	0.00	1.08	3.52	1.04	0.01	0.09	96.73	62.89
	BH175 A1 99	core	48.42	0.05	30.81	0.25	15.27	0.00	0.53	2.92	0.07	0.03	0.05	98.39	73.96
	BH175 A1 100	rim	43.56	0.01	30.21	0.16	18.31	0.01	0.77	1.76	0.46	0.02	0.00	95.29	83.01
	BH175 A1 99-100	average	45.99	0.03	30.51	0.21	16.79	0.00	0.65	2.34	0.27	0.02	0.02	96.84	78.48
	BH175 A1 103	core	46.42	0.00	32.85	0.18	17.50	0.00	0.53	1.67	0.05	0.02	0.02	99.24	85.00
	BH175 A1 103	rimwards	46.21	0.00	33.04	0.44	17.47	0.05	0.76	1.69	0.06	0.00	0.14	99.85	84.82
	BH175 A1 103	rimwards	46.79	0.07	33.36	0.18	17.69	0.00	0.52	1.60	0.07	0.00	0.07	100.35	85.57
	BH175 A1 103	rimwards	46.45	0.00	33.17	0.20	17.57	0.00	0.54	1.72	0.02	0.00	0.00	99.68	84.85
	BH175 A1 103	rimwards	47.02	0.01	32.98	0.37	17.37	0.00	0.70	1.60	0.03	0.00	0.01	100.08	85.56
	BH175 A1 103	rimwards	46.60	0.04	33.39	0.19	17.65	0.00	0.59	1.61	0.03	0.00	0.06	100.15	85.63
	BH175 A1 103	rimwards	49.30	0.01	31.66	0.24	15.94	0.00	0.54	2.56	0.06	0.00	0.04	100.33	77.27
	BH175 A1 103	rim	48.43	0.06	31.74	0.24	15.99	0.00	0.58	2.47	0.20	0.00	0.00	99.70	77.27
	BH175 A1 103	x average	47.15	0.02	32.77	0.26	17.15	0.01	0.59	1.86	0.06	0.00	0.04	99.92	83.25
	BH175 A1 104	core	46.02	0.04	33.17	0.18	17.86	0.00	0.54	1.55	0.04	0.05	0.07	99.51	86.15
	BH175 A1 104	rimwards	47.27	0.04	32.94	0.18	17.75	0.00	0.53	1.63	0.04	0.00	0.05	100.42	85.55
	BH175 A1 104	rimwards	45.38	0.00	32.13	0.92	16.95	0.00	1.20	1.51	0.09	0.02	0.04	98.22	85.58
	BH175 A1 104	rimwards	46.14	0.02	32.88	0.20	17.54	0.00	0.53	1.73	0.06	0.00	0.04	99.15	84.56
	BH175 A1 104	rimwards	46.79	0.01	33.19	0.21	17.61	0.00	0.51	1.73	0.05	0.03	0.00	100.12	84.62
	BH175 A1 104	rimwards	45.73	0.08	33.39	0.17	17.72	0.03	0.53	1.57	0.04	0.03	0.07	99.34	85.97
	BH175 A1 104	rimwards	46.32	0.01	33.33	0.19	17.50	0.00	0.56	1.67	0.03	0.00	0.05	99.64	85.12
	BH175 A1 104	rim	49.58	0.09	30.91	0.23	15.12	0.00	0.77	3.04	0.08	0.00	0.09	99.91	72.99
	BH175 A1 104	x average	46.65	0.04	32.74	0.28	17.26	0.00	0.64	1.80	0.05	0.01	0.05	99.54	83.82
	BH175 A1 105	core	39.88	0.00	29.46	0.17	19.73	0.00	0.57	0.34	2.77	0.00	0.02	92.94	83.47
	BH175 A1 106	rim	50.38	0.09	29.75	0.22	14.18	0.01	0.92	3.50	0.15	0.00	0.00	99.20	68.52
	BH175 A1 105-106	average	45.13	0.05	29.61	0.19	16.96	0.00	0.75	1.92	1.46	0.00	0.01	96.07	75.99
	BH175 A1 110	ground (rep)	51.30	0.08	30.20	0.26	0.33	0.03	0.97	0.14	11.71	0.00	0.09	95.10	2.25
	BH175 A1 117	rep	46.1	0.10	32.22	0.22	16.7	0.08	0.7	2.05	0.07	0.00	0.0	98.34	81.4

			3				0		1				7		6
	BH175 A1 118	ground (rep)	51.28	0.05	26.79	1.38	11.38	0.02	3.35	4.01	0.36	0.01	0.06	98.68	59.67
	BH175 A1 122	ground (rep)	54.98	0.10	26.76	0.06	10.14	0.00	0.99	5.44	0.46	0.03	0.10	99.05	49.35
	BH175 A1 128	rep	49.62	0.09	30.61	0.29	0.48	0.02	0.64	0.15	11.69	0.01	0.41	94.02	3.28
	BH175 A1 129	ground (rep)	49.55	0.02	29.11	0.16	14.33	0.00	1.20	3.33	0.32	0.02	0.04	98.07	69.10

Appendix G5 – SFDC sulphur isotope data

ZONE	SAMPLE ID	LITHOLOGY	DISTANCE FROM	$\delta^{34}S$(VCDT)	S (wt %)	Ni (ppm)	Cu (ppm)
			INTRUSIVE CONTACT (m)				
D	MH123A1	Wynniatt Fm	NA	7.41	0.17	16	12
	MH123B1	Gabbro	NA	2.98	0.077	132	189
	MH126A1	Gabbro	NA	4.54	0.078	110	166
	MH127A1	Wynniatt Fm	NA	11.47	0.30	b.d.l.	b.d.l.
	MH128A1	Gabbro	NA	2.74	0.091	125	161
C							
B	BH188A1	Wynniatt Fm	NA	19.55	0.18	9	b.d.l.
	BH193A1	Gabbro	NA	4.82	0.576	105	266
	BH195A1	Gabbro	NA	12.56	0.392	117	313
	BH196A1	Wynniat Fm	NA	12.74	0.27	b.d.l.	b.d.l.
	BH197A1	Gabbro	NA	8.24	0.244	78	178
E	BH366B1	Gabbro	-0.2	9.74	0.091	112	158
	BH366B1#2	Gabbro	-0.2	10.39	0.091	112	158
	BH366B1#3	Gabbro	-0.2	10.35	0.091	112	158
	BH371A1	Kilian Fm	1.8	16.96	0.13	15	8
	BH369A1	Kilian Fm	6.7	17.57	0.26	10	5
	BH368A1	Kilian Fm	-5.06	10.95	0.28	b.d.l.	b.d.l.
	BH367A1	Kilian Fm	12.45	17.15	0.43	7	9
	BH365A1	Kilian Fm	NA	24.06	0.92	6	27
	BH371A2	Kilian Fm	NA		0.27		
A	BH167A4	Gabbro	-22.7	8.86	0.076	88	204
	BH162A1	Gabbro	-13.9	5.03	0.070	121	162
	BH162A2	Gabbro	-4.9	8.00	0.074	96	179
	BH164A1	Kilian Fm	9.5	19.06	0.13	b.d.l.	7
	BH164A2	Kilain Fm	13.2	21.50	0.21	15	162
	BH166A1	Kilian Fm (evaps)	17	31.77	17.4	b.d.l.	11
	BH166A1#2	Kilian Fm (evaps)	17	31.92	17.4	b.d.l.	11
	BH166A2	Kilian Fm (evaps)	35	32.59	17.4	b.d.l.	b.d.l.
*b.d.l. = below detection limit							